When Galaxy Clusters Collide: the impact
of merger shocks on cluster gas and galaxy evolution

When Galaxy Clusters Collide: the impact of merger shocks on cluster gas and galaxy evolution

Proefschrift

door Andra Stroe
geboren te Constanța, Roemenië
in 1987

Promotiecommissie

Promotor:	Prof. dr. H. J. A. Röttgering	
Co-promotor:	Dr. David Sobral	
Overige leden:	Prof. dr. Annalisa Bonafede	(Hamburg Observatory)
	Dr. Jarle Brinchmann	
	Prof. dr. Marijn Franx	
	Prof. dr. Jelle Kaastra	
	Prof. dr. Koen Kuijken	
	Prof. dr. Tom Oosterloo	(ASTRON, Dwingeloo; Kapteyn Astronomical Institute)

In loving memory of my mother.
Thank you for being my best friend, my greatest
supporter and for always believing in me!

Contents

1

Introduction

1.1   Evolution and composition of the Universe

The 'Big Bang' theory proposes that the Universe started in a hot, dense state about 13.7 billion years ago (Planck Collaboration et al. 2015). Shortly after its birth (10^{-36} s), the Universe passed through 'inflation' (Guth 1981), a period of rapid expansion over a few orders of magnitude, when the Universe slowly cooled thus allowing the condensation of elementary particles, such as electrons, protons and neutrons. Between three and twenty minutes after the 'Big Bang', the temperature dropped to the point where hydrogen and helium nuclei could bind. Around $377,000$ years after the birth of the Universe, in the 'recombination' phase, the temperature dropped to the point where positively charged atoms were capable of capturing electrons to become neutral atoms and photons were now able to travel freely. We have observed the relic emission of the 'recombination' process as the Cosmic Microwave Background (CMB) radiation (Penzias & Wilson 1965).

In the currently adopted cosmological ΛCDM model, the Universe is a soup of different components. 'Normal' baryonic matter does not dominate, but currently only accounts for a little under 5 per cent of the content of the Universe (Planck Collaboration et al. 2015). Almost 27 per cent of the present Cosmos is dark matter, which does not emit any form of radiation. Dark matter was originally proposed by Zwicky (1933), who measured a velocity dispersion of the Coma cluster too large to be explained by the mass contained in the luminous matter. However, during the 'recombination' epoch, the Universe was dominated by dark matter, amounting to over 60 per cent.

The study of the CMB has revealed that the Universe on large scales is astonishingly uniform and isotropic. However, on smaller scales, inhomogeneities in the matter distribution left imprints in the CMB temperature (Mather et al. 1990; Smoot et al. 1992; Mather et al. 1994; Kovac et al. 2002). Under the influence of gravity, seed fluctuations in the the early Universe density field grew over the next 13 billion years to form structures hierarchically from small to large scales. In the gravitational potential wells created by the high densities of dark matter (White & Rees 1978), baryonic matter aggregates to form the first astronomical sources: Population III stars and quasars, followed by Population II and I stars which bound together to form galaxies. At the location of the highest primordial inhomogeneities, galaxies grouped together to form galaxy clusters and even larger superclusters connected in a cosmic web through low-density filaments. At the opposite pole, primordial negative peaks in the matter distribution resulted in the lowest density area which fill the space between galaxy clusters: voids (e.g. Peacock et al. 2001).

1.2 Galaxy clusters

Cluster of galaxies, located at the top of hierarchical structure formation, have masses of 10^{14-15} M$_\odot$ and contain hundreds of galaxies within a few Mpc^3 volume (Sarazin 1986, 2002).

Most of the mass in galaxy clusters is distributed in between the galaxies, in the form of dark matter and hot (10^{7-8} K), X-ray emitting plasma. The dense intra-cluster medium has a profound impact on the evolution of the cluster galaxies. Field star-forming spiral galaxies suffer a morphological transformation as they fall into a cluster environment, as the fraction of star-forming galaxies drops from void-like environments towards cluster cores (e.g. Dressler 1980; Goto et al. 2003). Ram pressure strips the gas fuelling star formation away from the host galaxy (Gunn & Gott 1972), while tidal forces truncate the halo and disk of infalling spiral galaxies or channel gas out of the host galaxy (Moore et al. 1996; Larson et al. 1980).

Clusters evolve through mergers, in the most energetic events after the 'Big Bang', releasing 10^{64} erg (40 orders of magnitude higher than an atomic bomb) on time scales of $1-2$ billion years (Hoeft et al. 2004). After two clusters pass through each other, dark matter and galaxies become separated from the cluster gas (e.g. Clowe et al. 2006; Dawson et al. 2012). This offers unique opportunities to study cosmological structure formation and the nature of dark matter. Part of the merger energy is dissipated through the intra-cluster medium (ICM) via turbulence and shocks. In this sense, cluster shocks are the largest particle accelerators in the Universe, 19 orders of magnitude larger than the Large Hadron Collider.

Enormous Mpc-wide, diffuse radio sources associated with the intra-cluster medium (ICM) are often found in merging galaxy clusters (e.g. reviews by Feretti et al. 2012; Brunetti & Jones 2014). Their spectral and polarisation properties indicate that they are synchrotron emission caused by relativistic electrons (cosmic rays) gyrating in a weak magnetic field ($1-10\ \mu$G).

Radio **relics** are arc-like patches of emission located at the periphery of clusters and are believed to be formed when relativistic particles are accelerated by low Mach number ($M = 1-5$) shocks produced at the merger of two massive clusters (Ensslin et al. 1998). Markevitch et al. (2005) propose the seed electrons are pre-accelerated, for example through past radio galaxy activity. The electrons, no matter if they are thermal or relativistic, are accelerated to a power-law energy distribution spectrum and emit over a broad radio range. Observations and simulations indicate that the shock also compresses and aligns the magnetic fields with the shock surface (e.g., Bonafede et al. 2009; Finoguenov et al. 2010; van Weeren et al. 2011a; Iapichino & Brüggen 2012). In terms of the cosmic evolution of radio relics, models predict for example that increasing merger rates at high redshift cause the fraction of clusters hosting relics to rise as well and that relics are hosted by the most massive clusters (Nuza et al. 2012).

Radio **halos** are diffuse emission that follows the X-ray ICM distribution, believed to form when particles are re-accelerated by turbulence injected by the cluster merger (Brunetti et al. 2001). Blasi & Colafrancesco (1999) propose that the emission comes from secondary electrons injected by proton-proton collisions (hadronic model).

Shocks and turbulence drive the evolution of clusters in the context of structure formation (Brunetti & Jones 2014). The study of clusters with diffuse radio emission can unveil particle acceleration in conditions which cannot be found in other astronomical contexts and cannot be reproduced on Earth (large scales, weak shocks, weak magnetic fields and low density). While the past decade has seen significant progress in our understanding of merging clusters, due to the lack of suitable instruments to detect relics and haloes, most research still relies on

a few individual, low-redshift sources observed in one or two radio frequency bands. With a mainly radio and X-ray focused view of merging clusters, the nature and evolution of the cluster star-forming and AGN galaxies remains unexplored. Unanswered questions in the field include:

Cosmic evolution of diffuse cluster emission: Are there massive, merging clusters hosting diffuse radio emission at high-redshift? What is their dynamical history? What is the cosmic evolution of diffuse sources?

Nature and physics of diffuse cluster radio emission: How are cosmic rays injected and accelerated to form relics and halos? How do Mach numbers and speeds of radio shocks relate to cluster mass, temperature, redshift? What is the magnetic field topology at cluster outskirts? How do electrons interact with the magnetic field such that they lose their energy?

Galaxy evolution in merging clusters with shocks: Do the merger, the shocks and the turbulence drive the evolution of cluster galaxies?

1.3 This thesis

This PhD thesis combines complementary broad-band radio data, optical imaging, spectroscopy and spectral modelling, to study merging clusters hosting radio relics. The thesis focuses on two massive merging clusters, nicknamed the 'Sausage' (van Weeren et al. 2010) and 'Toothbrush' (van Weeren et al. 2012b), which host Mpc-wide double-relics, with spectacular, regular morphologies. The clusters appear to have relatively simple merger histories, resulting from binary mergers of two equal mass systems in the plane of the sky. This thesis aims to obtain a complete picture of these two clusters focusing on the way shocks interact with electrons and magnetic fields to produce diffuse emission and on the the way the merger of massive systems affects star formation in cluster galaxies.

Chapter 2 deals with the influence of the cluster merger history on the radio galaxies and on particle acceleration in the context of diffuse radio emission. The analysis is based on the very wide range radio data of the 'Sausage' cluster from the Giant Metrewave Radio Telescope and the Westerbork Synthesis Radio Telescope ($150 - 2300$ MHz. Through spectral index, spectral curvature and radio color-color techniques, we show that the twin radio relics in the 'Sausage' cluster have most likely been accelerated by symmetrical merger shocks produced at the core-passage of two sub-clusters that are traced by tailed radio galaxies. The analysis indicates that the electrons are accelerated by the shock front, while their pitch angle to the magnetic field is continuously isotropised.

Chapter 3 tackles the issue of mismatching radio and X-ray measurements of the shock Mach number in radio relics. We perform the first spatially-resolved spectral modelling of a radio relic and alleviated the resolution effects which previously affected the radio measurement of the Mach number in the 'Sausage' relic and brought it in agreement with the X-ray. We find a systematic increase in spectral age from the northern side of the 'Sausage' relic into the downstream area. This indicates that the shock is moving northwards at about 2500 km s^{-1}and represents the first direct test that the steepening of the radio spectrum is a consequence of electrons losing energy through synchrotron emission and inverse Compton interactions. We show that there are other important effects (re-acceleration by turbulence and line-of-sight mixing) which have not been previously considered in the formation mechanism of relics.

Chapters 4 and 5 present the highest radio frequency measurements of diffuse emission to date, at 16 and 30 GHz, made possible with the Arcminute Microkelvin Imager and Combined Array for Research in Millimeter-wave Astronomy. Such measurements are crucial for quantifying the interaction of the electrons with the magnetic field and distinguishing between various models for the origin of the synchrotron emitting electrons. The high-frequency data indicates a trend of steepening in the integrated radio spectrum of the 'Sausage' relic, challenging the currently-accepted view of radio relic formation.

Chapters 6, 7 and 8 present the Hα mapping of the 'Sausage' and 'Toothbrush' clusters, which serve as the first direct proof that the shock affects star formation in cluster galaxies. We find numerous Hα emitting galaxies in close proximity to the radio relics in the 'Sausage' cluster, which are extremely massive, metal-rich and star-forming. There are no such examples in the 'Toothbrush' cluster. We interpreted these results in the context of the different timescales of the clusters, taking into account simulations which indicate that the 'Toothbrush' cluster is ~ 1 Gyr older than the 'Sausage'. We propose that the passing of the shock momentarily excites star-formation, accelerating the transformation of gas-rich spirals into ellipticals.

In **Chapter 9**, we use Westerbork Synthesis Radio Telescope HI observations of the 'Sausage' cluster to investigate the effect of the merger and the shocks on the gas reservoirs fuelling star formation in cluster galaxies. Contrary to previous research which finds that galaxies become increasingly HI deficient towards cluster cores, we find that the star-forming galaxies in the 'Sausage' cluster have as much HI as their field counterparts. We find evidence of vigorous supernova remnant emission in cluster galaxies, which indicates they have been forming stars for at least 100 Myr.

In **Chapter 10**, we carry out the largest survey of star forming galaxies at redshift $z \sim 0.2$. We build an Hα luminosity function which overcomes cosmic variance and samples the brightest and rarest galaxies. Luminous, strongly star-forming galaxies are more clustered than those weakly star-forming. Even though there is significant cosmic variance within our survey, we find that overdensities, such as the 'Sausage' cluster are extremely rare.

1.4   Future prospects

Detailed studies of individual sources can provide crucial insight into the physics of particles and galaxies in clusters at particular phases in their evolution. However, in order to trace the evolution of shocks and cosmic ray particles up to the epoch when the first massive clusters formed, we require a sample of clusters hosting radio relics and halos, with a wide spread in mass and redshift. Excellent multi-wavelength data will enable us to discover the required sources and study their properties in detail. With the recent availability of the first high-z massive cluster samples (e.g. Planck Collaboration et al. 2014) it has become clear that this next important step can now be taken.

Targeted observations of clusters recently discovered by the Planck mission with telescopes of unprecedented sensitivity over the entire radio spectrum (30 MHz $-$16 GHz, Low Frequency Array, Very Large Array, Giant Metrewave Radio Telescope, Arcminute Microkelvin Imager) will enable the detection of diffuse radio emission at the highest redshifts. With samples of clusters up to $z \sim 1$, evolution models of diffuse emission populations can be constrained.

By applying spectral modelling techniques to a sample of diffuse radio sources using wide-band radio data, we can obtain a consistent set of shock parameters (Mach number M, shock speed) and test whether the spatial distribution of shock strengths is consistent with hydrodynamical simulations. Simulations predict that strong shocks ($M > 3$) in clusters are rare, but low-Mach number shocks are ubiquitous (e,g, Pfrommer et al. 2006). Particle acceleration at high Mach number shocks ($M > 100$) is well understood from studies of supernova remnants. Theory predicts that low-Mach number shocks ($M < 5$), such as those in clusters are extremely inefficient at accelerating particles from the thermal pool and cannot account for the observed relic emission (see review by Brunetti & Jones 2014). From the spectrum and morphology of the relics we will be able to pinpoint the nature of the ICM electrons: pre-accelerated, rather than thermal, electrons originating from radio jets would alleviate the injection efficiency problem. Turbulent re-acceleration in the downstream area of the shock could also explain the observed emission. The re-acceleration model predicts ultra steep spectrum halos, which have yet to be detected because they are very faint in the typical frequency ranges explored. If this model is correct, deep, low-frequency data will enable the discovery of halos with steep spectra. The combination of radio and X-ray data breaks degeneracies due to magnetic field changes and adiabatic gains/losses to clearly measure the intrinsic spectral shape of the diffuse emission and help discriminate between formation models of relics and halos. By studying the filamentary morphology and radio polarization properties of the diffuse emission, we can test whether the magnetic field is constant, aligned, turbulent or intermittent. Future telescopes such as Astro-H will provide the first high-resolution X-ray spectral mapping of clusters, directly measuring bulk and turbulent motions in the ICM, which in comparison with radio data will provide key insights on the acceleration processes in radio halos.

By using the emission lines as a well-calibrated, sensitive indicator of recent star formation, we will unveil for the first time the role of the merger, turbulence and shocks in suppressing or enhancing star formation in cluster galaxies. With a proper sample of radio relic and halo clusters, we will be able to test whether the evolutionary path of star-forming galaxies is a function of host cluster mass, age, merger state and dynamical history. By following up the samples of star-forming galaxies with spectroscopy (e.g. optical and near-infrared multi-object spectroscopy), we will be able to determine the power source of the emission. From the metallicity of the HII regions, we can determine whether the line emission is coming from accretion of matter onto the super-massive black holes at galaxy nuclei or it is purely generated by star-formation. Integral field unit data will reveal any preferential alignment in the 3D distribution of gas. Could the gas be stripped or compressed at all scales, as expected from shock fronts, or does that only occur at the outer regions of the galaxy, indicative of small-scale motions induced by intra-cluster medium turbulence? High resolution Hubble and in the future James Webb Space Telescope imaging will clearly indicate the presence of star-forming tails, knots and filaments in the galaxies infalling into the cluster and in those that recently interacted with the shock front. By comparing these observations with simulations which predict that after a shock passes through a gas-rich galaxy, significant star formation occurs in the galactic disk only at radii where the gas will be stripped in due course and in knots throughout stripped tails (Roediger et al. 2014).

By comparing Hα measurements to Atacama Large Millimeter/sub-millimeter Array and Herschel data which trace dust-obscured SF over longer timescales (100 Myr), we can test

whether the number of dusty star-forming galaxies increases from low to high densities and from relaxed to merging clusters or the AGN activity and/or quenching rate is higher in denser, more disturbed regions. With new-generation sub-mm/mm facilities such as ALMA, we will be able to perform in-depth studies of the fuelling source for future SF and AGN episodes. CO rotational transitions are for example sensitive to dense and thermally excited gas in the central starburst/AGN regions, as well as the overall low-density sub-thermally excited molecular gas distribution. The radio jets coming from the galaxy nucleus can expel large amounts of cold gas, which is the raw ingredient for future formation of stars, but could also increase turbulence and lead to instabilities which induce SF. Does the merger shock induce outflows that will eventually lead to a shut-down of SF in a few hundred million years? Ultimately, we will be able to test the prediction that cluster shocks and turbulence compress the gas within galaxies, which then collapses and cools to form stars, dramatically changing the fates of galaxies within clusters.

2

Discovery of spectral curvature in the shock downstream region: CIZA J2242.8+5301

Giant cluster radio relics are thought to form at shock fronts in the course of collisions between galaxy clusters. Via processes that are still poorly understood, these shocks accelerate or re-accelerate cosmic-ray electrons and might amplify magnetic fields. The best object to study this phenomenon is the galaxy cluster CIZA J2242.8+5301 as it shows the most undisturbed relic. By means of Giant Metrewave Radio Telescope (GMRT) and Westerbork Synthesis Radio Telescope (WSRT) data at seven frequencies spanning from 153 MHz to 2272 MHz, we study the synchrotron emission in this cluster. We aim at distinguishing between theoretical injection and acceleration models proposed for the formation of radio relics. We also study the head-tail radio sources to reveal the interplay between the merger and the cluster galaxies. We produced spectral index, curvature maps and radio colour-colour plots and compared our data with predictions from models. We present one of the deepest 153 MHz maps of a cluster ever produced, reaching a noise level of 1.5 mJy beam^{-1}. We derive integrated spectra for four relics in the cluster, discovering extremely steep spectrum diffuse emission concentrated in multiple patches. We find a possible radio phoenix embedded in the relic to the south of the cluster. The spectral index of the northern relic retains signs of steepening from the front towards the back of the shock also at the radio frequencies below 600 MHz. The spectral curvature in the same relic also increases in the downstream area. The data is consistent with the Komissarov-Gubanov injection models, meaning that the emission we observe is produced by a single burst of spectrally-aged accelerated radio electrons.

2.1 Introduction

Galaxy clusters, the most massive gravitationally-bound objects in the Universe, have most of their baryonic mass in the form of hot intra-cluster gas visible in the X-rays. In the context of hierarchical structure formation, clusters mainly grow by mergers with other clusters and galaxy groups, events which release into the ICM enormous amounts of energy up to the order of 10^{64} erg on time scales of 1–2 Gyr (e.g., Sarazin 2002). In these extreme environments, radio emission can be found in the form of disturbed radio galaxies, relics and haloes.

The intra-cluster medium (ICM) interacts with the radio galaxies travelling at high speeds by shaping their radio jets into a head-tail morphology (Miley et al. 1972). A spectral index gradient across the tail is expected as the electrons in the ram pressure stripped lobes lose energy via synchrotron emission (O'Dea et al. 1987).

Haloes are centrally-located Mpc-wide diffuse, unpolarised, steep-spectrum objects, that follow the spatial distribution of the ICM as seen in the X-ray. To explain their origin, Brunetti et al. (2001) and Petrosian (2001) have proposed a turbulent re-acceleration mechanism, where cluster shocks induce turbulence, which in turn re-accelerates fossil relativistic particles. Other studies propose that the emission comes from secondary electrons injected by proton-proton collisions (e.g., Blasi & Colafrancesco 1999; Dolag & Ensslin 2000).

The main focus of this paper are relics, extended, Mpc-wide, diffuse, polarised radio emission in the form of arc-like, filamentary structures at the periphery of merging clusters. Their study can unravel not only how mergers affect structure formation and the evolution of clusters, but also detailed physics of the ICM and particle acceleration mechanisms in a cosmic framework. The origin of Mpc-scale relic emission has been debated, but observations suggest they are exclusively found in merging clusters with disturbed X-ray morphology, displaced X-ray peak from the galaxy distribution (e.g., Ferrari et al. 2008; Feretti et al. 2012). Ensslin et al. (1998) suggested that the merger produces cluster wide shock waves that travel through the ICM and accelerate thermal particles through the diffusive shock acceleration mechanism (DSA; e.g., Drury 1983). Another mechanism that has been proposed is shock re-acceleration of relativistic fossil electrons (Markevitch et al. 2005), which is similar to DSA, but instead of accelerating particles from the thermal pool, it assumes pre-accelerated mildly relativistic electrons that originate from, e.g., past radio galaxy activity. Both these models predict a connection between the injection and integrated spectral index and increasing spectral index and curvature into the post shock area. From an observational point of view, acceleration and re-acceleration are probably indistinguishable since the resulting spectra are similar (Markevitch et al. 2005; Giacintucci et al. 2008). From an observational point of view, relics are permeated by μG-level magnetic fields and emit synchrotron radiation with a spectral index between -0.8 and -1.6, ($F_\nu \propto \nu^\alpha$) and curved radio spectra due to synchrotron and inverse Compton losses (e.g., Ferrari et al. 2008; Feretti et al. 2012). Models suggest that the turbulence injected by the travelling shock in the downstream area produces these magnetic fields, which are then amplified through shock compression. Simulations by Iapichino & Brüggen (2012) predict strong magnetic fields aligned with the shock surface of the order of 6 μG at $0.5R_{vir}$, which are in agreement with observations (e.g., Bonafede et al. 2009; Finoguenov et al. 2010; van Weeren et al. 2011a). The electrons are accelerated to an initial power-law energy distribution spectrum. They emit at low radio frequencies and their emission spectrum is directly connected to the shock parameters, such as the Mach number. Synchrotron and inverse Compton

losses affect the high energy electrons more than the low energy ones. For an initial power-law distribution of electron energies spectral ageing causes a cutoff at the high frequency part of the emission spectrum. At lower frequencies the spectrum remains a power-law (Rybicki & Lightman 1979). The shape of the high-frequency fall-off is determined by physical processes such as the energy injection to the electrons and the pitch angle to the magnetic field. Both the Kardashev-Pacholczyk (KP; Kardashev 1962; Pacholczyk 1970) and the Jaffe-Perola (JP; Jaffe & Perola 1973) models assume a single-shot particle injection. The former considers the pitch angle to be constant in time. This leads to a power law fall-off with index $4/3\alpha_{\text{inj}} - 1$, where α_{inj} is the injection index. By contrast, the latter assumes a continuous isotropisation of the angle on timescales much shorter than the the time after which the radio emission diminishes significantly $(10 - 100$ Myr$)$. This leads to a faster, exponential fall-off. More complicated models include the continuous injection model (CI; Pacholczyk 1970), where fresh electrons are steadily injected and the Komissarov-Gubanov model (KGJP; Komissarov & Gubanov 1994) which extends the JP model to include a finite period of freshly supplied electrons.

To date, only ~50 examples of relic emission are known (e.g., Nuza et al. 2012; Feretti et al. 2012). Roughly ten of these systems contain two relics symmetrically positioned with respect to the cluster centre, e.g. A1240 and A2345 (Bonafede et al. 2009), A3376 (Bagchi et al. 2006), A3667 (Röttgering et al. 1997), PLCKG287.0 (Bagchi et al. 2011), ZwCl 2341.1+0000 (van Weeren et al. 2009), ZwCl 0008+52 (van Weeren et al. 2011a), MACS J1752.0+4440 (van Weeren et al. 2012a; Bonafede et al. 2012), RXC J1314.4-2515 (Venturi et al. 2007), 0217+70 (Brown et al. 2011). These are likely produced as a result of a major merger between two clusters of similar mass (e.g., Roettiger et al. 1999; van Weeren et al. 2011b).

CIZA J2242.8+5301 (from here on, C2242) is an extraordinary example of a merging cluster hosting a Mpc-wide double relics (van Weeren et al. 2010). At a redshift of $z = 0.1921$, it is a luminous X-ray cluster with $L_X = 6.8 \times 10^{44}$ erg s^{-1}, measured between 0.1 and 2.4 keV (Kocevski et al. 2007), and is marked by signatures of a major merger event. Analysis of recent XMM-Newton imaging by Ogrean et al. (2013a) confirm the merging nature of the cluster with X-ray morphology elongated along the north-south direction, significant substructure and hints for a shock front at the location of the relics. Because of the limited sensitivity in the X-rays, they are unable to to detect a joint density and temperature jump. Akamatsu & Kawahara (2013), via Suzaku data, were able to detect an X-ray density jump at the location of the northern relic, consistent with a Mach number $M = 3.15 \pm 0.52^{+0.40}_{-1.20}$. The two relics are located at 1.3 Mpc from the cluster centre. The northern relic (RN) is 1.7 Mpc across and very narrow (55 kpc). The spectral index (between 2272 MHz and 608 MHz) varies between -0.6 to -2.0 across the relic. This observed gradient towards the centre of the cluster is believed to be due to the spectral ageing of electrons. A Mach number M $= 4.6^{+1.3}_{-0.9}$ can be derived from the spectral index information (Landau & Lifshitz 1959; Sarazin 2002). The relic has been observed to be highly polarised up to 60%. Using the relationship between the width of the synchrotron emitting region, the characteristic time scale due to spectral ageing and the magnetic field, B was derived to lie between 5 and 7 μG (van Weeren et al. 2010). The southern relic (RS) is fainter and disturbed and is connected to the northern relic by a radio halo. van Weeren et al. (2011b) carried out hydrodynamical simulations of a binary cluster merger and varied the mass ratios, impact parameter, viewing angle etc., as to best fit the observed parameters of C2242. They concluded that the relics are seen close to edge-

Table 2.1: WSRT observations

Wavelength	24.5 cm	21.5 cm	17.5 cm	13.2 cm
Frequency range	1170-1289 MHz	1303-1460 MHz	1642-1780 MHz	2200-2344 MHz
Observation dates	Nov 17, 2009	Aug 30, Sept 4, 9, 14, 2009	Oct. 24, 2009	Sept 9, 2009
Integration time	60 sec	60, 30, 60, 60 sec	60 sec	60 sec
Total on-source time	11h 37min	36h 03min	11h 44min	11h 58min
Usable channels per IF	56	56	56	56
Usable bandwidth per IF	17.5 MHz	17.5 MHz	17.5 MHz	17.5 MHz
Channel width	312.5 kHz	312.5 kHz	312.5 kHz	312.5 kHz
Number of IFs	8	8	8	8
Polarisation	XX, YY, XY, YX	XX, YY, XY, YX	XX, YY, XY, YX	XX, YY, XY, YX

on ($i \lesssim 10°$) and that C2242 underwent a binary merger ~1 Gyr ago, with a mass ratio of the two components between 1.5:1 and 2.5:1. The above mentioned properties of the relic provide strong evidence for shock-acceleration in galaxy cluster shocks (van Weeren et al. 2010). Kang et al. (2012) performed time-dependent DSA simulations and concluded that the observational properties of C2242 can be accounted for with both a shock with Mach number $M = 4.5$ accelerating thermal electrons and a weaker shock of $M = 2.0$ with a relativistic particle pool.

In this paper we aim at distinguishing between theoretical injection models such as KP, JP and CI. Another process we investigate is the (re-)acceleration of electrons emitting at long radio wavelengths with the goal to discriminate between shock acceleration and other proposed relic formation mechanisms such as adiabatic compression (Ensslin & Gopal-Krishna 2001). We also study the cluster head-tail radio sources to reveal the interplay between the merger and the cluster galaxies. We therefore carry out a detailed radio analysis of C2242 using the Westerbork Synthesis Radio Telescope (WSRT) and the Giant Metrewave Radio Telescope (GMRT). C2242's relatively high radio surface brightness and large size, make it the ideal cluster for this analysis as the quality of the spectral index and curvature fits depends directly on the dynamic range, resolution and sensitivity of the radio maps employed. We present deep, high-resolution radio maps and the first integrated spectra, spectral index and curvature maps of four relics in C2242 to cover a frequency range of almost two orders of magnitude.

The layout of the paper is as follows: in Sect. 2.2 we give an overview of the radio observations and the data reduction, in Sect. 2.3 we present radio maps and a spectral index and curvature analysis, in Sect. 2.4 we discuss the implications for different injection and re-acceleration mechanisms. Concluding remarks can be found in Sect. 2.5. A flat, ΛCDM cosmology with $H_0 = 70.5$ km s^{-1} Mpc^{-1}, matter density $\Omega_M = 0.27$ and dark energy density $\Omega_\Lambda = 0.73$ is assumed (Dunkley et al. 2009). At the redshift of the cluster 1 arcmin corresponds to 0.191 Mpc. All images are in the J2000 coordinate system.

2.2 Observations & Data Reduction

In this section, we present the calibration and imaging steps performed on the WSRT and GMRT datasets.

Table 2.2: WSRT image parameters

Wavelength	24.5 cm	21.5 cm	17.5 cm	13.2 cm
Beam size	$22.4'' \times 17.1''$	$20.9'' \times 15.8''$	$16.0'' \times 13.1''$	$12.4'' \times 10.0''$
RMS noise (σ_{RMS})	51 μJy beam^{-1}	43 μJy beam^{-1}	34 μJy beam^{-1}	41 μJy beam^{-1}
Dynamic range	~4600	~3850	~4450	~3250
Mode	mfs*	mfs	mfs	mfs
Weighting	Briggs	Briggs	Briggs	Briggs
Robust	0.5	0.5	0.5	0.5

* multi-frequency synthesis

2.2.1 WSRT observations

C2242 was observed with WSRT at four different frequencies (1221 MHz, 1382 MHz, 1714 MHz and 2272 MHz) in August - November 2009. Eight frequency bands of 20.0 MHz bandwidth and 64 channels were centred around each of the frequencies. The observational details can be found in Table 2.1.

We used the Astronomical Image Processing System (AIPS)[1] and the Common Astronomy Software Applications (CASA)[2] package to reduce the data. Data for each of the four frequencies were independently flagged and calibrated. We set the fluxes of the calibrators 3C 286 and 3C 147 according to the Perley & Taylor (1999) extension to the Baars et al. (1977) scale. Initial phase solutions were obtained for the centre of each IF and were subsequently used to compute delay phase corrections. Twelve edge channels were excluded due to bandpass roll-off. The bandpass and phase solutions derived for the usable range of channels were transferred to C2242.

The science target data were split and all the IFs belonging to the same frequency setup (see Table 2.1) were combined for imaging (for imaging parameters, see Table 2.2). We reached dynamic ranges of above 3000 measured as the ratio between the peak in the map and the RMS noise. We then performed three rounds of phase only self-calibration and one round of phase and amplitude self-calibration.

The final image was produced using "Briggs" weighting (robust set to 0.5, Briggs 1995). The images were corrected for primary beam attenuation[3]:

$$A(r) = \cos^6(cvr) \tag{2.1}$$

where constant $c = 68$, r is the distance from the pointing center in degrees and v is the observing frequency in GHz. We adopt am uncertainty of 10% in the overall flux scale (e.g., Schoenmakers et al. 1998; Rengelink et al. 1997), which includes errors such as imperfect calibration, positional errors and flux calibration errors for different observations.

2.2.2 GMRT observations

153 MHz Observations

The target C2242 was observed with the GMRT at 153 MHz on Nov 2, 2010 during a single 8.5 hour daytime observing session, recording visibilities over an 8.5 MHz bandwidth. C2242 was observed in scans of ~1 hour, interleaved with 3 minute scans on phase calibrator J2148+611. The observation schedule also included initial and final scans on flux calibrators 3C 286 and 3C 48, respectively.

Data reduction was performed also making use of the Source Peeling and Atmospheric Modelling (SPAM) package (Intema et al. 2009), a Python-based extension to AIPS (Greisen 2003) including direction-dependent (mainly ionospheric) calibration and imaging. 3C 48 was used as the single flux and bandpass calibrator, adopting a total flux of 63.4 Jy. The bandpass filter edges and channels with strong RFI were flagged, yielding an effective bandwidth of 5.5 MHz. 3C 48 was also used to determine the phase offsets between polarisations, and for

---

[1]http://aips.nrao.edu/

[2]http://casa.nrao.edu/

[3]According to the WSRT Guide to observations

Table 2.3: GMRT observations

Frequency range	150-156 MHz	309-324 MHz	323-328 MHz	593-623 MHz
Observation dates	Nov 2, 2010	Jul 2, 2010	Jul 3, 2010	Nov 20, 2009
Integration time	4 sec	8 sec	8 sec	8 sec
Total on-source time	6h 15min	4h 35min	4h 35min	8h 11min
Total bandwidth	8.5 MHz	16.6 MHz	16.6 MHz	32 MHz
Channels	128	256	256	512
Usable bandwidth	5.5 MHz	14.7 MHz	14.7 MHz	30 MHz
Usable channels	88	226	226	480
Channel width	62.5 kHz	62.5 kHz	62.5 kHz	62.5 kHz
Polarisation	RR,LL	RR,LL,RL,LR	RR,LL,RL,LR	RR,LL,RL,LR

Table 2.4: GMRT image parameters

Frequency	153 MHz	323 MHz	608 MHz
Beam size	$28.4'' \times 23.6''$	$12.3'' \times 11.3''$	$6.9'' \times 5.1''$
σ_{RMS}	1.5 mJy beam^{-1}	0.2 mJy beam^{-1}	24 μJy beam^{-1}
Dyn. range	~650	~1180	~2750
Mode	mfs	mfs	mfs
Weighting	Briggs	Briggs	Briggs
Robust	0.5	0.5	0.5
Grid mode	widefield	widefield	widefield
w projection	150	150	150

estimating the instrumental, antenna-based phase offsets (needed for ionospheric calibration; see Intema et al. 2009).

All calibrations derived from 3C 48 were transferred to the target data. After clipping excessive visibility amplitudes and subtracting low-level RFI (Athreya 2009), visibilities were converted to Stokes I and averaged per 6 channels for more efficient processing, while keeping enough spectral resolution to suppress bandwidth smearing. The target was initially phase-calibrated against a point source model derived from the NVSS, VLSS and WENSS surveys (Condon et al. 1998; Cohen et al. 2007; Rengelink et al. 1997). This gives a starting model for the calibration and ensures fast convergence. This was followed by rounds of (phase-only) self-calibration and wide-field imaging. Bright outlier sources were included in the imaging. Additional flagging of bad data was performed in between rounds.

After a last round of (amplitude & phase) self-calibration and imaging, we performed two additional rounds of SPAM ionospheric calibration and imaging. This consists of "peeling" bright sources within the field-of-view, fitting a time and spatially varying ionosphere model to the resulting gain phase solutions, and applying this model during imaging. A peeling cycle consists of obtaining directional dependent gain solutions for the "peeled" source, which is now properly modelled and can be completely removed from the uv data (e.g., Noordam 2004). We peeled 16 sources in the first round and 17 sources in the second round of SPAM.
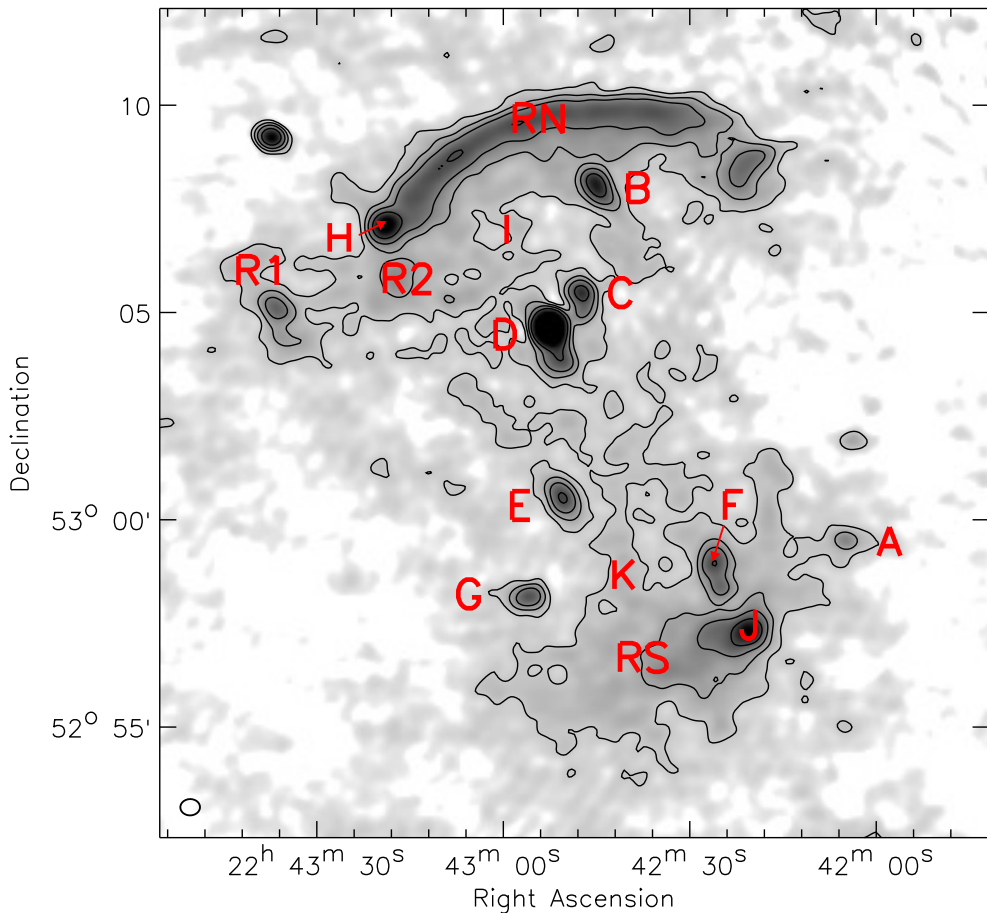
Figure 2.1: GMRT 153 MHz image with contours drawn at $[3, 8, 16, 32] \times \sigma_{RMS}$. The beam size at $28.41'' \times 23.60''$ is shown in the bottom left corner of the image.

This procedure removed a substantial fraction of the remaining residual artefacts around point sources after self-calibration. We imaged the data using the polyhedron method (Perley 1989; Cornwell & Perley 1992) to minimise effects of non-coplanar baselines. The final image (see Table 2.4), made using robust 0.5 weighting (Briggs 1995), has a central background RMS noise level of 1.5 mJy beam^{-1}. The image was corrected for primary beam attenuation[4]:

$$A(x) = 1 + \frac{-3.397}{10^3}x^2 + \frac{47.192}{10^7}x^4 + \frac{-30.931}{10^{10}}x^6 + \frac{7.803}{10^{13}}x^8 , \qquad (2.2)$$

with x the distance from the pointing centre in arcmin times the observing frequency in GHz.

We adopt an uncertainty in the calibration of the absolute flux-scale for GMRT of 10% (Chandra et al. 2004).

---

[4]According to the GMRT User's manual

316 MHz and 330 MHz Observations

C2242 was observed with the GMRT for a total of 15 hours on two subsequent nights, July 2 and July 3, 2010. Data were recorded in two slightly overlapping spectral windows centred at frequencies 316 MHz and 330 MHz. The 16.6 MHz bandwidth per spectral window was sampled in 256 channels in full polarisation mode. The observations are summarised in Table 2.3. 3C 48 and 3C 147 were used as flux calibrators and 2355+498 as phase calibrator.

We used CASA to reduce the data. The two spectral windows were independently flagged and calibrated. The first integration of each scan was flagged to account for system instabilities when moving between set-ups. On both nights there were malfunctioning antennas, resulting in 26 working antennas during the entire two nights of observations. The RFI in the calibrator data was manually removed. We set the fluxes of the primary calibrators according to the (Perley & Taylor 1999) scale. Initial phase solutions were obtained for a small number of channels free of RFI close to the centre of each bandpass, which were used to compute delay phase corrections. Thirty edge channels were not considered in the calibration due to bandpass roll-off, resulting in 14.7 MHz of effective bandwidth per spectral window. The bandpass and phase solutions derived for the full usable range of channels were transferred to C2242.

The science target data were split and averaged down to 56 channels per spectral window, which were afterwards combined for imaging (for imaging parameters, see Table 2.4). The egregious RFI was visually identified and excised. We then performed three rounds of phase only self-calibration and one round of phase and amplitude self-calibration.

A CLEANed image was produced from the flagged dataset, whose dynamic range was limited by the presence of very bright sources increasing the RMS in the field. The brightest sources were successively removed through the "peeling" method. The final image was produced using "Briggs" weighting (robust set to 0.5, Briggs 1995). Reasons for not reaching the thermal RMS include: residual RFI and calibration errors (Bhatnagar et al. 2008). The residual patterns around the positions of bright sources are caused by incomplete peeling due to imperfect models of the sources, pointing errors and non-circularity of the antenna beam pattern.

608 MHz observations

The cluster was observed at 608 MHz for over 8 hours on Nov 20, 2009 in full polarisation (see Table 2.3). 3C 286 and 3C 48 served as flux calibrators, while phase calibrator 2148+611 was observed every hour.

CASA and AIPS were used to reduce the data in a similar fashion as presented in Sect. 2.2.2. After peeling the brightest sources, we performed an additional step in simply subtracting from the uv data the contaminating sources towards the edges of the field. We then imaged the central part of the FOV with the parameters given in Table 2.4.

2.3 Results

In this section we present radio continuum maps, spectral index, spectral curvature and colour-colour plots.

Figure 2.2: GMRT 323 MHz image with overlaid contours at $[4, 8, 16, 32] \times \sigma_{RMS}$. The beam size at $12.26'' \times 11.27''$ is shown in the bottom left corner of the image. Added source labelling.

2.3.1 Radio continuum maps

van Weeren et al. (2010) presented a 1400 MHz image in their paper focussing on a discussion of two counter relics, pointing out the northern relic's narrow and elongated structure. Here, we discuss in detail the morphology of all the compact and diffuse radio sources in the field.

Relics

All of the radio maps present the two counter relics and two smaller areas of diffuse emission, plus a variety of radio sources (for labelling see Figs. 2.1 and 2.4). The sizes reported in the following text are measurements in the high-resolution 608 MHz image within $5\sigma_{RMS}$ levels and represent true sizes convolved with the synthesised beam at this particular frequency.

The northern relic (labelled RN), maintains its arc-like shape and impressive size (1.8 Mpc $\times$ 150 kpc) throughout more than one order of magnitude in frequency. The thickness of the

Figure 2.3: GMRT 608 MHz image with contour lines drawn at $[4, 8, 16, 32] \times \sigma_{\text{RMS}}$. The beam size is $6.87'' \times 5.12''$ and shown at the bottom left corner of the image.

relic in the north-south direction increases with decreasing frequency ($\sim$160 kpc), as expected for a source with a strong spectral index gradient across it. The tightness of the contours reveals the northern boundary to be extremely well defined and sharp (see Fig. 2.3). Towards the inner edge, the surface brightness drops smoothly and slowly. Towards the east of RN, source H has a much higher surface brightness than the relic at all frequencies and presents a typical tailed radio source morphology towards the north.

The southern relic (RS) does not posses the same well defined structure as RN, but generally follows a bow geometry. Its projected size is 590 kpc $\times$ 310 kpc. In the 2272 MHz map (Fig. 2.7) the relic is very faint, because of its steep spectrum. The WSRT and 608 MHz maps reveal a tail of fainter, diffuse emission extending towards the south that is not visible in the 153 and 323 MHz images (Figs. 2.1 and 2.2). At first glance this is puzzling if we do not take into consideration the noise levels of the GMRT measurements, which are an order of magnitude higher than the other maps. The spectrum of this extension should be steeper than $\alpha = -1.4$ for it to be detected in the low frequency maps.
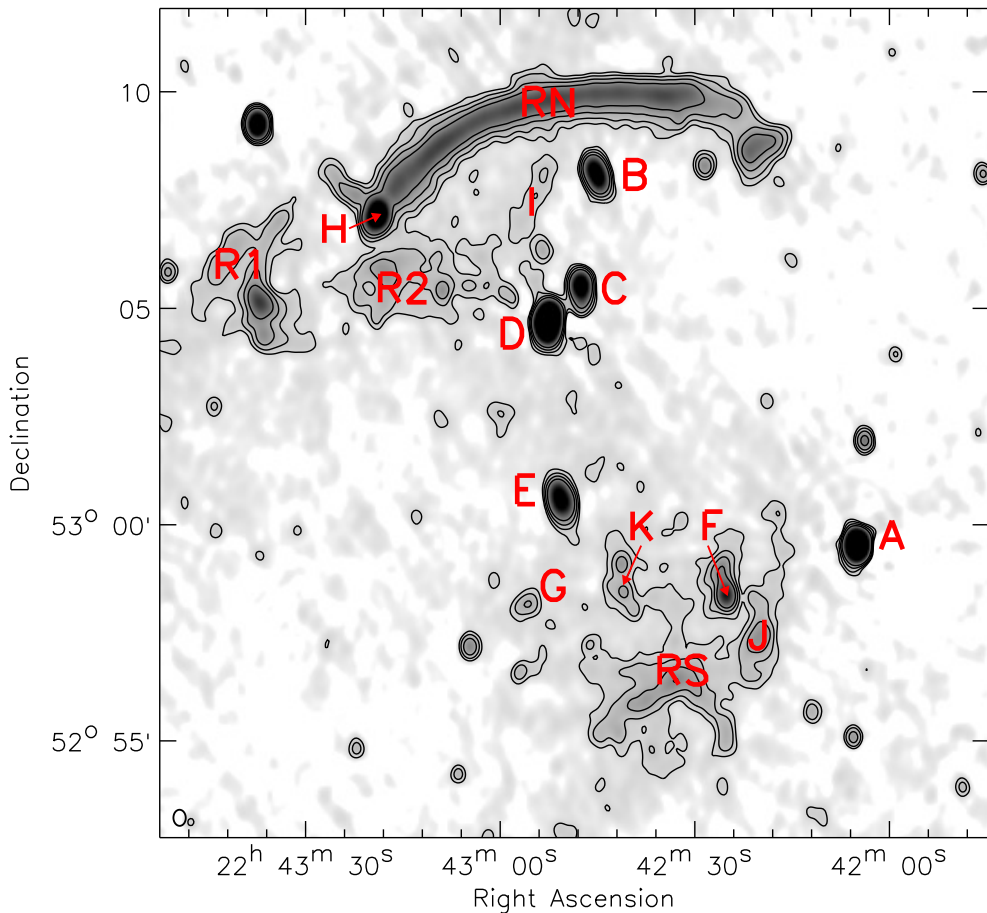
Figure 2.4: Left: WSRT 1221 MHz image with contour lines drawn at $[4, 8, 16, 32] \times \sigma_{\mathrm{RMS}}$. The beam size at $22.38'' \times 17.14''$ is shown in the bottom left corner of the image. Added source labelling.

To the north of RS, the 1221 MHz map (Fig. 2.4) reveals a patch of diffuse emission labelled as source K. The patch gets connected to RS in the 1221 and 1382 MHz maps (Fig. 2.4 and 2.5).

Diffuse source J is located at the west of RS and covers an area of 260 kpc $\times$ 350 kpc. In the lower frequency maps (below 1382 MHz), source J and RS become connected into a single area of diffuse emission with flux concentrated in two patches. The distinction between source J and RS will become evident in the spectral index maps (see Sect. 2.3.2).

Towards the east of RN, the maps reveal another smaller (350 kpc $\times$ 500 kpc) arc-like area of extended, diffuse emission (R1).

In all of the maps, a patch of extended emission (R2) is detected immediately south of the northern relic, with a size of 380 kpc $\times$ 290 kpc. In the high frequency maps (1221, 1382 and 1714 MHz) the emission has two peaks, but the 323 MHz map reveals that the western peak is actually a separate point source. This source, embedded in the relic emission, has a steeper,
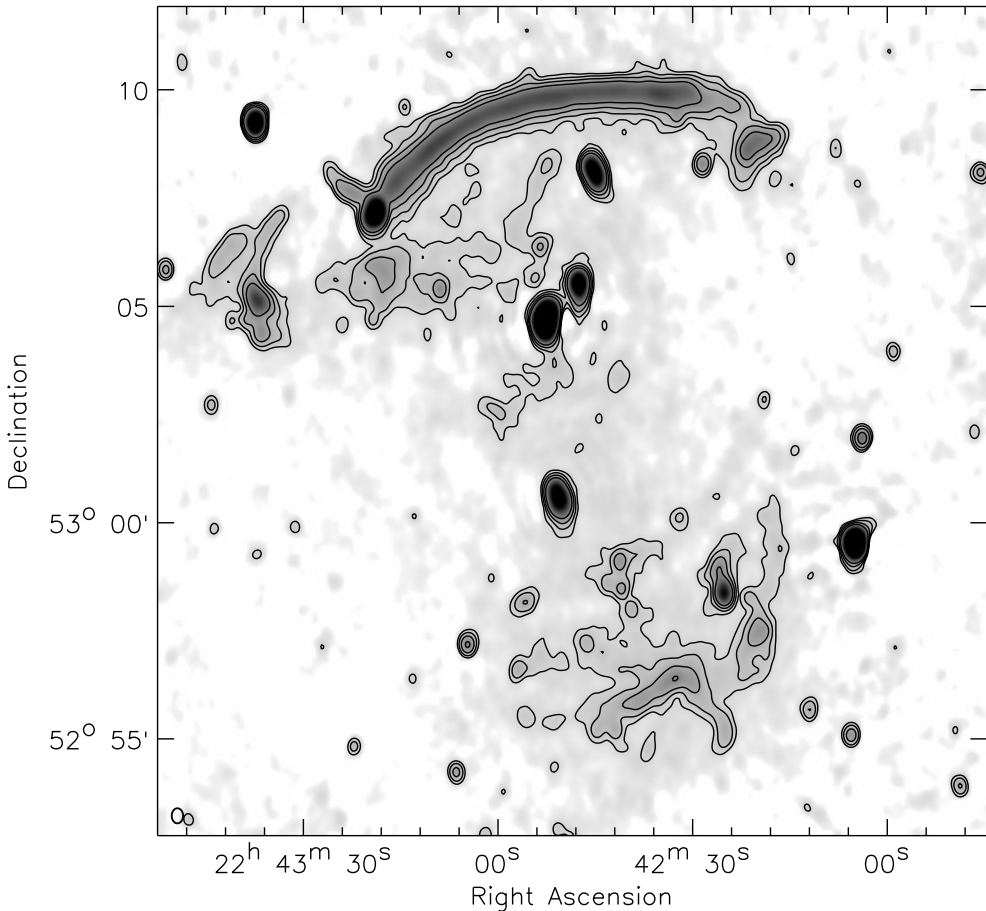
Figure 2.5: WSRT 1382 MHz image with contour levels at $[4, 8, 16, 32] \times \sigma_{\mathrm{RMS}}$. The beam size at $20.95'' \times 15.80''$ is shown in the bottom left corner of the image.

brighter spectrum than the surrounding diffuse emission which, at some frequencies, is below the noise levels. Towards the west, immediately south of RN, source I is an elongated patch of emission, which is visible only in the 608 MHz, the 1221 MHz and 1382 MHz images (Figs. 2.3, 2.4 and 2.5).

Radio galaxies

Within the sensitivity limits of our observations we detect five radio sources in the field with head-tail morphology. The 608 MHz image (Fig. 2.3) reveals object E to be a classical twin-tailed radio source with highly bent lobes. Interesting is also source G which is at the noise level in the 2272 MHz map, but a strong detection at the low frequencies. This means the source has an extremely steep spectrum. It has to be noted that source A has been peeled in the 153 MHz and 608 MHz. Since the source could not be perfectly removed from the uv data, the source itself is not visible, but there is some residual side lobe pattern in the images.

19
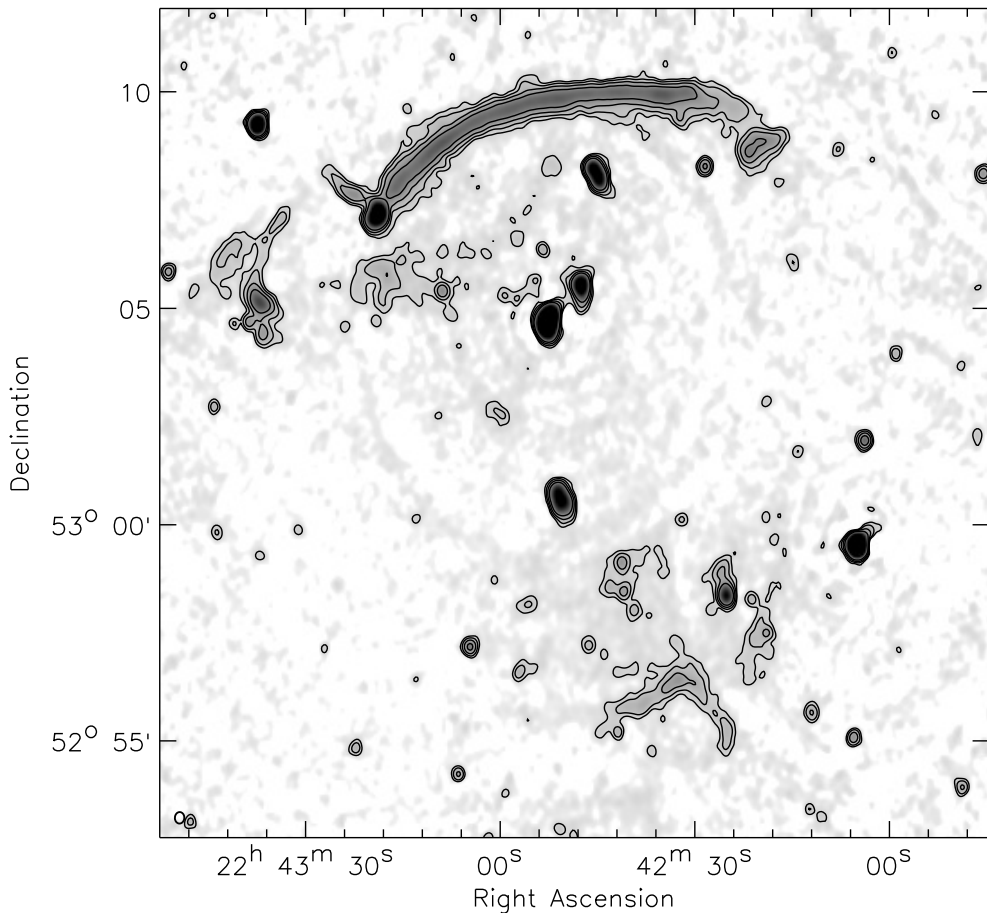
Figure 2.6: WSRT 1714 MHz image with contours at $[4, 8, 16, 32] \times \sigma_{\mathrm{RMS}}$. The beam size at $15.98'' \times 13.10''$ is shown in the bottom left corner of the image.

2.3.2 Spectral index and spectral curvature

For the purposes of spectral index and spectral curvature mapping, it is important to have consistent flux scales for all the seven frequencies. Despite the fact that the same flux standard was used throughout the calibration process, issues with the transfer of the flux scale from the calibrator to the target and differences in uv coverage result in the recovery of flux on scales that vary between observations and telescopes. In order to account for this, we produced new radio maps with a common, minimum uv cut at $0.2\mathrm{k}\lambda$ and uniform weighting to ensure recovery of flux on similar spatial scales. This uv cut accounts for the missing short uv spacings and causes the largest detectable scale to be $\sim 17'$. The resolution of these maps is, in ascending order of frequency: $16.2'' \times 13.8''$, $pa = 50.0°$; $10.0'' c \times 8.0''$, $pa = 0°$; $4.2'' \times 3.4''$, $pa = 60.0°$; $16.9'' \times 12.9''$, $pa = -1°$; $14.9'' \times 11.0''$, $pa = -1°$; $12.0'' \times 9.1''$, $pa = 0.0°$; $9.5'' \times 7.1''$, $pa = 0.0°$. We then convolved all the maps to the lowest resolution and regridded/aligned them with respect to the 1221 MHz image. The final effective resolution is: $18.0'' \times 14.8''$,
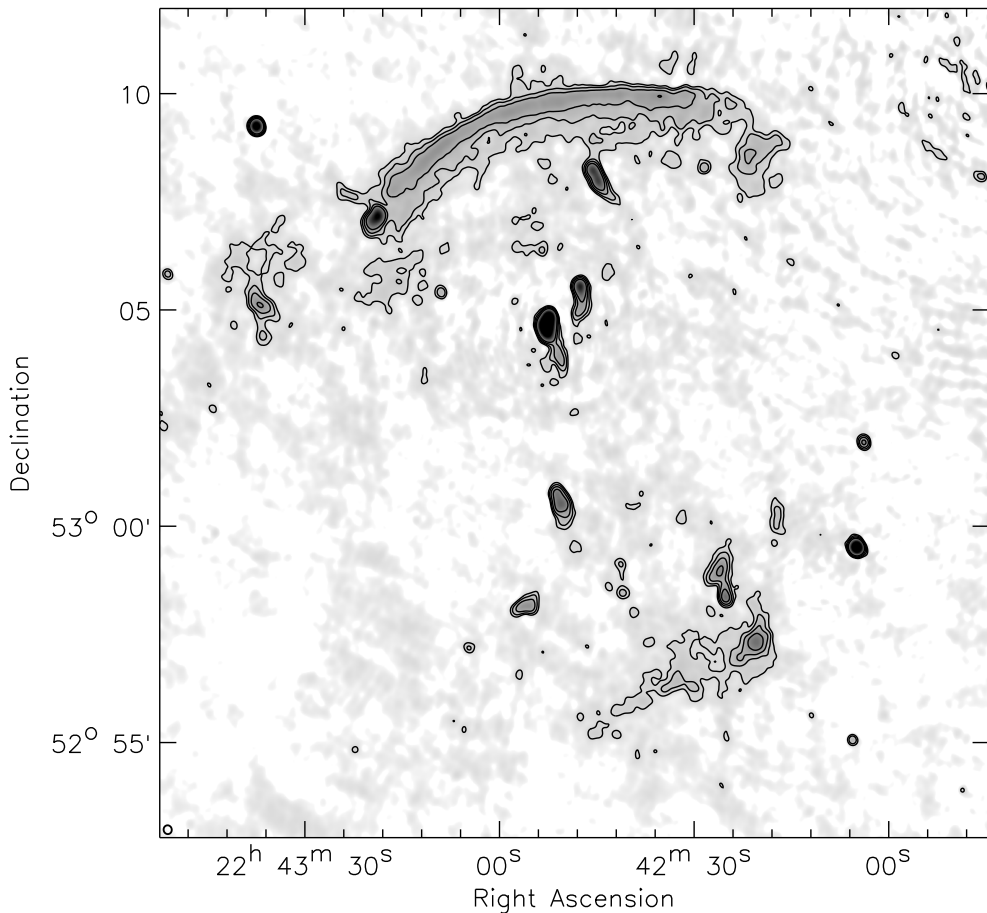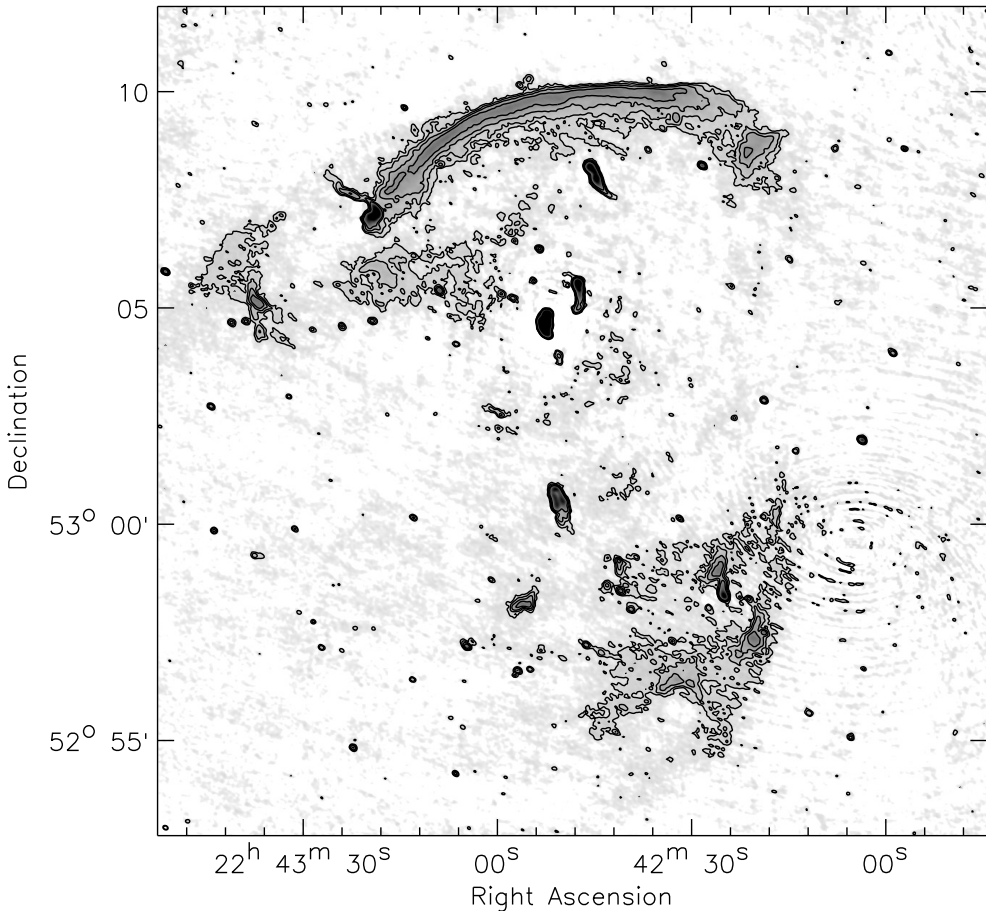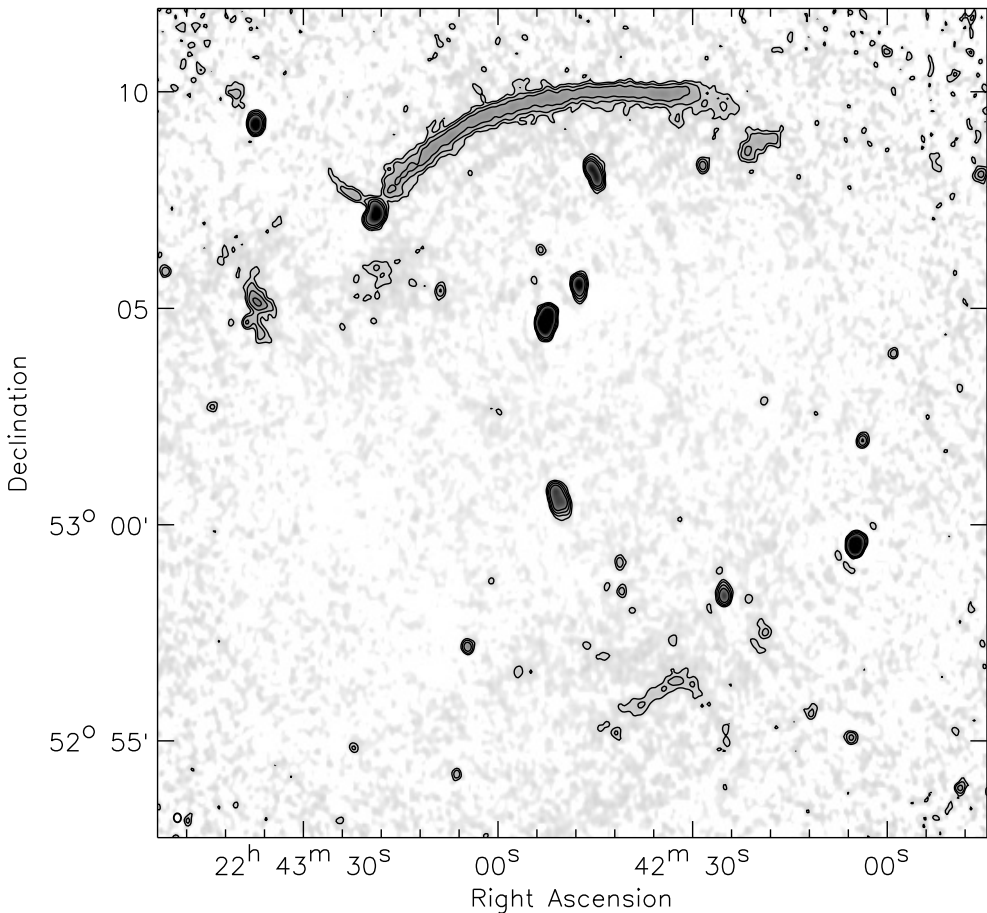
Figure 2.7: WSRT 2272 MHz image with contour lines drawn at $[4, 8, 16, 32] \times \sigma_{\text{RMS}}$. The beam size at $12.38'' \times 10.04''$ is shown in the bottom left corner of the image.

$pa = 20.0°$.

The uncertainty in the flux scale for both the WSRT and GMRT observations was considered 10%. We base this value on the studies of Schoenmakers et al. (1998), Rengelink et al. (1997) and Chandra et al. (2004). To ensure that the uncertainty is not underestimated, we studied the spectrum of seven compact sources in the field, using our measurements together with values from the NVSS (Condon et al. 1998), WENSS (Rengelink et al. 1997), VLSS (Cohen et al. 2007), Texas 365 MHz (Douglas et al. 1996), 4C (Gower et al. 1967) and 7C (Vessey & Green 1998) catalogues, where available. We derived linear fits to the measurements as function of frequency and measured the dispersion of the points with respect to the best fit. We concluded that our measurements were all within 10% of the fitted lines.

Integrated spectra

We produced integrated radio spectra for the four relics RN, RS, R1 and R2 using these maps with the common uv cut and same resolution. We measured the fluxes in fixed-size apertures across the seven frequencies. The uncertainty in the flux was computed as the RMS noise multiplied with the number of beams N_{beams} contained in the respective area and the 10% flux uncertainty, added in quadrature:

$$\Delta F = \sqrt{(\sigma_{\text{RMS}})^2 N_{\text{beams}} + 0.01 F^2}. \tag{2.3}$$

Figure 2.8 shows the flux measurements for RN, with a linear fit. Although the data is well described by a single power law, the spectrum falls off at 2272 MHz and becomes more curved. Figures 2.9, 2.10 and 2.11 present the linear fits for RS, R1 and R2, respectively. R1 is the only relic not well described by the straight spectrum. Diffuse source J is fitted with a power law with slope -1.55. The details of the fits for the relics are given in Table 2.5.

We also produced a linear fit to the spectrum of source G using six frequencies. Since it is not detected in the 2272 MHz image, we plotted, for reference, a $3\sigma_{\text{RMS}}$ upper limit value at this frequency (see Fig. 2.13).

Spectral index maps

For the spectral index maps, we blanked all pixels with values lower than $2\sigma_{\text{RMS}}$ and fitted linear functions to the data pixel by pixel. Errors were computed by adding in quadrature the flux uncertainty error of 10% and the σ_{RMS} in each map.

Figure 2.14 shows the low frequency GMRT spectral index map between 153 and 608 MHz. A spectral index gradient across the northern relic is immediately evident, varying from an average value of -0.6 at the outer to -2.5 at the inner edge, as was first observed at high radio frequencies by van Weeren et al. (2010). The gradient is smooth and consistently perpendicular to the relic from its east to its west tip. The beam is sampled only a few times over relic's thickness and, at the northern side, there is an abrupt drop in surface brightness where edge effects become important. This causes a sharp decrease in the spectral index in parts of the northern side of the relic. There is some spectral index steepening across relic R1, while R2 has a steep spectral index ($\alpha < -1.3$), but no strong gradient. A spectral index gradient is also noticeable across the head-tail sources B, C, D, E and F. The nuclei of these sources have $\alpha \sim -0.5$, whereas the tails steepen to values below -2.0. The most dramatic steepening can be observed across source F, whose tail reaches spectral index values of -3.5. Source G, which was below the noise level in the 2272 MHz map, has an ultra steep spectrum with $\alpha \sim -1.8$. The nuclei of tailed radio sources have a typical spectral indices of ~ -0.7 with tails steepening to -2. Röttgering et al. (1994) classify all sources with integrated spectral index $\alpha \leq -1.0$ as ultra steep spectrum sources. The point source embedded in the western part of R2 is now properly resolved. The spectral index is much flatter than the relic's and fairly constant across the source.

In Figure 2.15, we present seven frequency spectral index maps with a frequency coverage from 153 MHz to 2272 MHz. As before, the gradient across the northern relic is clearly visible. Although in the low-frequency radio maps, the southern relic and source J appear as a single object, in the spectral index map they are split in two areas with different properties.

Table 2.5: Integrated radio spectra of the relics and steep spectrum source G

Source	RN	RS	R1
α	-1.06 ± 0.04	-1.29 ± 0.04	-0.74 ± 0.07

Source	R2	J	G
α	-0.90 ± 0.06	-1.53 ± 0.04	-1.77 ± 0.05

RS, while not possessing the same orderly morphology as RN, still displays a gradient with steepening spectrum ($-3.0 < \alpha < -1.5$) towards the cluster centre. Source J has a much steep spectral index ($-2.0 < \alpha < -1.7$), while the RS is flatter ($-1.2 < \alpha < -0.6$).

Spectral curvature map

We produced a spectral curvature map using all of the seven maps available convolved to the same resolution. The wide frequency coverage enables us to better constrain the curvature and minimise errors. We follow the definition of Leahy & Roger (1998) for three frequencies:

$$C = -\alpha_{\nu_2}^{\nu_1} + \alpha_{\nu_3}^{\nu_2} \tag{2.4}$$

where ν_1 is the lowest of the three frequencies, ν_2 is the center one and ν_3 is the highest. In this convention, the curvature C for a normal, convex spectrum (e.g. spectral ageing) is negative. As we were unable to find a consistent definition of curvature when more than three frequencies are employed, we define spectral curvature in the following way:

$$C_{380}^{1650} = -\alpha_{low_{\nu}} + \alpha_{high_{\nu}} \tag{2.5}$$

where the low frequency spectral index was computed using the three GMRT frequencies centred at 380 MHz and the high frequency spectral index was obtained from the fit to the four WSRT measurements, centred at 1650 MHz. Thus the curvature depends on which frequencies one uses for the spectral indices. The two fits also produced standard errors of the spectral index ($\Delta\alpha_{low_{\nu}}$ and $\Delta\alpha_{high_{\nu}}$) which were added in quadrature to obtain the uncertainty in the curvature estimate:

$$\Delta C_{380}^{1650} = \sqrt{(\Delta\alpha_{low_{\nu}})^2 + (\Delta\alpha_{high_{\nu}})^2} \tag{2.6}$$

The results of a pixel by pixel curvature is presented in Fig. 2.16. We blanked all pixels with SNR smaller than 3. As expected, the relics and the tails of the radio galaxies have a convex spectrum, i.e. a negative curvature parameter.

RN is marked by a gradient of increasing curvature from north to south. At the front of the shock we have $C = 0$, which reinforces the results of the separate high and low frequency spectral index maps. The curvature increases into the downstream areas to values of -1.5. There are also small scale variations along the length of the source with a size of the order of a beam (~64 kpc). We treat these in more detail in the Discussion (Sect. 2.5)

R1 and R2 do not show any extreme curvature, while the division between source J and RS is still noticeable from their different curvature properties. The spectrum of RS is considerably less curved than J which reaches $C \sim -1.5$. There is smooth gradient over the tail of source E, which dips to -0.7. A pronounced spectral curvature is also visible in the tail of source
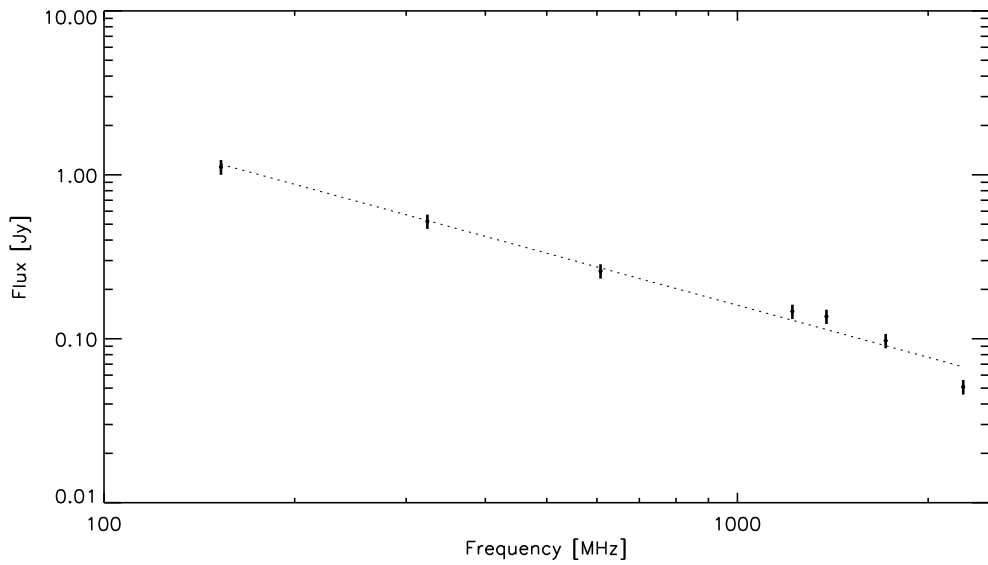
Figure 2.8: Integrated radio spectrum of RN.
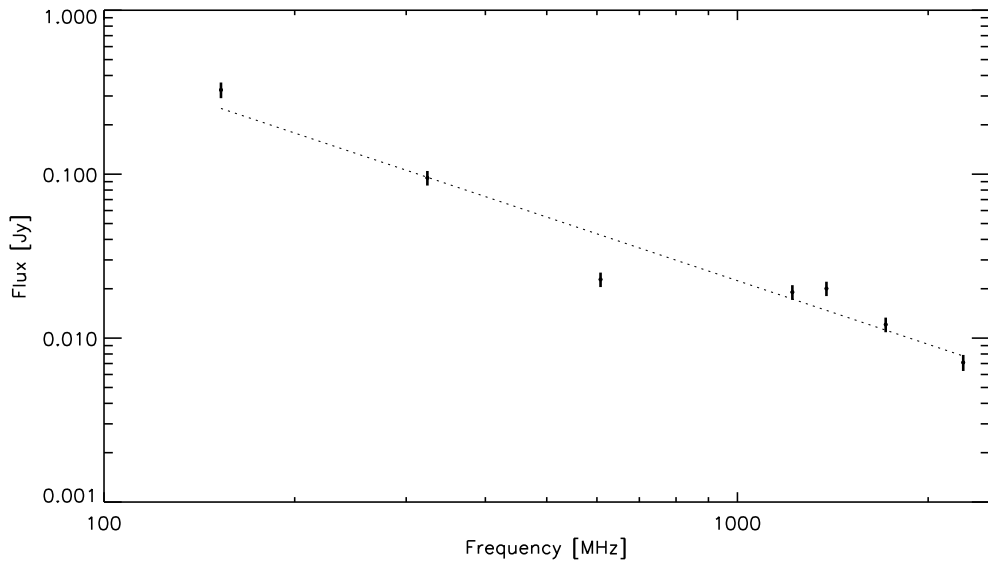
Figure 2.9: Integrated radio spectrum of RS.

F: values range from -1.0 to -1.4. We measure source G separately and it is also extremely curved with $C \sim -1.25$.
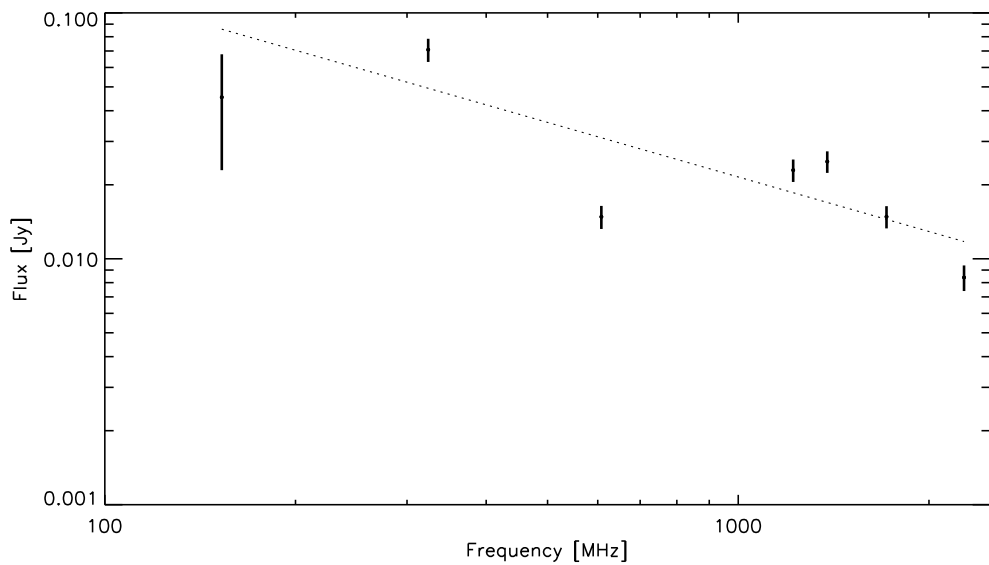
Figure 2.10: Integrated radio spectrum of R1.
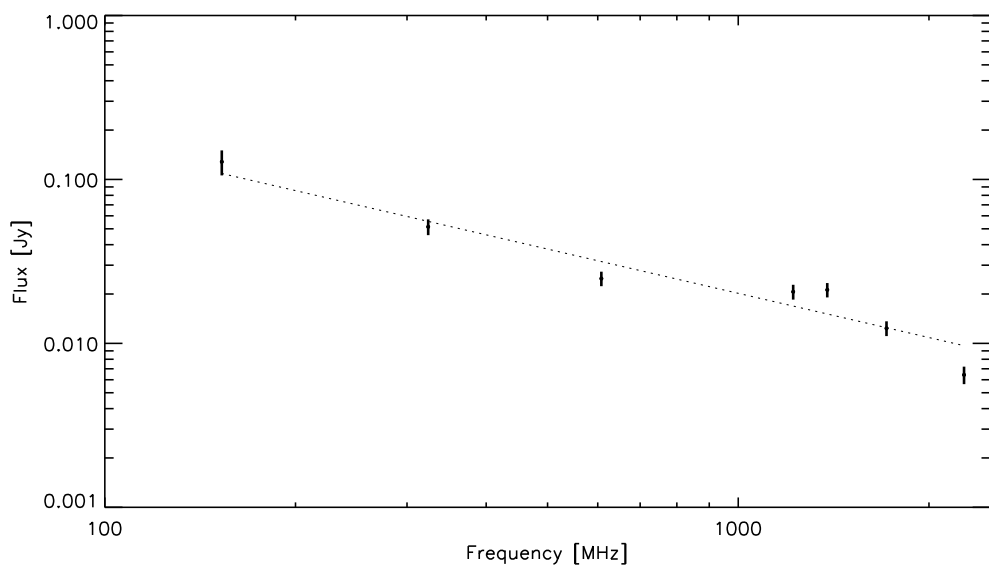
Figure 2.11: Integrated radio spectrum of R2.

2.3.3 Colour-colour plots

The spectral index and curvature maps were produced on a pixel by pixel basis. In order to increase the signal to noise ratio (SNR), we perform a spectral curvature analysis for RN on region with similar spectral properties based on the method of van Weeren et al. (2012b). For this, we bin pixels in seven spectral index groups ranging from $-0.75\cdots-1.35$, based on
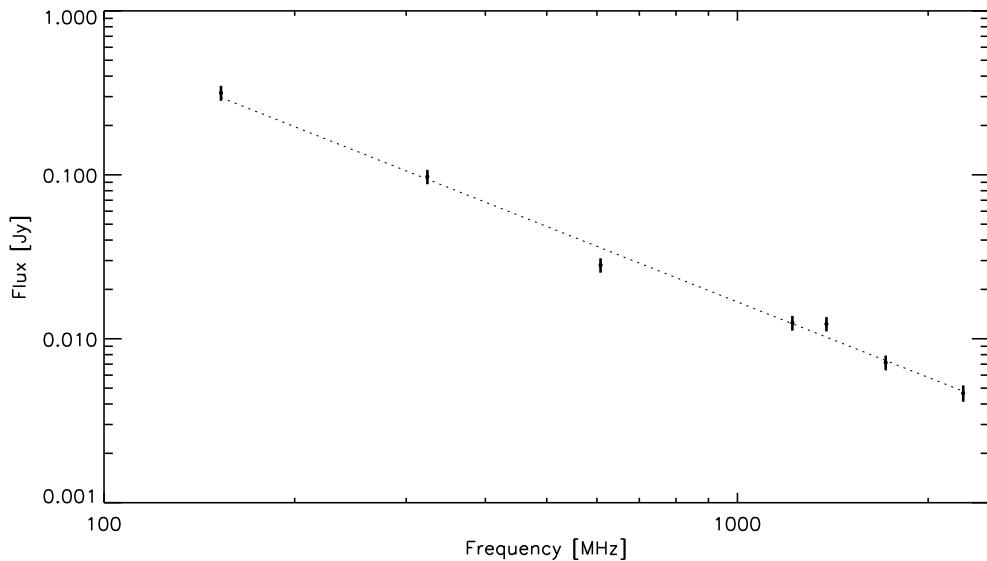
Figure 2.12: Integrated radio spectrum of source J.

their seven-frequency α in the spectral index map. The step size was chosen as 0.1, to gather enough pixels (> 800, pixel size is $1'' \times 1''$) to get high SNR in each bin, but to avoid too much mixing of electrons from different age populations. As compared to a pixel by pixel analysis, the binning increases the SNR with respect to the RMS at least a factor of 200.

The northern, outer edge of the relic is the front of the shock. The spectral index increases with distance into the back of the shock, towards the inner edge. Therefore, the spectral index criterion traces regions in a shell-like pattern from the shock into the post-shock area.

The spectral index selection criterion produces regions that vary in size, which makes it difficult to produce directly comparable spectra for each of these areas of the relic. In order to account for the difference in surface area, after we sum up the flux f_i of all of the pixels in each area, we normalise by the number of pixels to get an average flux per pixel:

$$\bar{F} = \frac{\sum_{i=1}^{N_{\text{pixels}}} f_i}{N_{\text{pixels}}}, \tag{2.7}$$

where $\bar{F}$ is the average flux for the region. The flux uncertainty derived in Sect. 2.3.2 is then normalised by the number of pixels in the respective area to get the standard error of the normalised flux $\bar{F}$. We fit second order polynomials to the normalised fluxes as a function of frequency. We then use the best-fit parameters to predict the flux at our reference frequencies. We thus have spectra predicted at seven frequencies for all the eight regions. In this way we are improving the SNR, by using all seven available flux measurements jointly to predict the flux at each of the seven frequencies. In the next analyses, we use these predicted fluxes for each of the α-selected regions, rather than the measurements themselves.

The spectra for the different regions of RN are plotted in Fig. 2.17, where the predicted flux was multiplied by the frequency on the y-axis to emphasise the differences between the regions. Linear fits were drawn through the points for reference. The colours from black to
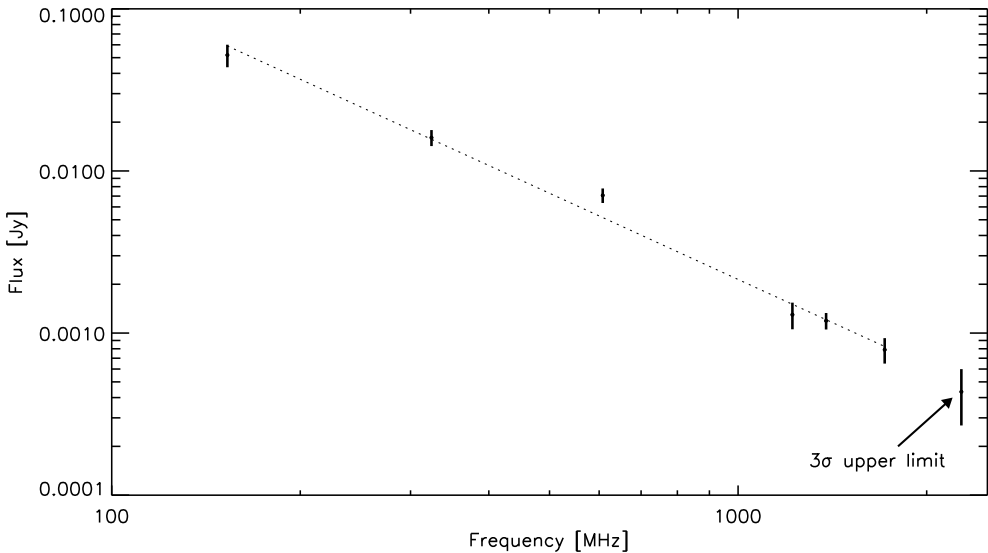
Figure 2.13: Integrated radio spectrum of source G.

red represent areas selected based on the pixels increasing spectral index. We compare the flux points with the fit in order to evaluate how strongly curved the RN spectrum is. The slope of the linear fit corresponds to the spectral index that describes the pixels summed up within an area. The areas with flatter spectra are well described by a power law, while the spectra become increasingly curved with steepening α and deviate from the linear fit.

The curvature was then computed using the formula defined in equation 2.5 with the same reference frequencies as before. In order to better visualise the dependence of the curvature on the spectral index, we have plotted these two quantities against each other in Fig. 2.18. The plot shows that the spectrum becomes more curved further from the shock. The dependence of the curvature on the spectral index fitted through the seven frequencies can be described by a linear function of the form $C_{380}^{1650} = (0.7 \pm 0.1) \cdot \alpha_{150}^{2274} + (0.3 \pm 0.1)$.

Injection in the northern relic

To test how well the RN data is described by some of the established injection models (see Sect. 2.1), we produced colour-colour plots (Katz-Stone et al. 1993), in which the high-frequency spectral index for multiple positions in the radio source is plotted against the low-frequency spectral index. Colour-colour diagrams have the advantage of emphasising spectral curvature and displaying data for all areas of the source in an empirical way. They can reveal trends which can be overlooked when fitting physical models directly to the data. They represent an easy way to visualise the models and to trace back the data to injection properties. This is possible because the shapes of spectral models are conserved under adiabatic and magnetic field changes and radiation losses. For this purpose, we used the same regions defined in Sect. 2.3.3, and fitted the low frequency (between 153 and 608 MHz) and high frequency (between 1221 and 2272 MHz) spectral index using the predicted fluxes from the second order fit to the data. For reference, we overplotted JP, KP, KGJP and CI models described in the
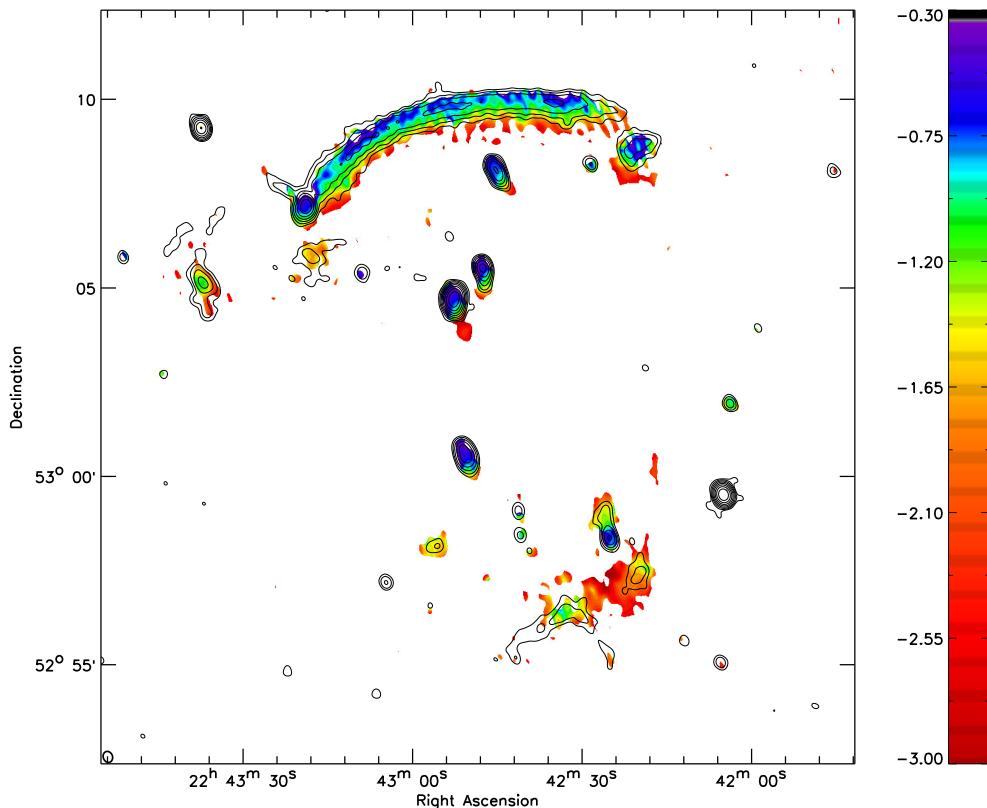
Figure 2.14: Three-frequency spectral index map between 153 MHz and 608 MHz. Contours from 1221 MHz are overlaid at $[4, 8, 16, 32] \times \sigma_{\mathrm{RMS}}$ level.

Introduction (Sect. 2.1) with injection spectral index of −0.6 and −0.7, in order to match the injection index derived from the spectral index maps. The intersection of the traced back data to the $\alpha_{153}^{608} = \alpha_{1221}^{2272}$ line gives an injection spectral index between −0.6 and −0.7, which is consistent with the one derived from the spectral index map.

2.4 Discussion

The northern relic in merging cluster CIZA J2242.8+5301 has been one of the best studied objects of its type owing to the size, regular morphology and high surface brightness. van Weeren et al. (2010) have performed a high radio frequency analysis focussed on the northern relic, discovered spectral index steepening and aligned magnetic field vectors and derived a Mach number of $M = 4.6^{+1.3}_{-0.9}$. Simulations of van Weeren et al. (2011b) managed to reproduce the morphology and spectral index trends of RN within a head-on collision of two similar-mass clusters in the plane of the sky. The merger produces the main counter-relics via opposite travelling shock waves.

The new low-frequency radio data combined with the existing GHz measurements provide an excellent opportunity to extend previous research to a cluster-wide analysis. This enables
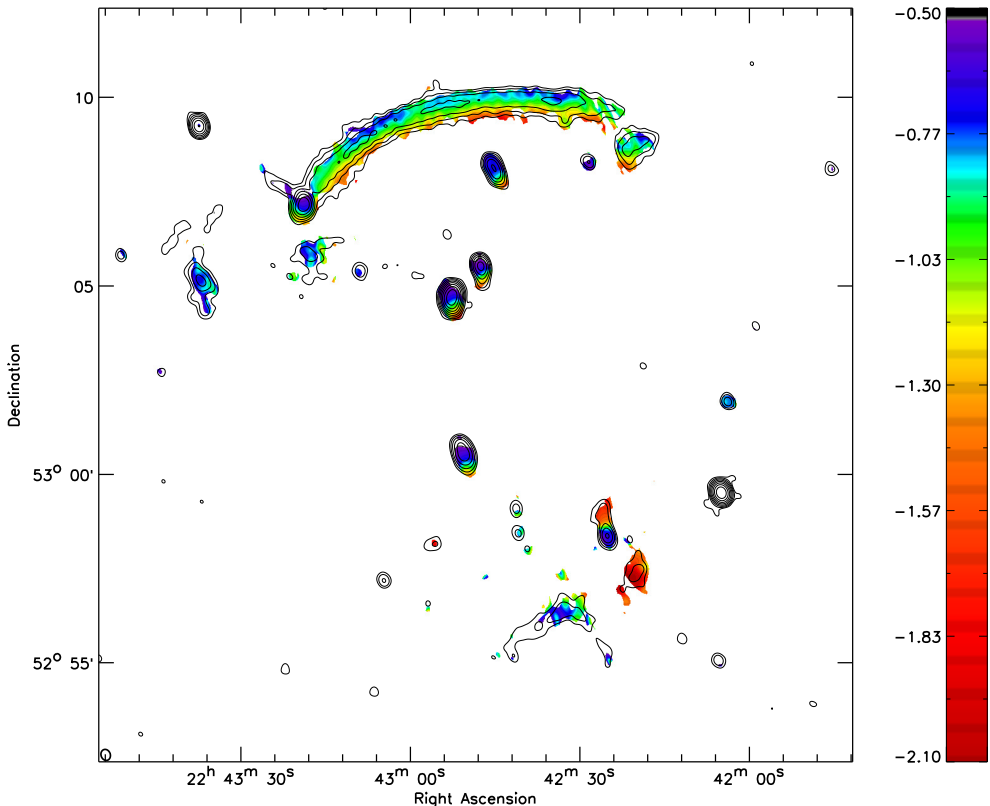
Figure 2.15: Seven-frequency spectral index map between 153 MHz and 2272 MHz. Contours from 1221 MHz are overlaid at $[4, 8, 16, 32] \times \sigma_{RMS}$ level.

us to answer some outstanding questions about spectral curvature and injection/acceleration mechanism. We will discuss the morphology of the sources across seven radio maps to provide clues about the nature and origin of the sources. We will interpret the spectral index and curvature map to fix the physical prescriptions for the four diffuse sources in the cluster, such as the Mach number and formation mechanism. The colour-colour analysis will focus on determining the injection mechanism responsible for accelerating the electrons within the northern relic.

2.4.1 Northern relic

Morphology

The northern relic possesses the morphological and spectral characteristics of shock wave in-duced emission. It maintains its arc-like shape over 1 Mpc and almost two orders of magnitude in frequency. Source H toward the east is most probably a separate physical system, whose position coincides with the projected location of the shock.
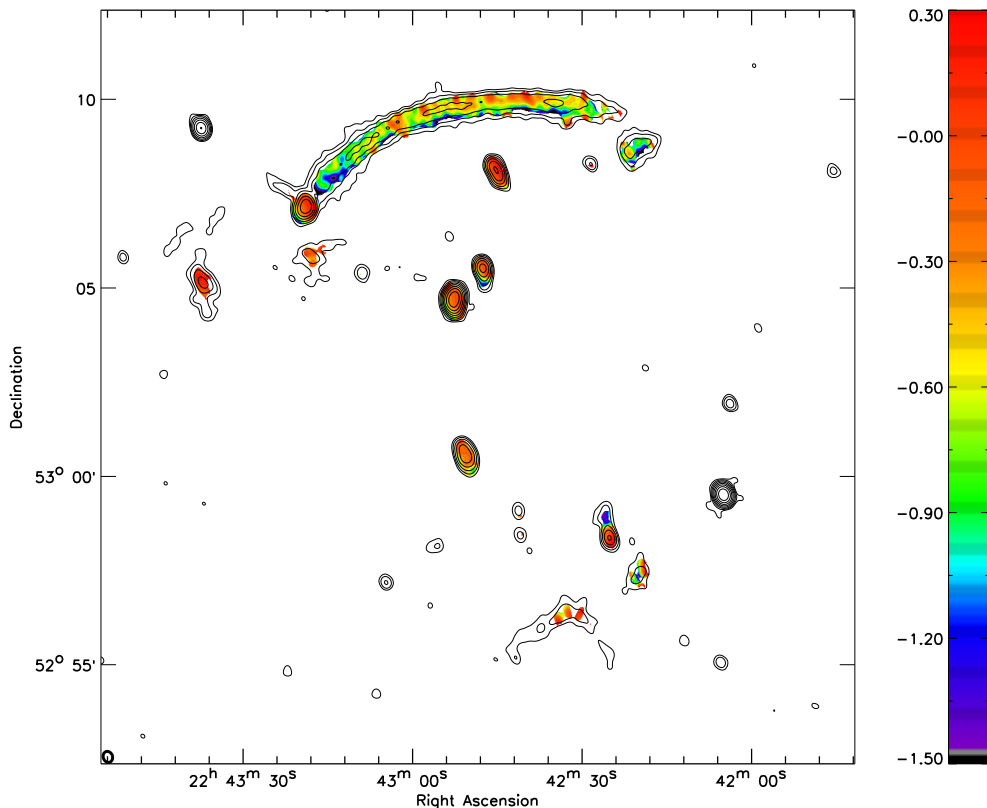
Figure 2.16: Seven frequency spectral curvature map between 153 MHz and 2272 MHz. Contours from 1221 MHz are overlaid at $[4, 8, 16, 32] \times \sigma_{\mathrm{RMS}}$ level.

Spectral analysis

In the acceleration scenario (Ensslin et al. 1998), at the front of the travelling shock we expect a straight and flat spectrum, as the entire electron population is similarly accelerated. The spectral index α at the outer edge of the RN, where acceleration is actively happening, has a value ~ -0.6 from 153 MHz to 2272 MHz. The injection spectral index between -0.6 and -0.7 derived from the spectral index maps matches the colour-colour analysis. Moreover, the spectra for regions selected based on spectral index in Fig. 2.17 can all be traced back to $\alpha_{\mathrm{inj}} \sim -0.60$ at the low frequency end, where radiation losses have not affected the spectral shape. The integrated spectrum of RN is well described by a power law with -1.06 ± 0.05 slope and does not show any flattening or turnover at low frequencies, which is expected from shock acceleration theory. This is confirmed by the fact that the α_{inj} derived from the low-frequency, high-frequency and seven-frequency map derived are consistent with each other at a value of ~ -0.60. α_{inj} is 0.5 flatter than the integrated spectral index which is expected for a simple shock model (e.g., Miniati 2002; Bagchi et al. 2002). The acceleration mechanism also predicts increasing spectral curvature with depth into the downstream area. We observe large scale trends of increasing curvature in our maps (Fig. 2.16) as well as in our colour-colour plot (Fig. 2.19). The curvature at the front of the shock is consistent with 0, which indicates
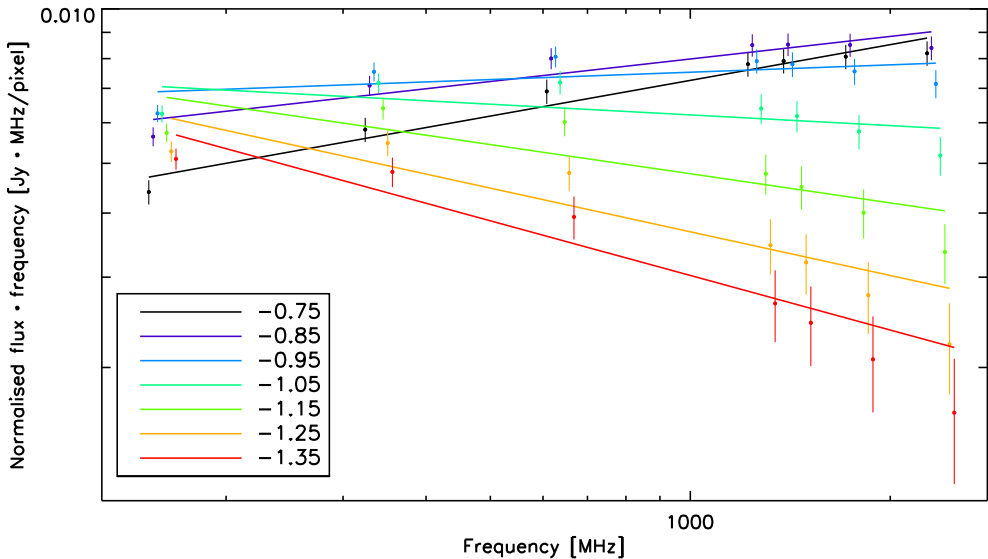
Figure 2.17: Normalised spectrum with linear fits for the regions selected based on spectral index. The flux was multiplied by the frequency on the vertical axis to better differentiate between the different regions. The data points were slightly shifted along the horizontal axis for clarity.

that all electrons emitting between 153 MHz and 2272 MHz are currently accelerated. The curvatures increases to $C_{380}^{1650} = -\alpha_{low_\nu} + \alpha_{high_\nu} = -1.5$ in the downstream area, showing a curved spectrum marked by energy losses.

Relic substructure

We found the significant curvature substructure along the length of the northern relic particularly puzzling. Are the variations due to real physical conditions or just noise peaks? In order to investigate the origin of these so-called "ripples" we placed circular bins across the relic, with a size matching the synthesised beam (radius~32 kpc). Their positions were chosen such that they follow the surface brightness distribution contours along the relic (see top map in Fig. 2.20).

In the bottom plot in Fig. 2.20 we plotted the flux measured within these circular regions. It is immediately obvious that the variations within the inner five frequencies (323 MHz to 1714 MHz) correlate well and show similar trends. This suggests there is real substructure associated with the shock. The radio maps at the bounding frequencies 153 MHz and 2272 MHz were heavily affected by the uv cut imposed for spectral analysis purposes. This leads to a reduction in relic brightness with respect to the background noise. We suspect spurious peaks in the brightness distribution across there two frequencies affected the curvature the most. To test this, we look at the curvature variations along the relic, fitted using the fluxes measured in the same circular regions. We detect suspicious maxima and minima at distances ~450 kpc, ~900 kpc and ~1150 kpc, which can be traced directly to noise peaks in the 153 MHz and 2272 MHz maps. We therefore suggest that the low curvature regions at $RA = 53°09'15''$,

$DE = 22^h43^m02^s$ and $RA = 53°10'00''$, $DE = 22^h42^m39^s$ and the curvature trough at $RA = 53°09'45''$, $DE = 22^h42^m48^s$ are probably noise effects. We have indicated the areas with poor signal to noise and low degree of confidence in red at the top of Fig. 2.20.

We notice the variations are stable on scales of roughly 100 kpc by following the average flux trends and the curvature variations. These are marked in green in the "confidence bar" in Fig. 2.20. Focussing on these correlated flux trends, we speculate the variations indicate complexity in the shock structure on similar scales. As shown by simulations (van Weeren et al. 2011b), the shock has travelled for hundreds of Myr since the core passage between the merging clusters. Breaking of shock surfaces along their path could result in brightness variations along relics when projected onto the sky (Vazza et al. 2012). Since the radio emission is most likely produced by electrons accelerated by the shock within a magnetic environment, variations in ICM density and temperature result in wiggles in the synchrotron emission/surface brightness along the relic (Hoeft et al. 2011). Simulations by Kang et al. (2012) also suggest that the surface of the shock that creates the northern relic should be highly elongated and that it would not be trivial to induce such a structure in cluster mergers. They argue that the relic might consist of a number of substructures, which is consistent with our observations.

Acceleration of emitting particles

The accepted model for acceleration of particles in the giant radio relic RN is (re-)acceleration (Ensslin et al. 1998; Markevitch et al. 2005). DSA and re-acceleration require the presence of a large scale shock wave and predict a single power law spectrum at the low frequencies, with steepening at the high frequencies due to energy loses into the post-shock area. There are two possible sources for the shock: accretion shocks at the interface between infalling material and an already formed cluster structure or merger shock that occur in major galaxy cluster mergers. The former predicts high Mach numbers (> 4) and occur at large distance from the cluster centre in low density environments, while the latter predicts average Mach numbers ($2 < M < 4$) (Bykov et al. 2008, and references therein).

As mentioned in Sect. 2.1, after the passage of the shock, the accelerated electrons start losing energy via inverse Compton and synchrotron processes, which affect the high energy particles first. For the physical parameters of RN, using the formalism from Hoeft & Brüggen (2007), we can derive an electron cooling time for the northern relic of a few 10 Myr, which peaks for a magnetic field of a few μG. By multiplying this time scale with the shock velocity, we obtain at the distance at which the electrons start to cool significantly: $\sim$ 50 kpc, which means in the northern relic we can resolve the downstream cooling.

The age of the electron population increases away from the shock, such that lower energy electrons also get affected. The decreasing spectral curvature at the back of the shock is to be expected as the cut-off frequency where the electrons start losing energy is shifted towards lower frequencies. The spectral curvature map (see Fig. 2.16) provides strong evidence that shock acceleration is the responsible physical process for RN, with no spectral curvature at the shock front and increasing curvature in the post-shock area. In the context of shock acceleration, the injection spectral index is connected to the Mach number M of the shock via $\alpha_{inj} = -\frac{M^2+3}{2M^2-2}$ (Blandford & Eichler 1987). van Weeren et al. (2010) have obtained a value of $M = 4.6^{+1.3}_{-0.9}$ using high frequency data only. Our results confirm their findings into the low frequency regime. Assuming an injection spectral index of $\alpha_{inj} = -0.60 \pm 0.05$, as mea-
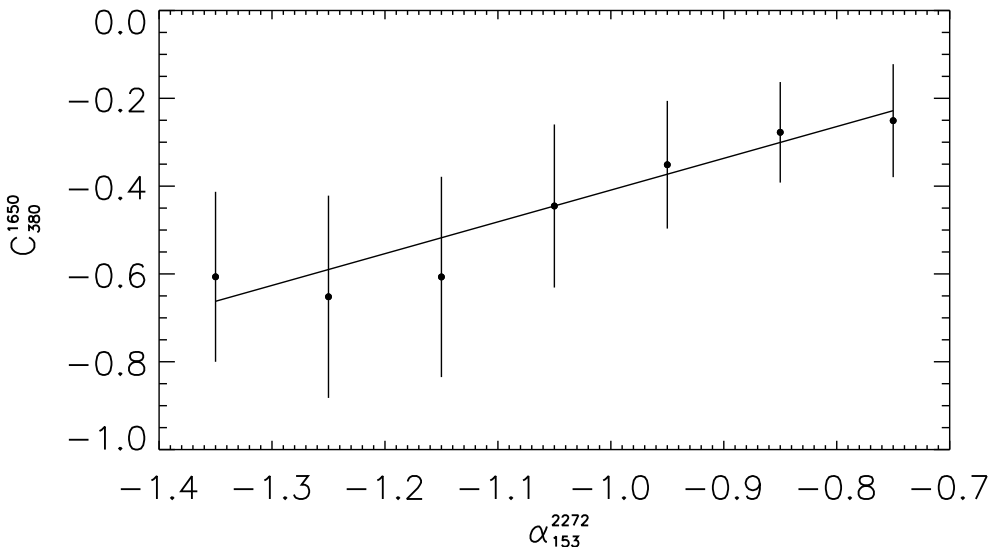
Figure 2.18: Curvature as function of seven-frequency spectral index for different regions in the northern relic.

sured from the spectral index maps and the colour-colour analysis, we obtain a Mach number $M = 4.58 \pm 1.09$.

The simulations performed by van Weeren et al. (2011b) provide evidence that Mach numbers as high as 3 can also occur in merger shocks, but this is dependent on the model of the pre-shock temperature. The highly aligned magnetic fields mapped by van Weeren et al. (2010) also suggest compression of the ICM at the shock location.

In terms of injection mechanisms, the models relate directly to physical processes operating at the shock front. The JP and KP models corresponds to a scenario at which electrons are accelerated at the shock front and cool while streaming downstream. These two models have been described as having a 'single burst' of electrons which means that the particles in a mass element of the ICM are only accelerated while passing through the shock. The CI model implies that there is injection all the way downstream. There are no published models for relic formation consistent with CI, but one could speculate that acceleration by small scale downstream turbulence induced by the shock (similar to haloes) would have such a signature. The KGJP model can be reduced to a continuous sum of JP events with different ageing. This is equivalent with the effect of mixing of different populations of electrons, which occurs because of projection effects. Because we see the relic side-on, there are parts of the spherical shock front that cause electron acceleration and are projected onto the downstream area. From our colour-colour plots, we exclude the continuous injection model as it does not match any of our data points. The data does not turn back to the line of equal low to high frequency spectral index, so it is also not well described by pure KP models. Despite the fact that the KP model does not fall within the error bars of most the points, we cannot fully rule it out. The SNR situation did not allow us to extend our spectral index coverage to steeper spectral index values in order to test whether the data turns back to the $\alpha_{153}^{608} = \alpha_{1221}^{2272}$. The JP models do not

provide a good fit of the extrema of the data. The KGJP model with $\alpha_{\mathrm{inj}} = -0.6$ provides the best description of the data. The deviations from this model can be explained by multiple factors. The effect of mixing is enhanced towards the centre of the cluster, where the steepest spectral indices appear. Another cause can be interfering emission from other sources, such as the radio source at the east end of the relic, the faint halo emission or unresolved compact sources. We also artificially introduced mixing when we binned pixels based on their spectral index. This acts as a complication to our analysis, since simple injection models are not applicable under these conditions. The additional mixing in the downstream area could cause the data to mimic a KP behaviour and turn back to the line of equal high and low frequency spectral index.

Kang et al. (2012) produced simulated colour-colour plots tailored to the physical prescriptions of C2242. While a direct comparison is difficult, since they used different reference frequencies, the general trends are the same. They also observe the effects of radiative cooling curving the data away from the line of equal low to high frequency spectral index and notice that the trends in the colour-colour plots are highly dependent on projection angle of the relic with respect to the sky.

The results of the colour-colour analysis are similar to the ones obtained by van Weeren et al. (2012b) for cluster 1RXS J0603.3+421. This indicates that in both clusters the same underlying mechanisms play a role producing spectral shapes consistent with acceleration to a power-law and then ageing in the post-shock region (JP model) and mixing effects.

2.4.2 Other relics

Morphology

By contrast to RN, the morphology of the counter relic RS changes significantly with frequency. At high radio frequencies, RS is connected with a flat-spectrum tail ($\alpha = -1.10 \pm 0.04$, measured between 1221 MHz and 1714 MHz) towards the south, but the tail is absent in the low frequency map. As mentioned in Sect. 2.3.1, the spectrum of the tail should be steeper than -1.4 for it to be detected in the 153 and 323 MHz maps. While RS is separated from source J at 1714 MHz map, the two patches are connected into a single system at low frequencies. Figure 2.21 reveals a point source with a red galaxy counterpart embedded in emission from J. The color of this galaxy is inconsistent with being a cluster member, but indicates it is a background source unrelated to the cluster.

Source K towards the north of RS between sources G and F gets resolved into multiple compact, elliptical areas of emission in the higher-resolution, low-frequency maps. There is also one head-tail source. All the components of source K have red optical counterparts.

R1 is positioned at a similar projected physical distance from the cluster centre as source RN, suggesting that R1 and RN could have been accelerated by a common merger interaction. R1 also has an arc-like morphology, suggesting that the source is seen edge-on. By contrast, the patchy nature of R2 could result in a scenario where the emission is extended in the plane of the sky (i.e. seen face-on). Both sources do not have obvious optical counterparts coinciding with the radio peak (see Fig. 2.21).

In the 153 MHz map the two relics R2 and RN and source I become connected with diffuse emission which was interpreted as a radio halo (van Weeren et al. 2010). R2 is most probably embedded in the halo that becomes prominent only at the lowest frequencies due to its steep

spectrum. Diffuse source I could be a flatter-spectrum part of the halo. The measured fluxes within a wide box around the emission give a spectral index of ~ -1.25, a typical value for haloes.

Spectral analysis

The division between the southern relic and source J is clear according to their different spectral properties. Source J has a very steep spectral index, which explains why the source is barely noticeable in the high-frequency radio maps. RS and the southern radio tail seem to form a system of flatter emission. We speculate that RS and J is produced by two main broken shocks with different acceleration parameters (i.e. Mach numbers). It is difficult to directly measure an injection spectral index for RS due to the disturbed nature of the relic. We can therefore, use the relation between the integrated ($\alpha_{inj} = -1.29 \pm 0.05$) and injection spectral index to derive $\alpha_{inj} = -0.79 \pm 0.05$, which could be produced by a weaker shock than RN.

R1 shows sign of spectral steepening from which supports the assumptions (see Sect. 2.4.2) that the source is viewed edge-on ($-2.5 < \alpha < -1.0$). There is no clear spectral index gradient across R2. In a scenario where the relic is viewed close to face-on, this is naturally expected as we are probing though electron populations with different ages. The shock front may have also broken off into different fragments, as expected from simulations (Paul et al. 2011).

Acceleration of emitting particles

Apart from DSA/re-acceleration, there is one competing scenario for the formation of relics. Adiabatic compression requires the presence of a nearby radio source (which could be inactive now) to supply radio fossil plasma younger than 2 Gyr. Due to the old age of the plasma, the spectra of these so-called phoenixes are expected to be extremely curved and steep with $\alpha < -1.5$ because of extensive energy losses. This scenario could explain why phoenixes do not trace an entire, spherical shock front, and predict most relics should be a few hundred kpc away from the cluster centres (Hoeft et al. 2004; Vazza et al. 2012).

RS, R1, R2 could also trace shock waves but they are probably produced by broken shock fronts and may also be viewed at an angle with respect to the line-of-sight which results in mixing of different electron populations and explains why clear spectral index trends are not visible. The prescriptions of adiabatic compression are not compatible with the observed position and integrated spectral index (~ -1.0) for these three relics. The flat integrated spectra of R1 and R2 ($\alpha_{int} = -0.74, -0.90$ respectively) are incompatible with pure (re-)acceleration theory, where the minimum injection index can be -0.5, given by an infinite Mach number. An explanation could be that R1 and R2 are produced via oblique shocks, where the relationship between the injection and integrated spectral index does not hold (Kirk & Heavens 1989). As well, a flatter integrated spectrum could arise due spectral ageing occurring in inhomogeneous downstream areas. A similar explanation has been given for the relic in cluster Abell 2256 (van Weeren et al. 2012c). It has to be noted that the scatter in the flux measurements is quite high, which makes the spectral index fits less reliable. One explanation could be that we are not measuring the total flux of the sources at all frequencies. R1 is the only relic that displays a possible spectral turnover which is particularly puzzling. For RS, we can use the relationship between the injection and integrated spectral index (derived in Sect. 2.4.1), to derive a Mach number of $M = 2.81 \pm 0.19$. The diffuse patch of emission J has a very steep
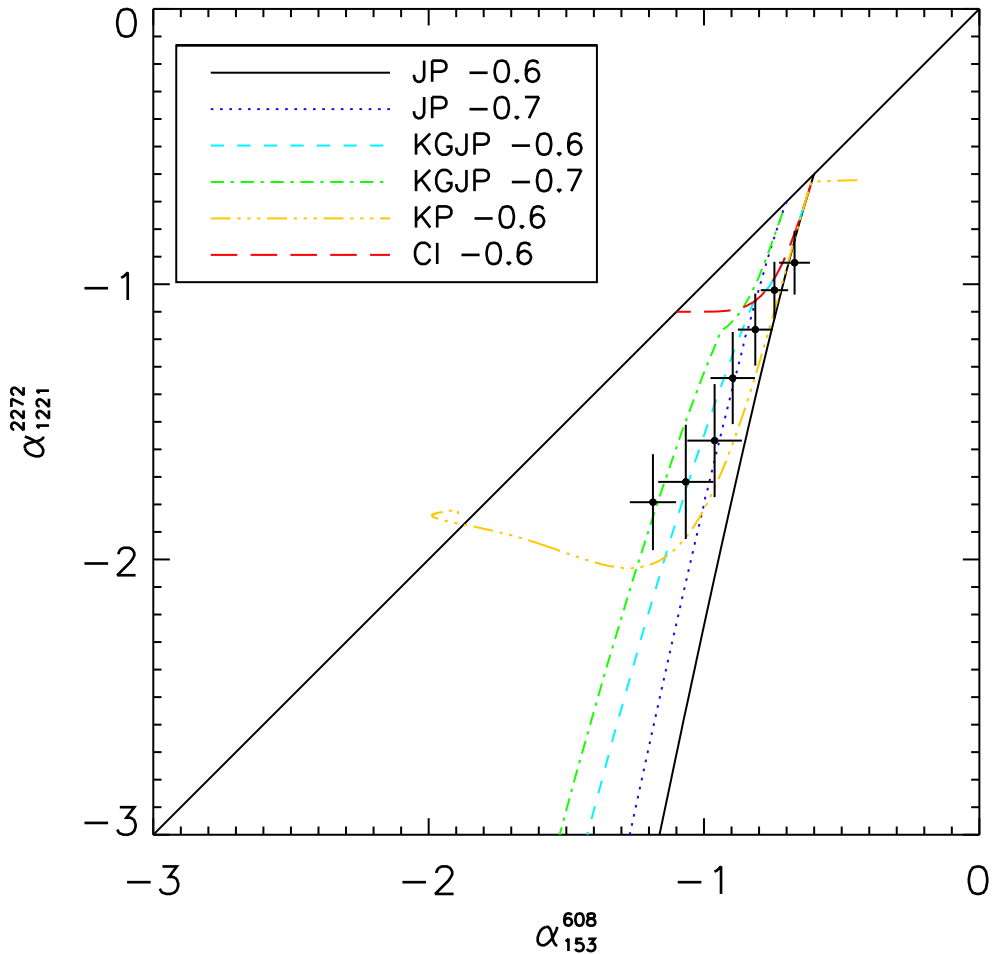
Figure 2.19: Colour-colour diagram showing RN data points in black dots. Different injection models have been overplotted for reference.

integrated spectrum (-1.53 ± 0.05) which suggests the source could be a phoenix embedded in the emission from RS. The high resolution 608 MHz image (Fig. 2.3) shows hints for a radio source with an optical counterpart (Fig. 2.21) that could supply the revived plasma. It is conceivable that source J and RS have been accelerated by a common shock front.

2.4.3 Radio galaxies

Morphology

Sources B, C, D, E and F are clear head-tail radio galaxies which have bright elliptical optical counterparts, coinciding with the peak of the radio emission. A spectral index gradient is noticeable across all of them. The nuclei of the sources have $\alpha \sim -0.5$, whereas the tails steepen to values below -2.0. The most dramatic steepening can be observed across source F, whose tail reaches spectral index values of -3.0. Source G, which was below the noise level

in the 2272 MHz map, has an ultra steep spectrum with $\alpha \sim -1.8$. This source has multiple possible optical counterparts. The point source embedded in the western part of R2 is only properly resolved in the 323 and 608 MHz radio maps. Its spectral index is much flatter than the relic's and fairly constant across the source, which is consistent with point source properties. We could claim that source H is part of the northern relic, owing to its proximity. The source morphology in the high-resolution 608 MHz map provides evidence the source is a radio galaxy (either a disturbed tailed galaxy or a highly asymmetric, double-lobed source), which also has an optical counterpart visible in the Fig 2.21. In addition, its spectral properties are different from the relic's, with no clear index gradient and flatter $\alpha \sim -0.75$.

Acceleration of emitting particles

The tails of radio galaxies are indicative of their relative motion with respect to the ICM. Assuming a geometry in the plane of the sky (van Weeren et al. 2011b), we can directly interpret the bi-modality in the orientation of the tails as a tracer of the two merging clusters. The axes of sources B, C, D and E are aligned with the merger axis, with tails pointing away from the northern shock. Strong evidence for the merger scenario is also the fact that source F near RS, is directed the opposite way. In merging, highly disturbed galaxy clusters, after core passage, there is a displacement between the dark matter and the gas pertaining to each of the clusters. Dark matter and galaxies act like collisionless particles, while the IGM of the two merging clusters interacts through ram pressure and slows down. This means that the dark matter concentration can be found ahead of the ICM peak for each of the clusters. As well, the galaxies decouple from the plasma and run in front of the gas of their parent clusters. This effect has been observed in a number of objects, most famous of which being the Bullet cluster (Clowe et al. 2006). Simulations by van Weeren et al. (2011b) and X-ray observations by Ogrean et al. (2013a) indicate that C2242 is a post-core passage cluster merger, with the main cluster at the north and the subcluster at the south. Therefore, galaxies B, C, D and E are part of the main merging cluster, while galaxy F belongs to the infalling subcluster. The radio head-tail morphology together with the spectral index gradients provide additional support for the merger scenario.

2.5 Conclusion

We presented a combined low and high radio frequency GMRT and WSRT analysis of CIZA J2242.8+5301. All of our maps, present two counter relics, three smaller patches of diffuse emission and several head-tail sources. The two main relics are perpendicular to the merging axis, while the radio sources are aligned with it.

We show the first deep, low-frequency maps of this cluster and integrated spectra for the five relics and a number of radio galaxies. The spectrum of the northern relic is very well described by a power law with integrated spectral index of -1.06 ± 0.05, which is consistent with the previous high frequency measurements. We derive a Mach number M = 4.58 ± 1.09. For the southern relic, we measure a steep spectral index of -1.29 ± 0.05, which suggests the source has been accelerated by a weaker shock of M = 2.81 ± 0.19. Embedded in the emission from the southern relic, we discover a possible radio phoenix revived by adiabatic compression. This source has an extremely steep spectrum $\alpha_{int} = -1.53 \pm 0.04$. The two
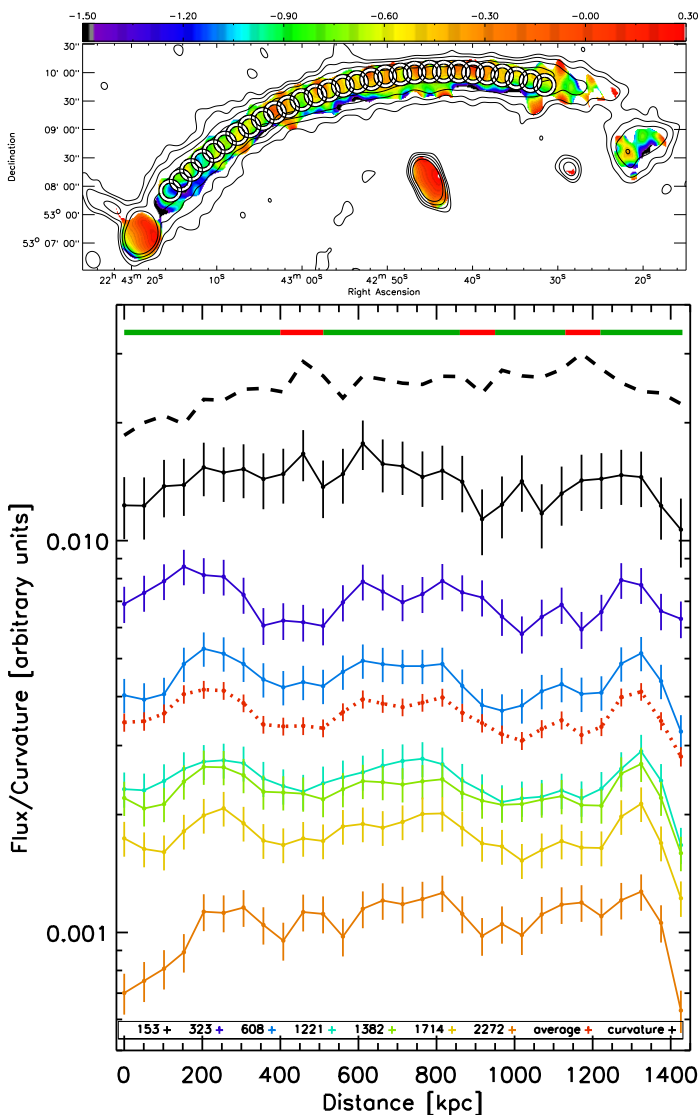
Figure 2.20: Top: areas selected for measuring the spectral curvature and flux. Bottom: Fluxes with error bars measured within the circular regions for seven frequencies 153 MHz to 2272 MHz. The x-axis measured distance along the relic measured in kpc from the first region to the east, towards west. The curves in solid lines represent increasing frequency from top to bottom. Average fluxes between 323 MHz and 1714 MHz are overplotted in a dashed red line. The curvature within the same regions is plotted in a dashed black line. The curvature values were shifted along the y-axis for plotting reasons and stretched for clarity. The colours in the solid line at the top of the plot indicate the level of confidence for the flux trends: red correlates to a noise dominated measurement, while green represents trustworthy measurements.

smaller patches of diffuse emission have flat radio spectra (-0.74 ± 0.07 and -0.90 ± 0.06),

which suggests electrons are cooling in an inhomogeneous medium behind the shock.

We find spectral index gradients across the northern and southern relic and the eastern patch of emission, indicative of shock acceleration with radiative losses into the downstream area. The smaller patch of radio emission to the south of the northern relic is probably seen face-on, as it does not have any clear spectral trends.

All of the proposed models for the formation of relics predict spectral curvature in the downstream area. The faint nature of radio relics impose a low SNR working regime that has proven detection of spectral curvature extremely challenging. We are able to find, for the first time, a curvature gradient across a relic, which suggests active acceleration towards the northern edge of RN, while towards the cluster area, in the downstream region, the spectrum is dominated by radiation losses. This is confirmed by the colour-colour diagram, where we obtained similar results to van Weeren et al. (2012b) for cluster 1RXS J0603.3+421.

We also analysed the small scale structure along the relic and conclude that variations in the spectrum on scales of ~30 kpc are most probably caused by noise peaks in one of our radio maps. This warns against over-interpreting local structure in cluster relics. We speculate that the variations on scales on ~100 kpc along the length of the relic are to be trusted and are probably caused a more complex shock surface.

We conclude that KGJP based models fits the data best, suggesting the electrons go through a phase of acceleration under a continuous isotropisation of the pitch angle to the magnetic field, followed by spectral ageing. Mixing of electron population is induced by projection and resolution effects. This also acts as a confirmation of the (re-)acceleration mechanism.

Most of the radio galaxies in the cluster have a head-tail morphology and have clear spectral trends across their lobes. We discover a very interesting radio source with an extremely steep ($\alpha \sim -1.8$) and curved spectrum. We also uncover a bi-modality in the distribution of radio galaxies, supported by the trends in the spectral index and curvature in their tails. This provides additional support for the the merger scenario where the northern and southern relic are accelerated through the shock acceleration mechanism in two outward travelling shocks waves.

The probing of the downstream area, where the radio spectrum is curved and steepest, is limited by the noise levels currently attainable. We therefore introduce a bias against faint emission by imposing an RMS cuf-off (e.g., Orrú et al. 2007). In our particular case, the limiting factors were the intrinsic lower GMRT sensitivity at 153 MHz map and the 2272 MHz map, with poor SNR given the low surface brightness of the extended emission at this frequency. In the future, telescopes like LOFAR and LWA, at the longest wavelength side, and the new upgraded Jansky Very Large Array, which samples the shortest radio wavelengths, are needed to better constrain the spectrum over more than three decades in frequencies. The high frequency data is crucial in determining which is the responsible injection mechanism, while the low frequency spectrum will further test shock acceleration up to the atmospheric cut-off frequency at 10 MHz. A further test on the merging scenario could be a weak lensing or optical analysis of C2242 that would point out a possible displacement of the mass concentration or galaxy distribution, respectively, from the X-ray peak.

Acknowledgements

2.6 Appendix

2.6.1 Optical counterparts of compact and diffuse sources

To identify optical counterparts for the compact and diffuse radio sources in the field, we overlaid 608 MHz contours on Isaac Newton Telescope (INT) optical images (Fig. 2.21). The images are composites of Wide-Field Camera images taken in the B, V, R and I filters between October 1-8, 2009. The total integration times per filter is ~ 4000s. The data were flat-fielded and bias-corrected with IRAF (Tody 1993) and the *mscred* package (Valdes 1998). The I and R band images were also fringe corrected. We removed cosmic rays and other artefacts by rejecting pixels above $3.0\sigma_{\text{rms}}$.

2.6.2 Spectral index and curvature error maps

In order to evaluate the uncertainties in the pixel-by-pixel spectral index and spectral curvature values, we produced error maps. Values in Figs. 2.22 and 2.23 represent 1σ uncertainties in the spectral index as resulting from the linear fit of the logarithm of the flux measurements as function of log frequency.

In the fitting procedure, errors on the flux consisted of 10% absolute flux calibration added in quadrature to the RMS noise. Figure 2.24 presents the curvature uncertainty, which is the average of the errors in the high and low frequency spectral index fits (these are subtracted to obtain the curvature values).
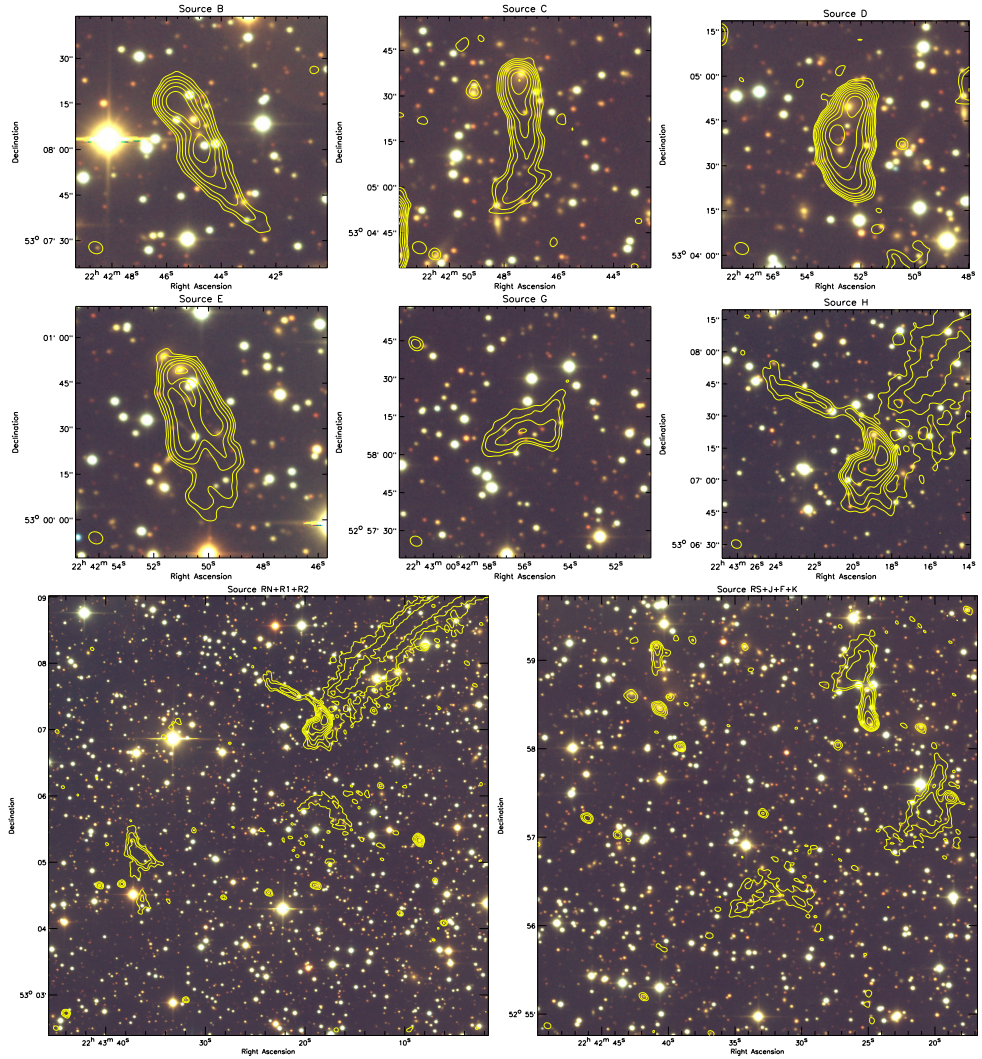
Figure 2.21: Optical images from the INT telescope. Contours from 608 MHz are overlaid at $[4, 8, 16, 32, 64, 128, 256, 512, 1024] \times \sigma_{\mathrm{RMS}}$ level. Sources are labelled as in Fig. 2.4
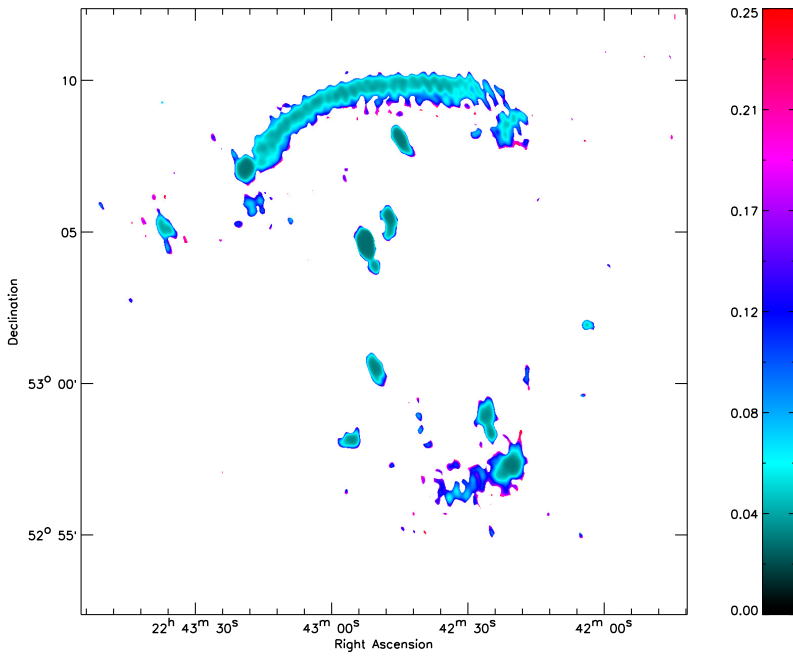
Figure 2.22: Spectral index error map corresponding to Fig. 2.14.
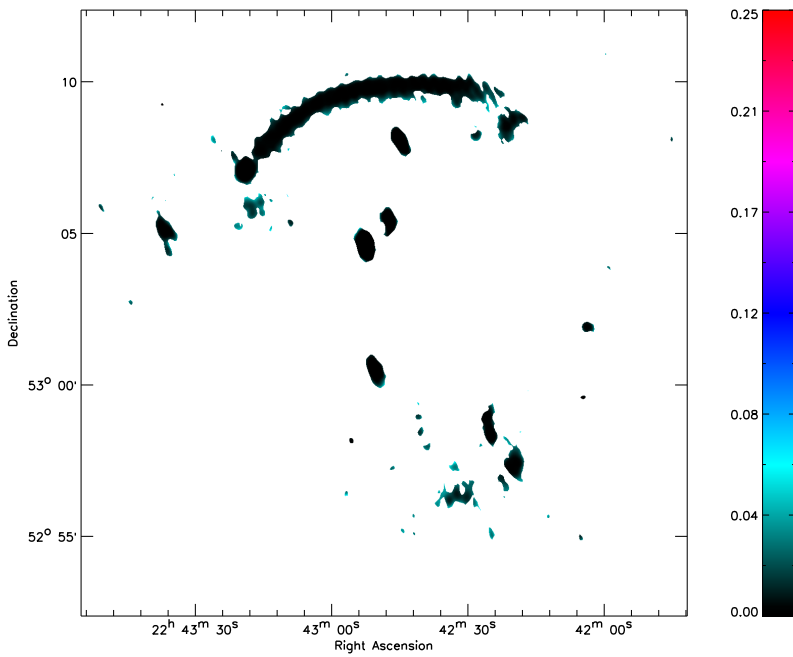
Figure 2.23: Spectral index error map corresponding to Fig. 2.15.
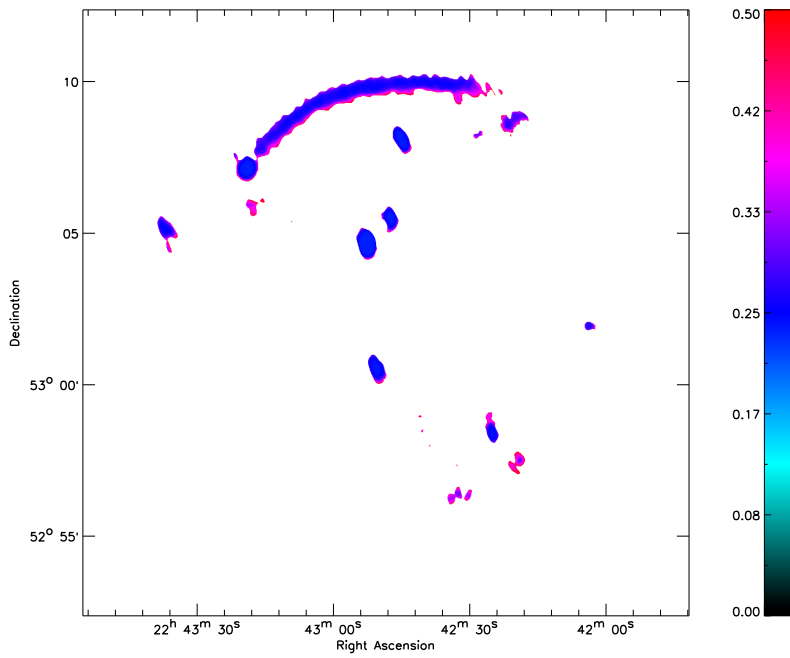
Figure 2.24: Spectral curvature error map corresponding to Fig. 2.16.

3

Spectral age modelling of the 'Sausage' cluster radio relic

CIZA J2242.8+5301 is a post-core passage, binary merging cluster that hosts a large, thin, arc-like radio relic, nicknamed the 'Sausage', tracing a relatively strong shock front. We perform spatially-resolved spectral fitting to the available radio data for this radio relic, using a variety of spectral ageing models, with the aim of finding a consistent set of parameters for the shock and radio plasma. We determine an injection index of $0.77^{+0.03}_{-0.02}$ for the relic plasma, significantly steeper than was found before. Standard particle acceleration at the shock front implies a Mach number $M = 2.90^{+0.10}_{-0.13}$, which now matches X-ray measurements. The shock advance speed is $v_{shock} \approx 2500$ km s^{-1}, which places the core passage of the two subclusters $0.6 - 0.8$ Gyr ago. We find a systematic spectral age increase from 0 at the northern side of the relic up to ~ 60 Myr at ~ 145 kpc into the downstream area, assuming a 0.6 nT magnetic field. Under the assumption of freely-ageing electrons after acceleration by the 'Sausage' shock, the spectral ages are hard to reconcile with the shock speed derived from X-ray and radio observations. Re-acceleration or unusually efficient transport of particle in the downstream area and line-of-sight mixing could help explain the systematically low spectral ages.

3.1 Introduction

3.1.1 Cluster radio relics

Acceleration of particles at shock fronts is an ubiquitous phenomenon in astrophysical contexts (e.g. Bykov et al. 2012). In the presence of magnetic fields, particles accelerated to relativistic speeds generate synchrotron radiation. Most of the observed radio emission in objects ranging from supernova remnants (SNR) to active galaxies and clusters of galaxies is due to synchrotron processes (Rybicki & Lightman 1979). Magnetic field strengths, shock strengths and spatial scales vary enormously between these different object classes. Shock fronts in SNR have Mach numbers of the order of 1000, but are limited in size to a couple of parsecs (e.g.; Reynolds 2008). In radio galaxies and quasars, particle transport occurs via a jet terminating in a $M \sim 10 - 100$, kpc-long shock (Bridle & Perley 1984). Some of the weakest (Mach number of a few), but most extended (Mpc-wide) observable astrophysical shocks are found in the intracluster medium (ICM) of clusters (see reviews by Brüggen et al. 2012; Feretti et al. 2012; Brunetti & Jones 2014). Galaxy clusters thus offer us the possibility to study the physics of weak shocks.

Since most of their observable mass is in the form of diffuse gas located in between the galaxies, clusters possess a huge reservoir of particles that could radiate synchrotron emission in the presence of magnetic fields and an accelerating shock. Shocks are expected given the violent merger history undergone by massive clusters within hierarchical structure formation (Sarazin 2002). Relatively strong (a few 10^{-10}T) magnetic fields can be found out to the outskirts of clusters which, in the presence of shocks, enable the production of synchrotron emission (e.g. Bonafede et al. 2009, 2010).

Direct evidence for shock-accelerated particles has been found at the periphery of approximately 40 merging clusters in the form of diffuse, extended, polarized, synchrotron emission (Feretti et al. 2012). These objects are known as giant radio relics. Sensitive observations show that, in the case of well behaved, non-disrupted, arc-like shocks, the spectral index of the radio emission becomes steeper from the shock into the downstream area. Examples include Abell 2744 (Orrú et al. 2007), Abell 521 (Giacintucci et al. 2008), CIZA J2242.8+5301 (van Weeren et al. 2010; Stroe et al. 2013) and 1RXS J0603.3+4214 (van Weeren et al. 2011b). The particles are thought to be accelerated via diffusive shock acceleration (DSA; Drury 1983) to a power law energy distribution at the shock front, which results in a power-law radio spectrum (with the slope called the 'injection index'). With time, under the effect of radiative losses which are proportional to the energy of the particle squared, the higher energy electrons preferentially cool, leading to a steepening of the spectrum at the higher frequencies (Rybicki & Lightman 1979).

3.1.2 The 'Sausage' cluster

CIZA J2242.8+5301 is a cluster that hosts a varied collection of bright, diffuse sources, including twin, double radio relics and smaller, patchy extended sources (for source labelling see Stroe et al. 2013). The peculiar morphology of the northern relic garnered the nickname the 'Sausage': the source has an arc-like shape, thought to trace a spherical shock, seen in projection, moving towards the north. van Weeren et al. (2010) performed a detailed study of the 'Sausage' relic and discovered steepening of the spectral index from the front towards

the back of the shock (north to south). They concluded that the source, at least in proximity to the shock front, is permeated by a coherent, aligned, strong magnetic field of $0.5 - 0.7$ nT. On the basis of spectral index and curvature maps and colour-colour plots, Stroe et al. (2013) concluded that the observed emission at each location within the relic is well described by a single injection spectrum with subsequent spectral ageing. The spectral analysis suggested that the outer edge of the northern relic is traced by a shock of Mach number 4.58 ± 1.09. The plasma trailing behind the shock shows systematic steepening of the spectrum further into the downstream area, indicative of spectral ageing. X-ray observations from the *XMM-Newton*, *Suzaku* and *Chandra* telescopes indicate the presence of weak discontinuities coinciding with the location of the radio shocks (Akamatsu & Kawahara 2013; Ogrean et al. 2013a; Ogrean et al. 2013b, 2014a). These discontinuities indicate a much weaker shock strength than the radio: $M \sim 2.5$. The shocks were also found to possibly interact with the cluster galaxies, boosting the Hα luminosity function of galaxies near the radio relics (Stroe et al. 2014a), leading to enhanced numbers of bright star-forming galaxies when compared to blank fields.

3.1.3 Main questions and aim of this paper

The general properties of relics have been broadly measured, but there are many open questions that have to be addressed (see review by Brunetti & Jones 2014). Does the relationship often expected between the injection α_{inj} and integrated index at high radio frequencies hold α_{int} ($\alpha_{int} - \alpha_{inj} = 0.5$, where $F_\nu \propto \nu^{-\alpha}$) hold (e.g. Pacholczyk 1970; Miniati 2002), given that the high-frequency integrated index of relics varies depending on the frequency window (Stroe et al. 2014b)? Is DSA efficient enough at low Mach numbers to inject/accelerate enough electrons to explain the total radio emission (e.g. Kang et al. 2007, 2012)? How can we explain the discrepancy between the radio and X-ray detected shocks, where the X-ray Mach number is systematically lower than the radio one (Akamatsu & Kawahara 2013; Ogrean et al. 2013a; Ogrean et al. 2013b, 2014a)? How are strong magnetic field generated within radio relics? Why is the surface brightness so uniform along some radio relics?

To address some of these questions we need to measure physical parameters such as the injection index, Mach number and spectral age precisely. The 'Sausage' relic is a bright, well resolved cluster relic, with excellent radio data available, which enables us to test spectral ageing models. In this paper we derive a consistent set of well understood physical parameters using some of the highest quality radio data available for any radio relic.

We present a spectral ageing analysis of the 'Sausage' relic using six radio frequency maps from the Giant Metrewave Radio Telescope (GMRT) and the Westerbork Synthesis Radio Telescope (GMRT) presented by Stroe et al. (2013), and references therein. Using the Broadband Radio Astronomy ToolS (BRATS[1]; Harwood et al. 2013), we fit spectral ageing models at the pixel-by-pixel level, with the aim of determining the physical model that best describes the spectral properties and morphology of the source. In order to do so, we test the Jaffe-Perola (JP; Jaffe & Perola 1973) and the Kardashev-Pacholczyk (KP; Kardashev 1962; Pacholczyk 1970) models of spectral ageing, which assume a single burst of electron injection, followed by radiative losses in a constant magnetic field. While the KP model assumes that the pitch angle between the electrons and the magnetic field stays constant over time, the JP model is more realistic in that it allows for the isotropisation of the pitch angle. We also test the

---

[1] http://www.askanastronomer.co.uk/brats/

Table 3.1: Sensitivity of the images used for the analysis of the 'Sausage' relic.

Frequency (MHz)	RMS μJy beam^{-1}	Telescope
153	1800	GMRT
323	240	GMRT
608	48	GMRT
1221	58	WSRT
1382	20	WSRT
1714	33	WSRT

more complex Tribble model, which accounts for emission arising from the more physically plausible case of an electron population subject to a spatially inhomogeneous magnetic field (Tribble 1993; Hardcastle 2013; Harwood et al. 2013). For the first time we derive precise injection indices (α_{inj}), the Mach numbers (M) and the ages of the electrons (t_{age}, time since last acceleration) in a self-consistent way using model fits to many different regions of the relic.

The structure of this paper is the following: in Section 3.2 we give an overview of the observations, in Section 3.3 we present the parameters and models tested with BRATS and in Section 3.4 we discuss the effect of finite resolution on our results. In Section 3.5 we discuss the results of the model fitting and the derived physical properties and the implications for cluster relics and ICM properties. The main results are summarised in Section 3.6. We assume a flat, ΛCDM cosmology with $H_0 = 70.5$ km s^{-1} Mpc^{-1}, matter density $\Omega_M = 0.27$ and dark energy density $\Omega_\Lambda = 0.73$ (Dunkley et al. 2009). At the 'Sausage' redshift of 0.19, 1 arcmin on the sky measures 0.191 Mpc. All images are in the J2000 coordinate system.

3.2 Observations and imaging

The 'Sausage' cluster was observed at eight radio frequencies spanning between 153 MHz and 16 GHz with the GMRT, WSRT and the Arcminute Microkelvin Imager telescopes between 2009 and 2013. A full description of the observations and data reduction is given by Stroe et al. (2013) and Stroe et al. (2014b). The flux calibration error on these maps was taken to be 10 per cent.

The 16 GHz AMI data of the relic published by Stroe et al. (2014b) is not suitable for fitting of spectral ageing models on a pixel-by-pixel basis, as the relic downstream area is not resolved. Hence the 16 GHz is not used the following analysis.

The WSRT measurements were taken in a single configuration. Due to the scaling of the angular sizes sampled by the same telescope configuration at different frequencies, the 2272 MHz data has the sparsest inner uv-coverage. This effectively means that the interferometer might be resolving out some parts of the largest scale diffuse emission. The brightness distribution of the 2272 MHz map is dominated by small-scale features (~ 30 kpc), an effect which is not seen in the lower frequency maps. We attribute this to the poor uv-coverage. In addition, because of the steep spectrum of the relic and the enhanced noise levels, the S/N in
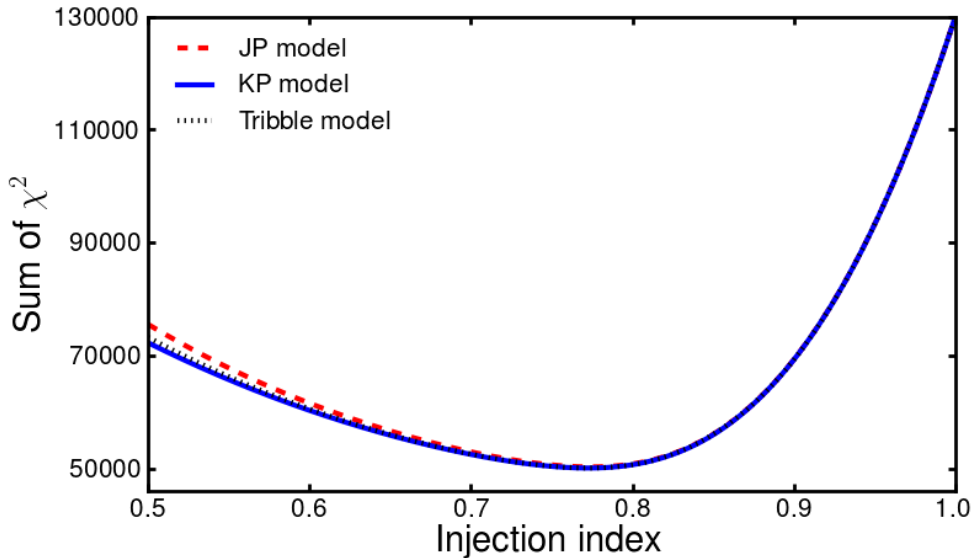
Figure 3.1: χ^2 value for varying injection index for the three injection models fitted with cubic splines. The JP is shown in the red, dashed line, the KP in a solid, blue line, while the Tribble is traced by a dotted, black line.

the 2272 MHz map is poor. Therefore, we prefer to map as much of the diffuse emission as possible using six radio frequencies and remove the 2272 MHz map from further analysis.

To ensure recovery of flux on the same spatial scales for the GMRT (153, 323, 608 MHz) and WSRT (1221, 1382, 1714 MHz) observations, we kept data on common uv-distances for all the remaining six frequencies. Data taken below 0.2 kλ was discarded, which limits the largest detectable radio features on the sky to approximately 17 arcmin in size. The data at each frequency was then imaged using multi-frequency-synthesis and uniform weighting at a common pixel scale of 1 arcsec pixel^{-1} and resolution of 18.0 arcsec×14.8 arcsec.

The central frequencies and root-mean-square (RMS) noise values of the images used in further analyses are given in Table 3.1.

3.3 Spectral age fitting with BRATS

As mentioned in Section 3.1, we have used the BRATS package to fit the JP, KP and Tribble models pixel-by-pixel in six frequency maps. We refer the interested reader to the work by Harwood et al. (2013) where a description of the BRATS software and its capabilities can be found.

The radio images of the 'Sausage' relic were loaded into BRATS, imposing a 5σ cutoff level of the radio emission based on the off-source RMS noise (see Table 3.1). The on-source S/N was high enough such that spectra could be fitted on a pixel-by-pixel basis, over 13999 pixels or an equivalent of almost 50 independent beams. As shown by Harwood et al. (2013), it is of utmost importance to use small regions for fitting synchrotron radio spectra, in order to

minimise effects of averaging across electron populations with different ages.

Spectral ageing models have four free parameters (flux normalisation, magnetic field B, injection index α_{inj}, time since last acceleration t_{age}). We set the magnetic field input value to 0.6 nT, as derived by van Weeren et al. (2010).

Note that inverse Compton losses because of interactions with the cosmic microwave background (CMB) are important and the code takes these effects into account. This interaction acts as an additional magnetic field B_{CMB}, added in quadrature to the magnetic field B that permeates the source. The CMB energy density in B field terms is (Longair 2010)

$$B_{CMB} = 0.318(1+z)^2 nT \tag{3.1}$$

where the redshift is $z = 0.19$. The equivalent magnetic field for the inverse Compton interactions at $z = 0.19$ is $B_{CMB} = 0.45$ nT.

We fit the JP, KP and Tribble model for a range of injection indices, keeping the flux normalisation and spectral age (time since last acceleration) as free parameters. We perform a broad index injection search between 0.5 and 1.0 in steps of 0.1, followed by a fine search between the initial minima of 0.7 and 0.8 in steps of 0.01. We note that the assumed magnetic field strength of 0.6 nT (as derived by van Weeren et al. 2010) does not affect the measurement of the injection index.

The goodness of fit (sum of χ^2) dependence on the assumed injection index contains a single minimum (see Fig. 3.1). We fix the injection index to the value where the fit reaches the minimum χ^2, i.e. where the model best describes the source brightness distribution.

An injection index of $\alpha_{inj} = 0.77$ minimises the χ^2 summed over all the regions for all three models. As shown in Fig. 3.1 the χ^2 curve is well known, hence the uncertainty in the injection index can be calculated using the method of Avni (1976) who shows that the 1σ error is given by a change in the χ^2 value from its minimum of $\Delta\chi^2 = 1$. However, as we are considering the source on a pixel-by-pixel basis, the sum of χ^2 is over weighted by a factor of the beam area A_{beam}. Assuming the injection index is approximately constant across the source, the errors on the injection index are therefore found by determining a $\Delta\chi^2$ of 1 for the corrected value given by $\chi^2_{cor} = \chi^2_{min}/A_{beam}$. This gives an injection index value for the 'Sausage' relic of $0.77^{+0.03}_{-0.02}$.

We fix the injection index value to 0.77 and run a final JP, KP and Tribble model fitting to obtain the best-fitting pixel-by-pixel spectral age t_{age} and its corresponding χ^2 map. The models have the same goodness-of-fit. The results for the three models are similar, with variations in ages of the order of 10% (see Fig. 3.2 for the Tribble model results).

3.4   Impact of finite resolution

We performed simulations to study how the intrinsic spectral ages and the injection index we derive for our 'Sausage' data are affected by the convolution of the 'true', intrinsic image with the beam of the telescope.

In order to test this effect, we modelled the 'Sausage' relic as a rectangular slab with a thin injection area with a corresponding 0.77 injection index, followed by JP spectral ageing, according to a shock advance speed of ~ 1500 km s^{-1} (see Section 3.5 for the derivation of these parameters from the real data). The JP, rather than the KP or Tribble models was used for
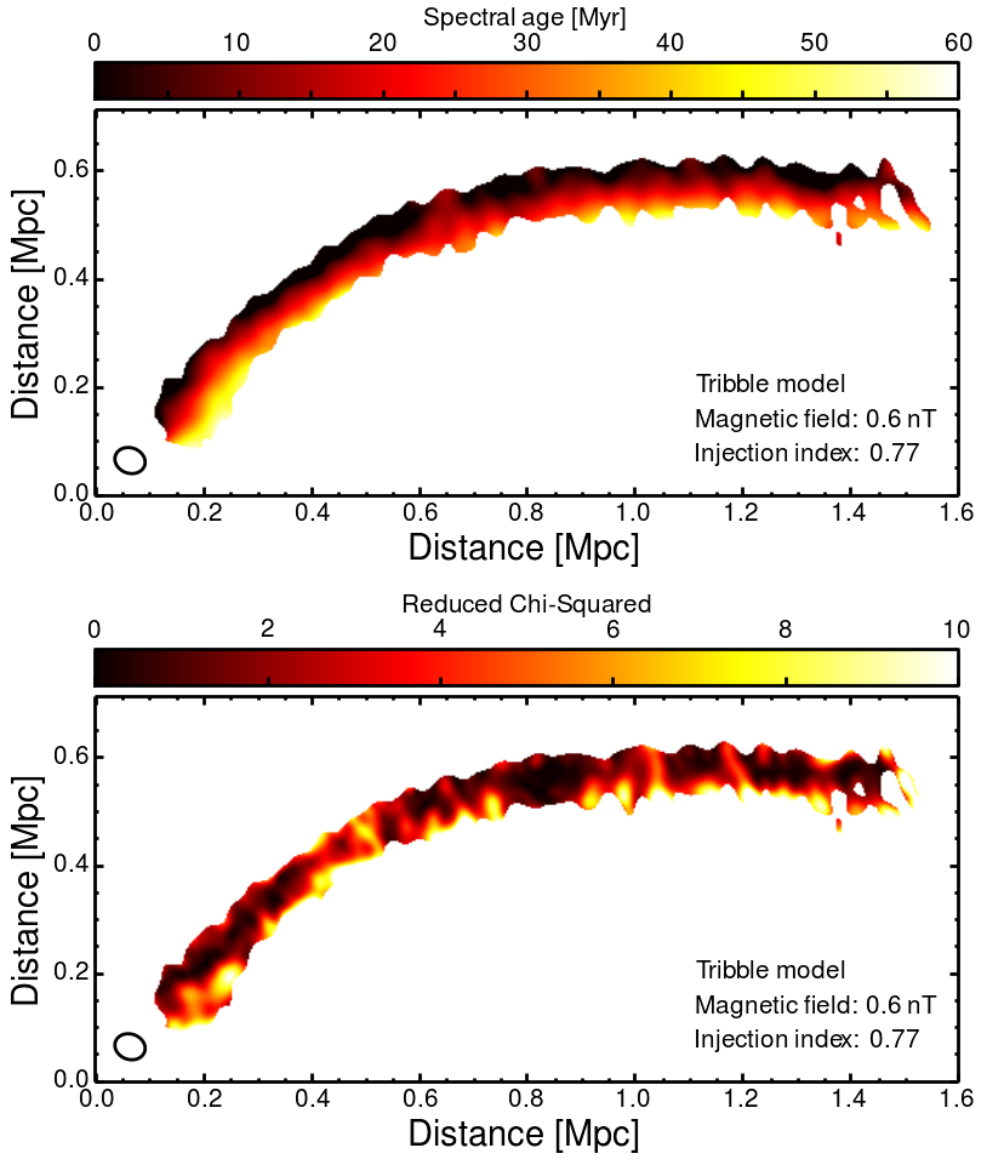
Figure 3.2: Tribble spectral ageing maps at the top and associated χ^2 maps at the bottom, using a magnetic field value of 0.6 nT, derived by van Weeren et al. (2010). The 18.0 arcsec ×14.8 arcsec beam is shown in the bottom-left corner of each image. Note that three models give similar results with a scaling of the ages: the Tribble model predicts the oldest ages, while the KP the youngest.

Table 3.2: 'Sausage' relic ageing model fitting results. The 0.6 nT magnetic field has been derived by van Weeren et al. (2010). The maximum lifetime of electrons is obtained for a 0.26 nT magnetic field (see Section 3.5.5 for details). 'Model' lists the model fitted for the corresponding row. 'Mean χ^2' lists the average χ^2 over the entire source with an equivalent reduced value shown in the 'Mean χ^2_{red}' column. 'Max age' shows the maximum age (time since last acceleration) we could map for each model. Given the S/N cut, we could map emission down to $\sim 10\%$ of the peak flux level in the downstream area. The last column represents the error on the maximum age.

Model	B field (nT)	Mean χ^2	Mean χ^2_{red}	Max Age (t_{age}) (Myrs)	± (Myrs)
JP	0.6	3.60	0.90	53.3	3.7
KP	0.6	3.58	0.90	54.2	3.7
Tribble	0.6	3.58	0.90	59.4	3.7
Tribble	0.26	3.58	0.90	83.1	5.8

processing power considerations. The KP model involves the calculation of an extra $\sin^2(\alpha)$ term, compared to the JP. The JP model entails two numerical integrations, and is therefore much faster than the Tribble, which requires an extra numerical integration over the Maxwell-Boltzmann distribution (Hardcastle 2013). Maps at the six frequencies (153, 323, 608, 1221, 1382 and 1714 MHz) were simulated, adding noise as measured in the real GMRT and WSRT maps. The model maps were convolved to 1^2, 2^2, 4^2, 8^2 and 18.0×14.8 arcsec beams. The five sets of maps were run through BRATS, in a similar fashion to the real data. We expect the parameters that we used in the simulations to be representative of the ones recovered from our data, but in any case, no matter which shock speed, magnetic field or model is assumed, the conclusions we draw from our simulations should be similar, apart from a multiplicative factor in the ages determined.

We searched for the best injection index via χ^2 minimisation and found that the 0.77 injection index is correctly recovered irrespective of resolution (see Fig. 3.3). The determination of the injection index is dominated by the spectrum at the lowest frequencies, where not much spectral curvature is expected. Moreover, all of the pixels in our radio maps are independently best-fitted by a model traced back to the injection spectrum of 0.77. We conclude that the injection index estimation in our real GMRT and WSRT maps is robust and consistent with the intrinsic injection index that would be recovered with an infinite-resolution telescope. The injection index can be recovered as long as the ageing, downstream area is still well resolved over at least $2 - 3$ beams across.

An important point to make is the noticeable effect of the beam convolution on the spectral index maps (see Fig. 3.4). Close to the injection area, the correct index is recovered in the higher resolution maps (up to 2 arcsec). As the beam size increases, the injection area is not resolved and the mixing of noise with fresh plasma leads to a flattening of the measured spectral index, up to ~ 0.6, in parts of the injection area. A noise maximum or minimum on top of radio emission in one of the radio maps can lead to an over-estimation or under-estimation of the spectral index within that region. For example, if our lower frequency map suffers from a

negative noise peak this artificially flattens the radio spectrum. The mixing of real emission with noise right in front of the shock, depending on the noise properties in each map, can also lead to a flattening of the measured injection index. This then naturally explains what is seen in the real 'Sausage' data, where the spectral modelling finds a best injection index of 0.77, while in the spectral index maps we measure values of about $0.60 - 0.65$ (Stroe et al. 2013). All previous studies of radio relics (e.g. MACSJ1149.5+2223, MACSJ1752.0+4440, Abell 521, Abell 2744, Abell 754, CIZA J2242.8+5301, 1RXS J0603.3+4214; Orrú et al. 2007; Giacintucci et al. 2008; van Weeren et al. 2010; Macario et al. 2011; van Weeren et al. 2011b; Bonafede et al. 2012; Stroe et al. 2013) use the flattest index measured in the spectral index map as the injection index or calculate the injection index from the integrated spectral index. The integrated spectral index of the 'Sausage' relic has been shown to vary significantly depending of the observed frequency window (Stroe et al. 2014b). We therefore caution against using the spectral index map or integrated index as a proxy for injection index determination.

We also tested the effect of resolution on the age determination (see Figs. 3.5 and 3.6). Decreasing the resolution of the radio data leads to mixing of different electron populations within an observed beam. With a decrease of resolution, the low-frequency spectrum index of each given region within the relic gets steeper, while its high-frequency index is measured as flatter, pushing the radio spectrum to a power-law. Therefore, this is equivalent to underestimating the curvature of the spectrum at high frequencies. While for lower-resolution images, the injection index derived is the same as in the higher-resolution maps, there is an effect of overestimating the spectral age, hence underestimating the spectral speed. For example, if we decrease the resolution from 1^2 arcsec to 18.0×14.8 arcsec, the derived age increases by ~ 10 per cent. These simulations at the lowest resolution, 18.0×14.8 arcsec, are comparable to our real GMRT and WSRT maps. 10 per cent is well within our measurement error in the real maps. Therefore resolution effects will not play a major role in our age measurements.

3.5 Discussion

3.5.1 Best-fitting model?

We fit the JP and KP models of spectral ageing, along with the more recent Tribble model directly to six radio-frequency data of the well-studied 'Sausage' relic, to derive a consistent set of shock parameters.

The three models have similar goodness of fit, with a mean $\chi^2 = 3.6$. All three models fit the data equally well. Nevertheless, we would expect, given the well-ordered magnetic fields measured in proximity to the 'Sausage' shock front, that the JP or KP would provide the better fit. Since the constant pitch angle of the KP is a less physically plausible scenario, the JP would be the preferred model. Stroe et al. (2013), by using a colour-colour analysis, concluded that the best description of the data was given by a superposition of JP models with different age. However, the comparison to the spectral ageing models was done on large areas, summing up many pixels with similar spectral index properties to increase S/N. This techniques does not allow the probing of the extremely steep spectrum plasma in the downstream area which would have allowed conclusive discrimination between the JP and KP model (the Tribble model was not tested by Stroe et al. 2013).

The source is highly-polarised (60 per cent) towards the location of the shock (van Weeren
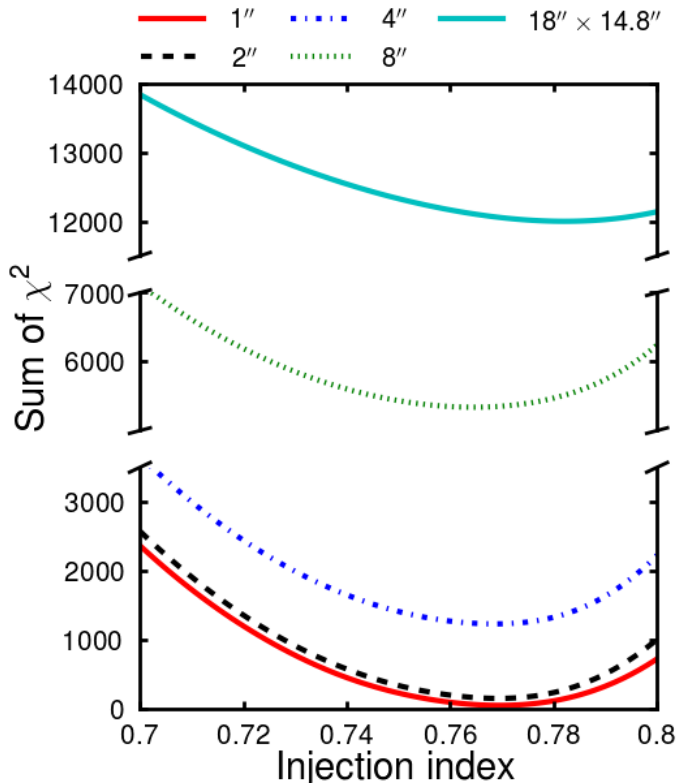
Figure 3.3: χ^2 value for varying injection index calculated for the simulated data, at five different resolutions. All models minimise at a $0.77 - 0.78$ injection index. The higher resolution maps have lower noise, hence lower χ^2 values.

et al. 2010), but this is not necessarily true for the much fainter downstream area. The measurement of the polarisation is dominated by the high surface brightness plasma close to the shock front. The amplification and alignment of the magnetic field vectors is likely a result of shock compression (e.g Iapichino & Brüggen 2012). While this is a reasonable assumption close to the shock front, in the downstream area there is the possibility of highly-turbulent magnetic fields, which motivates the use of a Tribble-like model. Steepening of the integrated relic spectrum towards 16 GHz also supports a scenario which includes either turbulent magnetic fields or ICM inhomogeneities (Stroe et al. 2014b).

In further analyses, parameters will be derived according to the best-fitting Tribble model.

3.5.2 Injection index

Assuming a Tribble model, we will derive a number of physical parameters for the 'Sausage' shock. The injection index $0.77^{+0.03}_{-0.02}$ we calculate is significantly steeper (6σ away) than what was found before from spectral index mapping and colour-colour plots ($\alpha_{\mathrm{inj}} = 0.65 \pm 0.05$; van Weeren et al. 2010; Stroe et al. 2013). The discrepancy between the steep injection index

derived from spectral modelling and the old measurement can be explained by convolution effects, as shown in Section 3.4.

3.5.3 Mach number

The Mach number M of a shock moving through a medium at speed v_{shock} is defined as

$$M = \frac{v_{\text{shock}}}{c_s} \tag{3.2}$$

where c_{s} is the sound speed in the upstream medium.

For simple shocks, the Mach number can be related to the radio injection index by (Blandford & Eichler 1987)

$$M = \sqrt{\frac{2\alpha_{\text{inj}} + 3}{2\alpha_{\text{inj}} - 1}} \tag{3.3}$$

Hence, for $\alpha_{\text{inj}} = 0.77^{+0.03}_{-0.02}$ (see Sect 3.5.2), we derive a Mach number of $2.90^{+0.10}_{-0.13}$ for the relic.

A number of papers based on *XMM-Newton* and *Suzaku* data (Akamatsu & Kawahara 2013; Ogrean et al. 2013a; Ogrean et al. 2013b, 2014a) reported a possible discrepancy between the X-ray and the radio shock Mach numbers (e.g. van Weeren et al. 2010; van Weeren et al. 2012b; Stroe et al. 2013). In the case of the 'Sausage' relic, the X-ray Mach number based of Suzaku data is $2.54^{+0.64}_{-0.43}$ (Ogrean et al. 2014a). Hence, the Mach number derived from the X-ray data also favours a steep injection index, close to 0.8 (via equation 3.3).

The weaker shock strength found here using spectral fitting would reconcile the differences found between radio and X-ray derived shock parameters for this radio relic. DSA happens to all charged, high energy particles when they encounter a collisionless shock too thin to capture them and depends only on the particle rigidity (momentum per charge). Simple DSA assumes that thermal particles are injected. Because of the much higher rigidity of thermal protons compared to thermal electrons, the injection efficiency of thermal protons is much higher than that of thermal electrons. For example, the electron efficiency for strong shocks ($M \gg 10$) is much lower than that of protons, at a ratio of ~ 0.001 (Brunetti & Jones 2014). If such a low DSA electron acceleration efficiency is assumed, the weak Mach number derived in this paper challenges even more the simple DSA theory of thermal particle acceleration proposed for radio relics. In the case of weak shocks ($M \ll 10$), the electron efficiency is not well constrained (Brunetti & Jones 2014). Simple DSA could in principle be reconciled with a low Mach number, given a very high electron efficiency, close to that of protons. Alternative theories including an injection of pre-accelerated rather than thermal particles (e.g. Kang et al. 2012), turbulent re-acceleration (pre-accelerated relativistic particles upstream can be maintained by several mechanisms including turbulent re-acceleration, e.g. Brunetti et al. 2001) or intermittent/highly turbulent magnetic fields could also explain the high level of radio emission, even with a low Mach number shock (e.g. Iapichino & Brüggen 2012). Our results also seem to support the simulations by Bykov et al. (2008) and Kang et al. (2012), which predict that a $M \approx 2$ shock could inject enough particles to reproduce the level of radio emission observed in the Sausage cluster, given a pre-existing low-energy, cosmic ray electron population.
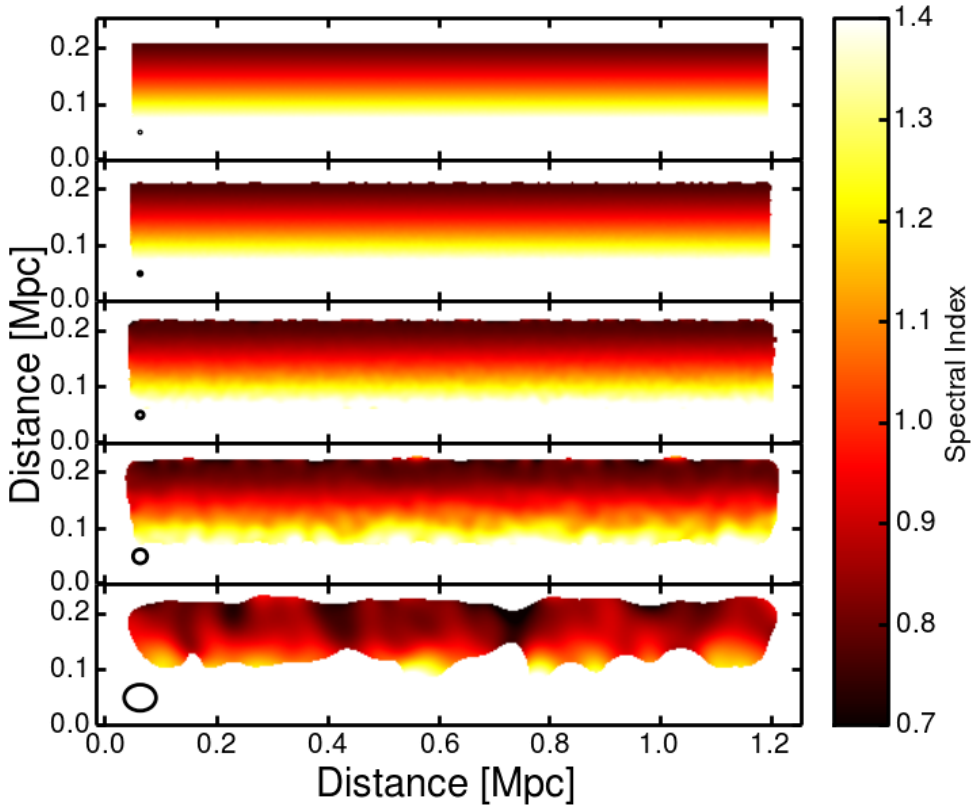
Figure 3.4: Spectral index maps calculated for the simulated data by fitting power laws through the six frequencies. The data are in ascending beam size from top to bottom. The beam is shown in the bottom-left corner of each image.

3.5.4 Shock and ageing speed from spectral modelling

The shock advance speed can be derived from the Mach number, in two independent ways, by using radio and X-ray data.

The X-ray ICM gas temperature in the upstream of the 'Sausage' shock front has been measured by Ogrean et al. (2014a) using *Suzaku* to be $3.35^{+1.13}_{-0.72}$ keV. Using the conversion $c_s = 1480\sqrt{T/(10^8 K)}$ km s^{-1} from Sarazin (1986), this results in a sound speed $c_s = 920^{+150}_{-110}$ km s^{-1} . The Mach number derived from the X-ray temperature data is: $M = 2.54^{+0.64}_{-0.43}$ (Ogrean et al. 2014a), thus a shock advance speed of $v_{shock} = 2340^{+700}_{-490}$ km s^{-1}.

A second measure of the shock speed can be obtained from the particle acceleration analysis. The new radio Mach number of $M = 2.90^{+0.10}_{-0.13}$ constrains the shock speed to $v_{shock} = 2670^{+450}_{-340}$ km s^{-1}.

With the injection index and X-ray Mach numbers being in agreement, we have two independent measurements of shock advance speeds in the context of cluster shock waves. We place the preferred shock speed v_{shock} at the average value between these two methods at
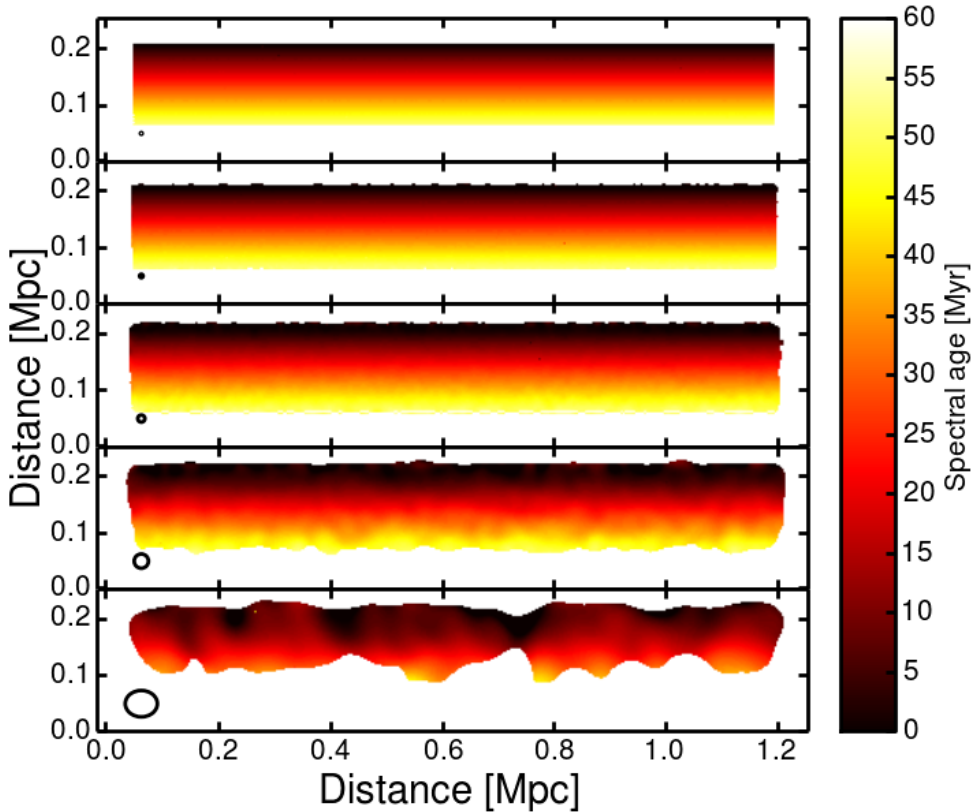
Figure 3.5: JP spectral ageing maps for the simulated data. The data are in order of ascending beam size from top to bottom: 1^2, 2^2, 4^2, 8^2, 18.0×14.8 arcsec. The beam is shown in the bottom-left corner of each image.

≈ 2500 km s^{-1}.

The spectral ageing data can also be used to derive a measurement of the ageing speed v_{age}, the speed at which the particles in the downstream area of the shock flow away from the shock, in the shock reference frame.

Standard shock physics says (Blandford & Eichler 1987)

$$v_{\text{age}} / v_{\text{shock}} = \frac{\gamma - 1 + 2/M^2}{\gamma + 1} \tag{3.4}$$

where v_{age} is the ageing speed (the speed at which the plasma flows away from the shock), v_{shock} is the shock upstream of the shock, i.e. the shock advance speed itself. $\gamma = 5/3$ is the ratio of specific heats and M is the Mach number. Therefore, the ageing speed is

$$v_{\text{age}} = c_s \frac{\gamma M - M + 2/M}{\gamma + 1}. \tag{3.5}$$

Given the Mach number derived above ($M = 2.90$) and $c_s = 920$ km s^{-1}, this leads to an expected ageing speed $v_{\text{age}} = 905^{+165}_{-125}$ km s^{-1}.
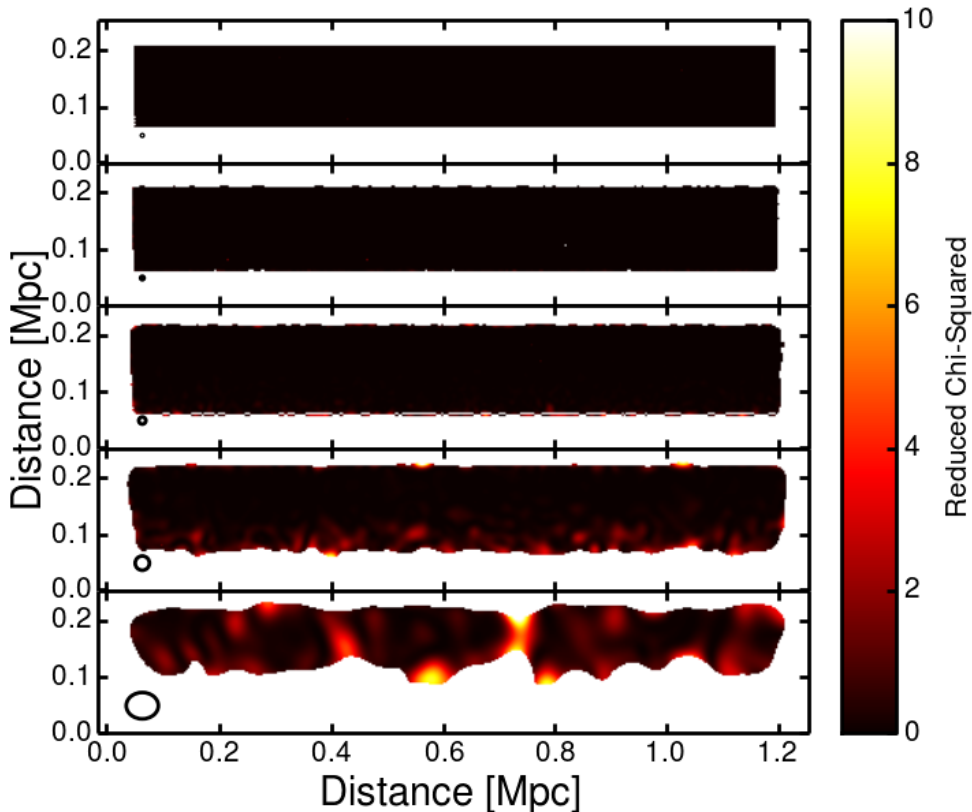
Figure 3.6: χ^2 maps associated to the JP spectral ageing fits to the simulated data. The data are in order of ascending beam size from top to bottom: 1^2, 2^2, 4^2, 8^2, 18.0×14.8 arcsec. The beam is shown in the bottom-left corner of each image.

3.5.5 Spectral age

In this section we consider the constraints on spectral age and magnetic field strength imposed by the observations.

Spectral age

Given the newly determined injection index (0.77) and assuming a magnetic field strength of 0.6 nT, we can derive spectral ages using the Tribble model (as explained in Sec 3.5.1).

We see clear ageing from north to south across the source, i.e. from the front of the shock front into the downstream area (left column of Fig. 3.2). The age t_{age} (time since initial acceleration) increases systematically across the source, with pixels located at the same projected distance from the expected location of the shock front having the same spectral age, meaning they were last accelerated at the same time. The ages along the length of the source are very similar at the same distances from the location of the shock (variations given by the noise are below 9 per cent). The age depends linearly on the distance from the shock front,

indicating that the shock speed has stayed constant for the past tens of Myr.

With a magnetic field of 0.6 nT, the maximum age is $\sim$ 60 Myr (see Fig 3.2). There are some age variations that come from small-scale, beam-size age variations across the length of the source (maximum of 5 Myr), which coincide with noise peaks in the 153 MHz map. This was also noted in the context of spectral index maps by Stroe et al. (2013). By excluding these peaks, we can see that the spectral speed varies little along the length of the relic, with a standard deviation of 300 km s^{-1}. To increase S/N, we average pixels along concentric circles fitted to describe the shape of the outer edge of the relic. The dependence of the average age with distance from the location of the shock front can be visualised in Figure 3.7. The typical standard deviation of pixels along these concentric circles is $\sim$ 3 Myr (per pixel). Assuming constant ICM temperature along the relic length, we can expect variations of at most 10 per cent in Mach number along the source.

While spectral index maps provide a proxy for spectral ageing, spectral steepening could be seen in some radio relics as a result of fortuitous superposition of filamentary radio structure. By using hydrodynamical simulations of cluster mergers, Skillman et al. (2013) argue that, even without prescribing spectral ageing, it is possible to observe spectral index trends caused by unrelated shock structures with different Mach numbers, seen in fortuitous projection at the same location. The authors therefore suggest that even the most basic assumptions of the formation mechanism of radio relics (shock-accelerated particles, with subsequent ageing) do not hold. In our analysis, we present the first direct measurement of aged plasma in the context of radio relics. We would like to stress that the age measurements are independently fitted on a pixel-by-pixel basis, therefore the systematic increase which is consistent across the entire 1.4 Mpc length of the source is undoubtedly a real effect, which cannot come from superposition of unrelated shock structures.

Magnetic field – constraints on spectral age

Spectral ageing models have four free parameters: flux normalisation, injection index α_{inj}, spectral age t_{age} and magnetic field strength B. Given a fixed flux normalisation F and injection index α_{inj}, to reproduce a given spectral shape at the high-frequency end, where losses dominate, the age of the electrons relates to the magnetic field in the following way (Tribble 1993; Hardcastle 2013):

$$t_{\mathrm{age}} = C(\alpha_{\mathrm{inj}}, F) \frac{\sqrt{B}}{B^2 + B^2_{\mathrm{CMB}}} \tag{3.6}$$

where $C(\alpha_{\mathrm{inj}}, F)$ is a constant that depends on the fixed flux normalisation and injection index, B is the source magnetic field and $B_{\mathrm{CMB}} = 0.45$ nT is the equivalent magnetic field exerted by the inverse Compton interactions at $z = 0.19$. By setting the derivative of equation 3.6 to 0, we can calculate the maximum lifetime of electrons t_{max} is obtained for a magnetic field

$$B = B_{\mathrm{CMB}} / \sqrt{3} \tag{3.7}$$

Equation 3.6 becomes:

$$t_{\mathrm{max}} \propto \frac{\sqrt{B_{\mathrm{CMB}}}}{\frac{4}{3} \sqrt[4]{3} B^2_{\mathrm{CMB}}} \tag{3.8}$$

The age obtained from the Tribble model fit with a 0.6 nT magnetic field at 10% flux level in the downstream area, or $\sim$ 150 kpc away from the shock location, is 59.4 Myr. t_{age} within

this equation has a clear maximum, attained for a magnetic field of 0.26 nT. By scaling the age using this magnetic field value, the maximum lifetime of electrons in the Tribble model is ~ 83.1 Myr, at a distance of ~ 150 kpc from the shock front.

Spectral age discrepancy

Our model fitting is sensitive to the time since the electrons population last underwent acceleration. Assuming the last agent of acceleration was the Sausage shock now located at the northern edge of the relic, the electrons should age freely in the magnetic field after the shock passage. The ageing speed v_{age}, or speed at which the electrons move away from the 'Sausage' shock in this scenario, is directly determined by t_{age} and the distance from the shock front. By taking into account the age dependence t_{age} on the distance d from the shock front, we can define an ageing speed $v_{age} = d/t_{age}$ (see Figure 3.7). At the distance of 150 kpc, the maximum lifetime of electrons is 83.1 Myr, hence the minimum ageing speed is ~ 1550 km s^{-1}. For any B field weaker or stronger than $B_{CMB}/\sqrt{3}$, the ageing speed must be higher (e.g. for 0.6 nT the speed rises to 2110 km s^{-1}).

Therefore, from our data, we can find a minimum on the speed at which the electrons can flow away from the shock front. The minimum ageing speed constrained here from the B field is $v_{age} > 1550$ km s^{-1}. Hence, the relationship between the shock speed and the ageing speed imposes $v_{age} = 905^{+165}_{-125}$ (derived in Section 3.5.4). These two derivations of the ageing speed are incompatible at $> 3\sigma$ level. This discrepancy suggests that the electrons are ageing too slowly given their distance from the northern edge of the 'Sausage' relic, in a scenario where the particles are last accelerated by the 'Sausage' shock front (see also Fig. 3.7).

Magnetic fields or turbulence?

In the spectral ageing models, magnetic field and ageing lifetime are interchangeable, as shown in Section 3.5.5. Therefore, we could bring the two ageing speeds into agreement by more closely inspecting these two parameters.

The magnetic field imposes a maximum electron lifetime, but from other constrains we expect the magnetic field to be significantly higher than the maximum electron lifetime B field of 0.26 nT. Estimates from simulated radio relic profiles from van Weeren et al. (2010) indicate a B field of $0.5 - 0.7$ nT. Rotation measure synthesis at similar cluster-centric distances for other clusters indicates values of $0.01 - 0.5$ nT (e.g. Clarke et al. 2001; Govoni et al. 2006; Bonafede et al. 2011). B can be increased by simple compression at the shock by up to the density compression factor (in the limit of a perpendicular shock), which is ~ 2.4 for the Mach number derived above; the fact that the Faraday-rotation-corrected B-field vectors are perpendicular to the shock (van Weeren et al. 2010) is consistent with a compression model, where the shock front magnifies and aligns the magnetic field vectors in its vicinity. Numerical modelling (e.g. Iapichino & Brüggen 2012) shows magnetic field amplification factors consistent with this in more realistic field configurations; it is possible that cosmic-ray-mediated magnetic field amplification, which would give a field increase over and above simple compression, occurs in relics in the same way as in supernova remnants (e.g. Völk et al. 2005). We have few other direct constraints on the field strength in the relic region. We have estimated from the *Chandra* data described by Ogrean et al. (2014a) an upper limit on the inverse-Compton emission which corresponds to a lower limit on the field strength of around

0.1 nT: this is extremely conservative because it attributes all the net X-ray emission from the relic region to the inverse-Compton process, whereas we would expect some of it to be thermal. The equipartition field strength in the relic region (assuming that the injection index that we measure extends to low energies) would be around 0.3 nT. Equipartition assumes that the energy is split between magnetic field energy and energy of the synchrotron electrons. This neglects the contribution to the energy density of the thermal protons and electrons, which is almost certainly dominant, so we can expect the real field strength to be higher than the equipartition value. Thus we conclude that the discrepancy between the two ageing speed determinations is likely even more substantial than what the limit on speed would indicate.

While testing the established JP, KP and Tribble models is a natural step forward from traditional techniques of spectral index maps and colour-colour plots, the ageing results are internally inconsistent, as shown above. There are a few effects that could ameliorate the inconsistency between the ageing solution and the shock speed. The following processes would affect the values of the ages derived in the downstream area of the shock.

Part of the discrepancy could be removed if, after the passage of the 'Sausage' shock front, there is another source of re-acceleration of the particles, which would bring the radio spectrum closer to an injection spectrum. However, re-acceleration would not necessarily allow the low-frequency, injection spectrum to remain unchanged (thus not preserving the measured injection index). Possible sources of re-acceleration in the case of radio relics could be through turbulence in the downstream area of the 'Sausage' shock or minor shock/instabilities created in the downstream area after the passage of the main shock front. Turbulence is also thought to be the main driver of re-acceleration within the ICM of merging clusters, leading to the formation of radio haloes, diffuse radio emission co-spatial with the X-ray emitting gas of some merging, luminous clusters (e.g. Brunetti et al. 2001). Small-scale turbulence would allow re-acceleration of particles, mimicking a spectral age lower than what would be expected from the distance to the 'Sausage' shock front, without leading to too much mixing of electron populations across the width and length of the relic. This way, the age gradient we observe across the radio relic could be preserved. Significant turbulence is expected in the downstream of merger shocks from simulations (e.g. Iapichino & Brüggen 2012). Higher-frequency, higher-resolution observations ($2 - 5$ GHz Very Large Array observations, van Weeren et al. in prep) would provide a good test for this theory, where spectral index fine structure across the relic is expected. Higher spatial resolution maps would also show saturating spectral index values with distance from the shock, as turbulence would overcome the ageing as soon as the ageing time approaches the turbulence acceleration time. However, there are challenges to this scenario. Firstly, the spectral evolution of a population of electrons undergoing re-acceleration via turbulence would most likely be different than what is expected from the JP, KP or Tribble models, which makes the good fits that we obtain using these models puzzling. Secondly, in the standard scenario only a relatively small fraction of the turbulent energy that is transported from large to small scales is channelled into electron re-acceleration (Brunetti & Lazarian 2007), with the result that the acceleration time-scales would be of the order of 100 Myrs, significantly larger than those needed in the 'Sausage' relic. Given its low Mach number, the 'Sausage' shock would not generate enough turbulent energy to re-accelerate particles to speeds beyond a few hundreds of km s^{-1} on small scales ($\ll$ 100 Myr). Boosting the acceleration efficiency in turbulent models requires special circumstances, including a reduced effective mean-free-path in the ICM (Brunetti & Lazarian 2011) or an efficient generation of

Alfvén waves at quasi-resonant scales (Ohno et al. 2002; Brunetti et al. 2004).

A second possibility is fast (super-Alfvénic) particle diffusion in the downstream area. However, this scenario requires very special conditions, such as highly intermittent magnetic fields (as in magnetic reconnecting regions) and/or an efficient damping of plasma instabilities (Wiener et al. 2013; Brunetti & Jones 2014).

Another point to note is that mixing along the line of sight will lead to the measurement of younger ages than expected given the distance from the shock front. In a simplified scenario, the 'Sausage' shock is a spherical cap front propagating northwards, seen in projection on the sky. Along any given line of sight, emission with a range of spectral ages actually located at different distances from the shock front is projected at the same apparent distance from the shock front. Mixing is expected to have the strongest effect furthest away from the shock, in the downstream area, along the merger axis of the cluster. The detailed arc-length and further 3D structure of the shock has been shown to have a significant effect on the surface brightness and spectral properties (Kang et al. 2012). We will explore the effects of this mixing on radio spectra in a later paper.

To summarize, all the effects we have considered above have difficulties in explaining the observations and none is expected to solely bridge the discrepancy between the ageing speed as derived from the spectral age and shock speed data. Further modelling is necessary to fully investigate the nature of the ageing behind the shock.

3.5.6   Merger history

Assuming a constant shock speed throughout the travel towards the outskirts of the cluster, we can trace back the formation time of the shock. We expect the shock speed to have been slightly different in the past given its dependence on the ICM temperature, density and pressure, which can vary across the cluster in a complex way, given how disturbed the cluster is (see Ogrean et al. 2013b, for temperature and density maps of the cluster). By fixing the cluster centre, from X-ray (emission peak, Ogrean et al. 2014a) or weak lensing (mass distribution, Jee et al. in prep) arguments, we can calculate the time required for the gravitationally-decoupled shock front to travel from the core-passage of the two merging sub-clusters. In the case of the 'Sausage' cluster, this analysis indicates that the time since core passage is $\sim 0.6 - 0.8$ Gyr. Albeit a very approximate value which should be considered with caution, the time since core passage is consistent with the results from a much more sophisticated Monte-Carlo dynamical analysis which will be presented in Dawson et al. (in prep), based on the method from Dawson (2013).

3.6   Conclusions

In this paper, we have performed the first spectral age model fitting of a radio relic. Multi-frequency GMRT and WSRT radio data spanning six equally-spaced bands between 153 and 1714 MHz enabled us to draw a number of conclusions. We have derived injection indices and spectral ages for the plasma using established electron injection models such as the JP, KP and Tribble models.

- Even with the best radio relic data available, we could not distinguish between the
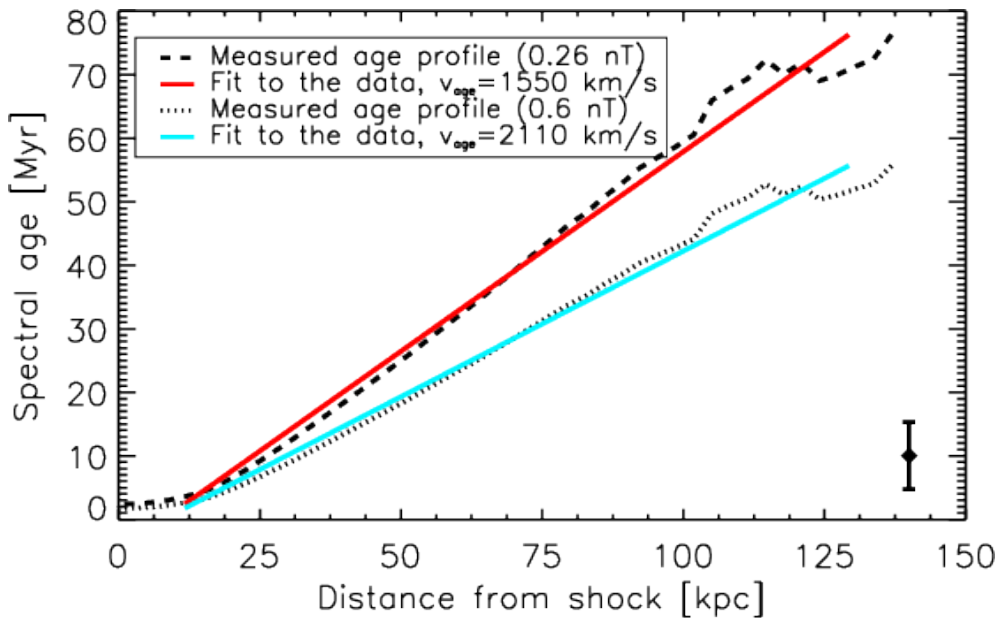
Figure 3.7: Spectral age profile as function of distance from the shock front. The age increases systematically with distance from the shock. In the scenario where the electrons are accelerated by the shock front located at the north of the relic, for a minimum B field value of 0.26 nT, yielding a maximum electron lifetime, a linear model yields a speed v_{age} of 1550 km s^{-1}. For a typical magnetic field measured in radio relics (~ 0.6 nT), the measured speed is higher (2210 km s^{-1}). We obtain the profile by averaging ages along the length of the relic. The typical standard deviation of each pixel-based average age value (for 0.26 nT) is shown in the bottom-right corner. The allowed spectral ages are too young to explain the very slow ageing speed imposed by the shock Mach number and upstream sound speed (see Section 3.5.5).

three spectral ageing models. Wider-bandwidth, higher-frequency and more reliable flux measurement would help distinguishing between ageing models.

- An injection spectral index of $0.77^{+0.03}_{-0.02}$ was derived, steeper than previously computed from radio data. The differences can be reconciled when taking beam smearing effects into account, which affect the old spectral index derivation only. We calculate a secure Mach number of $2.90^{+0.10}_{-0.13}$, based on a shock-acceleration model.

- We find a systematic increase in plasma age within the downstream area at the back of the shock front and uncover old plasma, with ages up to 60 Myr, assuming a 0.6 nT magnetic field.

- The new radio-derived Mach number is consistent with the X-ray results of Ogrean et al. (2014a), which imply a Mach number of $2.54^{+0.64}_{-0.43}$.

- We derive shock advance speeds of ~ 2500 km s^{-1} from X-ray data and radio particle acceleration arguments.

- The spectral ages allowed by a model of freely-ageing electrons behind the 'Sausage' shock front and the ages expected given the shock speed are incompatible. Part of the discrepancy between the two measurements can be attributed to line-of-sight mixing. They could be further brought into agreement if subsequent re-acceleration happens after the passage of the main shock front or if there is an usually efficient diffusion of particles in the downstream area.

The results presented here act as a proof-of-concept to display the power of multi-frequency data and to strengthen the necessity for broad-band observations of radio relics. Such observations for other clusters hosting radio relics could pose tight constrains on the clumpiness of the ICM. Very low frequency LOFAR measurement are crucial for the accurate determination of the injection index and Mach number.

Acknowledgements

4

The highest-frequency detection of a radio relic: 16-GHz AMI observations of the 'Sausage' cluster

We observed the cluster CIZA J2242.8+5301 with the Arcminute Microkelvin Imager at 16 GHz and present the first high radio-frequency detection of diffuse, non-thermal cluster emission. This cluster hosts a variety of bright, extended, steep-spectrum synchrotron-emitting radio sources, associated with the intra-cluster medium, called radio relics. Most notably, the northern, Mpc-wide, narrow relic provides strong evidence for diffusive shock acceleration in clusters. We detect a puzzling, flat-spectrum, diffuse extension of the southern relic, which is not visible in the lower radio-frequency maps. The northern radio relic is unequivocally detected and measures an integrated flux of 1.2 ± 0.3 mJy. While the low-frequency (< 2 GHz) spectrum of the northern relic is well represented by a power-law, it clearly steepens towards 16 GHz. This result is inconsistent with diffusive shock acceleration predictions of ageing plasma behind a uniform shock front. The steepening could be caused by an inhomogeneous medium with temperature/density gradients or by lower acceleration efficiencies of high energy electrons. Further modelling is necessary to explain the observed spectrum.

4.1 Introduction

Radio relics are diffuse, strongly-polarised, Mpc-wide synchrotron objects found at the periphery of disturbed galaxy clusters (e.g. Feretti et al. 2001). Relics are thought to trace large-scale, fast, outward-travelling shock fronts (Mach numbers up to 4) induced by major mergers between massive clusters (Ensslin et al. 1998; Sarazin 2002; Feretti et al. 2012). These objects usually extend perpendicularly to the merger axis of their host cluster and display narrow transverse sizes, resulting from a spherical-cap-shaped regions of diffuse emission seen side-on in projection (Feretti et al. 2012). Integrated radio spectral indices of elongated relics below < 1.2 GHz range between $-1.6 < \alpha < -1.0$ ($F_\nu \propto \nu^\alpha$) and the spectra display no curvature up to ~ 2 GHz (Feretti et al. 2012). Ensslin et al. (1998) suggest relics are formed through the diffusive shock acceleration mechanism (DSA; e.g., Drury 1983). In this scenario, intra-cluster-medium (ICM) particles are accelerated by shocks to relativistic speeds in the presence of μG level magnetic fields at the outskirts of clusters (e.g. Bonafede et al. 2009, 2010). Due to low acceleration efficiencies, mildly-relativistic (rather than thermal) electrons likely cross the shock surface multiple times by diffusing back through the shock after each passage. These re-accelerated electrons then exhibit synchrotron radio emission.

CIZA J2242.8+5301 ('Sausage' cluster; Kocevski et al. 2007; van Weeren et al. 2010) hosts a remarkable example of double, Mpc-wide, narrow radio relics. Twin relics are thought to form after a head-on collision of two roughly equal-mass clusters (Roettiger et al. 1999). The northern relic (RN) is bright (0.15 Jy at 1.4 GHz) with an integrated spectral index between 153 MHz and 2.3 GHz of $\alpha_{\mathrm{int}} = 1.06 \pm 0.04$ (Stroe et al. 2013). RN displays spectral index steepening and increasing curvature from the outer edge of the relic towards the inner edge, thought to be due to synchrotron and inverse Compton losses in the downstream area of a shock with an injection spectral index of ~ -0.65. The cluster contains a fainter counter-relic towards the south, a variety of diffuse patches of emission and a number of radio head-tail galaxies (Stroe et al. 2013).

Relics have been primarily studied at low radio frequencies (< 1.5 GHz), making accurate determination of the injection, acceleration and loss mechanisms difficult. Most of the ~ 40 radio relics with published spectra (Feretti et al. 2012) have measurements up to 2.3 GHz, while only two relics have spectra derived up to 5 GHz (Abell 521, 2163; Giacintucci et al. 2008; Feretti et al. 2001). The scarcity of high radio-frequency observations of relics is caused by two factors: (i) the steep spectrum means that relics are significantly fainter at high frequencies; (ii) there are few radio telescopes with the required compact uv coverage needed to detect relics. To begin to address this, we performed exploratory observations at 16 GHz with the Arcminute Microkelvin Imager (AMI; AMI Consortium: Zwart et al. 2008) of the 'Sausage' cluster. AMI is the only cm-wavelength radio telescope with the required capabilities for detecting Mpc-wide, low-redshift, diffuse targets at sub-arcminute resolution. In this letter, using two different AMI configurations, we image the 'Sausage' cluster at high (40 arcsec) and low (3 arcmin) resolutions. By combining the data with measurements from the Giant Metrewave Radio Telescope (GMRT) and the Westerbork Synthesis Radio Telescope (WSRT), we derive the RN spectrum over the widest frequency coverage ever performed for a radio relic (between 153 MHz and 16 GHz) and compare our results with predictions from spectral-ageing models. At the redshift of the 'Sausage' cluster, $z = 0.192$, 1 arcmin corresponds to a scale of 0.191 Mpc. All images are in the J2000 coordinate system.

4.2 Observations & Data Reduction

For our analysis, we combine the existing WSRT and GMRT observations with new AMI observations. We use the WSRT and GMRT datasets presented in Stroe et al. (2013) and refer the reader to that paper for details of the data reduction. In summary, the data were flagged, bandpass and gain calibrated and bright sources in the field were removed using the 'peeling' technique (Noordam 2004). A total of three frequencies were observed with the GMRT: 153, 323 and 608 MHz and four with the WSRT: 1.2, 1.4, 1.7 and 2.3 GHz.

4.2.1 AMI observations

AMI is a dual array of interferometers located near Cambridge, UK. The Small Array (SA) and the Large Array (LA), observe over $13.9 - 18.2$ GHz and measure the single Stokes polarisation I+Q (AMI Consortium: Zwart et al. 2008). The SA has ten 3.7-m antennas with baselines of $5 - 20$ m, while the LA has eight 12.8-m antennas with baselines of $18 - 110$ m, giving the instruments sensitivities to complimentary ranges of angular scale. Observations towards the X-ray cluster centre were taken between July 2012 and February 2013 on both SA and LA, with the field observed with a single pointing with the SA and with a series of multi-point hexagonal raster observations on the LA. The northern relic itself was also observed with the LA with four pointings centred along its axis. For all observations, flux calibration was performed using observations of 3C 48, 3C 286 and 3C 147, with 3C 286 calibrated against VLA measurements (Perley & Butler 2013). Raw data were flagged for hardware errors, shadowing and interference and phase and amplitude calibrated using the in-house software package REDUCE (AMI Consortium: Davies et al. 2009). All of the reduced LA data were concatenated into a single uv dataset before mapping.

Unlike the WSRT and GMRT arrays, that measure total intensity I, both AMI arrays measure the single polarisation Stokes I+Q. For the spectral work, it is necessary to correct the AMI values to make them consistent with those from the other telescopes. 4.9-GHz observations (van Weeren et al. 2010) show that RN is 60% polarised and that the magnetic field is tangent to the relic. The measured Faraday depth of -140 rad m^{-2} implies a rotation of 24 degrees between 5 and 16 GHz. We assume the same degree of polarisation at 16 GHz as at 4.9 GHz. AMI calibration assumes random polarisation, which in the case of RN is correct for only 40% of the measured flux. We multiply 60% of the measured I+Q flux by $1/(2\cos^2\phi)$, where ϕ is the angle between the electric field vector and the orientation of the I+Q AMI feeds, which is vertical on the sky. We take into account the variation of ϕ along the relic. The unpolarised RN flux is added to the corrected polarised flux: $I = 40\%(I+Q) + 60\%(I+Q)/(2\cos^2\phi)$. The I integrated flux density is obtained by decreasing 24% from the I+Q value.

4.2.2 Imaging

AMI radio maps

Figure 4.1 shows separate CLEANed maps for the LA and SA data, using 'Briggs' weighting (Robust set to 2.0 to enhance diffuse emission, Briggs 1995). The SA map resolution is 3.0 arcmin ×2.3 arcmin, while the LA has 44 arcsec ×22 arcsec. The RMS noise in the SA

map is ~ 0.1 mJy beam^{-1} near the northern radio relic, while in the LA map it is 35μJy beam^{-1}.

Combining the GMRT, WSRT and the AMI radio maps

To produce directly-comparable, multi-frequency radio images, a number of steps were taken before combining the maps for the study of the integrated spectrum. Due to the very low SA resolution compared to the WSRT and GMRT maps, we chose to combine only the LA map with the other datasets. We imaged the data using the CLEAN algorithm with the same pixel size (1 arcsec per pixel), image size and uniform weighting. The uv-coverage of the LA samples densely down to a uv-distance of 0.8 kλ. Therefore, only GMRT and WSRT data beyond a uv distance of 0.8 kλ were used, so that our radio maps image approximately the same spatial scales on the sky. We simulated an LA observation of a uniform brightness distribution with the angular dimensions of the northern relic as measured by the LA, with the uv coverage and pointings used for the real LA observation. We found that the LA could be resolving out a negligible part of the largest scale diffuse emission. The uv-cut is necessary for extended sources, as inconsistent inner-uv coverages can lead to non-comparable integrated fluxes. All of the maps were primary beam corrected and convolved to the beam of the AMI LA map.

We adopt an absolute flux-scale uncertainty of 10 per cent for the GMRT and WSRT data, following Stroe et al. (2013). This uncertainty results from telescope pointing errors and imperfect calibration. AMI flux scale errors are well-described by 5 per cent of the flux (AMI Consortium: Davies et al. 2011).

4.3 Results

4.3.1 Radio morphologies

SA map

The bottom panel of Figure 4.1 shows a 1.5-GHz WSRT image convolved to the resolution of the SA map, overlaid with SA contours. AMI recovers most of the bright sources detected by WSRT, while the fainter sources are below the noise. Due to the low resolution, sources close to the SA map centre will not only be blended and merged together, but will also have a negative contribution from SZ signal of the cluster. However, because of the excellent uv-coverage at short baselines down to 0.2 kλ, all of the diffuse emission visible at lower frequencies is recovered in the AMI SA map.

The northern relic (RN) displays an arc shape, but the emission is mixed with radio galaxies H and B and diffuse source I (see also top panel, Figure 4.1).

The complex of diffuse emission towards the south of the cluster arises as a blending of sources RS, J, A and tailed-radio source F. At lower frequencies, radio phoenix J is much brighter than the relic RS (Stroe et al. 2013). Since J has a much steeper spectrum than RS, they contribute comparably to the flux at 16 GHz. Puzzling is the ~ 2 mJy integrated flux, 1 Mpc, diffuse extension of RS towards the east, which has no counterpart in the low-resolution WSRT map (see labelling in Figure 4.1). By placing a 3σ upper limit on the WSRT flux (giving ~ 15 mJy), we would expect the spectral index of this extension to be flatter than
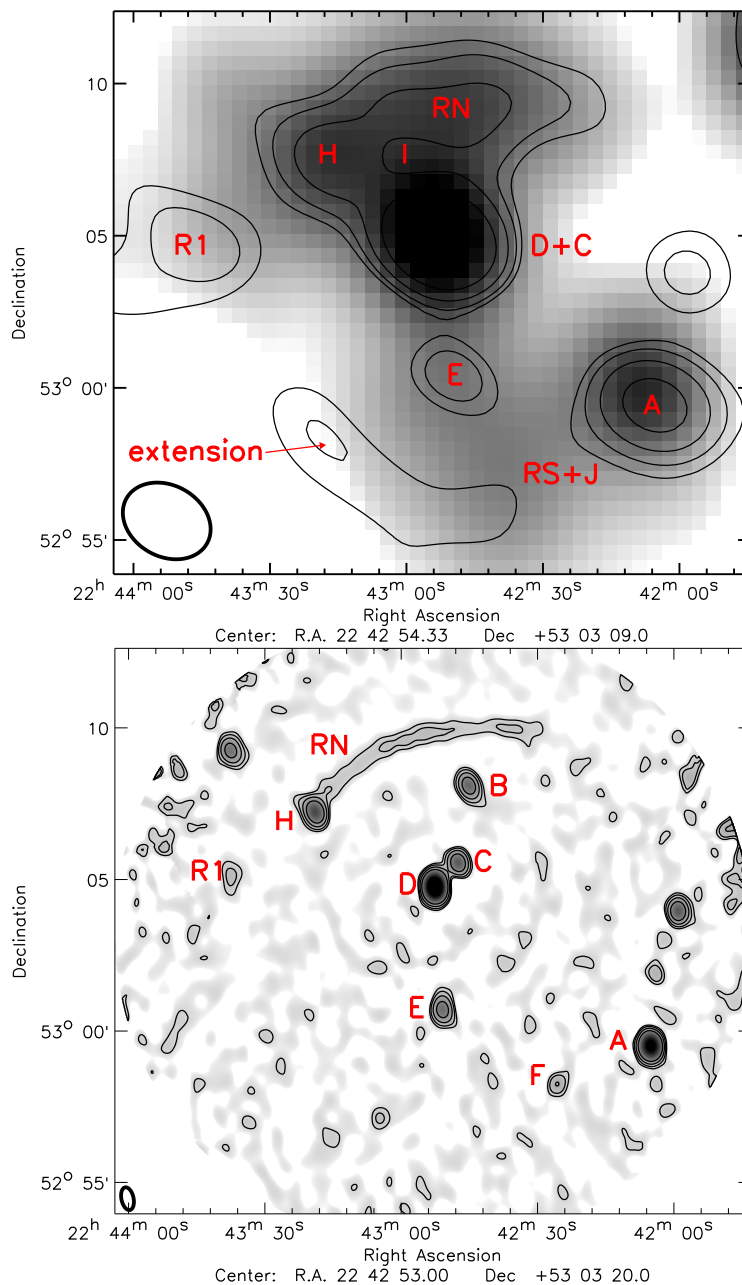
Figure 4.1: 'Briggs'-weighted AMI 16 GHz images (robust=2). Contours drawn at $[4, 8, 16, 32] \times \sigma_{RMS}$. *Top*: AMI SA. The beam size 3.0 arcmin $\times$2.3 arcmin is shown in the bottom-left corner of the image. The noise is ~ 0.1 mJy beam^{-1}. The grey intensity shows a low-resolution (3 arcmin) WSRT 1.5 GHz image. *Bottom*: AMI LA in intensity and contours, at 44 arcsec $\times$22 arcsec resolution, with $\sigma_{RMS} \approx 35 \, \mu$Jy beam^{-1}. Source labelling from Stroe et al. (2013) is shown.

−0.5. While the peak in the WSRT emission is towards the west, at the location of compact radio galaxy A, and it progressively wanes towards the east, the AMI SA emission shows the opposite trend. The peak at the emission is located where no counterpart is seen in the WSRT map. There could be some point-source contamination, but this should be minimal as the LA finds no significant sources in the area.

LA map

The top panel of Figure 4.1 shows the AMI LA map (imaged with robust=2). The higher resolution enables a better deblending of sources, but the poorer inner uv-coverage leads to loss of flux on large scales. This is evident as most diffuse sources (RS, J) detected in the SA effectively disappear in the LA map.

The northern relic is detected at the 11σ level at peak flux and clearly separated from its neighbouring source H towards the west. Only the central, brightest part of source R1 is visible. We also detect sources labelled A, B, C, D and E as point sources with high S/N ($> 32\sigma$). The nucleus of tailed-radio galaxy F is detected at 10σ, but its steep spectrum tail is not recovered, as expected (see Stroe et al. 2013). The 'extension' is not detected in the high-resolution 16 GHz, suggesting it may have a diffuse nature.

4.3.2 Integrated spectrum

Figure 4.2 and Table 4.1 present the spectrum of RN. The flux densities are measured in fixed boxes in uniform-weighted maps. Note that because of the uniform weighting, RN is detected at 6σ level significance at peak. We use a least-squares method to fit a single power law to the integrated flux-density of the relic from each of the eight radio maps, at common resolution and with the common uv-cut. This fitting takes into account a total flux error computed as the quadrature of the flux scale error of 10 per cent for the GMRT and WSRT measurements and 5 per cent in the AMI LA, and the RMS noise in each map multiplied by the square root of the number of beams contained in the box we measure the flux in.

From spatially-resolved, low-frequency observations of RN, we found a ~ -0.6 injection index, with an integrated spectrum between 153 MHz and 2.3 GHz well-described by a linear fit with slope −1.06 (Stroe et al. 2013). Figure 4.2 shows in the dotted line the injection spectrum of the freshly-accelerated electrons, while the dashed line presents the integrated spectrum, as derived from the low-frequency data. A single power law fit ($\alpha_{\rm int} = -1.33 \pm 0.03$) provides a poor description of the data up to 16 GHz, as the fitted line fails to pass through all but two error bars, with a reduced $\chi^2_{\rm red}$ of 163 (solid line in Figure 4.2). The 16 GHz measurement lies 12σ below the extrapolation of the low-frequency spectrum.

4.4 Discussion

Radio relics are thought to form at the wakes of travelling shock fronts produced by the major merger of galaxy clusters (Feretti et al. 2012). The physical processes underlying their formation, such as the injection and ageing mechanism, can be constrained using high-frequency measurements, which have not been performed until now. Here, we present the 16 GHz measurement of a relic through AMI observations of the 'Sausage' cluster.

Table 4.1: Integrated radio spectrum of the RN measured in the uniform-weighted radio maps with common uv-cut and resolution. The uncertainties of the measurements are computed as the quadrature of the flux error and the rms noise in each map, multiplied by the square root of the number of beams spanned by the source. Note that RN is detected at a total S/N of 24 in the integrated spectrum. Taking the lower bound given by the error in the integrated flux results in a 18σ detection.

Freq. [GHz]	0.15	0.32	0.6	1.2	1.4	1.7	2.3	16
Flux [mJy]	668	270	187	107	96	67	28	1.2
Error [mJy]	69	28	19	11	10	7	3	0.3

4.4.1 Northern relic

The 16 GHz measurement of the northern relic and its integrated spectrum are given in Fig. 4.2 and Table 4.1. We find strong evidence for high-frequency steepening in the integrated spectrum of RN. There are two reasons why this should be considered a robust measurement. Firstly, the integrated spectra of point sources in the GMRT, WSRT and AMI LA maps are well described by single power laws, implying a correct overall flux scale also for the 16 GHz measurements. Secondly, the dense AMI LA uv-coverage at the shortest spacings indicates minimal loss of flux at large spacial scales.

All of the lower-frequency measurements (GMRT and WSRT, < 2.3 GHz) present firm evidence for a scenario where the source traces an outward travelling shock wave. The ICM electrons are accelerated at the shock via the DSA mechanism, resulting in a relatively flat injection spectral index ($\alpha \sim -0.6$; van Weeren et al. 2010; Stroe et al. 2013). Energy losses due to synchrotron and inverse Compton processes lead to spectral index steepening and increasing spectral curvature in the downstream area (van Weeren et al. 2010; Stroe et al. 2013).

Ensslin et al. (1998) modelled the integrated radio spectrum for such a relic formation scenario. At the shock front the particles are accelerated to a power-law radio spectrum, followed by losses that steepen the spectra. The integrated spectrum results from the summation of particle spectra spanning a range of ages from different regions in the downstream area. This is equivalent to the continuous injection model which was proposed to explain the integrated spectra of radio galaxies, where the jet deposits freshly accelerated electron in the radio lobes at a constant rate (CI; Pacholczyk 1970).

In the CI model, the integrated spectrum has a critical frequency ν_{crit}, beyond which the spectrum steepens by 0.5 because of energetic losses (Pacholczyk 1970). Ensslin et al. (1998) follows this approach and assumes that the integrated spectrum is measured beyond this critical frequency (~ 100 MHz), where we observe the aged spectrum. Therefore, simple plane-shock theory in the context of DSA predicts that the relic integrated spectral index of a source should be 0.5 steeper than the injection index of the freshly-accelerated electrons, which has a hard upper limit at -0.5 (Pacholczyk 1970). In Stroe et al. (2013), we showed that the spectral index and curvature maps for the northern relic are consistent with this model. The relic injection index is -0.6, which defines a shock front Mach number of 4.6 ± 1.1 (Stroe et al. 2013). The difference between the injection index ~ -0.6 and the integrated index below 2.3 GHz of -1.06 ± 0.04 is consistent with the prediction from the CI model (Stroe et al. 2013).
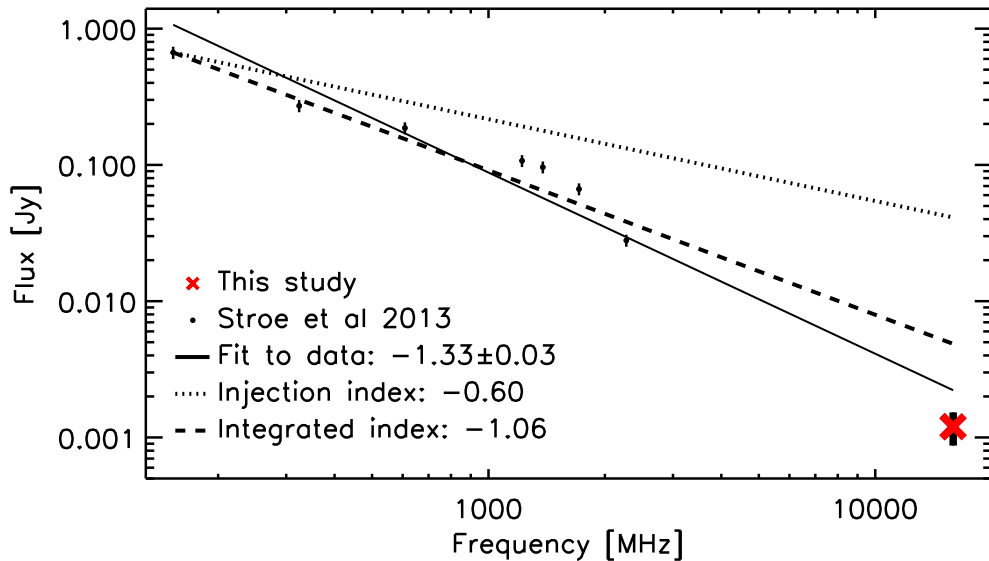
Figure 4.2: Integrated radio spectrum of the northern relic from 153 MHz up to 16 GHz (see also Table 4.1). The red cross marks the 16 GHz measurement. The uncertainties include a 10 per cent flux scale error added in quadrature to the σ_{RMS}. A power-law is fitted to the eight frequencies. The dotted line shows the injection spectrum and the dashed line the integrated spectrum, as derived from high-resolution GMRT and WSRT data (Stroe et al. 2013). The injection and integrated spectra below 2.3 GHz are consistent with a CI model. The 16 GHz measurement is 12σ below the CI prediction.

However, by extrapolating the RN low-frequency spectrum, we find that the 16 GHz measurement is in stringent tension with the CI prediction, at the 12σ significance level (see Fig. 4.2). The integrated 153 MHz to 16 GHz index is much steeper (~ 0.8) than the injection index, while if only the high-frequency data is considered, this difference increases to 1.2 spectral index units.

There are several explanations for this discrepancy between the 16 GHz and the lower frequency measurements:

- As mentioned previously, the Ensslin et al. (1998) model only holds for frequencies above the break frequency, where there is a balance between continuously, freshly injected plasma and ageing. In reality, there is a broad frequency range over which the steepening takes place. If the break occurs over a range of frequencies below ~ 100 MHz, then the steepening would gradually increase towards higher frequencies, giving a curved integrated spectrum, as the one we observe in the northern relic. In cases where the spectral break occurs across the observed frequency range, the results will be biased to flatter integrated spectra and hence stronger derived Mach number.

- The injection spectrum is not a power law. With a pool of thermal or pre-accelerated electrons, the injection spectrum is still expected to be a power law (Brunetti & Jones 2014). The acceleration efficiency for electrons beyond $\gamma \approx 3 \times 10^4$ Lorentz factors

(equivalent to a few GHz-peak emission frequency for μG magnetic fields) might be smaller than for the lower energy electrons. During their multiple crossings of the shock front, the electrons lose energy and radiatively cool during the acceleration, leading to a curved injection spectrum, assuming that the electron mean free path is larger than its gyro-radius (Keshet et al. 2003).

- A gradient of density and/or temperature across the source would result in different spectral components, resulting in a 16-GHz spectrum completely dominated by losses/aged electrons. Assuming an isothermal sphere ICM gas distribution (Sarazin 2002), we calculate a drop of $15 - 25$ per cent in electron gas density across the $50 - 100$-kpc width of the northern relic. The outward-movement of the shock, from regions of higher densities into lower densities, suggests that, in the past, the shock was crossing a region of higher electron density. The shock might have injected a larger pool of electrons in the past, compared to now. When summing up the particle spectra, the older electrons would have a higher normalisation, hence larger weight in the integrated spectrum. Therefore, the integrated spectrum would be dominated by the heavily-curved spectrum of the aged electrons.

- The magnetic field at the shock location might be stronger than in the downstream area, as a result of shock compression. Acceleration in the presence of ordered, strong magnetic fields at the shock front, combined with turbulent, lower magnetic fields in the downstream area, could lead to a curved integrated spectrum. Simulations of supernova remnant synchrotron emission under turbulent magnetic field conditions suggest that electrons in the cut-off regime can radiate efficiently (Bykov et al. 2008).

Nevertheless, higher-resolution data is required for distinguishing between these scenarios. At the moment, no relic formation mechanism can readily explain the high-frequency steepening, thus new theoretical models have to be developed (Brunetti & Jones 2014).

4.4.2 Diffuse extension

Towards the south of the cluster, we discover an extension at the 8σ significance level towards the east of RS in the low-resolution SA AMI map. This source does not have a counterpart in the lower frequency data, or in the high-resolution AMI LA map (Figure 4.1), excluding the possibility of a point source. The extension appears elongated (~ 1 Mpc) and has a spectrum flatter than ~ -0.5. Its arc-like shape and proximity to RS make the extension an ideal candidate for a relic, but its flat integrated spectral index means that the source cannot result from a shock front in the context of DSA. Striking also is the difference between the spectral index of the extension and RS, which points to very different shock properties towards the south and towards the south-west. This could be explained by different ICM temperature/densities in the two directions. Ogrean et al. (2013a) measured a sharp increase in ICM temperature in the direction of this extension, followed by a putative shock with a Mach number of 1.2, coincident with the location of the radio extension. Such an increase in temperature in the downstream area of travelling shock fronts has been also found in simulations (Roettiger et al. 1997). The source seems to trace an arc-like shock front, which suggests a shock seen in projection onto the plane of the sky, which means the radio emission detected is a mixture of different age-populations of electrons.

4.5   Conclusions

High radio-frequency observations of steep-spectrum, diffuse, cluster emission have not previously been made owing to a lack of suitable instrumentation. We have observed the 'Sausage' merging cluster at 16 GHz at low (3 arcmin) and high (40 arcsec) resolution with the AMI array and we successfully detect diffuse radio relic emission for the first time at frequencies beyond 5 GHz. Our main results are:

- The northern relic measures an integrated flux density of 1.2 ± 0.3 mJy (6σ peak detection in a uniformly-weighted map). We investigate in detail its integrated spectrum and conclude there are clear signs of spectral steepening at high frequencies. If thermal electrons are accelerated, the steepening can be caused by a lower acceleration efficiency for the high-energy ($\gamma > 3 \times 10^4$) electrons, a negative ICM density/temperature gradient across the source or turbulent downstream magnetic fields amplifying the emission of electrons in the cut-off regime. However, these scenarios are unlikely because of low-acceleration efficiencies at weak-Mach-number shocks. Further theoretical modelling is required.

- We also detect a peculiar, flat-spectrum ($\alpha_{\mathrm{int}} \approx -0.5$) patch of diffuse emission towards the south-east of the cluster, which cannot be explained by the CI model.

The surprising high-frequency spectral steepening results and flat-spectra presented here suggest that the simple CI model, which has been widely used in the literature to explain the formation of radio relics, needs to be revisited. Furthermore, there is a clear need for high-quality radio observations of relics at cm and mm-wavelengths that resolve radio relics.

Acknowledgements

5

The 'ultimate' cluster radio relic spectrum: observations from 150 MHz to 30 GHz

Radio relics are patches of diffuse synchrotron radio emission that trace shock waves. Relics are thought to form when intra-cluster medium electrons are accelerated by cluster merger induced shock waves through the diffusive shock acceleration mechanism. In this paper, we present observations spanning 150 MHz to 30 GHz of the 'Sausage' and 'Toothbrush' relics from the Giant Metrewave and Westerbork telescopes, the Karl G. Jansky Very Large Array, the Effelsberg telescope, the Arcminute Microkelvin Imager and Combined Array for Research in Millimeter-wave Astronomy. We detect both relics at 30 GHz, where the previous highest frequency detection was at 16 GHz. The integrated radio spectra of both sources clearly steepen above 2 GHz, at the $\gtrsim 6\sigma$ significance level, supports the spectral steepening previously found in the 'Sausage' and the Abell 2256 relic. Our results challenge the widely adopted simple formation mechanism of radio relics and suggest more complicated models have to be developed that, for example, involve re-acceleration of aged seed electrons.

Stroe, Shimwell, Rumsey et al.
MNRAS submitted (2015)

5.1   Introduction

Radio relics are polarized areas of diffuse, low-brightness radio emission often with arc-like morphologies and typical > 1 Mpc size (Feretti et al. 2012; Brunetti & Jones 2014). Relics are placed exclusively at the outskirts of massive, post-core passage merging galaxy clusters and preferentially oriented perpendicularly to the merger axis (Feretti et al. 2012). Whilst there are spectral index variations within individual relics (usually across the relic width, e.g. Orrú et al. 2007; van Weeren et al. 2010; van Weeren et al. 2012b; Bonafede et al. 2012; Stroe et al. 2013) the integrated radio relic spectra below 5 GHz are well described by a single power law with $\alpha < -1$, where radio spectral index α is described as the flux density F as function of the frequency ν: $F \sim \nu^{\alpha}$ (Feretti et al. 2012). The synchrotron nature of these sources, coupled with the strong polarization, indicates a significant ordering in the magnetic field structure: the magnetic field vectors are aligned with shock structure (van Weeren et al. 2010; van Weeren et al. 2012b, e.g.). The observational results regarding the morphology, spectrum and polarisation of radio relics led to a favoured interpretation. In this scenario, relics are produced by synchrotron-emitting cosmic ray electrons accelerated by shocks through the diffusive shock acceleration mechanism (DSA; Ensslin et al. 1998). Cluster merger events produce such weak shock waves in the ICM (Mach number $M < 5$), where part of the gravitational energy released during the merger event is dissipated (e.g. Pfrommer et al. 2006).

However, more recently, evidence has been found in tension with the simple DSA picture, as it was proposed by Ensslin et al. (1998). Simulations have found that producing substantial radio flux densities at low Mach number shocks with electrons accelerated out of the local thermal population would require extraordinarily large particle injection efficiencies (e.g. Kang et al. 2007). Furthermore, robustly detected X-ray shocks were found to have no radio counterpart or be associated with a radio shock at an offset position (e.g. Russell et al. 2011; Ogrean et al. 2013b, 2014b; Shimwell et al. 2015), while in cases with a joint shock detection, a discrepancy between the X-ray and the radio Mach number measurement was found (van Weeren et al. 2012b; Ogrean et al. 2013a). However, the initially measured discrepancy between the two Mach number estimates for the 'Sausage' relic in cluster CIZA J2242.8+5301, has since been partially attributed to resolution effects affecting the radio measurement (Stroe et al. 2014c).

High frequency flux measurements are useful to help resolving these issues. Very recently, high frequency radio measurements of relics have been published for the first time at 16 GHz with the Arcminute Microkerlvin Imager (AMI, Stroe et al. 2014b) and the Effelsberg telescope at 10 GHz (Trasatti et al. 2015). Both studies find evidence for steepening of the radio spectrum at frequencies higher than 2 GHz. Erler et al. (2015) proposed that the Sunyeav-Zeldovich effect (SZE; Sunyaev & Zeldovich 1972), the upscattering of cosmic microwave background photons by the intra-cluster medium electrons, could be responsible for the perceived steepening. Relics would sit in a negative 'bowl', which would result in a measured relic flux density smaller than the real value. Stroe et al. (2014b) propose that the cause for the steepening lies in the physics of the relic. A non-power-law injection spectrum could lead to a curved integrated index. Furthermore, if the magnetic field is ordered and boosted at the shock location, but turbulent in the downstream area, the integrated spectrum could steepen even more at high frequencies. Kang & Ryu (2015) use time-dependent DSA simulations of a spherical shock impinging on a magnetised cloud of pre-accelerated relativistic electrons to

obtain relic spectra which gradually steepen over the $(0.1 - 10)$ GHz range. However, the steepening is insufficient to fully explain the measurements by Stroe et al. (2014b). Testing theoretical models has been challenging due to a dearth of measurements above 2.5 GHz. For example, Trasatti et al. (2015) have integrated flux density measurements of the Abell 2256 relic only at 5 and 10 GHz, while Stroe et al. (2014b) have one measurement for the 'Sausage' relic, but at a much larger lever arm (16 GHz). This means the actual shape of the high-frequency spectrum is not well constrained.

The clusters CIZA J2242.8+5301 ('Sausage'; Kocevski et al. 2007; van Weeren et al. 2010) and 1RXS J0603.3+4214 ('Toothbrush'; van Weeren et al. 2012b) are ideal targets as both clusters host a bright relic ($F > 0.15$ Jy at 1.4 GHz). Both relics are located towards the northern periphery of the clusters, extending over more than 1.5 Mpc in length, but less than 200 kpc in width. The rich data below 2.5 GHz on the 'Sausage' and 'Toothbrush' relics were of sufficient quality to enable van Weeren et al. (2012b), Stroe et al. (2013) and Stroe et al. (2014c) to find gradients of increasing spectral index and spectral curvature from the northern towards the southern edge of the relics. Stroe et al. (2014c) fitted spectral ageing models to the 'Sausage' data to interpret the trends as increasing electron age across the relic.

We have performed new high-frequency observations of the two relics with the Karl G. Jansky Very Large Array (VLA) in the $2 - 4$ GHz range, with the Effelsberg telescope at 5 and 8 GHz, with AMI at 16 GHz and with the Combined Array for Research in Millimeter-wave Astronomy (CARMA) at 30 GHz. We combine the new observations with the radio data already available from the Giant Metrewave Radio Telescope (GMRT), the Westerbork Synthesis Radio Telescope (WSRT) and AMI (van Weeren et al. 2012b; Stroe et al. 2013, 2014b) to produce a well-sampled spectrum for the main radio relics over a frequency range spanning 2.3 dex.

Assuming a flat, ΛCDM cosmology with $H_0 = 70$ km s^{-1}, matter density $\Omega_m = 0.27$, dark energy density $\Omega_\Lambda = 0.73$, at the redshift of the two clusters, $z \sim 0.2$, 1 arcmin corresponds to a scale of ~ 0.2 Mpc. All images are in the J2000 coordinate system.

5.2 Observations and data reduction

For our analysis we combine existing observations with new data for the 'Sausage' and 'Toothbrush' relics. The frequencies of the observations can be found in Table 5.1. Standard calibration was applied to all the data sets, including flagging, bandpass and gain calibration. The details of the reduction of the existing GMRT and WSRT datasets can be found in van Weeren et al. (2012b) and (Stroe et al. 2013).

5.2.1 Jansky VLA data

Observations of the 'Sausage' cluster in S band were performed in D array configuration with the VLA on 27 January 2013. Data were recorded in full polarisation, in 16 spectral windows of 128 MHz each, spanning a bandwidth of 1 GHz between 2 and 3 GHz. Each spectral window was further subdivided into 64 channels. The 1.5 h on source-time were equally divided over three separate pointings to cover the cluster region. Two primary calibrators were observed, 3 C138 and 3 C147. J2202+4216 was used as a secondary calibrator. The pointing centres for the cluster were: RA=22:43:19, DEC=+53:05:28; RA=22:42:36,

Table 5.1: Summary of the frequencies at which observations have been made for the 'Sausage' and 'Toothbrush' radio relics. In both cases, the observations span from 150 MHz to 30 GHz.

Source	Telescope	Frequencies
	GMRT	150, 325, 610 MHz
	WSRT	1230, 1380, 1710, 2270 MHz
'Sausage'	VLA	2250, 2750, 3250, 3750 GHz
15 frequencies	Effelsberg	4.85, 8.35 GHz
	AMI	15.85 GHz
	CARMA	30 GHz
	GMRT	150, 240, 324, 608 MHz
	WSRT	1230, 1380, 1710, 2270 MHz
'Toothbrush'	Effelsberg	4.85, 8.35 GHz
12 frequencies	AMI	15.85 GHz
	CARMA	30 GHz

DEC=+53.07:29 and RA=22:42:41, DEC=+52:58:09. The data were calibrated with the Common Astronomy Software Applications package[1] (CASA version 4.3 McMullin et al. 2007). The data were first corrected for the antenna offset positions and elevation dependent gain curves. The data were also Hanning smoothed and strong radio frequency interference (RFI) was removed with the 'tfcrop' option of the task flagdata(). The flux scale for the primary calibrators was set using the calibrator model image provided by casapy and taking the Perley & Butler (2013) scale. We then determined an initial bandpass correction using the primary calibrator sources. This is done to remove the strong bandpass rolloff at the edges of the spectral windows which hinders the detection of RFI. RFI was then removed with AOFLAGGER (Offringa et al. 2010). After RFI removal, we determined initial gain corrections using the central 10 channels of the spectral windows. These corrections were pre-applied before finding the delay solutions and subsequent final bandpass solutions. By pre-applying the gain solutions we remove any temporal variations in the gains which would otherwise effect the bandpass and delay terms. The gain solutions were then re-determined for all calibrator sources but now pre-applying the bandpass and delay solutions. Next we bootstrapped the primary flux scale to the secondary calibrator. The final calibration solutions were applied to the target fields.

5.2.2 Effelsberg data

In the following section we describe the Effelsberg observations, data reduction and flux density measurements in detail.

Effelsberg observations

The observations were performed with the Effelsberg 100-m Radio Telescope in October/November 2010, January 2011, October 2011 and August 2014 using the 3.6 cm (8.35 GHz with 1.1 GHz bandwidth) single-horn and 6.3 cm (4.85 GHz with 0.5 GHz bandwidth) dual-horn receiving

---

[1] http://casa.nrao.edu/
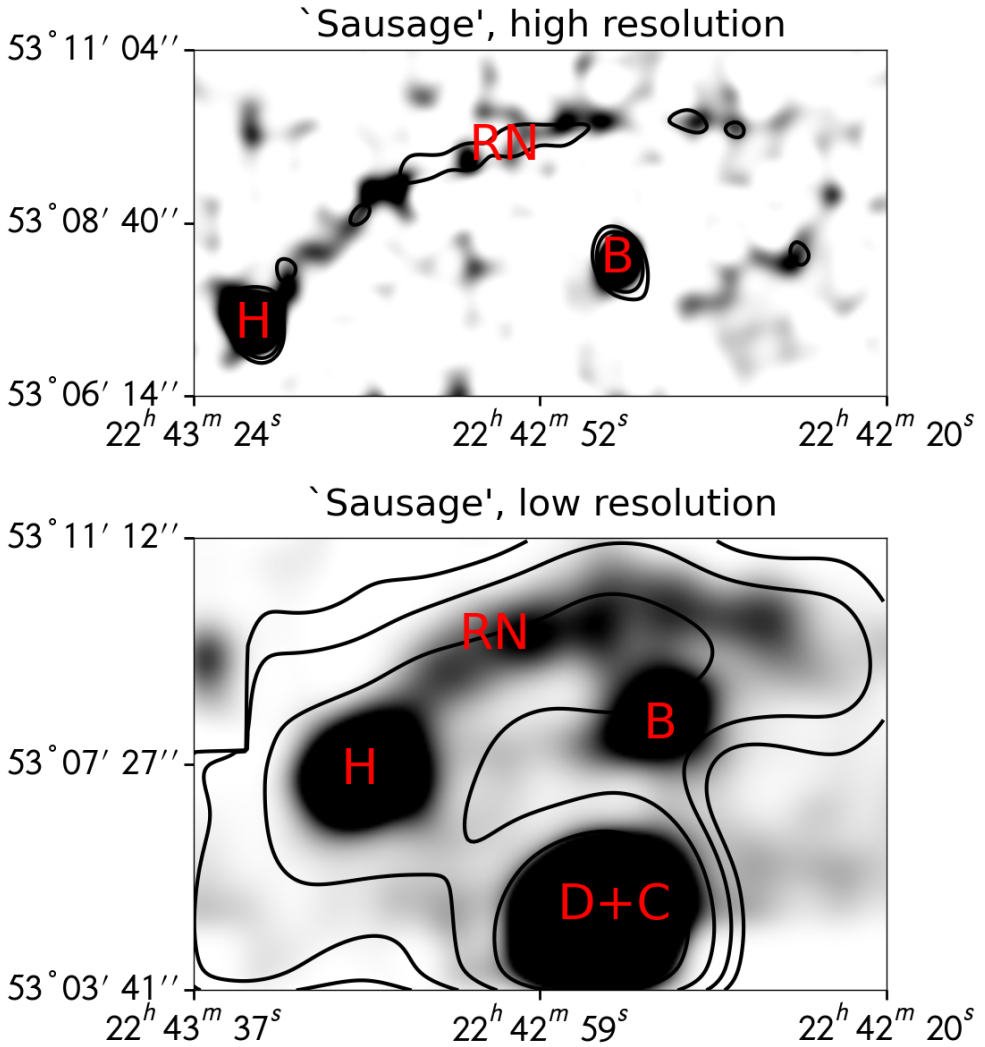
Figure 5.1: Low resolution total power and uniform-weighted high resolution images of the 'Sausage' cluster. The top panel shows the CARMA image (∼ 30 arcsec resolution) in grayscale and the AMI-LA (∼ 40 arcsec beam) image in contours drawn at $[4, 8, 16, 32] \times \sigma_{RMS}$. The bottom panel shows the Effelsberg 8.45 GHz (90 arcsec resolution) image in grayscale and the 4.85 GHz (159 arcsec resolution) in contours at $[4, 8, 16, 32] \times \sigma_{RMS}$. We label the source as Stroe et al. (2013). RN refers to the relic, which B, D, C and H and radio galaxies.
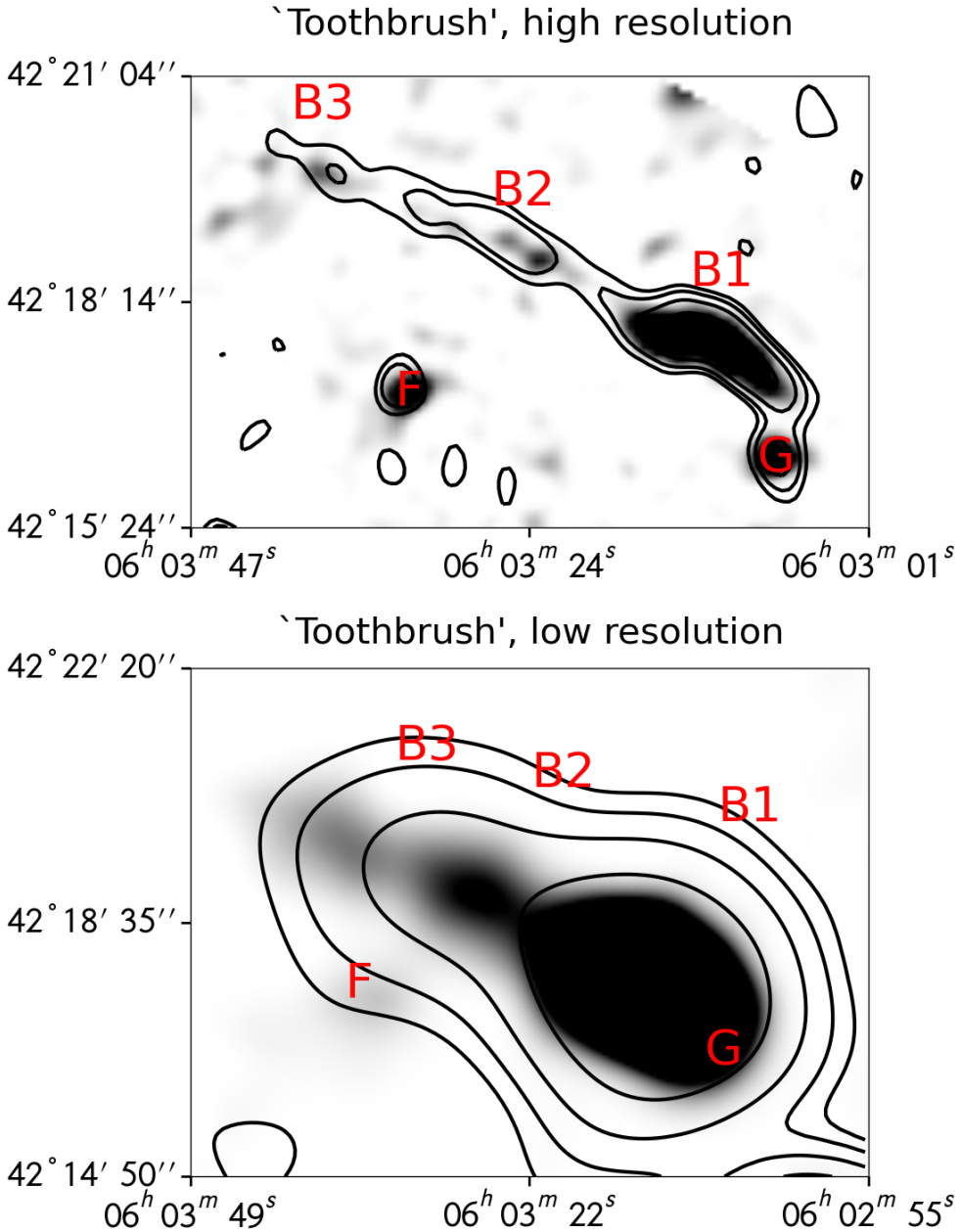
Figure 5.2: Same as Figure 5.1, but for the 'Toothbrush' relic. B1, B2 and B3 are subsections of the relic, labelled according to van Weeren et al. (2012b). Radio galaxy F (from van Weeren et al. 2012b) and G are also marked.

systems installed at the secondary focus. The radio sources 3C 48, 3C 138, 3C 147, 3C 286 and 3C 295 were observed as flux density and pointing calibrators, using the flux densities from Peng et al. (2000).

Firstly, a pointing check is performed. The telescope performs a cross scan of a well known, bright point source that is unresolved. This pointing check is repeated at regular intervals. To prevent long slewing movements of the telescope, the point source should be located close to the observed object. Secondly, a focus measurement is performed because the focus varies with temperature. The secondary mirror is moved back and forth (along the optical axis) to find the maximum amplitude. Then the pointing is repeated because an incorrect focus can shift the pointing. Finally, we measure a calibration map for the flux density and polarization calibration. A well-known, bright, not variable and unresolved radio source with constant flux density is used as a calibrator.

The 8.35 GHz observations were made with a single-horn system, located in the secondary focus of the telescope. The desired area were scanned alternatively in RA and DEC directions, where the sub-scans were separated by 30 arcsec. Baselevels were subtracted automatically by linear interpolation between pixels at both sides of each sub-scan. In the end, we obtained 46 maps for 'Sausage' and 40 for 'Toothbrush'.

The 4.85 GHz observations were made with a double-horn system. As the horns are fixed in the secondary focus, scanning has to be done in azimuth to allow the restoration of the signals (Emerson et al. 1979). The maps need to be larger in azimuth by the beam separation of 8 arcmin, plus one additional beamwidth on each side to improve the baselevel determination. The sub-scans were separated by 60 arcsec and the baselevels were subtracted. We obtained 32 maps for 'Sausage' and 12 for 'Toothbrush' scanned in azimuthal direction.

Effelsberg data reduction

All maps in Stokes parameters I, Q and U were averaged and combined using the basket-weaving method (Emerson & Graeve 1988) to improve the signal-to-noise (S/N) ratio. The raw maps include artefacts which need to be removed. Every single map was checked and edited if there were disturbances which result from weather effects or other problems such as, RFI, scanning effects due to clouds and baselevel distortions due to sources near the edge of a map. The main part of data reduction was accomplished using the NOD2-based software package called 'Ozmapax' (Haslam 1974). The software allows us to check individual maps for disturbances and edit them.

For the 8.35 GHz maps it was necessary to check every map for disturbances (RFI, scanning effects or baselevel distortions). In case of scanning effects or RFI, the entire affected scans must be set to dummy values. If a source is located near the edge, the baselevel of the entire scan can be incorrect. To make a baselevel modification one must define a new baselevel in a region further away from the source. All this has to be done separately for Stokes I, Q and U. After editing and separating all maps, we combined all reduced maps to one final map in Stokes I, Q and U using the basket-weaving method (Emerson & Graeve 1988).

For the 4.85 total power (Stokes I) data weather effects were removed by creating the difference of the maps from the two different horns. The result was a rectangular map in which the source appears twice: once with positive values and once with negative ones. Most weather effects were eliminated in the difference map. Nevertheless, it was necessary to correct all

Table 5.2: Imaging parameters and data used in combination for producing integrated spectra. For the interferometric spectrum made from comparable datasets, all the data were convolved to the image with the lowest resolution (imposed by the AMI-LA data). For the total-power measurements the data were left at their native resolution (best resolution obtained by the interferometric data with the robust weighting). Convolving the images to the lowest resolution of Effelsberg (the largest beam is 2.5 arcmin at 4.85 GHz) would result in heavy blending of diffuse flux with point sources.

Source	Type	uv range	Weighting	Max scale	Resolution	Telescope	Frequencies
		kλ		'	''		GHz
'Sausage'	Total power	all	robust	-	5 – 147	GMRT, WSRT, Effelsberg	0.15, 0.325, 0.61, 1.2, 4.85, 8.45
	Interferometric	> 0.8	uniform	~ 4	40	GMRT, WSRT, VLA, AMI-LA, CARMA	0.15, 0.325, 0.61, 1.2, 1.4, 1.7, 2.25, 2.3, 2.75, 3.25, 3.75, 15.85, 30
'Toothbrush'	Total power	all	robust	-	5 – 147	GMRT, WSRT, Effelsberg	0.15, 0.24, 0.325, 0.61, 1.2, 4.85, 8.45
	Interferometric	> 0.8	uniform	~ 4	40	GMRT, WSRT, AMI-LA, CARMA	0.15, 0.24, 0.325, 0.61, 1.2, 1.4, 1.7, 2.3, 15.85, 30

difference maps for residual disturbances. After editing all Stokes Q and U (see above) and all difference maps (Stokes I) we combined them to improve the S/N.

Further reduction steps were done by the NRAO AIPS [2] (Astronomical Image Processing System) software package. All Stokes maps are convolved to 90 arcsec at 8.45 GHz and 159 arcsec at 4.85 GHz to increase S/N ratios. These maps will be fully presented and discussed in an upcoming paper (Kierdorf et al. in preparation).

5.2.3 AMI data

The AMI telescope (AMI Consortium: Zwart et al. 2008) consists of two interferometers: the Large Array (AMI-LA) with baselines of 18-110 m has a resolution of approximately 30 arcsec; the shorter Small Array (AMI-SA) baselines of 5-20 m give a resolution of about 3 arcmin. The 'Sausage' AMI-LA data and its reduction are summarised in Stroe et al. (2014b). Initial AMI-LA observations for the 'Toothbrush' cluster were taken at ∼ 16 GHz with 61 pointings to cover the entire cluster area. The relic was subsequently observed in a 4-point mosaic on 7 November 2013. We follow the same reduction steps for the 'Toothbrush' as described in Stroe et al. (2014b) for the 'Sausage' cluster.

5.2.4 CARMA data

The 'Sausage' and 'Toothbrush' relics were observed with the CARMA 6.1 m and 10.4 m dishes in the compact E-configuration during 2014 July 9 to 2014 August 3 (project c1223). The data were recorded with eight 500 MHz frequency bands placed between 27.4 and 32.7 GHz where known 'birdies' (radio chirps caused by harmonics) in the 1cm system were avoided . To obtain close to uniform sensitivity across the large relics we observed using 11-point mosaics where pointings were separated by 1.4 arcmin which is sufficiently close to Nyquist sample the pointings at the highest observed frequency for the largest antenna. A total of 14 hrs and 21 hrs hours of on-source data were recorded for the 'Toothbrush' and 'Sausage' clusters, respectively, and observations were performed over a range of elevations to provide good uv-coverage. During an observation each pointing in the mosaic was observed for 1 minute before a calibrator was observed for three minutes, this cycle was repeated until the end of the observation. We used BL Lac as the interleaved gain calibrator for the 'Sausage' relic and 055+398 for the 'Toothbrush' cluster. During each observation a passband calibrator was also observed for 10 minutes, we used 0510+180 and 0927+390 for the 'Toothbrush' observations and MWC349 for the 'Sausage' observations. The calibration was done with the MIRIAD package (Sault et al. 1995) following the procedure described in Shimwell et al. (2013).

5.3 Imaging and flux density measurements

The goal for our analysis is to determine the integrated spectrum of the two radio relics. We make two sets of measurements: one using interferometric images made from comparable data using the same inner uv cut and same resolution, the second using the interferometric

---

[2]http://www.aips.nrao.edu

measurement with the best uv coverage going to low uv spacings in an attempt to combine the flux density measurement with total power flux densities as measured by Effelsberg.

5.3.1   Interferometric measurements

The integrated flux density at each frequency is measured from the map. Each data set is imaged with uniform weighting, sampling the same spatial scales of the sky. Such images can be produced if we have the same uv coverage in each interferometric observation. In practice, we approximate this by applying a uv range and a uniform weighting to visibilities when imaging. We image the data using the CLEAN algorithm with the same resolution, the same pixel (1 arcsec per pixel) and image size and correct all images for the effects of the primary beam attenuation.

Radio images

We produced interferometric images using the CLEAN algorithm and refined them through the process of self-calibration. In the case of the VLA data, we decided to split the data into four 0.5 GHz wide chunks to allow flux density measurements at central frequencies of 2.25, 2.75, 3.25, and 3.75 GHz with sufficient S/N and without being hindered too much by spectral variations within a 0.5 GHz bandwidth. For these four VLA images, the three pointings were jointly convolved and imaged, correcting for the VLA primary beam scaled for the central frequency and using the 'mosaic' option of the clean() task in CASA. To facilitate imaging from the heterogeneous CARMA array we used the CASA package with the default CARMA primary beams. As for the VLA data, we used the 'mosaic' mode in the imager to jointly deconvolve the entire 'Sausage' and 'Toothbrush' mosaics CLEANing to a depth of 0.15 mJy/beam. To improve the image quality our data were self calibrated with two rounds of phase-only calibration, followed by two final rounds of amplitude and phase calibration. The amplitude solutions were normalized to 1.0 to prevent drifting of the flux scale. For imaging during the self-calibration we used Briggs weighing with a robust factor of 0.0 (Briggs 1995). To aid the deconvolution we used clean boxes.

We produce primary beam corrected images using the same uv ranges from our interferometric data, in order to study the diffuse emission on different scales. The details of the imaging parameters and the data used can be found in Table 5.2. We calculate the largest spatial scale fully recovered using the conversion: $0.6\lambda/b_{\mathrm{min}}$, λ is the wavelength and b_{min} is the smallest baseline sampled in the uv plane[3]. To probe spatial scales of up to ~ 2.6 arcmin, we use only data at uv distances beyond $800\,\lambda$ and convolve the images to ~ 0.5 arcmin resolution, as imposed by the AMI-LA uv coverage. We probe the uv space over a factor of 8 in baseline length, ranging from $800\,\lambda$ and at least up to $\sim 6600\,\lambda$. Note that any flux at scales larger than this is mostly aligned with the shock (east-west direction). This means we are not resolving out any flux along the north-south direction (because there is not diffuse relic component in this direction). Therefore in the downstream direction we are capturing all

---

[3]Note that formally an interferometer is a matched filter and it is sensitive to emission on scales of $\sim \lambda/b_{\mathrm{min}}$. However, assuming a Gaussian brightness distribution the flux on scales of $\sim 0.6\lambda/b_{\mathrm{min}}$ can be fully recovered, while emission on scales up to $\sim \lambda/b_{\mathrm{min}}$ is partially recovered. This estimation comes from Fourier transforming the Gaussian source brightness distribution and estimating on what angular scale the recovered power drops to ~ 50 per cent.
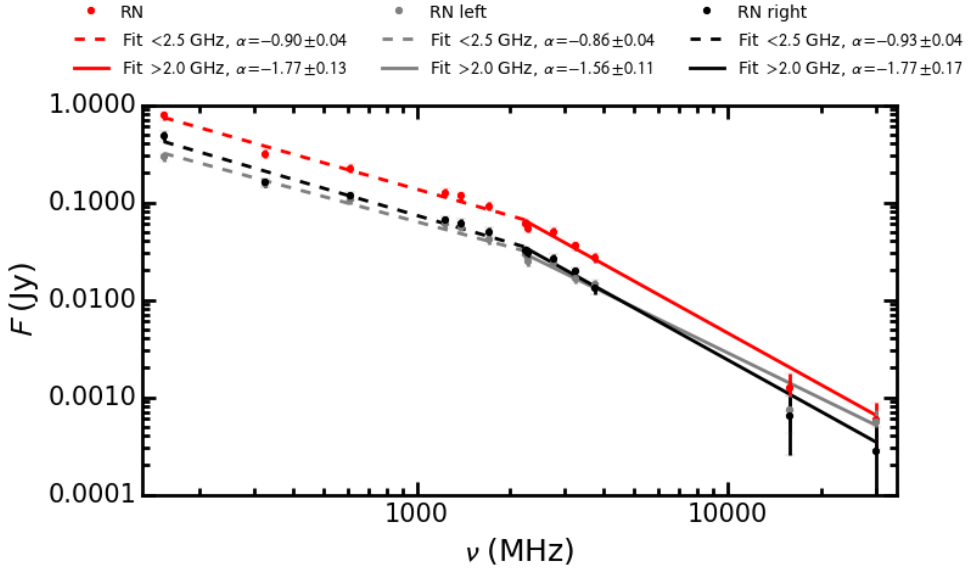
Figure 5.3: Integrated spectrum of the 'Sausage' radio relic measured at ~ 30 arcsec resolution from 150 MHz to 30 GHz. There is clear evidence for spectral steeping beyond 2.5 GHz. A single power law does not fit the data, while a broken power law provides a much better description. Note the results hold even when we split the source in two halves.
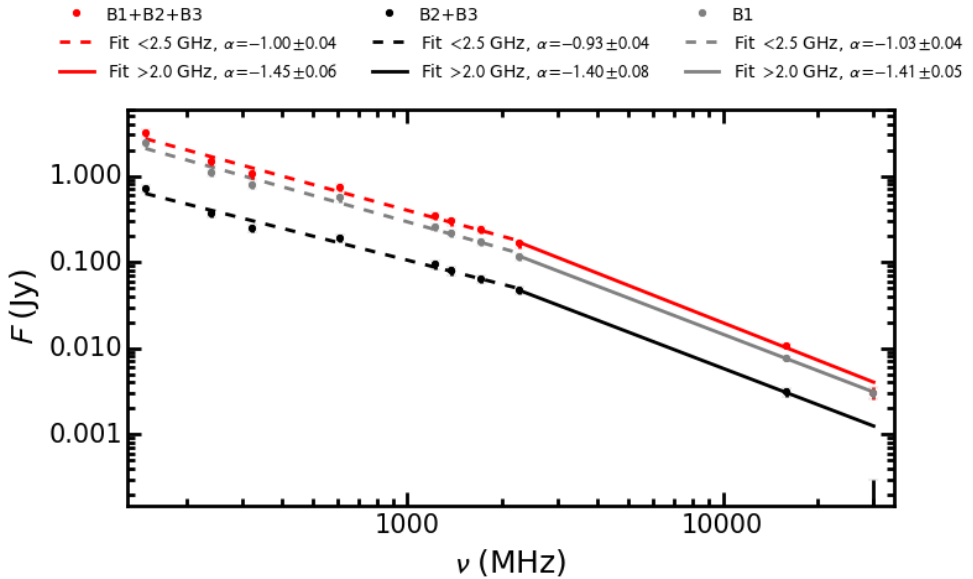
Figure 5.4: Same as Figure 5.3, but for the 'Toothbrush' relic.

the emission. For a given shock section we are capturing all the emission coming from the recently shock-accelerated electrons as well as the aged particles. Therefore the uv cut are not affecting the integrated flux density measurements, in the sense of biasing its shape because of preferential selection of young or old plasma in the downstream of the shock.

The images (as listed in Table 5.2), produced with uniform weighting and common uv-cut (from AMI-LA and CARMA) are shown in Figures 5.1 and 5.2 for the 'Sausage' and 'Toothbrush' relics, respectively. Note that even in uniform weighted images, which emphasise point sources and suppress diffuse emission, the relics are clearly detected till 30 GHz.

Obtaining flux density measurements

We measure the flux density of the relics using uniform weighted maps that sample the same scales on the sky and that are convolved to the lowest resolution available.

All the data were set to the same flux scale (e.g. note the very good agreement between the WSRT and VLA measurements at ∼ 2.3 GHz for the 'Sausage' relic). For all but the AMI data, we adopt a flux-scale uncertainty f of 10 per cent, following Stroe et al. (2013), resulting from telescope pointing errors and imperfect calibration. The AMI flux scale is precise within 5 per cent according to AMI Consortium: Davies et al. (2011). In the case of the interferometric images, the error ΔF on the integrated flux density F is calculated as function of the flux-scale error and image noise σ_{RMS}:

$$\Delta F = \sqrt{(fF)^2 + N_{\mathrm{beams}}\sigma_{\mathrm{RMS}}^2},$$ (5.1)

where N_{beams} is the number of beams spanned by the source.

Lower frequency, high resolution measurements show that the 'Sausage' and the 'Toothbrush' relics are both polarised (van Weeren et al. 2010; van Weeren et al. 2012b). As explained in Stroe et al. (2014b), both AMI sub-arrays measure a single polarisation (I+Q). The AMI reduction pipeline assumes random polarisation for the sources, therefore assuming that AMI measures only half the power. For randomly polarised sources the flux densities coming out of the pipeline are correct, however, the flux densities of polarised sources need to be reduced because the flux is overcorrected by the pipeline. Following the method from Stroe et al. (2014b), the AMI integrated flux density of the 'Sausage' relic has to be decreased by 24 per cent, compared to the single polarisation measured by AMI. In the case of the 'Toothbrush', the polarisation values from van Weeren et al. (2012b) were used to derive a flux density reduction of 12 per cent. The polarisation correction takes into account the polarisation fraction, the Faraday depth and the orientation of the electric vector with respect to the shock front at the lower frequencies to predict the rotation of the angle towards 16 GHz. Note however, that even if we assumed the sources to be fully unpolarised, their flux density would not change the overall integrated spectrum fits significantly (see below and Section 5.5).

Figures 5.8 and 5.9 display the areas used for integration for GMRT and WSRT, overlaid on a 1.2 GHz frequency map with the uv weighting and cut and resolution used for measuring the flux densities. We should note that flux densities of the 'Sausage' relic presented in this paper will be slightly different than those calculated in Stroe et al. (2014c) because of small differences in the area used for integration, which in the present paper follows more closely the distribution of the emission. For the VLA, AMI-LA and CARMA datasets we decided to

Table 5.3: Integrated radio spectrum of the 'Sausage' and 'Toothbrush' relics using comparable interferometric datasets. We list integrated flux densities, errors of the integrated flux densities (see equation 5.1) and the noise in the images. We use these measurements to probe emission up to ~ 2.6 arcmin on the sky.

Freq (GHz)	0.15	0.24	0.325	0.61	1.2	1.4	1.7	2.25	2.3	2.75	3.25	3.75	16	30
'Sausage'														
Flux density (mJy)	780.4		315.7	222.3	125.7	117.3	91.2	60.1	54.3	50.0	36.1	27.2	1.2	0.6
Error (mJy)	80.0		32.4	22.4	12.6	11.8	9.2	6.2	5.6	5.1	3.7	3.0	0.5	0.3
σ_{RMS} (mJy/beam)	2.4		1.0	0.30	0.16	0.13	0.15	0.14	0.16	0.14	0.06	0.17	0.06	0.04
'Toothbrush'														
Flux density (mJy)	3147.9	1466.7	1042.0	743.1	344.8	295.5	236.4		162.8				10.7	2.0
Error (mJy)	314.9	146.8	104.3	74.3	34.5	29.6	23.6		16.3				0.7	0.4
σ_{RMS} (mJy/beam)	1.0	0.89	0.24	0.17	0.062	0.05	0.05		0.10				0.05	0.05

measure the flux in boxes closely following the distribution of emission. Imperfect deconvo-
lution/cleaning can result in negative bowls appearing around bright sources. This effect is
mostly visible in our VLA, AMI-LA and CARMA data. In order to test this effect, we took
the interferometric GMRT, WSRT, VLA, AMI-LA and CARMA images with an 800 λ cut at
their native resolution and measured the flux in tight boxes, following the diffuse emission and
avoiding the negative bowls. We find that the 'Toothbrush' measurements for GMRT, WSRT
and AMI-LA are the consistent within the error bars to the values we get when convolving
to the lowest resolution and using a common integration area. The CARMA measurements
is a factor of ∼ 1.5 higher when we use a tight area and native resolution, than when using a
common integration area. We therefore use this new measurement in producing our integrated
spectrum. In the case of the 'Sausage', slightly higher flux values (factors < 1.5) are found
for the GMRT data, for the highest WSRT frequency, for the highest JVLA frequency and
for AMI-LA when use tight integration areas in the native resolution images. We use these
measurements in calculating the integrated spectrum to obtain the best values possibles.

We measure a flux density for the entire source as well as split the sources in two parts,
to test whether the integrated spectral trends we observed are dominated by one part of the
sources. Even when splitting the sources in two halves, the integrated spectrum should still
be characteristic for a summation of shock accelerated populations with ageing behind the
shock. The 'Sausage' and 'Toothbrush' relic flux density measurements at high resolution
from interferometric images can be found in Table 5.3.

Figures 5.3 and 5.4 show the flux density measurements and spectra of the 'Sausage' and
'Toothbrush' relic, respectively. As found by Stroe et al. (2014b), a single power law provides
a poor description of the data. We therefore fit the spectrum of each relic with two power
laws, one using the measurements below 2.5 GHz, and the other using the measurements
above 2.0 GHz. We use weighted least-squares regression, where each point is down-weighed
according to its error (as per equation 5.1). We fit the flux density for the entire source, as well
as split the source in two regions (left and right half for the 'Sausage' relic and the subareas
B1 and B2+B3, see Figure 5.2). The measurements and the results of the fit can be found in
Figures 5.3 and 5.4, for the 'Sausage' and 'Toothbrush' relics respectively. We find that the
low-frequency spectrum (< 2.5 GHz) greatly differs from the high frequency spectrum (> 2.0
GHz) for both sources. The low frequency spectrum for the 'Sausage' relic has a spectral
index of $\alpha = -0.90 \pm 0.04$, while beyond 2.5 GHz this steepens to -1.77 ± 0.13 (difference
significant at the 6.4σ level). In the 'Toothbrush', the low frequency spectrum differs from
the high frequency one at the $> 5.8\sigma$ level (-1.00 ± 0.04 versus -1.45 ± 0.06). The results
hold when splitting the source into two subareas, as explained above. Note than when we use
fluxes measured in the same box at all frequencies, we obtain spectra with slopes consistent
within the error bars with the slopes we obtain by using the fluxes obtained by best following
the emission.

5.3.2 Total power measurements

Radio relics are diffuse objects, so any spatial filtering applied by interferometers will affect
the measured total flux density. We also attempt to create a spectrum with our interferometric
data that have good short baseline coverage. This enables us to approximate a total power
measurement from interferometric dataset and compare them with Effelsberg data. For this

purpose we can use the GMRT data as well at the lowest frequency WSRT measurements which have baselines down to 100 λ corresponding to a largest spatial scale probed of ~ 21 arcmin. The rest of our interferometric data cannot properly pick up the largest scales of the relic emission, which Effelsberg detects.

Effelsberg data

The low resolution, total power images from Effelsberg are shown in Figures 5.1 and 5.2 for the 'Sausage' and 'Toothbrush' relics, respectively. In the low resolution images, the relics are detected at very high $S/N > 16$, but isolating the relic emission from the point sources is non-trivial.

Several radio galaxies are located nearby the relics which, could blend with the diffuse emission, depending on the resolution. In the interferometric images (with higher resolution, ~ 40 arcsec), blending is not a contaminant, since no radio sources are located too close to the diffuse emission. This can be clearly seen in very high resolution (~ 5 arcsec), deep (~ 25 μJy) GMRT images of the two relics (van Weeren et al. 2012b; Stroe et al. 2013).

However, contamination by radio galaxies is an important effect for the Effelsberg data. Radio galaxies are expected to have a flatter ($\alpha \sim -0.7$; Condon 1992) integrated index compared to the radio relics, and will, if anything, bias high the flux density measurement of the relics at higher frequencies. If the radio galaxy contribution is not properly subtracted, the relic flux density can be overestimated. The contamination is most important for the 'Sausage' relic, which is neighboured by an unrelated radio AGN (source H, see Figure 5.1) towards its eastern edge, which has a spectral index of -0.77 ± 0.04 (as measured from the interferometric images the with 800 λ inner uv cut).

The integrated flux densities for Effelsberg were measured using the option 'tvstat' in AIPS. For both relics and at both frequencies we defined integration areas around the relic down to a level where the intensity reaches the noise. Best efforts are made to properly subtract the compact sources from the diffuse emission. The point source flux densities are calculated by interpolating between their fluxes in the higher resolution images and subtracted from the relic flux density. For the 'Sausage' relic at 4.85 GHz, we subtract sources B and H (see Figure 5.1) from the flux density value by measuring their fluxes in higher resolution VLA C-array data at 4.9 GHz (data presented in van Weeren et al. 2010). At 8.35 GHz, source H was subtracted, as source B could be avoided for the integration. For the 'Toothbrush' relic, we subtract point sources F and G, using their fluxes measured in the 800 λ cut interreferometric measurements at 2.3, 16 and 30 GHz. Note however, the extrapolation of the flux density of contaminating radio sources is imperfect and could result in an overestimation of the relic flux density by $5 - 10$ per cent.

The uncertainties of the Effelsberg flux density measurements are dominated by the uncertainties in the baselevel of the maps. To correct the baselevel of each final map in Stokes I, Q and U, the mean intensity of each map was measured by selecting at least five boxes in regions where no emission from sources was detected. The average of these values was subtracted from the final map to result in maps with a baselevel near to zero. However there still is a possibility that the Effelsberg measurements do not lie on the same flux scale as the other interferometric data we aim to compare them with. The Effeslberg maps are too small to find large enough regions without signal: because of the large beams, the diffuse and compact flux
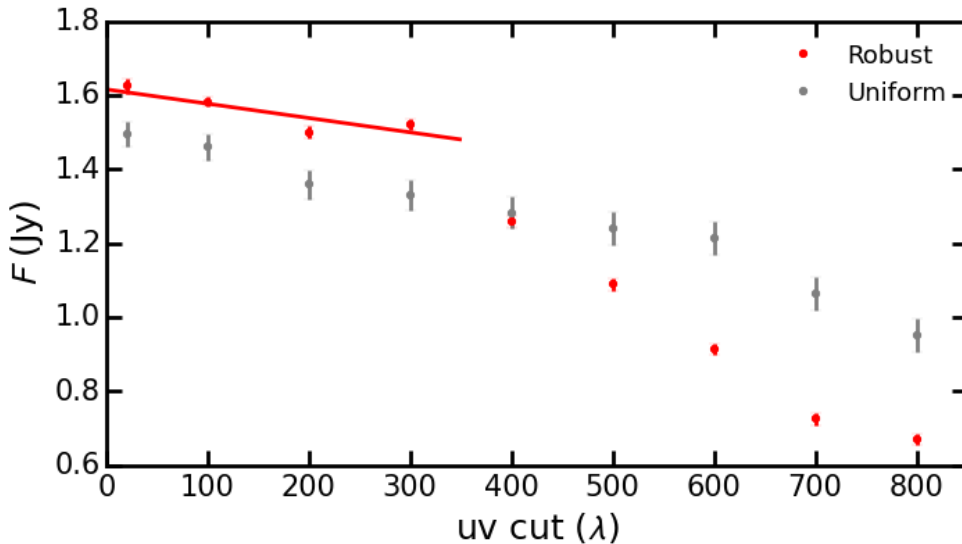
Figure 5.5: Dependence of the measured integrated relic flux density on the weighting and uv cut employed. Note that the uniform weighting is not as sensitive to the robust weighting. We use a fit to the points with uv cuts smaller than 300 λ to predict total power measurements for comparison with the Effelsberg data.

persists in the edges of the maps. Therefore the uncertainties in the baselevel corrections are quite large. Note, however, there is no diffuse cluster flux at the north of the relics, therefore setting the baselevel here does not result in a subtraction of the diffuse component from the Effelsberg measurements.

The error on the Effelsberg measurements is:

$$\Delta F = N_{\text{beams}} \sigma_{\text{b}}, \tag{5.2}$$

where N_{beams} is the number of beams spanned by the source and σ_{b} is the uncertainty of the baselevel (the standard deviation of the mean intensity in the boxes where the baselevel was measured). The errors on the Effelsberg flux densities could be in reality larger if we would account for any point source contamination remaining after the point source subtraction (which could be of up to 5-10 per cent).

The Effelsberg calibration was compared to the interferometric 4.9 VLA images of the 'Sausage' field (van Weeren et al. 2010), convolved to 90 arcsec resolution. The flux densities of sources B and H (see Figure 5.1) are consistent with −0.82 and −0.87 spectral indices between 4.9 GHz (VLA) and 8.35 GHz (Effelsberg).

Obtaining a total power measurement from interferometric measurements

We image the two relics at native resolution using the full uv coverage for GMRT and WSRT 1.2 GHz. We employ robust weighting to maximise the detection of large scale flux. The GMRT datasets at 150, 240 325 and 610 MHz have baselines down to 20, 40, 70 and 120 λ, respectively, while the WSRT 1.2 GHz dataset goes down to 100 λ uv distances.

The interferometric images, even imaged to best emulate a total power measurement, are not fully comparable to the Effelsberg observations, given interferometers resolve out flux detected by the single dish at Effelsberg. To assess how much flux can potentially be lost with interferometric imaging, we use the 150 MHz data for the 'Sausage' field, which has the best inner uv coverage going down to 20 λ. We image the data with different inner uv cuts, using both robust (with robust factor set to 0.5) and uniform weighting. The 150 MHz data set is suitable for this purpose since it covers spatial scales that are even larger than the cluster itself and has dense inner uv coverage. Figure 5.5 shows a plot of the integrated 'Sausage' flux density, measured in the same region, versus the minimum uv distance used for imaging. This plot is helpful in roughly estimating how much flux is lost depending on the inner uv cut. Note than the uniform weighting is not as affected as the robust weighting by the inner uv cut. For example, the 'Sausage' relic 150 MHz flux density drops by a factor of ~ 1.6 when using baselines beyond 800 λ instead of beyond 20 λ and uniform weighting. Therefore, we expect Effelsberg to measure a higher flux density than inferred from the > 800 λ interferometric observations only (such as those shown in Figures 5.3 and 5.4).

We fit the dependence of the relic flux density on the uv cut (using the uv cuts lower than 300 λ) and use this linear fit to predict total power measurements from the interferometric images. Note that the correction is imperfect given that structures at different frequencies and with different uv coverages will be recovered differently.

We measure the GMRT and WSRT radio relic flux densities in the native resolution of the images. If we were to smooth to the Effelsberg resolution, the flux densities would increase by a factor of at least 1.5. However, a correction for the contamination by radio sources would have to be included, which is imprecise as extrapolations need to be made. The flux density of radio galaxies can increase by a factor of up to 1.3, from a resolved to a heavily unresolved morphology. We tested the method of measuring the high resolution point source flux, smoothing the image and then subtracting the point source contamination but the results were within the error bars. Note that given the different resolutions of the interferometric and single dish data make it impossible for the flux densities to be measured in the same regions.

We calculate the error on the interferometric flux densities as in equation 5.1, however, we add 5 per cent to the flux-scale uncertainty to account for the different integration areas used in the low frequency maps and the Effelsberg measurements as well as to account for the extrapolation we make to total power flux densities.

Total power spectrum

The Effelsberg total power flux density measurements and the GMRT and WSRT fluxes emulating a total power measurement can be found in Figure 5.6 and Table 5.4. We fit the flux density measurements below 1.2 GHz with a power law and find that the slopes are consistent within the error bars with the slopes found from the higher resolution maps with 800 λ cut. For the 'Sausage' relic we find a slope of -0.99 ± 0.11 (compared to -0.90 ± 0.04 in the high resolution images), while for the 'Toothbrush' we obtain a slope of -0.92 ± 0.09 (versus -1.00 ± 0.04 in the high resolution maps). We use these fits to predict flux densities at 2.3 GHz and combine this prediction to obtain a high frequency slope, comparable with the fits in Section 5.3.1. We assume an error bar on the 2.3 GHz comparable with the 1.2 GHz error. In the case of the 'Sausage' relic, as found in Section 5.3.1, the high frequency spec-
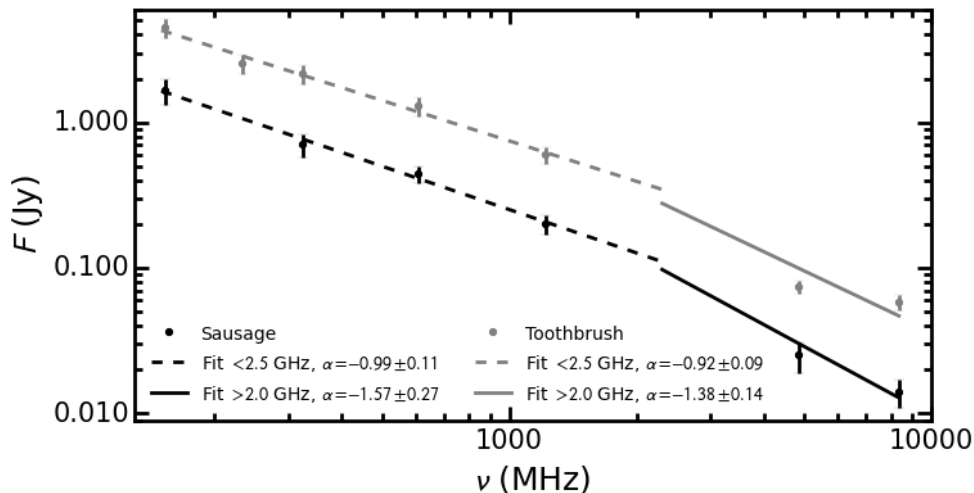
Figure 5.6: Integrated 'Sausage' and 'Toothbrush' relic spectrum using the Effelsberg measurements and interferometric observations corrected to obtain a total-power value. Note the values of the interferometric measurements are not fully comparable with the total power Effelsberg measurements, but this is included in the error bars. Note the spectrum is steepening towards high frequencies as observed from spectra made using comparable interferometric datasets probing the same spatial scales. A 2.0 GHz measurement is predicted using the low-frequency fit. This prediction is then combined with the Effelsberg flux densities to obtain a high frequency spectrum.

trum steepens with respect to the low frequency one with a slope of -1.57 ± 0.27, consistent with the steepening found in the high resolution maps (-1.77 ± 0.13). The 'Toothbrush' relic high frequency, total power measurements indicate a spectral index of -1.38 ± 0.15 (versus -1.45 ± 0.06). Therefore the low-resolution, total power measurements confirm the steepening found in Section 5.3.1.

5.4 Possible systematics decreasing high frequency flux densities

We explore possible systematic, instrumental effects which can cause the high frequency measurements to be biased low. We refer to the spectrum produced using comparable interferometric measurements as the interferometric spectrum and to the spectrum produced from Effelsberg and the interferometric data with best inner uv coverage as the total-power spectrum.

5.4.1 Mosaicking in the interferometric spectrum

The VLA, AMI-LA and CARMA data are all from mosaics, which means the primary beam correction might be imperfect, especially if the pointings are separated at large distances. AMI-LA has a primary beam of about 5.5 arcmin, which in principle means two pointings can cover the 'Sausage' and 'Toothbrush' relic over they full extent. However four pointings over

Table 5.4: Integrated radio spectrum of the 'Sausage' and 'Toothbrush' relics using the Effelsberg single dish and interferometric measurements best simulating a total-power measurement. We give the integrated flux densities and their errors. Single dish measurements are given with point sources subtracted.

Freq (GHz)	0.15	0.24	0.325	0.61	1.2	4.85	8.35
'Sausage'							
Flux density (mJy)	1655		700	440	200	25	14
Error (mJy)	337		126	60	30	6	3
'Toothbrush'							
Flux density (mJy)	4470	2510	2150	1290	600	74	58
Error (mJy)	680	380	320	190	80	8	7

the relics were used to alleviate the issue of the imprecise primary beam correction at large large distances from the pointing centre. Similarly, the CARMA observations were designed with 11 pointings over the sources. The VLA observations are also not susceptible to such errors, where two, closely spaced pointings were used to cover the 'Sausage' relic. Even at the highest VLA frequency, the radio relic is located in areas where the beam level is over 70 per cent of the peak sensitivity. At such levels, the primary beam is very well known and primary beam uncertainties are very small (<< 1 per cent). We further test the impact of the primary beams in the context of mosaicking, by measuring the VLA spectra of radio galaxies in the field (sources A, B, C, D, E, H using the labelling from Stroe et al. 2013, and unlabelled source located north of source H). The spectral indices of the these source vary between −1.26 and −0.93, with no systematic trends across the field of view (see also Figure 5.7. This indicates that primary beam uncertainties do not affect the measurements.

5.4.2 Flux scale

An issue with the flux scale at a particular frequency could result in an underestimation of the flux. The spectra for bright sources well detected at all frequencies are shown in Figure 5.7. The integrated spectra of these radio galaxies n the GMRT, WSRT, VLA, AMI-LA and CARMA data are described by smooth curves, indicating all the observations are on the same flux scale. Note that at higher resolution, galaxies C, D, H in the 'Sausage' field and F in the 'Toothbrush' field' are actually old, head-tail radio sources where ageing of electrons in the lobes can be clearly detected (van Weeren et al. 2012b; Stroe et al. 2013). The integrated spectrum of such sources is expected to slightly steepen at high frequencies because of synchrotron losses Condon (1992). However, there are no systematic breaks happening at a particular frequency, which could indicate a particular observation being on the wrong flux scale.

Also note the very good agreement between the WSRT and VLA measurements at ∼ 2.3 GHz for the 'Sausage' relic, indicating that the WSRT and VLA data are on the same flux scale. Moreover, we are finding a steepening in the spectrum of the two relics using data taken with three independent telescopes. It is highly unlikely that the flux scale of AMI, CARMA and VLA is biased low for independent measurements of two sources.

We therefore conclude that flux-scale issues cannot explain the steepening of the relic spectrum at high frequencies.
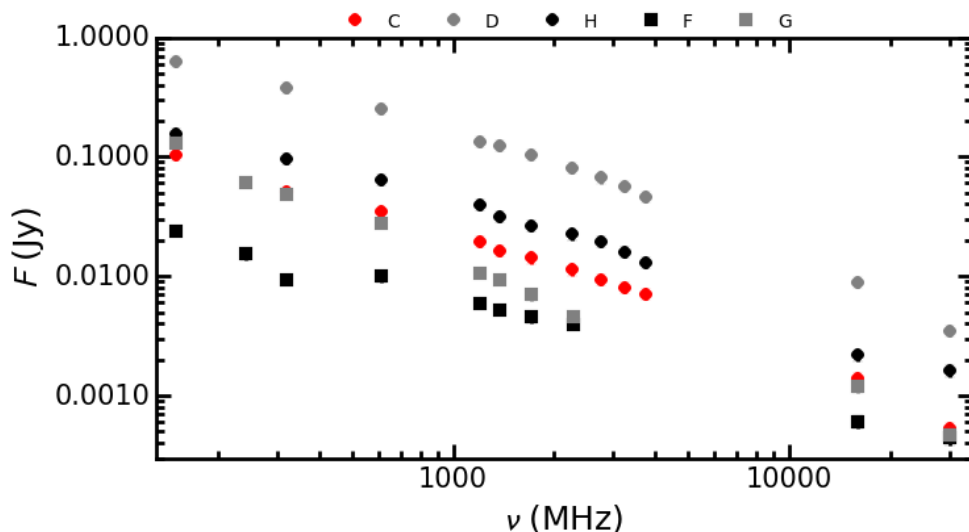
Figure 5.7: Integrated spectra for radio galaxies in the 'Sausage' (circles) and 'Toothbrush' (squares) fields. Source with clear detections at all frequencies are plotted. For labelling see Figures 5.1 and 5.4. The spectra show that there are no systematic flux-scale errors or primary beam imperfections affecting our data.

5.4.3 Sunyaev-Zeldovich decrement

At frequencies below ~ 217 GHz, the SZE is detected in decrement relative to the baseline given by the cosmic microwave background, causing a reduction in the measured flux densities of sources close to the cluster center, where the SZE is strongest. The SZE is a cluster-wide, large-scale effect. At the resolution of AMI-LA and CARMA the largest scale detectable is limited by virtue of interferometric observations. For example, AMI-LA observations of the clusters in the XMM Cluster Survey (XCS; AMI Consortium: Shimewell et al. 2013) and the Local Cluster Substructure Survey (LoCuSS; AMI Consortium: Rodríguez-Gonzálvez et al. 2012) resulted in no SZE detection. Additionally the AMI-SA observations measured a total SZE flux < 2 mJy, indicating the SZE contribution will be extremely small ($\lesssim 50\,\mu$ Jy, or less than ~ 5 per cent of the relic flux density) at AMI-LA resolution and at the large cluster-centric distances the 'Sausage' and 'Toothbrush' relics are located (1.5 Mpc). Even though the relics are located far away from the cluster centre, Erler et al. (2015) argue that shock compression could boost the SZE signal, leading to up to 30 per cent decrease at 10 GHz for Effelsberg observations of the relic of Abell 2256 (Trasatti et al. 2015). There is an important difference between our observations and Abell 2256: the relic in Abell 2256 is about 500 kpc from the cluster center, while the 'Sausage' and 'Toothbrush' clusters are 1.5 Mpc away from the cluster centre. Trasatti et al. (2015) argue that in the case of Abell 2256 the SZE decrement is of the order of 30 per cent at the distance of the relic from the cluster center (about 500 kpc). They estimate that at a distance of 750 kpc the SZE induced decrement drops to 15 per cent. However, the 'Sausage' and 'Toothbrush' relics are located about 1.5 Mpc away from the cluster centre, hence the SZE contamination would be very small. A linear extrapolation from the estimations of Trasatti et al. (2015) indicates a contamination at the level of < 5 per

cent, while a beta-profile for the ICM density would lead to even smaller numbers. Note that even if a significant decrement of a factor of 2 would be contaminating the AMI, CARMA or Effelsberg relic measurements, that would still not be enough to explain the discrepancy between the expected flux densities by extrapolation from the low frequency measurements and the measured fluxes. By extrapolating the low frequency spectrum of the 'Toothbrush', the AMI and CARMA flux densities would have to be 3.5 and 6 times higher than measured, respectively. In the case of the 'Sausage' the flux densities predicted from the low frequency spectrum are more than 10 times higher that those measured.

5.5 Why is the integrated relic spectrum steepening?

Using measurements at ~ 15 independent frequencies we find that the high frequency spectrum of the 'Sausage' and 'Toothbrush' relics differs significantly ($\gtrsim 6\sigma$) from the low frequency spectrum. Our estimates indicate systematic biases cannot account for the observed measurements.

In the simple radio relic formation scenario proposed by Ensslin et al. (1998) the shock strength is constant in time, the magnetic field is constant across the source and thermal particles are injected at the same rate. Under these assumptions, the index of the integrated spectrum should be 0.5 steeper than the injection index (Ensslin et al. 1998) and the injection index α_{inj} can be directly translated to a Mach number through $M = \sqrt{(2\alpha_{\mathrm{inj}} + 3)/(2\alpha_{\mathrm{inj}} + 1)}$ (Blandford & Eichler 1987). This only holds if we are observing the spectrum away from the break frequency (ν_{br}), where we detect the electrons which have started to lose energy through synchrotron and inverse Compton processes at a steady rate. Our measurements are incompatible with this simple model currently adopted for the formation of radio relics and explore other scenarios that could result in a curved integrated spectrum. If any of the assumptions of the model are broken, the integrated spectral steepening result can differ from the canonical 0.5.

We now discuss possible physical scenarios which would lead to a curved integrated relic spectrum. In the following discussion we focus on the spectra produced from comparable, high resolution (~ 40 arcsec) interferometric maps produced with an $800\,\lambda$ inner uv cut.

5.5.1 Non stationary shock conditions

Simulations by Kang (2015) show that stationary shock conditions (as in the model of Ensslin et al. 1998) cannot be assumed for cluster merger shocks as they are expanding into a medium with decreasing density and temperature. Our data supports these simulations, since the integrated spectral index of the two relics is about -0.9 at low-frequency and steepening to more than ~ -1.5 at higher frequencies. If we assume we are observing far away from ν_{br}, this is inconsistent with the simple Ensslin et al. (1998) model, as subtracting 0.5 would result in an injection index that is too flat and an infinite Mach number.

5.5.2 Structure in the Mach number or magnetic field distribution

If the magnetic field or Mach number are not uniform across the source causing anisotropies in the rate of particles injected, then the assumptions of the simple DSA scenario proposed by

Ensslin et al. (1998) are broken. The Mach number for example would mildly strengthen as it propagates outwards, impinging on lower density and lower temperature ICM gas (Brunetti & Jones 2014). However, observations of the brightness distribution, spectral index and electron age of the two relics indicate a relatively uniform structure, and hence a relatively constant Mach number throughout the source. Therefore anisotropies in the Mach number are not a pivotal factor in shaping the relic spectrum (van Weeren et al. 2010; van Weeren et al. 2012b; Stroe et al. 2013, 2014c).

Simulations indicate that magnetic fields at the location of the shock are aligned and amplified (Iapichino & Brüggen 2012), while significant turbulence develops in the shock downstream area (Paul et al. 2011). Note however, such effects are heavily dependent on the assumed model. A slowly decaying magnetic field from the shock region into the downstream area would lead to a decreasing cooling rate of the electron away from the shock.

A magnetic field stronger at the shock than in the downstream area would lead to an integrated spectrum dominated by the freshly accelerated electrons located in the immediate vicinity of the shock front. The spectrum will therefore be closer to what is expected for freshly DSA-accelerated electrons, so not 0.5 steeper spectrum as usually assumed in the case of a uniform mix of fresh and ages electron. If one would assume this integrated spectrum come from continuous injection of electrons, and subtract 0.5 to obtain an injection spectrum, the injection index derived will be too flat and the Mach number overestimated. However, the integrated spectra would depend on how the magnetic field varies (as the energy of electrons emitting at a given frequency changes as function of magnetic field). For instance, if the field is strong at the shock the high energy particles radiate their energy quickly. A field weakening into the downstream area means that the electrons needed to emit at a given frequency will disappear more quickly, so that the spectrum is actually steepened more. In order to reproduce a curving spectrum, we would need to amplify cooling in the downstream area.

The turbulence in the downstream area might re-accelerate the particles injected by the shock, instead of suppressing the high frequency emission. Any downstream re-acceleration would be expected to boost the brightness of emission of aged electrons, most likely leading to a very flat spectrum, rather than a curved one. Additionally, turbulent re-acceleration is a slow process as it requires the large bulk motions to cascade into small scale turbulence ($\gg$ 100 Myr) which are able to accelerate particles with sufficient efficiency (Brunetti & Lazarian 2007).

5.5.3 Seed population with energy distribution cut-off

Another scenario would be shock re-acceleration of a seed population with a cut-off in the energy distribution. Including both locally injected, thermal particles and particles coming from upstream area of the shock, DSA takes all the particles in a small energy range and redistributes them into a power law at higher energies with a certain slope (Drury 1983). If all the particles enter the process at energies well below ($4 - 5$ orders of magnitude) the one of interest then the appropriate slope at the energy of interest is the 'standard' test particle slope (Melrose & Pope 1993). If, on the other hand, the initial population being accelerated includes particles around the energy of interest ($\gamma \sim 10^4$), the relative contributions starting at different energies have to be considered, resulting from a blend of particles that entered at different starting energies which need to be weighted accordingly (e.g. Gieseler & Jones 2000). To a

first approximation, if the initial population at the energy of interest has a steeper spectrum than the classic DSA test particle slope, the outcome is the classic slope. For example, Kang (2011) and Kang & Ryu (2011) show that when pre-accelerated particles are considered, the overall spectral shape is conserved, as long as the seed population does not have a spectral break and the spectrum is flatter than the injection index given by the Mach number of the shock (hence the population is young, recently accelerated). Therefore, only the normalisation changes, because of the more efficient particle injection. Therefore, the DSA acceleration scenario, when modified for young relativistic particles, cannot explain the steepening of the spectrum towards high frequencies.

If, instead, the initial spectrum at or just below the one of interest is flatter than the classic slope for that shock, the outcome slope is the same as the one coming in (e.g. Kang & Ryu 2011). This was also observed in simulations tailored to the 'Sausage' relic, which find a good agreement to the observed low-frequency (< 1.5 GHz) spectrum (Kang et al. 2012).

If the incoming spectrum steepens or cuts off at high energies, then the output spectrum at high energies will take the flatter value of that coming in and the classic DSA slope for this shock. DSA always adds energy to the particle population (Drury 1983). Therefore, at a given energy, the number of particles after DSA acceleration will be higher than the number of particles at that energy before DSA (Drury 1983). Every particle gains, on average, an amount of energy proportional to its initial energy with a factor that depends on the number of times it bounces across the shock and the shock speed jump. The efficiency of energy transfer in DSA can be larger when an upstream, pre-accelerated population is involved, since the energy gain scales with the initial energy.

A few studies attempted to model radio relic spectra using DSA re-acceleration of seed, relativistic electrons with a break in the energy spectrum. Most recently, Kang & Ryu (2015) performed DSA simulations matched to the 'Sausage' relic, which indicate that a seed population with a break in the energy distribution, once re-accelerated by the shock, would result in a steepening integrated spectrum. The authors suggest that electrons sourced from past AGN activity or previous shocks, have since aged, resulting in a distribution with an exponential fall-off a high energies. Fossil electrons previously accelerated by accretion shocks would reside at a few 100 MeV energies and have a very long lifetime of a few Gyr, without being directly detectable in the radio. Observationally, this is supported by studies such as Shimwell et al. (2015) where an active radio galaxy is most likely feeding the plasma for a nearby relic. The authors suggest that pre-accelerated plasma could stream for Mpc distances along lines of equipotential ICM specific entropy, which at large cluster-centric distance can be approximated by spherical shells. However, none of the scenarios Kang & Ryu (2015) tested fully matched the GMRT, WSRT and AMI-LA observations from Stroe et al. (2014b) of the 'Sausage' cluster, and the authors conclude additional processes apart from radiative losses might be operating in radio relics.

However, Kang & Ryu (2015) only tested two basic models for the seed population. They did not vary the cut-off energy or the shape of the cut-off. For example, if the source of the plasma are radio galaxies, the break frequency of the population depends on the age of the plasma. A heavily aged seed population would have a strong, exponential cut-off spectrum which would translate into a curved integrated spectrum. However, as noted by Kang & Ryu (2015), the break in the spectrum is difficult to explain with synchrotron emission, as only a sharp break at $\gamma \sim 10^{4-5}$ in the seed electron population can explain the spectrum. A scenario

involving re-acceleration, namely one which preserves the break in the spectrum, is consistent with the observed spectrum.

5.5.4 Best scenarios?

All in all, scenarios with strong downstream magnetic fields or involving an aged electron population represent promising avenues for explaining the steepening of the spectrum. However more data and simulations are needed to explore these options.

High-resolution images at 4 GHz from VLA, which better resolve the 'Sausage' relic, point out possible anisotropies in the brightness distribution not visible at current resolutions (e.g. filaments; van Weeren et al. in prep.). Such filaments could be related to variations in the magnetic field strength, while polarisation measurements from the same data will be able to reveal the magnetic structure in more detail. Simulations probing the full parameters space of cut-off energy of the seed electrons and the strength of the cut-off are required, in order to match observations.

5.6 Conclusions

In this paper, we have presented high frequency (> 2.5 GHz) radio observations of the 'Sausage' and 'Toothbrush' relics. We combined these new measurements with GMRT and WSRT to study the relic spectrum over 2.5 dex in frequency.

- We successfully detect the 'Sausage' and 'Toothbrush' relics at high-radio frequencies up to 30 GHz.

- Using CARMA and AMI, we find compelling evidence for steepening in the high frequency spectrum of both relics. The low frequency (< 2.5 GHz) spectrum of both the 'Sausage' and 'Toothbrush' relics is well described by a single power law with spectral index ~ -0.9. The high frequency spectrum (> 2.0 GHz) is steeper than ~ -1.45 in both cases. The result hold when using predicted, total power flux densities.

- The Ensslin et al. (1998) model cannot explain the observed spectrum. A possible explanation would be that the relics are formed through shock acceleration of seed relativistic electrons with sharp spectral breaks at $\sim$ Gev energies, e.g. pre-accelerated from past AGN activity.

The models currently tested are all DSA-based with variations in the seed population. However, the mismatch between the models and the observations seems to suggest it is necessary we revisit the theory of radio relics. Therefore, the development of new theoretical models, building upon the observations presented here, is necessary. To attain this goal, high frequency data is crucial. To further remove uncertainties more measurements must be done and simpler, more compact relics are the ideal candidates to alleviate difficulties and minimise bias that may occur by missing flux when observing at high frequency. Unfortunately, given the impending decommissioning of CARMA, the spectral width of the observations presented here is likely to be unsurpassed until upcoming very low and very high frequency instruments are fully rolled out with accurate flux scales, high resolution (e.g. Low Frequency Array,

LOFAR, international baselines) and large field of view (e.g. low bands of Atacama Large Millimeter/submillimeter Array, ALMA). Till then, instruments such as Effelsberg and the Green Bank Telescope will be able to give us CARMA-like resolution at ~ 30 GHz.

Acknowledgements

5.7 Appendix

5.7.1 Areas used for measuring integrated flux densities for the interferometric spectrum

In the comparable interferometric images with 800 λ uv cut and uniform weighting, we use the same region at all frequencies for measuring the integrated spectra of the 'Sausage' and 'Toothbrush' relic. Using the same region ensures the summing up of emission from electrons with all ranges of ages, from recently accelerated particles to particles injected > 100 Myr in the past. This results in a spectrum measured given the assumptions laid out in Ensslin et al. (1998). Using a too large area would result in contamination from point sources or diffuse giant halo emission. However, a too small area would not fully probe the downstream area.
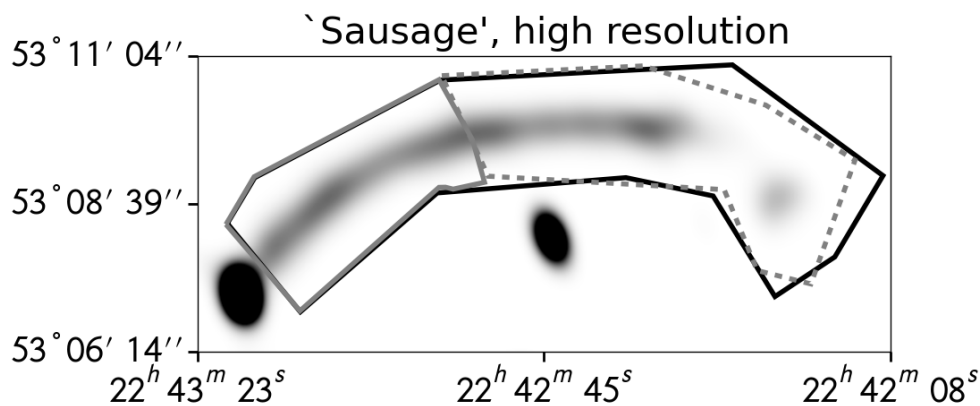
Figure 5.8: Area used for measuring the integrated spectrum of the 'Sausage' radio relic. The area is large enough to capture diffuse emission in the downstream area of the shock, while avoiding contamination from radio galaxies (such as source H and B in Figure 5.1).
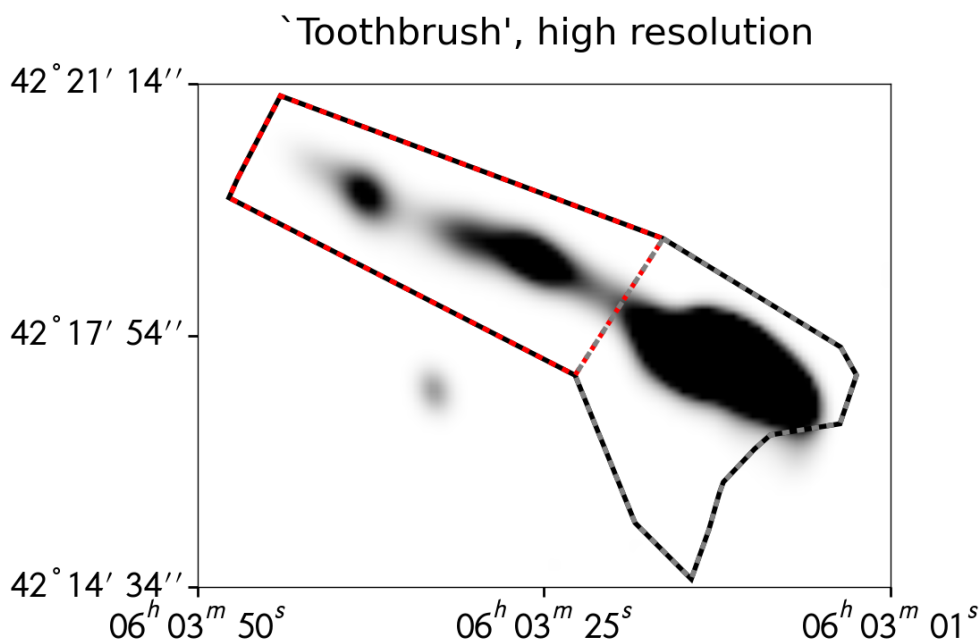
Figure 5.9: Area used for measuring the integrated spectrum of the 'Toothbrush' radio relic. The area was designed to avoid a point source close to component B1, which is very bright at high frequencies (see Figure 5.2).

6

The role of cluster mergers and travelling shocks in shaping the Hα luminosity function at z ~ 0.2: 'sausage' and 'toothbrush' clusters

The most extreme cluster mergers can lead to massive cluster-wide travelling shock waves. The CIZA J2242.8+5301 ('sausage') and 1RXS J0603.3+4213 ('toothbrush') clusters ($z \sim$ 0.2) host enormous radio-emitting shocks with simple geometry. We investigate the role of mergers and shocks in shaping the Hα luminosity function, using custom-made narrow-band filters matching the cluster redshifts mounted on the INT. We surveyed ~ 0.28 deg^2 for each cluster and found 181 line emitters in the 'sausage' (volume of 3.371×10^3 Mpc^3 for Hα at $z = 0.1945$) and 141 in the 'toothbrush' (4.546×10^3 Mpc^3 for Hα at $z = 0.225$), out of which 49 ('sausage') and 30 ('toothbrush') are expected to be Hα. We build luminosity functions for the field-of-view down to an average limiting star formation rate of 0.14 M$_\odot$ yr^{-1}, find good agreement with field luminosity functions at $z = 0.2$, but significant differences between the shapes of the luminosity functions for the two clusters. We discover extended, tens-of-kpc-wide Hα haloes in galaxies neighbouring relics, which were possibly disrupted by the passage of the shock wave. By comparing the 'sausage' cluster with blank fields and other clusters, we also uncover an order of magnitude boost (at 9σ level) in the normalisation ϕ^* of the luminosity function in the relic areas. Our results suggest that cluster mergers may play an important role in the evolution of cluster galaxies through shock-induced star formation.

6.1 Introduction

Tracing star formation across cosmic time and in different environments is instrumental to our understanding of galaxy evolution. Studies have shown that star formation (SF) activity has steadily declined since redshift $z \sim 2 - 3$ (Lilly et al. 1996; Hopkins & Beacom 2006; Sobral et al. 2013a). There is also a striking difference between field galaxies and systems within cluster environments: the fraction of blue, actively star forming, late-type galaxies is systematically lower in the latter (Dressler 1980; Goto et al. 2003). Multiple authors (e.g. Lewis et al. 2002; Gómez et al. 2003; Tanaka et al. 2004; Balogh et al. 2004) have therefore concluded that the SF rate is strongly dependent on local galaxy density. Early-type galaxies, predominately found in cluster environments, are more massive than their star-forming counterparts (Kauffmann et al. 2003). However, Peng et al. (2010) have shown that the effect of mass can be distinguished from that of environment, although both effects have important contributions. While the shape is similar, the overall normalisation of the Hα luminosity function (LF) in low-redshift $z \sim 0.2 - 0.4$ rich clusters is ~ 50 per cent lower than for the field (Balogh et al. 2002; Couch et al. 2001; Kodama et al. 2004). The difference between cluster and field spiral galaxies is evident also from radio observations of neutral hydrogen: cluster spirals contain significantly less HI gas than their field counterparts (e.g. Cayatte et al. 1990). There has been evidence of ram pressure stripping of the HI and Hα gas in infalling cluster galaxies, such as tidal tails and filaments (Gavazzi et al. 2001; Oosterloo & van Gorkom 2005). Interaction of galaxies with the intra-cluster medium is evident within high-redshift galaxies. Alignment of optical and radio continuum in active galaxies (e.g. Djorgovski et al. 1987; McCarthy et al. 1987) has prompted an interpretation where the travelling shock front at the wake of the radio lobes triggers star formation (Rees 1989). While the shock would evacuate the radio lobe of its hot gas and shock-heat the surrounding medium, the cool clouds within the radio lobes would collapse to form stars in this over-pressured environment.

The luminous components in galaxy clusters can reveal the complex evolution of baryonic matter through cosmic time and the interplay between the intra-cluster medium (ICM) and the cluster galaxies. Driven by mergers with other galaxy clusters and groups, the growth of clusters releases copious amounts of gravitational energy deposited into the ICM (e.g. Sarazin 2002), with direct evidence from the X-ray and radio in the form of shock fronts. The strongest cluster major mergers can produce cluster-wide shock waves that travel through the intra-cluster medium and accelerate particles through the diffusive shock acceleration mechanism (Drury 1983). Shock waves can be detected in the X-ray as density/temperature discontinuities (e.g. Markevitch et al. 2005) or in the radio bands as relics: elongated, diffuse synchrotron emitting areas located at the periphery of merging clusters (see review paper by Feretti et al. 2012).

The precise effect of the merging history of a cluster on the evolution of galaxies is unknown. The profound impact of the travelling shock waves on the ICM raises questions regarding the interaction between the galaxies within the cluster and the shock front, coupled with the merging nature of the cluster. What is the effect of the travelling shock wave on the ISM of galaxies and their star formation activity? Are there any morphological differences between galaxies in the pre- and post-shock regions?

To measure the effect of the travelling shock waves on the SF activity within clusters, we need to trace massive, newborn stars within the cluster galaxies. These stars emit strong,

ionising UV radiation. While this is often absorbed in nearby regions, it is then re-emitted through a variety of processes, such as far-infra-red (FIR) black-body emission (from the heated dust) and recombination lines, of which the Hα recombination line is the strongest and best calibrated. Hα suffers only from modest dust extinction and is much more sensitive to instantaneous SF than the UV/FIR. An excellent way to detect line emitters over large areas entails using narrow-band filters tuned to be sensitive to the Hα emission redshifted at the distance of your source of interest. Subtracting the broad-band (BB) emission from the narrow-band (NB) emission singles out sources which have line emission. In recent years, large Hα surveys of blank fields have been carried out up to redshift 2.23 (Fujita et al. 2003; Ly et al. 2007; Shioya et al. 2008; Villar et al. 2008; Geach et al. 2008; Sobral et al. 2009; Ly et al. 2011; Sobral et al. 2011; Drake et al. 2013; Sobral et al. 2013a). Studies of clusters have been limited to low-redshift relaxed, rich clusters (Couch et al. 2001; Balogh et al. 2002; Kodama et al. 2004) or higher redshift ($z = 0.8, 1.47$), almost virialised clusters (Koyama et al. 2010; Hayashi et al. 2010; Koyama et al. 2013).

Until now, it has been difficult to address the merging cluster Hα LF, owing to a lack of suitable systems. To directly interpret observables such as the radio/X-ray morphology and galaxy distribution in terms of simple physical parameters, we would like to study equal mass systems merging in the plane of the sky with a low impact parameter, ideally at a moment in time when shocks are prominently present. Recently, van Weeren et al. (2010) and van Weeren et al. (2012b) have discovered spectacular Mpc-size, coherent radio shocks in two merging clusters with the required properties. CIZA J2242.8+5301 (nicknamed the 'sausage') is a binary merging cluster at $z = 0.192$ (see Figure 6.6). A 2 Mpc relic at the northern periphery dwarfs a smaller one located symmetrically across the cluster centre. The northern relic is marked by signatures of cooling, synchrotron-emitting particles in the post-shock region. Stroe et al. (2013) discovered a bi-modality in the orientation of the head-tail radio galaxies which act as a tracer of the two merging clusters. Cluster 1RXS J0603.3+4213 (nicknamed the 'toothbrush'), at $z = 0.225$ (see Figure 6.7), hosts a 2.5 Mpc long and straight radio relic and also a smaller relic towards the south-east. Both clusters have a disturbed, elongated X-ray morphology (Ogrean et al. 2013a; Ogrean et al. 2013b; Akamatsu & Kawahara 2013), indicating they are post-core passage mergers. The different merger histories and post-merger timescales of the two clusters might provide valuable information about the evolution of the interaction between the galaxies and the shock front.

In this paper, we characterise the nature of galaxies in highly disturbed, $z \sim 0.2$, merging clusters hosting radio relics. We explore the imprint of the travelling shock wave on the morphology of the ionised gas within galaxies and on the Hα luminosity function. The paper is structured in the following way: in §6.2 we give an overview of the observations and the data reduction, in §6.3 we present the results, §6.4 shows the implications for galaxy evolution within merging clusters. The main points are summarised in §6.5. A flat, ΛCDM cosmology with $H_0 = 70.5$ km s^{-1} Mpc^{-1}, matter density $\Omega_M = 0.27$ and dark energy density $\Omega_\Lambda = 0.73$ is assumed (Dunkley et al. 2009). At the redshift of the 'sausage' cluster, 1 arcmin corresponds to 0.191 Mpc, while for the 'toothbrush' it measures 0.216 Mpc. All images are in the J2000 coordinate system. We use the online cosmological calculator described in Wright (2006). All magnitudes are in the AB system, except where noted otherwise.

Table 6.1: Filter properties: type (narrow band, NB, or broad band, BB), central wavelength, full width at half maximum and the redshift range $z_{H\alpha}$ for which the Hα line is detected within the FWHM of the narrow band filters.

Filter	Type	λ_c (Å)	FWHM (Å)	$z_{H\alpha}$
NOVA782HA	NB	7839.0	110	$0.1865 - 0.2025$
NOVA804HA	NB	8038.5	110	$0.2170 - 0.2330$
WFCSloanI	BB	7743.0	1519	–

6.2 Observations & Data Reduction

6.2.1 Isaac Newton Telescope observations

Optical imaging data were obtained with the Wide Field Camera (WFC)[1] installed at the prime focus of the Isaac Newton Telescope (INT) [2]. The large field of view (FOV) enables us to instantaneously capture each cluster and its outskirts within 0.3 deg^2 using a single method (equivalent to the area shown in the radio intensity in Figs. 6.6 and 6.7). This corresponds to an area of 6.5×6.5 Mpc, thirteen times the expected virial size of the cluster (Sarazin 1986). The instrument is a mosaic of four chips of 2048×4100 pixels, arranged in a square with a 1′ inter-chip spacing. The CCDs have a pixel scale of 0.33 arcsec pixel^{-1}. The FOV is $34.2′ \times 34.2′$, with the top north-western corner missing (e.g. Fig. 6.6). We used the WFCSloanI broad band (BB) filter centred at 7743 Å and full width at half maximum (FWHM) of 1519 Å, and custom made narrow band (NB) filters NOVA782HA ($\lambda_c = 7839$ Å) and NOVA804HA ($\lambda_c = 8038.5$ Å), both 110 Å wide at FWHM. The NB filters were designed to match the redshifted Hα (restframe $\lambda = 6562.8$ Å) emission at the redshift of the clusters ($z = 0.1945$ and $z = 0.2250$, respectively). Figure 6.1 presents the filter response and the redshift of Hα emission they trace. The values are also summarised in Table 6.1.

The two fields were observed between October 13–22, 2012. Conditions were photometric for six nights, when the seeing varied between 0.9 and 1.1 arcsec. Individual exposures of 200s in the BB and 600s in the NB were taken in 5 jittered positions to cover the chip gaps and obtain a contiguous coverage of the FOV.

Figure 6.1: Transmittance profiles for the three filters used in this analysis. The solid black line marks the profile of the BB filter. The solid yellow line defines filter NOVA782HA and the dashed red line the filter NOVA804HA. The top x-axis marks the redshifted Hα coverage of the filters. The vertical lines mark the redshifts of the two clusters.

Both clusters are found at low Galactic latitudes ($-5.1°$ for the 'sausage' and $9.7°$ for the 'toothbrush') and suffer from substantial dust extinction: 0.76 mag and 0.38 mag at the NB filter wavelength, respectively (see Fig. 6.2). The total integration times were driven by the

---

[1]http://www.ing.iac.es/engineering/detectors/ultra_wfc.htm
[2]http://www.ing.iac.es/Astronomy/telescopes/int/

different extinction values for the two clusters to reach a similar flux limit and obtain comparable results for the two targets. The details of the observations can be found in Table 6.2.

6.2.2   Reduction

We created a pipeline following the standard procedure for optical data reduction. Before reducing the data, bad frames were rejected, such as frames affected by significant cloud extinction (> 0.3 mag), drifting pointing, poor focussing and read-out issues. This resulted in removal of ∼ 40 per cent of the frames (see Table 6.2). The data were then split into individual frames for each camera chip and processed independently.

A 'master flat' was obtained for each filter by median-combining and normalising all of the available sky flats from all the nights. One 'master bias' was obtained for each night. After the science frames were bias-subtracted and flattened, astrometric solutions with $0.3 - 0.4$ arcsec root-mean-square (rms) were obtained with SCAMP (Bertin 2006) and the USNO-B1.0 catalogue red magnitude Imag (Monet et al. 2003).

The background noise level was not constant after flat-fielding, but presented regular, large-scale patterns not associated with real sky features. This effect, called fringing, is caused by thin-film interference in the CCD and specifically affects the red part of the optical spectrum, where our data were taken (Lewis et al. 2000). It is crucial to remove this additive contribution from the science frames to robustly extract even the lowest signal-to-noise (S/N) sources. The ripples across the image are tied to positions in the sky and cannot be simply removed with normal flattening. Therefore, we produced a 'super-flat' by median-combining the science frames with sources masked. We used this 'super-flat' to self-flatten the data, which eliminated the fringing.

In order to mask non-responsive or hot pixels, we blanked pixels that deviated by more than 3σ from the local median value of the flat.

6.2.3   Photometry

Each frame was photometrically calibrated before co-adding using the USNO-B1.0 catalogue. Typically 200-300 sources were matched to the USNO-B1.0 Imag catalogue (Monet et al. 2003) and the differences between the inferred magnitudes and the ones from the USNO-B1.0 were computed. We used the median of these differences as our initial zero-point (ZP), compared that with ZP=25, and derived the appropriate scaling factor to set the magnitude ZP of each image to 25. We note that the individual 0.2 mag uncertainties of the USNO-B1.0 Imag catalogue naturally lead to a scatter in the magnitude distribution of about 0.2 mag, but that we always match a sufficiently large number (∼ 250) of sources for the median to provide a robust ZP (error ∼ 0.05 mag) measurement. This step ensures the BB and NB frames are on the same magnitude scale. We finally combined all the calibrated frames, normalised to the same ZP, for each field and filter using SWARP (Bertin et al. 2002). This included a mesh-based sky background subtraction.

To check the consistency of these magnitudes with the Sloan AB system, we also performed an extra two-step calibration. The Sloan survey does not cover our targets, but the USNO-B1.0 catalogue (Monet et al. 2003) provides an all-sky coverage in three optical colours. In a first step, we found transformations between SDSS i magnitudes and USNO-B1.0 Imag

Table 6.2: Details of the observations: total integration times, effective integration times after removing bad frames and observing dates.

Field	RA	DEC	Filter	Int. Time (ks)	Eff. Time (ks)	Dates
'Sausage'	$22^h42^m50^s$	$53°06'30''$	NOVA782HA	66.9	35.4	October 13–15, 20–22, 2012
			WFCSloanI	7.4	3.2	October 15, 20–22, 2012
'Toothbrush'	$06^h03^m30^s$	$42°17'30''$	NOVA804HA	37.8	24.0	October 13–16, 20, 21, 2012
			WFCSloanI	5.0	5.2	October 15, 16, 21, 2012
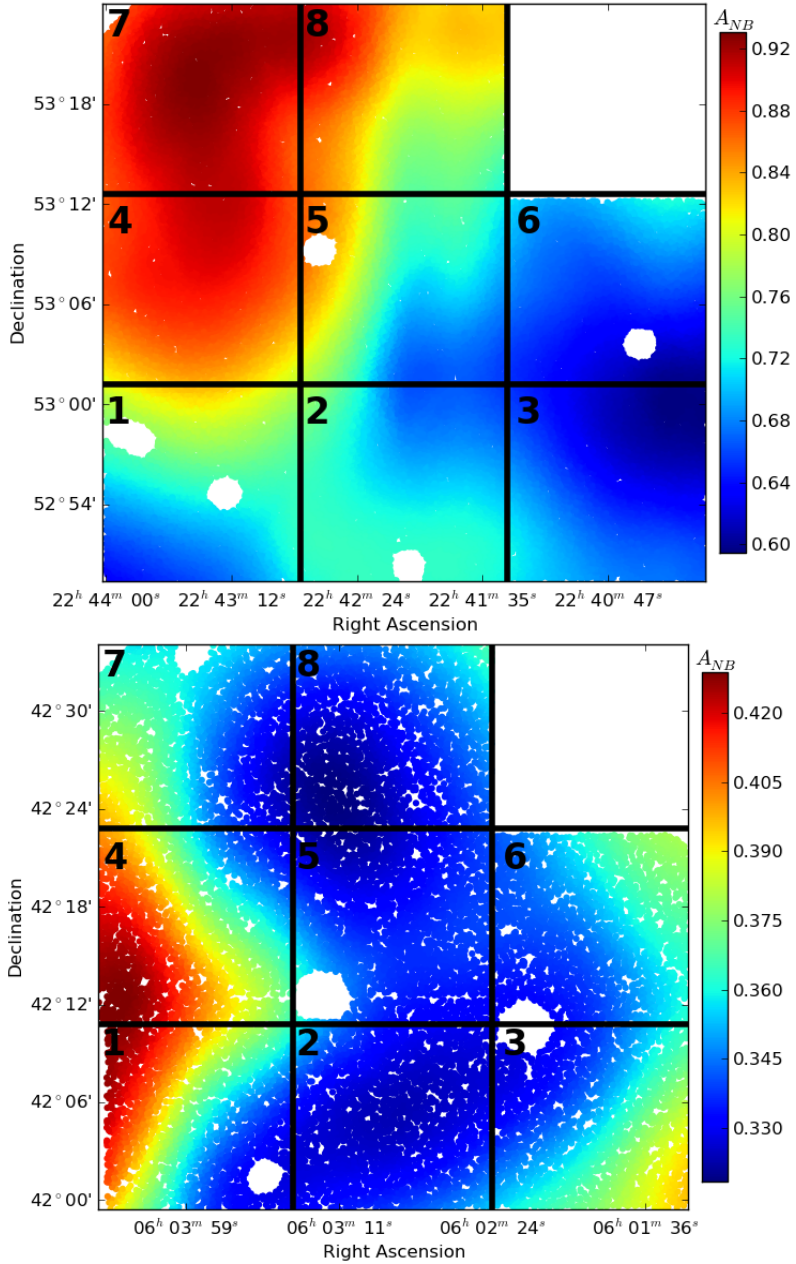
Figure 6.2: Narrow band 'dust screens' for the two fields in units of magnitudes. The dust extinction is predicted for wavelength 7839 Å for the 'sausage' and 8038.5 Å for the 'toothbrush'. The masked disks are the regions around bright stars that were not taken into account for the analysis. Notice the different scales of the two figures. The variations in dust extinction in the 'toothbrush' field are much smaller than the 'sausage'. *Top*: 'Sausage'. *Bottom*: 'Toothbrush'. Due to the high variability of the dust extinction, the FOV has been divided into eight areas to perform the completeness study.

magnitudes. Secondly, we tied our BB magnitude system to the USNO-B1.0 red magnitude Imag.

We chose a $3° \times 3°$ patch in the Galactic plane with both SDSS DR7 (Abazajian et al. 2009; Adelman-McCarthy et al. 2009) and USNO-B1.0 coverage. We matched the two catalogues using a search radius of 1 arcsec and flagged bright, saturated sources, faint sources where either catalogue became incomplete and sources which deviated by more than 3σ from the mean distribution. This resulted in a sample of 177000 sources. We used three USNO-B1.0 optical bands and four SDSS filters (u, g, r, i) to look for any correlations and concluded that the transformation between the SDSS i and USNO-B1.0 red magnitude Imag is well described by a constant offset of +0.54 mag. We matched the USNO-B1.0 catalogue with the BB catalogues for our two targets and removed sources at the bright and faint end. Using ~ 7800 matched sources for the 'sausage' and ~ 4300 for the 'toothbrush', we found constant offsets between our i band magnitudes and the USNO-B1.0 Imag measurements of -0.67 and -0.71, respectively.

We explored relationships with the red and blue USNO-B1.0 magnitudes, but found no significant trends. We concluded that the INT filters are comparable (within 5 per cent) to the SDSS DR7 ones, therefore we used the SDSS ZP to obtain correct BB magnitudes.

6.2.4   Source extraction

Source detection was performed using the SExtractor package (Bertin & Arnouts 1996). Bright stars were masked to prevent detection of spurious sources within the 'bright haloes' around them (see Figs. 6.6 and 6.7 for missing coverage). Fluxes were measured in 5 arcsec apertures corresponding to physical sizes of ~ 17 kpc for the 'sausage' and the 'toothbrush'. Because of the slightly different properties of the individual chips and different exposure times, sources were detected on each individual chip independently.

We measured the rms noise level in 1000 randomly placed apertures across the field. We repeated the experiment 100 times for each target and each filter to minimise statistical variance. The median of the rms measurements coincided with the values reported by SExtractor and we proceeded to use those. The average 3σ limiting magnitude (measured within 5 arcsec apertures) for the 'sausage' NB observations is 21.7, while the BB is limited to 22.1. The NB 'toothbrush' limiting magnitude is 22.2 and the BB goes down to magnitude 22.7. These are observed measurements, not corrected for Galactic dust extinction (see §6.2.5). The total number of sources detected by SExtractor in each filter is given in Table 6.3.

6.2.5   Galactic dust extinction correction

As mentioned in §6.2.1, both targets are affected by Galactic dust extinction. To correct for this effect, we linearly interpolated between SDSS i and z redenning values (Schlafly & Finkbeiner 2011) and used the fit to predict the Galactic extinction at the wavelength of our BB and NB filters. As the redenning varies significantly across the field, we produced 'dust screens' across the FOV, instead of using single values (see Fig. 6.2 for NB extinction maps). The spatial resolution of the dust map is given by the IRAS survey map which was used to derive the dust extinction corrections (4′). The error on the dust extinction correction is of the order of 0.05 mag. For this study, we are binning the sources based on their luminosity (i.e.
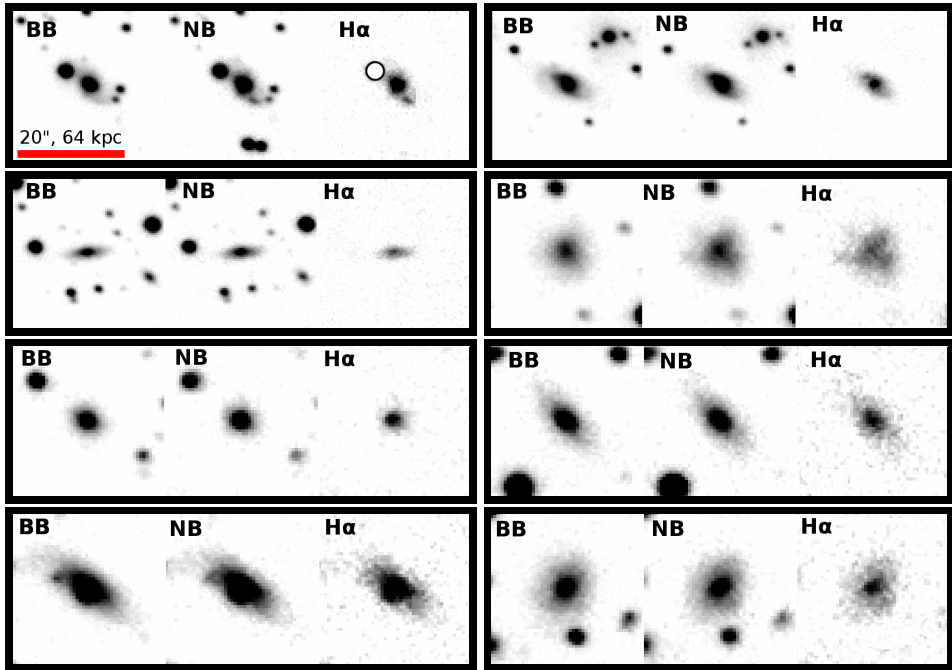
Figure 6.3: Eight examples of bright, extended Hα emitters found in the proximity of the radio relics in the 'sausage' cluster. Some examples show very disturbed, multi-tailed, asymmetric Hα morphologies. Very few such examples were found in the 'toothbrush' cluster. Within each group, the image to the left is the BB image, the central one is the NB and the right image is the BB subtracted from the NB. All images are on the same spatial scale. The red bar indicates a scale of 20 arcsec, equivalent to 64 kpc at the redshift of the 'sausage' cluster. The circle in the emission-line image for the top-left emitter masks out an artifact created around an imperfectly NB-BB subtracted bright star. The images are for illustration purposes only as the subtraction, colour palette and contrast were chosen specifically to emphasise the distribution of ionised gas in the galaxies.

magnitude) in bins which are much wider than the individual magnitude errors. Therefore random errors, such as the dust extinction correction error, are averaged out within a bin.

It should be noted that the varying dust extinction effect is also relevant for X-ray observations aiming at detecting shock fronts in galaxy clusters. Accurate subtraction of the background Galactic contribution to the number of photons is crucial for constraining shock parameters such as the Mach number. All X-ray observations of radio relics have taken a single off-cluster pointing which can lead to large biases in the derived model parameters (e.g. Ogrean et al. 2013a; Ogrean et al. 2013b; Akamatsu & Kawahara 2013).

6.2.6 Narrow band excess selection

We follow the method of Bunker et al. (1995) (see also Sobral et al. 2009, 2012) to select emission-line galaxies. In summary, we single-out emitters based on the colour excess signif-

icance of the narrow line with respect to the broad band emission (Σ) and the equivalent width (EW) of the line. We use these two cuts to model the scatter at the faint magnitudes and to reject bright sources with steep continuum that do not have an emission line. In our case, the colour significance Σ is defined by:

$$\Sigma = \frac{10^{-0.4(m_{BB}-m_{NB})}}{10^{-0.4(ZP_{AB}-m_{NB})}\sqrt{\pi r^2 \left(\sigma_{\mathrm{NB}}^2 + \sigma_{\mathrm{BB}}^2\right)}}, \tag{6.1}$$

where ZP_{AB} is the zero-point in magnitudes, m_{NB} and m_{BB} are the NB and BB magnitudes, respectively, r is the radius of the aperture in pixels, σ_{NB} and σ_{BB} are the rms noise levels in the NB and BB images, respectively. The Σ parameter is a signal-to-noise type of measurement that calculates the significance of the excess based on the RMS scatter of the intrinsic magnitudes at the faint end.

The EW is directly related to the BB − NB colour through the emission line flux. The NB or BB flux $f_{NB,BB}$ depend on the magnitude by:

$$f_{NB,BB} = \frac{c}{\lambda_{NB,BB}^2}10^{-0.4(m_{NB,BB}-ZP_{AB})}, \tag{6.2}$$

where c is the speed of light and λ_{NB} and λ_{BB} are the central effective wavelengths of the two filters. The line flux can then be derived as:

$$F_{line} = \Delta\lambda_{\mathrm{NB}}\frac{f_{NB}-f_{BB}}{1-\Delta\lambda_{NB}/\Delta\lambda_{BB}}, \tag{6.3}$$

where $\Delta\lambda_{\mathrm{NB}}$ and $\Delta\lambda_{\mathrm{BB}}$ are the widths of the NB and BB filters. The EW is then:

$$\mathrm{EW} = \Delta\lambda_{\mathrm{NB}}\frac{f_{NB}-f_{BB}}{f_{BB}-f_{NB}\left(\Delta\lambda_{NB}/\Delta\lambda_{BB}\right)} \tag{6.4}$$

$$= -\Delta\lambda_{\mathrm{BB}}\frac{1-\left(\lambda_{\mathrm{NB}}^2/\lambda_{\mathrm{BB}}^2\right)10^{-0.4(m_{BB}-m_{NB})}}{1-\left(\Delta\lambda_{\mathrm{BB}}/\Delta\lambda_{\mathrm{NB}}\right)\left(\lambda_{\mathrm{NB}}^2/\lambda_{\mathrm{BB}}^2\right)10^{-0.4(m_{BB}-m_{NB})}}. \tag{6.5}$$

The observed EW relates to the intrinsic EW_0 at emission via the redshift z:

$$\mathrm{EW}_0 = \mathrm{EW}/\left(1+z\right). \tag{6.6}$$

Because the NB filters do not fall at the centre of the BB filter there is a positive systematic offset of the colour excess (BB − NB). For the 'sausage', a constant median offset provides a good description of the data. For the 'toothbrush', we fit a linear regression to the non-saturated magnitudes at the bright end (NB magnitudes between 14.5 and 18.5) to correct the NB magnitudes and consequently the colour excess. The slope for the 'toothbrush' cluster is caused by the non-central location of its associated NB filter inside the BB filter. That means more red galaxies have a stronger positive colour excess and may be selected as emitters. The NB magnitudes, and the excess colour consequently, were corrected by −0.167 for the 'sausage'. NB magnitudes in the 'toothbrush' were corrected by $0.023(\mathrm{BB}-\mathrm{NB})-0.510$ (see Fig. 6.4).

The EW cut is imposed to distinguish true emission-line systems from sources which have positive excess because of random scatter in the magnitude measurements, such as foreground
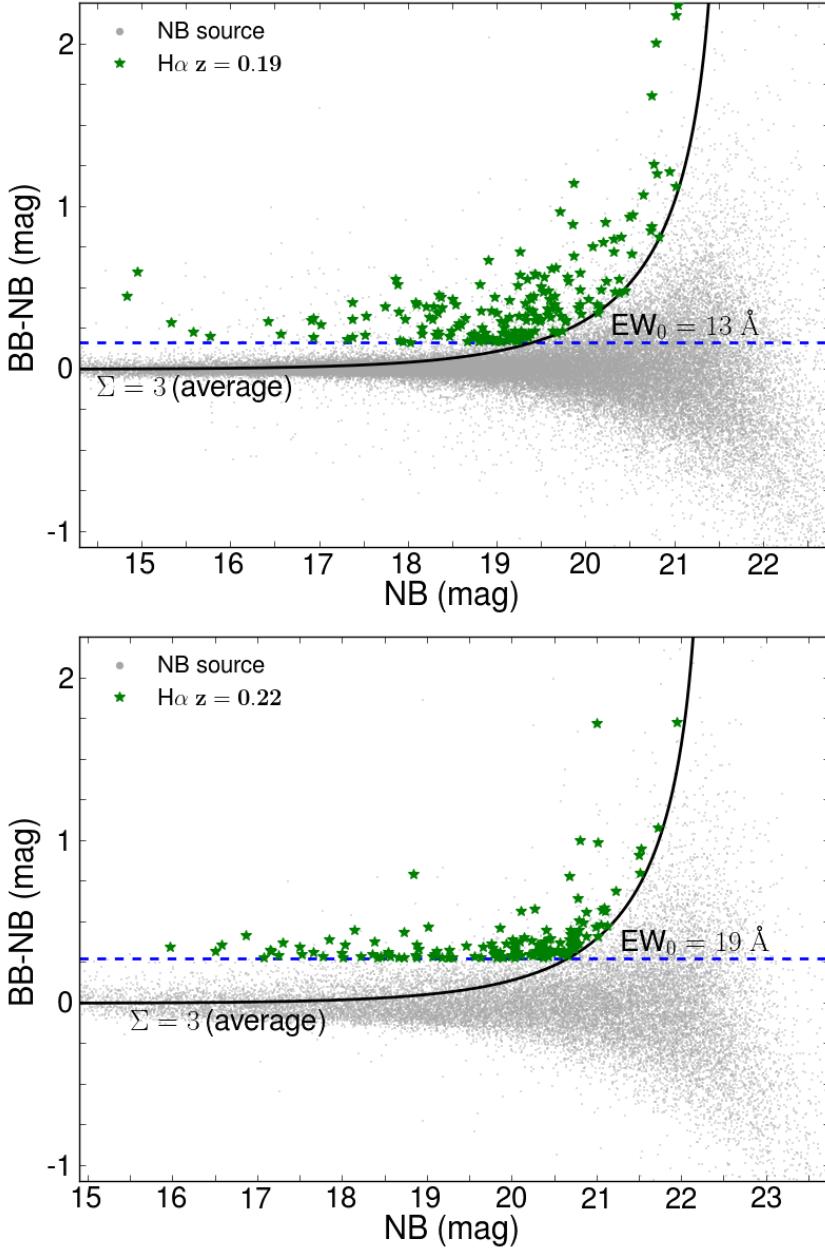
Figure 6.4: Colour-magnitude diagrams displaying narrow-band excess as function of NB magnitude. *Top*: 'Sausage'. *Bottom*: 'Toothbrush'. Notice that due to variations in dust extinction across the FOV and dissimilar chip properties, the selection of emitters was performed separately for each chip, allowing for different rms values. The data were corrected for the colour depence on the NB magnitude. The curves represent the average 3Σ colour significances (for the average depth, as the analysis is done individually for each chip). The horizontal dashed lines are the rest-frame EW cuts used in this study.

Table 6.3: Sources detected in our survey. The detected number of sources are within 5 arcsec diameter apertures down to 3σ magnitude limits within the NB matched to BB catalogues. The number of rejected stars, total number of NB emitters and extended NB emitters (sizes greater than 4 arcsec) for the two fields are also given. The seventh column presents the number of emitters found in the proximity of the radio relics, based on the arc-sectors defined in Figs. 6.6 and 6.7. The penultimate column shows the number of extended emitters located nearby radio relics. The last column tabulates the total number of sources likely to the Hα emitters at the redshift of the clusters. The total was calculated as the sum of the number of extended emitters plus a fraction of ∼ 20 of other emitters in the field (see §6.3.1).

Field	Filter	Detected (3σ)	Flagged stars	Emitters ($\Sigma > 3$)	Extended emitters
'Sausage'	NOVA782HA	36196	357	181	33
	WFCSloanI	40007			
'Toothbrush'	NOVA804HA	16776	207	141	12
	WFCSloanI	19418			

Field	Filter	Emitters close to the relics	Extended emitters close to the relics	Hα-likely sources
'Sausage'	NOVA782HA	31	13	49
	WFCSloanI			
'Toothbrush'	NOVA804HA	6	1	30
	WFCSloanI			

stars, or steep continuum. Therefore, we measure the standard deviation of the colour distribution σ_{excess} around zero and consider only sources with BB − NB larger than $3\sigma_{\mathrm{excess}}$. As shown in equation 6.4, colour excess can be directly related to equivalent width (Sobral et al. 2009). The data obtained with the two filters have different scatterings of the excess values, i.e. the standard deviation of the 'toothbrush' excess values is higher than for the 'sausage'. Therefore, we choose separate EW cuts that reflect the statistical properties of the magnitude measurements of the two fields. For the 'sausage' we use a colour cut at 0.16 mag and for the 'toothbrush' we use 0.27. These correspond to an observed EW of 16 Å and an intrinsic EW_0 at emission of 13 Å for the 'sausage' and EW = 24, EW_0 = 19 for the 'toothbrush'. The higher scatter in the 'toothbrush' is intrinsic to the filter and cannot be attributed to varying median colour offsets caused by different properties of the four chips. We also tested a single, common EW cut for the two clusters and found that a higher EW cut does not change the results.

A colour excess significance of $\Sigma > 3$ was imposed such that we remove most spurious sources and obtain a robust sample of emitters. This ensures we reject sources which have a low signal-to-noise. Because of the low Galactic latitude of both our targets, the fields are extremely crowded with stars, including old stars and frequent double-star occurrences, uniformly distributed across the field of view. Because of the rather large apertures used for source detection, light from companions in double-star systems can contaminate the measurement. All of the NB Hα imaging surveys to date have avoided observing in the Galactic

plane to obtain samples as clean as possible. One example is the COSMOS field (Scoville et al. 2007; Shioya et al. 2008), where the source density down to a magnitude of 22 is $\sim$ 5 sources/arcmin^2. We detect 17 sources/arcmin^2 in the 'toothbrush' field, which is at Galactic latitude 9.0°, while for the 'sausage', at latitude -5.1°, we detect an average of 45 sources/arcmin^2. The source density for the two fields discussed in the present work is significantly higher than for a typical Hα NB target field. The difference can be accounted for by the dense star field in the line of sight towards the Galactic plane, so an inspection of the dataset is crucial in obtaining robust samples of emitters. A first pass removal of stars was performed based on the source ellipticities reported by SEXTRACTOR. We further performed two independent visual inspections of the images to flag potential false positives around the edges of the chip where the noise increases or close to bright, saturated stars, mismatched NB to BB emitters and double stars blended into a single source which mimic line emission. We cross-checked the sources labelled as stars by SEXTRACTOR and the visual inspection and very good agreement was found.

Therefore, for a source to enter the emitters catalogue, it needs to fulfil three conditions (see Fig. 6.4):

- colour excess higher than $3\sigma_{excess}$ scatter at bright magnitudes (source has significant line emission)

- $\Sigma > 3$ colour excess significance (source has high signal-to-noise)

- pass visual inspection

The sample of sources that fulfil all criteria consists of: 181 emitters for the 'sausage' and 141 emitters for the 'toothbrush'. We visually inspected all of the sources in the fields by looking at a difference image obtained by subtracting the BB image from the NB image. Our visual inspection of the images revealed that all obvious 'sausage' line emitters pass our criteria. In the case of the 'toothbrush', because of the higher EW cut, we miss a few extended emitters with low surface brightness, but high integrated fluxes. We note that we fully correct for the emitters that do not fulfil the criteria by doing a completeness study (see §6.3.4).

Upon visual inspection, we also noted that there were sources significantly larger than the bulk of the emitters and thus flagged sources larger than 4 arcesc as extended. Examples of such bright, extended emitters (sizes greater than 4 arcsec, equivalent to $\sim$ 14 kpc) are given in Fig. 6.3 and they are predominantly found around the radio relics. We have to note that perfect subtraction of sources in the image plane is difficult because of non-matching point-spread-functions and different noise properties between the broad band and narrow band images. The BB $-$ NB images in Fig. 6.3 are displayed with contrast and colour scheme chosen to enhance the Hα gas distribution in the galaxies. We have displayed the distribution of extended line emitters in Figs. 6.6 and 6.7.

6.3 Results

6.3.1 Selecting Hα emitters

Hα NB surveys at moderately low redshift can also detect galaxies with shorter rest-frame wavelength lines located at much higher redshifts. In our survey, we are also sensitive to Hβ

($\lambda_{\text{rest}} = 4861$ Å) and [OIII]$\lambda\lambda$4959, 5007 emitters at $z \sim 0.61 - 0.65$, and [OII] ($\lambda_{\text{rest}} = 3727$ Å) emitters at $z \sim 1.15$. We also expect to detect 4000 Å break galaxies located over a wider range around $z = 0.8$.

Traditionally, when available, colour-colour information is used to separate higher redshift interlopers that fall within a NB filter designed to capture the Hα emission (e.g. Shioya et al. 2008; Sobral et al. 2013a). While we do not have multi-band imaging of the two fields, we can derive and apply a statistical correction by making use of the COSMOS (Capak et al. 2007; Ilbert et al. 2009) catalogue. Shioya et al. (2008) derived catalogues of NB816 line-emitters and Sobral et al. (2013a) observed the same field with the narrow band filter NB921. We predicted broad-band 5 arcsec magnitudes using their CFHT i magnitudes and measured narrow-band magnitudes in the COSMOS NB816 filter at 8160 Å and NB921 at $\lambda = 9120$ Å. In order to simulate the conditions of our two cluster catalogues, we made use of their ancillary z' filter information to apply a colour correction to the data. This is necessary because the NB816 filter is non-centrally located within the BB filter. We fully corrected for the colour dependence to best simulate the 'sausage' field where the NB filter is placed very close to the centre of the BB filter. We applied a partial colour correction to the COSMOS magnitudes to obtain a catalogue slightly affected by colour dependence as in the case of the 'toothbrush' dataset. We then passed the 'sausage'-like and the 'toothbrush'-like COSMOS catalogues through the same selection criteria presented in §6.2.6. In this way, we fully mimic our data selection process. We then combined the NB816 emitters with the NB912 emitters from the Sobral et al. (2013a) sample to minimise cosmic variance. The photometric redshift information from the COSMOS catalogue was used in conjunction to the selection criteria to classify the potential emitters as Hα, Hβ+[OIII] emitters, 4000 Å break galaxies or [OII] emitters. We used this information to derive Hα fractions relative to the total number of emitters as function of flux (see Fig. 6.10) and correct the Hα luminosity function. Typical Hα fractions are around 20 per cent. The expressions of the fractions frac$_{H\alpha}$ as function of flux are given below. We have explored functions of different order, but these provided the best description of the data. For the 'sausage' cluster:

$$
\begin{aligned}
\text{frac}_{H\alpha} = {} & 2.264 \log^4 (F_{line}) + 144.2 \log^3 (F_{line}) \\
& + 3441 \log^2 (F_{line}) + 3.646 \times 10^4 \log (F_{line}) \\
& + 1.447 \times 10^5,
\end{aligned}
\tag{6.7}
$$

where F_{line} is the line flux. For the 'toothbrush' field, the functional form is:

$$
\begin{aligned}
\text{frac}_{H\alpha} = {} & 3.945 \log^4 (F_{line}) + 248.1 \log^3 (F_{line}) \\
& + 5843 \log^2 (F_{line}) + 6.105 \times 10^4 \log (F_{line}) \\
& + 2.389 \times 10^5.
\end{aligned}
\tag{6.8}
$$

Extended sources (larger than 4 arcsec) are very likely to be real Hα emitters at the redshift of the cluster (see also §6.4, where we detail why this is so). However, for sources which are smaller, size cannot be used as an argument to derive the redshift. Therefore, for these smaller sources, we cannot say, on a case by case basis, which are Hα at redshift ~ 0.2 and which are Hβ+[OIII] emitters, 4000 Å break galaxies or [OII] emitters. We therefore apply the fractions derived above, which, in a statistical sense provide the correct number of counts for each luminosity bin, within the errors. We would like to stress that even though Shioya et al.
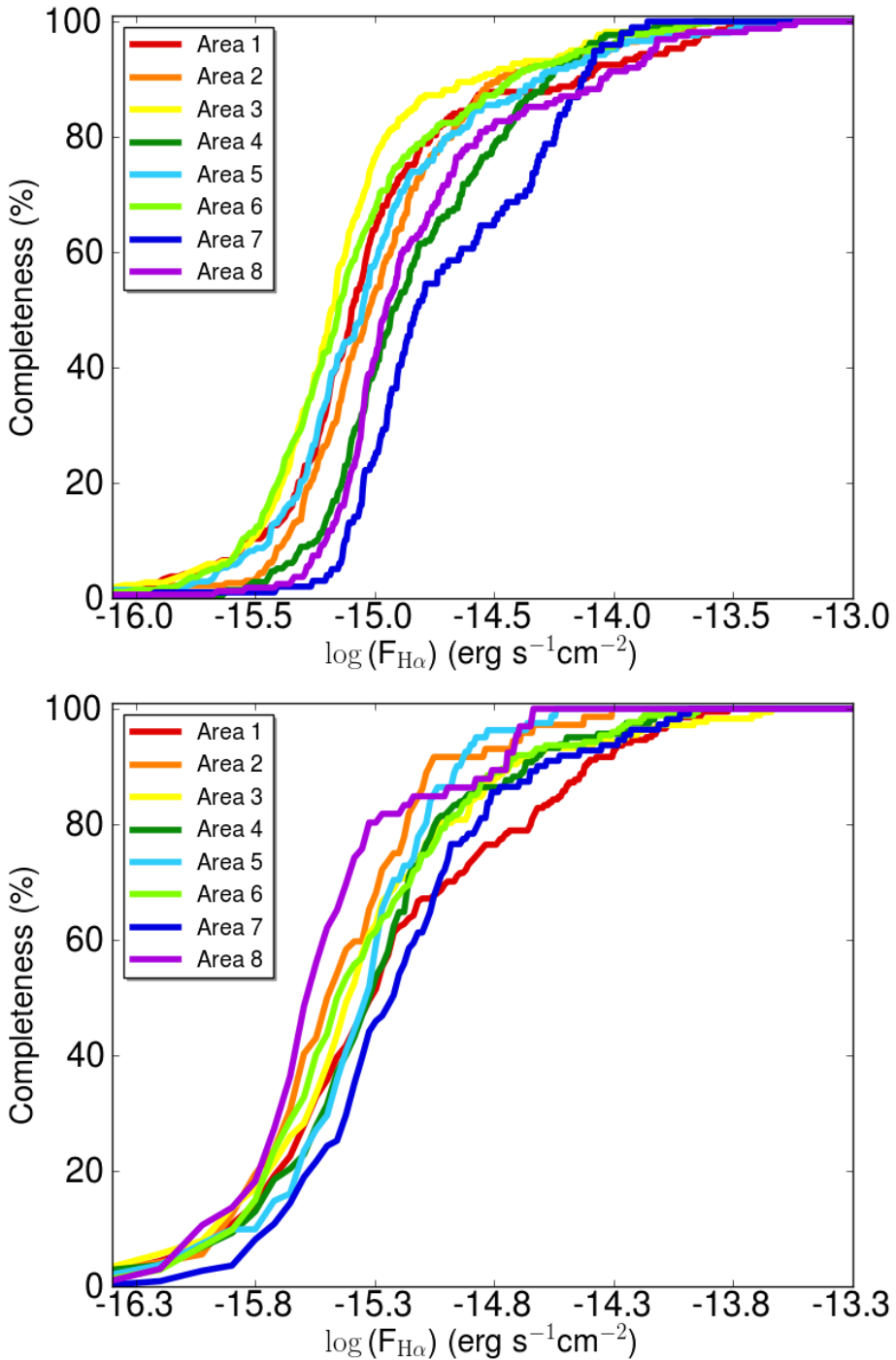
Figure 6.5: Completeness of the surveys for the 'sausage' and the 'toothbrush' clusters as function of Hα flux. The completeness study is performed separately on sub-areas of the FOV, as defined in Fig. 6.2. The differences in the curves between the sub-areas arises from their different dust extinction properties. *Top*: 'Sausage'. *Bottom*: 'Toothbrush'.

(2008) have separated the Hα from all others emitters and then computed the LF, the final statistical result is the same as in our method.

Fig. 6.10 reveals the increase of the Hα fraction with luminosity. Therefore, applying a constant fraction across all luminosity ranges is unsuitable. Studies performed with the Subaru telescope and long integration times, such as those by Shioya et al. (2008), Ly et al. (2007) and Drake et al. (2013), capture the fluxes where Hα contributes to less than 15 per cent and they become saturated when the Hα fraction is rising.

6.3.2   Removing [NII] contamination

The NB filters are wide enough to also capture the adjacent [NII] emission. It is crucial that we attempt to remove the contribution of this emission line from our fluxes. If unaccounted for, this contamination artificially increases the line fluxes and EWs. We follow the relation empirically calibrated by Sobral et al. (2012) against a large SDSS sample to remove the [NII] contribution. The relationship takes a functional form between the logarithm of the combined EW of the Hα and [NII] lines and the logarithm of the fractional contribution of [NII] towards the blended line flux:

$$f = -0.924 + 4.802E - 8.892E^2 + 6.701E^3 - 2.27E^4 + 0.279E^5, \qquad (6.9)$$

where f is the logarithmic ratio of [NII] flux to the total flux and $E = \log_{10}(\mathrm{EW}_0(\mathrm{H}\alpha + [\mathrm{NII}]))$. The average contamination by [NII] flux for our sample is 0.31 of the total blended flux.

6.3.3   Hα luminosity

Using emission line flux of a source, we compute its Hα luminosity. The luminosity is calculated as:

$$L_{\mathrm{H}\alpha} = 4\pi d_L^2 F(H\alpha), \qquad (6.10)$$

where $F(H\alpha)$ is the flux and d_L is the luminosity distance calculated assuming all sources are at redshift 0.1945 or 0.2250, for the 'sausage' or the 'toothbrush' respectively (see Table 6.1).

6.3.4   Completeness correction

For the purpose of building luminosity functions, we bin the sources based on their luminosity. It is essential to correct for incompleteness at the faint end of the source counts. Not doing so will result in a synthetically flat faint-end slope or even a turn-over in the LF. The completeness of the survey is determined from a set of simulations using the measured data itself. We follow the method developed by Sobral et al. (2012, 2013a). First, the distribution of recovered emitters as function of NB magnitude is modelled. A sub-sample is drawn from the pool of sources consistent with being non-emitters, following the same NB distribution as the population of emitters. Pure Hα emission line fluxes are added to the sources and the sample is passed through the selection criteria described in §6.2.6. Because of the irregular dust extinction (especially for the 'sausage') and the slightly different properties of the four WFC chips, we divided the FOV into eight areas (see Fig.6.2), for which we independently study the completeness properties. The 'extragalactic' depth of the observations is superior
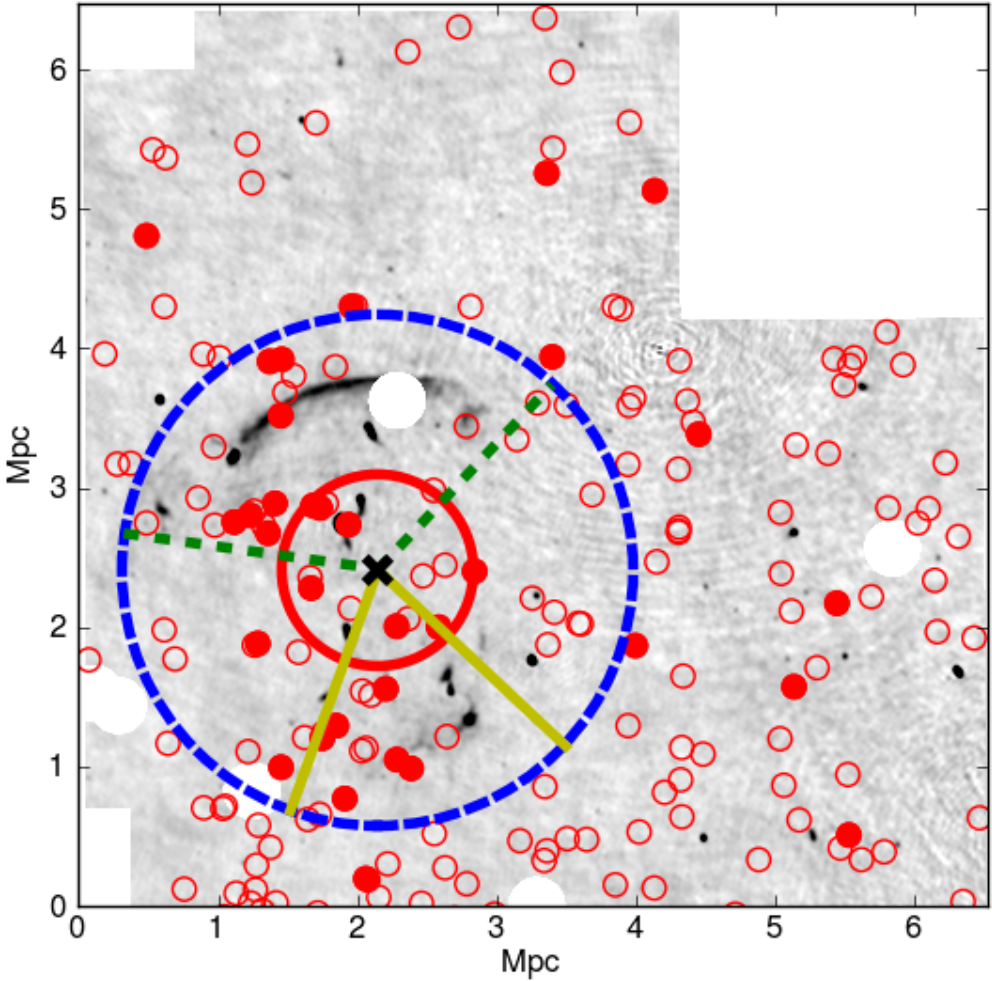
Figure 6.6: Giant Meterwave Radio Telescope 323 MHz radio images in grey intensity for the 'Sausage' FOV. The figure also shows the FOV of the two fields with masked areas in white. Circular masked areas are masked bright stars. The red circles show the position of the line emitters detected in the narrow band study. The filled circles indicate the location of the extended emitters (sizes greater than 4 arcsec), likely to be Hα emitters. Note the some source markers are overlapping. The arc-sectors define the areas around the radio relics which were considered for producing relic luminosity functions. The cluster centres are defined to be at the location of the black crosses. The Northern relic was captured by a section between the solid red and the dashed blue circles, bound by the dashed green lines. The Southern relic area was defined between the solid red and the dashed blue circles and the solid yellow radii.
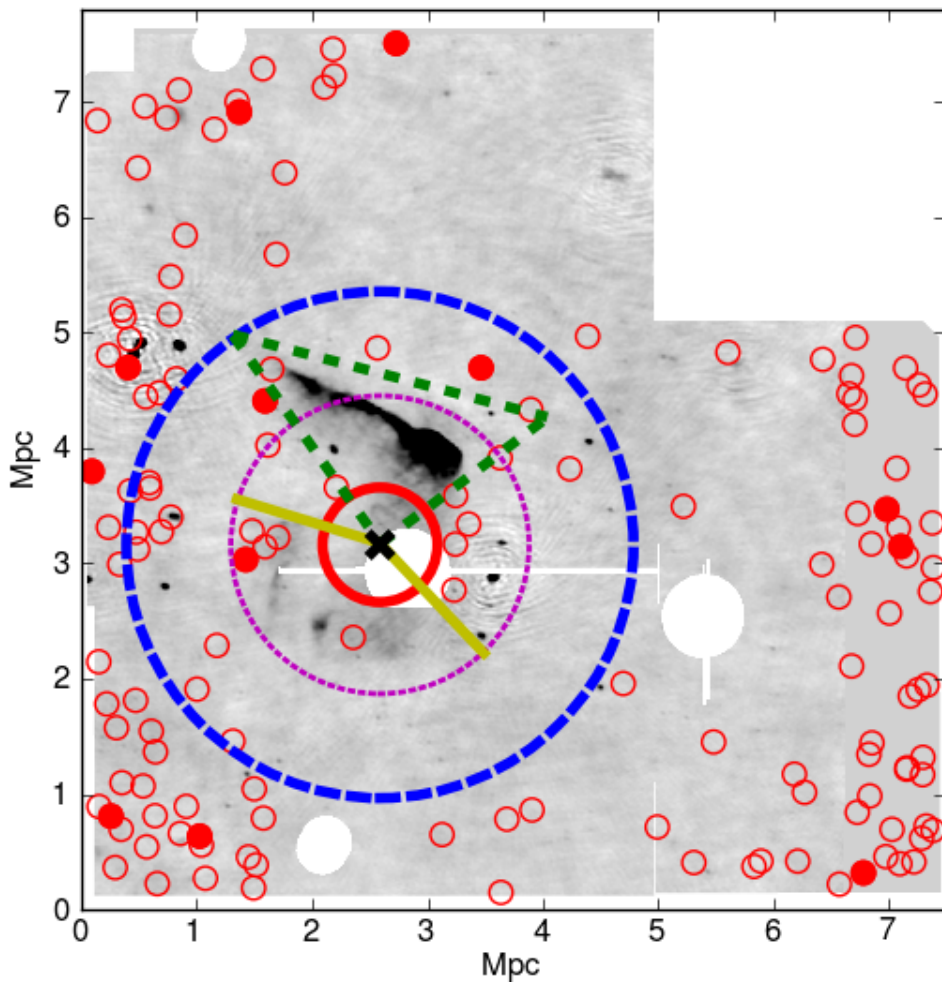
Figure 6.7: Same as Figure 6.6, but for the 'toothbrush' field. The Northern relic was captured by a section between the solid red and the dashed blue circles, bound by the dashed green lines. The Southern relic area was defined between the solid red and dotted purple circles and the solid yellow radii.

for areas with low dust extinction, while high-dust extinction areas will have a higher survey limit. This poses issues for computing the LF. Dividing the number counts detected over a restricted area with lower dust extinction by the entire FOV volume can simulate a turn-over in the faint-end slope of the LF. The results of the completeness study are presented in Fig. 6.5. As expected, the curves for the eight sub-areas are very similar for the 'toothbrush' where the dust extinction is almost constant across the field. The highly variable 'dust screen' for the 'sausage' is reflected in the completeness curves for the different sub-areas: the completeness for two cells with different dust properties can differ by as much as 50 per cent. We therefore correct the LF adaptively for the eight sub-areas. Sources whose flux falls below the 30 per cent completeness limit are disregarded and their associated comoving volume is not taken into account.

6.3.5 Volume

Both our NB filters have a width of 110 Å. Using a perfect top-hat (TH) approximation for the NB filters, at FWHM this translates to an Hα redshift coverage from 0.1865 to 0.2025 for the 'sausage' and to $0.2168 - 0.2328$ for the 'toothbrush'. The luminosity distance at the peak of the transmission curve is 936.2 Mpc and 1116.1 Mpc for the 'sausage' and the 'toothbrush', respectively. We survey a comoving volume density of 1.227×10^4 Mpc^{3}deg^{-2} and 1.600×10^4 Mpc^{3}deg^{-2}, respectively. Taking into account the masked edges and saturated stars (see Figs. 6.6 and 6.7), we are surveying an effective comoving volume of 3.371×10^3 Mpc^3 for the 'sausage' and 4.546×10^3 Mpc^3 for the 'toothbrush'. Our volumes are comparable ($\sim 1/3$) to the volumes of field surveys such as those by Ly et al. (2007) ($\sim 1.4 \times 10^4$ Mpc^3) and Drake et al. (2013) ($\sim 1.2 \times 10^4$ Mpc^3).

6.3.6 Filter profile correction

The volume covered by our NB filters is 90 per cent of that covered by an idealised TH profile with the same FWHM and maximum equal to the peak of our NB filters. Because neither NB filter is a perfect TH (Fig. 6.1), bright emitters will be detected in the wings of the filter profile as fainter sources. In order to estimate the magnitude of this bias effect, we performed a series of simulations based on the method of Sobral et al. (2009, 2012). This entails selecting emitters using a perfect TH filter and computing a first pass LF. Simulated Hα emitters are generated using the resulting best-fit Schechter function. This population is then folded through the true filter profile and the resulting LF is compared with the idealised one to study the rate of recovery of emitters.

6.3.7 Survey limits

Down to a 30% completeness limit, our LFs probe down to $10^{40.6}$ erg s^{-1} for the 'sausage' and $10^{40.4}$ erg s^{-1} for the 'toothbrush'. By using the relationship derived by Kennicutt (1998) corrected for the initial mass function from Chabrier (2003), we can obtain a limiting star formation rate of our survey of 0.17 and 0.11 M$_\odot$ yr^{-1} for the 'sausage' and the 'toothbrush', respectively. Our datasets become saturated at magnitude 14.5, which means we can probe up to luminosities of $10^{43.2}$ erg s^{-1}.
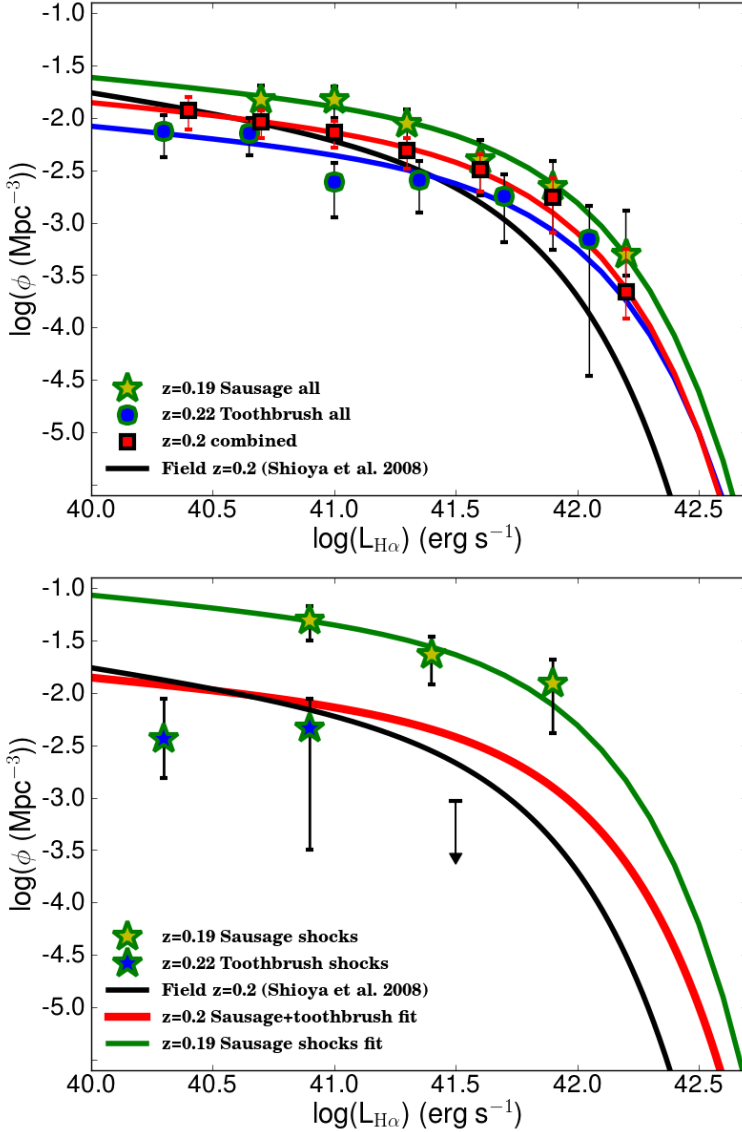
Figure 6.8: Luminosity function for the two clusters. *Top*: Luminosity functions using emitters from the entire FOV. The best-fitting parameters of the LFs are given in Table 6.4. We combined the data for the two clusters to obtain an average field-of-view wide LF. Overplotted is the LF derived by Shioya et al. (2008) for redshift 0.24. *Bottom*: The Hα LF for the regions projected around the 'sausage' and the 'toothbrush' cluster relics. The regions used are defined in Figs. 6.6 and 6.7. Overplotted is the average field-of-view LF derived in the present work. An upper limit of detection is shown for the 'toothbrush' cluster, corresponding to 1 source per bin. A fit was produced to describe the 'sausage' emitters nearby the two relics by fixing the L^* and α parameters to the value of the average LF and varying only ϕ^*, as this produces a very good fit to the data.

We should note that comparison to NB Hα surveys of blank fields such as COSMOS or the UKIDSS Ultra Deep Survey Field can be challenging. These studies have been carried out with wide-aperture telescopes using long individual integration times designed to target high-redshift Lyα. This means the data becomes saturated at magnitudes brighter $10^{41.0\sim41.5}$ erg s^{-1} and that bright Hα emitters can be missed (e.g. Shioya et al. 2008; Drake et al. 2013). These results are biased against high luminosities, which leads their fits to underpredict the high-luminosity behaviour of the LF. Therefore, luminosity functions derived from lower luminosity data cannot be easily translated to our luminosity coverage. This strengthens the importance of using smaller-diameter telescope for NB studies and/or short individual exposures that are not severely saturated at moderate magnitudes.

6.3.8 Hα luminosity function

We bin the data based on their luminosity to build LFs. We use the entire sample of Hα emitters, after applying all the relevant corrections (statistical removal of other line emitters, volume, completeness and filter profile corrections), to obtain a robust luminosity function of the field-of-view of the two clusters. We fit the data with a Schechter function (Schechter 1976) of the form:

$$\phi(L)\mathrm{d}L = \phi^* \left(\frac{L}{L^*}\right)^\alpha e^{-(L/L^*)} \mathrm{d}\left(\frac{L}{L^*}\right). \tag{6.11}$$

We combine the two datasets to obtain an average field-wide LF down to a limiting luminosity of $> 10^{40.5}$ erg s^{-1} (limiting SFR of 0.14). In the fit, we consider sources with line fluxes above the 30% completeness limit. We note that extended sources, likely to be at the redshift of the clusters, were assigned a weight of 1. For other line emitters, because of the ambiguity in the nature of the line/feature (Hα, Hβ+[O$\textsc{iii}$], 4000 Å break galaxies or [O$\textsc{ii}$]), the Hα fractions derived in §6.3.1 are applied (to recover the correct statistical number of Hα emitters). We first kept all three parameters free and, via a χ^2 minimisation scheme, found that the best description of the data is given by a faint-end slope of $\alpha = -1.2^{+0.2}_{-0.3}$. This value is placed between the results of Drake et al. (2013) ($-1.03^{+0.17}_{-0.15}$) and Shioya et al. (2008) ($-1.35^{+0.11}_{-0.13}$) at similar redshift. Ly et al. (2007) obtain an even steeper value of $\alpha = -1.7 \pm 0.1$. Values obtained by Shioya et al. (2008) for the COSMOS blank field at a similar redshift of ~ 0.24 are given for reference (see also: Dale et al. 2010; Drake et al. 2013). One can immediately notice that the average field-wide LF matches the field data points obtained by Shioya et al. (2008). This is expected, since by combining two distinct datasets we minimise the effects of cosmic variance, as well as the contribution of the cluster environment to the overall shape of the luminosity function. Note the differences at the bright end: these are likely driven by Shioya's data being saturated at these luminosities (see §6.3.7). We do not observe changes in the faint-end slope α, although there are hints of flattening compared to the canonical -1.35. To confirm this point, we also inspect LFs derived from the field outside the cluster areas (top and right CCDs, resulting in 69 emitters or 18 Hα-likely for the 'sausage' and 77 or 15 Hα for the 'toothbrush') and conclude that the LFs move in the direction of matching the Shioya et al. (2008) field LF, as is expected from cosmic variance.

We then fix α to -1.2 and vary only the normalisation and L^*. We fit the data for two cluster field-of-views with Schechter functions down to an observed Hα luminosity of $> 10^{40.6}$ erg s^{-1} for the 'sausage' and $> 10^{40.4}$ erg s^{-1} for the 'toothbrush'. For this step, we use all emitters found across the entire field mapped by the WFC as shown in Figs. 6.6

Table 6.4: Schechter fit parameters according to equation 6.11 for the 'sausage' and the 'toothbrush' clusters at redshift ~ 0.2. The data for the two fields was combined and fitted separately with a Schechter function for comparison. All errors represent 1σ uncertainties estimates on the fitted parameters. The uncertainty in α was obtained by keeping all parameters free and minimising the χ^2 of the fit. We then fixed α, and refitted the Schechter functions with $\log \phi^*$ and $\log L^*$ as free parameters. The errors on $\log \phi^*$ and $\log L^*$ are 1σ uncertainties determined from Schechter with two free parameters. For the fit on the Hα emitters located around the relic area within the 'sausage' cluster, we fixed both α and $\log L^*$ and varied the normalisation. The fit from Shioya et al. (2008) derived for a blank field at a similar redshift is given as reference (after being uncorrected for 'extragalactic' Hα dust extinction). The last column gives the number of emitters employed in building the LFs. The first value tabulates extended emitters likely to be at the redshift of the clusters, while the second value gives the number of other sources, which could be Hα or other, higher-redshift line emitters. For this second group of sources, a fraction was applied to account for the actual percentage we expect to be Hα at the redshift of the cluster (see eq. 6.7 and 6.8).

Field	α	$\log \phi^*$ Mpc^{-3}	$\log L^*$ erg s^{-1}	Number of Hα (extended+other)
'Sausage'	-1.2	$-2.33^{+0.11}_{-0.11}$	$41.73^{+0.08}_{-0.06}$	$33 + 16$
'Toothbrush'	-1.2	$-2.82^{+0.16}_{-0.31}$	$41.77^{+0.91}_{-0.21}$	$12 + 18$
Combined	$-1.2^{+0.2}_{-0.3}$	$-2.57^{+0.09}_{-0.09}$	$41.72^{+0.11}_{-0.07}$	$45 + 50$
'Sausage' relic area	-1.2	$-1.77^{+0.09}_{-0.09}$	41.72	$13 + 2$
Shioya et al. (2008)	$-1.35^{+0.11}_{-0.13}$	$-2.65^{+0.27}_{-0.38}$	$41.57^{+0.38}_{-0.23}$	

and 6.7. We obtain LFs for each cluster field-of-view by using χ^2 minimisation with two free parameters (ϕ^* and L^*). The results with 1σ uncertainties are summarised in Table 6.4 and seen in Figure 6.8 (left panel). Errors of data points are Poissonian. The overall normalisation of the 'sausage' field LF (ϕ^*) is significantly higher than the field LF, while the 'toothbrush' seems to be underdense as compared to Shioya et al. (2008) fit. Nevertheless, such differences are expected due to cosmic variance.

Shock areas

In order to study the effect of the travelling shock waves in shaping the Hα luminosity function of the cluster galaxies we define circular areas that trace the shock fronts in a shell-like pattern. The areas can be visualised in Figs. 6.6 and 6.7. As mentioned in §6.1, both clusters probably result from a major merger between two massive clusters, which in turn produces outward-travelling spherical shock waves. This motivates the choice of symmetrical, sector-of-arc regions to capture the relic areas. Both clusters host a strong Mach $M \sim 4.5$, ~ 1.5 Mpc-wide shock front at their northern outskirts traced by the dominating radio relic. Towards the south and east of the 'sausage', there are smaller, patchier relics which probably trace broken shock fronts (Stroe et al. 2013), where turbulence leads to mixing of different electron populations. Our samples of emitters in the proximity of the relic areas contains 31 sources for the 'sausage'

cluster (15 likely to be Hα) and 6 for the 'toothbrush' cluster (2 likely to be Hα). We note that these samples are derived over comparable volumes and we thus find that the 'sausage' has a density of Hα emitters nearby relics $\approx$ 7.5 times higher than the equivalent area for the 'toothbrush'.

The measurements of the 'toothbrush' Hα emitters in the proximity of shock fronts are consistent with field properties. The non-detection at the high-luminosity end is significant: an upper limit corresponding to 1 source detected in the surveyed volume indicates that there are no emitters brighter than $10^{41.5}$ erg s^{-1}. However, the 'sausage' LF is in stringent tension with the field properties, being boosted by an order of magnitude with respect to a blank field, as well as our combined field-wide LF. We fit the 'sausage' relic data with a Schechter function with α and $\log L^*$ fixed to the values we obtained from our combined fit (see Table 6.4). This allows us to obtain a value of the normalisation of the LF 0.8dex higher than what is found for the field (equivalent to a significance level of 9σ).

Comparison to other clusters

There are few NB studies of the Hα luminosity function of clusters at $z \approx 0 - 0.2$. We compare our LF for the cluster areas projected onto the vicinity of the relics with the results from cluster Abell 521 at redshift 0.25 (Umeda et al. 2004) and Abell 1367 and Coma at $z = 0.02$ (Iglesias-Páramo et al. 2002). For this purpose, we follow the method of Umeda et al. (2004) and Iglesias-Páramo et al. (2002) and estimate the cluster volume as a sphere with radius equal to projected size of the cluster on the sky (2 Mpc). In order to be fully consistent with the cluster studies of (Iglesias-Páramo et al. 2002) and (Umeda et al. 2004), we assume all emitters within the relic areas to belong to the cluster. We renormalise the line-emitter number counts to this estimated cluster volume, instead of using the entire surveyed volume. To produce comparable results, we also remove the $A_{H\alpha}$ correction for 'extragalactic' Hα extinction from the LFs of Umeda et al. (2004) and Iglesias-Páramo et al. (2002).

We plot the resulting bins for the 'sausage' and the 'toothbrush' clusters on top of the LFs derived for Abell 521, 1367 and Coma in Fig. 6.9. The overall LF normalisation for all clusters is above the field measurement of Shioya et al. (2008) by several orders of magnitude. The measurements for the 'toothbrush' relic areas now fall on the LF for local clusters at $z = 0.02$, while our 'sausage' measurements are in stringent disagreement with the local cluster results and an order of magnitude higher than the Abell 521 LF (at the 9σ level).

6.4 Discussion

We have carried out the first wide-area Hα survey of two merging galaxy clusters that host radio relics. These Mpc-wide synchrotron structures trace twin-outward travelling shock waves that accelerate ICM electrons. Being interested in the possible effects the shock front has on the member galaxies, we study their properties, with a particular focus on the general cluster Hα luminosity function and the Hα LF around the relic areas.

We used all of the potential Hα emitters in the field of view to derive general LFs. We corrected for variable Galactic dust extinction, incompleteness, volume, filter profile and statistically corrected for the Hα fraction. The 'toothbrush' data is consistent with the field
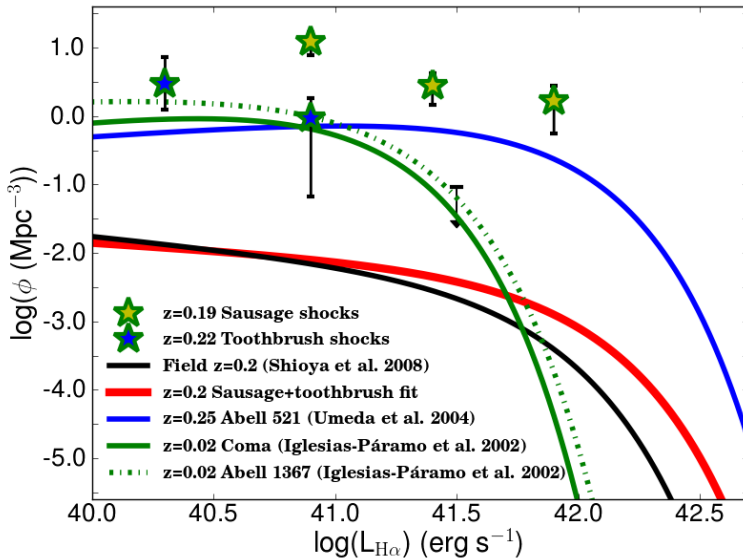
Figure 6.9: Hα narrow-band luminosity functions for clusters. The Hα luminosity function for the regions projected around the relics in the 'sausage' and the 'toothbrush' clusters are shown as stars. An upper limit of detection is shown for the 'toothbrush' cluster, corresponding to 1 source within the surveyed volume. Note that here we have calculated the LF of the 'sausage' and 'toothbrush' clusters using a cluster volume corresponding to a sphere of radius of 2 Mpc in order to compare to other cluster studies. Overplotted are the average cluster LF derived in the present work by using the entire cluster and field volume. We also plot the $z = 0.2$ field LF from the work of Shioya et al. (2008). We also plotted LFs for cluster Abell 521 at $z = 0.24$ (Umeda et al. 2004) and local clusters Abell 1367 and Coma at $z = 0.02$ (Iglesias-Páramo et al. 2002).

results derived by Shioya et al. (2008) for the blank COSMOS field, while the 'sausage' field LF indicates a larger number of bright emitters.

The LF of Hα galaxies around the relics in the 'sausage' is significantly boosted compared to the field around the cluster, as well as the COSMOS field (Shioya et al. 2008) at a significance of 9σ. The effect becomes more pronounced if we compare to the LFs by Drake et al. (2013) or Ly et al. (2007). Particularly important to note here is that our narrow band filters are wide enough to probe the background and foreground field behind and in front of the clusters, respectively. Our filters probe 30 Mpc behind and 30 Mpc in front of the cluster centre. The virial radius of the largest, richest clusters such as the Coma cluster is 2 Mpc, while clusters like ours are expected to be comparable in size. Therefore, a small percentage of the volume we are probing is populated by the cluster (up to 10 per cent), while the rest is foreground and background field.

Excluding the volume not contained in the clusters themselves would lead to an increase in the normalisation of the LF by a factor of 10 and would further strengthen our results. We attempt to account for this and follow the method of Iglesias-Páramo et al. (2002) and Umeda et al. (2004) and approximate the 'sausage' and 'toothbrush' clusters to be contained

within a spherical volume of radius 2 Mpc. This enables a comparison to cluster studies of Abell 521, Abell 1367 and Coma (see Fig. 6.9). The results for the relic areas in the 'sausage' cluster are an order of magnitude higher than the LF derived for the three clusters Abell 521, 1367 and Coma. The normalisation ϕ^* of Abell 1367, Coma and Abell 521 is ~ 2 orders of magnitude above the field LF at redshift 0.2. For the relaxed, local clusters Abell 1367 and Coma the characteristic luminosity L^* is below the field, which indicates a lack of bright emitters within the cluster volume, whereas the Abell 521 LF predicts the presence of many luminous emitters. Umeda et al. (2004) suggest this enhancement can be attributed to the merging nature of the cluster. Giacintucci et al. (2008) have found that Abell 521 also hosts a radio relic, but without a distribution of Hα emitters, we cannot confirm whether the majority of the emitters are located around the relic areas (Umeda et al. (2004) do not present a distribution of their Hα emitters). The measurements for the 'sausage' cluster indicate a possible LF shape similar to that of Abell 521, driven by the merging nature of the cluster, but with a factor of 10 increase in the overall normalisation.

The visual inspection of the BB, NB and BB-NB subtracted images revealed the same effect (see Figs. 6.6 and 6.7). Around the smaller relics in the 'sausage' cluster, where we expect the weaker, broken shock fronts to reside, we find numerous galaxies with haloes extended up to 60 kpc Hα (for some examples, see Fig. 6.3). Some of these emitters are highly disturbed and asymmetric and present tailed, clumpy Hα morphologies. We do not find any such examples in the 'toothbrush' cluster, nor in the field around the cluster. Sources extended beyond 4 arcsec were classified as extended, which corresponds to 14 kpc at the redshift of the clusters. Were these sources higher-redshift emitters, then their linear sizes would be extremely large: Hβ and [OIII] emitters at $z \sim 0.61 - 0.65$ would measure 27 kpc, 4000 Å break galaxies around $z = 0.8$ would be 30 kpc wide and [OII] emitters at $z \sim 1.15$ would be 33 kpc. A typical physical diameter of star-forming galaxies/line emitters at these redshift is $7 - 8$ kpc, with the largest galaxies being ~ 15 kpc in diameter (Stott et al. 2013a). This would render our extended emitters, were they at high redshift, two times larger than the largest galaxies and at least five times larger than typical galaxies at their redshift.

It has been known since the 1970s (Miley et al. 1972) that the cluster galaxies interact strongly with their environment: the ICM ram pressure strips the gas from the galaxies and bends their radio jets in a head-tail or twin-tail morphology. From our studies of the 'sausage' cluster (Stroe et al. 2013), we have discovered a clear bimodal distribution of galaxies with radio morphological orientations indicative of two sub-clusters, to the North and South of the cluster centre, moving in opposite directions, behind the radio shock fronts (for definition of cluster centres, see Figs. 6.6 and 6.7; the cluster centre was chosen as the middle of the distance between the radio relics, on the peak of the X-ray emission). The radio morphologies of the sources can be visualised in Figs. 6.6 and 6.7. Simulations suggest both clusters are post-core passage, meaning that the two initial clusters that participated in the merger, under the influence of gravity, have fallen into and passed through each-other once (van Weeren et al. 2011b; Brüggen et al. 2012). Because both clusters are post-core passage mergers, the shock fronts have travelled more than 1 Mpc though the ICM, potentially interacting with the cluster members. It is conceivable that travelling shock fronts could have an extra effect on the morphology of the galaxies, particularly on their Hα haloes.

We speculate that the disturbance of the 'sausage' Hα haloes and the increased number of bright Hα emitters may be an effect of shock induced star-formation. Most of the galaxies

in the cluster have interacted with the travelling shock wave sometime since core passage (∼ 1 Gyr). The shock front passage effectively compressed and injected turbulence into the ionised gas. The results indicate that the shock front has not stripped the ionised materials from the host galaxy, but has compressed the gas, which then may have collapsed into star forming clouds. A similar scenario has been proposed for high redshift galaxies, albeit with a different source and scale for the shock front. In the case of high-redshift radio galaxies the alignment of the optical and radio continuum emission was interpreted by Rees (1989) as shock induced star formation. These objects are still in the process of formation and their radio lobes would be advancing at Mach numbers of $M \simeq 10 - 100$. Such high Mach numbers are difficult to attain in the context of cluster mergers, where they are limited by the relative speeds of the infalling clusters driven by gravitational attraction. Lower Mach numbers are pervasive in merging clusters and this is exemplified by the radio relics in the 'sausage' cluster which trace shock fronts with Mach numbers between ∼ 2 − 4.5. Simulations of merging clusters show that the travelling shock fronts have higher Mach numbers in the past, compared to the shock strengths we measure via the relic radio properties (e.g. Roettiger et al. 1993; van Weeren et al. 2011b). It is therefore conceivable that large scale shocks with currently observed low Mach number could induce Jeans instabilities in the galactic gas clouds and cause them to collapse into star formation.

The boost in the Hα LF around the relic area in the 'sausage' cannot be attributed to accretion shocks, as these are expected to be generally symmetrical around the cluster outskirts, in the absence of a nearby obvious mass donor. ROSAT imaging (Voges et al. 1999) reveals that the 'sausage' is possibly connected to another cluster located to the north-east via a filament. Despite many galaxies being expected to lie along this filament, we do not find any evidence of enhanced star-forming galaxy counts in its direction. We stress that despite the fact the 'sausage' and the 'toothbrush' clusters are in the Galactic plane and are affected by differential dust extinction across the FOV, we have corrected for effects arising from incompleteness.

We find that the morphologies and star-forming properties of the galaxies hosted by the 'sausage' and 'toothbrush' clusters are vastly dissimilar. Despite having matching masses, temperatures, orientations and radio morphologies, there is one crucial factor that might explain the striking difference between the two clusters. Simulations (van Weeren et al. 2011b; Brüggen et al. 2012) tailored to reproduce the radio morphologies of the two fields indicate that, while the 'sausage' is a pure merger between two massive clusters, in the 'toothbrush' an extra smaller sub-cluster is participating in the merger towards the end of the merging process. Moreover, the core passage in the 'toothbrush' might have occurred ∼ 2 Gyr ago, while in the 'sausage' only ∼ 1 Gyr ago. The 'toothbrush' could be in a more advanced stage of relaxation, possibly close to virialisation (typical virialisation times for clusters are ∼ 1 Gyr), and the galaxy population evolved into gas-poor ellipticals. X-ray observations of the two clusters (Ogrean et al. 2013a; Ogrean et al. 2013b) also reveal that the more massive subcluster is located to the north of the 'sausage', in the proximity of the Mpc-wide relic, while for the 'toothbrush' it is located towards the southern relic. Hα is particularly sensitive to young, massive stars and it captures only recent episodes of star-formation. Shock compression is expected to be an 'instantanous' process, exciting star formation momentarily as it passes through a galaxy. In order to detect a boost in the luminosity function, we need to observe a cluster at the adequate time when shock-induced star formation is still active within gas-rich galaxies. Since we are viewing the 'toothbrush' cluster at a more evolved 'time-slice', it is

possible that there are fewer gas-rich galaxies for the shock to 'light-up'.

6.5   Conclusion

In this paper we have analysed Hα/emission-line galaxies within vastly disturbed clusters hosting radio-identified shock fronts. As test cases, we studied the 'sausage' and 'toothbrush' clusters at redshift ~ 0.2, which have been likely formed through major mergers in the plane of the sky. The merger gave rise to Mpc-wide coherent shock waves that produced spectacular examples of radio-relics. We used the Hα recombination line, observing the clusters via the narrow-band technique with the Isaac Newton Telescope. We inspected individual Hα morphologies and looked at global, statistical properties via Hα luminosity functions.

- We surveyed a comoving volume of 3.371×10^3 Mpc^3 for the 'sausage' cluster and 4.546×10^3 Mpc^3 for the 'toothbrush'. We detected a total of 181 line emitters for the former and 141 for the latter, out of which 49 and 30 are expected to be Hα emitters.

- We produced field LFs encompassing the entire field-of-view of the two clusters and found good agreement with the COSMOS blank field LF derived by Shioya et al. (2008) for a similar redshift.

- We discovered numerous extended galaxies around the radio relics in the 'sausage' cluster. The normalisation of the Hα luminosity function is an order of magnitude above that of luminosity functions derived for both local, relaxed clusters like Abell 1367 and Coma, and similar redshift, disturbed clusters like Abell 521. We speculate these extended Hα haloes result from interactions with the travelling shock waves that are responsible for accelerating the radio-electrons.

- In the 'sausage' cluster we uncover a clear boost (9σ) in the number counts of luminous Hα emitters around the radio relics and speculate that the passage of the shock wave might have induced star-formation within the disks of the cluster galaxies.

- We do not find such bright emitters in the 'toothbrush' cluster. We speculate that the difference between the emitter populations in the 'sausage' and 'toothbrush' clusters by examining their different merger history, particularly the time since core-passage.

The results presented here show the potential of multi-wavelength studies of clusters hosting radio relics. Surveying a statistical sample of clusters containing radio relics would enable us to test the statistical properties of galaxies under the influence of travelling shock waves. Do shock fronts lead to a boost in the star formation activity, or is it the case only in the 'sausage' cluster? Larger samples of clusters could reveal any dependence of shock-induced star-formation on the merging history of the clusters.

Acknowledgements

6.6 Appendix

6.6.1 Hα fractions

Figure 6.10: Hα and other emitters' fractions with respect to the total number of emitters detected by the narrow band filters, as a function of total line flux. *Top*: 'Sausage'-like data. *Bottom*: 'Toothbrush'-like catalogue. We used the COSMOS catalogue to simulate 'sausage'-like and 'toothbrush'-like catalogues. Error bars are overplotted, but in some cases they are smaller than the plotting symbol.

7

The rise and fall of star-formation in z ∼ 0.2 merging galaxy clusters

$$z \sim 0.2 \text{ merging galaxy clusters}$$

CIZA J2242.8+5301 ('Sausage') and 1RXS J0603.3+4213 ('Toothbrush') are two low-redshift ($z \sim 0.2$), massive ($\sim 2 \times 10^{15} M_\odot$), post-core passage merging clusters, which host shock waves traced by diffuse radio emission. To study their star-formation properties, we uniformly survey the 'Sausage' and 'Toothbrush' clusters in broad and narrow band filters and select a sample of 201 and 463 line emitters, down to a rest-frame equivalent width (13Å). We robustly separate between Hα and higher redshift emitters using a combination of optical multi-band (B, g, V, r, i, z) and spectroscopic data. We build Hα luminosity functions for the entire cluster region, near the shock fronts, and away from the shock fronts and find striking differences between the two clusters. In the dynamically younger, 1 Gyr old 'Sausage' cluster we find numerous (59) Hα emitters above a star-formation rate (SFR) of 0.17 $M_\odot$ yr^{-1} surprisingly located in close proximity to the shock fronts, embedded in very hot intra-cluster medium plasma. The SFR density for the cluster population is at least at the level of typical galaxies at $z \sim 2$. Down to the same star-formation rate, the possibly dynamically more evolved 'Toothbrush' cluster has only 9 Hα galaxies. The cluster Hα galaxies fall on the SFR-stellar mass relation $z \sim 0.2$ for the field. However, the 'Sausage' cluster has an Hα emitter density > 20 times that of blank fields. If the shock passes through gas-rich cluster galaxies, the compressed gas could collapse into dense clouds and excite star-formation for a few 100 Myr. This process ultimately leads to a rapid consumption of the molecular gas, accelerating the transformation of gas-rich field spirals into cluster S0s or ellipticals.

7.1 Introduction

Galaxy clusters grow by merging with other clusters and via accretion of galaxies (e.g. Sarazin 2002). Even at low redshifts ($z < 0.5$), a significant population of galaxy clusters are undergoing mergers, with clear evidence from their disturbed intra-cluster medium (ICM) X-ray emission. Merging clusters are a unique probe of the interaction between dark matter, the ICM and the galaxies. They provide us with a way to test hierarchical structure formation, cosmic ray physics and galaxy evolution in dense environments. Major mergers have been argued to lead to increased turbulence within the ICM. In a number of cases merging clusters have been observed to produce travelling shock waves with Mach numbers (M) below 4 (e.g. Brunetti & Jones 2014). The shock fronts (re-)accelerate ICM electrons, which radiate synchrotron emission, observed in the radio as giant relics at cluster peripheries (Brunetti & Jones 2014).

7.1.1 Star-forming galaxies in clusters

The ICM interacts strongly with the cluster galaxies and is efficient in transforming the star-forming properties of member galaxies and/or maintaining them quenched (e.g. Butcher & Oemler 1978a,b; Dressler 1980). The cluster galaxy population is dominated by passive, massive elliptical galaxies. The total galaxy number density in cluster environments is higher than in the field. Nevertheless, owing to a low fraction of blue, late-types within clusters, the number density of star-forming cluster galaxies is generally lower than in the field, (e.g. Dressler 1980; Goto et al. 2003). For example, by using the Hα emission line which traces recent (< 10 Myr) star-formation, multiple authors have found that the number density of star-forming galaxies is ~ 50 per cent lower than in blank fields (e.g., Couch et al. 2001; Balogh et al. 2002; Kodama et al. 2004). Neutral hydrogen (HI) observations also show that cluster spirals contain significantly less HI gas than their field counterparts (e.g. Cayatte et al. 1990).

Hence, dense cluster environments seem to suppress star-formation and probably lead to a morphological transformation from gas-rich spirals into gas-poor ellipticals. The deficit of star-forming galaxies in clusters is thought to occur through the process of ram pressure stripping (e.g. Gunn & Gott 1972; Fumagalli et al. 2014). Evidence of ram pressure stripping of the HI and Hα gas in infalling cluster galaxies has been observed in the form of tails, knots and filaments (e.g. Gavazzi et al. 2001; Oosterloo & van Gorkom 2005). N-body, smooth particle hydrodynamical simulations by Steinhauser et al. (2012), in line with previous work by Bekki & Couch (2003), Kronberger et al. (2008) and Bekki (2009), show that relatively weak ram pressure can compress the inter-stellar medium of the galaxy and lead to an increase of star-formation. By contrast, high environmental densities and strong ram pressure can remove most of the gas from the host galaxy.

Other processes, such as galaxy harassment (Moore et al. 1996), where galaxies are distorted by tidal forces, are also important. Tidal forces can be caused by the gravitational potential of the cluster or by encounters with other galaxies. The relative movement of galaxies as they fall into the cluster potential with respect to the ICM leads to a truncation of the outer galactic halo and disk. Simulations by Moore et al. (1998) indicate that galaxy harassment of small disk galaxies in clusters produces distorted spirals, often seen in $z \sim 0.4$ clusters (e.g. Couch et al. 1994), which evolve into spheroidal systems observed in local clusters.

Larson et al. (1980) proposed the process of galaxy strangulation as another means of transforming field spirals into cluster ellipticals and S0s. Gas from infalling galaxies escapes its host because of tidal forces created by the cluster potential well. With a limited supply of its main ingredient, the star-formation in the galaxy is effectively shut-down after over the course of a few Gyr.

7.1.2 Merging clusters with shocks

Even though the majority of galaxies in relaxed clusters are quenched, recent observations suggest that vigorous star-formation can be observed in merging clusters. By studying a sample of $z > 0.3$ clusters, Ebeling et al. (2014) found that gas within infalling galaxies is first shock compressed and then removed from the host galaxies. Therefore, if observed at the right time, gas-rich galaxies possibly shocked by infalling into the cluster or by the passage of a shock wave can exhibit high star-formation rates.

There has been recent evidence that merging cluster processes such as increased turbulence and shocks affect the star formation properties of associated galaxies. Pranger et al. (2013) find a population of quenched spirals at $3 - 4$ Mpc distances from the core of Abell 3921, which they attribute to shocks and cluster mergers. In the post-merger cluster Abell 2384, Pranger et al. (2014) find a significant population of disk galaxies in the cluster core, which is expected to be devoid of star-forming galaxies. Owers et al. (2012) find three star-forming tails and filaments in galaxies nearby the X-ray shock front in Abell 2744. Ferrari et al. (2003) and Umeda et al. (2004) find a significant population of luminous, Hα-emitting, star-forming galaxies in the merging cluster Abell 521 (Ferrari et al. 2003, 2006), which hosts a radio-detected shock front (Giacintucci et al. 2008).

Galaxy formation simulations can be used to model the impact of mergers on galaxy properties. For example, models of ram pressure stripping indicate that star-formation in galaxies within merging clusters can be quenched (e.g. Kapferer et al. 2009). More recently, hydrodynamical simulations of shocks passing through galaxies have reproduced star-forming tails trailing behind their parent galaxy (Roediger et al. 2014). The star-formation persists for a few 100 Myr after the shock passage, in line with observations of star-forming tails in cluster infalling galaxies by Owers et al. (2012).

7.1.3 The 'Sausage' and 'Toothbrush' clusters

To probe the effects of shocks in transforming cluster galaxies, we started an observing campaign of two major-merging, $z \sim 0.2$ clusters hosting some of strongest radio shocks detected to date: CIZA J2242.8+5301 (nicknamed the 'Sausage', van Weeren et al. 2010) and 1RXS J0603.3+4213 (nicknamed the 'Toothbrush', van Weeren et al. 2012b). The peculiar morphology of the relics explains the nickname of each cluster (see Figs. 7.1 and 7.2). The bright radio relics show clear signs of steepening and curving radio spectrum from the shock front into the downstream area, suggesting a scenario where the synchrotron electrons are shock accelerated and subsequently cool (van Weeren et al. 2010; van Weeren et al. 2012b; Stroe et al. 2013). Nevertheless, the high-frequency, 16 GHz observations of the 'Sausage' relic suggests a more complicated scenario in which the electrons are injected and accelerated also in the downstream area (Stroe et al. 2014b). Both clusters are massive, X-ray luminous and present elongated X-ray morphologies suggesting a merger in the plane of the sky (Akamatsu

& Kawahara 2013; Ogrean et al. 2013a; Ogrean et al. 2013b, 2014a). They host two radio relics, which trace $M \sim 2-4$ Mach number shocks. In both clusters, one relic is significantly larger and brighter than its counterpart, suggesting the merging sub-clusters were at close, but not $1:1$ mass ratio. A weak lensing analysis by Jee et al. (2015) indicates that the 'Sausage' cluster is among the most massive clusters discovered to date, with a total mass exceeding of $M_{200} > 2.5 \times 10^{15} M_{\odot}$. The northern ($M_{\mathrm{N}} = 11.0^{+3.7}_{-3.2} \times 10^{14} M_{\odot}$) and the southern sub-clusters ($M_{\mathrm{S}} = 9.8^{+3.8}_{-2.5} \times 10^{14} M_{\odot}$ Jee et al. 2015) are very similar in mass. Dawson et al. (2015) derive velocity dispersion based mass estimates ($M_{\mathrm{N}} = 16.1^{+4.6}_{-3.3} \times 10^{14} M_{\odot}$ and $M_{\mathrm{S}} = 13.0^{+4.0}_{-2.5} \times 10^{14} M_{\odot}$), which are in agreement with the weak-lensing results.

On the basis of its X-ray luminosity, van Weeren et al. (2012b) and Brüggen et al. (2012) conclude the 'Toothbrush' is also a very massive cluster of about $1 - 2 \times 10^{15} M_{\odot}$.

Hydrodynamical simulations, radio spectral modelling and an analytical dynamics analysis suggest that the 'Sausage' core-passage has happened ~ 1.0 Gyr ago, at a relative speed of $\sim 2000 - 2500$ km s^{-1} (Dawson et al. 2015; van Weeren et al. 2011b; Stroe et al. 2014c), making it a younger merger than the possibly ~ 2 Gyr old 'Toothbrush' merger (Brüggen et al. 2012).

7.1.4 This paper

In this paper, we aim to study the star-formation properties of galaxies within the 'Sausage' and the 'Toothbrush' clusters. We derive star-formation rates and masses for the Hα sample and build luminosity functions for different environments in and around the cluster volumes.

By using narrow band observations, Stroe et al. (2014a) constrained the Hα luminosity function (LF) of the cluster galaxies and found striking differences between the 'Sausage' and the 'Toothbrush' clusters. Stroe et al. (2014a) observed a notable enhancement in the normalisation of the LF around the relics within the 'Sausage' cluster, where the travelling shock is expected to have passed $10 - 100$ Myr ago. By contrast, the 'Toothbrush' cluster is almost devoid of line emitters, similar to a relaxed cluster. The relatively short time span when enhanced star-formation is seen in the 'Sausage' cluster could explain the differences found between the two clusters, in line with simulations from Roediger et al. (2014).

In Stroe et al. (2014a), lack of multi-band photometry prevented the galaxy-by-galaxy separation between Hα emitters and higher redshift, lower rest-frame wavelength emission lines. Without such data, disentangling the drivers of the enhanced Hα emission in the 'Sausage' clusters is not possible, specifically the role of the post-merger timescales in shaping the Hα properties of the galaxies. Instead, Stroe et al. (2014a) applied a statistical correction for the fraction of Hα emitters from the total number of emitters, which was based on deep, narrowband observations on the Cosmic Evolution Survey field (COSMOS; Shioya et al. 2008).

In this paper, we present an optical multi-wavelength analysis of the 'Sausage' and 'Toothbrush' clusters. A combination of photometric and spectroscopic data from the Isaac Newton, William Herschel, Canada-France-Hawaii, Subaru and Keck telescopes spanning the entire optical spectrum through the B, V, g, r, i, z bands enables us to properly separate Hα emitters from higher redshift emitters. Compared to Stroe et al. (2014a), we are going $0.2 - 0.4$ magnitudes (mag) deeper in our detection band (i) and in the narrow band data, resulting in a larger sample of emitters, of which more than 50 per cent have been followed up spectroscopically and confirmed as Hα emitters.

Figure 7.1: The emitters for the 'sausage' field in red circles and sources selected as Hα emitters in the filled circles, overlaid on a Giant Metrewave Radio Telescope 323 MHz radio images in grey intensity. The red circles with black dots at the centre represent spectroscopically confirmed Hα emitters. The radio image is cut according to the NB FOV coverage, which was used for the selection of the emitters. The arc-sectors define the areas around the radio relics which were considered for producing relic luminosity functions. The cluster centres are defined to be at the location of the black crosses. The Northern relic was captured by a section between the solid red and the dashed blue circles, bound by the dashed green lines. The Southern relic area was defined between the solid red and the dashed blue circles and the solid yellow radii. The weak lensing area is marked by the solid black curve. The non-relic areas are defined as the arcsectors between the solid red and dashed blue circles and the dashed green and solid yellow lines. The entire cluster was assumed to occupy the volume defined by the dashed blue circle, which has an ~ 1.85 Mpc radius.
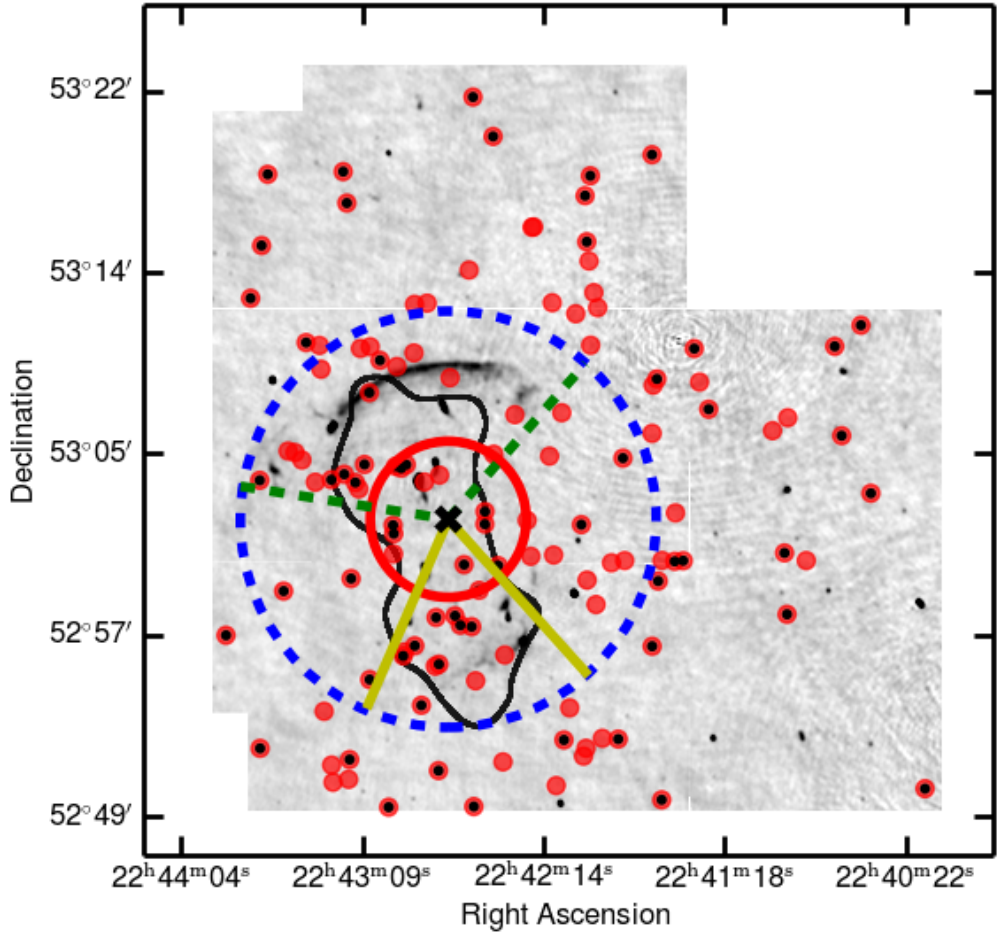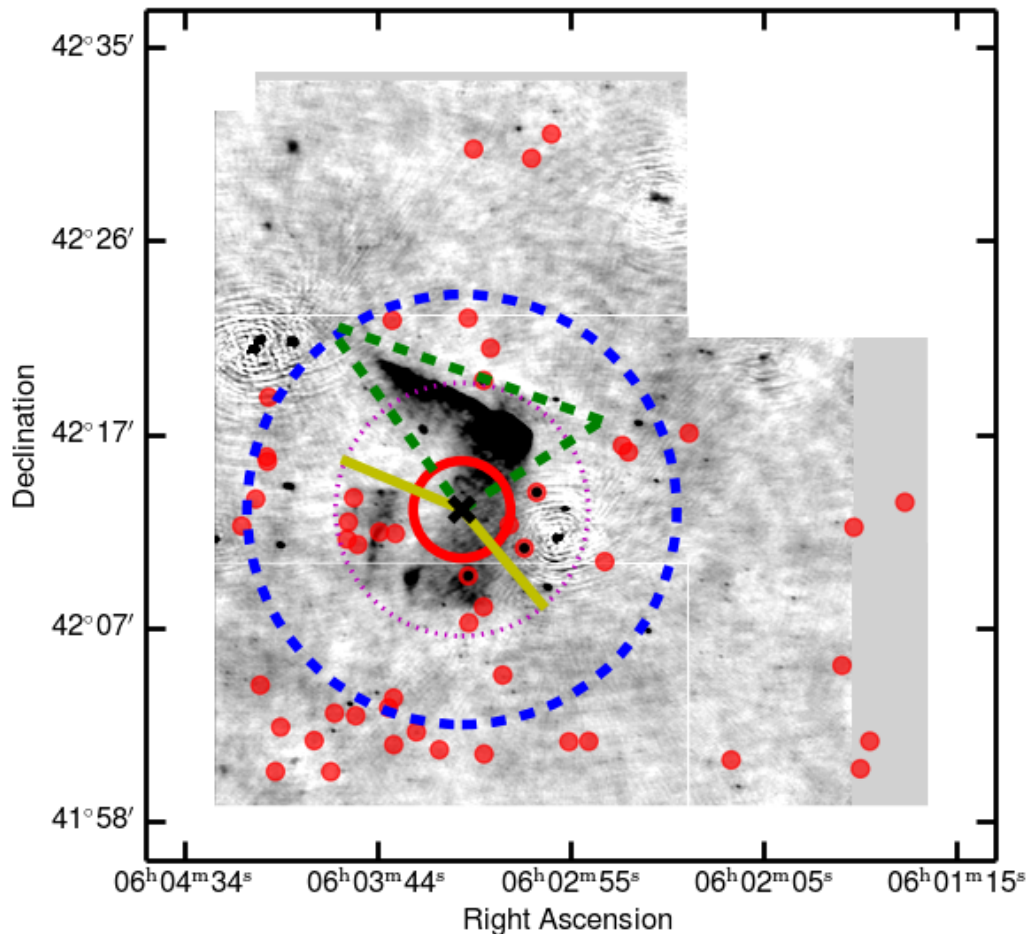
Figure 7.2: The emitters for the 'toothbrush' field in red circles and sources selected as Hα emitters in the filled circles, overlaid on a Giant Metrewave Radio Telescope 323 MHz radio images in grey intensity. The red circles with black dots at the centre represent spectroscopically confirmed Hα emitters. The radio image is cut according to the NB FOV coverage, which was used for the selection of the emitters. The arc-sectors define the areas around the radio relics which were considered for producing relic luminosity functions. The cluster centres are defined to be at the location of the black crosses. The Northern relic was captured by a section of the solid red circle, bound by the dashed green lines. The Southern relic area was defined between the solid red and dotted purple circles and the solid yellow radii. The non-relic areas are defined as the arcsectors between the solid red and dotted purple circles and the dashed green and solid yellow lines. The cluster was assumed to occupy the volume defined by the dashed blue circle of ~ 2.2 Mpc radius.

Table 7.1: Filter properties: type (narrow band, NB, or broad band, BB), weighted central wavelength and full width at half maximum. The redshift range $z_{H\alpha}$ for which the Hα line is detected within the FWHM of the narrow band filters is also given.

Filter	Type	λ_c (Å)	FWHM (Å)
NOVA782HA	NB	7839.0	110
($z_{H\alpha} = 0.1865 - 0.2025$)			
NOVA804HA	NB	8038.5	110
($z_{H\alpha} = 0.2170 - 0.2330$)			
INT i	BB	7746.0	1519
WHT B	BB	4332.7	1065
Subaru g	BB	4705.5	1393
INT g	BB	4857.3	1290
WHT V	BB	5488.1	990
INT V	BB	5483.4	990
CFHT r	BB	6257.9	1200
Subaru i	BB	7676.0	1555
WHT Z	BB	8720.9	–
INT Z	BB	8749.3	–

In §7.2 we present the reduction of the photometric and spectroscopic observations and the source extraction. §7.3 describes the emitter selection and separation, the luminosity functions and properties we derive for the galaxies. In §7.4 we compare our results with those for field galaxies and galaxies hosted in other clusters. We assume a flat ΛCDM cosmology with $H_0 = 70.5 \text{ km s}^{-1} \text{ Mpc}^{-1}$, matter density $\Omega_M = 0.27$ and dark energy density $\Omega_\Lambda = 0.73$ (Dunkley et al. 2009). We make use of Edward Wright's online cosmological calculator (Wright 2006). One arcmin measures 0.191 Mpc at $z = 0.192$ ('Sausage'), while at $z = 0.225$ ('Toothbrush') it corresponds to a physical size of 0.216 Mpc. All images are in the J2000 coordinate system. Magnitudes are in the AB system.

7.2 Data Reduction & Analysis

We use a multitude of photometric and spectroscopic instruments mounted on a range of optical telescopes. We describe the data acquisition, reduction and processing below. Table 7.1 and Fig. 7.3 display the filter properties, while the observations and integration times can be found in Table 7.2.

7.2.1 Observations & data processing

Isaac Newton Telescope observations

The broad band (BB) i and narrow band (NB) NOVA782HA and NOVA804HA imaging data presented in Stroe et al. (2014a), have been supplemented with new g, V, z, i and NB data

taken in 4 photometric nights in October-November 2013 with the Wide Field Camera (WFC)[1] mounted on the Isaac Newton Telescope (INT, PI Stroe) [2]. The camera, a mosaic of four chips, has a 0.33 arcsec pixel^{-1} scale and a square field of view (FOV) of 34.2 arcmin $\times$ 34.2 arcmin, with the top north-western corner missing. Individual exposures of 200 s for the BB and 600 s for the NB were taken in 5 dithered positions to cover the chip gaps, under seeing conditions varying from 0.7 to 2.0 arcsec. A total of $\sim$ 90 ks and $\sim$ 51 ks were observed in the NB and $\sim$ 13 ks and $\sim$ 12 ks in the BB for the 'Sausage' and 'Toothbrush', respectively. For details see Table 7.2.

Note that the NB filters have a full width at half maximum of 110 Å. They were designed to capture Hα emission ($\lambda_{restframe} = 6562.8$ Å) at the redshift of the 'Sausage' and 'Toothbrush' clusters. See Stroe et al. (2014a) for further details.

Canada France Hawaii Telescope observations

Under OPTICON programme 13B055 (PI Stroe), service mode r-band images were taken using the Megacam imager[3] installed on the 3.6-m Canada-France-Hawaii Telescope (CFHT)[4], under excellent seeing conditions (< 0.8 arcsec), between July and December 2013. The 36-chip camera has a $\sim$ 1 deg^2 FOV, with a 0.187 arcsec pixel^{-1}. To obtain a contiguous FOV coverage, 600 s exposures were taken in two dither positions spaced at 15 arcmin. 18 ks were observed in the 'Sausage' field and 5.4 ks in the 'Toothbrush'.

Subaru observations

Images in the g and i band (PI Wittman) were taken with Subaru's[5] Prime Focus Camera (Suprime-Cam)[6], a 10-chip mosaic with a 34 arcmin $\times$ 27 arcmin FOV and 0.2 arsec pixel scale. For the full details of the observations we refer the reader to Dawson et al. (2015) and Jee et al. (2015).

William Herschel Telescope Imaging

B, V and z band data were taken on 1-3 November 2013 with the newly-commissioned Prime Focus Imaging Platform (PFIP)[7] on the 4.2-m William Herschel Telescope (WHT, PI Stroe)[8]. The single-chip camera has a pixel scale of 0.27 arcsec with a FOV of 18.0 arcmin $\times$ 18 arcmin. We took a series of 600-s exposures in three pointings, jittered over five positions, to roughly cover the FOV of INT's WFC. The seeing varied between 0.7 and 2.0 arcsec. See table 7.2 for the integration times.

---

[1] http://www.ing.iac.es/engineering/detectors/ultra_wfc.htm
[2] http://www.ing.iac.es/Astronomy/telescopes/int/
[3] http://www.cfht.hawaii.edu/Instruments/Imaging/Megacam/
[4] http://www.cfht.hawaii.edu/
[5] http://www.naoj.org
[6] http://www.naoj.org/Observing/Instruments/SCam/index.html
[7] http://www.ing.iac.es/Astronomy/instruments/pfip/index.html
[8] http://www.ing.iac.es/Astronomy/telescopes/wht/
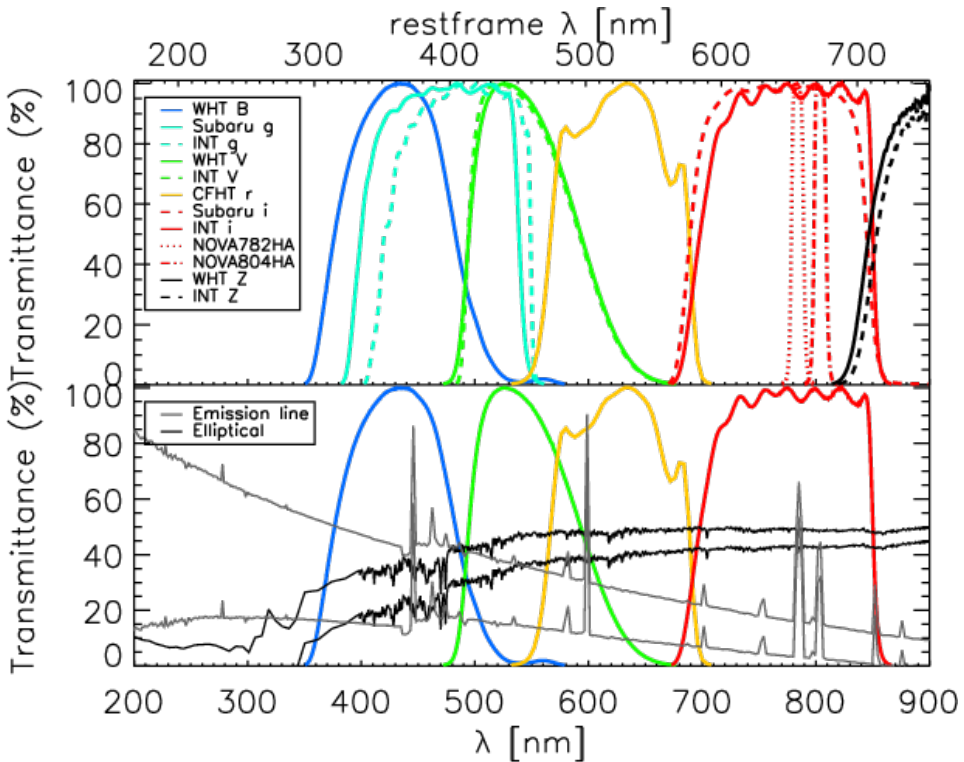
Figure 7.3: Top panel: Normalised transmittance profiles for the filters used in the analysis. The top x-axis marks the restframe wavelength coverage of the filters, assuming a redshift of 0.2. Bottom panel: Emission spectra for passive and emission line galaxies redshifted to $z = 0.2$, at arbitrary normalisation, taken from the PEGASE 2.0 template set (Grazian et al. 2006). Note how the Hα line falls within the corresponding narrow-band filter NOVA782HA, as expected. Both intrinsic and dust-attenuated spectra are shown. Notice the effect of Galactic dust extinction, especially in the blue-side of the spectrum.

7.2.2 Spectroscopy

We have also obtained spectroscopic data using two instruments. Spectra of a sample of 27 emission line, star-forming galaxies in the 'Sausage' and the 'Toothbrush' clusters were taken with the DEep Imaging Multi-Object Spectrograph (DEIMOS, Faber et al. 2003)[9] mounted at the Nasmyth focus of the Keck II telescope at the W. M. Keck Observatory (PI Wittman)[10]. These observations are described in detail in Dawson et al. (2015).

Spectra of line emitters within the 'Sausage' cluster roughly covering the $5500 - 8500$Å range were obtained on 2 and 3 July 2014 with the multi-object, wide-field AutoFib2 (AF2)[11] fibre spectrograph mounted at the prime focus of WHT (PI Stroe). A series of 30 min exposures in two configurations allowed us to observe ~ 100 sources within the cluster and

---

[9]http://www2.keck.hawaii.edu/inst/deimos/

[10]http://www.keckobservatory.org/

[11]http://www.ing.iac.es/Astronomy/instruments/af2/index.html

its northern periphery. Six line emitters in this sample were also targeted with DEIMOS. The data were analysed similarly to the method described in Dawson et al. (2015). In short, the fibre traces on the CCD was corrected for curvature using the lamp flats. After bias-subtracting, flattening and sky-background subtracting the data, the spectra were extracted and wavelength-calibrated using the lamp flats and sky lines. Full details can be found in Sobral et al. (in prep) and Dawson et al. (2015).

Note that the observing strategies for the DEIMOS and AF2 data were fundamentally different. The DEIMOS observations, tailored for a redshift analysis were mainly targeting the red sequence galaxies. The AF2 observations, however, specifically targeted emission line galaxies presented in this paper.

7.2.3 Photometric reduction and source extraction

We reduced the BB and NB optical photometry from the INT, WHT, Subaru and CFHT using the standard approach for reducing imaging data, implemented in our in-house PYTHON-based pipeline. We rejected data affected by cloud extinction, pointing, focussing, read-out issues and very poor seeing (> 2 arcsec). The data for each chip and each filter in the WFC (INT), Suprime-Cam (Subaru) and Megacam (CFHT) CCD mosaics were processed independently. Note that PFIP (WHT) imager contains a single CCD.

The sky flats for each filter on each instrument were median-combined to obtain a 'master-flat'. A 'master-bias' for each night of observing was obtained by median-combining biases taken with each instrument. The individual exposures were bias-subtracted and sky-flattened to remove electronic camera noise, shadowing effect and normalise for the pixel quantum efficiency. Science exposure pixels that deviated by more than 3σ from the local median were blanked as non-responsive, hot or as cosmic rays. We additionally normalised the WHT and INT i and z bands by a 'super-flat', obtained by combining science frames with masked sources. This step is necessary to remove the effects of significant thin-film interference ('fringing') for images taken in the red and near infra-red part of the spectrum.

We used recursive rounds of SCAMP (Bertin 2006) to find astrometric solutions for the processed exposures. $0.2 - 0.3$ arcsec root-mean-square (rms) accuracy per object was obtained by comparing source positions with 2MASS astrometry (Skrutskie et al. 2006). The exposures were normalised to the same zero-point (ZP) by referencing to the closest photometric band measured in the fourth United States Naval Observatory (USNO) CCD Astrograph Catalog (UCAC4; Zacharias et al. 2013). The fully-processed science exposures for each filter and each instrument were median-combined to obtain final stacked images using SWARP (Bertin et al. 2002).

The Sloan Digital Sky Survey (SDSS) does not cover our fields. We therefore used the USNO-B1.0 catalogue (Monet et al. 2003) to derive the photometric calibration, as outlined in Stroe et al. (2014a). The USNO-B1.0 magnitudes were converted to Johnson system B, V, z and Sloan system g, r, i based on relations derived from SDSS Data Release 7 (SDSS DR7 Abazajian et al. 2009; Adelman-McCarthy et al. 2009) on a 9 deg^2 field with overlapping SDSS DR7 and USNO-B1.0 coverage. Bright, but not saturated stars in our fields were matched to magnitudes of USNO-B1.0 sources, converted to the equivalent filter, in order to obtain the photometric ZP. Given the high number of sources matched an accuracy of ~ 0.05 mag was attained in the calculation of the ZP. The calibration was performed independently

Table 7.2: Details of the observations: total integration times, effective integration times after removing bad frames and observing dates.

Field	RA	DEC	Filter	Int. Time (ks)	Eff. Time (ks)	Dates
			NOVA782HA	78.9	47.4	October 13–15, 20–22 2012;
						November 1–6 2013
			INT i	13.2	9.0	October 15, 20–22, 2012;
						November 1–6, 2013
'Sausage'	$22^h42^m50^s$	$53°06'30''$	WHT B	12.0	9.6	November 1,3 2013
			Subaru g	3.3	3.3	July 13, 2013
			WHT V	9.0	9.0	November 1,3 2013
			CFHT r	18.0	18.0	July 3, 5–8, 11, 12 2013
			Subaru i	3.3	3.3	July 13, 2013
			WHT Z	10.8	9.0	November 1,3 2013
			INT Z	1.0	1.0	November 1–6 2013
			NOVA804HA	51.0	37.2	October 13–16, 20, 21 2012;
						November 1–6 2013
			INT i	11.8	11.8	October 15, 16, 21 2012;
						November 1–6 2013
			WHT B	12.0	9.6	November 1,3 2013
'Toothbrush'	$06^h03^m30^s$	$42°17'30''$	INT g	6.0	6.0	November 1–6 2013
			WHT V	9.0	9.0	November 1,3 2013
			INT V	2.0	2.0	November 1–6 2013
			CFHT r	5.4	5.4	December 4, 5 2013
			WHT Z	10.8	9.0	November 1, 3 2013
			INT Z	5.0	5.0	November 1–6 2013

141

Table 7.3: Observed 1σ error and 3σ limiting magnitudes (measured in 5 arcsec apertures) for the 'Sausage' and 'Toothbrush' observations, uncorrected for the effects of Galactic dust attenuation. The extinction A_λ ranges for that filter are also given.

'Sausage'	INT NB	INT i	INT z	WHT B	WHT V
1σ	21.7	21.8	19.4	24.0	23.1
3σ	20.5	20.7	18.2	22.8	21.9
A	$0.6 - 1.0$	$0.6 - 1.0$	$0.5 - 0.8$	$1.3 - 2.1$	$1.0 - 1.6$
'Sausage'	WHT Z	Subaru g	Subaru i	CFHT r	
1σ	21.5	24.2	23.7	23.4	
3σ	20.2	23.1	22.5	22.2	
A	$0.5 - 0.8$	$1.2 - 1.9$	$0.6 - 1.0$	$0.8 - 1.3$	
'Toothbrush'	INT NB	INT i	INT g	INT V	INT z
1σ	21.9	22.5	23.5	22.8	20.8
3σ	20.7	21.3	22.3	22.3	19.6
A	$0.32 - 0.43$	$0.34 - 0.46$	$0.27 - 0.37$	$0.65 - 0.88$	$0.57 - 0.76$
'Toothbrush'	WHT B	WHT V	WHT Z	CFHT r	
1σ	24.0	23.6	21.5	23.8	
3σ	22.8	22.4	20.3	22.6	
A	$0.74 - 1.00$	$0.56 - 0.76$	$0.27 - 0.37$	$0.47 - 0.68$	

for the four WFC chips (INT) and the three PFIP (WHT) pointings.

We extracted sources using SExtractor (Bertin & Arnouts 1996), measuring magnitudes in 5 arcsec apertures, corresponding to a physical diameter of ~ 17 kpc at the redshift of the clusters. This aperture ensures that we encompass the full disk of the galaxies. Subsequently, the magnitudes were corrected for dust absorption by the Milky Way, using the reddening values from Schlafly & Finkbeiner (2011), interpolated to the effective wavelength of each of our filters. The clusters are located at low Galactic latitude and suffer from significant dust extinction (A_λ) which varies across the relatively large FOV of our observations (see Figs. 7.15 and 7.16). If uncorrected for, the dust extinction can shift galaxy B-V colours by up to 0.5 magnitudes and B-z up to 1.5 mag.

We used the RMS noise reported by SExtractor to calculate the 1σ and 3σ limiting magnitudes for our observations. Note that the Galactic dust extinction is substantial for our field and rises steeply in the blue side of the spectrum (see Table 7.3).

7.3 Methods and Results

7.3.1 Narrow band emitter selection

In order to select line-emitting candidates, we study the excess of the NB emission as compared to the BB continuum. If an emission line is present, the source will have a significant BB-NB colour excess. We use the same approach described in detail in Stroe et al. (2014a), based on the methods of Bunker et al. (1995) and Sobral et al. (2009, 2012). We refer the

interested readers to those papers for the details of the selection criteria.

The different effective central wavelengths of the NB and BB filters (see Table 7.1, ~ 100Å for the 'Sausage' and ~ 300Å for the 'Toothbrush') cause systematic BB-NB colour offsets. A constant offset was sufficient to correct the excess in the 'Sausage' field, as there was no dependence of NB-BB excess on the NB magnitude. The NOVA804HA filter peaks 300Å redder than the INT i BB filter. Therefore, the i and z magnitudes were used to correct for the colour offsets that vary with NB magnitude. For sources without a z band magnitude, a statistical correction was applied based on the average z-i colour. Note this is a significant improvement, greatly reducing scatter compared to Stroe et al. (2014a), where z band data was not available.

The selection of emitters is performed anew, since our new NB and BB data are deeper by $0.2 - 0.4$ mag than in Stroe et al. (2014a), with a better colour correction, allowing us to probe fainter and lower equivalent width (EW) emitters. In short, to be selected as a line emitter, a source must fulfil three criteria (for details, see Stroe et al. 2014a):

- Significant excess (Σ) narrow band (NB) emission with respect to the broad band (BB, $\Sigma > 3$), based on the scatter of the faint-end of the NB magnitudes. This criterion rejects faint, low signal-to-noise sources from entering the emitter catalogue.

- A NB minus BB colour cut, intended to retain sources with an intrinsic emission line equivalent width (EW) higher than 13Å (assuming the sources are at $z \sim 0.2$). This ensures that we select sources with strong spectral features and remove stars or sources without an emission line, but which have steep continuum. The EW cut value was chosen to reflect the 3σ scatter of the BB-NB excess around 0, for bright, but not saturated NB magnitudes.

- Visual inspection to remove saturated stars, double stars and false positives at the edge of chips. These types of sources can mimic line emitters.

Our sample consists of 201 emitters for the 'Sausage' field (0.020 sources per kpc^2, down to a line flux of 5.2×10^{-16} erg s^{-1} cm^{-2}) and 463 for the 'Toothbrush' field (0.036 sources per kpc^2, see also Table 7.4, down to a line flux of 9.8×10^{-17} erg s^{-1} cm^{-2}). This is a substantial increase compared to Stroe et al. (2014a), where 181 emitters were found for the 'Sausage' field and 141 in the 'Toothbrush' FOV.

7.3.2 Identifying Hα emitters among the line emitters

Our NB emitter population is composed of a sample of Hα sources at $z \sim 0.2$, together with other strong, higher-redshift line-emitters that fall within the passband of our NB filter. Nevertheless, given the moderate depth of our NB survey, we expect our emitter population to have a higher fraction of Hα emitters compared to what is measured from deep surveys such as COSMOS, which are saturated at bright luminosities because of long individual integration times. Emission line sources strong enough to potentially be detected are: Hβ ($\lambda_{\rm rest} = 4861$ Å), [O$_{\rm III}$]$\lambda\lambda$4959, 5007 emitters at $z \sim 0.61 - 0.65$ and [O$_{\rm II}$] ($\lambda_{\rm rest} = 3727$ Å) emitters at $z \sim 1.15$. We might also be contaminated by $z \sim 0.8$ 4000 Å break galaxies.

In order to differentiate between these emitter populations, we use colour-colour separation (e.g. Shioya et al. 2008; Sobral et al. 2013a), in combination with spectroscopic and
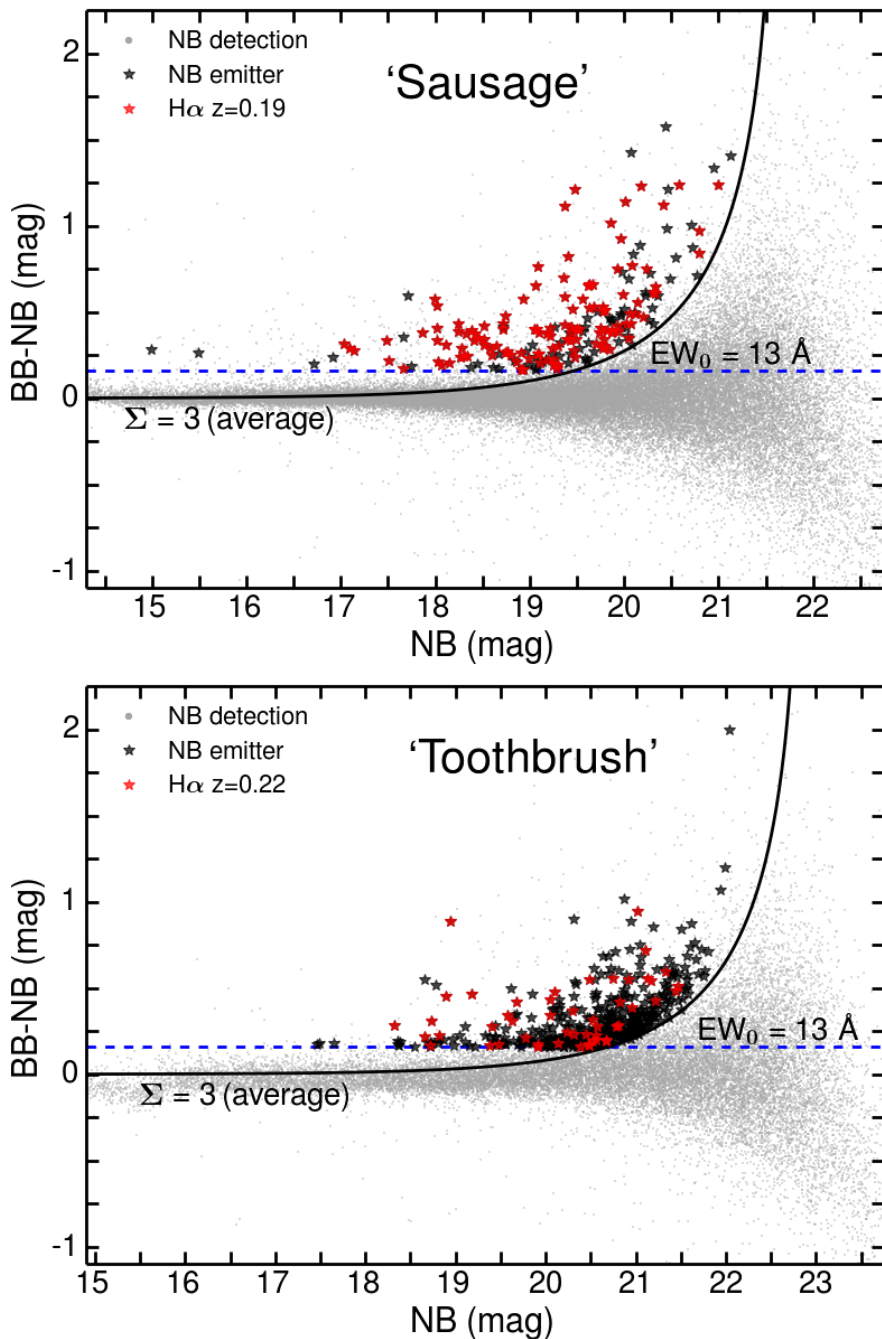
Figure 7.4: BB minus NB as function of NB magnitude for the 'sausage' (top) and 'toothbrush' (bottom) fields. The INT i band was used for BB subtraction. The blue dashed, horizontal line represents the limiting rest-frame EW, while the curve marks the 3Σ colour significance limit for choosing sources as NB emitters (masked in the black stars). The sources selected as Hα emitters at $z \approx 0.2$ (according to Fig. 7.5) are shown in the red stars.

photometric redshifts. In order to do so, we fully exploit the wealth of multiband photometry we have acquired. We use our INT i catalogue as our main detection catalogue (used for subtraction of the continuum, with the INT NB data). The Subaru i band catalogue, albeit deeper than the INT i, does not have perfectly matching FOV coverage to our NB observations. We note that all our emitters have a detection in the BB and NB. We further use all the data available from the other bands ranging from B up to z band. Given the different depths and FOV coverage of these data, not all emitters have detections in all seven ancillary bands. About 40 per cent of sources have detections in all bands and another ~ 45 per cent miss a detection in one single band. The remaining ~ 15 per cent of sources lack 2 or more bands.

Colour-colour separation

We base our colour-colour selection on the $z = 0.24$ Hα emitters selected in COSMOS (Capak et al. 2007; Ilbert et al. 2009) from Subaru NB NB816 imaging (Shioya et al. 2008). Since COSMOS goes to much fainter magnitudes than our data, we select only emitters with line emission greater than 2.5×10^{-16} erg s^{-1} cm^{-2} to match the range observed in our survey. We explore possible colour-colour selections which best separate the low-redshift Hα emitters from the higher-redshift interlopers. We use the photometric and spectroscopic redshifts available for COSMOS to test how many emitters are correctly classified by each colour-colour selection. We adopt the B $-$ g versus r $-$ i colour-colour plane as best discriminator between the low and high redshift emitters (see Fig. 7.5). Sources are selected as potential Hα emitters if they simultaneously fulfil the two colour requirements:

$$(B - g) > (0.6(r - i) - 0.3) \tag{7.1}$$

$$(B - g) > (1.6(r - i) - 1.1) \tag{7.2}$$

These separation lines are marked in Fig. 7.5 by thick red lines.

Spectroscopic and photometric redshifts

The redshift of the sources was found by measuring the position of the brightest emission lines (e.g. Hα, Hβ, [OIII] [NII] and [SIII]) in each spectrum. For the 'Sausage' cluster, based on Keck spectra, there are 23 emitters which have been spectroscopically confirmed as Hα line galaxies at $z \sim 0.2$ (Sobral et al. in prep, Dawson et al. 2015). Forty-eight Hα sources are detected among the WHT spectra (see Sobral et al. in prep for details). Six emitters were targeted by both surveys and are detected as Hα in both data sets, confirming the robustness of our analysis. Therefore, we have 65 spectroscopically confirmed Hα sources out of a sample of 201 emitters. We confirm 8 Hβ/[OIII] emitters at $z \sim 0.6$, 1 [OII] emitter at $z \sim 1.1$ and 1 passive galaxy at $z \sim 0.8$. Hence out of 75 emitters with spectra, 65 are Hα (87 per cent) and the rest are higher redshift emitters. This low number of non-Hα sources is partly driven by our selection of bright emitters (with a mean 5 arcsec i band magnitude of 19.6 compared to 19.9 for the entire emitter population) for spectroscopic follow up, which have very high chances of being low rather than high-redshift. In addition, the Keck spectra confirm only 3 stars which contaminate our emitter population and we note that we have not done any star rejection due to the lack of near infra-red data. We exclude these sources from our Hα catalogue.
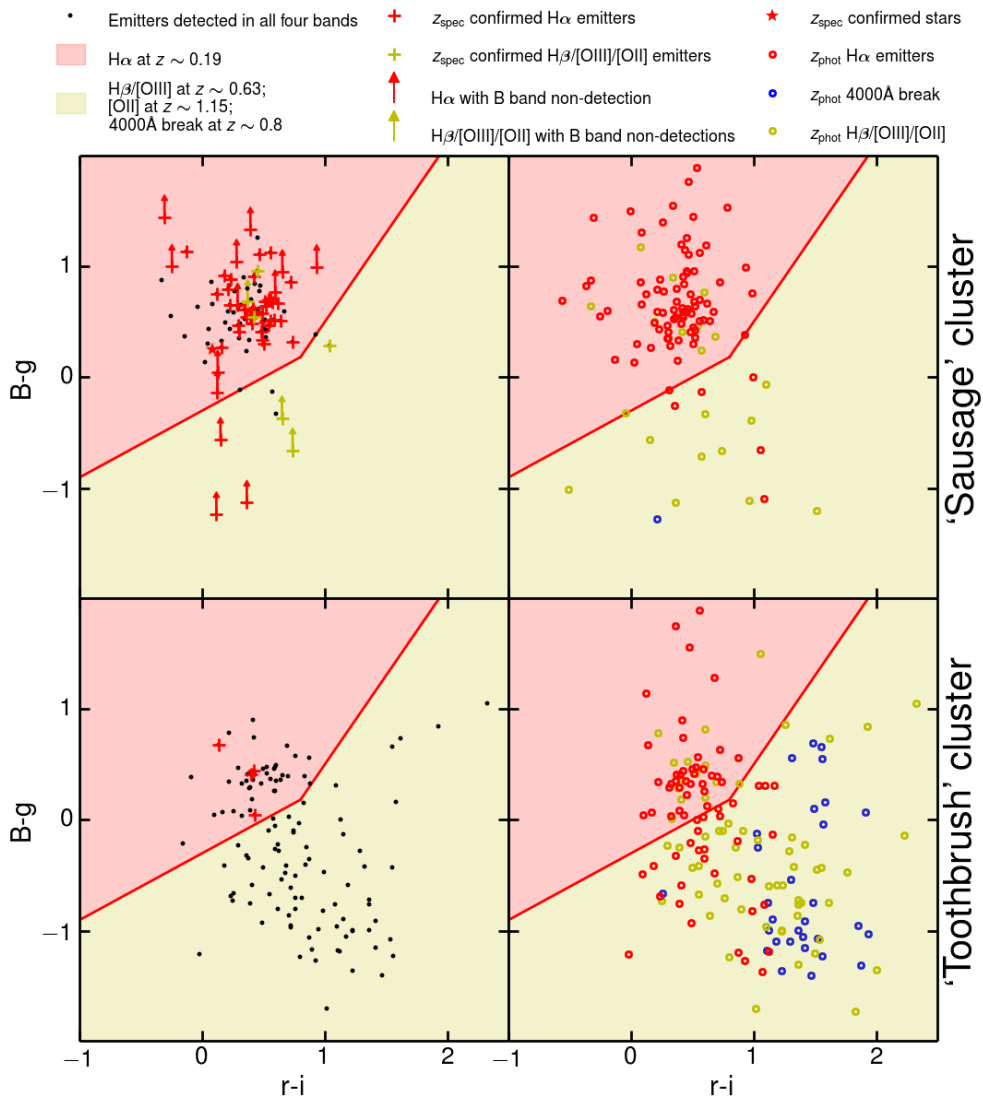
Figure 7.5: Colour-colour plot of 'Sausage' (top) plot and 'Toothbrush' (bottom plot) emitters, selected according to the criteria described in Fig. 7.4. $B - g$ versus $r - i$ colours are plotted. Hα emitters are expected to lie above and to the left of the thick red lines, in the red shaded areas. Hβ, [OIII], [OII] emitters and 4000Å break galaxies lie in the yellow shaded area. *Left panels*: Sources with clear detections are plotted with black dots. Spectroscopically confirmed Hα emitters are plotted in red crosses. *Right panel*: Sources with photometric redshifts consistent with being Hα emitters at $z \sim 0.2$ are plotted with red circles. Possible 4000Å break galaxies are plotted in blue. Sources with photo-z's around 0.63 (between 0.5 and 0.7) and 1.15 (between 1.0 and 1.2) are selected as Hβ, [OIII] and [OII] emitters (plotted in yellow).

For the 'Toothbrush' cluster, we have only 4 spectroscopically confirmed Hα emitters from Keck data. Only these 4 emitters were serendipitously targeted as the survey was targeting passive members.

As we do not have spectroscopy for all sources, we compute photometric redshifts. Using the comprehensive optical photometry available for these two fields (B, g, V, r, i, z, NB), relatively precise photometric redshifts (with errors $\Delta z_{\mathrm{phot}}/z_{\mathrm{phot}} < 20$ per cent) can be derived. For this purpose, we performed a grid-based redshift search between 0.01 and 1.3 with the EAZY code (Brammer et al. 2008). Full freedom has been otherwise allowed in the fitting process of the full set of PEGASE 2.0 templates (described in Grazian et al. 2006), which includes a range of early to late type galaxies, with a range of stellar ages. We used magnitudes measured in 5 arcsec apertures. The large apertures bias against the detection of high-redshift emitters, which are more compact and faint and are likely missed by our selection. Therefore, we expect our emitter population to be predominantly Hα emitters at $z \sim 0.2$. The distribution of photometric redshifts z_{phot} can be found in Fig. 7.6. A natural spread in the redshifts is expected given the uncertainties in fitting photometric redshifts, especially for star-forming galaxies, which can be relatively featureless in the continuum, e.g. they do not have strong 4000Å breaks. The majority of the line emitters ($> 85\%$) are correctly fit with templates that include line emission features, while galaxies at $z \sim 0.8 - 0.9$ are fit with passive galaxy templates marked by absorption features. Therefore, not only the redshifts, but also the correct spectral type can be recovered from the template fitting.

The effect of Galactic extinction (see Figs. 7.15 and 7.16) is evident in the photometric redshift fitting: if we use magnitudes uncorrected for dust attenuation, the bulk of the line emitters are fitted as higher redshift passive galaxies. Hence, as explained in Section 7.2.3, correcting for Milky Way dust is of the utmost importance.

Emitters are selected as Hα emitters if the photometric redshift lies between 0.16 and 0.23. Hβ/[OIII] explains the emission if $0.5 < z_{\mathrm{phot}} < 0.7$, [OII] if $1.0 < z_{\mathrm{phot}} < 1.2$ and 4000Å break galaxies if $0.7 < z_{\mathrm{phot}} < 0.9$ (Figs. 7.5 and 7.6).

Hα emitter selection

A source is selected as an Hα emitter if it fulfils any of the criteria listed below (see Fig. 7.5). We give the number of sources selected through each criterion for each field in the parentheses. Note that the spectroscopic confirmation overlaps with the other criteria in most cases, confirming the robustness of our selection.

- passes the colour-colour selection (equation 7.1, either has clear detections in all bands B, g, r, i or an upper limit in B, i.e. the source is not detected in the B band below the detection limit in the B band, see Table 7.3) and a z_{phot} placing it at the cluster redshift (63 sources for the 'Sausage' and 24 sources for the 'Toothbrush' field) *or*

- passes the colour-colour selection (either has clear detections in all bands B, g, r, i or significant upper limit in B), but not the z_{phot} criterion due to insecure z_{phot} (the χ^2 distribution does not have a clear minimum around $z \sim 0.2$, with minima of similar significance at other redshifts; we selected sources with a difference greater than 0.15 between the primary redshift solution and the redshift marginalised over $p(z|C) = exp(-0.5\chi^2)$, or z_{m1} as denoted in `eazy`) (42 sources for the 'Sausage' and 15 sources for the 'Toothbrush' field) *or*

147

Table 7.4: Statistics for the emitters detected in our 'sausage' and 'toothbrush' surveys. A non-detection in a particular band can be caused by lack of FOV coverage or limited depth. For emitters with detections in all bands or with significant upper limits, a colour–colour selection criterion could be applied to select Hα emitters. Additionally, spectroscopic or photometric redshifts were used to select potential Hα sources. Note that even though the sample of emitters is larger for the 'toothbrush' FOV, the number of Hα emitters is smaller, reinforcing the effect seen in Figure 7.6, where the photometric redshift distribution is dominated by high-z emitters.

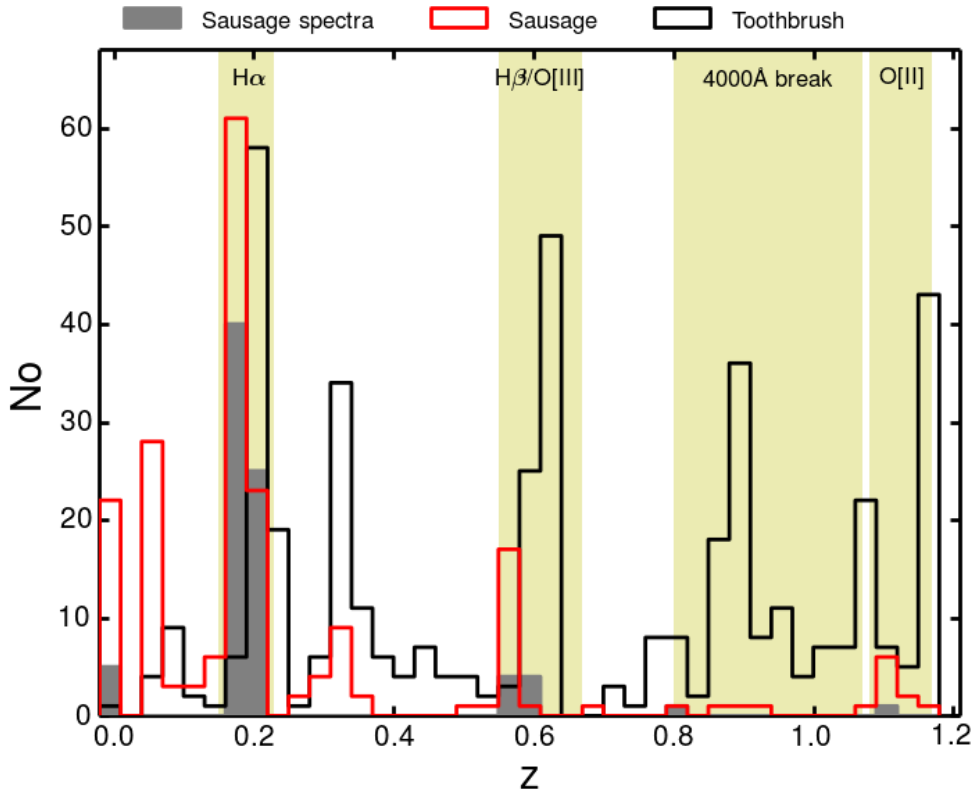| Field	Emitters	Detected in							Not detected in B, g, r	z_{spec} selected	Hα selected
		B, g, r, i	B, g, i	B, r, i	g, r, i	B	g	r			
'Sausage'	201	79	0	2	95	0	0	25	0	65	124
'Toothbrush'	463	120	9	51	114	3	6	141	19	4	50

Figure 7.6: Redshift distribution of emitters in the 'Sausage' and 'Toothbrush' FOV, as reported photometrically by EAZY. Spectroscopic redshifts obtained from Keck and WHT are also overplotted. Notice the clear peaks around $z \approx 0.2$. The 'toothbrush' Hα emitter distribution peaks at a slightly higher redshift than the 'Sausage' which is in line with the design of the NB filters. The ranges of higher redshift emitters possibly captured by our NB filters are marked in green. More high redshift emitters are captured in the 'Toothbrush' field, given its slightly deeper data.

- does not pass the colour-colour selection, but has a secure z_{phot} (the χ^2 distribution has a clear minimum around $z \sim 0.2$, without minima of similar significance at other redshifts, i.e. difference between the primary redshift solution and z_{m1} is lower than 0.15) (2 sources for the 'Sausage' and 11 sources for the 'Toothbrush' field) *or*

- z_{spec} confirms it is at the cluster redshift (65 sources for the 'Sausage' and 4 sources for the 'Toothbrush' field).

The fraction of spectroscopically confirmed Hα emitters in the 'Sausage' is extremely high ($\sim$ 52.5 per cent, see Fig. 7.6). The location of the spectroscopically confirmed sources fully validates the colour-colour selection (Fig. 7.5). Based on the colour-colour selection the photometric redshift catalogue suffers from 20 per cent mis-classifications. Most of these are sources where the photometric redshift probability distribution was roughly equal for classi-

fying the source as Hα, Hβ/[O$\textsc{iii}$] or [O$\textsc{ii}$]. In the case of the 'Sausage' field, out of 95 sources that would be classified as Hα by the photo-z, 37 were targeted by spectroscopy. Out of 76 emitters confirmed through spectroscopy, 40 were also correctly classified by the photometric redshift method. Another 11 sources were assigned as Hβ/[O$\textsc{iii}$] or [O$\textsc{ii}$] emitters, instead of their right type. For the rest of the sources photometric redshifts between 0.05 and 0.35 were assigned. In the case of the 'Sausage' cluster, out of 129 potential Hα emitters selected through the criteria above, 5 were removed as confirmed stars of higher redshift emitters (amounting to a contamination of less than < 4 per cent). The emitters were also visually inspected to check for possible interlopers and obvious Hα emitters not selected by our method. The visual inspection indicates a rate of ~ 10 per cent possible Hα sources not categorised as Hα by our method (or 90 per cent incompleteness), which is similar to Shioya et al. (2008).

We select a total of 124 Hα emitters located at the 'Sausage' cluster redshift and 50 for the 'Toothbrush' FOV (Table 7.4 and Figs. 7.5 and 7.2). For similar Hα luminosities, the typical fraction for Hα emitters at $z \sim 0.2$ out of a population of emitters selected in blank fields with a NB filter is $\sim 15 - 20$ per cent (e.g. Shioya et al. 2008). The fraction of Hα emitters (based on Table 7.4) in the 'Toothbrush' FOV resembles that of blank fields (11 per cent, 50 Hα out of 463 emitters), while in the 'Sausage' the fraction (~ 62 per cent, 124 out of 201) is significantly above field levels.

7.3.3   Removing [N$\textsc{ii}$] contamination

The [N$\textsc{ii}$] forbidden line is very close in wavelength to the Hα line (~ 20 Å away, restframe). Since our filters are 110 Å wide, we expect to pick up emission from both the Hα and [N$\textsc{ii}$]. We remove the contribution to the line flux, using the relation from Sobral et al. (2012). The median contribution of [N$\textsc{ii}$] to the Hα+[N$\textsc{ii}$] flux is 0.32, consistent with solar metallicity.

7.3.4   Hα luminosity

The Hα luminosity $L_{\mathrm{H}\alpha}$ can be calculated from the Hα flux $F(\mathrm{H}\alpha)$, corrected for [N$\textsc{ii}$], as described in §7.3.3.

$$L_{\mathrm{H}\alpha} = 4\pi d_L^2 F(\mathrm{H}\alpha). \tag{7.3}$$

where d_L is the luminosity distance (941 Mpc for a redshift of 0.1945 and 1107 Mpc for 0.2250, respectively for the two clusters). The emitters are binned based on their luminosity and normalised by the survey volume to form a luminosity function.

7.3.5   Completeness correction

Fainter Hα emitters and the emitters with lower line EWs will not enter our Hα emitter catalogue given our emitter selection criteria on limiting Σ and EW. This results in incompleteness. We study the way our completeness rate varies as a function of line luminosity following the method of Sobral et al. (2012). For this, we pass sub-samples of our emitters population through our selection criteria for Hα emitters described in Section 7.3.2.

We select a sample of sources, consistent with being non-emitters, but which pass our colour-colour criteria as being located at the cluster redshift. We add fake Hα emission lines to the flux of these galaxies and fold them through our EW and Σ emitter selection criteria

(as shown in §7.3.1) and study the recovery fraction. We perform this study independently for eight areas, given the variation of the dust extinction across the FOV (as noted by Stroe et al. 2014a, see also Fig. 7.15). The variable dust extinction has a non-trivial effect on the recovery rate of Hα emitters, given the different way dust extinction affects the blue side and the red side of the spectrum, affecting the perceived colours of the emitters.

The recovery rate of Hα emitters as function of their flux, for the eight areas of the FOV can be found in Fig. 7.7.

7.3.6 Volume and filter profile corrections

Assuming a top-hat (TH) shape with FWHM of 110 Å for the NB filter transmission profiles and given the FOV coverages (see Figs. 7.1 and 7.2), we are surveying a total comoving volume of 3.435×10^3 Mpc^3 for the 'Sausage' and 4.625×10^3 Mpc^3 for the 'Toothbrush'. Since our filters are not perfect THs (Fig. 7.3), we correct the volumes for the possible sources which might be missed in the wings of the filter as shown in Sobral et al. (2009, 2012).

7.3.7 Survey limits

We probe luminosities down to a 10 per cent completeness limit (see Fig. 7.7). This is equivalent to an average limiting Hα luminosity of $10^{40.64}$ erg s^{-1} for the 'Sausage' field and $10^{40.14}$ erg s^{-1} for the 'Toothbrush' field. The actual limiting magnitude will vary across the FOV much as the completeness varies, due to the varying dust extinction. Assuming all the Hα luminosity comes from star formation, we can use the Kennicutt (1998) relation, with a Chabrier (2003) initial mass function (IMF) to obtain the limiting star formation rate (SFR) of our surveys (see equation 7.5 in Section 7.3.10). The 'Sausage' field average limiting SFR is 0.17 $M_\odot$ yr^{-1}, while for the 'toothbrush' we reach down to an average of 0.06 $M_\odot$ yr^{-1}.

7.3.8 Hα luminosity function and star formation rate

We fit LFs to different regions within the two clusters (e.g. relic areas that are aligned with the merger axis, the sides of the cluster perpendicular to the axis where there is no radio emission, weak lensing area where most of the mass is contained etc.). For this purpose, we bin the data based on luminosity over each area. We bin the data using a range of bins. We define the bins by varying the minimum luminosity and bin width (100 random choices with uniform distribution). The errors on the $\log \phi$ values are Poissonian. By resampling the LF in different ways we can obtain a more robust determination of the fit parameters, which are not dominated by a particular choice of binning. To compare with other studies, we use the popular parametrisation of the LF defined by Schechter (1976):

$$\phi(L)\mathrm{d}L = \phi^* \left(\frac{L}{L^*}\right)^\alpha e^{-(L/L^*)} \mathrm{d}\left(\frac{L}{L^*}\right), \tag{7.4}$$

where L^* is the characteristic luminosity of the emitters where the power-law cuts off. ϕ^* is the density of Hα emitters and provides the normalisation. α is the faint-end slope of the LF, which we fixed to -1.2 (Stroe et al. 2014a).

We produce a 2D distribution of number of realisations as function of LF parameters (i.e. how many of the randomly generated binnings were best fitted with a particular combination
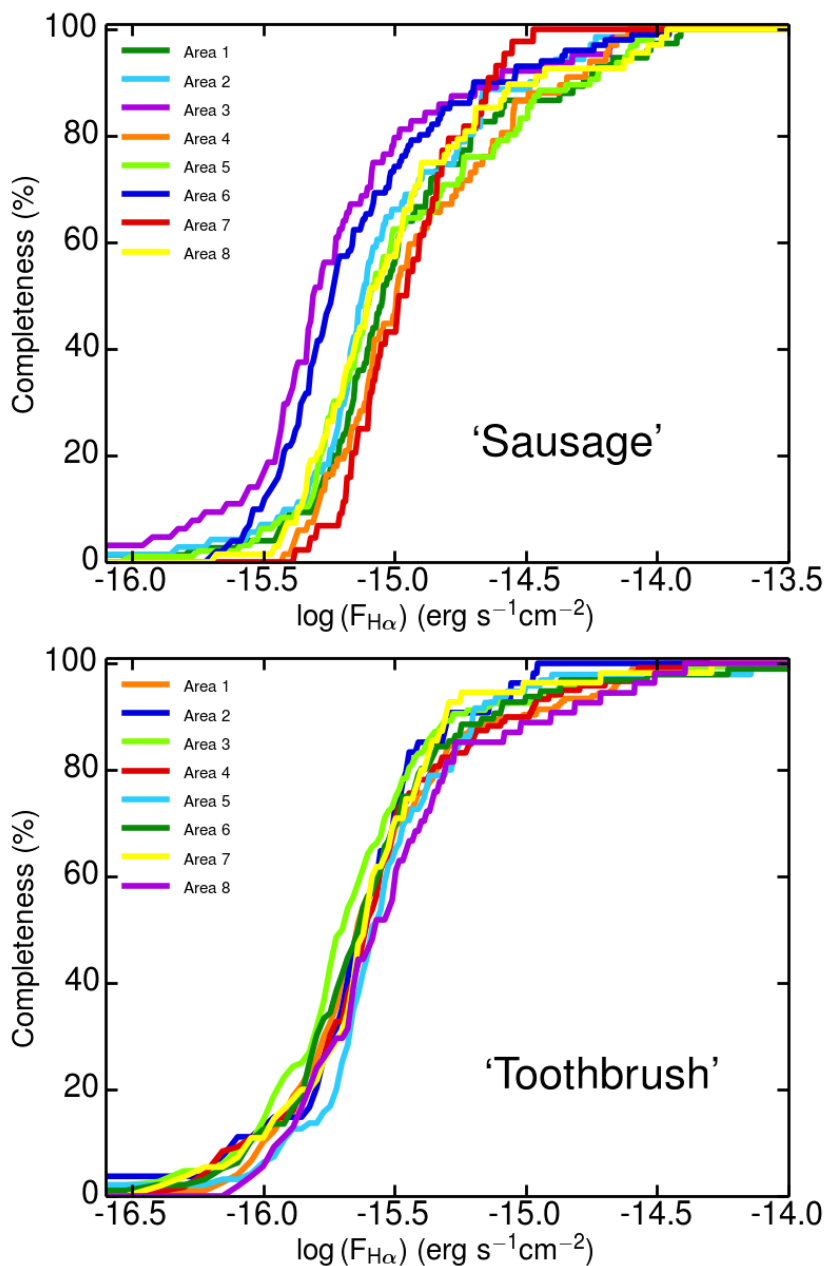
Figure 7.7: Survey completeness for the 'Sausage' (left) and 'Toothbrush' (right) fields as a function of Hα flux, performed separately for eight sub-areas within the FOV, to account for the varying dust extinction (see Figs. 7.15 and 7.16). The areas are colour-coded according the dust extinction, from low dust extinction in indigo, though blue, green yellow, orange and red for the highest extinction. Note the correlation between completeness and amount of extinction: areas 3 and 6 in the 'Sausage' field have the highest level of completeness, being the least affected by dust.

of ϕ^* and L^*). The reported $\log \phi^*$ and $\log L^*$ are determined as the mean of this distribution obtained by resampling the LF. The errors are 1σ standard deviations away from the mean. The results of the fit for different regions within and around the clusters (as defined in Figs. 7.1 and 7.2) can be found in Table 7.5 and Fig. 7.8. There is a striking difference between the normalisation of the two cluster LFs, as discussed in more detail in Section 7.4. The 'Toothbrush' LF is similar to a blank field, while the 'Sausage' ϕ^* is about a factor of 10 larger than that (Fig. 7.8).

We can use the Kennicutt (1998) conversion from Hα luminosity to star formation activity, using a Chabrier IMF Chabrier (2003) IMF:

$$SFR(M_\odot \text{yr}^{-1}) = 4.4 \times 10^{-42} L_{H\alpha}(\text{ergs}^{-1}).$$ (7.5)

7.3.9   Stellar masses

Galaxy spectral energy distributions were generated with the Bruzual & Charlot (2003) software package. We used stellar synthesis models from Bruzual (2007), a Chabrier IMF with exponentially declining star formation histories and a range of metallicities. These models were fitted to the full broad-band data (BgVrIz) to obtain stellar masses for the Hα galaxies, following the method presented in Sobral et al. (2011); Sobral et al. (2014) (for further details, see Sobral et al in prep). A histogram of the masses of Hα emitters in the 'Sausage' and 'Toothbrush' field is shown in Fig. 7.9. The values are normalised by the volume of each survey. The masses of the 'Sausage' Hα emitters are on average $\sim 10^{9.8}$ M$_\odot$. On average, the 'Toothbrush' Hα emitters are ~ 3 times less massive than those in the 'Sausage' ($\sim 10^{9.3}$ M$_\odot$). Note that this is driven by the deeper 'Toothbrush' data: the faintest Hα flux detected in the 'Sausage' survey is 3.4×10^{-16} erg s^{-1} cm^{-2}, while in the 'Toothbrush' we probe down to 4.2×10^{-17} erg s^{-1} cm^{-2}, a factor of ~ 8 deeper. Note that despite the similar volumes probed by the two surveys, there are significantly fewer massive Hα emitters in 'Toothbrush' compared to the 'Sausage'.

In Fig. 7.10, we plot the SFR versus the mass of the cluster Hα emitters, on top of the results for the blank field obtained from COSMOS (Shioya et al. 2008). We compute SFR for individual galaxies using the dust correction based on stellar mass (Garn & Best 2010). While our cluster Hα emitters fall on the SFR-mass relationship as defined from blank fields, it is important to note that the COSMOS data was obtained over a volume ~ 10 times higher than the volume probed by our 'Sausage' and 'Toothbrush' surveys. We are detecting high numbers of very high-mass, highly-star forming galaxies which are relatively rare in the field.

7.3.10   The star formation rate density

Given a LF and using the conversion from Hα luminosity and SFR, we can also calculate the star formation rate density ρ_{SFR} within that particular volume. The luminosity density is obtained by integrating the LF:

$$\rho_L = \int_0^\infty \phi(L) L dL = \Gamma(\alpha+2)\phi^* L^*,$$ (7.6)

where $\Gamma(n) = (n-1)!$ is the gamma function. ρ_{SFR} is then:

$$\rho_{SFR} = \Gamma(\alpha+2)10^{\phi^*}10^{L^*}10^{0.4}(1-f_{AGN})$$ (7.7)

where we are assuming that part of the Hα emitters are powered by active galactic nuclei, rather than star formation. From the spectroscopic observations of the 'Sausage' Hα emitters, emission lines ratios (comparison of [O$\textsc{iii}$]/Hβ versus [N$\textsc{ii}$]/Hα (BPT diagram; Baldwin et al. 1981) enable the separation between star-forming galaxies and AGN (Sobral et al. in prep). This analysis indicates a fraction of 10 per cent pure AGN-powered Hα emitters. We thus assume that a fraction f_{AGN} of the emitters is powered by AGN activity, chosen to be 10 per cent according to Sobral et al (in prep) and in line with Garn & Best (2010) and Sobral et al. (2013a). We also correct the luminosity for the dust extinction intrinsic to the line emitter. A conservative value of 1.0 magnitude has been shown to be appropriate by various authors (e.g. Sobral et al. 2012; Ibar et al. 2013) and has been widely assumed in the literature (e.g. Fujita et al. 2003; Ly et al. 2007; Geach et al. 2008; Sobral et al. 2009). The error on the ρ_{SFR} is $\Delta\rho_{SFR}$:

$$\Delta\rho_{\text{SFR}} = \rho_{\text{SFR}} \ln(10) \sqrt{(\Delta\phi^*)^2 + (\Delta L^*)^2} \tag{7.8}$$

The comparison of ρ_{SFR} in and around our clusters and the field is illustrated in Fig. 7.11. We also overplot the value obtained by Shioya et al. (2008) for the COSMOS field. For comparison, we show the parametrisation derived by Sobral et al. (2013a) using a method similar to ours from a set of consistent Hα NB observations at four redshift slices (2.23, 1.47, 0.84 and 0.40). The dependence of the ρ_{SFR} on redshift for the blank field is:

$$\log_{10}\rho_{\text{SFR}} = -2.1(1+z)^{-1}. \tag{7.9}$$

We find that ρ_{SFR} for the Sausage cluster is significantly enhanced compared to the field. See Section 7.4 for a more detailed discussion.

7.4 Discussion

The fraction of star-forming galaxies drops steeply from field environments towards the cores of massive, hot, relaxed clusters (e.g. Gómez et al. 2003). To study the effect of cluster mergers and shocks on the star forming properties of cluster galaxies, we performed observations of two disturbed, $z \sim 0.2$ clusters hosting radio relics, tracers of ICM shock waves of Mach number $3 - 4$. We look at the trends in the normalisation and specific luminosity of the Hα luminosity function for the clusters and the masses, star-formation rate and star-formation rate density for the cluster star-forming galaxies. We discuss possible scenarios in which we expect differences between the Hα population of the two clusters.

7.4.1 Hα luminosity function for the clusters

'Sausage' Hα luminosity function

In the case of the 'Sausage', we build independent Hα LFs for the areas around the relics, along the merger axis of the cluster, and also away from the relics, perpendicular to merger axis (see Fig. 7.1). We study the LF for the entire cluster, by encompassing it with a circular aperture of ~ 1.85 Mpc radius. This radius was chosen as function of the X-ray temperature peaks Ogrean et al. (2013a) and the positions of the radio relics, which should be located at the cluster outskirts. A weak lensing analysis of the cluster (Jee et al. 2015), indicates a

Table 7.5: Parameters of the luminosity functions fitted with a Schechter function (see equation 7.4). The faint-end slope was fixed to a value of $\alpha = -1.2$, which was obtained by Stroe et al. (2014a) by combining data for the entire FOV of the two clusters. The fits were possible only for some areas within the cluster, as the number statistics were not in all cases high enough to allow the fitting of the independent Schechter parameters. For each area, the data was binned in range of different ways (by varying the luminosity of the first bin and the bin width) and fit independently to obtain an average, characteristic fit that best describes the LF shape. The average and standard deviation over these independent fits is reported in the table. The blank field fit for the COSMOS field by Shioya et al. (2008) is also reported. We also list ρ_{SFR} corresponding to each fit. The number of Hα emitters employed in each fit is given in the last column.

| Field	α	$\log \phi^*$ Mpc^{-3}	$\log L^*$ erg s^{-1}	SFRD $M_\odot$ yr^{-1} Mpc^{-3}	Number of Hα	z_{spec} confirmed Hα
'Sausage' field						
Cluster relics area	-1.2	-1.37 ± 0.04	41.69 ± 0.09	0.22 ± 0.05	32	15
RN area	-1.2	-1.22 ± 0.04	41.51 ± 0.06	0.21 ± 0.04	20	7
RS area	-1.2	-1.29 ± 0.04	41.72 ± 0.19	0.29 ± 0147	12	8
Weak lensing area	-1.2	-1.07 ± 0.04	41.40 ± 0.05	0.23 ± 0.03	26	19
Entire cluster area	-1.2	-1.21 ± 0.02	41.33 ± 0.02	0.14 ± 0.01	59	30
Cluster - no relics area	-1.2	-1.46 ± 0.03	41.38 ± 0.06	0.09 ± 0.01	14	5
'Toothbrush' field						
Cluster environment	-1.2	-1.76 ± 0.04	40.75 ± 0.01	0.01 ± 0.001	25	4
Shioya et al. (2008)	$-1.35^{+0.11}_{-0.13}$	$-2.65^{+0.27}_{-0.38}$	$41.57^{+0.38}_{-0.23}$	$0.018^{+0.007}_{-0.004}$		
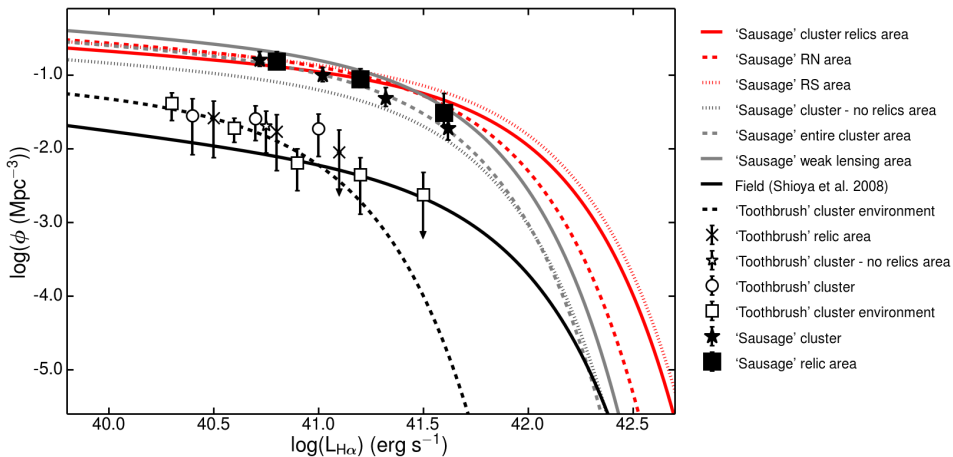
Figure 7.8: Luminosity function for the two clusters, obtained by fixing the faint end slope α to -1.2 (as derived in Stroe et al. 2014a) and varying the normalisation $\log \phi^*$ and the characteristic luminosity $\log L^*$. The regions are defined according to Figs. 7.1 and 7.2. Downward pointing arrows represent upper limits equivalent to 1 source per volume element, per bin. The fit for a $z = 0.24$ blank field from Shioya et al. (2008) is oveplotted. Note the difference in normalisation between the two clusters: the density of Hα emitters in the 'Sausage' is a factor of 10 higher than in the 'Toothbrush'. The typical luminosity L^* of 'Toothbrush' emitters is lower than the blank field.

value of $r_{200} = 2.63$ Mpc for the radial extent, assuming the cluster is fitted with a single Navarro-Frenk-White dark matter halo (Navarro et al. 1997). Therefore, our chosen radius for the cluster is smaller than r_{200}. We also build LFs for the area where most of the weak lensing mass in contained, as per Jee et al. (2015). We smooth the luminosity density map with a Gaussian kernel of 125 arcsec. We consider the weak lensing area to be contained within the contour defined by a 0.4 value of the peak in the smoothed map. This corresponds to a mass of about $1 \times 10^{15} M_\odot$ (half the mass of the entire cluster) that is enclosed within this contour.

The normalisation of the Hα LF for all areas within the 'Sausage' cluster is higher by a factor > 15 compared to the fit for a blank field at $z = 0.24$ by Shioya et al. (2008). The field LF parameter fits are expected to be only moderately affected by cosmic variance given the volume probed (3.1×10^4 Mpc^3) and the small correlation length of $r_0 = 1.8 \pm 0.2$ Mpc of the observed Hα emitters at $z = 0.24$, roughly corresponding to emitters residing in typical dark matter halos of $10^{11} M_\odot$ masses (Sobral et al. 2010). There is evidence that the number of emitters within the weak lensing area, which traces the direction of the merger, is enhanced compared to other areas within the cluster. The LF normalisation $\log \phi^*$ in the weak lensing area is -1.07 ± 0.04 compared to an average of -1.37 ± 0.04 near the relics (difference of 5.0σ) and -1.46 ± 0.03 in the region away from the relics (7.8σ), perpendicular to the merger axis. This fully confirms the results from Stroe et al. (2014a), where, even if a conservative, low fraction of Hα emitters was considered, an enhancement in the $\log \phi^* = -1.77$ around the relics area was observed by comparison to field galaxies ($\log \phi^* = -2.65$).

These very high numbers of Hα galaxies within the densest parts of the 'Sausage' cluster
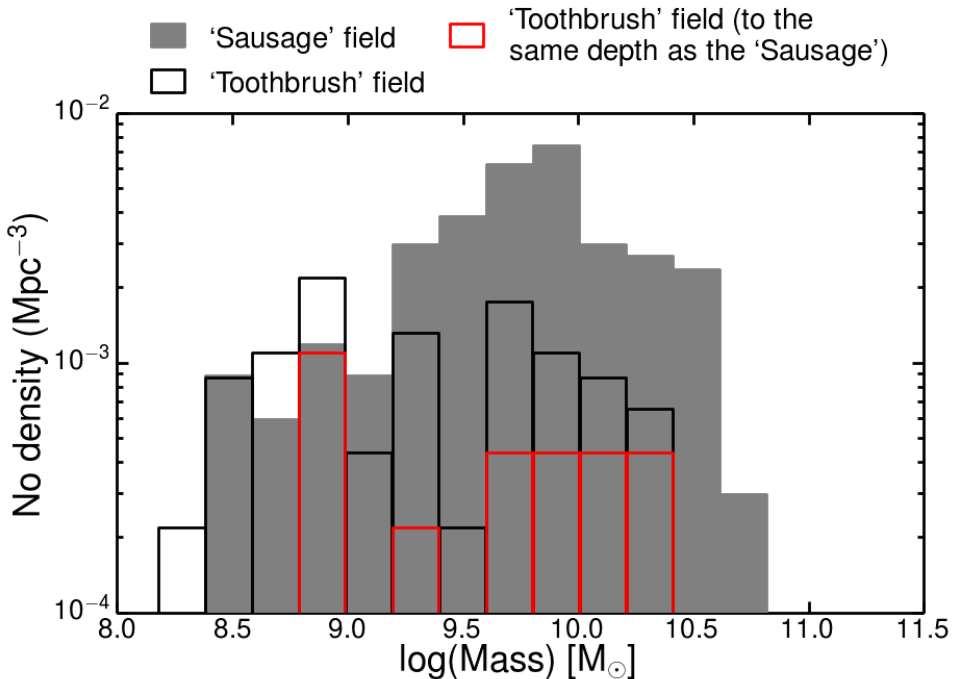
Figure 7.9: Mass distribution of Hα emitters in the fields of the two clusters, normalised to the volume of each respective survey. Note than even though the 'Toothbrush' data probes to Hα fluxes fainter by a factor of 8 compared to the 'Sausage', the 'Toothbrush' cluster is almost devoid of massive star-forming galaxies.

are surprising, given the number of studies showing that the fraction of star-forming galaxies drops steeply towards the cluster core. Even in the case of medium redshift clusters such as the $z = 0.81$ RXJ1716.4+6708 cluster, Koyama et al. (2010) have found that the fraction of Hα emitters drops steeply towards the regions of highest density, down to values of just 10% of the total population. The authors use a similar method to ours: a narrow-band Hα selection technique to identify star forming galaxies. A different trend is found at higher redshifts, in dynamically young clusters. For example, Hayashi et al. (2011) have found that at $z \sim 1.5$, the centre of a dynamically young cluster is still full of star-forming galaxies and AGN. Therefore, the 'Sausage' cluster presents features very similar to a young cluster at the time where the progenitors of the most massive clusters have started forming.

Note that we calculate the volume by taking the entire redshift slice captured by the NB filter. The volume occupied by the cluster which, given its projected dimension, is expected to be < 3 Mpc (real-space) across in the redshift direction. If we were to assume the cluster occupies a cylindrical volume, with a circular shape projected onto the sky, the cluster volume would be a maximum of ~ 32 Mpc^3 (real-space volume). We subtract the typical level of field emitters ($\log \phi^* = -2.65$, as per Shioya et al. 2008) and consider all additional Hα emitters projected on the cluster area to be cluster members. Note that this method assumes that there are field galaxies mixed within the cluster volume, but this is not expected to make a big
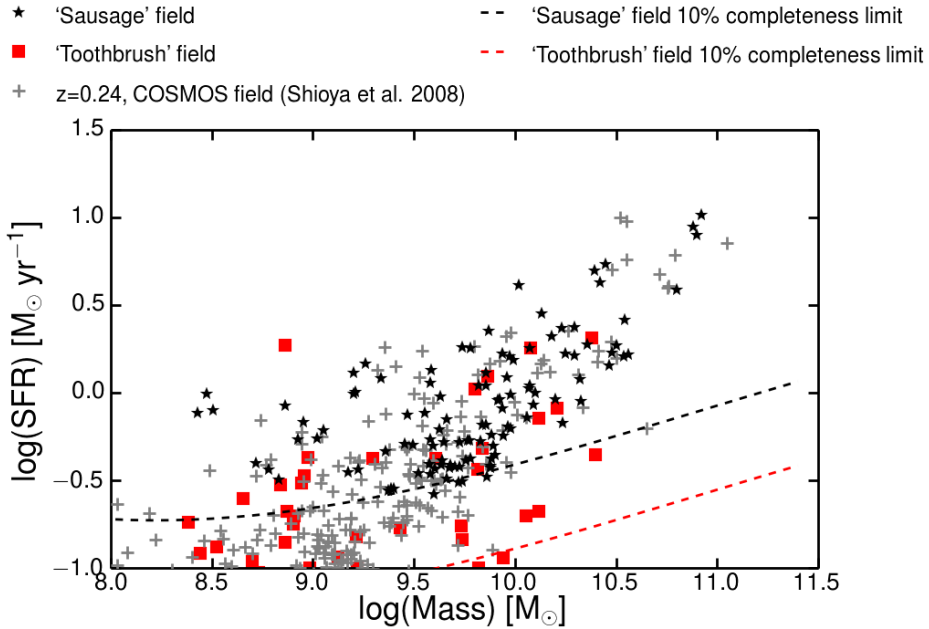
Figure 7.10: Star-formation rate as function of stellar mass for the two clusters and the blank field (Shioya et al. 2008), using a Chabrier IMF. The Shioya et al. (2008) results for the COSMOS field were corrected for the different aperture sizes. The average 10% completeness line for the 'Sausage' and 'Toothbrush' surveys is shown in the dashed lines. The SFR-mass relation holds for both the blank field and the two clusters. Note the overdensity of high-mass, high-SFR galaxies within the 'Sausage' cluster, which surveys a volume ~ 10 times smaller than the COSMOS field. This point is illustrated further in Figs. 7.13 and 7.14.

difference in the final numbers. This exercise leads to an enhancement by ~ 1.5 dex (a factor of 30) compared to the $\log \phi^*$ calculated in Table 7.5 (0.10 versus -1.27). If the background level of field Hα galaxies is not subtracted $\log \phi^*$ is 0.12. The same enhancement would be seen in all areas if the volume was adjusted.

Even more so, there are a high number of spectroscopically confirmed Hα cluster members close to the relics and along the merger axis. Within the entire cluster encompassed by the large circle there are 30 confirmed cluster members, compared to 59 sources in total. This means that even if we build an Hα LF using the spectroscopically confirmed members and a cluster volume of ~ 32 Mpc^3, $\log \phi^*$ is -0.18, significantly above the field where $\log \phi^* = -2.65$. The difference lies at $> 8\sigma$ significance.

We also detect a mild boost in the characteristic luminosity $\log L^*$ of the cluster galaxies located in proximity of the relics compared to the field (41.69 ± 0.09 versus $41.57^{+0.38}_{-0.23}$). By contrast, the population located away from the shocks seems to have lower luminosities on average, pointing towards a quenching of luminous Hα emitters in that direction. The difference between the Hα emitters located around the relics and away from the relics is at the level of at least 3σ. Hα luminosity scales with SFR, which means the 'Sausage' relic emit-
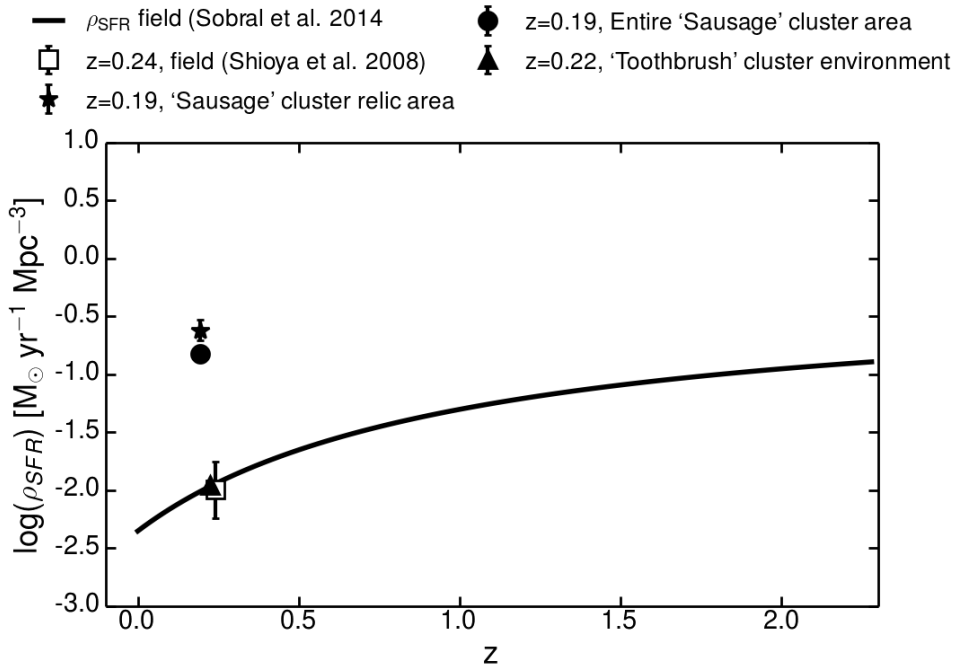
Figure 7.11: ρ_{SFR} for the 'Sausage' and 'Toothbrush' fields plotted over the Hα parametrisation of the ρ_{SFR} history from Sobral et al. (2013a), corrected for a Chabrier IMF. The entire volume spanned by the NB filter is considered. Note that ρ_{SFR} for the 'Sausage' cluster relic area is at the level of $z \sim 2.3$ field galaxies. By contrast the 'Toothbrush' cluster environment is at the level of $z \sim 0.2$ field galaxies. The 'Toothbrush' behaves more like one would expect for a cluster, where the fraction of Hα galaxies steeply drops towards the cluster core. Error bars are plotted, but sometimes they are smaller than the symbol.

ters are slightly more star-forming than field galaxies at the same redshift and cluster galaxies located away from the shock fronts. Balogh et al. (1998) found, from comparing a sample of field star-forming galaxies with galaxies in X-ray luminous, $0.18 < z < 0.55$ clusters, that the dense cluster environment suppresses the star-formation rate of galaxies. This is consistent with the galaxies located away from the shock fronts, which have average SFR 1 $M_{\odot}$ yr^{-1}, compared to 2 $M_{\odot}$ yr^{-1} for the Hα emitters located close to the radio relics.

Comparison with other clusters is challenging, because there are only a few studies that use a uniform NB, Hα selection method. Umeda et al. (2004) derive Hα luminosity functions for the merging cluster Abell 521, assuming that all the Hα emitters captured by their filter are encompassed in a spherical volume of radius 2 Mpc (with a volume of 33.5 Mpc^4). The volume is therefore comparable to our method. The LF normalisation obtained by Umeda et al. (2004) is -0.25 ± 0.20 compared to our estimation of 0.12. Note that the authors do not subtract a background level of field galaxies, which would make the difference between the two results more significant. The typical log10 luminosity of Abell 521 is 41.73 ± 0.17, which is consistent with the values obtained for the 'Sausage' cluster relic areas. Note that the

luminosity distance depends on the chosen cosmology and affects the derived Hα luminosity, when converting from Hα flux. To correct for this, we correct for the different cosmology used by the other authors.

Iglesias-Páramo et al. (2002) derived LFs for the local cluster Abell 1367 and Coma, which have also have a lower $\log \phi^*$ of $0.06^{+0.14}_{-0.12}$ and $-0.07^{+0.03}_{-0.02}$, estimated in the same way as Umeda et al. (2004). The typical luminosities are $\log L^* = 41.00^{+0.07}_{-0.09}$ and $\log L^* = 40.97^{+0.01}_{-0.02}$, which are much lower than the overall cluster and sub-areas ($\log L^* = 41.33 - 41.72$), at the level of $5.0 - 8.0\sigma$.

Abell 1367 is a relatively cold, but dynamically active cluster with temperature averages for its two subclusters of 4.2 ± 0.3 keV and 3.2 ± 0.01 keV (using Advanced Satellite for Cosmology and Astrophysics data Donnelly et al. 1998). Coma is a dynamically more evolved cluster with a low spiral fraction of ~ 13 per cent (Bahcall 1977) and an average temperature of 7.9 ± 0.03 keV (Mushotzky & Smith 1980). By contrast, in the 'Sausage' cluster the numerous emitters along the merger axis are located within areas of extremely hot ICM. As shown in Ogrean et al. (2013a), the cluster temperatures along the merger axis are higher than 9 keV, reaching 13 keV. The enhanced numbers of SF galaxies seems to indicate that there is an inversion of the environmental trends in the 'Sausage' cluster. Typically, the interaction with the hot ICM should quench the SF by removing gas from the galaxies, while the 'Sausage', a dynamically active cluster, has a very high fraction of star-forming galaxies.

'Toothbrush' Hα luminosity function

In the case of the 'Toothbrush', because of a lack of emitters within the cluster potential, we could not separate the cluster in multiple areas. There are no emitters in the region close to the northern relic and a few (9) close to the southern relic, with 3 emitters towards the right side of the cluster, away from the relic areas. Compared to the blank field around the cluster there is an under-density of emitters within the cluster. The few Hα emitters within the cluster region, between and around the relics are clumped together close to the southern relic. To gain enough statistics, we produce an Hα LF only for the cluster environment encompassed by a large circular aperture of ~ 2.2 Mpc radius, chosen to reflect the locations of the X-ray peak and the radio relics. A very preliminary weak lensing analysis of the cluster (James Jee, private communication), coupled with the X-ray temperature of this cluster (Ogrean et al. 2013b), indicates the 'Toothbrush' cluster is similarly massive to the 'Sausage' cluster, suggesting a similar or slightly larger radial extent of $r_{200} > 2.6$ Mpc. The four spectroscopically confirmed Hα emitters are located towards the south-west of the cluster.

The number density of emitters is typical of what is measured for the COSMOS field (Shioya et al. 2008). Over comparable volumes and down to the same Hα flux, the 'Toothbrush' field of view has only about ~ 12 per cent of the number of Hα galaxies hosted by the 'Sausage'. Within the cluster volumes, down to the same Hα flux, the 'Toothbrush' cluster contains only 9 emitters compared to 59 in the 'Sausage'. In the case of the 'Toothbrush', there is evidence for a suppression of Hα emission at high luminosities, as indicated by the lower value of the specific luminosity $\log L^*$ compared to the field (40.75 vs 41.57). Nevertheless, because of low number statistics, the error in the 'Toothbrush' $\log L^*$ measurement is high. The suppression of bright Hα emission is consistent with the dense, hot environment in which galaxies are residing. X-ray observations of the 'Toothbrush' cluster from Ogrean
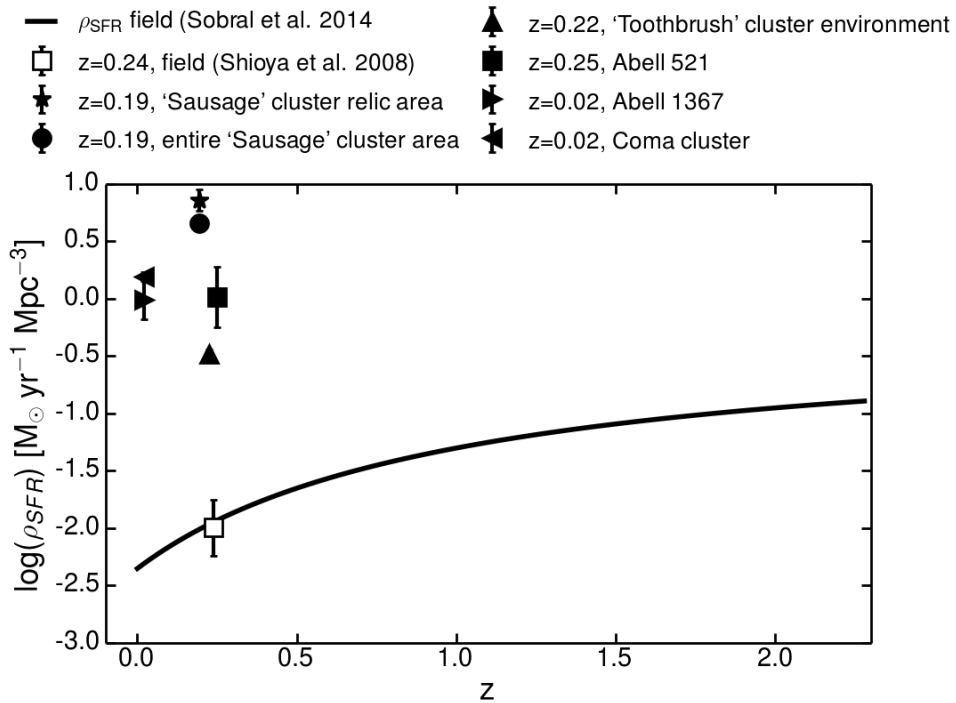
Figure 7.12: ρ_{SFR} for the 'Sausage' and 'Toothbrush' clusters, plotted over the parametrisation of the ρ_{SFR} history from Sobral et al. (2013a) (corrected for a Chabrier IMF) together with Abell 521, 1367 and the Coma cluster. We correct for the cluster volume.

et al. (2013b) indicate that the cluster, while highly disturbed in its temperature structure, has temperatures towards the southern part of the cluster ranging between $6 - 8$ keV.

Following the procedure described in Section 7.4.1, we subtract the background level of field emitters and assume all other Hα emitters located in projection in the cluster area are actually cluster members and we adjust the volume as we did in Section 7.4.1 (the cluster volume is ~ 46 Mpc^3), pushing the LF normalisation to a value of $\log L^* = -0.41$.

7.4.2 Star formation rate density for the two clusters

The ρ_{SFR} values for the 'Sausage' relic area and the entire cluster area are significantly above what is expected for galaxies at redshift 0.2 (Fig. 7.11). Note that these values are obtained if one uses the entire redshift span of the filter, hence using co-moving volumes. The emitters in the cluster and the relic area behave on average like typical blank field galaxies at $z \sim 2.3$.

If we correct for the limited real-space volume the cluster is expected to occupy (as shown in Section 7.4.1), ρ_{SFR} for the cluster is $6.9~M_\odot$ yr^{-1} Mpc^{-3}, more than 15 times the level of typical galaxies located at the peak of the SFR history (Fig. 7.12). Note that here we calculate the SFR for the cluster volume using real-space volumes, while the volume for the blank fields are calculated using co-moving volumes. If we use only the spectroscopically confirmed galaxies, ρ_{SFR} is at least at the level 7 times the peak of the SFR. Note, however,
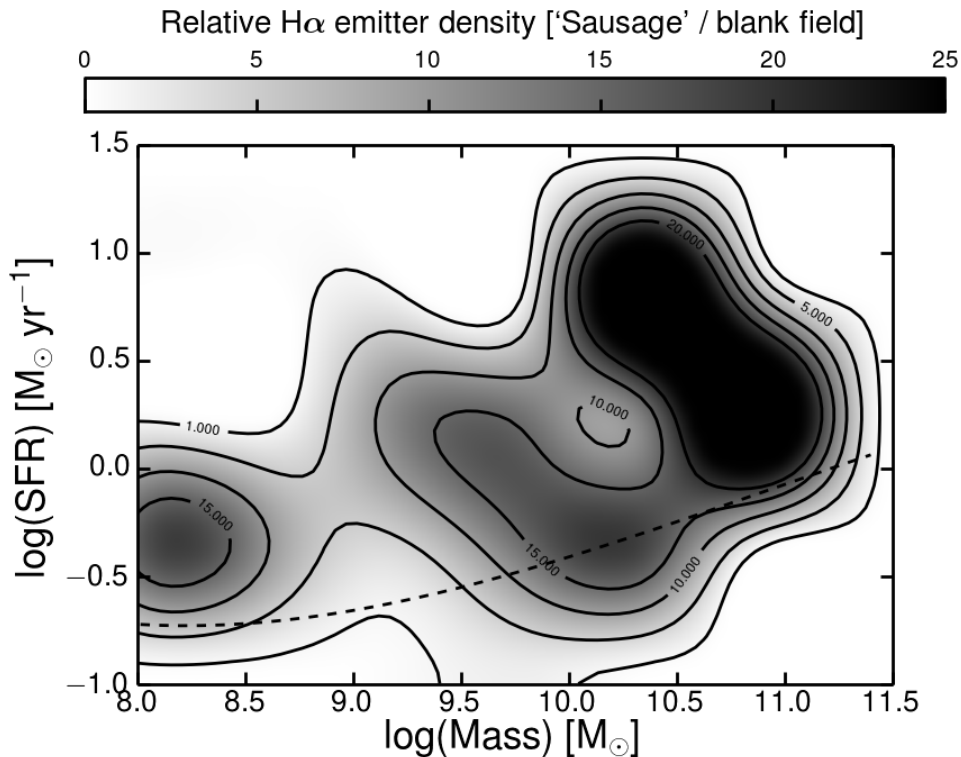
Figure 7.13: Relative density of Hα emitters of the 'Sausage' field compared to a blank field from Shioya et al. (2008), plotted in the stellar mass - star-formation rate plane. The 10% completeness in the SFR measurements is plotted in the dashed line. The 'Sausage' field has a higher density of Hα emitters at all SFRs and stellar masses, as compared to a blank field. The 'Sausage' cluster contains up to $15-20$ times more highly star-forming, high-mass galaxies than a blank field.

that the volume is small and the stellar mass density added is therefore very little, equivalent to adding until z 0.2 just on galaxy with a stellar mass of about $4.5 \times 10^{10} M_\odot$ (see also Section 7.4.4).

By contrast, the lower LF normalisation and specific Hα luminosity in the 'Toothbrush' cluster drive ρ_{SFR} to very low values, consistent with $z = 0.2$ blank field galaxies.

7.4.3 Stellar masses of cluster galaxies

The cluster galaxies ($10^{8-10.5}$ $M_\odot$) fall on the mass-SFR relation (see Fig. 7.10). Therefore, even though an exceptionally high-fraction of galaxies are star-forming, given they are located in a cluster, they have SFR typical for their mass. This is in agreement with Koyama et al. (2013) that study the star forming properties of the cluster Cl0939+4713 at $z = 0.4$. Nevertheless, the distribution of Hα galaxies within the mass-SFR relation is strikingly different from the field. To quantify the distribution of Hα galaxies in our two clusters in the stellar
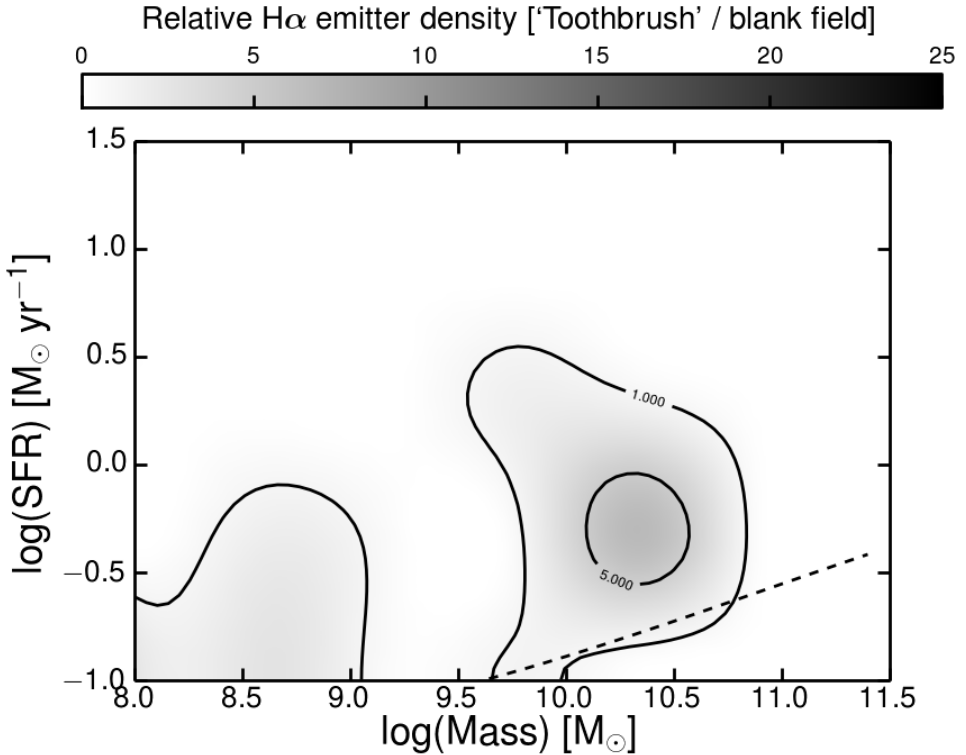
Figure 7.14: Relative density of Hα emitters of the 'Toothbrush' field compared to a blank field from Shioya et al. (2008), plotted in the stellar mass - star-formation rate plane. The 10% completeness in the SFR measurements is plotted in the dashed line. Note the stark difference with the 'Sausage' field. The 'Toothbrush' field contains a lower or similar number of emitters as compared to blank fields at all masses and SFRs. The slight enhancement up to a factor of 5 can be explained by Poissonian errors or cosmic variations. The 'Toothbrush' not only follows the SFR-mass relation, but also has the same density of Hα emitters as blank fields in each part of the relation.

mass-SFR plane, we compare with the results from Shioya et al. (2008), obtained over volumes ∼ 10 times larger than the survey of the 'Sausage' and 'Toothbrush' clusters. We bin the Hα emitters in mass and SFR and divide the 2D histogram by the different volumes probed by the three surveys. This ensures we obtain comparable results for the clusters and the blank field. We then divide the normalised mass-SFR distribution of emitters for the clusters by the normalised Hα distribution for the COSMOS blank field. The bicubicly-interpolated results for the 'Sausage' and the 'Toothbrush' fields can be visualised in Figs. 7.13 and 7.14, respectively. The 'Sausage' field contains elevated numbers of Hα emitters at all masses and SFRs. The cluster is exceptionally abundant in high-mass ($> 10^{10} M_\odot$), highly-star forming ($1 - 10 M_\odot$ yr^{-1}) galaxies. The 'Sausage' has a density of Hα emitters $20 - 25$ times higher than a blank field. Note that towards low SFRs, our results suffer from incompleteness so the relative abundance of Hα emitters is underestimated. In conclusion, the enhancement in the

'Sausage' Hα emitter density is seen at all masses, but particularly at the high masses. The 'Toothbrush' field Hα emitters density is consistent with results obtained from blank fields, with mild over-densities of relatively high-mass, low SFRs Hα emitters ($\sim 10^{10} M_\odot$, $\sim 0.3 M_\odot$ yr^{-1}). However, this enhancement in one mass-SFR bin could easily be explained by Poissonian errors and/or cosmic variance.

7.4.4   Cause for enhanced star formation in the 'Sausage' cluster

Both the 'Sausage' and the 'Toothbrush' clusters have undergone mergers that induced travelling shock waves to propagate through the ICM and accelerate ICM electrons to relativistic speeds. In the case of the 'Sausage' cluster, a binary merger lead to the formation of two unequal relics along the merger axis (van Weeren et al. 2011b). The northern relic has a stronger Mach number than the southern one by a factor of ~ 2 (Stroe et al. 2013). In the 'Toothbrush' cluster, simulations and X-ray data indicate a more complicated merger scenario with a main binary merger, possibly followed by a smaller mass interloper participating in the merger towards the end (Brüggen et al. 2012; Ogrean et al. 2013b). The northern relic is also larger than the relic located towards the south-east side of the cluster. Simulations indicate that the 'Toothbrush' could also be a more advanced merger than the 'sausage' with a core passage time of the main sub-clusters happening ~ 2 Gyr ago, compared to $\sim 0.5 - 1$ Gyr ago for the 'Sausage' (van Weeren et al. 2011b; Brüggen et al. 2012).

Through our Hα observations we discover and confirm numerous star-forming galaxies nearby the relics in the 'Sausage' cluster and along the merger axis. Also in the 'Toothbrush' cluster there is a clump of star-forming galaxies in the vicinity of the southern shock. The concentration of emitters close to the southern relic in the 'Toothbrush' shows that the shock front might have passed through a group of gas-rich galaxies. There is indication that the cluster is a more complicated merger with a third smaller cluster responsible for the straight northern relics and that could also cause the formation of the southern relic, at a later stage than the northern one. If this smaller sub-clump was a low-mass group and still contained numerous gas-rich galaxies that could explain why there is a striking difference between the galaxy populations towards the northern and the southern relic in the 'Toothbrush' cluster.

Another point to note is that the distribution of Hα emitters around the clusters is very different. The environment of the 'Toothbrush' cluster is at the level expected for the field, while the 'Sausage' clusters seems to be embedded in a more SFR-rich region with filamentary Hα structures.

The gravitationally decoupled shock travels ahead of the ICM gas, dark matter and galaxies and therefore could have interacted with these components at some point since the sub-clusters merged. In terms of its interaction with galaxies, a shock wave will heat any available intra-galactic gas and increase turbulence and induce instabilities in the gas. The gas can then collapse into clouds which are dense enough to start forming stars. The scenario was proposed by Rees (1989) for high redshift galaxies where the powerful radio jet was suggested to induce star-formation along its propagation axis. Radio jets with high Mach numbers ($M \sim 10 - 100$) at their terminating shocks have too much power and entrain the low-entropy gas away from the galaxy uplifting it in buoyant bubbles (e.g. Werner et al. 2010). Werner et al. (2010) found Hα filaments in the immediate downstream area from the jet-termination shock front in M87. Crockett et al. (2012) and Hamer et al. (2014) found evidence for shock-induced shells

around star-forming clumps. The locations of these shells along the optical filaments connecting the two radio jets in the Centaurus A galaxy is consistent with material being swept along the back flow of the jet and ionised through shocks. In the case of the high-redshift galaxy 4C+41.17, Steinbring (2014) confirmed the presence of a bow-shock structure inducing star-formation near the core of the galaxy. In the context of interacting galaxies, smooth particle hydrodynamical simulations by Barnes (2004) show that a shock-induced star-formation prescription fits very well observations of NGC 4676. Saitoh et al. (2009) similarly found in their simulations a vigorous, shock-induced starburst event at the interface of two colliding disk galaxies. By contrast to radio-jet terminating shocks, the merger shocks in the 'Sausage' and the 'Toothbrush' cluster have Mach numbers of at most 4. Ogrean et al. (2014a) have shown using Chandra data that minor shock fronts are ubiquitous within the ICM of the 'Sausage' cluster.

We speculate that low Mach number, extended shocks might have a higher chance of not removing the gas from the galaxy, but increasing the turbulence. We suggest that there is a tight correlation between the strength of the shock and the ultimate fate of the gas. If the shock is too strong then the gas can be stripped from the host galaxy in the same fashion as it happens when a galaxy is infalling into the cluster potential with relative speeds of $1000 - 2000$ km s^{-1}. For example, there is evidence that the galaxies in the 'Sausage' cluster are moving along the merger axis, following the merger direction (Stroe et al. 2013). Given the speed at which the collissionless shock front travels with respect to the ICM (~ 2500 km s^{-1}, Stroe et al. 2014c) and the relative collision speed (~ 2250 km s^{-1}, Dawson et al. in preparation), the galaxies seem to be trailing behind the shock front, but are ahead of the ICM, indicating they are possibly moving at a speed of $500 - 2000$ km s^{-1} with respect to the ICM gas. This is comparable or lower than the speeds reached by galaxies infalling into the cluster via accretion. Note that there is a velocity dispersion of ~ 1000 km s^{-1}, so some galaxies will be going much faster/slower relative to the shock.

The shock-induced SF interpretation is in line with simulations by Roediger et al. (2014). They show that star formation lasting for up to a few 100 Myr can happen with a delay of ~ 10 Myr after a passage of the shock. The newly-born stars build up with a tail trailing the shock direction. Multiple episodes of SF can happen after the passage of the shock and therefore a gradient of ages within these tails or between galaxies located at different distance from the shock is not necessarily expected. Given the delayed start of SF, our Hα selection might miss the galaxies very close to the shock fronts, where the star-formation might not have started yet.

A requirement for the shock and merger to increase the SFR is that the galaxies within the sub-clusters are still relatively gas rich. The Hα emitters in the 'Sausage' cluster are relatively massive (significant numbers of star-forming galaxies with stellar masses over 10^{10} $M_\odot$, see Fig. 7.9). The shock is expected to traverse a galaxy within a very short timescale of about $10 - 50$ Myr. Hence the shock quickly induces turbulence in the gas, after which the gas cools and collapses. The high rate of SF following the shock passage can quickly deplete the gas reservoir. Part of the gas fuels SF, while the rest, is removed from the galaxy through strong outflows. A fraction of the gas located towards the outer disk of the galaxy could be easily stripped by the shock. We therefore expect the passage of the shock to lead to a steep rise in SF for $10 - 100$ Myr, followed by a quick quenching of the galaxy and a shut-down in the formation of new stars.

As shown in Sobral et al (in prep), there is evidence for strong outflows in some of the 'Sausage' cluster galaxies with asymmetric and P-cygni profiles in the Hα, [N$\textsc{ii}$] and [S$\textsc{ii}$] lines and broad components for the [N$\textsc{ii}$] and [S$\textsc{ii}$] forbidden lines. This suggests that even though galaxies are highly star-forming as we observe them, they will quickly evolve into gas-poor galaxies. Given the galaxies reside in a very massive cluster, any outflowing material will easily escape the host galaxy. The high mass-loss rate caused by these outflows leads to a quick depletion of the gas reservoir effectively shutting down star-formation. Hence, the outflows indicate that Hα galaxies will be transformed into passive galaxies within a short time scale. We can make an estimate of the rate at which this can happen by comparing the two clusters. The 'Toothbrush' cluster hosts about 60 per cent (34) fewer Hα galaxies than the 'Sausage' cluster. If the time since core passage is 2 Gyr for the 'Toothbrush' compared to 1 Gyr for the 'Sausage' cluster, SF in these galaxies is being shut-down at a rate of 34 galaxies per Gyr, or one galaxy every $\sim$ 30 Myr. If no additional accretion of fresh matter happens, the 'Toothbrush' will have a complete shut-down of star formation within 1 Gyr of when we observe it. 'Right now', the 'Toothbrush' galaxy population is fully passively-evolving. For the 'Sausage', the process of star-formation shut down will take another 2 Gyr. Given that the stellar mass of the 'Sausage' galaxies is $10^{8-10.5}$ $M_\odot$, and assuming a molecular gas M_{gas} to gas plus stellar mass $M_{\mathrm{gas}} + M_\star$ ratio of 0.1 (Young & Scoville 1991), our galaxies have about $10^{7-9.5}$ $M_\odot$ molecular gas. The molecular gas has two possible fates: it either contributes to star-formation or it is removed from the host galaxy, either via outflows or ram pressure stripping. The characteristic Hα luminosity of the 'Sausage' galaxies of $10^{41.6}$ erg s^{-1} is equivalent to a rate of $\sim$ 3 $M_\odot$ yr^{-1} of molecular gas being converted into new stars. If all the molecular gas is consumed through SF, the low mass galaxies would use up their molecular gas within 1 Myr, while the galaxies located at the high mass end would require 1 Gyr. Assuming a maximal mass loss through outflows equal to the rate of conversion to SF, star formation in the 'Sausage' galaxies would last up to 0.5 Gyr.

Another calculation we can make using the difference of age between the clusters is the quantity of stellar mass being added to the cluster volume. We assume that the two clusters are relatively similar in their properties apart from the 'Toothbrush' being an older merger compare to the 'Sausage'. In this scenario, the 'Toothbrush' represents a "look into the future" of a 'Sausage'-like cluster in 0.5 Gyr. The 'Sausage' cluster ρ_{SFR} is $\sim$ 6.9 $M_\odot$ yr^{-1} Mpc^{-3} (corrected for the volume occupied by the cluster), while the 'Toothbrush' is only $\sim$ 0.3 $M_\odot$ yr^{-1} Mpc^{-3}, a drop which could happen, given the simulations of the two clusters, over 0.5 Gyr. Within every Mpc^3, a mass of $\sim$ 1.5×10^9 $M_\odot$ of stars would be formed. Given the entire cluster volume is expected to be about 30 Mpc^3, the total stellar mass added to the cluster is $\sim$ 4.5×10^{10} $M_\odot$, less than 3 per cent of the mass of the Milky Way. A similar mass is lost through outflows. Therefore, even though many galaxies within merging clusters can go through episodes of vigorous star-formation, once enough time passes, this will not necessarily reflect in the total mass of passive galaxies.

As an interpretation for our results, we suggest that even in a hot cluster atmosphere, as long as galaxies retain some of their gas content until the passage of the merger shock, it is possible to observe high levels of star formation in a large fraction of cluster galaxies. The influence of shocks seems to supersede the passive evolution of galaxies within the cluster environment and prevent the rapid loss of gas through interactions with the ICM. Rather, the shock favours the retainment of gas within its host galaxy. This is consistent with the find-

ing that the number of high-mass star-forming galaxies is especially boosted in the 'Sausage' cluster. High stellar-mass galaxies reside in massive dark matter haloes with a strong gravitational pull capable of holding the gas. Shocks probably induce instabilities in the gas which collapses into star-forming clouds and also increase AGN activity that produces large mass outflows. Therefore, while momentarily the galaxies close to the shock front will exhibit high levels of Hα emission, the fast consumption of their gas will lead to an accelerated evolution from gas-rich to gas-poor ellipticals or S0s, compared to other cluster galaxies allowed to passively evolve.

7.5 Conclusions

We conducted an Hα survey of two post-core passage, merging clusters which host Mpc-wide travelling shock waves (the 'Sausage' and the 'toothbrush clusters). Using optical broad and narrow band data and spectroscopy, we are able to draw a number of conclusions.

- We robustly select line emitters towards the two clusters using custom-made narrow-band filters. Down to a similar equivalent width, but different luminosity limits, we select 201 and 463 line emitters towards the 'Sausage' and the 'Toothbrush' field of view, respectively. We separate between Hα emitters at the cluster redshift and other higher-redshift emitters using colour-colour diagnostics, photometric and spectroscopic data.

- Based on photometric redshifts, the emitter population for the 'Sausage' cluster is clearly dominated by Hα emitters with a fraction of 62 per cent, 52.5 per cent of which are confirmed by spectroscopy. The bulk of the emitters are located in the cluster.

- In the case of the 'Toothbrush', 89 per cent of the emitters are not Hα. The bulk of the Hα emitters are located in the field environment around the cluster.

- We find a clear enhancement in the number density of Hα emitters in the 'Sausage' compared to a blank field $\log \phi^*$ (-1.37 ± 0.04 versus $-2.65^{+0.27}_{-0.38}$), pointing towards a very high fraction of the cluster population being star-forming. This is a highly surprising result given the high X-ray temperature of the ICM ($9 - 13$ keV). The results also hold if we look only at emitters around the shock fronts or within the cluster volume (as defined from weak lensing data). The star-formation rate density for the cluster is at the order of 15 times the peak of the star-formation history of the Universe. The average star-formation rate of galaxies along the merger axis is higher than away from the shock fronts. The cluster has a density of high-mass, highly star-forming galaxies $20 - 25$ higher than blank fields.

- The normalisation $\log \phi^*$ of the Hα luminosity function in the 'Toothbrush' cluster is -1.76 ± 0.02, compared to $-2.65^{+0.27}_{-0.38}$ for a blank field. Owing to a specific luminosity $\log L^* = 40.75 \pm 0.01$ in the cluster lower than the field ($41.57^{0.38}_{-0.23}$), the 'Toothbrush' overall star-formation rate density is consistent with blank fields at $z = 0.2$.

- We find that the relation between the SFR and stellar mass for the two clusters is very similar to that of blank fields. However, the density of Hα emitters in the 'Sausage'

cluster is boosted compared to the field, especially in the high mass, high SFR regime, where the cluster is $20 - 25$ times denser than the COSMOS field.

- Accounting for the different ages of the two clusters, we measure a rate of 1 star-forming galaxy being transformed into a non-star forming galaxy every ~ 30 Myr to transform a star-formation rich, 'Sausage'-like cluster into a 'Toothbrush'-like cluster devoid of star-forming galaxies.

- We interpret our results as shock-induced star-formation. In line with simulations and other observational results, the merger and shock waves lead to a momentary increase in star-formation in gas rich galaxies. This is turn accelerates the turn-off of star-formation owing to a rapid consumption of the molecular gas supply. This effects seems to be happening at all masses and star-formation rates, but predominantly in the high-mass regime.

Acknowledgements

Table 7.6: Sample catalogue of line emitters in the 'Sausage' field. The first two rows indicate the coordinates of the sources, the FLUX column is the total line flux of each source. The observed equivalent width of the emission line can be found in the penultimate column. The last column indicate whether the line emitter is an H*alpha* emitter. The full table of line emitters for both the 'Sausage' and the 'Toothbrush' can be found on the online version of the paper.

RA	DE	FLUX	EW	Hα?
(deg)	(deg)	(erg s^{-1} cm^{-2})	(Å)	
340.595947	52.825943	5.54×10^{-16}	21.1	No
340.790497	52.826099	5.96×10^{-16}	154.1	No
340.790100	52.827122	1.01×10^{-15}	46.4	No
340.754944	52.828049	1.29×10^{-16}	70.6	Yes
340.646942	52.828678	5.68×10^{-16}	33.1	Yes

7.6 Appendix
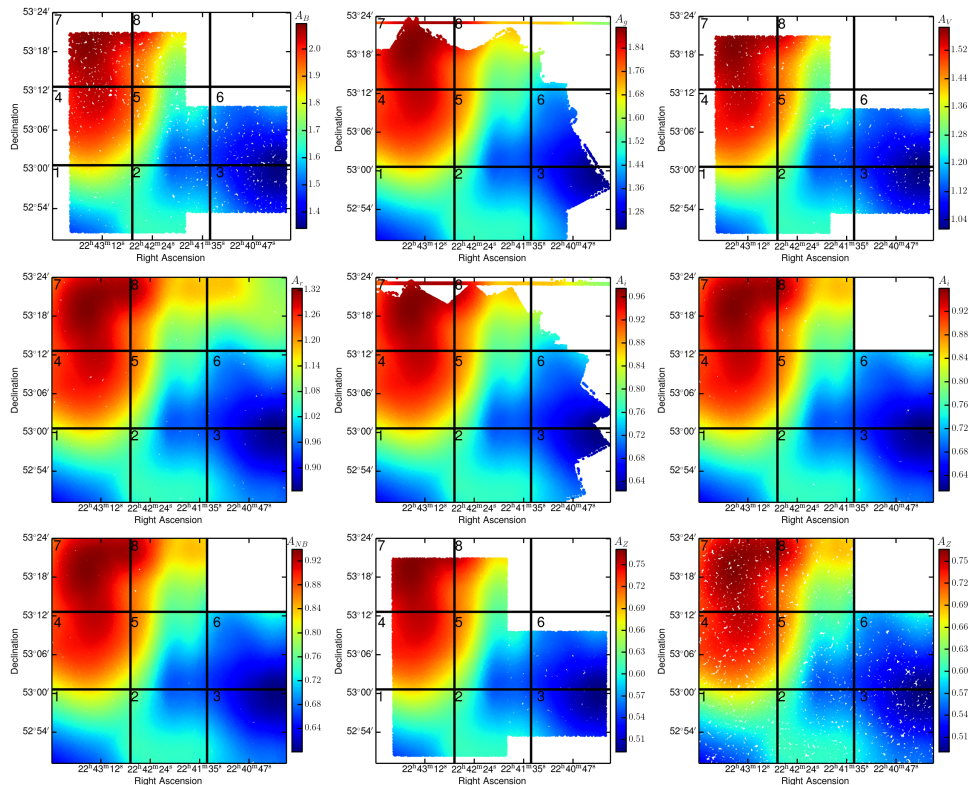
7.6.1 Dust extinction screens

Figure 7.15: 'Dust screens' for the 'Sausage' for the different filters from top-left to bottom right: WHT B, WHT V, Subaru g, CFHT r, Subaru i, INT i, INT NB, WHT z, INT z. The figures are all on the same RA & DEC scale and serve to display the FOV coverage with each camera. The values of the dust attenuation are calculated for each source in the FOV and all sources are plotted as individual points. All filters cover the full extent of the cluster. Note the NB extinction is effectively the same as for the i band filter, as the NB filter is centred close to the central wavelength of the i band filter. The dust extinction, measured in magnitudes, is based on measurements from Schlafly & Finkbeiner (2011). Note the different scales of the figures: the dust extinction and its variation across the FOV increase significantly towards the blue side of the optical spectrum. The dust extinction variations across the FOV lead to differences in depth across the FOV, therefore the FOV has been divided into eight areas for completeness study purposes.
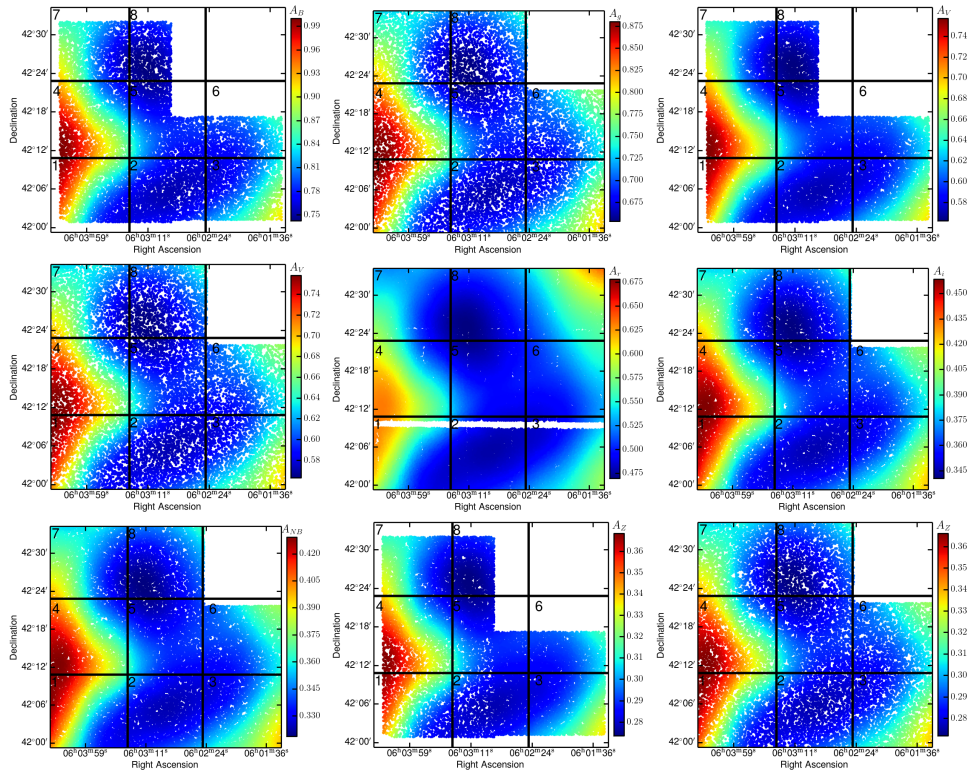
Figure 7.16: The same as Fig. 7.15, but for the 'Toothbrush' field. The figures are in order from top-left to bottom right: WHT B, INT g, WHT V, INT V, CFHT r, INT i, INT NB, WHT z, INT z. Note that because the dust attenuation is plotted for individual sources, the lower source density than the 'Sausage' field is apparent.

8

MC²: Boosted AGN and star-formation activity in CIZA J2242.8+5301, a massive post-merger cluster at z = 0.19

Cluster mergers may play a fundamental role in the formation and evolution of cluster galaxies. Stroe et al. (2014a) revealed unexpected over-densities of candidate Hα emitters near the ~ 1 Mpc-wide shock fronts of the massive ($\sim 2 \times 10^{15}$ M$_\odot$) "Sausage" merging cluster, CIZA J2242.8+5301. We used Keck/DEIMOS and WHT/AF2 to confirm 83 Hα emitters in and around the merging cluster. We find that cluster star-forming galaxies in the hottest X-ray gas and/or in the cluster sub-cores (away from the shock fronts) show high [S$\textsc{ii}$] 6716/[S$\textsc{ii}$] 6761 and high [S$\textsc{ii}$] 6716/Hα, implying very low electron densities ($< 30\times$ lower than all other star-forming galaxies outside the cluster) and significant contribution from supernovae, respectively. All cluster star-forming galaxies near the cluster centre show evidence of significant outflows (blueshifted Na D $\sim 200 - 300$ km s^{-1}), likely driven by supernovae. Strong outflows are also found for the cluster Hα AGN. Hα star-forming galaxies in the merging cluster follow the $z \sim 0$ mass-metallicity relation, showing systematically higher metallicity ($\sim$0.15-0.2 dex) than Hα emitters outside the cluster (projected $R > 2.5$ Mpc). This suggests that the shock front may have triggered remaining metal-rich gas which galaxies were able to retain into forming stars. Our observations show that the merger of impressively massive ($\sim 10^{15}$ M$_\odot$) clusters can provide the conditions for significant star-formation and AGN activity, but, as we witness strong feedback by star-forming galaxies and AGN (and given how massive the merging cluster is), such sources will likely quench in a few 100 Myrs.

8.1 Introduction

Star-forming galaxies have evolved dramatically in the 11 Gyr between $z \sim 2.5$ (the likely peak of the star formation history of the Universe) and the present day (e.g. Madau et al. 1996; Sobral et al. 2009; Karim et al. 2011; Sobral et al. 2014). The co-moving star formation rate density of the Universe has dropped by more than an order of magnitude over this time in all environments (Rodighiero et al. 2011; Karim et al. 2011; Gilbank et al. 2011; Sobral et al. 2013a), and also specifically in clusters (e.g. Kodama et al. 2013; Shimakawa et al. 2014). The bulk of this evolution is described by the continuous decrease of the typical star formation rate, SFR^*, which is found to affect the star-forming population at all masses (Sobral et al. 2014). Surprisingly, the decline of SFR^* seems to be happening (for star-forming galaxies) in all environments, at least since $z \sim 2$ (e.g. Koyama et al. 2013).

Locally, star formation activity has been found to be very strongly dependent on environment (e.g. Lewis et al. 2002; Gómez et al. 2003; Tanaka et al. 2004; Mahajan et al. 2010). Clusters of galaxies are dominated by passively-evolving galaxies, while star-forming galaxies are mostly found in low-density/field environments (Dressler 1980). It is also well-established (e.g. Gómez et al. 2003; Kauffmann et al. 2004; Best 2004) that both the typical star formation rates of galaxies and the star-forming fraction decrease with local environmental density both in the local Universe and at moderate redshift ($z \sim 0.4$, e.g. Kodama et al. 2004). This is in line with the results at $z \sim 0.2 - 0.3$ from Couch et al. (2001) or Balogh et al. (2002) who found that the Hα luminosity (an excellent tracer of recent star-formation activity) function in rich, relaxed clusters have the same shape as in the field, but have a much lower normalisation (~ 50 per cent lower), consistent with a significant suppression of star formation in highly dense environments.

The strong positive correlation between star formation rate (SFR) and stellar mass (e.g. Brinchmann et al. 2004; Noeske et al. 2007; Peng et al. 2010), while being a strong function of cosmic time/redshift, seems to depend little on environment (Koyama et al. 2013), even though cluster star-forming galaxies seem to be more massive than field star-forming galaxies. Thus, the fundamental difference between cluster and field environments (regarding their relation with star formation) seems to be primarily the fraction of star-forming galaxies, or the probability of being a star-forming galaxy: it is much lower in cluster environments than in field environments. Studies looking at the mass-metallicity relation with environment also seem to find relatively little difference at $z \sim 1$ (comparing groups and fields; Sobral et al. 2013a), or just a slight offset ($+0.04$ dex) for relaxed cluster galaxies in the Local Universe, as compared to the field (using Sloan Digital Sky Survey, SDSS; Ellison et al. 2009). Further studying the mass-metallicity relation (and the Fundamental Metallicity Relation, FMR, e.g. Maiolino et al. 2008; Mannucci et al. 2010; Stott et al. 2013b) in clusters and comparing to the field could provide further important information.

While there are increasing efforts to try to explain the SFR dependence on the environment, by conducting surveys at high redshift (e.g. Hayashi et al. 2010; Sobral et al. 2011; Matsuda et al. 2011; Muzzin et al. 2012; Koyama et al. 2013; Tal et al. 2014; Darvish et al. 2014), so far such studies have not been able to fully reveal the physical processes leading to the ultimate quenching of (satellite) star-forming galaxies (e.g. Peng et al. 2010; Muzzin et al. 2012, 2014). Several strong processes have been proposed and observed, such as harassment (e.g. Moore et al. 1996), strangulation (e.g. Larson et al. 1980) and ram-pressure stripping

(e.g. Gunn & Gott 1972; Fumagalli et al. 2014). Observations are also showing a variety of blue-shifted rest-frame UV absorption lines which indicate that most star-forming galaxies at least at $z \sim 1 - 2$, are able to drive powerful gas outflows (e.g. Shapley et al. 2003; Weiner et al. 2009; Kornei et al. 2012) which may play a significant role in quenching, particularly if those happen in high density environments. Evidence of such galactic winds have also been seen in e.g. Förster Schreiber et al. (2009) through broad components in the rest-frame optical Hα and [N$_{II}$] emission line profiles (e.g. Genzel et al. 2011). Spatially resolved observations allow for constraints on the origin of the winds within galaxies, and on the spatial extent of the outflowing gas, which are essential to derive mass outflow rates. In field environments, it is expected that such outflows will not be able to escape the halo (as long as it is massive enough and it is not a satellite), and in many conditions would likely come back and further fuel star formation (e.g. Hopkins et al. 2013). However, in the most massive clusters, such strong outflows will likely result in significant amounts of gas being driven out of the sub-halos that host star-forming galaxies, enriching the ICM and quickly quenching star-forming galaxies (SFGs) with the highest SFRs/highest outflow rates.

Many studies often have environmental classes simply divided into (relaxed) "clusters" or "fields". However, in a ΛCDM Universe, most clusters are expected to be the result of group/smaller cluster mergers – some of which can be extremely violent. Little is known about the role of cluster and group mergers in galaxy formation and evolution, and whether they could be important in setting the environmental trends which have now been robustly measured and described. It is particularly important to understand if cluster mergers trigger star formation (e.g. Miller & Owen 2003; Owen et al. 2005; Ferrari et al. 2005; Hwang & Lee 2009; Wegner et al. 2015), if they quench it (e.g. Poggianti et al. 2004), or, alternatively, if they have no direct effect (e.g. Chung et al. 2010). Results from Umeda et al. (2004), studying a merging cluster at $z \sim 0.2$ (Abell 521) found tentative evidence that merging clusters could perhaps trigger star-formation. More recently, Stroe et al. (2014a) conducted a wide field Hα narrow-band survey over two merging clusters with a simple geometry, with the merger happening in the plane of the sky. Stroe et al. (2014a) find a strong boost in the normalisation of the Hα luminosity function of the CIZA J2242.8+5301 ("Sausage") cluster, several times above the field and other clusters. The authors suggest that they may be witnessing star-formation enhancement or triggered due to the passage of the shock wave seen in the radio and X-rays. Interestingly, Stroe et al. (2014a) do not find this effect on the other similar merging cluster studied ("Toothbrush"), likely because it is a significantly older merger (about 1 Gyr older, c.f. Stroe et al. 2014a, 2015), and thus displays only the final result (an excess of post-starburst galaxies instead of Hα emitters). The results are in very good agreement with simulations by Roediger et al. (2014) and recent observational results by Pranger et al. (2014).

In order to investigate the nature of the numerous Hα emitter candidates in and around the "Sausage" merging cluster, we have obtained deep spectroscopic observations of the bulk of the sample presented in Stroe et al. (2015), using Keck/DEIMOS (PI Wittman; Dawson et al. 2015) and the William Herschel Telescope (WHT) AutoFib2+WYFFOS (AF2) instrument (PI: Stroe; this paper). In this paper, we use these data to confirm candidate Hα emitters, unveil their nature, masses, metallicities and other properties. We use a cosmology with $\Omega_\Lambda = 0.7$, $\Omega_m = 0.3$, and $H_0 = 70 \, \mathrm{km \, s^{-1} \, Mpc^{-1}}$. All quoted magnitudes are on the AB system and we use a Chabrier initial mass function (IMF; Chabrier 2003).

8.2 Sample Selection, Observations & Data Reduction

8.2.1 The "Sausage" Merging Cluster

The CIZA J2242.8+5301 cluster (nicknamed "Sausage" cluster, referred simply as Sausage for the rest of the paper; see Figure 8.1) is a $z = 0.1921$, X-ray luminous ($L_{0.1-2.4\text{keV}} = 6.8 \times 10^{44}$ erg s^{-1}; Kocevski et al. 2007), disturbed (Akamatsu & Kawahara 2013; Ogrean et al. 2013a; Ogrean et al. 2014a, Akamatsu et al. 2015) cluster that hosts double radio relics towards its northern and southern outskirts (van Weeren et al. 2010; Stroe et al. 2013, see Figure 8.1). The radio relics (Mpc-wide patches of diffuse radio emission) trace Mpc-wide shock fronts travelling through the intra-cluster medium (see Figure 8.1) thought to have been produced at the core-passage of two massive clusters during major merger in the plane of the sky (van Weeren et al. 2010; Stroe et al. 2013, 2014c,a). Despite being an interesting cluster, the CIZA J2242.8+5301 cluster (Sausage cluster from now on) remained mostly unexplored until very recently, due to significant Galactic extinction (c.f. Stroe et al. 2014a; Jee et al. 2015; Stroe et al. 2015).

Dynamics inferred from spectroscopic observations suggest the two sub-clusters each have masses of $\sim 1.3 - 1.6 \times 10^{15} M_\odot$ (Dawson et al. 2015), in agreement with independent weak lensing analysis which points towards $\sim 1.0 - 1.1 \times 10^{15} M_\odot$ (Jee et al. 2015). The weak lensing (Jee et al. 2015), and the dynamics (Dawson et al. 2015) point towards a total mass of $\approx 2 \times 10^{15}$ M$_\odot$, making it one of the most massive clusters known to date. The virial radius for the total system from weak lensing (Jee et al. 2015) is r$_{200} \sim 2.63$ Mpc..

Dawson et al. (2015) presents a detailed dynamics analysis of the cluster merger. Observations and information from lensing, spectroscopy, broad-band imaging, radio and other constraints imply that the merger likely happened around 0.7±0.2 Gyrs ago (see also Akamatsu et al. 2015, in very good agreement). Clusters were likely travelling at a velocity of $\sim 2000 - 2200$ km s^{-1} towards each other when they merged (Dawson et al. 2015, Akamatsu et al. 2015). This is in excellent agreement with the analysis presented in Stroe et al. (2014c) that shows that the shock wave seems to be moving with a similar speed ($\sim 2000 - 2500$ km s^{-1}). Because the shock does not slow down due to gravitational effects, it can be thought as a proxy of the collisional velocity, further supporting a speed of ~ 2000 km s^{-1} (see also Akamatsu et al. 2015 who find this is also the case from X-rays). We use the detailed information from Dawson et al. (2015), Jee et al. (2015), Akamatsu et al. (2015), Stroe et al. (2015), and references therein, to put our results into context and to explore potential interpretations of the results. The reader is referred to those papers for more information on the cluster itself.

8.2.2 Narrow-band survey and the sample of Hα candidates

By using a custom-designed narrow-band filter ($\lambda = 7839 \pm 55$Å, PI: Sobral) mounted on the Wide Field Camera at the prime-focus of the Isaac Newton Telescope, Stroe et al. (2014a) imaged the Sausage cluster over 0.3 deg^2 and selected 181 potential line emitters, down to a Hα luminosity of $10^{40.8}$ erg s^{-1} (see Stroe et al. 2014a). They discover luminous, extended, tens-of-kpc-wide candidate Hα emitters in the vicinity of the shock fronts, corresponding to a significant boost in the normalisation of the Hα luminosity function, when comparing to not only the field environment (Shioya et al. 2008; Drake et al. 2013), but also to other relaxed and merging clusters (e.g. Umeda et al. 2004).
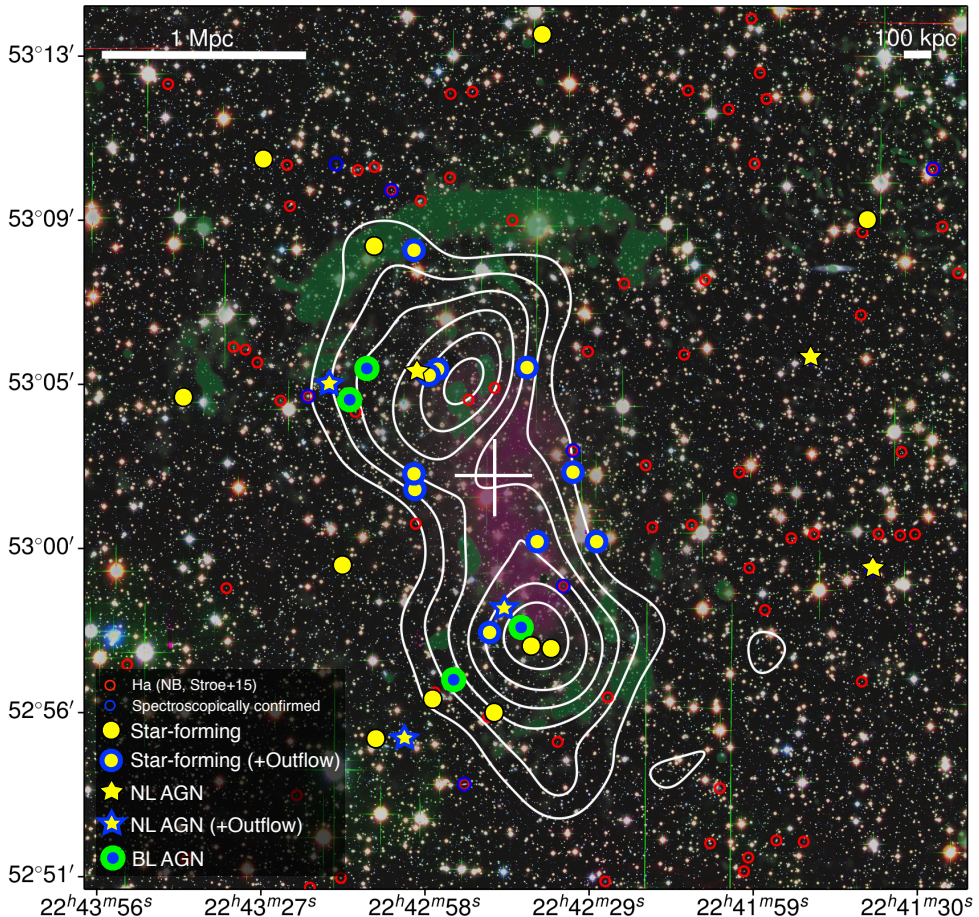
Figure 8.1: The distribution of Hα emitters in the Sausage cluster. The cross marks what we define as the "centre" of the cluster. The background shows a false RGB image from the combination of broad-band images presented in Stroe et al. 2015, while white contours present the weak lensing map (Jee et al. 2015) and in green the 323 MHz radio emission (Stroe et al. 2013). The Hα emitters in our sample reside in a range of different regions, but are found preferably near the shock fronts. Hα emitters also seem to be found just on the outskirts of the hottest X-ray gas – but where the temperatures are still very high (Ogrean et al. 2013a). We also find that all AGN are located relatively close to the post-shock front, but all at a couple of hundred projected kpc away from the radio relics. Note that our sample extends beyond this region, as the field of view of the narrow-band survey, and the spectroscopic follow-up of such sources, cover a larger area (see Stroe et al. 2015). We also show star-forming galaxies showing signatures of outflows, mostly from systematically blue-shifted Na D in absorption from 150 to 300 km^{-1}. Note that 100% of the cluster star-forming galaxies which are closest to the hottest X-ray gas (very close to the "centre" of the cluster), have strong signatures of outflows. Potentially, these are also the sources that, if affected by the shock, may have been the first to be affected, up to ~ 0.7 Gyr ago.

Stroe et al. (2015) presents deeper narrow-band and *i* band imaging, along with new multi-band data (*BVriZ*), and find a total of 201 candidate line emitters. Here we use the full sample of candidate line emitters in and around the Sausage merging cluster, without any pre-selection on the likelihood of them being Hα, along with the corrected broad-band photometry (due to Galactic dust extinction, see Stroe et al. 2015). We take this approach in order to increase the completeness of our Hα sample and avoid any biases (even if small) caused by the need to use broad-band colours and/or photometric redshifts (photo-*z*s). Spectroscopic redshifts obtained here are used in Stroe et al. (2015) to test their selection, improve completeness, and reduce contamination by other emission lines.

8.2.3 Follow-up spectroscopy with Keck and WHT

Keck/DEIMOS observations

We conducted a spectroscopic survey of the Sausage cluster with the DEep Imaging Multi-Object Spectrograph (DEIMOS; Faber et al. 2003) on the Keck II 10 m telescope over two observing runs on 2013 July 14 and 2013 September 5. For full details on the observations and data reduction, see Dawson et al. (2015). Here we provide just a brief summary.

We observed a total of four slit masks with approximately 120 slits per mask. For each mask we took three 900 s exposures, for a total exposure time of 2.7 ks. The average seeing was approximately 0.7″. For both observing runs we used 1″ wide slits with the 1200 line mm^{-1} grating, tilted to a central wavelength of 6700 Å, resulting in a pixel scale of 0.33 Å pixel^{-1}, a resolution of ~ 1 Å (~ 45 km s^{-1}, observed and just below 40 km s^{-1} rest-frame for our cluster Hα emitters), and typical wavelength coverage of 5400 Å to 8000 Å. The actual wavelength coverage is in practice shifted by $\sim \pm 400$ Å depending where the slit is located along the width of the slit-mask. For most cluster members this enabled us to observe Hβ, [OIII]$_{4959\&5007}$, MgI (b), FeI, NaI (D) , [OI], Hα, [NII] and [SII]. We used the DEEP2 version of the SPEC2D package (Newman et al. 2013) to reduce the data. SPEC2D performs wavelength calibration, cosmic ray removal and sky subtraction on slit-by-slit basis, generating a processed two-dimensional spectrum for each slit. The SPEC2D pipeline also generates a processed one-dimensional spectrum for each slit. This extraction creates a one-dimensional spectrum of the target, containing the summed flux at each wavelength in an optimised window.

Our primary DEIMOS targets were candidate red sequence/cluster galaxies and for details on the full sample, the reader is referred to Dawson et al. (2015). Here we focus on the observed 40 Hα emitters within the DEIMOS data-set (see e.g. Figure 8.2), out of which 32 are found to be cluster members (see Dawson et al. 2015). The remaining 8 sources were found to be at slightly higher and slightly lower redshifts, and will be used as part of the comparison sample (Hα emitters outside the cluster, which are either at a different redshift from the cluster, or are at a projected distance higher than 2.5 Mpc from the cluster).

WHT/AF2 observations

We followed up 103 candidate line emitters from Stroe et al. (2015) using AF2 on the WHT in La Palma on two nights during 2014 July 2–3. In order to allocate spare fibres, we used our *BVriZ* photometric catalogue (Stroe et al. 2015) to select other potential cluster candidates (using colour-colour selections; see Stroe et al. 2015). We observed six of these sources. We
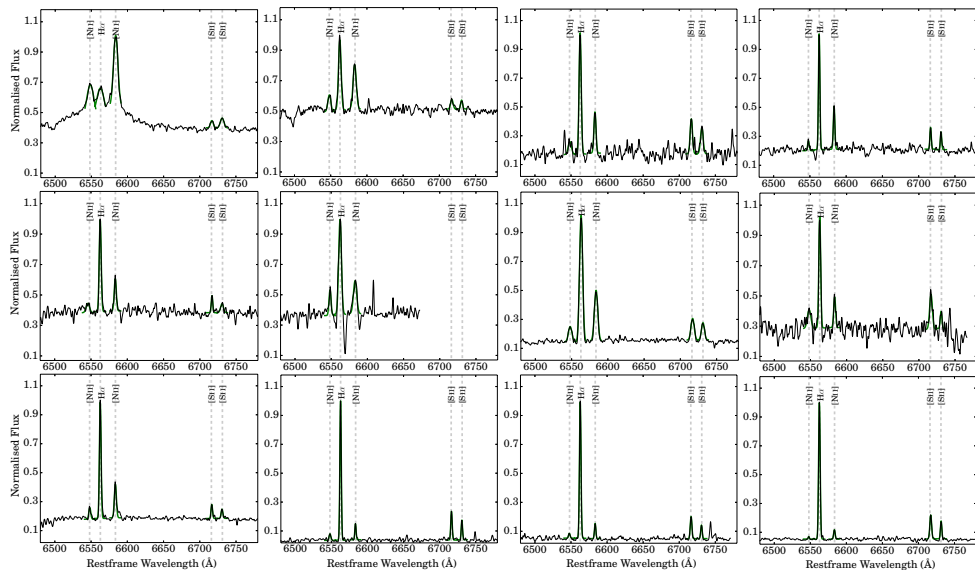
Figure 8.2: Some examples of our Hα emitters from the Keck/DEIMOS data and the Gaussian fits we derived in order to measure emission line ratios. We find a variety of line ratios and FWHMs, but are able to fit all emission lines with simple Gaussian profiles.

found no evidence of emission lines in any of these sources, but have a very high success rate in detecting emission lines for the main sample of emission line candidates.

The seeing was 0.8-1.0″ throughout the observing run. The AF2 instrument on WHT is made of ∼ 150 fibres, each with a diameter of 1.6″, which can be allocated to sources within a ∼ 30 × 30 arcmin² field of view, although with strong spatial constraints/limitations. The spectral coverage varies slightly depending on the fibre and field location, but for a source at $z = 0.19$ all our spectra cover the main emission lines we are interested in: Hβ, [OIII], Hα, [NII] and [SII]. We obtained 2 different pointings: one centred on the cluster, with a total exposure time of 9 ks (where we were able to allocate 63 fibres to targets, and 3 fibres to sky), and one slightly to the North, with a total exposure time of 5.4 ks (46 fibres allocated to targets and 4 to sky). We also obtained some further sky exposures to improve the sky subtraction (2.7 ks per field).

We took standard steps in the reduction of optical multi-fibre spectra, also mimicking the steps followed for DEIMOS. Biases and lamp flats were taken at the beginning of each night. Arcs using neon, helium and mercury lamps were taken on the sky for each fibre configuration. The traces of the fibres on the CCD were curved in the dispersion direction (y axis on the CCD). The lamp flats were used to correct for this distortion. Each fibre shape was fit with a Y pixel coordinate polynomial as function of X coordinate. All CCD pixels were corrected according to the polynomial for the closest fibre. This was done separately for each configuration, on the biases, flats, lamp arcs and the science data.

The final 2D bias subtracted and curvature corrected frames were then sky subtracted using the sky position exposure(s). In order to improve the sky subtraction we also used sky-dedicated fibres (which observe sky in all positions) to scale the counts. We further obtained the best scaling factor by minimising the residuals after sky subtraction. After subtracting the
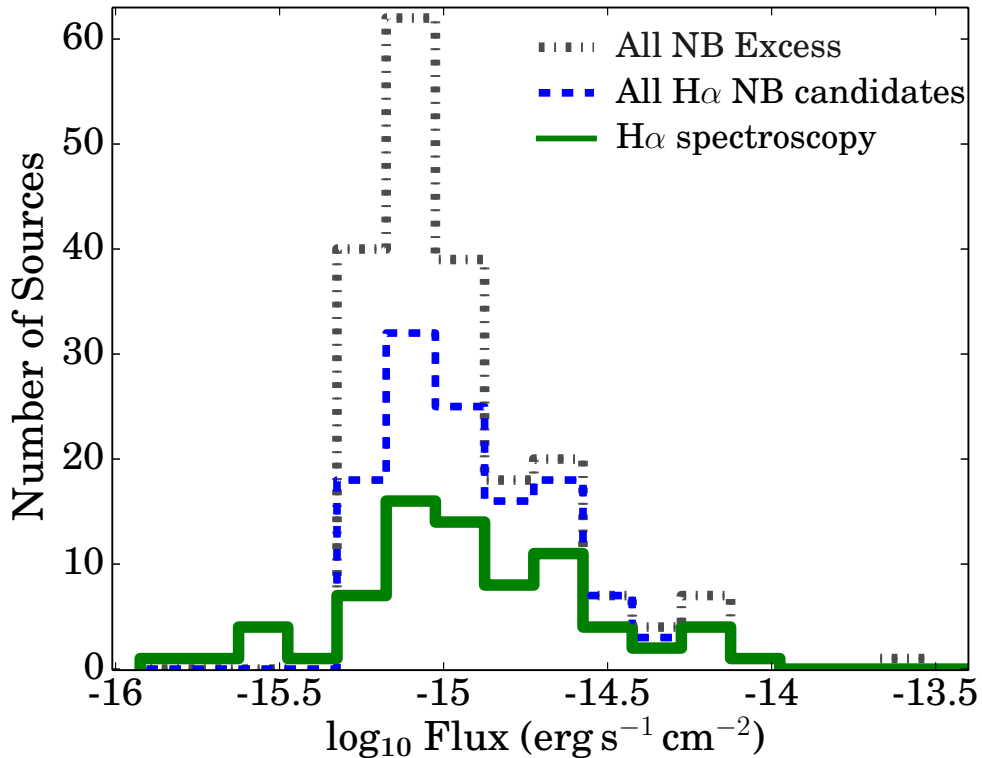
Figure 8.3: The distribution of emission line fluxes in the full sample of narrow-band selected Hα emitters, and those in our spectroscopic sample. Fluxes shown here are derived from narrow-band photometry (full flux, including both Hα and [Nɪɪ] fluxes), and corrected for Galactic extinction. This shows that we are complete down to $\sim 6 \times 10^{-16}\,\mathrm{erg\,s^{-1}\,cm^{-2}}$, but that, particularly due to the use of Keck, we also have Hα emitters with significantly lower emission line fluxes in our sample, although we are clearly not complete for those fluxes.

sky, we extracted sources along the dispersion axis, summing up the counts. We obtained a first order wavelength calibration by using the arcs and obtain a final wavelength calibration per fibre by using the wealth of sky lines on that particular fibre. This gives a wavelength calibration with an error (rms) of less than 1 Å.

In total, out of the 109 targeted sources, we obtained high enough S/N to determine a redshift for 73 sources (65 candidate line emitters selected with the NB). The remaining sources either had very low S/N, were targeted by fibres with low throughput and/or for which sky subtraction was only possible with the dedicated (different) sky fibre (thus resulting in poor sky subtraction). All the sources for which we did not get high enough S/N to detect an emission line are the emitters with the lowest emission line fluxes, expected to remain undetected with the achieved flux limit. Figure 8.3 shows the distribution of fluxes for the full sample of candidate Hα emitters (only a fraction of those were targeted) and those we have detected at high S/N – this shows that we are complete for "intrinsic" (i.e., after correcting for Galaxy extinction) fluxes of $> 6 \times 10^{-16}\,\mathrm{erg\,s^{-1}\,cm^{-2}}$ (see Figure 8.3). We note that while our the Keck spectroscopy was targeting red sequence galaxies (see Dawson et al. 2015), our WHT

follow-up was specifically targeted at NB-selected line emitter candidates (dominated by Hα at $z \sim 0.19$), thus giving an unbiased spectroscopic sample to study Hα emitters. Most importantly, our AF2 sample targets line emitters both in and around the merging cluster, thus allowing us a direct comparison between cluster Hα emitters and those outside the cluster, observed with the same instrument/configuration/exposure times.

8.2.4 Redshifts and Emission line Measurements

We extract the 1D spectra (e.g. Figure 8.2) by detecting the high S/N trace (continuum), or by detecting the strong emission lines, and extracting them across the exposed pixels. We obtain a reasonable flux calibration with broad-band photometry available from g, r, and i observations and improve it further by using our own NB observations. However, we note that the focus of this paper is on line ratios (which do not depend on flux calibration), not emission line fluxes.

Spectroscopic redshifts for the Keck/DEIMOS data-set are obtained as described in Dawson et al. (2015). We find 40 Hα emitters within the DEIMOS/Keck data-set, but 5 (3) are at higher (lower) redshift, and thus clearly outside the merging cluster. These will be part of our comparison/field sample together with the AF2 spectra at the same redshift of the cluster but far away from it (non-cluster members). In total, 32 Hα emitters are cluster members within the DEIMOS data-set. From these, 6 were targeted with both DEIMOS and AF2 and show perfect agreement in the redshift determination (see Dawson et al. 2015, for a redshift comparison), flux and emission line ratios, showing that no systematics are affecting our analysis, and that spectra from both instruments are fully comparable – see Figure 8.4.

For the WHT/AF2 data-set, we determine an initial estimate for each redshift by identifying strong emission lines around $\sim 7600 - 8000$Å. In most cases emission lines are detected at high S/N (> 10) and a redshift is then found with several emission lines, with the vast majority of sources being at $z \sim 0.19$ with strong Hα emission (see Figure 8.5 for the redshift distribution of Hα emitters). Given the proximity to the Galaxy (see e.g. Jee et al. 2015), the stellar density is many times higher than in a typical extragalactic field. We find objects with many clear absorption features which are easily classified as stars by identifying $z = 0$ absorption lines (including Hα). The complete set of redshifts of Hα emitters in our sample is given in Table 8.1.

Out of the 73 (65 line emitters) sources with high enough S/N we find 49 Hα emitters at $z \sim 0.19$, 8 Hβ/[OIII] emitters at $z \sim 0.6$, 2 [OII] emitters at $z \sim 1.1$ and one 4000 Å break galaxy at $z \sim 0.8$. In total, for the AF2 spectra, we find 5 stars among our full sample of candidate line emitters. All other sources that were targeted and that were not in our NB-selected catalogue were found to be stars. Thus, within the sample of line emitters from Stroe et al. (2015), we find that 75 % are Hα emitters.

Emission line fluxes for both AF2 and DEIMOS spectra are measured by fitting Gaussian profiles (see e.g. Figure 8.2), and measuring the continuum directly red-ward and blue-ward of the lines (masking any other features or nearby lines). We also obtain the line FWHM (in km s^{-1}), taking advantage of the high resolution, high S/N Keck spectra. We measure (observed, aperture/slit/fibre corrected) line fluxes in the range $1.7 - 35 \times 10^{-16}$ erg s^{-1} cm^{-2} in Hα, and FWHMs of 40-466 km s^{-2} – full details are given in Table 8.1. We find the best redshift by fitting all the available spectral lines and do this independently on the Keck/DEIMOS
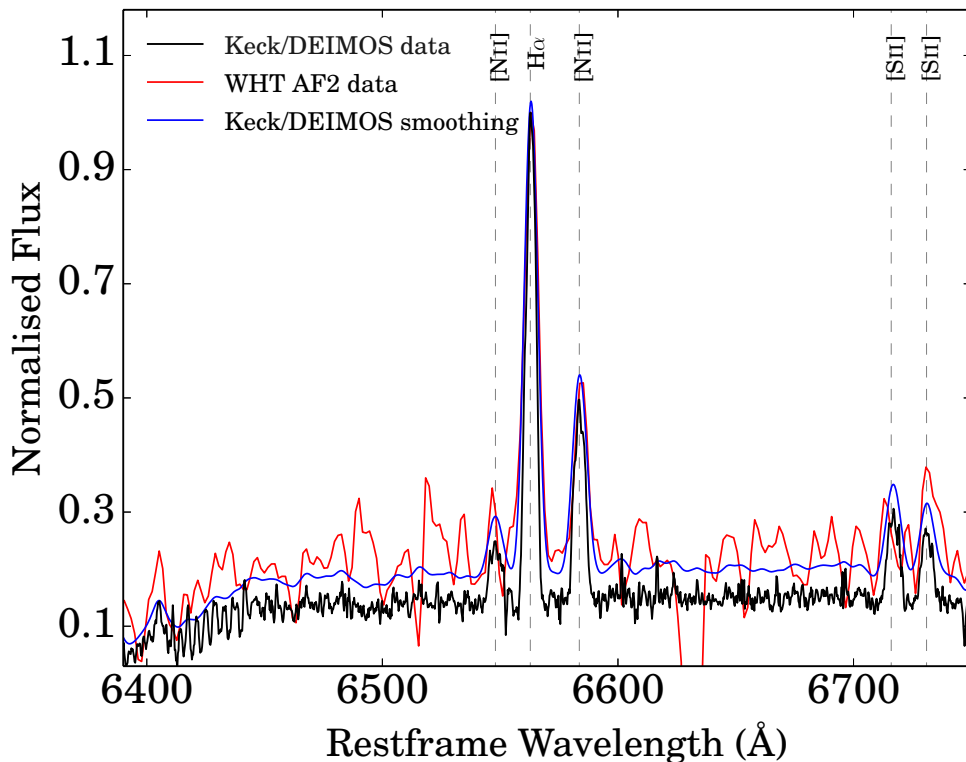
Figure 8.4: An example of one of the typical/faint sources that was targeted with both WHT/AF2 and Keck/DEIMOS. We find perfect agreement and recover the same line ratios, within the errors, although Keck/DEIMOS spectra have much higher individual S/N ratio and much higher resolution, as this clearly shows. Nevertheless, both data-sets provide consistent measurements with no biases and thus can be used together.
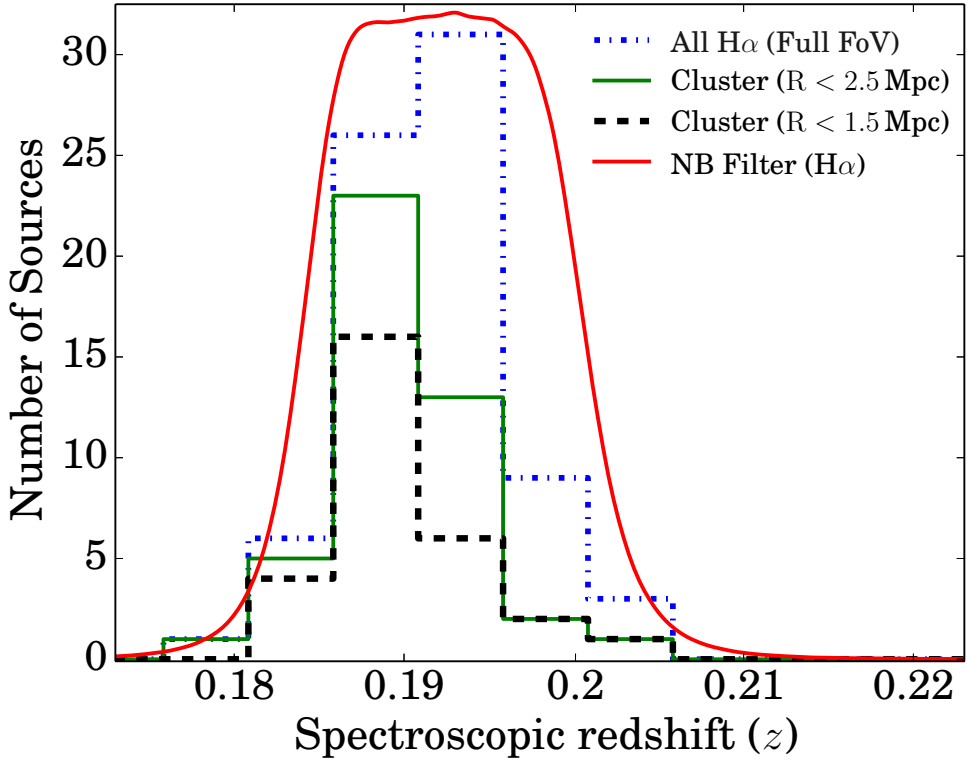
Figure 8.5: Spectroscopic redshift distribution of our sample of Hα emitters in the full FoV of the INT survey (Stroe et al. 2015), compared with the spectroscopic distribution of Hα emitters within the projected "central" 1.5 Mpc radius (physical) of the Sausage cluster and those within a 2.5 Mpc radius (physical) of the "centre" of the Sausage cluster. We also scale our narrow-band filter transmission. Sources outside the 2.5 Mpc radius are used as a comparison sample, together with a few sources at significantly higher and lower redshift found with DEIMOS (not shown here). We note that our narrow-band filter profile encompasses the 95% confidence interval of the full cluster redshift dispersion (Dawson et al. 2015) for Hα emission.

ID	z_{spec}	I_{AB}	$F_{H\alpha}$ $\log_{10}$	FWHM km/s	[NII]/Hα	[SII]/[SII]	[OIII]/Hβ	[SII]/Hα	Mass $M_\odot$	C dist.	AGN
SSSD-02	0.1838	18.3	-15.1	198	0.71	1.3	—	0.3	10.3	2	—
SSSD-04	0.1895	19.3	-15.7	50	1.02	0.2	—	—	9.6	2	1
SSSD-06	0.1910	20.2	-15.0	102	0.07	1.8	4.2	0.2	8.5	1.5	0
SSSD-07	0.2291	21.2	-16.0	136	0.28	3.4	0.9	0.5	8.7	10	0
SSSD-08	0.1844	21.4	-16.1	104	0.31	1.9	2.4	0.2	8.7	2	—

Table 8.1: Notes: Here we show just the five first entries: the full catalogue is published in the on-line version of the paper. The C column indicates the environment/sub-sample of each source (distance from cluster center, Mpc), with sources flagged as 10 being outside the cluster. The AGN column distinguishes between likely AGN which present narrow-lines (1; NLA), broad lines (2; BLA), likely star-forming galaxy (0; SFG) and unclassified (—; UNC).

and WHT/AF2 data-sets. Given that we have an overlap of six sources, we can check if the different resolution and the use of fibres versus slits can introduce any biases/differences. We find that all these six sources yielded the same redshift and we find that the fluxes and the line ratios all agree within the errors (see an example in Figure 8.4). We therefore combine the samples for the following analysis, taking into account the different errors given by each data-set. For the six sources with measurements in both data-sets we use the DEIMOS results for four out of the six sources (due to a much higher S/N). For the remaining two (detected at very high S/N in AF2), we use the AF2 measurements because they also cover [SII], Hβ and [OIII], while these lines are not covered by DEIMOS. In total, we have 83 Hα emitters in our sample (for 6 we have measurements from both DEIMOS and AF2). Out of these, 75 Hα emitters are all at the redshift of the cluster ($z = 0.18 - 0.197$), but some are far from the centre: 52 Hα emitters are found within a (projected) radius of 2.5 Mpc from the cluster "centre", defined as in Stroe et al. (2015) (RA[J2000] 22:42:45.6, Dec[J2000] +53:03:10.8), while 44 are within a 2 Mpc (projected) radius, 36 are within a 1.5 Mpc (projected) radius.

8.2.5 Multiband photometry and stellar masses

We use multi-band catalogues derived in Stroe et al. (2015) to obtain information on all the emitters and here we explore the *BgVrIz* photometry to compute stellar masses by spectral energy distribution (SED) fitting. All the photometry is corrected for Galactic extinction (see details in Stroe et al. 2015). We use the spectroscopic redshift of each source, but using $z = 0.19$ for all sources does not significantly change any of the results. We compute stellar masses for all candidate Hα emitters, regardless of having been targeted spectroscopically or not, so we can compare our spectroscopic sample with the full parent sample. The full sample is explored in Stroe et al. (2015).

Stellar masses are obtained by SED fitting of stellar population synthesis models to *BgVrIz*, following Sobral et al. (2011); Sobral et al. (2014). The SED templates are generated with the Bruzual & Charlot (2003) package using Bruzual (2007) models, a Chabrier (2003) IMF, and exponentially declining star formation histories with the form $e^{-t/\tau}$, with τ in the range 0.1 Gyrs to 10 Gyrs. The SEDs were generated for a logarithmic grid of 200 ages (from 0.1 Myr to the maximum age at $z = 0.19$). Dust extinction was applied to the templates using the Calzetti et al. (2000) law with $E(B - V)$ in the range 0 to 0.5 (in steps of 0.05), roughly

corresponding to $A_{H\alpha} \sim 0 - 2$. The models are generated with five different metallicities ($Z = 0.0001 - 0.05$), including solar ($Z = 0.02$). Here we use the best-fit template to obtain our estimate of stellar mass, but we also compute the median stellar mass across all solutions in the entire multi-dimensional parameter space for each source, which lie within 1σ of the best-fit and thus also obtain the median mass of the 1σ best-fits.

8.2.6 Completeness: Stellar Mass

We show the distribution of stellar masses for the samples of Hα emitters in Figure 8.6. Hα emitters in our full sample have an average stellar mass of $\sim 10^{9.4}$ M$_\odot$. As a whole, the sample of Hα emitters at $z \sim 0.19$ has a similar stellar mass distribution to samples of field Hα emitters at similar redshifts (e.g. Shioya et al. 2008; Sobral et al. 2014), but with cluster Hα emitters having higher stellar masses than Hα emitters outside the cluster. Figure 8.6 also shows that our main limitation at lower masses is our parent sample from Stroe et al. (2015), which is complete down to roughly $\sim 10^9$ M$_\odot$, and thus our results, particularly for the mass-metallicity relation, only take into account star-forming galaxies with stellar masses $> 10^9$ M$_\odot$.

8.2.7 Completeness: SFR-Stellar Mass

Figure 8.7 shows the relation between Hα(+[N$\textsc{ii}$]) flux (based on narrow-band photometry, so we can fully compare it with the parent NB sample) and stellar mass, for both the parent sample, and for our spectroscopic sample. We also highlight sources confirmed to be outside the cluster, and those in the cluster and outskirts. The comparison with the parent sample shows that our sample is representative of the full parent sample, at least down to stellar masses of $> 10^9$ M$_\odot$, and for fluxes (corrected for Galactic extinction and for 5″ apertures, and thus in practice after a full aperture correction) of Hα flux $> 10^{-15.25}$ erg s^{-1} cm^{-2} (roughly corresponding to SFRs> 0.2 M$_\odot$ yr^{-1}).

8.2.8 The comparison sample: DEIMOS+AF2 non-cluster Hα emitters

We explore our Hα emitters in the DEIMOS dataset (8) that are found to be at higher ($0.23 < z < 0.3$) and lower redshift ($0.14 < z < 0.17$) , and 31 Hα emitters from the AF2 data-set that are more than 2.5 Mpc away from the Sausage cluster "centre" but at a similar redshift. As mentioned in §8.2.4, we use RA(J2000) 22:42:45.6, Dec(J2000) +53:03:10.8 as the "centre" of the Sausage merging cluster, and compute projected distances from this position. This sample of 39 Hα emitters is compared with a similar number of Sausage cluster Hα emitters and allows us to directly compare their properties, AGN contamination and search for any differences. We use this sample for direct comparisons.

8.3 Results

The redshift distribution of our final sample of Hα emitters belonging to the merging cluster is shown in Figure 8.5 and compared to the distribution of spectroscopic redshifts for Hα emitters within different radii from the cluster centre. We confirm that the narrow-band filter
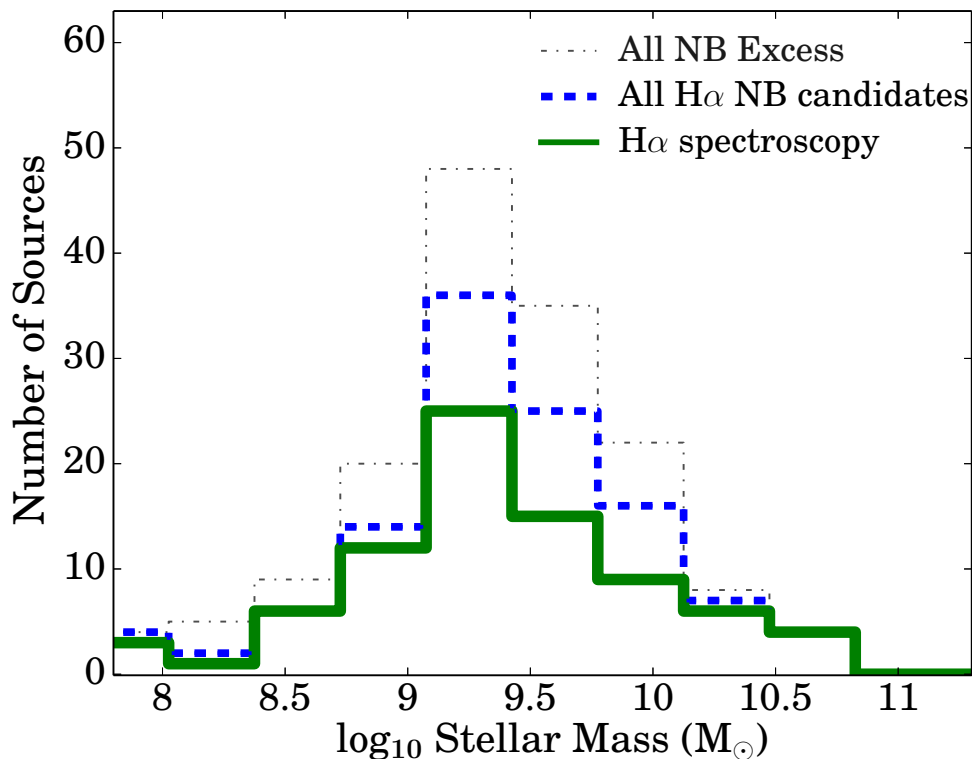
Figure 8.6: Stellar mass distribution for our full spectroscopic sample and comparison with the parent NB sample of all emitters ("All NB Excess"; stellar masses computed assuming all would be at $z = 0.19$ and be Hα emitters, just shown for comparison, as many sources here are clearly not Hα emitters) and the sample of Hα emitters at $z = 0.19$ after colour-colour, photometric redshift and spectroscopic redshift selection ("All Hα NB candidate"). This shows that we are almost fully complete at both low and high masses (compared to the parent sample). Even at intermediate to high masses, where the number of sources is higher, we still have a very high spectroscopic completeness of $\sim 50\%$ or more. Most importantly, the sources that are not in our spectroscopic sample are those that i) we could not target due to fibre configuration constraints and ii) that have very low fluxes.
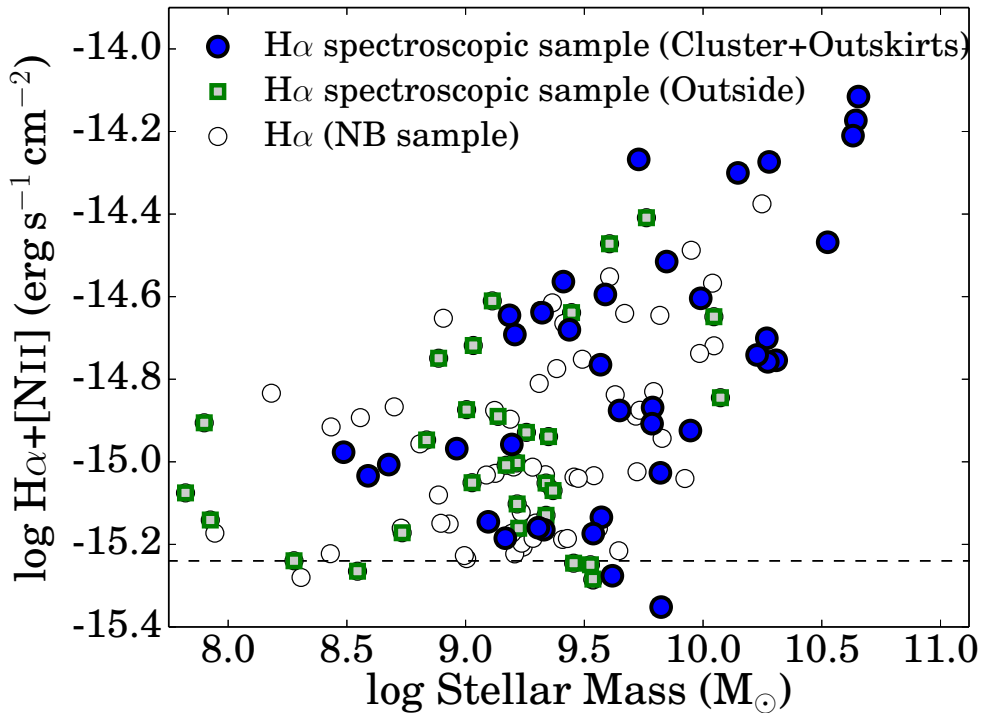
Figure 8.7: The relation between Hα+[Nɪɪ] flux (corrected for Galactic extinction, but not corrected for intrinsic dust extinction), based on 5″ narrow-band photometry and stellar mass, for the parent sample, selected using narrow-band, and our spectroscopic sample. Our spectroscopically confirmed sources sample the vast majority of the parameter space, both for galaxies in the cluster ($R < 1.5\,\mathrm{Mpc}$) and outskirts ($1.5 < R < 2.5\,\mathrm{Mpc}$) and for those outside the cluster. We are particularly complete, relative to the parent sample, for stellar masses $> 10^9\,\mathrm{M_\odot}$. We preferentially miss sources with the lowest fluxes and with stellar masses lower than $\sim 10^9\,\mathrm{M_\odot}$.
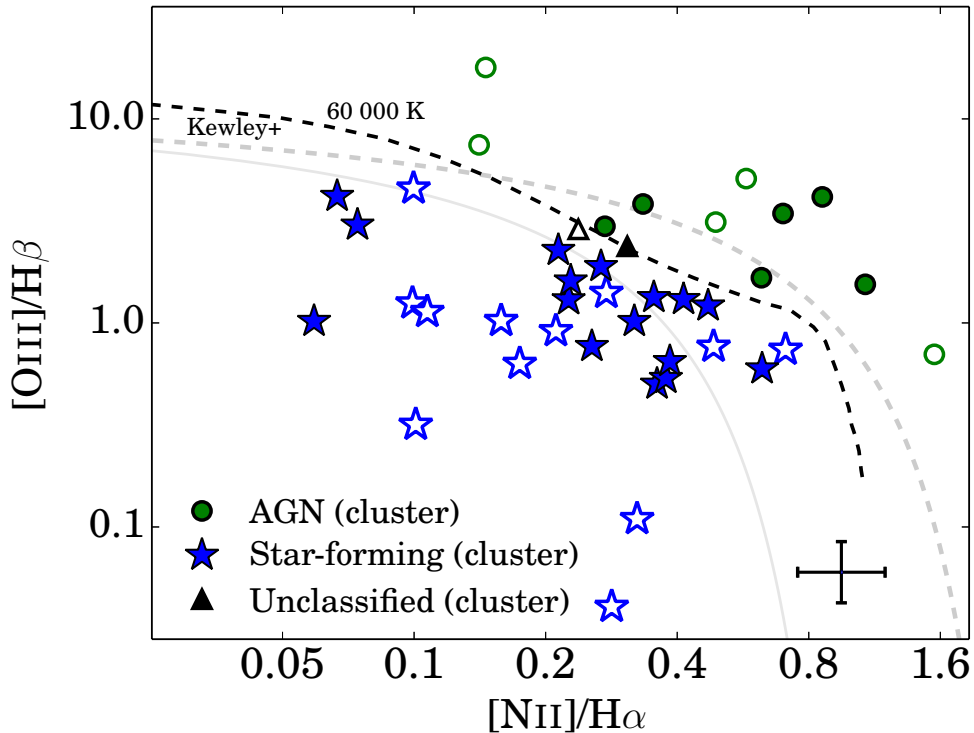
Figure 8.8: Emission line ratio diagnostics (Baldwin et al. 1981; Rola et al. 1997) separate star-forming dominated from AGN dominated Hα emitters (black dashed line). We also show emission line diagnostics from Kewley et al. (2001) for comparison, which show the location of pure, "typical" star-forming galaxies (gray solid line), and the separation line between maximal starbursts and AGN (gray dashed line). We only show galaxies with detections in all emission lines. Filled symbols are Hα emitters within a 1.5 Mpc radius of the cluster, while the unfilled symbols are either at higher, lower redshift, or are at the redshift of the cluster, but at distances higher than 1.5 Mpc. These results reveal a similar fraction of AGN in ($36 \pm 8\%$) and outside ($29 \pm 7\%$) the cluster. Note that, due to the significant dust extinction, particularly on the line of sight, the [O$\textsc{iii}$]/Hβ line ratio is slightly overestimated for all galaxies (likely by ~ 0.06 dex), making it easier to classify galaxies as AGN, and making the sample of star-forming galaxies even cleaner from potential AGN contamination.
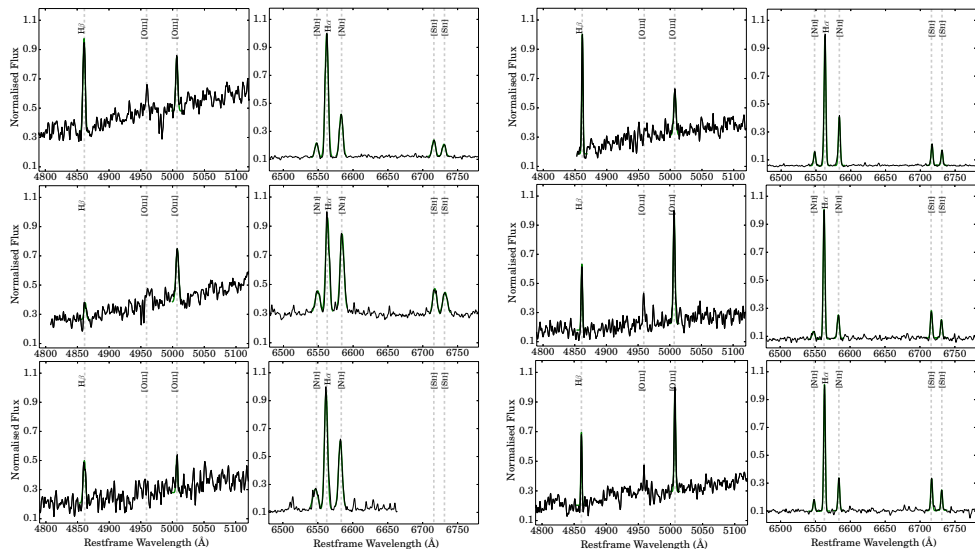
Figure 8.9: Some examples of our Hα emitters, the coverage that extends to Hβ and [OIII] and the gaussian fits we derived in order to measure emission line ratios. This extended coverage is particularly important in order to allow us to distinguish between star-forming dominated and AGN-dominated sources by measuring [OIII] 5007/Hβ and [NII]/Hα line ratios and placing them on the Baldwin et al. 1981 classification scheme.

used in Stroe et al. (2015) effectively selects all Hα emitters belonging to the merging cluster, and that such selection is not biased towards galaxies at the outskirts (in the redshift direction) of the cluster. We fully confirm the very high number of Hα emitters in this merging cluster. Given the mass of the cluster ($\sim 1.0 - 1.1 \times 10^{15} M_\odot$, see Jee et al. 2015), and its very high ICM temperature (Ogrean et al. 2013a, Akamatsu et al. 2015) – 7-12 KeV –, it is puzzling that there are so many Hα emitters. With a final sample of 39 field Hα emitters and samples of 52, 44 and 36 Hα emitters (within 2.5, 2.0 and 1.5 Mpc from the cluster "centre", respectively) we now investigate their nature and unveil their properties. For the remaining analysis in the paper, we divide our sample in three different environments: i) Cluster (sources at the redshift of the cluster and within R< 1.5 Mpc), ii) Cluster outskirts (sources at the redshift of the cluster and at projected distanced $1.5 < R < 2.5$ Mpc) and iii) Outside the cluster (sources at the redshift of the cluster that are found to be $R > 2.5$ Mpc away and sources at a significantly higher and lower redshift). For some parts of the analysis, we also split the cluster sample into galaxies in the i) cluster, near to the hottest intra-cluster medium, $R < 0.5$ Mpc away from the "centre" of the cluster and ii) post-shock region, within the North and South radio relics, close to the relics and further away from the "centre". We refer to ii) as "post-shock" region and to i) as "elsewhere in the cluster".

8.3.1 Nature of Hα emitters: SF vs AGN

In order to differentiate between star-forming and AGN, the [OIII] 5007/Hβ and [NII] 5007/Hα line ratios were used (see Figure 8.8); these have been widely used to separate AGN from star-

forming galaxies (e.g. Baldwin et al. 1981; Rola et al. 1997; Kewley et al. 2001, 2013). We show some examples of spectra in Figure 8.9. These line ratios are also for emission lines sufficiently close that dust extinction has little effect. However, for the case of the [O III] 5007/Hβ emission line ratios, due to the significant total dust extinction affecting our galaxies, particularly due to the Galaxy, line ratios may be over-estimated by ~ 0.06 dex. Because we do not correct for this, the [O III] 5007/Hβ line ratios are all closer to AGN. This means, however, that our sample of star-forming galaxies will be even more conservative and robust (if anything, some star-forming galaxies may be classified as AGN). Because corrections are relatively unreliable, and because applying unreliable corrections could lead to including potential AGN in our samples of star-forming galaxies, we opted not to correct for this effect. Only spectra with all lines detected at S/N > 3.0 were used, but we also place limits on those with lower S/N. Figure 8.8 shows data-points for the line ratios, while the black dashed curve shown represent maximum line ratios for a star-forming galaxy (from OB stars with effective temperatures of 60000 K; Baldwin et al. 1981; Rola et al. 1997). We also show curves from Kewley et al. (2001) and Kewley et al. (2013) encompassing "pure", "typical" star-forming galaxies (gray solid line), and encompassing up to maximal starbursts (gray dashed line).

Over our full AF2 and DEIMOS sample, we find 4 broad line AGNs. All these broad line AGNs are found to be in the cluster. Furthermore, in total, we have measurements of [O III] 5007/Hβ and [N II]/Hα line ratios with individual line detections above 3 σ which allow us to distinguish between AGN and SF for 42 sources. For these 42 sources, we find 14 AGN (10 narrow-line AGN and 4 BL-AGN), and 28 likely star-forming dominated Hα emitters. We show the location of these sources in Figure 8.1, revealing that AGN in the cluster are all in the post-shock regions, just behind both the North and South radio relics/shock fronts.

For the sources we can classify we also have measured the FWHM of the narrow emission lines. We show the fraction of AGN sources as a function of FWHM of the narrow lines in Figure 8.10. This clearly shows that at the highest FWHM, the AGN fraction is very high. We note that these are FWHM of narrow lines, and thus this is likely indicative of outflows happening in the AGN in our sample, dominated by those in the Sausage cluster.

We split sources between those in the cluster (see Figure 8.1) and outskirts (25 classified sources) and those outside the cluster (17 classified sources). We find 9/25 sources in the cluster+outskirts to be AGN (including the 4 broad-line AGN), resulting in an AGN fraction of 36 ± 8 % (Poissonian errors), while outside the cluster we find 5/17 sources to be AGN, resulting in an AGN fraction of 29 ± 7 %, lower than in the cluster, but still consistent. It should be noted that both samples have very similar median Hα luminosities, and thus should be fully comparable. For Hα emitters within the Sausage merging cluster (R< 1.5 Mpc), we find an AGN fraction of 35 ± 6% (see Figure 8.1).

8.3.2   Morphologies

By exploring deep i band Subaru images (see also Stroe et al. (2014a)), we investigate the morphologies of our Hα emitters. We show thumbnails of all our Hα cluster galaxies, also labelling them as AGN or star-forming galaxies, in Figure 8.3.2. We find little to no indication of merger activity (note that the stellar density from the Galaxy is extremely high: point-like sources are stars). We however note that most star-forming galaxies show relatively compact morphologies and hint that most star-formation is occurring in relatively central re-
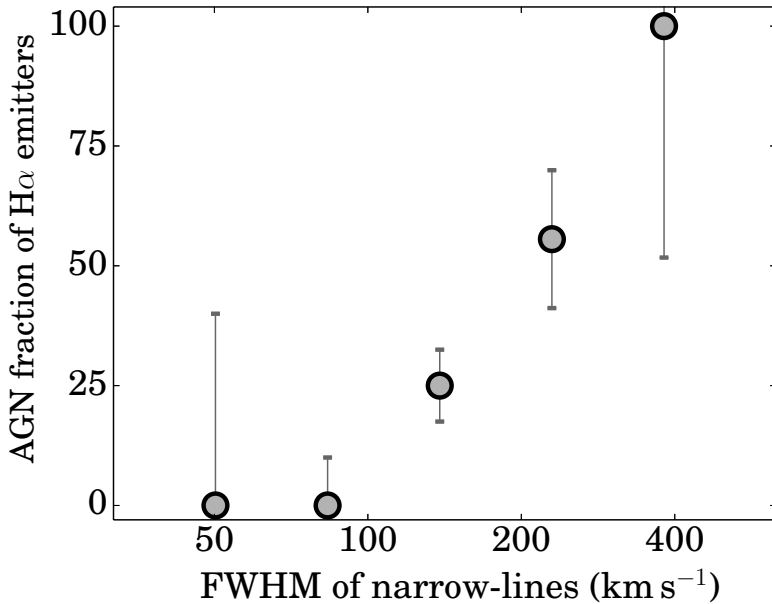
Figure 8.10: Fraction of AGN-dominated galaxies as a function of emission line FWHM in km s^{-1} for the narrow lines (broad emission lines are neglected here). We find that at higher FWHM of Hα, [NII], [SII] lines, the prevalence of AGN increases, likely indicating that AGN are the cause for such high FWHM in narrow lines, and indicative of outflows.

gions, where molecular gas is likely still available to form stars. However, a more detailed morphological analysis is beyond the scope of this paper.

Field star-forming galaxies at these Hα luminosities present a typical fraction of mergers on the order of $\sim$ 10% (e.g. at $z = 0.24$ in the COSMOS field; Sobral et al. 2009), and our Hα emitters in the cluster do not present a larger fraction than that. Thus, the elevated activity in our cluster Hα emitters is definitely not being driven by mergers as, if anything, our Hα emitters have a lower fraction of mergers than those in the field. This is, nonetheless, not surprising. The cluster we are studying is incredibly massive, with a high velocity dispersion of over 1000 km s^{-1}, and thus the chances of a galaxy-galaxy mergers are relatively small.

8.3.3 Electron densities and Ionisation Potential

We make clear individual detections of the [SII]$_{6716,6761}$ doublet. We also (median) stack the entire sample to find [SII]$_{6716}$/ [SII]$_{6761}$= 1.22 ± 0.05, corresponding to an electron density of $10^{2.4\pm0.1}$ cm^{-3}(Osterbrock 1989). If we only consider star-forming galaxies, we find [SII]$_{6716}$/ [SII]$_{6761}$= 1.36 ± 0.07, corresponding to $10^{2.00\pm0.25}$ cm^{-3}.

In order to compare several sub-samples, based on membership and nature, we further split the sample in i) all (all sources), ii) cluster, iii) outskirts and iv) outside. Within the cluster sample, we further split it into sources within the post-shock regions (both North and South, see Figure 8.1), and those elsewhere, including in the two cluster cores and within the hot X-ray gas. We further split samples with respect to the dominating nature of the sources: i) all sources, ii) sources clearly dominated by star formation (SFGs) and iii) sources dominated
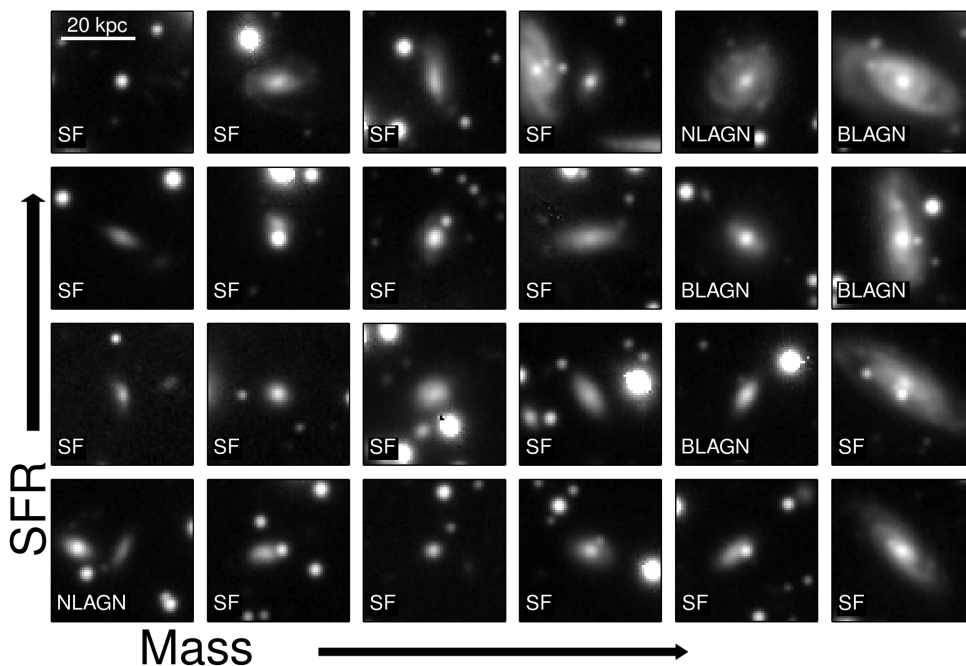
Figure 8.11: Thumbnails of our Hα cluster members. Each square is ∼ 40 × 40 kpc and we organise galaxies in respect to their estimated stellar mass and estimated star-formation rate. We also indicate which sources are likely AGN and which are star-forming. We do not find any evidence for significant galaxy-galaxy (major) merging. This implies that the enhanced star-formation and AGN activity within the merging cluster is not being driven by galaxy-galaxy mergers, and thus is it more likely driven by the interaction with the environment, and in particular with the shock wave. We note that the bright point sources, which show up in most images are stars within the Milky Way, not galaxies.
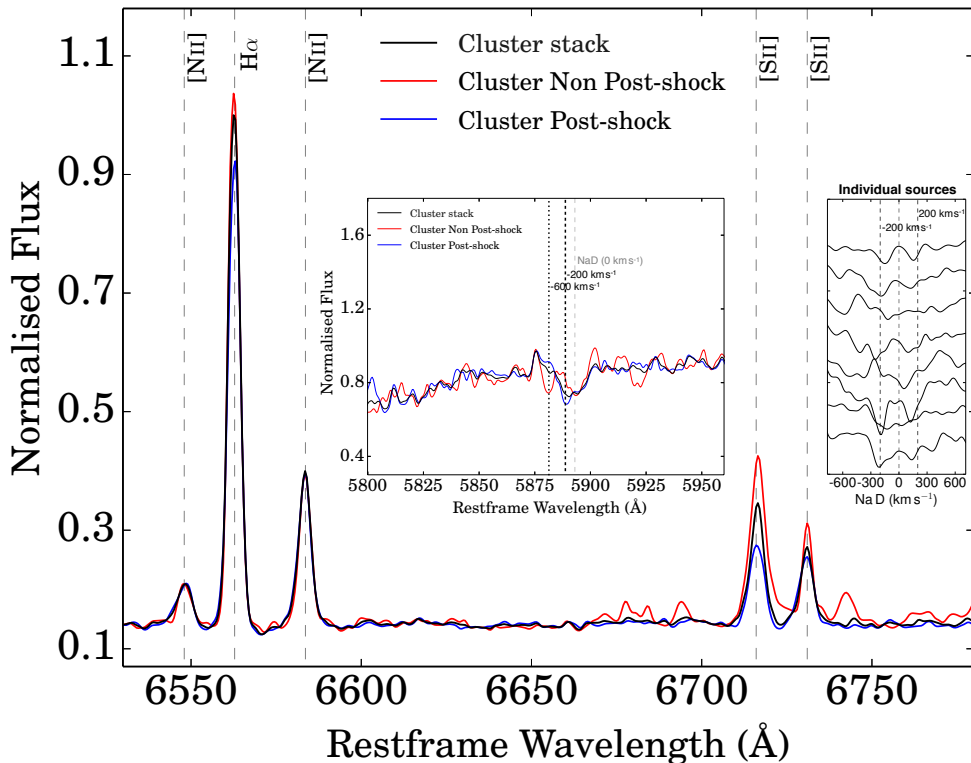
Figure 8.12: Stacks for our full merging cluster star-forming galaxies, and when splitting the sample in post-shock regions and non post-shock regions (mostly those in the very hot intra-cluster medium and in the sub-cluster cores). While as a whole cluster galaxies show significant differences from field and outskirts star-forming galaxies, post-shock and non post-shock star-forming galaxies also show a drastic difference in their stacked spectra regarding the [SII] emission lines, and particularly for [SII]$_{6716}$, which is significantly boosted for non post-shock cluster star-forming galaxies. This may be evidence of significant supernova activity. We also find a significant red-shifted component of the [SII]$_{6716}$ emission line, potentially indicative of outflows, and is relatively broad. Further evidence for outflows is found even for the stack of both sub-samples: we find NaD absorption line significantly blue-shifted, from 200 to 600 km s^{-1}, a clear sign that, as a whole, cluster star-forming galaxies are driving rapid outflows (Heckman et al. 2000). We note that Na D in absorption with significant velocity offset from the systematic redshift within the range 200 to 600 km s^{-1} is also found for individual sources with even stronger S/N (as the stack mixes different velocity offsets); we show those in the right panel.

RESULTS FROM THE STACKS FOR DIFFERENT SUB-SAMPLES.

SAMPLE	number sources	[Nɪɪ]/Hα	12 + log(O/H)	[Sɪɪ]/[Sɪɪ]	[Sɪɪ]/Hα
Full Sample	83	0.338 ± 0.007	8.632 ± 0.005	1.22 ± 0.05	0.249 ± 0.003
All in Cluster	24	0.443 ± 0.007	8.698 ± 0.004	1.48 ± 0.08	0.285 ± 0.002
All in Post-shock (PS)	17	0.655 ± 0.01	8.795 ± 0.004	1.24 ± 0.06	0.32 ± 0.003
All Cluster non-PS	7	0.265 ± 0.005	8.571 ± 0.005	2.23 ± 0.18	0.372 ± 0.004
All in Outskirts	20	0.287 ± 0.007	8.591 ± 0.006	0.96 ± 0.04	0.209 ± 0.004
All Outside	31	0.168 ± 0.006	8.458 ± 0.009	1.26 ± 0.04	0.234 ± 0.005
All SFGs	28	0.284 ± 0.006	8.588 ± 0.005	1.43 ± 0.07	0.259 ± 0.002
Cluster SFGs	11	0.311 ± 0.005	8.611 ± 0.004	1.73 ± 0.11	0.265 ± 0.002
Post-shock (PS) SFGs	6	0.339 ± 0.005	8.632 ± 0.004	1.22 ± 0.04	0.201 ± 0.002
Cluster non-PS SFGs	5	0.285 ± 0.005	8.590 ± 0.004	2.5 ± 0.2	0.430 ± 0.004
Outskirts SFGs	5	0.180 ± 0.002	8.476 ± 0.003	1.57 ± 0.10	0.193 ± 0.002
Outside SFGs	10	0.152 ± 0.010	8.433 ± 0.016	0.82 ± 0.04	0.212 ± 0.007
All AGNs	17	0.731 ± 0.009	—	0.93 ± 0.02	0.250 ± 0.003
Cluster AGNs	6	0.938 ± 0.014	—	0.82 ± 0.02	0.251 ± 0.003
Post-shock (PS) SFGs	6	0.938 ± 0.014	—	0.82 ± 0.02	0.251 ± 0.003
Cluster non-PS SFGs	0	—	—	—	—
Outskirts AGNs	5	1.054 ± 0.031	—	0.58 ± 0.02	1.1 ± 0.1
Outside AGNs	7	0.513 ± 0.007	—	0.62 ± 0.03	0.13 ± 0.01

Table 8.2: Notes: The Full sample contains all Hα emitters, the Sausage Cluster sample is defined with sources within 1.5 Mpc radius of what we assign as the central position of the cluster. The sample in the outskirts is defined as Hα emitters within 1.5 and 2.5 projected Mpc from the central position, and sources defined as outside are at higher distances than 2.5 Mpc projected.

by AGN activity (AGNs). The results are presented in Table 8.2.

Our results clearly show that all sub-samples of Sausage cluster members have higher $[\text{Sɪɪ}]_{6716}/[\text{Sɪɪ}]_{6761}$ line ratios than similar sub-samples. In particular, the merging cluster star-forming galaxies show a very high $[\text{Sɪɪ}]_{6716}/[\text{Sɪɪ}]_{6761} = 1.73 \pm 0.11$, implying an extremely low electron density of $< 5\,\text{cm}^{-3}$ (the higher the line ratio, the lower the electron density; Osterbrock 1989), < 30 times lower electron density than star-forming galaxies outside the cluster and other star-forming galaxies found in the literature. On the other hand, it should be noted that AGNs (see Table 8.2) all have $[\text{Sɪɪ}]_{6716}/[\text{Sɪɪ}]_{6761}$ line ratios below 1, as expected, so completely opposite to what is found for the cluster star-forming galaxies.

By further splitting the cluster sample into galaxies in the post-shock region (within the North and South radio relics, close to the relics and the furthest away from the "centre") and those elsewhere, and particularly in the hot intra-cluster medium (see Table 8.2), we show that the high $[\text{Sɪɪ}]_{6716}/[\text{Sɪɪ}]_{6761}$ line ratio is being strongly driven by star-forming galaxies within the hottest inter-cluster medium (those closest to the "centre", and further away from the shock fronts). These star-forming galaxies (no AGNs are found, but 2 are unclassified) show very high $[\text{Sɪɪ}]_{6716}/[\text{Sɪɪ}]_{6761} = 2.5 \pm 0.2$, corresponding to extremely low electron densities. This is likely evidence that such star-forming galaxies are substantially affected by their surrounding environment. Most importantly, the stack of the non-post-shock galaxies (see Figure 8.12) reveals asymmetric $[\text{Sɪɪ}]_{6716}$ emission line, with significantly blue-shifted emission, likely indicating stripping/outflows.

The $[\text{Sɪɪ}]_{6716}/\text{H}\alpha$ line ratio can be used to estimate the ionisation strength (Osterbrock 1989; Collins & Rand 2001) of the inter-stellar medium (ISM). We derive, for our full sample (median stack), $[\text{Sɪɪ}]_{6716}/\text{H}\alpha = 0.249 \pm 0.003$ (see Table 8.2), which corresponds to an ionisation parameter $\log_{10}(U, \text{cm}^3) = -4.06 \pm 0.05$ (Collins & Rand 2001). Cluster mem-

bers show the highest $[S_{II}]_{6716}/H\alpha$ ratios. Focusing on the $H\alpha$ star-forming galaxies in the Sausage merging cluster, we find $[S_{II}]_{6716}/H\alpha = 0.265 \pm 0.002$, which corresponds to a ionisation strength of the ISM about half of that of the field and outskirts sample. However, $H\alpha$ star-forming galaxies in the outskirts and outside the cluster are significantly more metal poor (see §8.3.5), which is enough to explain the difference. When matched in metallicities, we find no significant difference within the errors.

When we further split the cluster sample into sources in the post-shock region and those elsewhere (mostly in the hottest X-ray gas region, near the "centre" of the cluster and/or in the sub-cluster cores), we find that the high $[S_{II}]_{6716}/H\alpha$ ratio within the cluster is mostly driven by cluster star-forming galaxies outside the post-shock region, again indicating that these galaxies are affected by their surroundings. In practice, with a $[S_{II}]_{6716}/H\alpha = 0.430 \pm 0.004$, cluster star-forming galaxies away from the post-shock regions have an ionisation parameter $\log_{10}(U, cm^3) = -4.5 \pm 0.05$, more than 4 times lower than all other star-forming galaxies in the cluster. This could be interpreted as further evidence that these galaxies are already having their star-formation activity quenched. However, we note that this very high $[S_{II}]_{6716}/H\alpha$ ratio could also be interpreted as a significant contribution from supernova remnants. Since we do not find any difference in the typical SFRs of these galaxies relative to the other star-forming galaxies in and outside the cluster, the supernova explanation is strongly favoured. Furthermore, as we find evidence for outflows (see Figure 8.12), both in redshifted $[S_{II}]_{6716}$ emission, but particularly in strongly blue-shifted Na D (see e.g. Heckman et al. 2000) absorption ($\sim 600\,km^{-1}$) for these star-forming galaxies, it may well be that these outflows are being driven by supernovae.

8.3.4 Outflows

Particularly focusing on the Keck/DEIMOS sample (where the S/N is the highest, detecting the continuum for the bulk of the sample), we inspect the $H\alpha$, $[N_{II}]$ and $[S_{II}]$ lines to look for asymmetric profiles, broad components (for the forbidden lines) and P Cygni profiles, all potential signatures of strong outflows. We find strong evidence for at least one of such signatures in 7 of our 24 cluster galaxies, while we find no such signatures for galaxies outside the cluster (but the Keck/DEIMOS sample outside is smaller). For the Keck/DEIMOS sample only (as it is the only data-set that actually allows us to detect such signatures at the necessarily high S/N in a complete way), we find such signatures in $\sim 22\,\%$ of the cluster sample, and 100% of these are in the post-shock regions (see Figure 8.1). For the 7 sources, the absorption features show offsets of 600-1000 km/s. Many of these are AGNs and, as discussed in §8.3.1, all cluster AGNs are in the post shock-front regions of both north and south relics/shock-waves (see Figure 8.1).

We also attempt to fit emission lines with a combination of a narrow and a broad component. Whenever the S/N for the bluer lines ($H\beta$ and $[O_{III}]$) is lower than 10 we use only $H\alpha$, $[N_{II}]$ and $[S_{II}]$. We find that a single Gaussian profile (with a FWHM of up to $500\,km\,s^{-1}$) is able to fully fit all the spectra apart from the BL-AGNs. This also holds true for the stacks. We note that given the lower spectral resolution of WHT/AF2 when compared to Keck/DEIMOS (and lower S/N per Å, see e.g. Figure 8.4), we find that we can only reliably measure FWHM of emission lines with AF2 if they are larger than $160\,km\,s^{-1}$. With DEIMOS, we can measure FWHM down to 60-80 $km\,s^{-1}$. For the Keck/DEIMOS sample, we find that that the average

FWHM is $156 \pm 84\,\mathrm{km\,s^{-1}}$ (for AF2 we find an average of $174 \pm 70\,\mathrm{km\,s^{-1}}$). The line ratios and other properties for our full sample are given in Table 8.1. We find that the fraction of AGN correlates with increasing FWHM of narrow lines (see Figure 8.10), indicating that AGN are likely driving strong outflows.

Finally, for the sources with the highest S/N in the continuum, for which we can detect clear absorption lines, we also measure systematic velocity offsets from the absorption and emission lines. We find strong evidence for outflows (see Figure 8.12), both in redshifted $[\mathrm{S\,II}]_{6716}$ emission, but particularly in strongly blue-shifted Na D absorption ($\sim 200 - 600\,\mathrm{km^{-1}}$) for cluster star-forming galaxies as a whole (median stack). We also look at Na D in absorption which may be offset significantly on a source by source basis. We do this by fitting Na D with a Gaussian profile, and then comparing net velocity offsets when compared to the median redshift given by all the emission lines. We find strong evidence for outflows in all cluster star-forming galaxies except one (see Figure 8.12). We find an average velocity offset of $210\pm70\,\mathrm{km\,s^{-1}}$, in line with the stack. The most important result is that the vast majority of the Sausage merging cluster star-forming galaxies are driving strong outflows, and thus are experiencing (stellar) feedback. An alternative would be that these galaxies are having their gas stripped into the intra-cluster medium. However, if the latter was the case, one would expect that the velocity offsets would largely average out to zero, since the relative motion of the galaxies with respect to the gas should be random. We therefore argue that it is much more likely that we are witnessing strong stellar feedback which, of course, given the environment, will likely mean all the gas is permanently removed from the galaxies.

8.3.5 Metallicities

We use the $[\mathrm{N\,II}]/\mathrm{H}\alpha$ emission line ratio to infer the metallicity of the gas for each star-forming galaxy (AGNs are neglected). We obtain metallicities for each star-forming source, but also for sub-samples: see Table 8.2. For our full sample (median stack), we find $[\mathrm{N\,II}]/\mathrm{H}\alpha = 0.338 \pm 0.007$. The $[\mathrm{N\,II}]/\mathrm{H}\alpha$ line ratio can be used to obtain the metallicity of our star-forming galaxies (oxygen abundance), $[12 + \log(\mathrm{O/H})]$, by using the conversion of Pettini & Pagel (2004): $12 + \log(\mathrm{O/H}) = 8.9 + 0.57 \log([\mathrm{N\,II}]/\mathrm{H}\alpha)$. The galaxies in our full sample (without excluding AGN) have a median metallicity of 8.632 ± 0.005, which is consistent with solar (8.66 ± 0.05), but we note that we are sampling galaxies with a range of masses, and thus we need to take that into account when properly comparing the samples – this is done in §8.3.6.

Our results reveal that cluster Hα emitters have the highest $[\mathrm{N\,II}]/\mathrm{H}\alpha = 0.443 \pm 0.007$ line ratios. However, AGN typically have high $[\mathrm{N\,II}]/\mathrm{H}\alpha$ line ratios, and it is mandatory to exclude them if metallicities are to be robustly estimated from this line ratio. Nevertheless, even when considering only Hα star-forming galaxies (in the cluster, outskirts or field), we find cluster star-forming galaxies to be significantly metal rich, with a median metallicity $12 + \log(\mathrm{O/H}) = 8.611 \pm 0.004$, which compares with $12 + \log(\mathrm{O/H}) = 8.476 \pm 0.003$ for the cluster outskirts and $12 + \log(\mathrm{O/H}) = 8.433 \pm 0.016$ for outside the cluster. Our results thus clearly indicate that star-forming galaxies in the merging clusters are significantly metal rich, practically solar, being about $\sim 0.15\,\mathrm{dex}$ more metal rich than other star-forming galaxies outside the cluster.

We find that star-forming galaxies in the cluster show significantly higher metallicities than star-forming galaxies in the outskirts or in the field environment, although star-forming
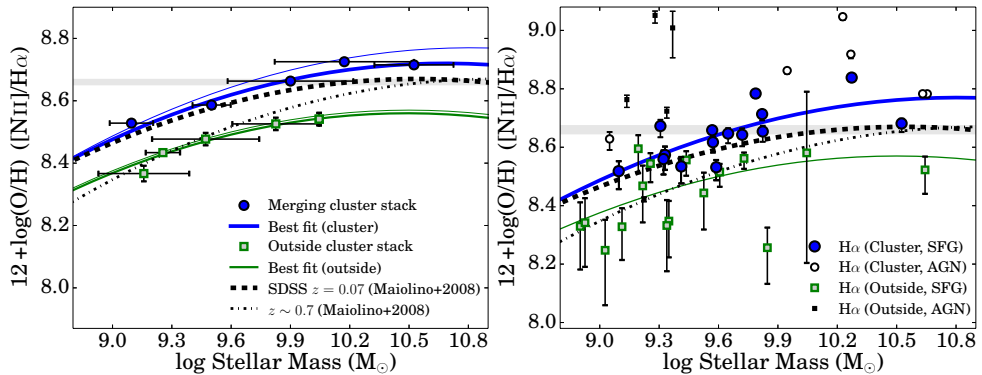
Figure 8.13: The mass metallicity relation for our Hα emitters. Grey lines indicate solar metallicity, for reference. We find a good correlation between (stacked, left panel; individual measurements, right panel) metal abundance (excluding all AGN), traced by [NII]/Hα, and stellar mass of each galaxy, for both Hα emitters in the cluster (within a radius of 1.5 Mpc), and for Hα emitters in our comparison sample, outside the cluster, observed with the same instruments and with the same selection functions. Hα emitters in the cluster are systematically more metal rich at fixed mass than those in the comparison sample, and follow closely the local SDSS mass-metallicity relation, or even higher, particularly at high masses. On the other hand, Hα emitters outside the Sausage cluster reveal some evolution relative to the SDSS $z = 0$ relation (Maiolino et al. 2008, after applying the appropriate corrections for a different metallicity indicator and a different IMF). When directly comparing our sample of Hα emitters in the Sausage cluster and those outside the cluster, we find a systematic offset of about 0.2 dex, which gets tentatively higher for higher stellar masses. This shows that Hα emitters in the Sausage are more metal rich.

galaxies in the post-shock regions show an even higher metallicity, fully consistent with solar metallicity. We note, however, that star-forming galaxies in the post-shock regions also have a slightly higher median stellar mass (+0.12 dex), and thus the slightly higher metallicities when compared with the remaining galaxies in the cluster, can be fully explained by the mass-metallicity relation (see §8.3.6). Thus, both sub-samples show a very high metal-enrichment.

We note that star-forming galaxies in the cluster are also slightly more massive, as a whole, than those in the other environments, and thus it is very important to look at the mass-metallicity relation, in order to address whether the higher metallicity is simply a consequence of higher stellar masses, or a genuine higher metallicity even at fixed mass.

8.3.6 The Mass-Metallicity relation for the Sausage merging cluster

Having found that our merging cluster star-forming galaxies have higher metallicities than those in lower density environments, we investigate the mass-metallicity relation. We show our results in Figure 8.13. We find a strong relation between metallicity (here traced by the [NII]/Hα ratio and using the conversion of Pettini & Pagel 2004 for star-forming galaxies) and stellar mass, both when we look at individual sources (Figure 8.13: right panel) and particularly when we look at stacks as a function of stellar mass (Figure 8.13: left panel). We find that Hα emitters in both the cluster and the field have metallicities that correlate with stellar mass. We also show where AGNs would be placed had they not been excluded from our analysis, clearly showing that they would bias the metallicities to higher values. We note that all AGNs were excluded from the metallicity analysis, both for the fits with individual sources and for all the stacks that measured metallicities (the only exceptions are for "full" samples in Table 2, but we make explicit notes that those values are still contaminated by AGN). We also note that because of significant dust extinction on the line of sight, the [OIII] 5007/Hβ ratio is overestimated, thus making our cuts even more conservative in excluding potential AGN.

Our results clearly reveal, both based on the combination of individual measurements, and based on the stacks for each sub-sample, that our merging cluster star-forming galaxies are significantly more metal-rich than those outside the cluster. We find this to be valid for masses higher than $10^9 \, M_\odot$ (for which we are reasonably complete), although the difference seems to be even higher for masses $> 10^{10} \, M_\odot$. We note that this difference, of about 0.15 to 0.2 dex, found at all masses, is based on two fully comparable samples, with the same selection function, same completeness, with the sole difference being the environment in which these star-forming galaxies reside in. We also compute metallicities using the O3N2 indicator (Alloin et al. 1979) and recover similar results. However, measurements based on O3N2 have much lower S/N, due to the high level of dust extinction affecting both [OIII] 5007 and Hβ (up to $\sim$ 3 mag). In addition, because of the difference in wavelength between the two lines ($\sim$ 176 Å), the [OIII] 5007 and Hβ emission lines suffer from different dust extinction values. Therefore, the [OIII] 5007/Hβ line ratio is biased high (average $\sim$ 0.06 dex), while [NII]/Hα ratio provides, in this case, a much better metallicity estimator. With [NII]/Hα we can measure metallicities at much higher S/N, in exactly the same way for our fully comparable samples in and outside the cluster and without the potential biases from dust extinction, as [NII] and Hα are only separated by 20.8 Å.

We also compare our results with those in the literature, particularly with SDSS (Maiolino et al. 2008, after applying the appropriate corrections for a different metallicity indicator and

a different IMF). In practice, we find that star-forming galaxies in the Sausage merging cluster follow the local ($z \sim 0$) mass-metallicity perfectly, even though they are being studied 2.3 Gyr before it was established. On the other hand, star-forming galaxies outside the cluster follow a mass-metallicity relation more applicable to slightly higher redshift galaxies (Maiolino et al. 2008). We also use the parameterisation of Maiolino et al. (2008) to fit our mass-metallicity relations for cluster and star-forming galaxies outside the cluster. The parameterisation is given by: $12 + \log(O/H) = -0.0864 \times (\log M - M_0)^2 + K_0$. For Cluster star-forming galaxies we find $M_0 = 10.68 \pm 0.04$ and $K_0 = 8.72 \pm 0.01$, while for star-forming galaxies outside the cluster the best fit is given by $M_0 = 10.49 \pm 0.14$ and $K_0 = 8.56 \pm 0.03$.

While we find evidence that the Fundamental Metallicity Relation (Mannucci et al. 2010) is somewhat applicable to our data (at all environments), our sample (particularly when split in different environments and only focusing on robust star-forming galaxies) is too small to properly address how these sources fit into the FMR and particularly to attempt to constrain it. However, we note that both samples (cluster and outside the cluster) are very well matched in SFR (see Figure 8.7 and Stroe et al. (2015)), and thus the difference in metallicity for a fixed mass cannot be explained by a typically lower SFR. Nevertheless, it should be noted that the scatter on individual measurements in Figure 8.13 (right panel) seems to be mostly driven, at fixed stellar mass and fixed environment, by SFR.

8.4 Discussion: Shock induced star-formation, cooling or turbulence?

By obtaining high S/N spectra of the bulk of the sample of candidate line emitters in the Sausage cluster, we were able to confirm them as Hα emitters. We find that about 65% are consistent with being powered by star-formation, with about 35% being AGN. We find Hα star-forming galaxies in the cluster to be highly metal-rich and to already follow the SDSS $z \sim 0$ mass metallicity relation. We also find striking evidence of ubiquitous outflows in the majority of our cluster Hα emitters: not only strong P Cygni profiles, mostly in cluster AGN, but also for star-forming galaxies, where we find redshifted emission lines and particularly significantly blue-shifted Na D emission. We find that such outflows are consistent with being driven by AGN for sources with clear AGN activity, while for star-forming galaxies in the cluster, and particularly for those with very high [S$_{II}$]$_{6716}$/Hα, away from the post-shock regions, these are likely driven by supernova. It is also likely that star-forming galaxies in the post-shock region are in a relatively earlier evolution phase compared to those away from it (which are likely in final phase of star-formation, showing the strongest outflows and the strongest evidence for supernova). We argue that the merger must have had a significant effect on all these Hα emitters. This is because the cluster, despite being extremely massive, shows a surprising number of active Hα emitters, but also because all Hα emitters in the cluster show significant differences in their properties to field galaxies.

A requirement for the shock and cluster merger to increase star formation and AGN activity is that the galaxies within the sub-clusters are still relatively gas rich or have at least some remaining amount of relatively cool molecular gas, capable of being turned into stars in a few Myrs, or be accreting such gas at a sufficient rate. The Hα emitters in the 'Sausage' cluster present masses $10^{9-10.7}$ M$_\odot$ and are in general very metal-rich, particularly given their mass,

following the SDSS relation at $z = 0$. Field Hα emitters at the same redshift but outside the cluster show systematically lower metallicities at all masses (see Figure 8.13). The metallicity as measured from nebular lines for the H$_{II}$ regions is essentially solar for cluster star-forming galaxies, suggesting that these Hα emitters are using relatively metal rich gas to form new stars at all stellar masses. What is the source of these reservoirs of gas?

A source of gas would be a reservoir of high-metallicity $Z \sim 0.3$ ICM gas (Leccardi & Molendi 2008), compared to field galaxies which may preferentially accrete low(er)-metallicity gas ($Z \sim 0.01$ at $z \sim 0.2$, Fox 2011) from their inter-galactic (filamentary) medium. Accretion of ICM gas was also proposed as an interpretation for the metal-rich ($Z \sim 1.1Z_\odot$) spirals found in the Virgo cluster (Skillman et al. 1996). By contrast, if we assume the galaxies to be closed-boxes, supernova explosions (SN) of asymptotic giant branch (AGB) stars would enrich the intra-galactic medium with metals and, given the higher-mass of the galaxies and the large potential of the cluster, this gas could be retained and fall back into the galaxies.

A slight elevation of 0.04 dex was also found in the metallicities of a large sample of cluster galaxies, as compared to the field (Ellison et al. 2009) – our results go in the same direction, but we find an even higher offset. Cooper et al. (2008) also find that galaxies at low redshift residing in higher density environments tend to have higher metallicities, at fixed mass, than those in lower density regions, in agreement with our findings. Interestingly, this trend is also being found at higher redshift. By studying an over-density of Hα emitters at $z = 0.8$ with KMOS, Sobral et al. (2013a) find that star-forming galaxies in the high-density group-like or filamentary structure are more metal rich than those in the field. However, the difference can be explained by the fact that galaxies residing in higher density regions are also more massive. On the other hand, and at higher redshift, Kulas et al. (2013) used MOSFIRE to study a "proto-cluster" at $z \sim 2.3$. They also find that galaxies in the proto-cluster environment are, on average, more metal rich than those in the field comparison (which the authors also obtain with the same instrument and set-up, to be fully comparable), particularly for stellar masses of $\sim 10^{10}$ M$_\odot$. Similar results are found by Shimakawa et al. (2015), who study two rich over-densities at $z \sim 2.2$ and $z \sim 2.5$. Shimakawa et al. (2015) find that galaxies residing in over-densities likely have higher metallicities than those in the field sample presented by Erb et al. (2006).

As long as there is some relatively cool gas in cluster galaxies, and even if that gas is relatively unlikely to form stars on its own (e.g. not dense enough/too stable), the passage of a shock wave can likely introduce the turbulence needed for that to happen. Given the shock properties and velocity, the shock is expected to traverse galaxies within a relatively very short timescale of about $10 - 50$ Myr. Hence the shock induces turbulence quickly, which may lead to further gas cooling and collapse of any gas that is still available in the galaxies – although due to the time needed for that to happen, a time delay is expected from the passage of the shock wave to the star-formation episodes. However, the enhancement of star formation and AGN activity following the shock passage can quickly deplete the gas reservoir. This is because while part of the gas fuels SF and goes into stars, we also find evidence of strong outflows in our cluster Hα star-forming galaxies, and also for our Hα cluster AGN: these can easily further remove gas and lead to relatively short depletion times. We therefore expect the passage of the shock to lead to a steep rise in SF for a few $10 - 100$ Myr, followed by a quick quenching of the galaxy and a shut-down in the formation of new stars. Given the evidence for strong outflows and supernova in cluster Hα star-forming galaxies not in the post-shock

region (which may have been affected even longer ago), such galaxies may be in the final phase of quenching. This is a very likely scenario, particularly because the latter are satellites of extremely massive dark matter haloes of $> 10^{15} \, M_\odot$. Therefore, any gas that is expelled from the galaxy by strong outflows will easily be lost to the ICM.

We also note that a high number of our Hα emitters in the Sausage cluster are located near the shock fronts, in the post-shock region, fully consistent with the shock front affecting them 100-200 Myrs ago. At the passage of the shock wave two potentially important things happen: i) firstly, magnetic fields are amplified and aligned and they funnel material to infall only along the field lines (this may have helped sources to accrete ICM gas in some conditions and/or to force gas in the galaxies to become denser) and ii) after the shock passes, turbulence takes over and the fields also get tangled; thus, such conditions (provided galaxies still have some molecular gas) should enhance/promote star formation.

We therefore conclude that whatever process is driving the enhanced star-formation activity in the merging cluster, it will contribute to the build-up of the red sequence, as even though new stars will form, the feedback processes that we see happening will quickly quench any galaxy that still had enough gas to form stars and that was able to cool/accrete gas.

8.5   Conclusions

We presented spectroscopic observations of 83 strong Hα emitters in the "Sausage" merging cluster and in surrounding regions. Our sample, split into cluster, outskirt and field Hα emitters, selected in the same way, and with very high S/N, allows us to unveil the nature and properties of sources, and directly compare them across environment. Our main results are:

- We find that $\sim 35\,\%$ of the cluster Hα emitters are AGN, similar to what is found in the field ($29 \pm 7\%$). We do not find any significant evidence for galaxy-galaxy (major) mergers in our Hα emitters in the cluster, thus ruling out that the elevated activity is due to galaxy-galaxy mergers.

- Cluster star-forming galaxies in the hot X-ray gas and/or in the cluster sub-cores show exceptionally high [S II] 6716, implying very low electron densities ($< 50\times$ lower than all other star-forming galaxies) and/or significant contribution from supernova.

- Cluster star-forming galaxies show evidence of significant outflows (blueshifted NaD, $200 - 600 \, \mathrm{km \, s^{-1}}$), likely driven by supernova. Individual signatures of strong, massive outflows are also found for the cluster Hα AGN, including P Cygni profiles. All cluster star-forming galaxies near the centre of the merging cluster show significant outflows, and thus this will likely lead to star-formation being quenched rapidly.

- Cluster star-forming galaxies are highly metal-rich, roughly solar, and those in the post-shock region are the most metal rich ($12 + \log(\mathrm{O/H}) = 8.632 \pm 0.004$).

- Hα star-forming galaxies in the Sausage merging cluster follow the local Universe mass-metallicity relation. However, Hα star-forming galaxies in the Sausage merging cluster also show systematically higher metallicity ($\sim$0.15-0.2 dex) for $M > 10^9 \, M_\odot$ when directly comparing with our Hα emitters outside the cluster. This suggests that the shock

front may have triggered remaining gas which galaxies were able to retain into forming stars.

Our observations show that the merger of massive ($\sim 10^{15}$ M$_\odot$) clusters can provide the conditions for significant star-formation and AGN activity, but, as we witness strong feedback by star-forming galaxies and AGN (and given how massive the merging cluster is), and particularly because these sources reside in very massive haloes of $> 10^{15}$ M$_\odot$ which will not likely allow galaxies to re-accrete gas, such sources will likely be quenched in a few 100 Myrs.

Acknowledgements

9

Neutral hydrogen gas, past and future star-formation in galaxies in and around the 'Sausage' merging galaxy cluster

CIZA J2242.8+5301 ($z = 0.188$, nicknamed 'Sausage') is an extremely massive ($M_{200} \sim 2.0 \times 10^{15} M_\odot$), merging cluster with shock waves towards its outskirts, which was found to host numerous emission-line galaxies. We performed extremely deep Westerbork Synthesis Radio Telescope HI observations of the 'Sausage' cluster to investigate the effect of the merger and the shocks on the gas reservoirs fuelling present and future star formation (SF) in cluster members. By using spectral stacking, we find that the emission-line galaxies in the 'Sausage' cluster have, on average, as much HI gas as field galaxies (when accounting for the fact cluster galaxies are more massive than the field galaxies), contrary to previous studies. Since the cluster galaxies are more massive than the field spirals, they may have been able to retain their gas during the cluster merger. The large HI reservoirs are expected to be consumed within $\sim 0.75 - 1.0$ Gyr by the vigorous SF and AGN activity and/or driven out by the outflows we observe. We find that the star-formation rate in a large fraction of Hα emission-line cluster galaxies correlates well with the radio broad band emission, tracing supernova remnant emission. This suggests that the cluster galaxies, all located in post-shock regions, may have been undergoing sustained SFR for at least 100 Myr. This fully supports the interpretation proposed by Stroe et al. (2015) and Sobral et al. (2015a) that gas-rich cluster galaxies have been triggered to form stars by the passage of the shock.

9.1 Introduction

Galaxy cluster environments have a profound impact on the evolution of cluster galaxies. At low redshifts ($z < 0.5$) and focusing on relaxed clusters, the fraction of galaxies which are star-forming drops steeply from field environments, to cluster outskirts and cores (Dressler 1980; Balogh et al. 1998; Goto et al. 2003). The morphological transformation of field spirals into cluster ellipticals or S0s has been attributed to a number of processes. The dense intracluster medium (ICM) could lead to the ram pressure stripping of the gas content of field spirals as they accrete onto the cluster (e.g. Gunn & Gott 1972; Fumagalli et al. 2014). Tidal forces produced by gradients in the cluster gravitational potential or by encounters with other galaxies, can distort infalling galaxies, truncate their halo and disk (harassment, Moore et al. 1996) or remove gas contained in the galaxy and deposit it into the ICM (strangulation, Larson et al. 1980). All these processes ultimately lead to the removal of gas and a truncation of star-formation (SF).

The effect of relaxed cluster environments on galaxies is evident using a wide range of diagnostics, which trace different phases and time-scales of SF. Using UV data produced by young OB stars, Owers et al. (2012) found galaxies with star-forming trails, which they attribute to gas compression by the high-pressure merger environment. The UV radiation coming from massive, short-lived stars excites emission lines. Lines such as Hα or [OII]3727Å probe SF on time scales of < 10 Myr. Emission line studies confirm that the fraction of star-forming galaxies increases from cluster cores towards field environments (e.g. Gavazzi et al. 1998; Balogh et al. 1998; Finn et al. 2005; Sobral et al. 2011; Darvish et al. 2014). Using far infra-red data (tracing dust obscured SF), Rawle et al. (2012) find that the fraction of dusty star-forming galaxies, compared to the total star-forming galaxies, increases from low to high densities, an effect they attribute to dust stripping and heating processes caused by the cluster environment. Similar results are found by Koyama et al. (2013).

Synchrotron emission from supernovae traces SF on longer timescales of about 100 Myr (Condon 1992). Deep radio surveys at GHz frequencies indicate that below $100 - 200$ μJy, the number of star-forming galaxies dominates over radio-loud active galactic nuclei (AGN, e.g. Padovani et al. 2011). The number of radio-faint radio star-forming galaxies (Morrison & Owen 2003), in clusters was found to increase with redshift (Morrison 1999). Radio broad-band emission from cluster spirals was also found to be enhanced with respect to field counterparts, an effect which can be caused by compression of the magnetic fields (Gavazzi & Jaffe 1985; Andersen & Owen 1995).

In addition to probes of past or current SF, CO rotational transitions can be used as an excellent tracer of molecular gas, which is the raw fuel for future SF episodes (e.g. Leroy et al. 2008). Other gas phases cannot form stars directly, but they have to cool sufficiently to form cold, dense molecular clouds (see review by Carilli & Walter 2013). However, a conversion factor between the CO mass and the total molecular gas is needed, which is highly uncertain (see review by Bolatto et al. 2013). Instead of using CO or other direct tracers of molecular gas, many studies use neutral hydrogen HI as a proxy for the molecular gas. Relaxed cluster spirals become increasingly more HI deficient towards cluster cores, an effect which does not depend on cluster global properties such as X-ray luminosity, temperature, velocity dispersion, richness or spiral fraction (e.g. Magri et al. 1988; Cayatte et al. 1990; Solanes et al. 2001; Chung et al. 2009). Oosterloo & van Gorkom (2005) and Scott et al.

(2012) have found galaxies with HI tails, knots and filaments, which are possibly caused by ram pressure stripping. Until very recently, HI measurements have been limited to the local Universe ($z \sim 0$). At low redshifts ($z \sim 0.06$), Chengalur et al. (2001) studied the A3128 cluster and found that the average HI mass for emission-line and late-type cluster members is about $(8.6 - 8.7) \times 10^8$ M$_\odot$. They did not find a statistically significant difference between the HI content of emission-line galaxies inside and outside the cluster, but the field spirals contain about two times more HI than their cluster counterparts. Pioneering work by Verheijen et al. (2007), Lah et al. (2007) and Lah et al. (2009) used direct detections and stacking to measure the HI content of cluster galaxies up to $z \sim 0.4$. Verheijen et al. (2007) surveyed two $z \sim 0.2$ clusters with very different morphologies: the relaxed, massive galaxy cluster A963 and the low-mass, diffuse cluster A2192. They detect only one HI galaxy within 1 Mpc of the centre of each cluster. By stacking galaxies with known redshifts, they make a clear detection of HI for blue galaxies outside the clusters, but no such detection was made for cluster galaxies. In a detailed study of the cluster A370 at $z \sim 0.37$, Lah et al. (2007) use spectral stacking to measure HI in gas-rich galaxies lying outside or at the outskirts of the cluster.

As discussed previously, relaxed cluster environments are believed to suppress SF by removing cold gas form their host galaxies. At $z < 0.3$ between $10 - 20$ per cent of clusters are undergoing mergers (Katayama et al. 2003; Sanderson et al. 2009; Hudson et al. 2010) and this fraction is expected to increase steeply beyond $z = 0.4$ (Mann & Ebeling 2012). The effect of cluster mergers on the SF activity and gas content of galaxies is disputed. Most studies find that cluster mergers trigger SF (Miller & Owen 2003; Umeda et al. 2004; Ferrari et al. 2005; Owen et al. 2005; Johnston-Hollitt et al. 2008; Cedrés et al. 2009; Hwang & Lee 2009; Stroe et al. 2014c; Wegner et al. 2015; Stroe et al. 2015; Sobral et al. 2015a), but a few studies find they quench it (e.g. Poggianti et al. 2004) or that they have no direct effect (e.g. Chung et al. 2010).

An interesting subset of clusters are those hosting radio relics, extended patches of diffuse radio emission tracing merger-induced shocks (e.g. Ensslin et al. 1998). The Hα properties of radio-relic clusters Abell 521, CIZA J2242.8+5301 and 1RXS J0603.3+4214 (Umeda et al. 2004; Stroe et al. 2014c, 2015) indicate that the merger and the passage of the shocks lead to a steep SF increase for < 0.5 Gyr. The fast consumption of the gas ultimately quenches the galaxies within a few hundred Myr timescales (Roediger et al. 2014).

The Hα studies of Umeda et al. (2004), Stroe et al. (2014c) and Stroe et al. (2015) are tracing instantaneous (averaged over 10 Myr) SF and little is known about SF on longer timescales and the reservoir of gas that would enable future SF. An excellent test case for studying the gas content of galaxies within merging clusters with shocks is CIZA J2242.8+5301 (Kocevski et al. 2007). For this particular cluster unfortunately, its location in the Galactic plane, prohibits studies of the rest-frame UV or FIR tracing SF on longer timescales, as the emission is dominated by Milky Way dust. However, the rich multi-wavelength data available for the cluster give us an unprecedented detailed view on the interaction of their shock systems with the member galaxies. CIZA J2242.8+5301 is an extremely massive (Jee et al. 2015; Dawson et al. 2015, $M_{200} \sim 2 \times 10^{15} M_\odot$) and X-ray disturbed cluster (Akamatsu & Kawahara 2013; Ogrean et al. 2013a; Ogrean et al. 2014a) which most likely resulted from a head-on collision of two, equal-mass systems (van Weeren et al. 2011b; Dawson et al. 2015). The cluster merger induced relatively strong shocks, which travelled through the ICM, accelerated particles to produce relics towards the north and south of the cluster (van Weeren et al. 2010; Stroe

et al. 2013). There is evidence for a few additional smaller shock fronts throughout the cluster volume (Stroe et al. 2013; Ogrean et al. 2014a). Of particular interest is the northern relic, which earned the cluster the nickname 'Sausage'. The relic, tracing a shock of Mach number $M \sim 3$ (Stroe et al. 2014c), is detected over a spatial extent of ~ 1.5 Mpc in length and up to ~ 150 kpc in width and over a wide radio frequency range (150 MHz -16 GHz; Stroe et al. 2013, 2014c). There is evidence that the merger and the shocks shape the evolution of cluster galaxies. The radio jets are bent into a head-tail morphology aligned with the merger axis of the cluster. This is probably ram pressure caused by the relative motion of galaxies with respect to the ICM (Stroe et al. 2013). The cluster was also found to host a high fraction of $H\alpha$ emitting galaxies (Stroe et al. 2014c, 2015). The cluster galaxies not only exhibit increased SF and AGN activity compared to their field counterparts, but are also more massive, more metal rich and show evidence for outflows likely driven by super-novae (SN) (Sobral et al. 2015a). Stroe et al. (2015) and Sobral et al. (2015a) suggest that these relative massive galaxies (stellar masses of up to $\sim 10^{10.0-10.7}$ $M_\odot$) retained the metal-rich gas, which was triggered to collapse into dense star-forming clouds by the passage of the shocks, travelling at speeds up to ~ 2500 km s^{-1} (Stroe et al. 2014c), in line with simulations by Roediger et al. (2014).

In this paper we focus on the effect of the massive cluster merger and travelling shocks in the 'Sausage' cluster on the HI content of the galaxies, tracing the gas that may fuel future SF. We place this in context of other phases of SF, averaged over short timescales (~ 10 Myr, $H\alpha$ data) and averaged over longer timescales (~ 100 Myr, radio broad band data) SF episodes.

The structure of the paper is as follows: in §9.2 we discuss the observations and the reduction of the HI, optical and broad band data; in §9.3 we discuss the HI detections, stacking, masses and how these correlate with $H\alpha$ and radio luminosities; in §9.4 we discuss the implication of our results for future SF episodes and compare them with other HI studies of clusters. Finally, §9.5 presents a summary of the results, placing them in context of the SF history of the cluster. At the redshift of the 'Sausage' cluster, $z \sim 0.188$, 1 arcsec covers a physical scale of 3.18 kpc and the luminosity distance is $d_L \approx 940$ Mpc. All coordinates are in the J2000 coordinate system. We use a Chabrier (2003) initial mass function (IMF) throughout the paper. We correct measurements from other papers accordingly.

9.2 Observations & Data Reduction

In our analysis, we combine radio spectral line data tracing HI, broad-band radio data, optical imaging and spectroscopy of passive and star-forming galaxies in and around the cluster.

9.2.1 HI data

The 'Sausage' cluster was observed with the Westerbork Synthesis Radio Telescope[1] in the maxi-short configuration during the second half of 2012, for a total of 26 12-h tracks. The observations were taken in 4, slightly-overlapping bands of 10 MHz each and central frequencies 1180, 1188, 1995 and 1203 MHz, respectively, therefore fully covering the $1175 - 1208$ MHz range. Re-circulation was used to have 512 channels per band (with XX and YY polarisations only). Sources CTD93 and 3C 147 were used as flux calibrators.

---

[1] http://www.astron.nl/radio-observatory/astronomers/observing-wsrt/observing-wsrt

Table 9.1: Details of the JVLA observations of the 'Sausage' cluster taken in L band (1.5 GHz), combining all four configurations of the telescope for a total of > 26 h of observing time.

	L-band A-array	L-band B-array	L-band C-array	L-band D-array
Observation dates	May 11, 2014	Oct 31, 2013	Sep 2, 2013; Jul 3, 2013	Feb 3, 2013; Jan 31, 2013; Jan 27, 2013
Total used on source time (h)	~ 6.5	~ 6.5	~ 10	~ 3.5
Integration time (s)	1	3	5	5

Table 9.2: Number of sources with spectroscopic data, separated by galaxy type. Not all spectroscopic sources are covered by the redshift range of the HI observations.

Sample	Total number	Sources within HI z range	Reference
Emission line, field	39	22	Sobral et al. (2015a); Stroe et al. (2015)
Emission line, cluster	54	45	Sobral et al. (2015a); Stroe et al. (2015)
Cluster star-forming	48	39	Sobral et al. (2015a)
Cluster AGN	6	6	Sobral et al. (2015a)
All emission-line	93	67	Sobral et al. (2015a); Stroe et al. (2015)
Passive, cluster	184	154	Dawson et al. (2015)
All	277	221	

The velocity resolution (after Hanning smoothing), at the redshift of the cluster, is about 20 km s^{-1}, sampled a channel width of ~ 9.9 km s^{-1}. The velocity range covered is about 4700 km s^{-1}, corresponding to an HI redshift range of $0.184 - 0.199$. The redshift range covers the cluster volume within -1σ to $+3\sigma$ of the cluster redshift $z = 0.188$, where $\sigma = 0.04$ is the cluster velocity dispersion (Dawson et al. 2015). The HI observations cover well the distribution of the Hα emitting galaxies ($z = 0.190 \pm 0.010$; Sobral et al. 2015a).

Significant radio frequency interference (RFI) is known to be present at the WSRT at frequencies covering the HI redshift range of 0.1 to 0.25, caused by geo-positional systems such as GPS and GLONASS. However, at the time of our observations, the frequencies corresponding to the redshift of the cluster ($1185 - 1200$ MHz) were still fairly free of such RFI. With the foreseen deployment of the GALILEO geo-positional system, the situation in this frequency range will worsen dramatically in the near future.

To remove any residual RFI, we performed our RFI flagging on the Stokes Q (i.e. XX-YY) component on the data. Given the polarised nature of RFI, this removed most of the astronomical signal, but left the RFI mostly intact. The flags found for Stokes Q were then applied to original XX and YY visibilities. Moreover, because the RFI in our data is broad band, before flagging we performed a smoothing in frequency to enhance the 'sensitivity' for RFI. These procedures worked very well and the final data cubes do not show any effects of residual RFI, while the noise level (75 μJy beam^{-1} over 20 km s^{-1}) is very close to what is expected for the integration time.

Once the data were flagged, we applied standard calibration procedures to the data using the miriad software (Sault et al. 1995). The continuum emission was removed from the data by fitting, to all channels, a 3rd order polynomial to each visibility spectrum ('uvlin'). The choice of the order depends on out to which radius there are significant continuum sources and on bandwidth. The higher the order, the better the sources are removed, however the noise, after subtraction, increases. A 3rd order polynomial fit represents a compromise between sufficient removal of the continuum and little increase in the noise level of the line cube, as shown by Sault (1994). Because this does not take into account the presence of any possible HI emission, the spectra of individual detections, and of the stacked spectra we discuss below, are corrected for this over-subtraction (see Section 9.3.3).

The synthesised beam of the WSRT observations is 24.9×18.5 arcsec^2 at a position angle of 165.8°, or 79.3×58.9 kpc^2.

9.2.2 Optical imaging and spectroscopy

In order to locate the spatial and velocity position of the HI signal, we use the Keck and William Herschel Telescope spectroscopy. Data of both passive and star-forming galaxies in the field of the cluster were presented in Sobral et al. (2015a), Dawson et al. (2015) and Stroe et al. (2015).

Galaxies are categorised as passive or emission-line based on spectral features. Emission line galaxies were selected through the presence of the Hα emission-line (with a Hα+[NII] rest-frame equivalent width larger than 13Å), tracing hot ionised gas, indicating the presence of SF and/or radio-quiet AGN (broad and narrow line AGN). The spectra of passive galaxies display Balmer absorption features and/or no Balmer series emission lines. The passive galaxies are undetected in Hα at the 13 Å level equivalent width level. The sample was divided into three categories:

1. passive galaxies inside the cluster,

2. emission-line galaxies within the cluster,

3. emission-line galaxies in the field around the cluster.

The number of sources in each sub-sample can be found in Table 9.2. The emission-line galaxy sample is dominated by star-forming galaxies with a $\sim 20 - 30$ per cent contribution from broad and narrow line optical AGN (see Table 9.2; Sobral et al. 2015a). The cluster members were chosen to be located at a projected distance of less than 1.85 Mpc away from the cluster 'centre', in line with the definition of cluster membership from Stroe et al. (2015). Line-emission galaxies outside the cluster were defined to lie outside of the 1.85 Mpc radius. The redshift distribution of the galaxies is plotted in Figure 9.1. We note that, as shown by Sobral et al. (2015a), the samples of cluster and field line emitters are selected uniformly, down to a similar star-formation rate (SFR).

The spectroscopy is supplemented with Subaru, Canada-France-Hawaii, William Herschel Telescope and Isaac Newton Telescope broad band (BB) and narrow-band (NB) imaging tracing the Hα emission-line in galaxies at the cluster redshift (Stroe et al. 2015). Hα luminosities for each source were calculated using the excess of NB emission compared to the i BB filter (for method and details see Stroe et al. 2015). In the analysis, we also employ stellar masses derived using the method described in Sobral et al. (2015a).

9.2.3 Broad-band radio data

We identified radio counterparts to the optical sources by cross-matching with a deep, high resolution (~ 1.5 arcsec) image of the cluster, centred at 1.5 GHz, produced using the upgraded Jansky Very Large Array.

Deep JVLA observations of the cluster were taken in the $1 - 2$ GHz L-band in A, B, C, and D-array configurations. An overview of the observations is given the Table 9.1. In total, 16 spectral windows with 64 channels, each covering 64 MHz of bandwidth, were recorded. The data reduction for each observing run was carried out separately, using `CASA`[2] version 4.2.
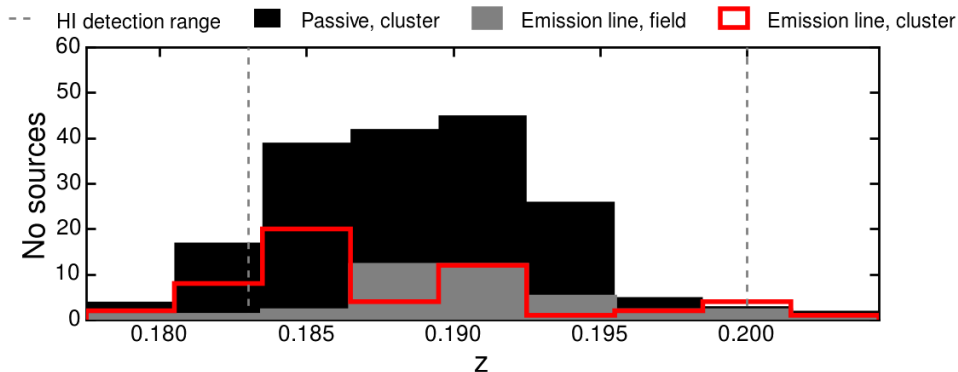
---

[2]http://casa.nrao.edu

Figure 9.1: Redshift distribution of sources in each galaxy sample (emission-line cluster members, emission-line field galaxies and cluster passive galaxies). The HI redshift coverage of the WSRT data is marked by the vertical dashed lines.

As a first step, the data was Hanning-smoothed and corrections for the antenna positions and elevation dependent gains were applied. We then obtained an approximate bandpass solution using observations on the primary calibrators (3C147, 3C138). We applied the bandpass solutions to the data and flagged RFI in an automated way using the `AOFlagger` (Offringa et al. 2010). This initial bandpass correction was performed to avoid flagging of data due to the bandpass variations across the spectral windows. After flagging, we obtained gain corrections on the primary calibrators using 5 channels centred at channel 30. These gain solutions were obtained to remove the time-varying gains. We pre-applied these solutions to find delay terms and bandpass solutions. We then re-determined the gain solutions but now using the full channel range pre-applying the bandpass and delay corrections. We then pre-applied these solutions to obtain gain solutions on our secondary calibrator J0542+4951. The cross-hand delays were solved for using the calibrator 3C 138. The channel dependent polarization leakage terms and polarization angles were set using 3C 147 and 3C 138, respectively. For observing runs longer than four hours the leakage terms were determined from scans on the secondary calibrator J0542+4951[3].

We bootstrapped the flux-scale from our primary calibrator observations to find the flux-density of J0542+4951. The flux-scale was set using the default settings of the task `setjy`. As a final step, the calibration tables were applied to the target data. We averaged the target field data by a factor of 3 in time and frequency, to reduce the data volume for imaging.

In the next steps, the calibration solutions were refined using several cycles of phase-only and amplitude and phase self-calibration. For the imaging we employed w-projection (Cornwell et al. 2008, 2005) and MS-MFS clean (Rau & Cornwell 2011) with `nterms=3`. Clean boxes were set by running the Python Blob Detection and Source Measurement (`PyBDSM`[4]). A few additional clean regions were added manually for diffuse sources.

After self-calibrating the individual datasets, we combined all the datasets to make one deep image. Two more rounds of amplitude and phase self-calibration (on a 1 h timescale) were carried out on the combined dataset. During the self-calibration the amplitude scale

---

[3] The polarization results will be discussed in a forthcoming paper (van Weeren et al. in prep.)

[4] http://dl.dropboxusercontent.com/u/1948170/html/index.html

Table 9.3: Properties of the direct detections. The positional uncertainties are 15 arcsec, the error in the redshifts is 0.0005 and the error in the HI mass about $0.4 \cdot 10^9$ M$_\odot$. The stellar masses reported are for the closest face-on spiral found within 7 arcsec.

RA	DEC	z	M_{HI}	$M_\star$	$M_{HI}/M_\star$
(h m s)	(° ′ ″)		(10^9 M$_\odot$)	(10^9 M$_\odot$)	
22 41 51.1	52 52 55	0.18893	2.1	2.0	1.0
22 42 56.5	52 57 21	0.18916	2.6	*	–
22 43 14.3	53 04 57	0.18536	1.2	9.7	0.1
22 43 23.2	53 04 41	0.18536	2.2	**	–
22 41 30.4	53 05 58	0.18486	1.7	**	–
22 43 43.7	53 09 43	0.18994	1.6	7.9	0.2

* A bright star overlaps the position of the galaxy, so no reliable counterpart can be found.
* No face-on spiral was found nearby the HI detection indicating the detection is spurious.

was allowed to drift freely. This was needed to fully align the different datasets and spectral windows and avoid strong artefacts around a few bright sources located in the field of view (FOV)[5]. We made a final image using Briggs (`robust=0`) weighting and corrected for the primary beam attenuation. We checked the flux-scale of the image against our previous 1.38 GHz WSRT observations of the cluster (van Weeren et al. 2010; Stroe et al. 2013). This was done by checking the integrated fluxes of 10 sources and scaling the fluxes from 1.4 to 1.5 GHz assuming a spectral index of −0.7, the canonical spectral index for bright radio sources (e.g. Condon 1992). The JVLA fluxes were divided by a correction factor of 1.4 ± 0.1 to re-align the flux-scale to the WSRT scales. The resolution of the VLA image is 1.5 arcsec ×1.4 arcsec, with a position angle of 86.5 degrees.

9.3 Results

9.3.1 Direct detections

Six galaxies are tentatively detected in HI. The detection criterion is signal above 5σ over at least two consecutive channels. Table 9.3 lists the redshifts and HI masses of the direct detections. The narrow HI profiles (~ 40 km s^{-1}) of the directly detected sources indicates, if real, they are most probably oriented in the plane of the sky. For a given HI mass, the peak flux for a face on galaxy is higher than for an edge-on galaxy because the same amount of flux divided up in fewer channels. Therefore, we are biased towards detecting face-on galaxies. However, given the very narrow profiles of these tentative detections, they could also be high noise peaks.

We note that none of the six HI direct detections have counterparts (matches within 10 arcsec) in our spectroscopic data or in the Hα catalogue. This indicates that the sources have faint Hα emission, below the equivalent width detection threshold (13Å). Their SFR are therefore below ~ 0.35 $M_\odot$ yr^{-1}.

Given the positional accuracy coupled with the large beam of WSRT finding the right optical counterpart is very challenging. A few ($1 - 6$) potential optical hosts are found for the

---

[5]In principle, the global amplitude scale could have been preserved, but such an option is not offered in CASA at the moment.

tentative HI direct detections, but most sources are unresolved and faint (*i* band magnitude on average fainter than 20). Therefore reliable photometric redshifts could not be derived and we cannot confirm them as being located at $z \sim 0.2$. However, even if these sources were $z \sim 0.2$ galaxies, they would have small stellar masses. For example, using the closest optical match as galaxy host, we find that their stellar masses are very small ($< 1 \times 10^9 M_\odot$). This would imply unrealistically high gas to stellar mass ratios. Additionally, the morphology of these close optical sources does not match face-on spiral galaxies, as we expect. These arguments indicate that the closest sources are not the correct matches. For three out of the six HI detections there are large, face-on spiral galaxies in their vicinity (within 7 arcsec), which could be the correct optical counterpart. These three galaxies have stellar masses of $\sim (2 - 10) \times 10^9 \ M_\odot$, which indicates $0.1 - 1$ atomic gas to stellar fractions. For two detections only small sources are located in the vicinity and no obvious face-on galaxies are found nearby the HI, indicating these are spurious detections (noise peaks in adjacent channels mimicking a signal). In one case, a bright star located at the location of the HI detection prevent correct optical identification.

9.3.2   HI stacking

Since only six galaxies were directly detected, we use spectral stacking to measure the average HI content of the galaxy samples.

We use the optical positions to extract radio spectra for each galaxy, summing the flux within an elliptical aperture equal to the FWHM of the synthesised beam (24.9×18.5 arcsec^2). This corresponds to a spatial scale of 79.3×58.8 kpc^2, matched to the physical size of the galaxies, which at $z \sim 0.19$ are unresolved in the HI observations (Verheijen et al. 2007) (also in line with the galaxy sizes presented in Stroe et al. 2014c, 2015). We further tested the effect of the aperture size on the final stack using apertures of sizes ranging from 0.1 of the FWHM up to 2 times the FWHM.

To test the effect of aperture size on the final HI stack, we use elliptical apertures in size equal to a fraction of the FWHM on both the width and height of the synthesised beam. We use apertures from 0.1 to 2 times the FWHM of the radio beam. We follow the procedure described in § 9.3.2 to extract spectra at the positions of the cluster emission-line members. We find that the peak of the HI detection remains relatively stable if the aperture is at least 0.9 of the FWHM size (see top panel, Figure 9.2).

For each aperture size (from 0.1 to 2.0 times the FWHM of the radio beam, see Figure 9.2), we also measure the HI mass in the way described in §9.3. As shown in the bottom panel of Figure 9.2, we find that the HI mass is relatively stable as function of aperture, but it peaks when the size of the aperture is equal to the FWHM of the synthesised beam. The FWHM size of WSRT is also well matched to the expected HI disk size of galaxies at $z \sim 0.19$ (Verheijen et al. 2007). We therefore choose to measure HI quantities within apertures equal to the FWHM of the synthesised beam.

We extract spectra for all galaxies whose redshift falls within the HI redshift range probed by our WSRT observations ($0.184 < z < 0.199$). To study the noise properties, we extract spectra in sky positions shifted by -60 arcsec in the RA direction, but using the same redshifts as the sample of galaxies. This method captures the effect of increasing noise towards the edges of the bandpass. Note however that the noise could be overestimated. Given the
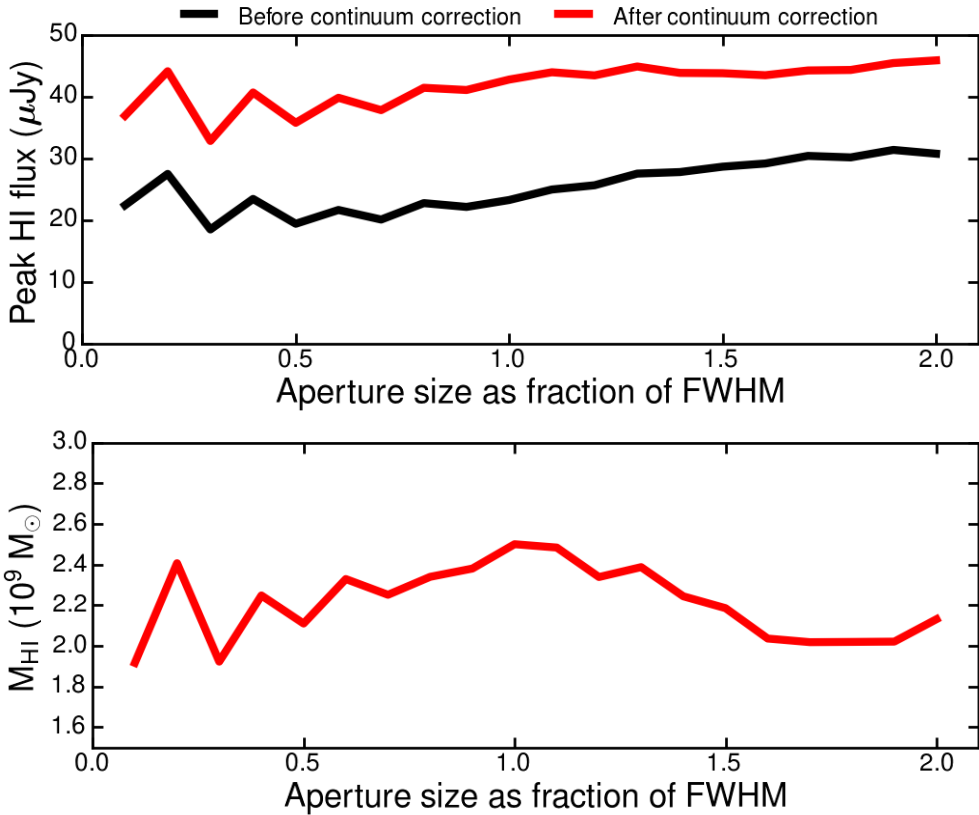
Figure 9.2: Top: HI peak emission flux in the cluster line emitter stack as function of the aperture size used for extracting the individual spectra. The horizontal scale indicates the fraction by which the aperture width and height are scaled as a function of the FWHM. The trend in the peak emission does not change before and after correcting for the continuum over-subtraction (see §9.3.3). Bottom: Average HI mass of cluster line emitters (see §9.3), as function of the aperture size used for extracting the individual spectra. The horizontal scale indicates the fraction by which the aperture width and height are scaled as a function of the FWHM.

large source density of the cluster field, a shift in sky position does not guarantee we will be measuring pure noise, but some apertures could partially fall on undetected source.

Before stacking, we correct the galaxy and noise spectra for the WSRT primary beam, which is a function of distance from the pointing centre and observing frequency:

$$A(r, \nu) = \cos^6(c\nu r) \tag{9.1}$$

where $c = 68$ is a constant, r is the distance from the pointing center in degrees and ν is the observing frequency in GHz. By correcting for the primary beam, we account for the effect of noise increasing towards the FOV edges in both the galaxy and their associated noise spectra.

The spectra are then shifted to the rest-frame velocity using their spectroscopic redshift. We use the radio definition of velocity: $V = c(\nu_{HI} - \nu_{observed})/\nu_{HI}$, where c is the speed of light, ν_{HI} is the restframe frequency of HI and $\nu_{observed}$ is the observing frequency. The galaxy spectra and the noise spectra are co-added using a weight based on the primary beam ($\propto A^2(r, \nu)$), which accounts for the fact that the noise for galaxies away from the field centre is larger in proportion to the primary beam. To obtain the correct flux density scale, we normalise the stacked spectrum by the integral of the synthesised beam, integrated over the same spatial region used for extracting the galaxy spectra.

After stacking and normalising the spectra, we filter the data using a second-order Savitzky-Golay filter (SG; Savitzky & Golay 1964), which convolves the data with a polynomial filter. Given that our line profiles are resolved (FWHM of the stacks with detection are > 150 km s^{-1}, compared to a channel width of > 20 km s^{-1}, see Table 9.4), the method reduces the noise, while preserving line profiles (see for example Morabito et al. 2014). We tested the method using different window sizes. The effect of the SG filtering with increasing window lengths is shown in Figure 9.3. Out of the window size tested, we finally choose a filter window of ~ 300 km s^{-1}, which provides minimal noise, while preserving the width and height of the signal, thus maximising the signal to noise of the possible HI detection peaks. We also tested other smoothing kernels (e.g. moving boxcar), which resulted is similar results, but with a widening of the profile and reduction of the peak strength.

Separate stacks are produced for the sample of passive cluster galaxies, line emission cluster members and line emission galaxies located within the field environment around the cluster. Line emitters include both star-forming galaxies and optical AGN (see also § 9.2.2). Finally, we produce a master stack of all the galaxies available. The number of galaxies per each velocity channel for each stack is shown in Figure 9.4 and Table 9.4. The number of sources in the stack naturally peaks at the 0-velocity position, but dwindles towards higher relative velocities. This effect is governed by where the redshift of each source falls within the WSRT HI bandpass. Due to extensive spectroscopy from Keck aimed at obtaining a dynamical analysis of the cluster that specifically targeted the red sequence, the number of passive cluster galaxies far outnumbers the number of emission-line galaxies.

The asymmetry (about the central position) in the number of sources for which data exists, especially visible in the passive cluster galaxy sample, is caused by the discrepancy in the nominal redshift of the cluster ($z = 0.188$, recently derived from more than 200 spectra by Dawson et al. 2015) and the outdated $z = 0.192$ (Kocevski et al. 2007) which was used for creating the WSRT HI setup. Our spectroscopic measurements are therefore biased towards lower redshifts, compared to the HI coverage of the WSRT data (see §9.2.2 and Figure 9.1). If a redshift of a source falls at the middle of the WSRT HI band coverage, the frequency
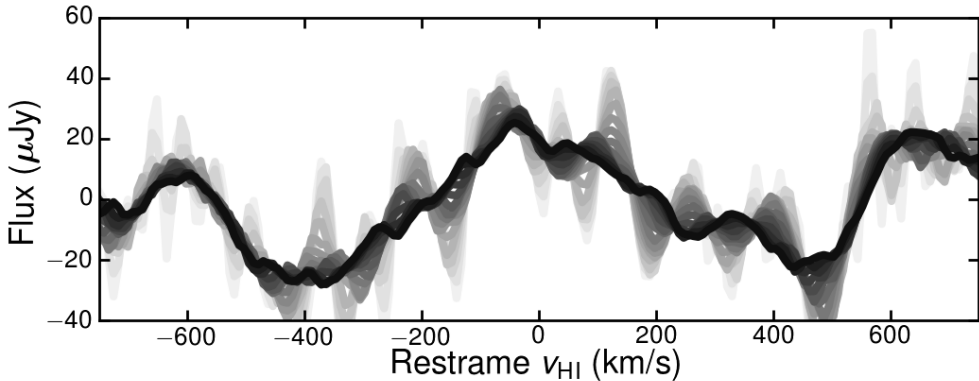
Figure 9.3: Noise reducing properties of the Savitzky-Golay filter with increasing filter window width demonstrated on the cluster member galaxy stack. Colours of the lines go from lighter to darker shades in increasing window length. The black line at the foreground of the figure is smoother spectrum after applying the final window length choice, ~ 300 km s^{-1}, which is also the one we finally applied to the data. Similar results are obtained for the galaxy stacks, as well as their associated noise stacks.

coverage is symmetric about the observed frequency of the HI. However, a lower redshift (than the central redshift) is equivalent to a source having a wider frequency coverage at frequencies lower than the HI and a narrower coverage at higher frequencies. When translating to a rest-frame velocity, there is a preferential data coverage of the positive restframe velocities. The missing data at larger absolute restframe velocities drives the noise to higher values in those regions.

9.3.3 Correcting for the over-subtracted continuum emission

As mentioned previously, the bulk of our galaxies do not have a direct detection of the HI line. Hence, the continuum emission subtraction (see §9.2.1) could not take into account the presence of HI emission and leads to an over-subtraction of the continuum where the putative HI line is located. The over-subtraction is not visible (and relevant) in the individual spectra, but it shows up in the stacked spectrum. As expected, the over-correction of the continuum is evident in the case of the emission-line galaxy samples, where the HI signal is located on top of a broad, negative dip. No evident negative trough is present in the passive member sample, where less HI is expected.

We apply a two step process to correct for the over-subtraction of the continuum. Firstly, to measure the possible extent of the HI in the Hα galaxies, we fit Gaussian profiles to their stacked profiles. We select data at least $4\sigma_{\text{Gauss}}$ away from the peak of the Gaussian, where σ_{Gauss} is the dispersion of Gaussian profile. Additionally, we discard the data at relative restframe velocities higher than 1000 km s^{-}1. These cuts are employed to exclude any HI signal from the estimation of the continuum, but not include very noise edge channels, where only a few galaxies are stacked (see Figure 9.4). In the case of the passive members, a similar procedure is applied, but since we do not have a clear detection of emission, the velocity range between 250 and 1000 km s^{-1} is used.
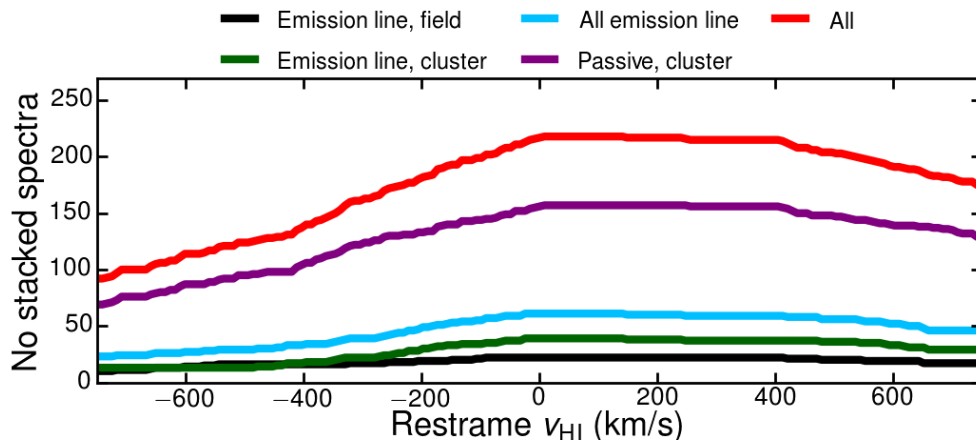
Figure 9.4: Number of sources stacked in each velocity channel, for the separate stacks. The passive cluster galaxy stack (purple line) benefits from a factor of > 5 more sources than the stacks for the Hα line emitters (mostly star-forming and some AGN) galaxies inside (green line) and outside the cluster (black line). Note how the number of sources dwindles towards the edges of the WSRT HI bandpass. The asymmetry in the number of sources is caused by the redshift distribution of the stacked sources (see Figure 9.1), preferentially located at redshifts lower than the central WSRT HI coverage.

We fit the channels free of HI with a 2nd order polynomial and subtract the fit from the data to correct for the over-subtracted continuum (see example in Figure 9.6). The correction is substantial for the cluster Hα line galaxies, but the results indicate that the continuum has not been significantly over-subtracted for passive cluster members and those line emitters located in the field environment.

9.3.4 Measuring the HI signal and its significance

After the stacked spectra are filtered and corrected for the continuum over-subtraction, we fit Gaussian profiles around the 0-velocity position. Results are shown in Figure 9.5. The parameters of the Gaussian fits can be found in Table 9.4. We calculate the RMS from the noise stack. Note that even though the number of galaxies in the cluster and field stacks is similar, the noise levels achieved are a factor of ∼ 4 different. This is because field galaxies are preferentially located at large distances away from the FOV centre, meaning that the noise levels at their location are higher.

In the case of the Hα emission-line galaxies, a clear peak is found around the 0-velocity position and a Gaussian profile could clearly be fit. In the cluster line emitter stack, we reach a noise level σ_{RMS} of 5.9 μJy and detect HI at a peak significance of 7.2σ. The results are virtually unchanged if the 6 AGN are removed from the stack. No clear detection of HI is made in the case of the passive galaxies, despite the much larger number (2.5 times) of galaxies stacked, as compared to the line emitter sample (HI measured with a peak of 5.3 μJy, with a $\sigma_{RMS} = 2.1$ μJy). The velocity position of the putative peak (~ -100 km s^{-1}), highly offset from 0, is likely a spurious peak and also indicative of a non-detection of HI. The high

offset is highly unlikely to be caused by stripping, given we are averaging across 150 passive galaxies within the cluster, which have random motions in the cluster potential. In some of the stacks (e.g. emission cluster galaxy stack and the emission line field galaxy stack), there are additional peaks off-centred from the 0-velocity. In theory, additional peaks in cluster stack, for example, could be caused by tidally stripped tails, pointing in the same redshift direction, such that they add coherently when stacked. However, this is highly unlikely as the cluster galaxies are moving on a range of orbits within the cluster potential. Even if HI tails existed, they would have a variety of orientations. When stacking the galaxies, the tails would therefore not add coherently. Therefore, we believe these to peaks to be caused by noise variations and low-level systematics. Note that at higher restframe velocities, the number of sources for which data exists dwindles (as shown in Figure 9.4). For example, at ±600 km s^{-1}, the number of sources with data in that velocity channel is already half that at velocity 0. That means that the noise at larger restframe velocities will be higher than the noise around the 0-velocity. Therefore the significance of off-center peaks is actually very low (at least a factor $\sqrt{2}$ lower than if located at 0-velocity).

The stack using all the galaxies reaches a very low noise level of 3.1 μJy. The HI signal peaks at a significance of $4.6\sigma_{\mathrm{RMS}}$, value mainly due to the contribution of SF and AGN galaxies.

9.3.5   HI masses

We use the following relation to convert from radio flux S into HI mass (M_{HI}; Wentzel & van Woerden 1959; Roberts 1962):

$$\frac{M_{\mathrm{HI}}}{M_\odot} = \frac{236}{1+z} \left(\frac{D_L}{\mathrm{Mpc}} \right)^2 \left(\frac{\int S_V dV}{\mathrm{mJy\ km\ s^{-1}}} \right), \tag{9.2}$$

where $M_\odot$ is the mass of the Sun, $z = 0.192$ is the mean redshift of the sample of galaxies, $D_L = 940.7$ Mpc is the luminosity distance at that redshift and $\int S_V dV$ is the average of the HI emission over a restframe velocity range. As mentioned in §9.3.2, the velocity is defined as $V = c(\nu_{\mathrm{HI}} - \nu_{\mathrm{observed}})/\nu_{\mathrm{HI}}$.

For the stacks with HI detections (Figure 9.5), the HI mass is averaged over $2\sigma_{\mathrm{Gauss}}$ (2 times the Gaussian dispersion) on either side of the peak position. For the passive population, we use the range within 200 km s^{-1} from 0-velocity position. The error in the HI mass is calculated by propagating the RMS error through equation 9.2, using the same velocity range used for the integration of the signal.

Note that even though we use the filtered stacks to calculate the HI masses, similar results would be obtained even if the original data is used. Although the quality of the spectra improve, the errors on the final HI mass do not heavily depend on the filtering. As shown in equation 9.2, the mass is effectively an integral over the profile. Hence, the effects of SG filtering are reduced because averaging over a velocity range equivalent to smoothing down to a resolution equal to that velocity range.

We find that the average HI mass for the emission-line cluster galaxies ($M_{\mathrm{HI}} = (2.50 \pm 0.62) \times 10^9 M_\odot$) is a factor of 1.3 higher than the mass of cold neutral gas in their field counterparts ($M_{\mathrm{HI}} = (1.86 \pm 1.20) \times 10^9 M_\odot$). However the difference is not significant. Additionally, the cluster galaxies are on average ~ 1.5 times more massive than their field counterparts (see

Table 9.4: Peak number of sources in every stack created for the different galaxy samples, the RMS noise value obtained for each stack and the parameters of the Gaussian fit to the HI signal. HI emission is securely detected, at its peak, in the emission-line galaxy and all galaxy stacks, but not in the cluster passive galaxies. When integrating the HI signal to estimate an HI mass, we obtain clear detections for the line-emitters.

| Sample	Number	σ_{RMS} (μJy)	HI peak (μJy)	Peak significance σ_{RMS}	HI velocity (km s^{-1})	HI width (km s^{-1})	M_{HI} (10^9 M$_\odot$)	$M_\star$ (10^9 M$_\odot$)	$M_{HI}/M_\star$
Emission line, field	22	21.3	60.4	2.8	1.0	69.3	1.86 ± 1.20	4.8 ± 0.8	0.39 ± 0.26
Emission line, cluster	45	5.9	42.7	7.2	4.6	137.0	2.50 ± 0.62	7.4 ± 0.5	0.34 ± 0.09
All emission-line	67	8.2	45.1	5.5	−0.7	104.7	2.00 ± 0.67		
Passive, cluster	154	2.1	5.3	2.5	−97.4	90.1	0.21 ± 0.15	25.6 ± 0.4	< 0.008 ± 0.006
All	221	3.1	14.3	4.6	−29.5	107.0	0.60 ± 0.30		
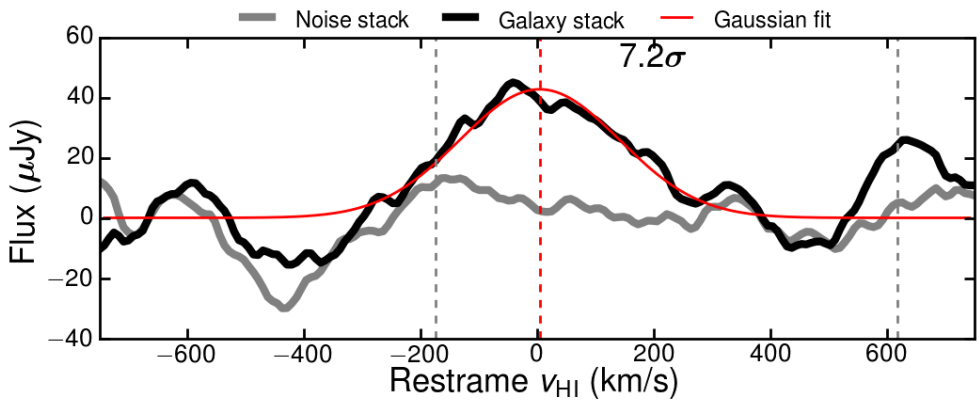
(a) Emission line cluster galaxies.
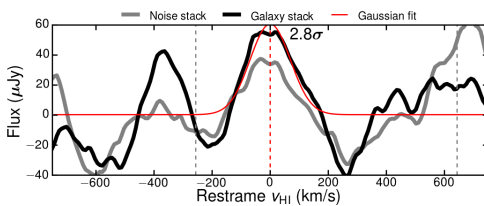
(b) Emission line field galaxies.
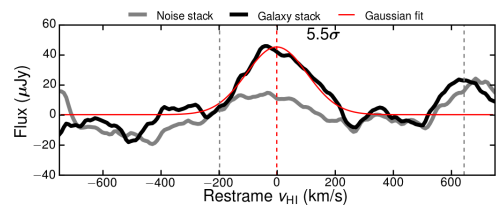
(c) All emission-line galaxies.
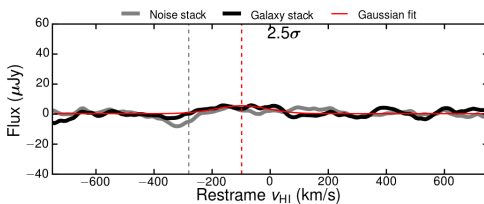
(d) Cluster passive galaxies.
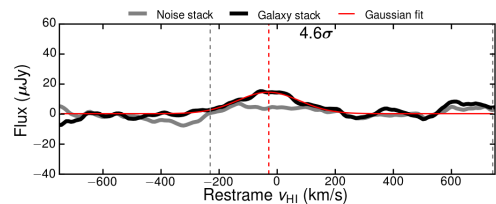
(e) All galaxies.

Figure 9.5: Final HI stacks after filtering and correcting for continuum over-subtraction. The solid black lines show the galaxy stacks and the gray lines show the corresponding noise properties. The thin, solid red lines show the Gaussian fits to the profiles located around a 0 restframe velocity. The vertical, dashed red line show the position of the peak, which is labelled with its significance based on the underlying noise properties. The RMS noise is calculated using only the data between the vertical, dashed gray lines, where at least 80% of the peak number of sources are stacked. Note clear detections of HI are made for the line emitters, while no detections are made in the case of the cluster passive galaxies.
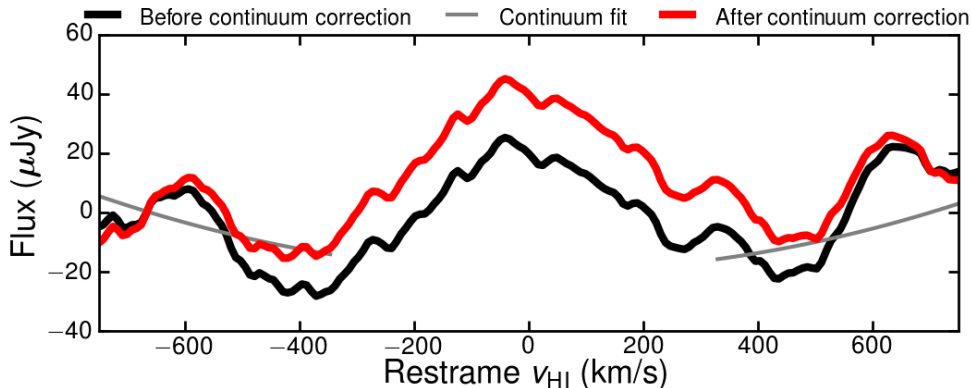
Figure 9.6: Correction for the continuum over-subtraction in the case of the cluster line emitter HI stack.

also Table 9.5). The average stellar masses ($M_\star$) are calculated over the same galaxies stacked for the HI analysis and the error reported is the standard deviation of the sample. Therefore, when accounting for the differences in stellar masses between the cluster and the field galaxies, the cluster line emitters are consistent with being as gas rich as the field counterparts. The fraction of neutral atomic gas to stellar mass $M_{\mathrm{HI}} / M_\star$ is 0.39 ± 0.26 and 0.34 ± 0.09 for field and cluster galaxies, respectively. This is a surprising result, as cluster galaxies have been found to contain less HI than galaxies in the field (e.g. Solanes et al. 2001).

The HI masses of the directly detected sources (Table 9.3) are in the same range as the values for the average emission-line stacks (Table 9.4). However, we do not directly detect any of the emission-line systems. This indicates that we are biased towards detecting face-on sources, while the galaxies used for stacking have random orientation (with the bulk being oblique to edge on).

Within our noise limits, we do not detect any significant HI within the passive cluster galaxy population ($M_{\mathrm{HI}} = (0.21 \pm 0.15) \times 10^9 M_\odot$). The passive population has at least nine times less HI gas than field line emitters (although not statistically significant) and about 12 times less than the cluster star-forming galaxies and AGNs (2.8σ significance, where σ is calculated as the errors on the passive galaxy mass and the cluster line emitter mass, added in quadrature). Note, however, that the velocity range used for the integration of the HI signal is larger for the passive cluster members than what was used for the line-emitters. The cluster emission-line systems have on average much lower masses compared to the passive galaxies. Therefore, the ratio of HI to stellar mass for the passive cluster galaxies is less than 0.008, a factor of~ 30 times lower than the cluster line emitters. Taking into account the errors on the gas fractions for the two populations summed in quadrature, the difference between the gas fraction in passive and cluster active galaxies is significant at the 4σ level.

9.3.6 Hα - HI correlation

We compare the amount of cold gas and ionised content in each galaxy stack by investigating their Hα ($L_{\mathrm{H}\alpha}$) and HI (L_{HI}) luminosities.

The HI luminosity is calculated from the peak flux. The Hα luminosity is calculated from

Table 9.5: Optical properties of each galaxy stack. The average Hα luminosities for each stack are calculated from data from Stroe et al. (2015). The SFRs are calculated using the (Kennicutt 1998) conversion. Stellar masses are obtained using the method from Sobral et al. (2015a).

Sample	Number	$\log_{10}(L_{H\alpha})$ (erg s^{-1})	SFR ($M_\odot$ yr^{-1})	$M_\star$ (10^9 $M_\odot$)
Emission line, field	22	41.53	1.49	4.8 ± 0.8
Emission line, cluster	45	41.45	1.23	7.4 ± 0.5
Passive, cluster	154	< 40.9	< 0.35	25.6 ± 0.5

the Hα flux estimated from the NB observations (see § 9.2.2), after correcting for extinction by Galactic dust, as well as for 1 mag for intrinsic dust attenuation (Sobral et al. 2012) within each galaxy. We also remove the contribution of the adjacent [NII] line from the line flux (for details please see Stroe et al. 2014c, 2015). We average the corrected Hα luminosities for galaxies within each stack to obtain a mean value for the ionised gas content as function of galaxy type.

The luminosities are calculated in the following way:

$$L_{HI,H\alpha} = 4\pi d_L F_{HI,H\alpha} \tag{9.3}$$

where F is the Hα total flux and HI peak flux, respectively and $d_L = 940$ Mpc is the luminosity distance at the redshift of the cluster.

The Hα can be converted into a SFR value using the relationship from Kennicutt (1998), which we correct for the Chabrier (2003) IMF, according to Salim et al. (2007):

$$\frac{SFR}{M_\odot yr^{-1}} = \frac{4.4 \times 10^{-42} L_{H\alpha}}{\text{erg s}^{-1}}. \tag{9.4}$$

Note that not all HI stacked galaxies have an Hα flux measurement (see Table 9.6 for numbers). This may be because the sources have too faint Hα line fluxes, below the limits of our NB Hα survey. To test how the full HI sample differs from the HI sample with Hα measurements, we followed the procedure outlined in §9.3.2-9.3.4 and stacked only the HI sources with Hα measurements. We find that the peak HI fluxes and the average HI masses for subsamples with Hα counterparts matches their parent sample within the error. Therefore, the subsamples with Hα measurements are representative of the parent sample. Given the more robust measurement of the average HI properties for the full HI samples (driven by the higher number statistics), in comparing the Hα and HI properties, we use average HI properties derived for the full samples.

As Figure 9.7 shows, the Hα line emitters tend to be more luminous in HI. This is equivalent to galaxies which are more star-forming possessing larger reservoirs of atomic gas (Figure 9.8).

9.3.7 Hα - radio correlation

We extract sources from the VLA 1.5 GHz image using PyBDSM at the positions of the passive and Hα line emitter galaxies with spectra (for number of sources see Table 9.6). The software
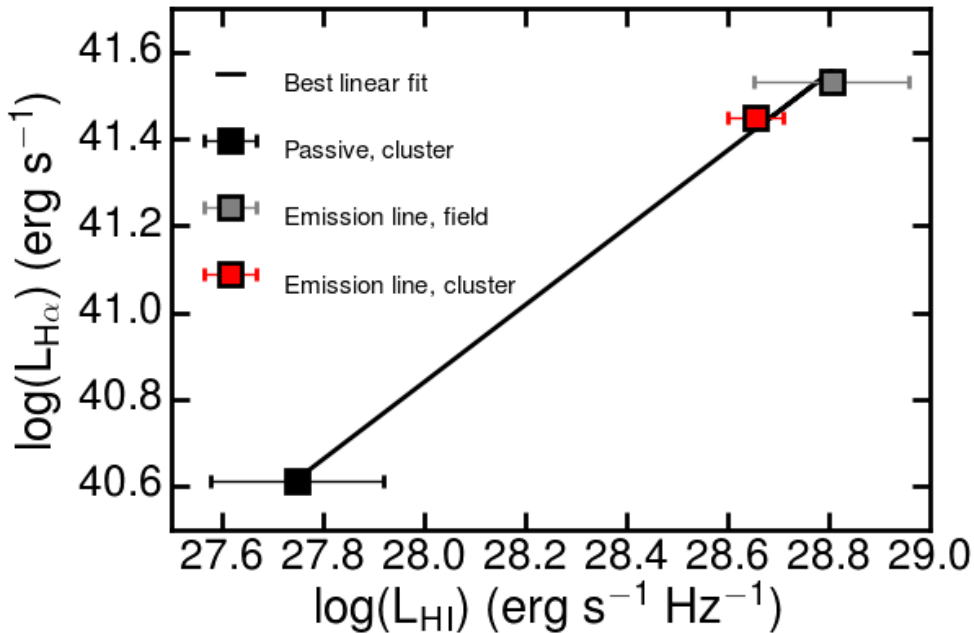
Figure 9.7: Relationship between Hα luminosity and peak HI luminosity. As expected the cluster passive galaxies, selected to be non-line emitters contain less HI than emission-line galaxies. Line emitters are selected to be Hα luminous, indicating the presence of vigorous SF and/or AGN activity.

detects single sources as islands and fits the flux distribution with Gaussians and also calculates the background noise levels using emission-free regions of the sky nearby each source. We assign a source a radio flux density by summing up the flux from all Gaussians belonging to its island. We cross-match radio sources with optical counterparts in our optical spectroscopic catalogue, using a maximum search radius of 5 arcsec, to account for the positional accuracy of the optical and radio images as well as any extent the radio sources may have.

In case a source is not detected in the radio map, we assign it an upper limit flux equivalent to $3\sigma_{RMS}$, where the σ_{RMS} is calculated from the noise level at the position of the source. Note that the FOV of the VLA image is large enough (FWHM of $\sim$ 30 arcmin) that is covers all the optical source positions.

We calculate observed 1.4 GHz measurements from the 1.5 GHz values assuming a -0.7 radio spectral index value, and then convert the values to restframe 1.4 GHz measurements.

A plot showing the relationship between the Hα luminosities and 1.5 GHz luminosities (calculated using equation 9.3) can be found in Figure 9.9. The fluxes of the radio counterparts and their morphologies can be found in the Appendix in Table 9.7. The emission-line galaxies have, on average, 1.5 GHz luminosities $1 - 2$ orders of magnitude lower than the passive galaxies. Interestingly, even though the emission-line cluster members have similar Hα luminosities, and hence SFRs, to the field line emitters, their radio BB detection rate is a factor of > 5 higher. However, for all emission-line sources with radio detections, the Hα luminosity correlates with the amount of radio emission.

9.4 Discussion

Despite being extremely massive ($M_{200} \sim 2 \times 10^{15} M_\odot$, Jee et al. 2015; Dawson et al. 2015) and hot ($T = 6 - 12$ keV, Ogrean et al. 2013a), the 'Sausage' merging cluster hosts numerous massive, Hα emission-line galaxies displaying elevated levels of SF and AGN activity, outflows, high metallicities and low electron densities compared to galaxies in the field (Sobral et al. 2015a; Stroe et al. 2015). In the present study, we find that the emission-line cluster galaxies have similar HI neutral gas fraction as the field galaxies. The data reveal linear correlations of the HI, Hα line emission and radio BB luminosity (Figures 9.7, 9.9, 9.8). By combining tracers of SF on different time scales, HI, Hα and radio BB data, we can understand the circumstances under which the elevated activity can be triggered and also the possible future evolution of the SF properties in the cluster galaxies.

9.4.1 HI & Hα - tracing the gas that fuels future star formation episodes

We make a clear detection of HI for the emission-line cluster galaxies giving an average mass of $(2.50 \pm 0.62) \times 10^9$ M$_\odot$, while the average HI mass for the field galaxies is $(1.86 \pm 1.20) \times 10^9$ M$_\odot$. Stroe et al. (2015) and Sobral et al. (2015a) find that the stellar masses of Hα cluster galaxies are on average higher than their field counterparts. For the samples used in the HI stacks, the cluster galaxies are about 1.5 times more massive than the field line emitters (see Table 9.6).

Note that the cluster and field line emitters are selected in the same way and that the spectroscopic samples are representative of their parent samples (see Sobral et al. 2015a). Therefore the cluster and field emission-line galaxy samples within the 'Sausage' field are fully comparable.

As mentioned in § 9.1, previous studies of the HI content in cluster galaxies find that starforming galaxies become increasingly HI deficient towards cluster cores, when controlling for stellar mass or optical disk size (e.g. Solanes et al. 2001; Verheijen et al. 2007; Lah et al. 2007). Contrary to previous work in the field, we find that our emission-line cluster galaxies are as gas rich as their field counterparts, despite the two samples having similar Hα luminosities and hence similar SFR (see Table 9.5 and Figure 9.7).

The studies of Lah et al. (2009) and Lah et al. (2007) indicate that a cluster at $z \sim 0.37$ and a blank field at $z \sim 0.24$ follow a similar relationship between SFR and HI mass to local field galaxies (Doyle & Drinkwater 2006). Even though our galaxies show evidence for a correlation between the amount of Hα emission (or the SFR) and the HI mass, both the emission-line and passive galaxies do not follow the Doyle & Drinkwater (2006) relationship (see Figure 9.8). The HI masses of our sample are $> 5\sigma$ away from the masses predicted by the relationship at the same SFR. This could be entirely driven by the different SF tracers used in the different studies (Doyle & Drinkwater (2006) use infrared data, Lah et al. (2009) use [OII] and Lah et al. (2007) the Hα emission line) or the spatial or velocity range over which the HI signal was integrated over.

Given the massive cluster galaxies may reside in massive dark matter haloes, they could have retained their cold HI gas more easily during the cluster merger. Interestingly, while spiral galaxies in the Virgo cluster are highly HI deficient, they are not deficient in molecular gas (Kenney & Young 1986, 1989; Stark et al. 1986). The authors attribute this to the preferential stripping of low-density gas located at the galaxy outskirts, therefore not affecting dense
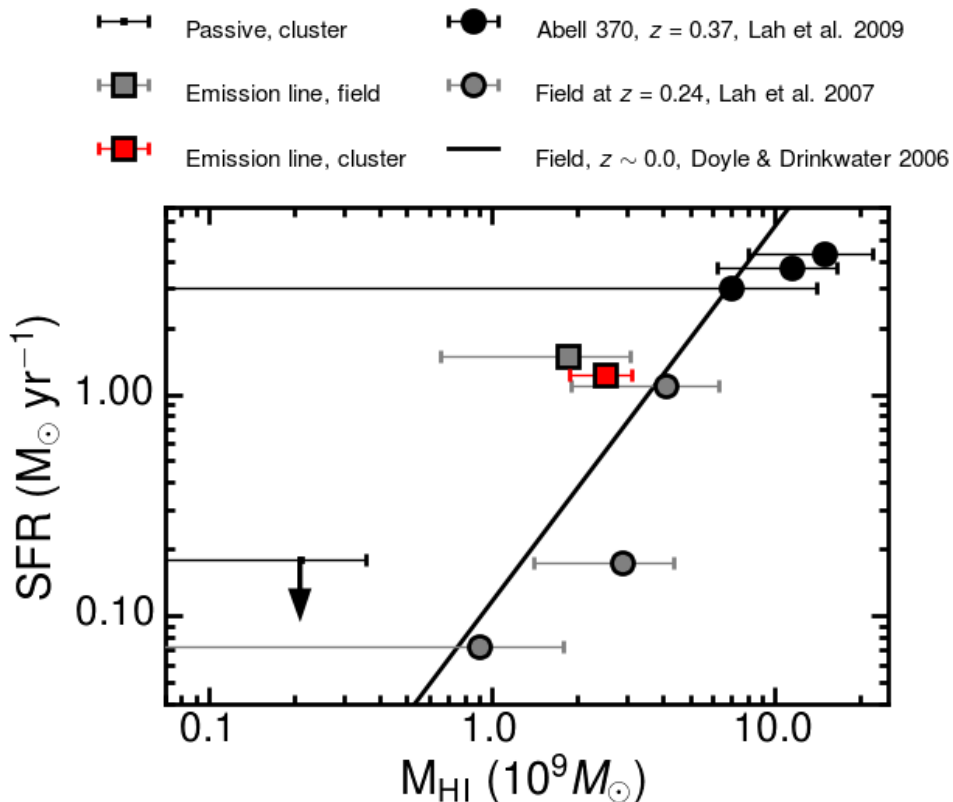
Figure 9.8: Relationship between SFR and integrated HI mass. All SFRs are calculated with a Chabrier IMF. For the passive population, the SFR is an upper limit. Overplotted are the data points for cluster Abell 370 at $z = 0.37$ (Lah et al. 2009) and a blank field at $z = 0.24$ (Lah et al. 2007), together with the SFR-M_{HI} relationship for the local Universe (Doyle & Drinkwater 2006). Note that it is difficult to compare our dataset with other work because of the different ways of measuring the HI mass and the different SF tracers used (Hα, [OII] or IR).

molecular gas located towards the galaxy centre. Therefore, in the case of the 'Sausage' line emitters, with little to no ram pressure stripping of neutral and molecular gas, the larger reservoirs could fuel increased SFR in the cluster galaxies. If the cluster galaxies maintain their current average level of SF ($\sim$ 1.23 $M_\odot$ yr^{-1}, see Table 9.6), and assuming 100% efficiency in converting cold gas into stars, the HI reservoir would be depleted in $\sim$ 2.0 Gyr. If we assume a molecular gas content equal to the HI mass, it would take about $\sim$ 4.0 Gyr to consume the gas. However, as shown in Sobral et al. (2015a), the cluster galaxies also lose gas through outflows. Assuming a maximal mass outflow rate similar to the SFR (Förster Schreiber et al. 2009; Genzel et al. 2011), the HI gas will have been used up in about $\sim$ 1.0 Gyr ($\sim$ 2.0 Gyr if we include molecular gas). Assuming a more realistic outflow rate of about $0.1 - 0.5$ SFR (as observed by Swinbank et al. submitted), the HI gas would be depleted in $1.35 - 1.85$ Gyr, or $2.7 - 3.7$ Gyr if molecular gas is considered. This is in line with calculations from Stroe et al. (2015) where the molecular gas content was estimated using the total stellar mass, but atomic gas was not taken into account.

9.4.2 Radio broad data - tracing the SN emission

As shown by Sullivan et al. (2001), synchrotron radio emission in star-forming galaxies is generated in super-nova remnants (SNR). Given the time required for a $7 - 8$ $M_\odot$ star to evolve to the red giant phase and undergo core-collapse, SNRs are good tracers of SF episodes happening $\sim$ 100 Myr ago (Condon 1992).

In the case of Hα luminous cluster galaxies, undergoing strong SF and optical AGN activity, the Hα luminosity correlates well with the radio BB continuum (see Figure 9.9 and Table 9.7 in the Appendix). The values fall on the same correlation as the large sample ($\sim$ 350) of typical $z = 0.24$, Hα luminous field galaxies studied by Lah et al. (2007) and follow the tight relationship found by Sullivan et al. (2001) for local field galaxies. For both samples, the galaxies classified as purely star-forming or as hosting an optical AGNs follow the Hα - radio correlation. However, the AGN dominated cluster galaxies are expected to posses reasonable amounts of SF, as indicated by the spiral arm patters in many of their hosts (for images see Sobral et al. 2015a). Therefore, the sample includes photoionised broad line and narrow line regions (Sobral et al. 2015a) hosted by spiral galaxies, constituting examples of Seyfert galaxies. Even though some of the cluster galaxies are currently dominated by AGN, they have undergone significant SF activity in the past.

Despite their similar average Hα luminosities, the fraction of Hα luminous cluster members with radio counterparts is a factor > 5 higher than their field counterparts, down to a similar sensitivity limit (see Table 9.6 and Figure 9.9). This is consistent with results from Sobral et al. (2015a) where they found evidence for strong outflows, probably driven by SN, only in the cluster galaxies and not in their field counterparts. Therefore, cluster galaxies have been undergoing SF for at least 100 Myr, while field galaxies have been relatively inactive or less active in the past. Increased SF episodes tens to a few hundred Myr ago triggered by the cluster merger and its associated shock would also lead to higher SN rates. Field galaxies have not undergone any interaction with the shock front, hence in their case, there was no trigger for SN.

Overall, line emission galaxies both inside and outside the 'Sausage' cluster follow the local relationship between Hα and radio emission. Field emission line galaxies from a larger

Table 9.6: As Table 9.5 but only for sources with Hα measurements. Optical and broad-band radio properties of the sources in the line emitter and passive stacks. The average Hα luminosities for each stack are calculated from data from Stroe et al. (2015). The SFRs are calculated using the Kennicutt (1998) conversion, with a Chabrier (2003) IMF.

Sample	Number HI sources with Hα counterparts	$\log_{10}(L_{H\alpha})$[1] (erg s^{-1})	SFR[1] $M_\odot$ yr^{-1}	Number Hα sources	Number Hα sources with radio counterparts	$\log_{10}(L_{H\alpha})$[2] (erg s^{-1})
Emission line, field	20 ($\sim$ 91%)	41.53	1.49	39	3 ($\sim$ 8%)	41.30
Emission line, cluster	29 ($\sim$ 65%)	41.45	1.23	54	24 ($\sim$ 44%)	41.20
Passive, cluster	79 ($\sim$ 51%)	< 40.9	< 0.35	90	11 ($\sim$ 12%)	40.15

[1] Average over the HI stacked sources with Hα counterparts. [2] Average over all spectroscopic sources with Hα measurements.
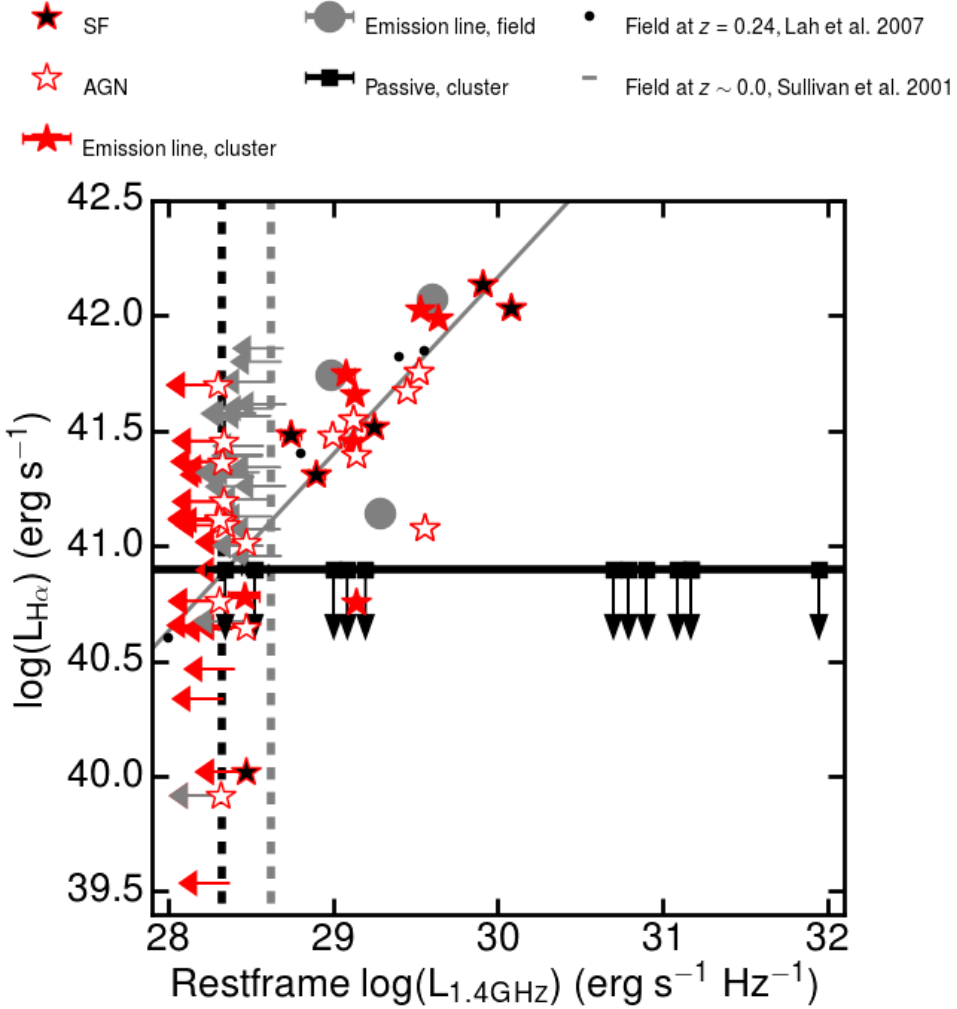
Figure 9.9: Relationship between Hα luminosity and restframe 1.4 GHz radio luminosity. The vertical black dashed line marks the RMS noise at the centre of the radio image, while the gray line represents the detection limit towards the edges of the FOV. The horizontal, solid, black line indicates the detection limit of the Hα NB survey. Passive galaxies, undetected in Hα, are only plotted if they have a detection in the radio. Error bars are plotted but in most cases they are smaller than the symbol size. On average, the galaxies undergoing SF and optical AGN episodes have lower radio luminosities, probably driven by SNRs, while the passive cluster galaxies host powerful jetted and tailed radio sources. It is noteworthy that, in the case of line emission sources with radio detections the Hα luminosity correlates well with the radio luminosity. We overplot for comparison data points for field galaxies at $z = 0.24$ from Lah et al. (2007) and the linear correlation between Hα and radio luminosity for local galaxies found by Sullivan et al. (2001).

sample at $z \sim 0.24$ (~ 150 field galaxies Lah et al. 2007) fall on the same relation. This indicates that the relationship between Hα and BB radio emission does not evolve from $z \sim 0.2$ to the present and that it does not depend on environment. The stellar populations in all galaxies that have been undergoing SF for longer periods (~ 100 Myr), irrespective of redshift or environment, seem to evolve similarly from the massive, short-lived stars which are responsible for producing the bulk of Hα emission to the slightly less massive stars whose explosions dominate the SN population. These results indicate that the star formation history for the 'Sausage' cluster galaxies is relatively constant, without any strong recent (~ 10 Myr) busts of star formation or in the past 100 Myr.

A little bit over 10 per cent of the passive galaxies have a radio BB counterpart, a similar rate to field emission line galaxies, much 4 times lower than the cluster line emitters. The passive cluster members that have radio counterparts are giant ellipticals hosting radio jets and tails as indicated by the radio morphologies and luminosities. By contrast to the emission-line galaxies, where the radio emission is most likely produced by SNR, the radio emission in the elliptical galaxies traces shock-accelerated electrons in the jets and their back-flow (see also the Appendix).

9.4.3 Relationship to cluster merger state and shocks

As the radio BB and Hα data indicate, the 'Sausage' cluster galaxies have been undergoing intense SF and AGN activity for at least 100 Myr and this is likely to last a further ~ 1 Gyr, given the large reservoirs of neutral hydrogen. The SF can last for an another ~ 2 Gyr if comparable amounts of molecular gas are present. However, in the field galaxies around the cluster, we only find evidence of very recent SF episodes (~ 10 Myr). Despite the comparable amounts of HI, the cluster galaxies therefore underwent a significant event triggering SF about ~ 100 Myr ago, evolving differently than their field counterparts. The most significant difference between the cluster and field line emitters is the cluster merger and the passage of the merger-induced shock waves only affected the cluster members.

The 'Sausage' cluster is a result of a massive merger about 0.5 Gyr ago (e.g. van Weeren et al. 2011b), which produced shocks travelling through the ICM at about 2500 km s^{-1} (Stroe et al. 2014c). As the HI data indicate, the massive cluster members seem to have retained most of their neutral gas during the merger. Given their travelling speed, we expect the shocks to have traversed most cluster galaxies about $100-300$ Myr ago. The SF time scale imposed by the radio and optical tracers therefore matches well with the cluster merger time line. Our results fully support the interpretation previously proposed by Stroe et al. (2015) and Sobral et al. (2015a), where the cluster merger induced shocks trigger gas collapse as they traverse the gas rich cluster galaxies. This interpretation is also supported by simulations (Roediger et al. 2014).

9.5 Conclusions

We presented deep HI observations combined with Hα and broad band radio data to study the past, present and future SF activity in the 'Sausage' merging cluster. Our main results are:

- The cluster Hα emission-line galaxies (star-forming and radio-quiet broad and narrow line AGN), selected down to the same SFR limit, have as much HI gas ((2.50 ± 0.62) $\times$

$10^9 M_\odot$) as the field counterparts around the cluster ($(1.84 \pm 1.20) \times 10^9 M_\odot$), when accounting for the different stellar masses of the two samples. This indicates the massive cluster line emitters retained their gas during the cluster merger.

- A stringent upper limit is placed on the average HI content of the passive galaxies in the 'Sausage' cluster: $M_{HI} = (0.21 \pm 0.15) \times 10^9 M_\odot$. The ratio of HI to stellar mass for the passive galaxies is almost 40 times less than for cluster line emitters (significant at 4σ level).

- If the present SF and outflow rate is maintained in the emission-line cluster galaxies, their HI reservoirs will be depleted in $\sim 0.75 - 1.0$ Gyr.

- A large fraction of the emission-line cluster galaxies have radio BB detections, indicating the presence of SNR. These sources have been therefore undergoing vigorous SF for at least 100 Myr.

- The relationship between Hα and radio continuum emission shows no evolution from $z \sim 0.2$ to the present and also no dependence on environment.

Our HI observations represent an important milestone in the study of the 'Sausage' cluster SF history. The member galaxies are gas-rich (gas to stellar mass ratio of ~ 0.34) and thus capable of sustaining the increased SF and AGN activity measured in the cluster.

Acknowledgements

9.6 Appendix

9.6.1 Radio fluxes and morphologies

We tabulate the flux values of the 1.5 GHz VLA counterparts to the spectroscopic sources in Table 9.7. We also describe the morphology of the radio sources. Passive galaxies are hosts to jetted radio AGN, mainly pushed in wide or narrow angle tail morphologies by the interaction with the ICM. Emission line galaxies have mostly disk or spiral-like morphologies, indicating the radio emission is coming star formation.

Table 9.7: Table with the radio fluxes, errors and morphologies of the VLA 1.5 GHz counterparts to the spectroscopic sources. The same sources tabulated here are plotted in Figure 9.9.

RA (deg)	DEC (deg)	Flux (mJy)	Error (mJy)	Morphology
Passive, cluster				
340.6978	53.0939	15.034	0.022	NAT
340.7687	53.1234	0.023	0.006	unresolved
340.6048	52.9719	6.304	0.033	WAT
340.7073	53.0401	0.034	0.007	unresolved
340.8293	53.1228	12.420	0.094	WAT
340.7072	53.0081	5.109	0.125	unresolved
340.7051	53.0920	0.160	0.013	unresolved
340.7191	53.0806	90.106	0.090	tailed
340.7132	53.0139	8.084	0.053	WAT
340.7385	53.1344	0.124	0.008	unresolved
340.7720	52.9552	0.103	0.010	unresolved
Emission line, field				
340.3917	53.0163	0.194	0.014	unresolved
340.6917	52.8561	0.404	0.025	unresolved
340.9183	52.8727	0.097	0.013	unresolved
Emission line, cluster				
340.4575	53.0954	0.138	0.011	unresolved
340.5930	53.0083	0.029	0.006	unresolved
340.6151	52.9683	0.185	0.011	unresolved
340.6518	53.0904	0.073	0.007	unresolved
340.6598	53.0138	0.100	0.010	unresolved
340.6642	52.9674	0.361	0.012	unresolved
340.6711	52.9746	0.817	0.026	disk
340.7136	52.9061	0.133	0.015	disk
340.7225	52.9517	0.080	0.009	unresolved
340.7369	52.9439	0.439	0.015	disk
340.7401	53.0874	0.336	0.022	disk
340.7475	53.0889	0.179	0.017	disk
340.7502	53.0439	0.139	0.010	unresolved
340.7796	52.9257	0.122	0.013	disk
340.7870	53.0902	1.207	0.018	unresolved
340.7941	53.0716	0.135	0.011	disk
340.7985	53.0764	0.055	0.008	unresolved
340.8037	53.0029	0.285	0.016	disk
340.9204	53.0778	0.344	0.016	disk

NAT: narrow angle tailed galaxy; WAT: wide angle tailed galaxy;
Disk: galaxies with a disk or spiral-like morphology.

10

A large narrow band Hα survey at z ∼ 0.2: the bright end of the luminosity function, cosmic variance and clustering across cosmic time

We carried out the largest ($> 3.5 \times 10^5$ Mpc^3, 26 deg^2) Hα narrow band survey to date at $z \sim 0.2$ in the SA22, W2 and XMMLSS extragalactic fields. Our survey covers a large enough volume to overcome cosmic variance and to sample bright and rare Hα emitters up to an observed luminosity of $\sim 10^{42.4}$ erg s^{-1}, equivalent to $\sim 11 M_\odot$ yr^{-1}. Using our sample of 220 sources brighter than $> 10^{41.4}$ erg s^{-1} ($> 1 M_\odot$ yr^{-1}), we derive Hα luminosity functions, which are well described by a Schechter function with $\phi^* = 10^{-2.85\pm0.03}$ Mpc^{-3} and $L^*_{H\alpha} = 10^{41.71\pm0.02}$ erg s^{-1} (with a fixed faint end slope $\alpha = -1.35$). We find that surveys probing smaller volumes ($\sim 3 \times 10^4$ Mpc^3) are heavily affected by cosmic variance, which can lead to errors of over 100 per cent in the characteristic density and luminosity of the Hα luminosity function. We derive a star formation rate density of $\rho_{\mathrm{SFRD}} = 0.0094 \pm 0.0008\ M_\odot$ yr^{-1}, in agreement with the redshift-dependent Hα parametrisation from Sobral et al. (2013a). The two-point correlation function is described by a single power law $\omega(\theta) = (0.159 \pm 0.012)\theta^{(-0.75\pm0.05)}$, corresponding to a clustering length of $r_0 = 3.3 \pm 0.8$ Mpc/h. We find that the most luminous Hα emitters at $z \sim 0.2$ are more strongly clustered than the relatively fainter ones. The $L^*_{H\alpha}$ Hα emitters at $z \sim 0.2$ in our sample reside in $\sim 10^{12.5-13.5}\ M_\odot$ dark matter haloes. This implies that the most star forming galaxies always reside in relatively massive haloes or group-like environments and that the typical host halo mass of star-forming galaxies is independent of redshift if scaled by $L_{H\alpha}/L^*_{H\alpha}(z)$, as proposed by Sobral et al. (2010).

Table 10.1: Area and volumes covered by the narrow band observations. Only the common area between the two filters is listed. The same area is used to calculate the co-moving volume.

Field	No pointings	Area deg^2	z	Volume 10^4 Mpc^3
SA22	24	6.1	0.19	7.5
			0.22	9.8
W2	12	3.6	0.19	4.4
			0.22	5.7
XMMLSS	13	3.1	0.19	3.9
			0.22	5.0
Total	49×2	12.8×2		36.3

10.1 Introduction

The star formation (SF) activity in the Universe was significantly higher in the past, reaching a peak $\sim 10 - 11$ Gyrs ago ($z \sim 2 - 3$, e.g. Lilly et al. 1996; Karim et al. 2011; Bouwens et al. 2011; Gunawardhana et al. 2013; Sobral et al. 2013a; Bouwens et al. 2015), and with the typical star formation rate (SFR) of galaxies (SFR*) at $z \sim 2$ being a factor ~ 10 times higher than at $z = 0$ (Sobral et al. 2014). However, the understanding of how and through which physical mechanisms the typical SFRs of galaxies have declined over the last 11 Gyrs is still poor.

In order to study SF across cosmic time, a number of tracers can be used. Ultra violet (UV) data can be used to trace radiation coming from massive, short-lived stars. Dust heated by the UV radiation emits in the far infra-red (FIR). The radiation from the massive stars also ionises the surrounding gas and leads to numerous recombination lines such as Hα (6563Å) and [OII] (3727Å). Radio observations can be used to trace emission from super nova remnants. However, it is not trivial to combine these SF indicators, given they trace different phases of SF (averaged on short, ~ 10 Myr, or long, ~ 100 Myr, timescales, dust obscured, etc.), with different selection functions. Some selections are significantly biased: UV-selected samples miss dusty/metal enriched star forming galaxies, while the FIR exclusively selects dusty star-forming regions. Therefore, one of the main challenges in obtaining a complete picture of the SF evolution is the direct comparison of equally selected large samples of SF galaxies at a range of redshifts. Samples at high redshift tend to be obtained with a completely different selection than those at lower redshift, which can result in misinterpreted evolutionary trends which are more likely connected with the different selections at different redshifts than the actual evolution of galaxies across time (e.g. Stott et al. 2013a).

An effective way of overcoming such limitations is by using a single technique and a single SF indicator up to the peak of the star formation activity. This can be achieved by tracing the Hα emission line, which is one of the most sensitive and well-calibrated SF traces and also benefits from low intrinsic dust extinction within the host galaxy (when compared to e.g. UV). Hα surveys performed using the narrow-band (NB) technique can provide clean, large and complete samples SF galaxies (c.f. Oteo et al. 2015).

A successful example of the NB technique put into practice is the High Redshift Emission Line Survey (HiZELS, Geach et al. 2008; Best et al. 2010; Sobral et al. 2013a), but also see the

pioneering works of Bunker et al. (1995), Moorwood et al. (2000), Kurk et al. (2004), Ly et al. (2007) and Shioya et al. (2008). At $z \sim 1-2$, the volumes probed by HiZELS over a number of different fields ($\sim 5-10$ deg^2) virtually overcome cosmic variance (Sobral et al. 2015b). However, at $z < 0.4$, the volumes probed over $1-2$ deg^2 areas are only a minor fraction of those at high-redshift. Indeed, the samples at low redshift are greatly limited by cosmic variance, and even the widest surveys (e.g. Shioya et al. 2008, Cosmological Evolution Survey (COSMOS)) struggle to reach the characteristic Hα luminosity ($L^*_{H\alpha}$). An additional limitation is saturation, which means missing the luminous population of Hα emitters (with $> 1-3$ M$_\odot$ yr^{-1}, for discussion of this effect see Stroe et al. 2014a). This can lead to an underestimation of Hα luminosity function (LF) bright end and an exaggeration of the evolution of $L^*_{H\alpha}$ from high to low redshift.

The combination of all these issues and the different selection techniques applied by each study makes it extremely hard to fairly compare between $z < 0.4$ and $z > 1$ samples when based on the same surveys. While it is possible to use other samples at lower redshift (e.g. spectroscopic selection, Gunawardhana et al. 2013), the importance of using the same selection in order to obtain clean and clear evolutionary trends cannot be stressed enough: without the guarantee of a unique selection, any evolutionary trends become hard/impossible to understand and interpret, limiting our understanding.

In order to overcome the current shortcomings we clearly require a large Hα survey at lower redshifts which can be directly matched to higher redshift. In this paper we present a large survey at $z \sim 0.2$, covering a similar co-moving volume (3.5×10^5 Mpc^3, spread over 3 independent fields to overcome cosmic variance) and complete down to similar luminosity limits relative to $L^*_{H\alpha}$ as surveys at $z > 1$. The structure of the paper is as follows: in Section 10.2 we present the observations and the reduction of the narrow-band data, while in Section 10.3 we show the selection of the Hα emitters. Section 10.4 deals with the $z \sim 0.2$ Hα luminosity function and Section 10.5 the clustering of bright Hα sources and the implications of our results for the cosmic SF evolution are presented. We present concluding remarks in Section 10.6.

At the two redshifts probed, $z \sim 0.19$ and 0.22, 1 arcsec covers a physical scale of 3.2 kpc and 3.6 kpc, respectively. The luminosity distance is $d_L \approx 940$ Mpc at $z \sim 0.19$ and ≈ 1110 Mpc at $z = 0.22$. All coordinates are in the J2000 coordinate system. We use the Chabrier (2003) initial mass function (IMF) throughout the paper, and results from other studies are also converted to this IMF.

10.2   Observations & Data Reduction

We obtain NB data tracing Hα at $z \sim 0.19$ and ~ 0.22 in three well studied extragalactic fields located at high Galactic latitude. W2 is part of the Canada-France-Hawaii Telescope Legacy Survey (CFHTLS) 155 deg^2, wide and shallow survey (Gwyn 2012), aimed at studying the large scale structure and matter distribution using weak lensing and galaxy distribution. SA22 is part of the W4 field in CFHLS and multiwavelength data has been compiled by Matthee et al. (2014) and Sobral et al. (2015b). The XMM Large Scale Structure Survey (XMMLSS, Pierre et al. 2004) is aimed at mapping large scale structures through clusters and groups of galaxies.

Table 10.2: Typical 3σ limiting magnitudes for the three fields (including the standard spread in values), for each filter. The depth for each pointing (and within each CCD of out of the four WFC CCDs) varies across the fields over the ranges reported in the third and last column.

Field	Filter	3σ
		mag
SA22	NB1	$17.5^{+0.4}_{-0.3}$
	NB2	$17.4^{+0.4}_{-0.3}$
W2	NB1	$16.8^{+1.5}_{-0.6}$
	NB2	$16.7^{+0.7}_{-0.4}$
XMMLSS	NB1	$17.7^{+0.4}_{-0.3}$
	NB2	$17.5^{+0.5}_{-0.3}$

10.2.1   Narrow band Hα observations

We obtained narrow band data using the NOVA782HA and NOVA804HA (Stroe et al. 2014a, 2015; Sobral et al. 2015a) filters on the Wide Wide Field Camera (WFC)[1] mounted on the Isaac Newton Telescope (INT, I13BN008, PI Sobral) [2]. For brevity, we label the filters as NB1 (NOVA782HA) and NB2 (NOVA804HA). Given the central wavelengths of the filters are 7852.4Å and 8036.15Å, with a full-width-half-maximum (FWHM) of 110Å, the two filters trace Hα emission in the $z = 0.1865 - 0.2025$ and $z = 0.2170 - 0.2330$ redshift ranges. Note that given the large field of view of WFC, a slight blue shift in the filter central wavelength is expected at large off-axis distances. However, given the WFC focal ratio ($f/3.29$), this effect is expected to be very low (a few per cent Bland-Hawthorn et al. 2001). Sobral et al. (2015a) and Stroe et al. (2015) characterised the filters with spectroscopy from the Keck and Willam Herschel Telescopes with sources located both towards and away from the pointing centre and found that the redshift distribution of Hα emitters matches that expected from the filter profile, without any noticeable offset.

Observations were conducted in five bright nights, between 22 and 26 of October 2013, under $\sim$ 1 arcsec seeing conditions. A five-position dither pattern was employed for the individual exposures (of 600 s each) to cover the spacings between the four WFC CCDs. Forty-nine individual pointings (of ~ 0.3 deg^2 each with WFC) split between the three fields (SA22, W2 and XMMLSS) cover an area of almost 13 deg^2 at each of the two redshifts (thus an effective area of $\sim$ 26 deg^2 combined), tracing a total co-moving volume of about 3.63×10^5 Mpc^3. The overlap with the multiwavelength data extends to about 10 deg^2 per redshift.

10.2.2   Narrow band data reduction

We reduce the data using the PYTHON based pipeline described in Stroe et al. (2014a). In short, we median combine the sky flats and biases and use the stacks to correct the science data. After detecting sources using the SExtractor package (Bertin & Arnouts 1996) and masking them in each science exposure, we median combine the exposures to obtain a 'super-flat'. We divide

---

[1]http://www.ing.iac.es/engineering/detectors/ultra_wfc.htm
[2]http://www.ing.iac.es/Astronomy/telescopes/int/

the data through the 'super-flat' to correct for 'fringing'. We then use SCAMP (Bertin 2006) to find astrometric solutions for the science exposures. The exposures are normalised to the same zero-point (ZP) by comparison to the red magnitude in the fourth United States Naval Observatory (USNO) Catalog (UCAC4; Zacharias et al. 2013). We combine the processed data into final stacked images using SWARP (Bertin et al. 2002). We photometrically calibrate our data against the i band magnitude from the Sloan Digital Sky Survey (SDSS) Data Release 9 (SDSS DR9 Ahn et al. 2012), which covers all our fields (SA22, W2 and XMMLSS). We extract magnitudes within 5 arcsec apertures using SEXTRACTOR (Bertin & Arnouts 1996). This corresponds to a physical diameter of $\sim$ 18 kpc at $\sim$ 0.2 redshift.

We calculate 3σ limiting magnitudes using the RMS noise reported by SEXTRACTOR (see Table 10.2). The depth of the observations varies across the pointings and even between the different chips of the WFC. Hence, we calculate the RMS noise individually for each CCDs, for each pointing, across the three fields.

We apply the NB technique to select line emitters, using a NB filter tracing line emission within a narrow range in redshift, in combination with another NB or broad band (BB) filter used for the estimation of the continuum emission underlying the emission line. We use two NB filters to trace Hα emission in two redshift ranges (0.1865 − 0.2025 and 0.2170 − 0.2330). For each NB filter, we use the other NB filter to estimate the continuum BB emission. In this way, for line emitters, one NB filter captures the BB emission as well as the line emission, while the other NB filter only captures the stellar continuum emission. Our method is similar to that of Dale et al. (2010), who use twin NB filters for continuum subtraction. In further text, we use labels according to the filter which was used as NB filter in that particular case. Therefore, when we label with NB1, we refer to line-emitters in the 0.1865 − 0.2025 redshift range, while NB2 refers to the 0.2170 − 0.2330 range. The details of the selection method are laid down in Section 10.3.2.

10.2.3 Optical and IR data

In our analysis, we use the rich multi-wavelength optical and infra-red (IR) data available for the SA22, W2 and XMMLSS fields.

All three fields are part of the CFHTLS wide and shallow surveys (SA22, W2 and XMMLSS are in fields W4, W2 and W1). We make use of the g, r, i and z photometry (Erben et al. 2013) and photometric redshifts (Ilbert et al. 2006) available through the CFHTLS T0007 release.

We also employ near IR data in the J and Ks filters, down to magnitude $\sim$ 21.2 and $\sim$ 20.0 respectively, obtained as part of the Visible and Infrared Survey Telescope for Astronomy (VISTA) Hemisphere Survey (VHS, McMahon and the VHS Collaboration, 2012, in preparation). Where available, in the XMMLSS field, we preferentially use data from the VISTA Deep Extragalactic Observations (VIDEO) Survey (Jarvis et al. 2013), which is about 3.5 magnitudes deeper than VISTA. We also make use of the IR photometric data taken in the SA22 field as part of the second data release of the UKIDSS Deep Extragalactic Survey (Warren et al. 2007), which reaches magnitudes 23.4 and 22.8 in the J and Ks bands, respectively, with a catalogue from Sobral et al. (2015b).

We make use of the photometric and spectroscopic redshift compilation in the UKIDSS Ultra Deep Survey (part of XMMLSS) available as part of their 8th data release[3], as well as

---

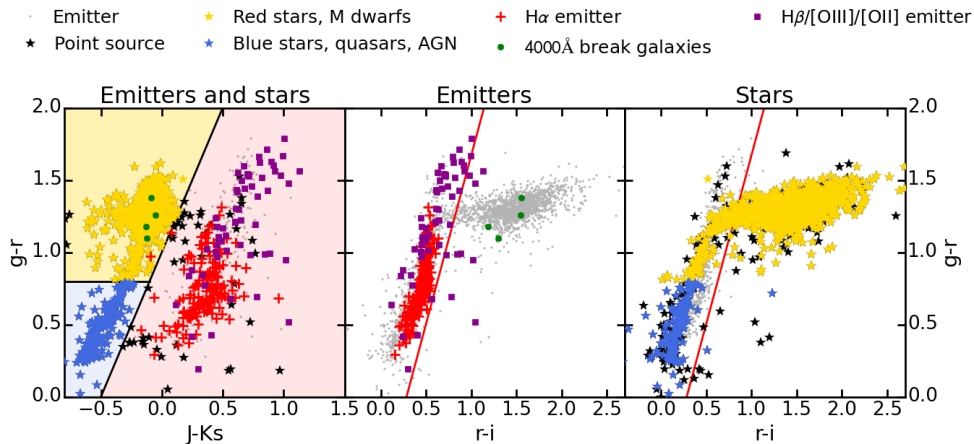[3] http://www.nottingham.ac.uk/astronomy/UDS/data/data.html

Figure 10.1: Colour-colour plots for the SA22, W2 and XMMLSS fields, mainly used to remove stars. The first plot shows $g - r$ versus $J - Ks$ while the middle and last plots show $g - r$ versus $r - i$. We first separate stars and emitters using the $g - r$ versus $J - Ks$, and the apply an extra cut using the optical colours to further remove stars with absorption features in one of the filter. The solid red and black lines display the colour cuts used to select point-like objects. Hα emitters are plotted in red crosses, while point-like sources are plotted as stars. 4000Å break galaxies are plotted in green crosses and high redshift sources in purple crosses.

other publicly available spectroscopy in the XMMLSS field (Garcet et al. 2007; Polletta et al. 2007; Tajer et al. 2007; Melnyk et al. 2013).

10.3 Methods and selecting the Hα samples

Once sources are detected in the NB images, we cross-match the NB catalogues with the optical and IR catalogues presented in Section 10.2.3, using a 1 arcsec positional tolerance. Note that because the BB catalogues are deeper than our data by at least 2 mag, we have 100 per cent optical and IR coverage in the areas we have FOV overlap with all the multiwavelength data. We use each NB catalogue as base catalogue for the cross-match.

10.3.1 Star removal

As explained in Section 10.2.2, we use the two NB filters to trace Hα emission at two redshifts ranges ($0.1865 - 0.2025$ and $0.2170 - 0.2330$). However, given the wavelength coverage of the two adjacent filters our samples of line emitters is contaminated by stars (see also Stroe et al. 2014a). Stars could mimic having an emission line if they have extremely red or a broad absorption feature, which would lead to a strong colour between the two NB filters. We expect the line emitters selected in the NB2 filter to be particularly contaminated with a population of (L, M) dwarf stars (Kirkpatrick et al. 1991, 1999). They will be selected as having excess in NB2 because their continuum has a broad absorption feature falling within the NB1 filter, leading to an underestimation of the continuum emission. The extremely red BB colours of these sources are also consistent with them being red dwarfs.
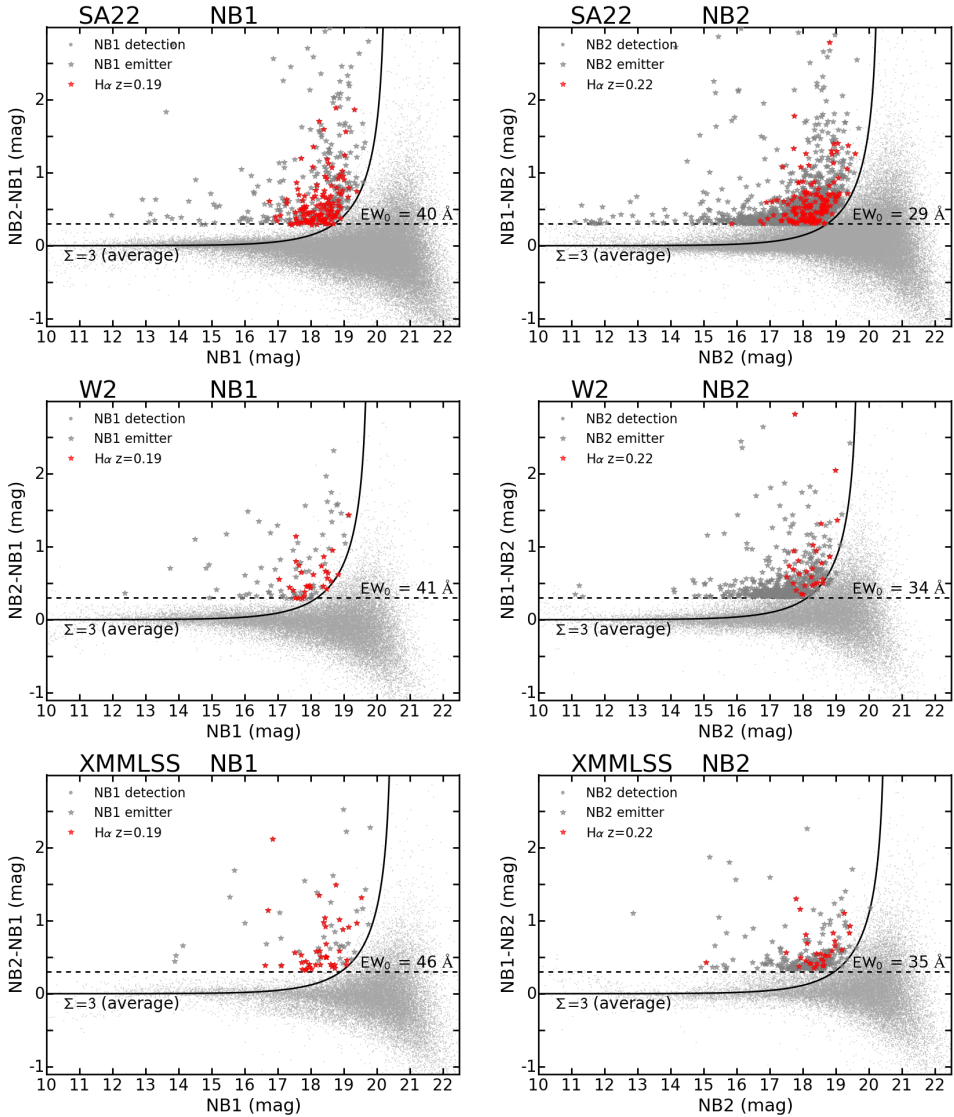
Figure 10.2: Colour-magnitude diagrams showing the excess as function of NB magnitude. The selection is performed separately for each CCD/pointing, field and NB filter, using the other NB filter for continuum estimation. Each panel is labelled with the corresponding field and the filter which is used as NB. The curves show average 3Σ colour significances for the average depth, as the RMS value varies between the pointings and CCDs. The horizontal dashed, black lines represent the intrinsic EW cuts. Note that we correct for incompleteness arising from our slightly different EW and colour significance cuts.

Table 10.3: Number of line emitters and Hα emitters selected in each field and filter. We also list the average limiting observed Hα luminosity at 50 per cent completeness and the equivalent SFR (using equation 10.11).

Field	Filter	Emitters	Hα emitters	$\log(L_{\text{H}\alpha})$ (erg s^{-1})	SFR ($M_{\odot}$ yr^{-1})
SA22	NB1	153	59	41.4	1.1
	NB2	238	91	41.4	1.1
W2	NB1	33	13	41.4	1.1
	NB2	55	15	41.6	1.7
XMMLSS	NB1	51	23	41.1	0.5
	NB2	50	19	41.4	1.1
Total	both	576	220		

We exclude stars using a colour-colour selection criterion using optical and IR colours based on Sobral et al. (2012), keeping in mind the distribution of sources in the colour-colour diagram. This is illustrated in Figure 10.1.

Red stars are selected using:

$$(g - r) > 2(J - Ks) + 1 \quad \& \quad (g - r) > 0.8 \quad \& \quad (J - Ks) > -0.7 \qquad (10.1)$$

We select dwarf stars via:

$$(g - r) > (7/3(r - i) - 2/3) \quad \& \quad (g - r) > 1.0 \qquad (10.2)$$

Optically blue stars and dwarf stars with absorption features are selected by:

$$(g - r) > 2(J - Ks) + 1 \quad \& \quad (g - r) < 0.8 \qquad (10.3)$$

We additionally use the 'StarGal' parameter in the CFHTLS photometric redshift catalogue to select stars (Ilbert et al. 2006), which categorises sources as point-like or extended objects.

Thus, in summary, we label sources as stars if:

- Source passes the red star selection criterion (equation 10.1) or

- Source passes the blue star selection criterion (equation 10.3) or

- Source passes the dwarf star selection criterion (equation 10.2) or

- Source is classified as star by the CFHTLS 'StarGal' parameter.

About $60 - 80$ per cent of the sources mimicking emission lines are marked as stars. Spectroscopic observations using NB1 and NB2 (e.g Stroe et al. 2015; Sobral et al. 2015a) confirm the presence of such stars. All the sources masked as stars are removed from catalogues such that they are not selected as line emitters.

10.3.2 Selection of line emitters

We use the formalism developed by Bunker et al. (1995), which is widely used in the literature (e.g. Shioya et al. 2008; Sobral et al. 2009; Stroe et al. 2014a) to select large numbers of line emitters. We refer the interested readers to those papers for the details of the selection criteria.

We select line emitters separately in each field and each NB filter. For brevity, in the following equations, we label the filter used to select emitters as NB, while we name the other NB filter, used to quantify the continuum emission, as BB filter. Note that we attempted the selection of line emitters using the i band filter, following Stroe et al. (2014a) and Stroe et al. (2015). However, the relatively deep CFHTLS data becomes saturated at magnitude $17 - 18$ and would prevent the selection of bright line emitters. Therefore using each NB filter for continuum subtraction of the other represents the optimal strategy, enabling the selection of line emitters up to magnitude 10. Using much deeper broad band i data would allow us to probe down to fainter emitters, but our aim for the paper is to study the bright population. By comparison, the widest Hα survey at $z \sim 0.2$ to date, performed by Shioya et al. (2008), can only probe sources as bright as ~ 18 mag, but excels at the faint end (going down to 24 mag).

We select emitters in each NB filter based on their excess emission compared to the BB emission (quantified using the other NB filter). We first correct for any systematic colour offset between the two NB filters. Colour is defined here as the difference in magnitude between the filter used as NB and the filter used to measure broad band. We estimate a median offset of this colour, based on the scatter in the colours at non-saturated, but still bright NB magnitudes. We then apply this correction to the colour and the NB magnitude. However, because the filters are close in wavelength this correction is small (0.02 and 0.03 mag, for NB1 and NB2 respectively).

The excess emission is then quantified through the colour excess significance Σ, which is used to separate sources with real colour excess, compared to excess caused by random scatter (Sobral et al. 2009, 2012):

$$\Sigma = \frac{10^{-0.4(m_{BB}-m_{NB})}}{10^{-0.4(ZP_{AB}-m_{NB})} \sqrt{\pi r^2 \left(\sigma_{\mathrm{NB}}^2 + \sigma_{\mathrm{BB}}^2\right)}}, \tag{10.4}$$

where ZP_{AB} is the magnitude system zero-point, m_{NB} and m_{BB} are the NB and BB magnitudes (where NB is the filter used for detection of line emitters and BB is the other NB filter used for quantifying the continuum emission), r is the radius of the aperture in pixels and σ_{NB} and σ_{BB} are the rms noise levels.

The NB or BB flux $f_{NB,BB}$ are calculated as:

$$f_{NB,BB} = \frac{c}{\lambda_{NB,BB}^2} 10^{-0.4(m_{NB,BB}-ZP_{AB})}, \tag{10.5}$$

where c is the speed of light, λ_{NB} and λ_{BB} are the central wavelengths of the two NB filters and $ZP_{AB} = 48.574$ is the ZP of the AB magnitude system. The line flux is:

$$F_{\mathrm{line}} = \Delta\lambda_{\mathrm{NB}}(f_{NB} - f_{BB}). \tag{10.6}$$

Note that the two filters are independent, hence there is no overlap in wavelength between NB1 and NB2. Therefore, if one filter captures line emission on top of the continuum, automatically the other NB filter picks up only continuum emission. Therefore, the line flux formula accounts for the fact the filter used as BB does not contain any line emission.
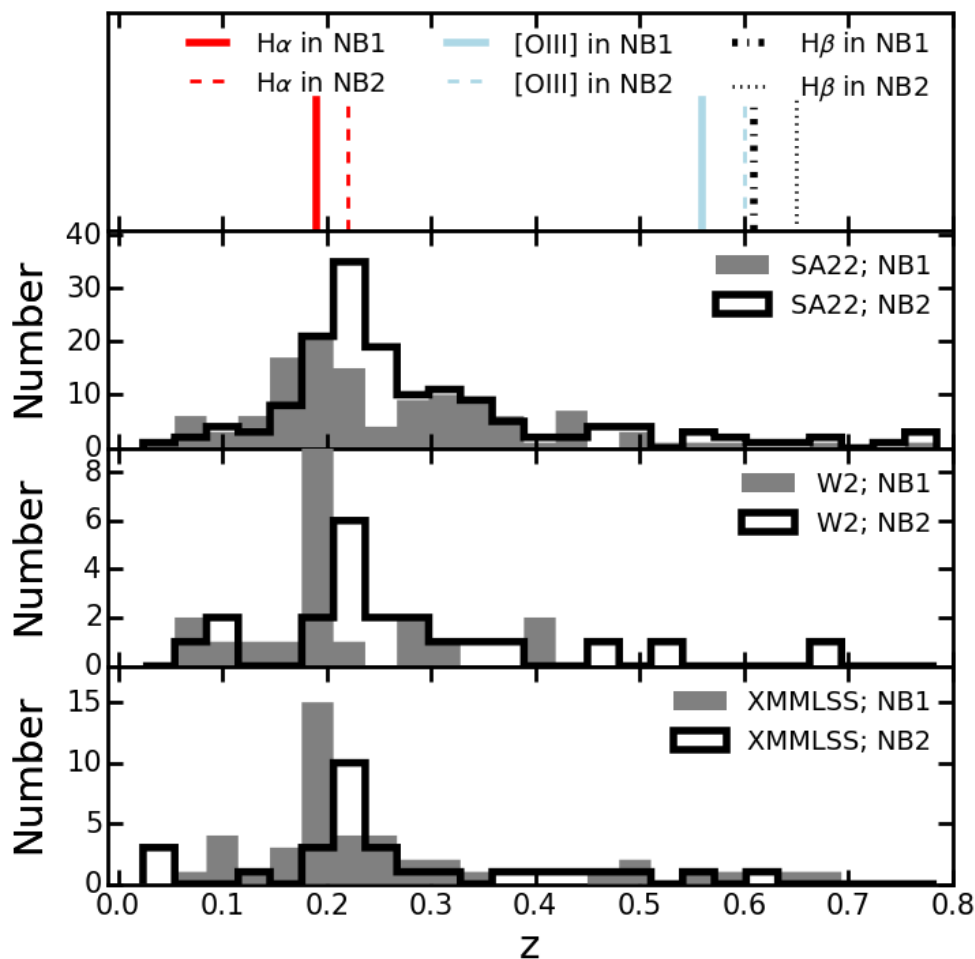
Figure 10.3: Photometric redshift distribution of line emitters for each field. Note the quality of the photometric redshifts varies between the fields. The top panel shows the main line we expect to capture with out two narrow band filters. The distribution contains clear peaks around $z \sim 0.2$, indicating our sample is dominated by Hα emitters, with little contamination from higher redshift emitters.

We use the Σ parameter in conjunction with an equivalent width (EW) cut, which ensures that we select only sources which have a ratio of the line to continuum flux larger than the scatter at bright magnitudes. The observed EW is defined as:

$$EW = \Delta\lambda_{NB} \frac{f_{NB} - f_{BB}}{f_{BB}},$$
(10.7)

where $\Delta\lambda_{NB} = 100$ Å is the FWHM of the NB filters, while f_{NB} and f_{BB} are the NB and continuum fluxes. Note this formula is a simplified version of those presented in, e.g., Bunker et al. (1995) and Sobral et al. (2009), because we do not expect our BB filter to contain any emission line flux.

In the restframe of the sources, the intrinsic EW_0 is:

$$EW_0 = EW / (1 + z).$$
(10.8)

In conclusion, we select sources as emitters if:

- Their colour significance Σ is higher than 3 and

- Their equivalent width is higher than 3σ, where σ is the colour excess (BB-NB) scatter at bright, but not saturated magnitudes.

The $\Sigma = 3$ colour significance and the 3σ excess depend on the depth of the observations in each field (see Figure 10.2). We choose to not impose a single, common cut, to follow the natural depth of the data, rather than cutting the sample at excessively high EW and Σ. However, we note that we fully correct for the sources missed by our cuts, as explained in Section 10.4.1.

10.3.3 Selection of Hα candidates

The line emitter population is made of Hα emitters at $z \sim 0.2$, as well as higher redshift line emitters: Hβ ($\lambda_{rest} = 4861$ Å), [OIII]$\lambda\lambda4959, 5007$ emitters at $z \sim 0.61 - 0.65$ and [OII] ($\lambda_{rest} = 3727$ Å) emitters at $z \sim 1.15$ (see Figure 10.3). Our sample could be contaminated by a population of 4000 Å break galaxies at $z \sim 0.8$. As shown in Stroe et al. (2014a), at ~ 8000 Å and lower line fluxes, the line emitter population is dominated by [OII]$\lambda3727$ emitters and $z \sim 0.8$ 4000 Å break galaxies. However, at high fluxes, the number of Hα and Hβ/[OIII] steeply rises, each amounting to about 50 per cent of the line emitter population. Therefore, given the shallow depth of our survey, we are strongly biased against detecting high-redshift ($z > 0.6$) sources. We expect the Hα emitters to amount to about half of the emitter population. Figure 10.3, presenting the photometric redshift distribution of the line emitters, confirms these findings. The steps we undertake to robustly separate the Hα emitters from the other sources are described in the following paragraphs.

We first visually inspected all line emitter candidates to flag any spurious sources coming from noisy edge regions of the chips or from false detections within the haloes of bright sources.

Hα emitters are selected in the following way:

- The photometric or spectroscopic redshift of the source does not lie in the expected ranges for Hβ/[OIII]/[OII] emitters ($0.37 < z < 0.7$ and $0.9 < z < 1.2$) and 4000 Å break galaxies ($0.7 < z < 0.9$) and
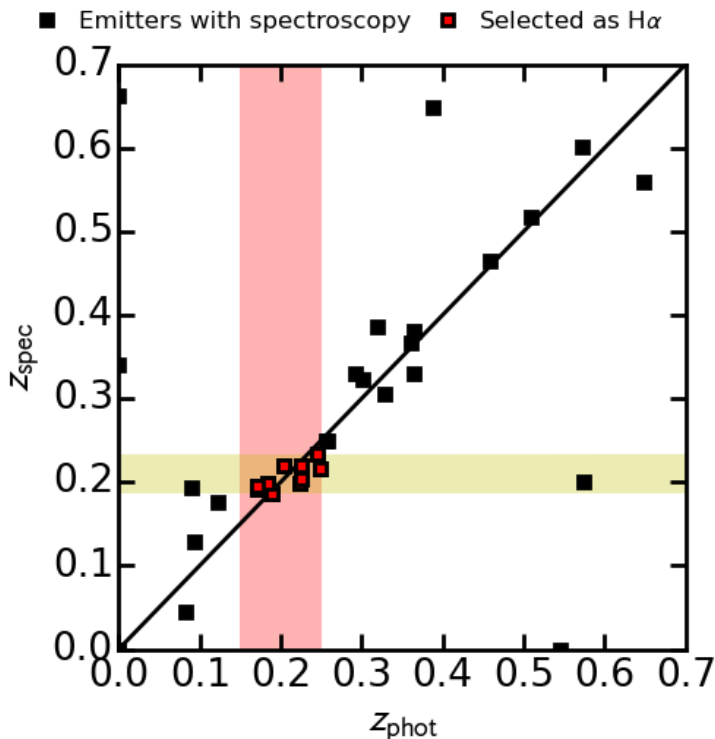
Figure 10.4: Photometric versus spectroscopic redshift for sources selected as emitters. The shaded red area indicates sources which based on their photometric redshift were selected as Hα. The yellow shaded area indicates the redshift range captured by the filters.

- The photometric or spectroscopic redshift of the source lies in the $0.15 < z < 0.25$ range.

Figure 10.1 displays the colour-colour distribution of line emitters, the cut employed to separate the source types and highlights the location of the Hα emitters. All three fields and both filters are shown in the same plot. Separating the data per field and filter results in colour-colour diagrams which are consistent with Figure 10.1, indicating there are no systematic differences between the populations selected with the two NB filters. The number of Hα emitters selected in each field can be found in Table 10.3, amounting to a total of 220 Hα emitters. This amounts to almost 40 per cent of the total number of emitters, as expected and explained in Section 10.3.3.

Purity of the Hα sample

We compare the spectroscopic and photometric redshifts in order to study the purity of the Hα sample (Figure 10.4). We find that the photometric redshifts are within 0.05 of the spectroscopic ones. From the sources spectroscopically confirmed to be at lower or higher redshift, none make it into the Hα catalogue, implying a very low contamination. Note that the range we used for selecting sources as Hα from photometric redshifts is $0.15 - 0.25$, which is

large enough to capture Hα emitters in both filters, while minimising contamination. Out of 12 spectroscopically confirmed emitters we miss two sources, implying completeness higher than 80 per cent. However, the spectroscopy is limited and the low number statistics could lead to an overestimation or underestimation of the completeness and contamination. Future spectroscopic observations will allow us to further investigate this.

10.4 Hα luminosity function and star-formation rate density

We use the sample of 220 Hα sources to build luminosity functions.

Our filters are sensitive not only to Hα, but also to the adjacent [Nɪɪ] double (6450 and 6585 Å) forbidden line. We subtract the [Nɪɪ] contribution from the line fluxes using the method from Sobral et al. (2012) to obtain Hα fluxes (F_{Hff}), which has been spectroscopically confirmed by Sobral et al. (2015b). The average [Nɪɪ] contribution is about 30 per cent of the total line flux.

After we obtain pure Hα fluxes $F_{\mathrm{H}\alpha}$, we calculate the Hα luminosity $L_{\mathrm{H}\alpha}$:

$$L_{\mathrm{H}\alpha} = 4\pi d_L^2(z) F_{\mathrm{H}\alpha}, \tag{10.9}$$

where $d_L(z)$ is the luminosity distance (940 Mpc for the NB1 filter and 1110 Mpc for NB2).

10.4.1 Completeness, volume and filter profile corrections

We use the method of Sobral et al. (2012) to correct for the incompleteness arising from missing sources with faint Hα fluxes and/or low *EW*. We select random samples of sources passing the selection criteria for being located at the redshifts traced by the two filters, but which are not selected as Hα emitters. Fake Hα emission lines are added to these sources which are then passed through the Hα selection criteria (*EW* and Σ) described at the end of Section 10.3.3.

Because of the different depth between the pointings and between the four CCD chips, we independently study the recovery rate as function of the Hα flux for each chip, pointing, filter and field. The results of the completeness study can be found in the Appendix in Figure 10.15. Our results are corrected for the effects of incompleteness, especially the Hα luminosity function (see Sections 10.4.3 and 10.4.4 and, e.g., Figures 10.5, 10.6 and 10.7).

The volumes probed in each field and at each redshift assuming that the filters have a perfect top-hat shape are listed in Table 10.1. The total co-moving volume probed is 3.63×10^5 Mpc^3, by far the largest volume ever surveyed in Hα at $z \sim 0.2$. However, since the filter transmission does not follow perfectly an idealised top hat, we follow the method of Sobral et al. (2009) and Sobral et al. (2012) and correct the volumes to account for sources missed at the edges of the filter.

10.4.2 Survey limits

A 50 per cent completeness (see Figure 10.15) translates to average limiting Hα luminosities of $10^{41.1-41.6}$ erg s^{-1} for our survey. This is equivalent to limiting star formation rates (SFR) of
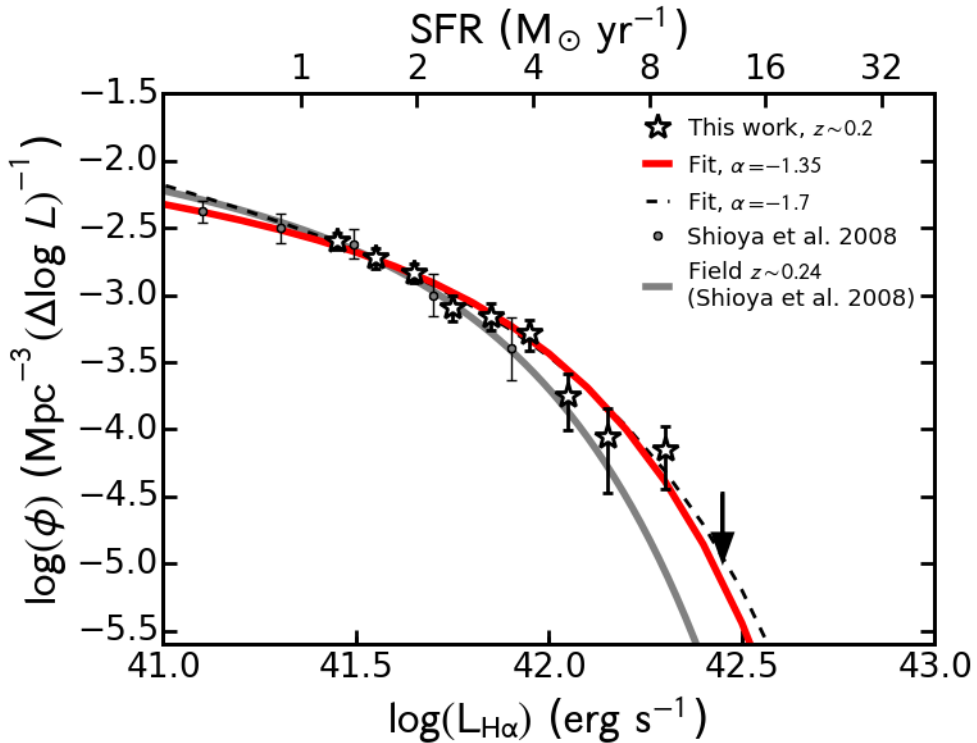
245

Figure 10.5: The Hα luminosity function at $z \sim 0.2$ from our study and the best fit Schechter function. The $L_{H\alpha}$ is not corrected for intrinsic dust attenuation. For comparison, the results from Shioya et al. (2008) are also shown. Note the excellent agreement between the data in the overlapping luminosity range. However, our data probes brighter luminosities, enabling the first determination of the bright end of the Hα luminosity function at $z \sim 0.2$.

Table 10.4: Best fit luminosity function at $z \sim 0.2$ obtained from combining data in the three fields (SA22, W2 and XMMLSS) and two NB filters. Since our data is not very deep, but probes the bright-end really well, we fix the faint-end slope α at two values. For comparison, we also list the results and volumes probed from other studies at a similar redshift. Note that none of the $L_{H\alpha}^*$ are corrected for Hα extinction.

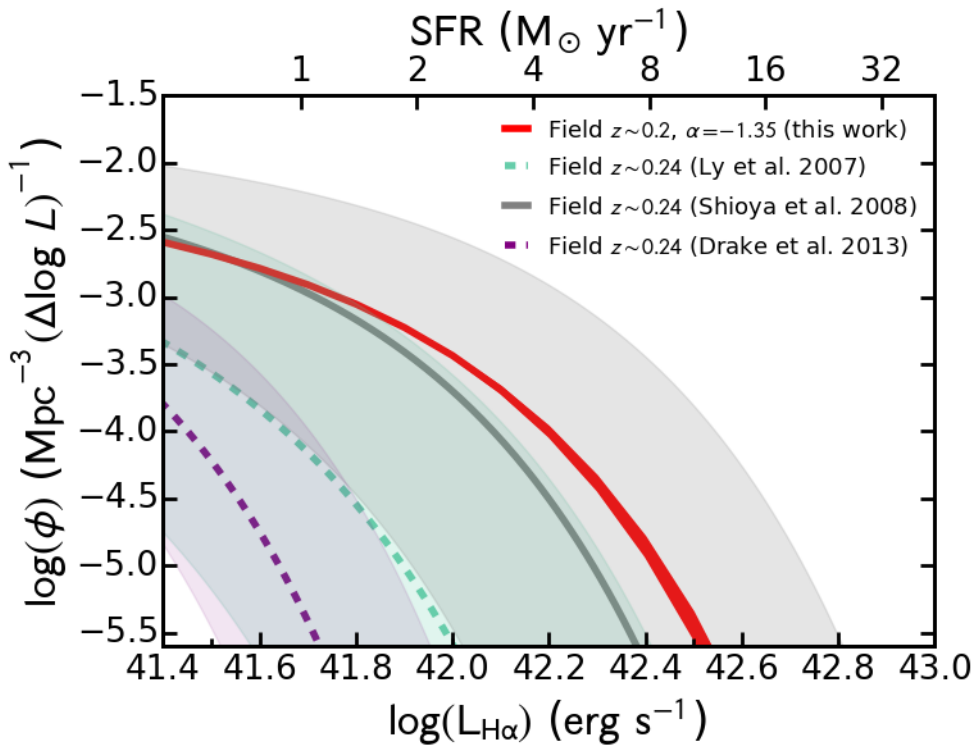| Source	z	V (10^4 Mpc^3)	α	$\log \phi^*$ (Mpc^{-3})	$\log L_{H\alpha}^*$ (erg s^{-1})
This study	~ 0.2	36.3	-1.35	-2.85 ± 0.03	41.71 ± 0.02
			-1.70	-3.06 ± 0.04	41.83 ± 0.03
Shioya et al. (2008)	~ 0.24	3.1	$-1.35^{+0.11}_{-0.13}$	$-2.65^{+0.27}_{-0.38}$	$41.54^{+0.38}_{-0.29}$
Ly et al. (2007)	~ 0.24	0.5	-1.70 ± 0.10	-2.98 ± 0.40	41.25 ± 0.34
Drake et al. (2013)	~ 0.25	1.2	$-1.03^{+0.17}_{-0.15}$	$-2.53^{+0.17}_{-0.21}$	$40.83^{+0.19}_{-0.16}$

Figure 10.6: A range of luminosity functions at $z \sim 0.2$, from the current work and the works of Shioya et al. (2008), Ly et al. (2007) and Drake et al. (2013). In shaded areas, we overplot the ranges allowed by the 1σ error bars of the LF parameters. The works of Shioya et al. (2008), Ly et al. (2007) and Drake et al. (2013) explore the faint end part of the luminosity. The shaded areas indicate the 1σ uncertainties of the Schechter function parameters. Our measurements are consistent with previous work, but significantly improve the previously unexplored bright end. While our measurement error is given by cosmic variance, as shown in Section 10.4.6. However the other measurement do not include the error given by cosmic variance, which would add an error of about $100 - 200$ per cent in the parameters.

$0.5 - 1.8$ $M_\odot$ yr^{-1}, with no intrinsic dust extinction applied. If 1 magnitude of dust extinction is applied this is equivalent to $0.2 - 0.8$ SFR* (see equation 10.11 in Section 10.4.4).

The maximum observed Hα luminosity our survey probes is $\sim 10^{42.4}$ erg s^{-1}, equivalent to SFRs of 11 $M_\odot$ yr^{-1} (or $\gtrsim 27$ $M_\odot$ yr^{-1} if 1 mag of dust extinction is applied). By comparison, the widest Hα survey at a similar redshift, performed by Shioya et al. (2008), reaches $\sim 10^{41.9}$ erg s^{-1}, or 3.5 $M_\odot$ yr^{-1} (8.7 $M_\odot$ yr^{-1} with dust extinction). This means our survey probes galaxies more than three times more star forming than previous surveys.

10.4.3 Hα luminosity function

Using our final sample of Hα emitters, we build luminosity functions (LF) which characterise the density of sources at any given Hα luminosity. To do so, we bin sources based on their

luminosity (corrected for the [NII] contribution, Section 10.4, but not for intrinsic dust extinction), by adding their associated inverse co-moving volume, corrected for the real filter profile and incompleteness (as shown in Section 10.4.1).

We fit the binned data with a Schechter (1976) parametrisation:

$$\phi(L_{\text{H}\alpha})\mathrm{d}L_{\text{H}\alpha} = \phi^* \left(\frac{L_{\text{H}\alpha}}{L_{\text{H}\alpha}^*}\right)^\alpha e^{-\frac{L_{\text{H}\alpha}}{L_{\text{H}\alpha}^*}} \mathrm{d}\left(\frac{L_{\text{H}\alpha}}{L_{\text{H}\alpha}^*}\right),$$
(10.10)

where $L_{\text{H}\alpha}^*$ is the characteristic Hα luminosity, ϕ^* is the characteristic density of Hα emitters and α is the faint-end slope of the LF. Since our data is not deep enough to properly constrain the faint end slope of the LF (see Table 10.3), we fix α to two values previously derived in the literature using deep data: -1.35 from Shioya et al. (2008) and -1.7 from Ly et al. (2007). In fitting the LFs, we assume Poissonian errors.

Our best fit Hα LF is described by a typical luminosity $\log(L_{\text{H}\alpha}^*) = 10^{(41.71\pm0.02)}$ erg s^{-1} and a characteristic density $\log(\phi^*) = 10^{(-2.85\pm0.03)}$ Mpc^{-3} (see Table 10.4 and Figure 10.5). Our data samples really well the bright-end of the LF, which enables us to place tight constraints on ϕ^* and $L_{\text{H}\alpha}^*$ (errors lower than 15 per cent). However, we lack depth (lowest bin at $\sim 10^{41.4}$ erg s^{-1}), so we fix the faint-end slope to -1.35, as obtained by Shioya et al. (2008) from the previously widest Hα survey, which benefits from high-quality, deep data reaching luminosities of $10^{39.3}$ erg s^{-1}, but is limited at the bright end. Therefore, the two surveys are highly complementary. Within the overlapping regions with data from both the Shioya et al. (2008) and our survey, the measurements are in excellent agreement. However, our LF, constrained up to $L_{\text{H}\alpha} = 10^{42.5}$ erg s^{-1}, indicates a slightly larger value of $L_{\text{H}\alpha}^*$, but still consistent with Shioya et al. (2008) within their large error bars (see Figure 10.6). Note that their uncertainties do not include the error from cosmic variance, which can results in $100 - 200$ errors in the parameters of the LF (see Section 10.4.6). Any discrepancy between the results can be explained by cosmic variance, given Shioya's volume is ~ 10 times smaller than ours and probes a single field. The differences between the ϕ^* results could also be explained by the different colour-colour methods used to separate the Hα emitters from higher redshift line emitters.

The discrepancy with other studies is much larger however (see Figure 10.6). Compared to our results, Ly et al. (2007), slightly overestimate ϕ^* (not significant) and underestimate $L_{\text{H}\alpha}^*$ (at the 2σ level). Drake et al. (2013) obtain an $L_{\text{H}\alpha}^*$ which is highly underestimated ($10^{40.83}$ erg s^{-1}). The difference to our value is significant at the 11σ level. This is entirely driven by Drake's small volume (~ 30 times smaller than ours) and the long exposures they were using in their study which prevented the study of sources brighter than 20 mag in the NB filter. Given the large variations in the LF parameters from cosmic variance, we expect all theses results to be consistent with our measurement, once the cosmic variance error is folded in (see Section 10.4.6).

10.4.4 Star formation rate density

We can calculate the star formation rate density (SFRD) at $z \sim 0.2$ by integrating the luminosity function and converting Hα luminosity to SFR. We use the $L_{\text{H}\alpha}$ to SFR conversion from Kennicutt (1998), corrected for the Chabrier (2003) IMF:

$$SFR(\text{M}_\odot\text{yr}^{-1}) = 4.4 \times 10^{-42} L_{\text{H}\alpha}(\text{erg s}^{-1}).$$
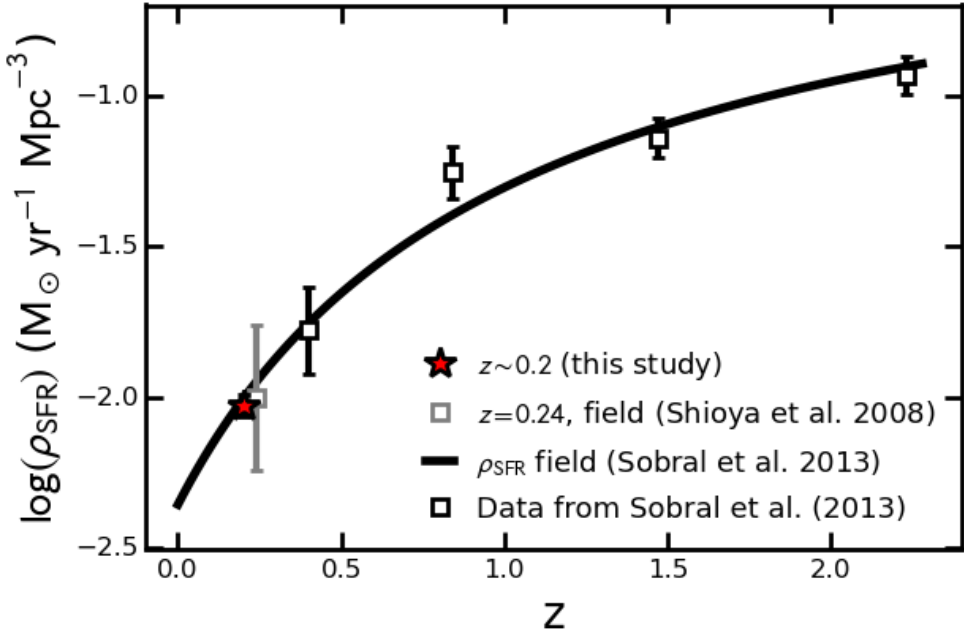(10.11)

Figure 10.7: Evolution of the SFRD from $z \sim 2.23$ to $z \sim 0.2$. Our measurement at $z \sim 0.2$ confirms the previously discovered decline in SFRD, which can be simply parametrised as a function of redshift (Sobral et al. 2013a).

The luminosity density is obtained by integrating the Hα LF:

$$\rho_{L_{H\alpha}} = \int_0^\infty \phi(L_{H\alpha}) L_{H\alpha} dL_{H\alpha} \tag{10.12}$$

$$= \Gamma(\alpha + 2)\phi^* L_{H\alpha}^*, \tag{10.13}$$

where $\Gamma(n) = (n-1)!$ is the Gamma function. By converting from luminosity to SFR through equation 10.11, the SFRD ρ_{SFR} is:

$$\rho_{SFR} = \Gamma(\alpha + 2)\phi^* L_{H\alpha}^* 10^{0.4 A_{H\alpha}} (1 - f_{AGN}) \tag{10.14}$$

where $A_{H\alpha}$ is the intrinsic Hα dust extinction which we assume to be 1 mag and $f_{AGN} = 0.15$ is the fraction of the Hα luminosity expected to be due to contributions from broad line and narrow line AGN emission (e.g. Garn & Best 2010; Sobral et al. 2015a).

Our measurement of the SFRD, $\rho_{SFRD} = 0.0094 \pm 0.0008$ M$_\odot$ yr^{-1} Mpc^{-3}, which matches with the value of Shioya et al. (2008) (0.010 ± 0.006 M$_\odot$ yr^{-1} Mpc^{-3}). Sobral et al. (2013a) derive a redshift-dependent parametrisation of the SFRD ($\rho_{SFRD} = -2.1/(1+z) + \log 10(4.4/7.9)$, corrected for the Chabrier IMF) based on their measurements and results from Ly et al. (2007) at $z \sim 0.08$ and Shioya et al. (2008) at $z \sim 0.24$ (see Figure 10.7). Our measurement perfectly agrees with the parametrisation, which predicts a value of 0.01 at $z \sim 0.2$.
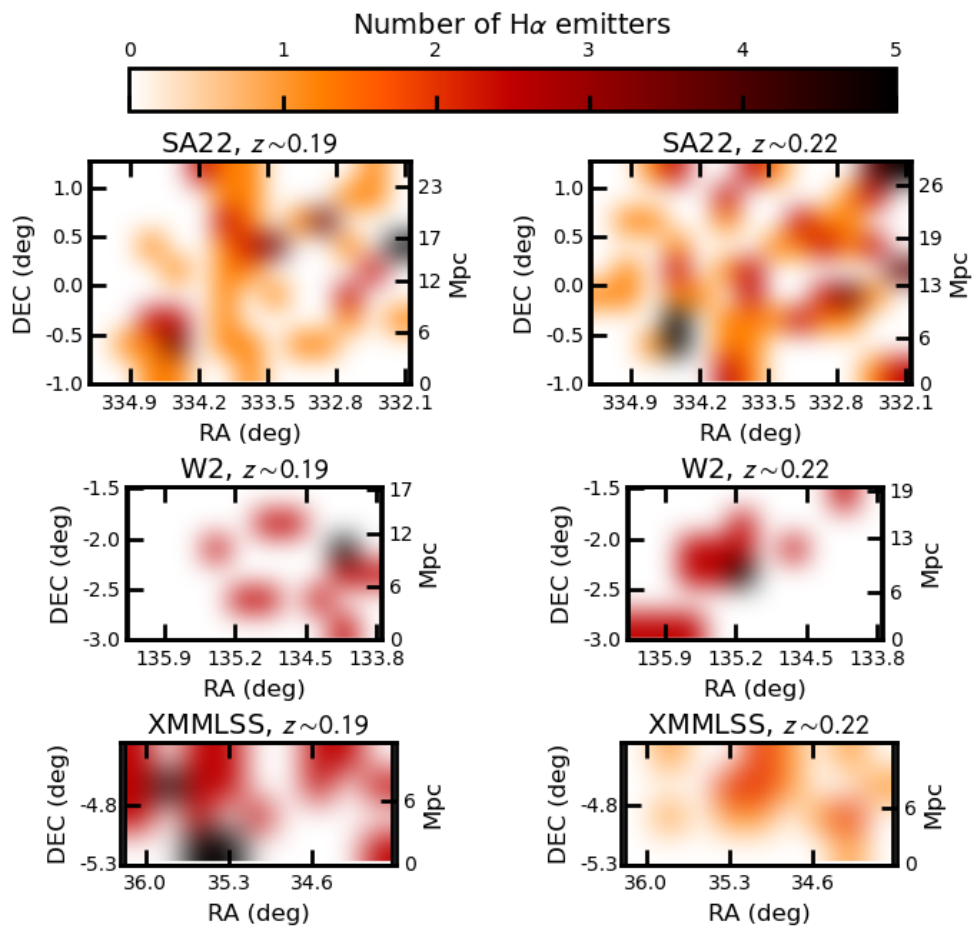
Figure 10.8: Smoothed sky distribution of the Hα emitters. Note the amount of cosmic variance within the fields. On average 2 emitters are found per deg^2, but the values vary between 0 and 5 sources per deg^2.
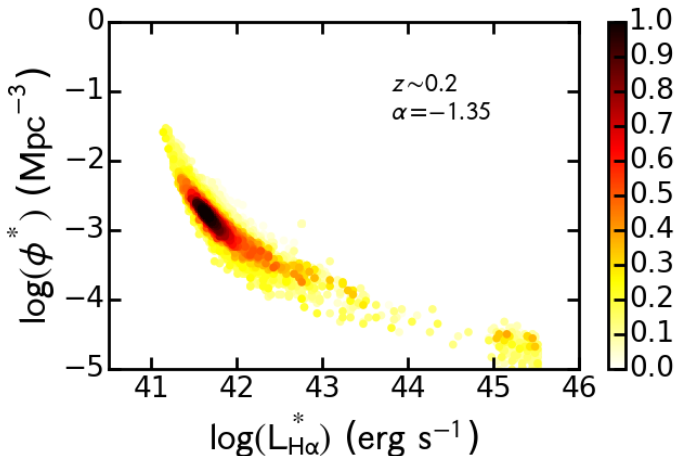
Figure 10.9: The values of LF Schechter parameters ϕ^* and $L_{H\alpha}^*$, when we fix $\alpha = -1.35$. For fitting the LF, we create 1000 random sub-samples of Hα emitters, at a range of probed volumes. The data points are colour coded with the co-moving volume probed in units of 1000 Mpc^3. Note how at small volumes the scatter is the value is extremely large (up to $4 - 5$ dex), while at large volumes the values for ϕ^* and $L_{H\alpha}^*$ converge. We obtain similar results with a different value of α or when we use the data for the two filters separately (see Figure 10.16)

10.4.5 Distribution of Hα emitters

Figure 10.8 shows the distribution of the Hα emitters in the three fields at the two redshifts, as selected in Section 10.3.3. Note the high degree of cosmic variance within and between the field and at the adjacent redshifts.

On average, down to a limiting Hα luminosity of $10^{41.4}$ erg s^{-1} or $SFR \sim 1\ M_\odot\ yr^{-1}$, we find ~ 2 Hα emitters per square degree (or ~ 3 per Mpc^3). However, there are large areas with no emitters, while parts of the W2 and XMMLSS fields have densities of up to 20 sources per square degree. The 'Sausage' massive, young post-merger galaxy cluster Stroe et al. (2014a, 2015), where Hα emitters were selected with the NB1 filter, was found to be extremely dense in star-forming galaxies and AGN, compared to blank fields. Down to the faintest Hα luminosities as our current data surveys ($10^{41.1}$ erg s^{-1}), the density is ~ 140 emitters per square degree, about 70 times above the average we find over an area of 20 deg^2. Assuming Poissonian noise, the 'Sausage' cluster overdensity is significant at the $> 11\sigma$ level.

The older 'Toothbrush' galaxy cluster merger, where the two subclusters collided about 2 Gyr ago, behaves differently. The density is about ~ 16 emitters per square degree, densities similar to the densest parts of our wide, shallow Hα survey. Our results thus corroborate the conclusions from Stroe et al. (2014a) and Stroe et al. (2015).

10.4.6 Quantifying cosmic variance

One of our goals is to understand the impact of cosmic variance and low number statistics on the determination of the LF parameters, especially motivated by the differences in LF found with the previous studies of Ly et al. (2007) and Drake et al. (2013). We generate random
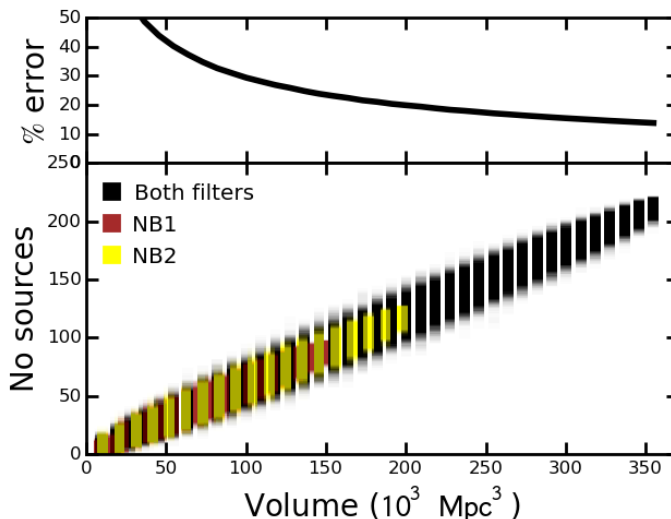
Figure 10.10: Distribution of the number of Hα emitters randomly selected within a range of volumes. As expected the larger the volume, the larger the number of sources, with a spread at each volume size caused by cosmic variance. The Poissonian error relative to the mean number of sources does not dominate over the spread caused by cosmic variance, except where cosmic variance is minimised through the sampling of a large volumes.

subsamples of Hα emitters, probing a range of volumes. We perform 1000 realisations starting from the smallest volumes for which we can fit a LF, up to the entire volume of our survey. We perform this experiment using Hα emitters in each NB filter and also combine all the data together, following Sobral et al. (2015b).

The number of sources for each realisation is plotted in Figure 10.10. As expected the average number of sources increases with the volume surveyed. We calculate the standard deviation of the spread in number of sources at each volume and compare that to the Poissonian error. In the calculation of the Poissonian error we take into account the fact that the sources are divided into bins. At very low volumes, the relative Poissonian error dominates over the spread in the number of sources, which is caused by cosmic variance. Given the depth of our survey, at the very small volumes ($< 2 \times 10^4$ Mpc^3) the Poissonian error essentially goes to infinity. Overall, the total relative error, calculated as the sum in quadrature of the Poissonian and cosmic variance error, goes down with increasing volume.

Naturally, when surveying a smaller volume, the number of Hα sources is proportionally smaller. We therefore adapt the number of bins (N), the bin width $\Delta \log L_{H\alpha}$ and the starting bin $\log L_{H\alpha}$, depending on the volume V probed, as detailed in Table 10.5.

The results from the different realisations of the LF calculated from Hα emitters extracted over a range of volumes can be found in Figure 10.9. At small volumes ($< 4 \times 10^4$ Mpc^3), the random realisations of the LF give wildly different results, with values spanning $4-5$ dex. This is driven by two main factors: low number statistics and cosmic variance. The low number of Hα emitters in small volumes imposes wide and few $L_{H\alpha}$ bins to gain enough number statistics. With few bins, the LF function is barely constrained. Additionally, small volumes
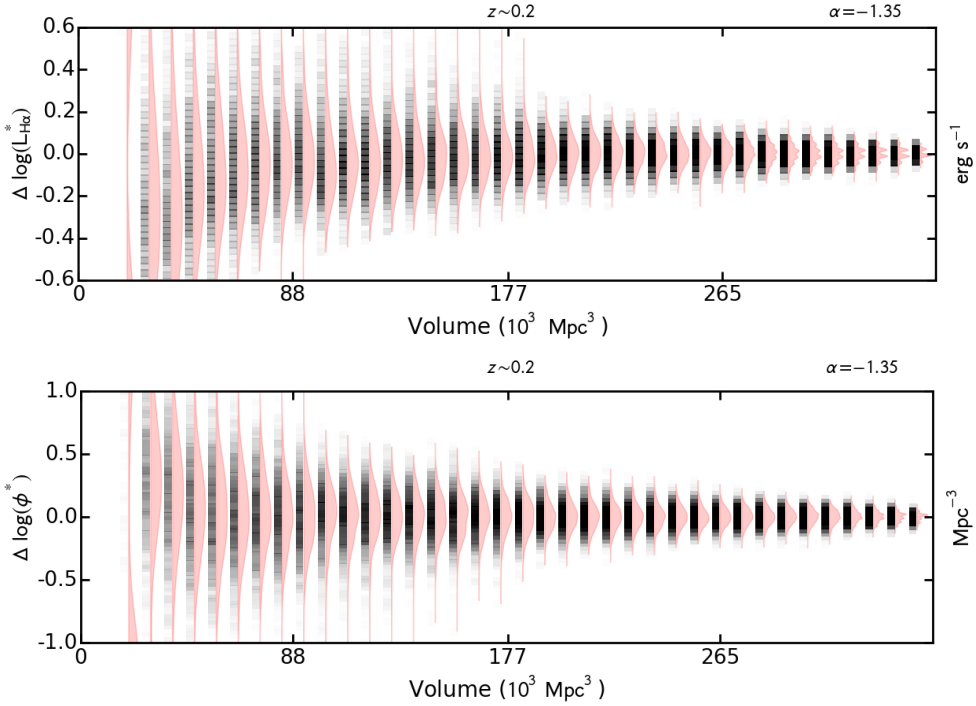
Figure 10.11: The error distribution of the characteristic Hα luminosity $L^*_{H\alpha}$ and number density ϕ^*, as function of the volume probed. The error is calculated as fitted value minus the mean of the distribution at each volume. The results are obtained when combining data from both NB filters, with faint end slope fixed to -1.35 (see Figures 10.17, 10.18 and 10.19 for results for other α and for the two filters independently). At each volume, 1000 realisations are performed, based on random samples of sources. Each figure shows the values obtained from the LF fitting in gray-black stripe. Darker colours mean more of the realisations found that particular $L^*_{H\alpha}$ or ϕ^* value. The violin plot next to each stripe encodes the $L^*_{H\alpha}/\phi^*$ histogram. The top panel shows the standard deviation σ of the $L^*_{H\alpha}$ values at each volume size. Note that spread of values drops the larger the volume probed, indicating a convergence in the values of $L^*_{H\alpha}$ and ϕ^*.

Table 10.5: Bin width $\Delta \log L_{H\alpha}$, starting bin $\log L_{Hff,min}$ and number of bins (N) chosen for studying the luminosity function, depending on the volume V probed.

V range	$\Delta \log L_{H\alpha}$	$\log L_{Hff,min}$	N_{bins}
$< 2 \times 10^4$ Mpc^3	0.3	41.5	4
$2 \times 10^4 - 9 \times 10^5$ Mpc^3	0.2	41.5	4
$9 \times 10^5 - 18 \times 10^5$ Mpc^3	0.15	41.4	5
$18 \times 10^5 - 27 \times 10^4$ Mpc^3	0.15	41.4	6
$> 27 \times 10^5$ Mpc^3	0.1	41.4	8

do not fully sample the LF at the brightest $L_{\mathrm{H}\alpha}$, where Hα emitters are rare. Therefore, when the volumes are small cosmic variance is significant. However, with the increase of the probed volume, we can much better constrain ϕ^* and $L^*_{\mathrm{H}\alpha}$ parameters, by overcoming both Poissonian errors and cosmic variance. This is exemplified in Figure 10.11. The standard deviation of the $L^*_{\mathrm{H}\alpha}$ and ϕ^* parameters at each volume size becomes smaller with increasing volume. Note however the values of $L^*_{\mathrm{H}\alpha}$ and ϕ^* are highly correlated (Figure 10.16).

As shown in this section, cosmic variance can fully explain the differences found in the literature regarding the Hα LF at $z \sim 0.2$. By accounting for cosmic variance our LF results can be reconciled with those of Drake et al. (2013) and Ly et al. (2007). Our results indicate that at $z \sim 0.2$, volumes of at least 10^5 Mpc^3 are required to overcome cosmic variance.

10.5   Clustering of Hα emitters

To study the clustering of our sample of 220 bright Hα emitters at $z \sim 0.2$, we start by generating a random catalogue with 1 million sources. The random catalogue sources follow the geometry of the actual observed fields and masked areas (due to saturated stars) and their number in each CCD of each pointing is normalised according to the depth attained (and hence the density of sources in that area).

We follow the method described in detail in Sobral et al. (2010), which evaluates the two-point angular correlation function minimum variance estimator proposed by Landy & Szalay (1993):

$$\omega(\theta) = 1 + \left(\frac{N_R}{N_D}\right)^2 \frac{\mathrm{DD}(\theta)}{\mathrm{RR}(\theta)} - 2\frac{N_R}{N_D}\frac{\mathrm{DR}(\theta)}{\mathrm{RR}(\theta)}, \tag{10.15}$$

where θ is the angle on the sky and N_R and N_D are the number of sources in the random and real catalogue of Hα sources. $\mathrm{DD}(\theta)$, $\mathrm{RR}(\theta)$ and $\mathrm{DR}(\theta)$ are the number pairs of sources located at distances between θ and $\theta + \delta\theta$ in the real data, random data and between real and random data, respectively.

Errors on $\omega(\theta)$ are then (Landy & Szalay 1993):

$$\Delta\omega(\theta) = \frac{1 + \omega(\theta)}{\sqrt{\mathrm{DD}(\theta)}}. \tag{10.16}$$

We determine $\omega(\theta)$ using 1000 different randomly selected sub-samples of sources selected from the randomly generated catalogue. We perform our analysis separately on emitters selected in each filter, but combine the data for the SA22, W2 and XMMLSS fields. We use the full luminosity range ($L_{\mathrm{H}\alpha} = 10^{41.0-42.4}$ erg s^{-1}) of the Hα emitters, as well as split the sample in two roughly equal halves: a faint sample with luminosities in the range $10^{41.0-41.55}$ erg s^{-1} and a bright one with luminosities $10^{41.55-42.40}$ erg s^{-1}. We bin the data using a range of angular scale bins (with different starting bin $\theta_{\min}$, bin width $\delta\theta$ and maximum bin $\theta_{\max}$).

The results are presented in Figure 10.12 and Table 10.6. The two-point correlation function for the samples is well described by a single power law. The results for the two filters are considered separately and when combined give fully consistent results within the error bars.

Note we studied only the range 0.02 deg $< \theta <$ 3.0 deg, where there was enough signal. At scales smaller than < 0.02 deg, a flattening of $\omega(\theta)$ occurs, maybe caused by bright Hα emitters not being able to reside in a single halo. Additionally, since our survey is not very
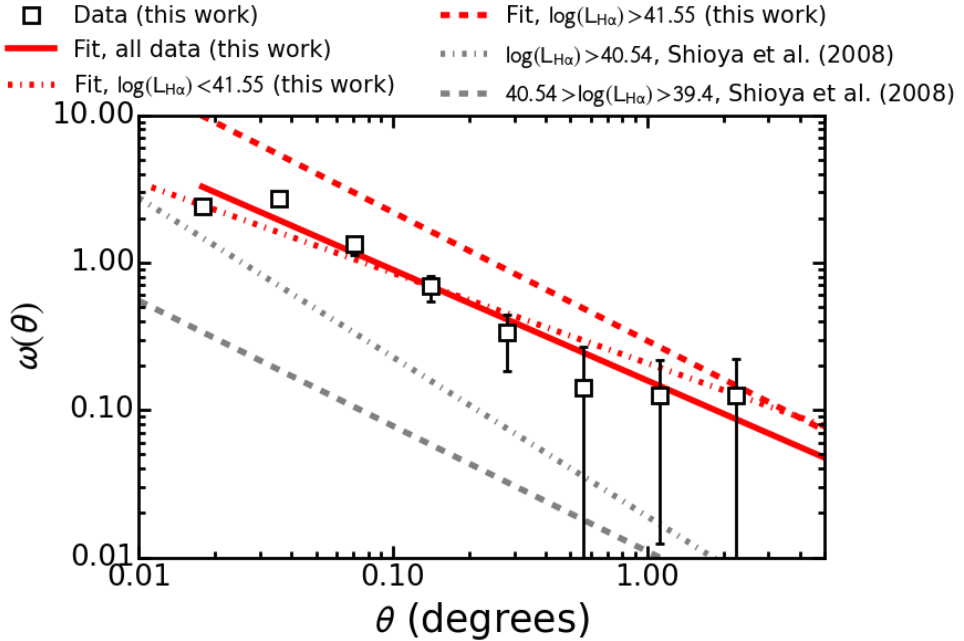
Figure 10.12: Angular two-point correlation function for bright Hα emitters ($L_{Hα} \gtrsim 10^{41.0}$ erg s^{-1}) at $z \sim 0.2$. The best fit power law relation is: $\omega(\theta) = (0.109 \pm 0.005)\theta^{(-0.79 \pm 0.04)}$. For comparison, we plot the results for fainter emitters ($L_{Hα} \lesssim 10^{41.5}$ erg s^{-1}) from Shioya et al. (2008). We find that more luminous Hα emitters are more clustered.

Table 10.6: Two-point correlation function for Hα emitters at $z \sim 0.2$. Best fit as a single power law of the form $\omega(\theta) = A\theta^{\beta}$. Note taht the filters and redshift distribution is different for Shioya et al. (2008) than for our study, so the amplitudes cannot be directly compared.

Source	$\log(L_{Hα})$ (erg s^{-1})	A	β
This study	$41.00 - 42.40$	0.159 ± 0.012	-0.75 ± 0.05
Faint	$41.00 - 41.55$	0.208 ± 0.035	-0.61 ± 0.07
Bright	$41.55 - 42.40$	0.295 ± 0.026	-0.87 ± 0.06
Shioya et al. (2008)	$40.54 - 41.50$	0.019 ± 0.004	-1.08 ± 0.05
Shioya et al. (2008)	$39.40 - 40.54$	0.011 ± 0.002	-0.85 ± 0.05

deep, we do not probe the regime where satellites are expected. Therefore, we cannot evaluate the departure of the two-point correlation function from a single power, which is caused by the transition from the large scale (two galaxies residing in separate dark matter halo) to the small scale clustering regime (galaxies sharing a single halo, e.g. Ouchi et al. 2005).

Previous research indicates that bright Hα galaxies as well as Lyman break galaxies are more clustered than the faint ones. Shioya et al. (2008) found that the two-point correlation function for faint Hα emitters ($L_{H\alpha} < 10^{40.54}$ erg s^{-1}) at $z \sim 0.24$ follows the relationship: $\omega(\theta) = (0.011 \pm 0.002)\theta^{(-0.84 \pm 0.05)}$, while brighter emitters with $10^{40.54} < L_{H\alpha} \lesssim 10^{41.5}$ erg s^{-1} follow the relationship: $\omega(\theta) = (0.019 \pm 0.004)\theta^{(-1.08 \pm 0.05)}$. The amplitude of the two-point correlation function for our faint sample is 0.208 ± 0.035, while for the bright sample it is slightly larger: 0.295 ± 0.026. The relation is also steeper for the bright sample than for the faint sample. Our results therefore support and extend the claim that brighter (and hence more star-forming galaxies) are more clustered than faint ones to very high luminosities beyond $10^{41.0}$ erg s^{-1} up to $10^{42.4}$ erg s^{-1} ($L/L_{H\alpha}^* \sim 5.0$).

We use the inverse Limber transformation and the redshift distribution of the NB filters to translate the two-point correlation function into a 3D spatial correlation (Peebles 1980), assuming the latter is well described by $\epsilon = (r/r_0)^\gamma$, where r_0 is the real-space correlation length of the Hα emitters. Following the method of Sobral et al. (2010), we assume that the two filters have a perfect top-hat shape. We compute r_0 for each realisation of $\omega(\theta)$ in each filter, by fixing $\beta = -0.8$. We finally combine the data for the two filters. The dependence of r_0 on redshift is shown in Figure 10.13.

For the full sample, we obtain a correlation length $r_0 = 3.3$ Mpc/h with a standard deviation 0.8 Mpc/h. We obtain $r_0 = 3.5 \pm 1.1$ Mpc/h for our fainter Hα sample and 5.0 ± 1.5 Mpc/h for the brighter one. Our measurements are larger than those of Sobral et al. (2010) at $z \sim 0.24$ (based on the sample from Shioya et al. (2008)), which find a value of 1.8 ± 0.2 Mpc/h for their sample with $10^{39.4} < L_{H\alpha} < 10^{41.5}$ erg s^{-1}. As expected, fainter Hα galaxies have smaller correlation lengths than brighter ones (Norberg et al. 2001; Shioya et al. 2008; Sobral et al. 2010). The correlation length also depends on redshift, but the evolution is driven by the typical luminosity: at high redshift, Hα emitters are on average brighter and have larger r_0 than lower redshift sources.

Similar results are found by Hartley et al. (2010), who select galaxies using K band luminosity as proxy for stellar mass. The authors find that red galaxies, likely mostly ellipticals, are more clustered than the blue galaxies. Selecting star-forming galaxies based on colours, they find that r_0 drops with redshift. However, no dependence of r_0 on broad band luminosity was found. By contrast, Bielby et al. (2014) use a mass selected sample and find that higher mass galaxies tend to have larger clustering lengths. Additionally, they find that the clustering strength increases with stellar mass. Stellar mass correlates well with SFR (e.g. at $z \sim 0.2$ Stroe et al. 2015), which can then be translated to an equivalent Hα luminosity though equation 7.5. The results from Bielby et al. (2014) may indicate that more star forming, more luminous galaxies have larger r_0 which is consistent with our findings. Note however that Sobral et al. (2010) controlled for both Hα luminosity and mass (K band luminosity) and found both are important for the evolution of r_0: r_0 increases with both higher $L_{H\alpha}$ and K band luminosity.

The clustering of the Hα emitters depends on the clustering of their host dark matter (DM) haloes. The bias parameter $b(z)$ describes how the matter distribution traces the DM distri-
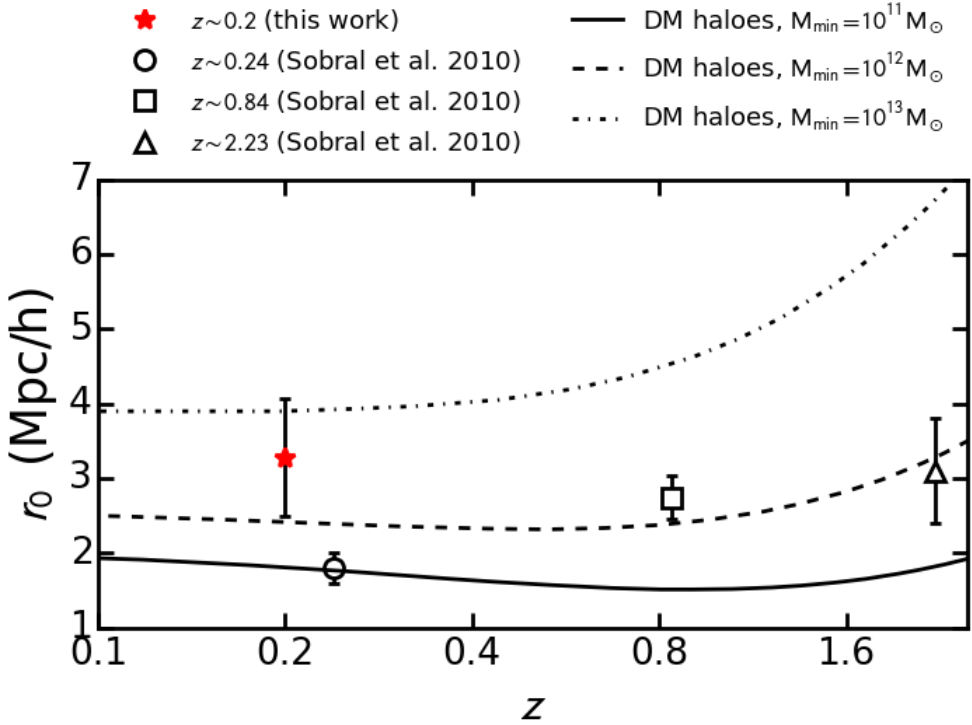
Figure 10.13: The dependence of the clustering length r_0 on redshift, using a consistent set of Hα emitters selected through NB surveys. For comparison, we are also showing data from Sobral et al. (2010). The plot suggests that typical ($L^*_{H\alpha}$) emitters have very similar r_0 across cosmic time. At $z \sim 0.2$, there is a sharp increase in the typical DM halo mass with luminosity of the Hα sample. Note however, as shown in Figure 10.14, that once corrected for the redshift evolution of the characteristic luminosity, $L_{H\alpha}$ sets the position of galaxies in relation to DM halo host.
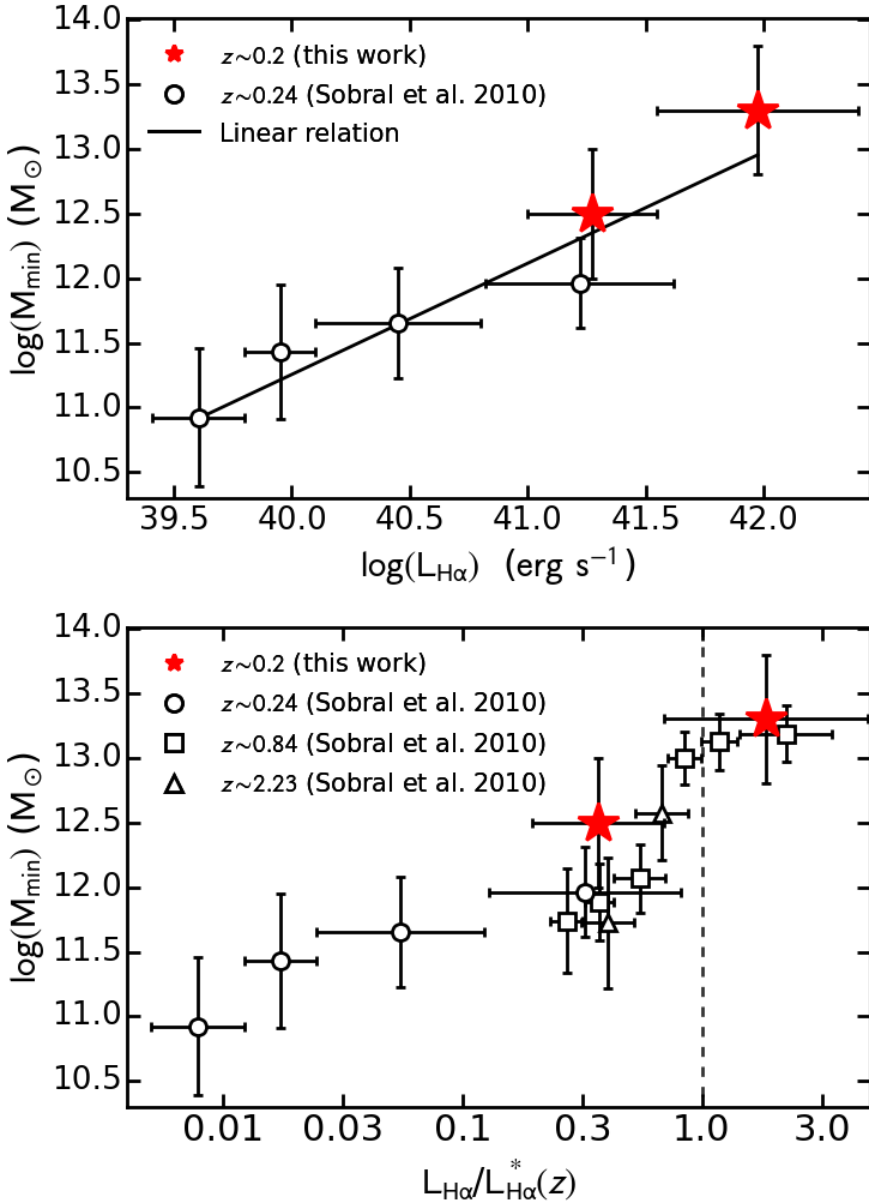
Figure 10.14: The minimum DM halo mass (M_{DM}) as function of luminosity ($L_{\mathrm{H}\alpha}$, left) and luminosity scaled by the characteristic luminosity at the respective redshift ($L_{\mathrm{H}\alpha}/L_{\mathrm{H}\alpha}^*(z)$, right). The data from Sobral et al. (2010), split per luminosity bin, are shown for comparison. The ~ 0.2 points are renormalised using the $L_{\mathrm{H}\alpha}^*$ derived in this paper. All luminosities are not corrected for intrinsic dust extinction. Note the relation between the Hα luminosity and host mass. When scaled for the typical luminosity, a clear relation between DM halo mass and luminosity is observed from $z \sim 2.23$ to $z \sim 0.2$.

bution, as function of redshift. In the bias model of Matarrese et al. (1997), the physical parameters of galaxies are determined by their host dark matter halo mass. In such a model, $b(z)$ depends on the minimum mass of the DM halo. Figure 10.13 also contain r_0 predictions for dark matter (DM) haloes with fixed minimum mass of $M_{\min} = 10^{11-13} M_\odot$, as calculated by Geach et al. (2008) assuming a ΛCDM cosmology and an evolving bias model from Matarrese et al. (1997) and Moscardini et al. (1998). Note however, the r_0 prediction is highly dependent on the model, see for example Hartley et al. (2010). We thus note that while the trends are valid, the normalisation of the $M_{\min}$ could be higher than that used here, leading to lower masses than derived here.

The emitters from Shioya et al. (2008), probing fainter Hα regimes with $L_{H\alpha} < 10^{41.5}$ erg s^{-1}, reside in DM haloes of $10^{11} M_\odot$ mass. These are most likely dwarf galaxies. By contrast, our faint sample is hosted by DM haloes of about $10^{12.5} M_\odot$ mass, about the mass of the Milky Way. The bright Hα emitters are hosted by $\sim 10^{13-13.5} M_\odot$ DM haloes, which are most probably already galaxy groups.

Figure 10.14 shows how the DM halo minimum mass varies as function of Hα luminosity and the luminosity scaled by the characteristic luminosity at that redshift ($L_{H\alpha}/L^*_{H\alpha}(z)$). By comparing our results, with the results from Sobral et al. (2010) (based on data from Shioya et al. (2008)), we find a linear correlation between the host minimum DM halo mass and luminosity (in log-log space, see Figure 10.14). This indicates that more luminous, more star-forming galaxies reside is more massive dark matter haloes.

Accounting for the evolution of the characteristic luminosity with redshift, we find that more luminous emitters reside in more massive DM haloes, irrespective of redshift. Such a comparison between $z < 0.4$ and $z > 4$ samples has been previously difficult because of the different $L_{H\alpha}/L^*_{H\alpha}(z)$ ranges probed in the different redshift ranges. With our measurements, we probe beyond $L^*_{H\alpha}$ at $z \sim 0.2$ for the first time to be fully comparable with samples up to $z \sim 2.23$. Our measurements therefore confirm the results from Sobral et al. (2010) and Geach et al. (2012), who find that $L^*_{H\alpha}$ galaxies reside in $\sim 10^{13} M_\odot$, Milky Way size DM haloes, at all redshifts. The results indicate the the position of a star forming galaxies within the Hα luminosity function is dictated by the host DM halo mass, at all cosmic times since ~ 2.3.

10.6 Conclusions

In order to constrain the evolution of the star-forming galaxies across cosmic time, large samples of sources are necessary. Such samples are available at high redshifts ($z > 0.8$) through NB selected Hα emitter samples which probe large volumes ($> 10^5$ Mpc^3) and overcome cosmic variance. However, at low redshifts ($z < 0.8$), large areas (> 15 deg^2) need to be surveyed in order to match the volumes at high redshift. By carrying out the largest survey of Hα emitters at $z \sim 0.2$, we produce a luminosity function describing typical galaxies within representative volumes of the Universe. With our large sample of bright emitters we study their distribution and clustering and place it in the context of the evolution of the SFRD throughout cosmic history. Our main results are:

- The Hα luminosity function at $z \sim 0.2$ is well described by a Schechter function with $\log(\phi^*) = -2.85 \pm 0.03$ (Mpc^{-3}) and $\log(L^*_{H\alpha}) = 41.71 \pm 0.02$ (erg s^{-1}). We find that previous studies, probing far smaller volumes, underestimate the characteristic lu-

minosity $L_{\text{H}\alpha}^*$, but are reconciled with our results if cosmic variance uncertainties are taken into account. For volumes typically probed in previous Hα works at $z \sim 0.2$ of $< 5 \times 10^4$ Mpc^3, cosmic variance can account to more than 50 per cent variance in the LF parameters.

- By assuming a 15 per cent AGN fraction, we derive a star formation rate density of $\rho_{\text{SFRD}} = 0.0094 \pm 0.0008$ M$_\odot$ yr^{-1} Mpc^{-1}.

- We find significant cosmic variance in the distribution of the Hα emitters, but on average $1 - 4$ bright ($L_{\text{H}\alpha} > 10^{41.1}$ erg s^{-1}) Hα emitters are found per square degree.

- We study the clustering of the Hα emitters. The two-point correlation function is well fit by a single power law $\omega(\theta) = (0.159 \pm 0.012)\theta^{(-0.75\pm0.05)}$, with a spatial clustering length $r_0 = 5.0 \pm 1.1$ Mpc/h for the bright sample ($10^{41.0-41.55}$ erg s^{-1}) and $r_0 = 3.5 \pm 1.1$ Mpc/h for the faint sample ($10^{41.55-42.40}$ erg s^{-1}). Our results confirm that luminous, strongly star-forming galaxies are more clustered than those weakly star-forming.

- We find that, at $z \sim 0.2$, the higher the SFR, the more massive the DM halo host is. When accounting for the redshift dependence of the characteristic Hα luminosity, there is no redshift dependence of the host mass, but a strong dependence on $L_{\text{H}\alpha}/L_{\text{H}\alpha}^*(z)$.

Acknowledgements

Figure 10.15: Survey completeness as a function of Hα flux, plotted separately for each field and NB filter used to select Hα candidates. Each curve is associated with the the completeness study for a different CCD chip within each pointing. The darker the colour the more completeness curves fall within that region. Note the XMMLSS field is significantly more complete than the W2 field.

10.7 Appendix

10.7.1 Survey completeness

The method for studying the completeness is detailed in Section 10.4.1. The dependence of the completeness on line flux is shown in Figure 10.15.

10.7.2 Survey completeness

The results of the resampling of the LF at $z \sim 0.2$ with different binnings is presented for a range of data selections. The faint end slope is fixed at -1.35 and -1.7 and ϕ and L are fit using data selected from the two NB filters independently and combined. The results are shown in Figures 10.16, 10.17, 10.18 and 10.19.
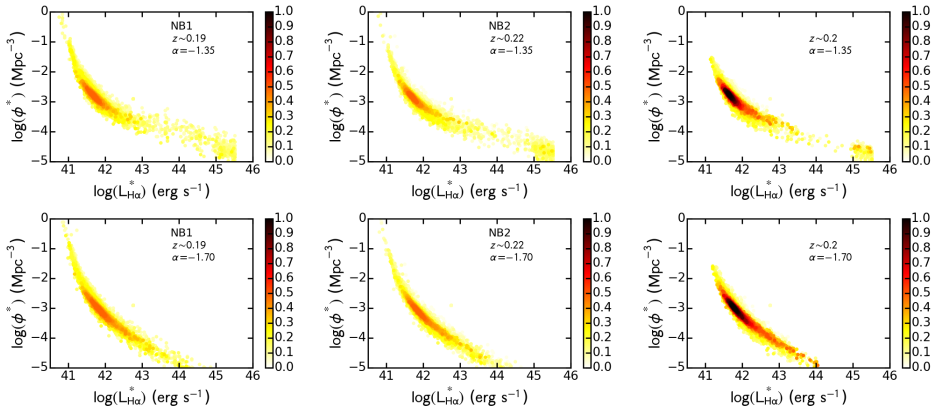
Figure 10.16: As for Figure 6.8, but with different values of α and when using the data for the two filters separately or together.
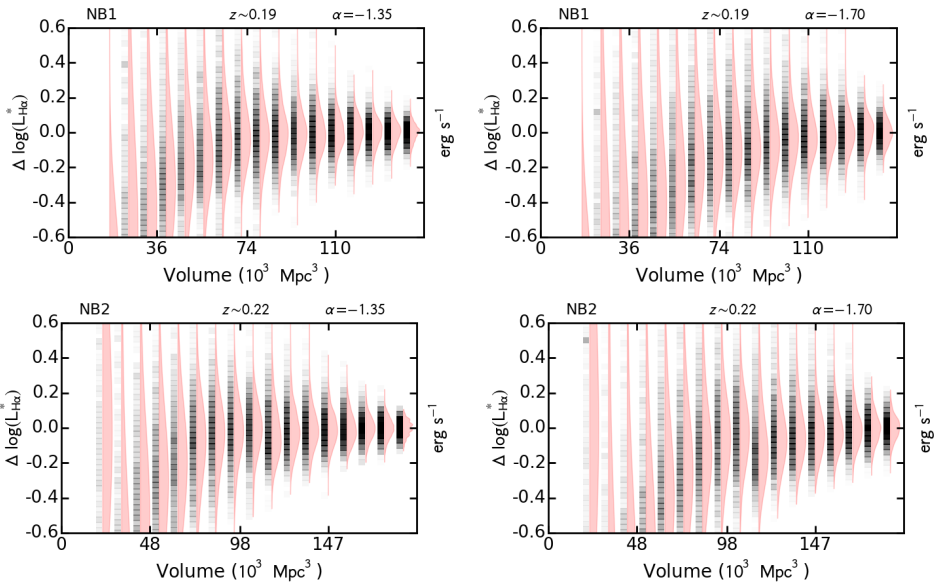
Figure 10.17: As Figure 10.11, but for data samples from the two NB filters independently. Note that similar results are found for the two filters, even when considered separately.
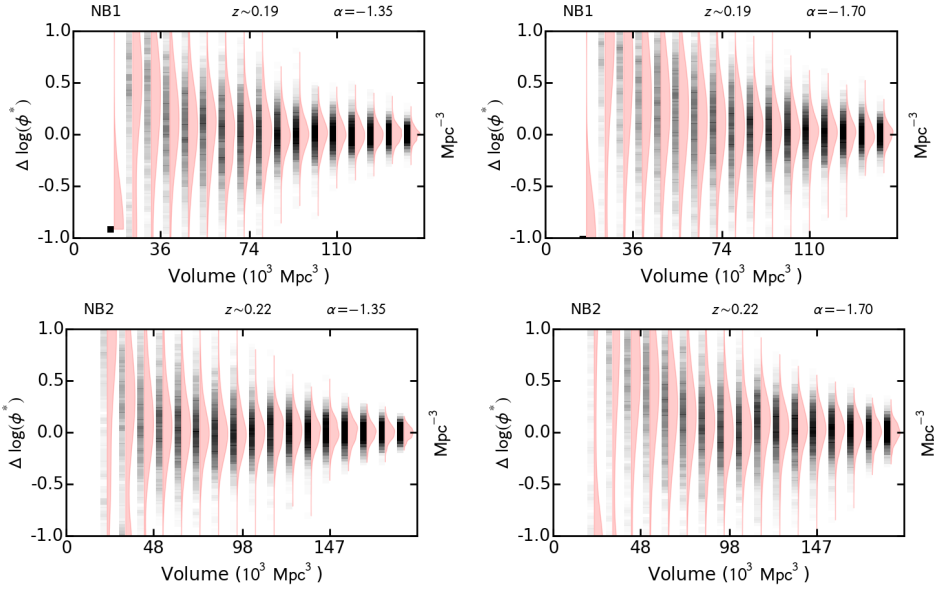
Figure 10.18: As Figure 10.11, but for data samples from the two NB filters independently. Note that similar results are found for the two filters, even when considered separately.
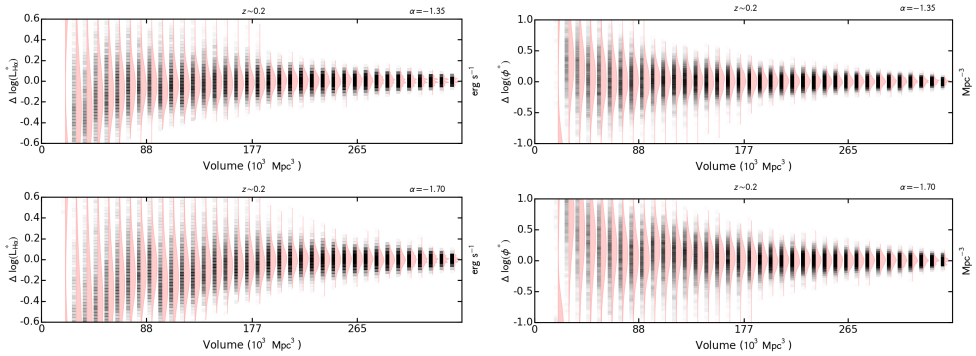
Figure 10.19: As Figure 10.11, but for different α values.

Bibliography

Abazajian, K. N., Adelman-McCarthy, J. K., Agüeros, M. A., et al. 2009, ApJS, 182, 543

Adelman-McCarthy, J. K., et al. 2009, VizieR Online Data Catalog, 2294, 0

Ahn, C. P., Alexandroff, R., Allende Prieto, C., et al. 2012, ApJS, 203, 21

Akamatsu, H., & Kawahara, H. 2013, PASJ, 65, 16

Alloin D., Collin-Souffrin S., Joly M., Vigroux L., 1979, A&A, 78, 200

Andersen, V., & Owen, F. N. 1995, AJ, 109, 1582

Athreya, R. 2009, ApJ, 696, 885

Avni, Y. 1976, ApJ, 210, 642

Baars, J. W. M., Genzel, R., Pauliny-Toth, I. I. K., & Witzel, A. 1977, A&A, 61, 99

Bagchi, J., Ensslin, T. A., Miniati, F., et al. 2002, *New Astronomy*, 7, 249

Bagchi, J., Durret, F., Neto, G. B. L., & Paul, S. 2006, Science, 314, 791

Bagchi, J., Sirothia, S. K., Werner, N., et al. 2011, ApJL, 736, L8

Bahcall, N. A. 1977, ApJL, 218, L93

Baldwin, J. A., Phillips, M. M., & Terlevich, R. 1981, PASP, 93, 5

Balogh, M. L., Schade, D., Morris, S. L., et al. 1998, ApJL, 504, L75

Balogh, M. L., Couch, W. J., Smail, I., Bower, R. G., & Glazebrook, K. 2002, MNRAS, 335, 10

Balogh, M., Eke, V., Miller, C.,et al. 2004, MNRAS, 348, 1355

Barnes, J. E. 2004, MNRAS, 350, 798

Bekki, K., & Couch, W. J. 2003, ApJL, 596, L13

Bekki, K. 2009, MNRAS, 399, 2221

Bertin, E., & Arnouts, S. 1996, A&AS, 117, 393

Bertin, E., Mellier, Y., Radovich, M., et al. 2002, Astronomical Data Analysis Software and Systems XI, 281, 228

Bertin, E. 2006, Astronomical Data Analysis Software and Systems XV, 351, 112

Best P. N., 2004, MNRAS, 351, 70

Best, P., Smail, I., Sobral, D., et al. 2010, arXiv:1003.5183

Bhatnagar, S., Cornwell, T. J., Golap, K., & Uson, J. M. 2008, A&A, 487, 419

Bielby, R. M., Gonzalez-Perez, V., McCracken, H. J., et al. 2014, A&A, 568, A24

Bland-Hawthorn, J., van Breugel, W., Gillingham, P. R., Baldry, I. K., & Jones, D. H. 2001, ApJ, 563, 611

Blandford, R. & Eichler, D. 1987, Phys. Rep., 154, 1

Blasi, P., & Colafrancesco, S. 1999, Astroparticle Physics, 12, 169

Bolatto, A. D., Wolfire, M., & Leroy, A. K. 2013, ARA&A, 51, 207

Bonafede, A., Feretti, L., Giovannini, G., et al. 2009, A&A, 503, 707

Bonafede, A., Giovannini, G., Feretti, L., Govoni, F., & Murgia, M. 2009, A&A, 494, 429

Bonafede, A., Feretti, L., Murgia, M., et al. 2010, A&A, 513, A30

Bonafede, A., Govoni, F., Feretti, L., et al. 2011, A&A, 530, A24

Bonafede, A., Brüggen, M., van Weeren, R., et al. 2012, MNRAS, 426, 40

Bouwens, R. J., Illingworth, G. D., Oesch, P. A., et al. 2011, ApJ, 737, 90

Bouwens, R. J., Illingworth, G. D., Oesch, P. A., et al. 2015, ApJ, 803, 34

Brammer, G. B., van Dokkum, P. G., & Coppi, P. 2008, ApJ, 686, 1503

Bridle, A. H., & Perley, R. A. 1984, ARA&A, 22, 319

Briggs, D. S. 1995, PhD thesis, New Mexico Institute of Mining Technology, Socorro, New Mexico, USA

Brinchmann J., Charlot S., White S. D. M., Tremonti C., Kauffmann G., Heckman T., Brinkmann J., 2004, MNRAS, 351, 1151

Brown, S., Duesterhoeft, J., & Rudnick, L. 2011, ApJL, 727, L25

Brüggen, M., Bykov, A., Ryu, D., Röttgering, H. 2012, Space Sci. Rev., 166, 187

Brüggen, M., van Weeren, R. J., Röttgering, H. J. A. 2012, MNRAS, 425, L76

Brüggen, M. 2013, MNRAS, 436, 294

Brunetti, G., Setti, G., Feretti, L., & Giovannini, G. 2001, MNRAS, 320, 365

Brunetti, G., Blasi, P., Cassano, R., & Gabici, S. 2004, MNRAS, 350, 1174

Brunetti, G., & Lazarian, A. 2007, MNRAS, 378, 245

Brunetti, G., & Lazarian, A. 2011, MNRAS, 410, 127

Brunetti, G., & Jones, T. W. 2014, International Journal of Modern Physics D, 23, 30007

Bruzual, G., & Charlot, S. 2003, MNRAS, 344, 1000

Bruzual, G. 2007, From Stars to Galaxies: Building the Pieces to Build Up the Universe, 374, 303

Bunker, A. J., Warren, S. J., Hewett, P. C., & Clements, D. L. 1995, MNRAS, 273, 513

Butcher, H., & Oemler, A., Jr. 1978a, ApJ, 226, 559

Butcher, H., & Oemler, A., Jr. 1978b, ApJ, 219, 18

Bykov, A. M., Dolag, K., & Durret, F. 2008, Space Sci. Rev., 134, 119

Bykov, A. M., Uvarov, Y. A., & Ellison, D. C. 2008, ApJL, 689, L133

Bykov, A. M., Ellison, D. C., & Renaud, M. 2012, Space Sci. Rev., 166, 71

Calzetti D., Armus L., Bohlin R. C., Kinney A. L., Koornneef J., Storchi-Bergmann T., 2000, ApJ, 533, 682

Capak, P., Aussel, H., Ajiki, M., et al. 2007, ApJS, 172, 99

Carilli, C. L., & Walter, F. 2013, ARA&A, 51, 105

Casali, M., Adamson, A., Alves de Oliveira, C., et al. 2007, A&A, 467, 777

Cayatte, V., van Gorkom, J. H., Balkowski, C., & Kotanyi, C. 1990, AJ, 100, 604

Cedrés, B., Iglesias-Páramo, J., Vílchez, J. M., et al. 2009, AJ, 138, 873

Chabrier, G. 2003, PASP, 115, 763

Chandra, P., Ray, A., & Bhatnagar, S. 2004, ApJ, 612, 974

Chengalur, J. N., Braun, R., & Wieringa, M. 2001, A&A, 372, 768

Chung, A., van Gorkom, J. H., Kenney, J. D. P., Crowl, H., & Vollmer, B. 2009, AJ, 138, 1741

Chung, S. M., Gonzalez, A. H., Clowe, D., Markevitch, M., & Zaritsky, D. 2010, ApJ, 725, 1536

Clarke, T. E., Kronberg, P. P., Böhringer, H. 2001, ApJL, 547, L111

Clowe, D., Bradač, M., Gonzalez, A. H., et al. 2006, ApJL, 648, L109

Cohen, A. S., Lane, W. M., Cotton, W. D., et al. 2007, AJ, 134, 1245

Collins J. A., Rand R. J., 2001, ApJ, 551, 57

Condon, J. J. 1992, ARA&A, 30, 575

Condon, J. J., Cotton, W. D., Greisen, E. W., et al. 1998, AJ, 115, 1693

Cooper M. C., Tremonti C. A., Newman J. A., Zabludoff A. I., 2008, MNRAS, 390, 245

Cornwell, T. J. & Perley, R. A. 1992, A&A, 261, 353

Cornwell, T. J., Golap, K., & Bhatnagar, S. 2005, Astronomical Data Analysis Software and Systems XIV, 347, 86

Cornwell, T. J., Golap, K., & Bhatnagar, S. 2008, IEEE Journal of Selected Topics in Signal Processing, 2, 647

Couch, W. J., Ellis, R. S., Sharples, R. M., & Smail, I. 1994, ApJ, 430, 121

Couch, W. J., Balogh, M. L., Bower, R. G., et al. 2001, ApJ, 549, 820

Cowie, L. L., Songaila, A., Hu, E. M., & Cohen, J. G. 1996, AJ, 112, 839

Crockett, R. M., Shabala, S. S., Kaviraj, S., et al. 2012, MNRAS, 421, 1603

Dale, D. A., Barlow, R. J., Cohen, S. A., et al. 2010, ApJL, 712, L189

Darvish, B., Sobral, D., Mobasher, B., et al. 2014, ApJ, 796, 51

AMI Consortium, Davies, M. L., Franzen, T. M. O., Davies, R. D., et al. 2009, MNRAS, 400, 984

AMI Consortium, Davies, M. L., Franzen, T. M. O., et al. 2011, MNRAS, 415, 2708

Dawson, W. A., Wittman, D., Jee, M. J., et al. 2012, ApJL, 747, L42

Dawson, W. A. 2013, ApJ, 772, 131

Dawson, W. A., Jee, M. J., Stroe, A., et al. 2015, ApJ, 805, 143

Djorgovski, S., Spinrad, H., Pedelty, J., Rudnick, L., & Stockton, A. 1987, AJ, 93, 1307

Dolag, K., & Ensslin, T. A. 2000, A&A, 362, 151

Donnelly, R. H., Markevitch, M., Forman, W., et al. 1998, ApJ, 500, 138

Douglas, J. N., Bash, F. N., Bozyan, F. A., Torrence, G. W., & Wolfe, C. 1996, AJ, 111, 1945

Doyle, M. T., & Drinkwater, M. J. 2006, MNRAS, 372, 977

Drake, A. B., Simpson, C., Collins, C. A., et al. 2013, MNRAS, 433, 796

Dressler, A. 1980, ApJ, 236, 351

Drury, L. O. 1983, Reports on Progress in Physics, 46, 973

Dunkley, J., Komatsu, E., Nolta, M. R., et al. 2009, ApJs, 180, 306

Ebeling, H., Stephenson, L. N., & Edge, A. C. 2014, ApJL, 781, L40

Ellison, S. L., Simard, L., Cowan, N. B., et al. 2009, MNRAS, 396, 1257

Ensslin, T. A., Biermann, P. L., Klein, U., & Kohle, S. 1998, A&A, 332, 395

Ensslin, T. A., & Gopal-Krishna 2001, A&A, 366, 26

Ensslin, T. A., & Brüggen, M. 2002, MNRAS, 331, 1011

Emerson, D. T., Klein, U., & Haslam, C. G. T. 1979, A&A, 76, 92

Emerson, D. T., & Graeve, R. 1988, A&A, 190, 353

Erb, D. K., Shapley A. E., Pettini M., et al. 2006, ApJ, 644, 813

Erben, T., Hildebrandt, H., Miller, L., et al. 2013, MNRAS, 433, 2545

Erler, J., Basu, K., Trasatti, M., Klein, U., & Bertoldi, F. 2015, MNRAS, 447, 2497

Faber, S. M., Phillips, A. C., Kibrick, R. I., et al. 2003, Proc. SPIE, 4841, 1657

Fanaroff, B. L., & Riley, J. M. 1974, MNRAS, 167, 31P

Feretti, L., Fusco-Femiano, R., Giovannini, G., & Govoni, F. 2001, A&A, 373, 106

Ferrari, C., Govoni, F., Schindler, S., Bykov, A. M., & Rephaeli, Y. 2008, Space Sci. Rev.,
    134, 93

Feretti, L., Giovannini, G., Govoni, F., & Murgia, M. 2012, A&Ar, 20, 54

Ferrari, C., Maurogordato, S., Cappi, A., & Benoist, C. 2003, A&A, 399, 813

Ferrari C., Benoist C., Maurogordato S., et al. 2005, A&A, 430, 19

Ferrari, C., Arnaud, M., Ettori, S., Maurogordato, S., & Rho, J. 2006, A&A, 446, 417

Finn, R. A., Zaritsky, D., McCarthy, D. W., Jr., et al. 2005, ApJ, 630, 206

Finoguenov, A., Sarazin, C. L., Nakazawa, K., Wik, D. R., & Clarke, T. E. 2010, ApJ, 715,
    1143

Förster Schreiber, N. M., Genzel, R., Bouché, N., et al. 2009, ApJ, 706, 1364

Fox A. J., 2011, ApJ, 730, 58

Fujita, S. S., Ajiki, M., Shioya, Y., et al. 2003, ApJL, 586, L115

Fumagalli, M., Fossati, M., Hau, G. K. T., et al. 2014, MNRAS, 445, 4335

Garcet, O., Gandhi, P., Gosset, E., et al. 2007, A&A, 474, 473

Garn, T., & Best, P. N. 2010, MNRAS, 409, 421

Gavazzi, G., & Jaffe, W. 1985, ApJL, 294, L89

Gavazzi, G., Catinella, B., Carrasco, L., Boselli, A., & Contursi, A. 1998, AJ, 115, 1745

Gavazzi, G., Boselli, A., Mayer, L., et al. 2001, ApJL, 563, L23

Geach, J. E., Smail, I., Best, P. N., et al. 2008, MNRAS, 388, 1473

Geach, J. E., Sobral, D., Hickox, R. C., et al. 2012, MNRAS, 426, 679

Genzel, R., Newman, S., Jones, T., et al. 2011, ApJ, 733, 101

Giacintucci, S., Venturi, T., Macario, G., et al. 2008, A&A, 486, 347

Gieseler, U. D. J., & Jones, T. W. 2000, A&A, 357, 1133

Gilbank D. G., Bower R. G., Glazebrook K., et al. 2011, MNRAS, 414, 304

Gómez, P. L., Nichol, R. C., Miller, C. J., et al. 2003, ApJ, 584, 210

Goto, T., Yamauchi, C., Fujita, Y., et al. 2003, MNRAS, 346, 601

Govoni, F., Murgia, M., Feretti, L., et al. 2006, A&A, 460, 425

Gower, J. F. R., Scott, P. F., & Wills, D. 1967, MmRAS, 71, 49

Grazian, A., Fontana, A., de Santis, C., et al. 2006, A&A, 449, 951

Greisen, E. W. 2003, Information Handling in Astronomy - Historical Vistas, 285, 109

Gunawardhana, M. L. P., Hopkins, A. M., Bland-Hawthorn, J., et al. 2013, MNRAS, 433, 2764

Gunn, J. E., & Gott, J. R., III 1972, ApJ, 176, 1

Guth, A. H. 1981, Phys. Rev. D, 23, 347

Gwyn, S. D. J. 2012, AJ, 143, 38

Hamer, S., Salomé, P., Combes, F., & Salomé, Q. 2014, arXiv:1409.7700

Hardcastle, M. J. 2013, MNRAS, 433, 3364

Hartley, W. G., Almaini, O., Cirasuolo, M., et al. 2010, MNRAS, 407, 1212

Harwood, J. J., Hardcastle, M. J., Croston, J. H., & Goodger, J. L. 2013, MNRAS, 435, 3353

Haslam, C. G. T. 1974, A&A, 15, 333

Hayashi, M., Kodama, T., Koyama, Y., et al. 2010, MNRAS, 402, 1980

Hayashi, M., Kodama, T., Koyama, Y., Tadaki, K.-I., & Tanaka, I. 2011, MNRAS, 415, 2670

Heckman T. M., Lehnert M. D., Strickland D. K., Armus L., 2000, ApJs, 129, 493

Hewett, P. C., Warren, S. J., Leggett, S. K., & Hodgkin, S. T. 2006, MNRAS, 367, 454

Hodgkin, S. T., Irwin, M. J., Hewett, P. C., & Warren, S. J. 2009, MNRAS, 394, 675

Hoeft, M., Brüggen, M., & Yepes, G. 2004, MNRAS, 347, 389

Hoeft, M., & Brüggen, M. 2007, MNRAS, 375, 77

Hoeft, M., Nuza, S. E., Gottlöber, S., et al. 2011, Journal of Astrophysics and Astronomy, 32, 509

Hopkins, A. M., & Beacom, J. F. 2006, ApJ, 651, 142

Hopkins P. F., Keres D., Onorbe J., et al. 2013, arXiv:1311.2073

Hudson, D. S., Mittal, R., Reiprich, T. H., et al. 2010, A&A, 513, AA37

Hwang H. S., Lee M. G., 2009, MNRAS, 397, 2111

Iapichino, L., & Brüggen, M. 2012, MNRAS, 423, 2781

Ibar, E., Sobral, D., Best, P. N., et al. 2013, MNRAS, 434, 3218

Iglesias-Páramo, J., Boselli, A., Cortese, L., Vílchez, J. M., & Gavazzi, G. 2002, A&A, 384, 383

Ilbert, O., Arnouts, S., McCracken, H. J., et al. 2006, A&A, 457, 841

Ilbert, O., Capak, P., Salvato, M., et al. 2009, ApJ, 690, 1236

Intema, H. T., van der Tol, S., Cotton, W. D., et al. 2009, A&A, 501, 1185

Jaffe, W. J., & Perola, G. C. 1973, A&A, 26, 423

Jarvis, M. J., Bonfield, D. G., Bruce, V. A., et al. 2013, MNRAS, 428, 1281

Jee, M. J., Stroe, A., Dawson, W., et al. 2015, ApJ, 802, 46

Johnston-Hollitt, M., Sato, M., Gill, J. A., Fleenor, M. C., & Brick, A.-M. 2008, MNRAS, 390, 289

Kang, H., Ryu, D., Cen, R., & Ostriker, J. P. 2007, ApJ, 669, 729

Kang, H. 2011, Journal of Korean Astronomical Society, 44, 49

Kang, H., & Ryu, D. 2011, ApJ, 734, 18

Kang, H., Ryu, D., & Jones, T. W. 2012, ApJ, 756, 97

Kang, H. 2015, Journal of Korean Astronomical Society, 48, 9

Kang, H. 2015, Journal of Korean Astronomical Society, 48, 155

Kang, H., & Ryu, D. 2015, arXiv:1505.04256

Kapferer, W., Sluka, C., Schindler, S., Ferrari, C., & Ziegler, B. 2009, A&A, 499, 87

Kardashev, N. S. 1962, Soviet Ast., 6, 317

Karim A., Schinnerer E., Martínez-Sansigre A., et al. 2011, ApJ, 730, 61

Katayama, H., Hayashida, K., Takahara, F., & Fujita, Y. 2003, ApJ, 585, 687

Katz-Stone, D. M., Rudnick, L., & Anderson, M. C. 1993, ApJ, 407, 549

Kauffmann, G., Heckman, T. M., White, S. D. M., et al. 2003, MNRAS, 341, 33

Kauffmann G., White S. D. M., Heckman T. M., et al. 2004, MNRAS, 353, 713

Kenney, J. D., & Young, J. S. 1986, ApJL, 301, L13

Kenney, J. D. P., & Young, J. S. 1989, ApJ, 344, 171

Kennicutt, R. C., Jr. 1998, ARA&A, 36, 189

Keshet, U., Waxman, E., Loeb, A., Springel, V., & Hernquist, L. 2003, ApJ, 585, 128

Kewley L. J., Dopita M. A., Sutherland R. S., Heisler C. A., Trevena J., 2001, ApJ, 556, 121

Kewley L. J., Maier C., Yabe K., et al. 2013, ApJl, 774, L10

Kirk, J. G., & Heavens, A. F. 1989, MNRAS, 239, 995

Kirkpatrick, J. D., Henry, T. J., & McCarthy, D. W., Jr. 1991, ApJS, 77, 417

Kirkpatrick, J. D., Reid, I. N., Liebert, J., et al. 1999, ApJ, 519, 802

Kocevski, D. D., Ebeling, H., Mullis, C. R., & Tully, R. B. 2007, ApJ, 662, 224

Kodama, T., Balogh, M. L., Smail, I., Bower, R. G., & Nakata, F. 2004, MNRAS, 354, 1103

Kodama T., Hayashi M., Koyama Y., et al., eds, IAU Symposium Vol. 295 of IAU Symposium, Mahalo-Subaru: Mapping Star Formation at the Peak Epoch of Massive Galaxy Formation. pp 74–77

Komissarov, S. S., & Gubanov, A. G. 1994, A&A, 285, 27

Kornei K. A., Shapley A. E., Martin C. L., et al., 2012, ApJ, 758, 135

Kovac, J. M., Leitch, E. M., Pryke, C., et al. 2002, Nature, 420, 772

Koyama, Y., Kodama, T., Shimasaku, K., et al. 2010, MNRAS, 403, 1611

Koyama, Y., Smail, I., Kurk, J., et al. 2013, MNRAS, 434, 423

Koyama, Y., Kodama, T., Tadaki, K.-i., et al. 2014, ApJ, 789, 18

Kronberger, T., Kapferer, W., Ferrari, C., Unterguggenberger, S., & Schindler, S. 2008, A&A, 481, 337

Kulas K. R., McLean I. S., Shapley A. E., et al. 2013, ApJ, 774, 130

Kurk, J. D., Pentericci, L., Röttgering, H. J. A., & Miley, G. K. 2004, A&A, 428, 793

Lah, P., Chengalur, J. N., Briggs, F. H., et al. 2007, MNRAS, 376, 1357

Lah, P., Pracy, M. B., Chengalur, J. N., et al. 2009, MNRAS, 399, 1447

Landau, L. D. & Lifshitz, E. M. 1959, Fluid mechanics, ed. Landau, L. D. & Lifshitz, E. M.

Landy, S. D., & Szalay, A. S. 1993, ApJ, 412, 64

Larson, R. B., Tinsley, B. M., & Caldwell, C. N. 1980, ApJ, 237, 692

Lawrence, A., Warren, S. J., Almaini, O., et al. 2007, MNRASs, 379, 1599

Leahy, D. A., & Roger, R. S. 1998, ApJ, 505, 784

Leccardi, A., & Molendi, S. 2008, A&A, 487, 461

Leroy, A. K., Walter, F., Brinks, E., et al. 2008, AJ, 136, 2782

Lewis, J. R., Bunclark, P. S., Irwin, M. J., McMahon, R. G., & Walton, N. A. 2000, Astronomical Data Analysis Software and Systems IX, 216, 415

Lewis, I., Balogh, M., De Propris, R., et al. 2002, MNRAS, 334, 673

Lilly, S. J., Le Fevre, O., Hammer, F., & Crampton, D. 1996, ApJL, 460, L1

Longair, M. S. 2010, High Energy Astrophysics, Cambridge University Press, 2010. ISBN: 9780521756181,

Ly, C., Malkan, M. A., Kashikawa, N., et al. 2007, ApJ, 657, 738

Ly, C., Lee, J. C., Dale, D. A., et al. 2011, ApJ, 726, 109

Macario, G., Markevitch, M., Giacintucci, S., et al. 2011, ApJ, 728, 82

Madau P., Ferguson H. C., Dickinson M. E., et al. 1996, MNRAS, 283, 1388

Magri, C., Haynes, M. P., Forman, W., Jones, C., & Giovanelli, R. 1988, ApJ, 333, 136

Mahajan S., Haines C. P., Raychaudhury S., 2010, MNRAS, 404

Maiolino R., et al., 2008, A&A, 488, 463

Mann, A. W., & Ebeling, H. 2012, MNRAS, 420, 2120

Mannucci F., Cresci G., Maiolino R., Marconi A., Gnerucci A., 2010, MNRAS, 408, 2115

Markevitch, M., Govoni, F., Brunetti, G., & Jerius, D. 2005, ApJ, 627, 733

Matarrese, S., Coles, P., Lucchin, F., & Moscardini, L. 1997, MNRAS, 286, 115

Mather, J. C., Cheng, E. S., Eplee, R. E., Jr., et al. 1990, ApJL, 354, L37

Mather, J. C., Cheng, E. S., Cottingham, D. A., et al. 1994, ApJ, 420, 439

Matsuda Y., Smail I., Geach J. E., et al. 2011, MNRAS, 416, 2041

Matthee, J. J. A., Sobral, D., Swinbank, A. M., et al. 2014, MNRAS, 440, 2375

McCarthy, P. J., van Breugel, W., Spinrad, H., & Djorgovski, S. 1987, ApJL, 321, L29

McMullin, J. P., Waters, B., Schiebel, D., Young, W., & Golap, K. 2007, Astronomical Data Analysis Software and Systems XVI, 376, 127

Melnyk, O., Plionis, M., Elyiv, A., et al. 2013, A&A, 557, AA81

Melrose, D. B., & Pope, M. H. 1993, Proceedings of the Astronomical Society of Australia, 10, 222

Miley, G. K., Perola, G. C., van der Kruit, P. C., & van der Laan, H. 1972, Nature, 237, 269

Miller N. A., Owen F. N., 2003, AJ, 125, 2427

Miniati, F. 2002, MNRAS, 337, 199

Monet, D. G., Levine, S. E., Canzian, B., et al. 2003, AJ, 125, 984

Moore, B., Katz, N., Lake, G., Dressler, A., & Oemler, A. 1996, Nature, 379, 613

Moore, B., Lake, G., & Katz, N. 1998, ApJ, 495, 139

Moorwood, A. F. M., van der Werf, P. P., Cuby, J. G., & Oliva, E. 2000, A&A, 362, 9

Morabito, L. K., Oonk, J. B. R., Salgado, F., et al. 2014, ApJL, 795, LL33

Morrison, G. E. 1999, Ph.D. Thesis,

Morrison, G. E., & Owen, F. N. 2003, AJ, 125, 506

Moscardini, L., Coles, P., Lucchin, F., & Matarrese, S. 1998, MNRAS, 299, 95

Mushotzky, R. F., & Smith, B. W. 1980, Highlights of Astronomy, 5, 735

Muzzin A., van der Burg R. F. J., McGee S. L., et al. 2014, arXiv:1402.7077

Muzzin A., Wilson G., Yee H. K. C., et al. 2012, ApJ, 746, 188

Navarro, J. F., Frenk, C. S., & White, S. D. M. 1997, ApJ, 490, 493

Naylor, T. 1998, MNRAS, 296, 339

Newman J. A., et al., 2013, ApJs, 208, 5

Noeske K. G., Weiner B. J., Faber S. M., et al. 2007, ApJL, 660, L43

Noordam, J. E. 2004, in SPIE Conference Series, Vol. 5489, ed. J. M. Oschmann, Jr., 817–825

Norberg, P., Baugh, C. M., Hawkins, E., et al. 2001, MNRAS, 328, 64

Nuza, S. E., Hoeft, M., van Weeren, R. J., Gottlöber, S., & Yepes, G. 2012, MNRAS, 420, 2006

O'Dea, C. P., Sarazin, C. L., & Owen, F. N. 1987, ApJ, 316, 113

Offringa, A. R., de Bruyn, A. G., Biehl, M., et al. 2010, MNRAS, 405, 155

Ogrean, G. A., Brüggen, M., Röttgering, H., et al. 2013a, MNRAS, 429, 2617

Ogrean, G. A., Brüggen, M., van Weeren, R. J., et al. 2013b, MNRAS, 433, 812

Ogrean, G. A., Brüggen, M., van Weeren, R. J., et al. 2014a, MNRAS, 440, 3416

Ogrean, G. A., Brüggen, M., van Weeren, R. J., Burgmeier, A., & Simionescu, A. 2014b, MNRAS, 443, 2463

Ohno, H., Takizawa, M., & Shibata, S. 2002, ApJ, 577, 658

Oosterloo, T., & van Gorkom, J. 2005, A&A, 437, L19

Orrú, E., Murgia, M., Feretti, L., et al. 2007, A&A, 467, 943

Osterbrock D. E., 1989, Astrophysics of gaseous nebulae and active galactic nuclei

Ouchi, M., Shimasaku, K., Akiyama, M., et al. 2005, ApJL, 620, L1

Owen F. N., Ledlow M. J., Keel W. C., Wang Q. D., Morrison G. E., 2005, AJ, 129, 31

Owers, M. S., Couch, W. J., Nulsen, P. E. J., & Randall, S. W. 2012, ApJL, 750, L23

Pacholczyk, A. G, 1970, Radio astrophysics : nonthermal processes in galactic and extra-galactic sources

Padovani, P., Miller, N., Kellermann, K. I., et al. 2011, ApJ, 740, 20

Paul, S., Iapichino, L., Miniati, F., Bagchi, J., & Mannheim, K. 2011, ApJ, 726, 17

Peacock, J. A., Cole, S., Norberg, P., et al. 2001, Nature, 410, 169

Peebles, P. J. E. 1980, Research supported by the National Science Foundation. Princeton, N.J., Princeton University Press, 1980. 435 p.

Peng, Y.-j., Lilly, S. J., Kovač, K., et al. 2010, ApJ, 721, 193

Penzias, A. A., & Wilson, R. W. 1965, ApJ, 142, 419

Perley, R. A. 1989, in Astronomical Society of the Pacific Conference Series, Vol. 6, 259–+

Perley, R. T. & Taylor, G. B. 1999, VLA Calibrator Manual, Tech. rep., NRAO

Perley, R. A., & Butler, B. J. 2013, ApJS, 204, 19

Pettini M., Pagel B. E. J., 2004, MNRAS, 348, L59

Petrosian, V. 2001, ApJ, 557, 560

Pierre, M., Valtchanov, I., Altieri, B., et al. 2004, JCAP, 9, 011

Pfrommer, C., Springel, V., Enßlin, T. A., & Jubelgas, M. 2006, MNRAS, 367, 113

Planck Collaboration, Ade, P. A. R., Aghanim, N., et al. 2014, A&A, 571,A29

Planck Collaboration, Ade, P. A. R., Aghanim, N., et al. 2015, arXiv:1502.01589

Poggianti, B. M., Bridges, T. J., Komiyama, Y., et al. 2004, ApJ, 601, 197

Polletta, M., Tajer, M., Maraschi, L., et al. 2007, ApJ, 663, 81

Pranger, F., Böhm, A., Ferrari, C., et al. 2013, A&A, 557, A62

Pranger, F., Böhm, A., Ferrari, C., et al. 2014, A&A, 570, A40

Rau, U., & Cornwell, T. J. 2011, A&A, 532, AA71

Rawle, T. D., Rex, M., Egami, E., et al. 2012, ApJ, 756, 106

Rees, M. J. 1989, MNRAS, 239, 1P

Rengelink, R. B., Tang, Y., de Bruyn, A. G., et al. 1997, A&As, 124, 259

Reynolds, S. P. 2008, ARA&A, 46, 89

Roberts, M. S. 1962, AJ, 67, 437

Rodighiero G., Daddi E., Baronchelli I., et al. 2011, ApJL, 739, L40

AMI Consortium, Rodríguez-Gonzálvez, C., Shimwell, T. W., et al. 2012, MNRAS, 425, 162

Roediger, E., Brüggen, M., Owers, M. S., Ebeling, H., & Sun, M. 2014, MNRAS, 443, L114

Roettiger, K., Burns, J., & Loken, C. 1993, ApJL, 407, L53

Roettiger, K., Loken, C., Burns, J. O., 1997, ApJS, 109, 307

Roettiger, K., Burns, J. O., & Stone, J. M. 1999, ApJ, 518, 603

Rola C. S., Terlevich E., Terlevich R. J., 1997, MNRAS, 289, 419

Röttgering, H. J. A., Lacy, M., Miley, G. K., Chambers, K. C., & Saunders, R. 1994, A&As, 108, 79

Röttgering, H. J. A., Wieringa, M. H., Hunstead, R. W., & Ekers, R. D. 1997, MNRAS, 290, 577

Russell, H. R., van Weeren, R. J., Edge, A. C., et al. 2011, MNRAS, 417, L1

Rybicki, G. B., & Lightman, A. P. 1979, New York, Wiley-Interscience, 1979. 393 p.,

Saitoh, T. R., Daisaka, H., Kokubo, E., et al. 2009, PASJ, 61, 481

Salim, S., Rich, R. M., Charlot, S., et al. 2007, ApJS, 173, 267

Salpeter, E. E. 1955, ApJ, 121, 161

Sanderson, A. J. R., Edge, A. C., & Smith, G. P. 2009, MNRAS, 398, 1698

Sarazin, C. L. 1986, Reviews of Modern Physics, 58, 1

Sarazin, C. L. 2002, in Astrophysics and Space Science Library, Vol. 272, 1–38

Sault, R. J. 1994, A&A, 107, 55

Sault R. J., Teuben P. J., Wright M. C. H., 1995, ASPC, 77, 433

Savitzky, A., & Golay, M. J. E. 1964, Analytical Chemistry, 36, 1627

Schechter, P. 1976, ApJ, 203, 297

Schlafly, E. F., & Finkbeiner, D. P. 2011, ApJ, 737, 103

Schoenmakers, A. P., Mack, K.-H., Lara, L., et al. 1998, A&A, 336, 455

Scott, T. C., Cortese, L., Brinks, E., et al. 2012, MNRAS, 419, L19

Scoville, N., Aussel, H., Brusa, M., et al. 2007, ApJS, 172, 1

Shapley A. E., Steidel C. C., Pettini M., Adelberger K. L., 2003, ApJ, 588, 65

Shimakawa R., Kodama T., Tadaki K.-i., Hayashi M., Koyama Y., Tanaka I., 2015, MNRAS, 448, 666

Shimakawa R., Kodama T., Tadaki K.-i., et al. 2014, MNRAS, 441, L1

Shimwell T. W., et al., 2013, MNRAS, 433, 2036

AMI Consortium, Shimwell, T. W., Rodríguez-Gonzálvez, C., et al. 2013, MNRAS, 433, 2920

Shimwell, T. W., Markevitch, M., Brown, S., et al. 2015, MNRAS, 449, 1486

Shioya, Y., Taniguchi, Y., Sasaki, S. S., et al. 2008, ApJS, 175, 128

Skillman, E. D., Kennicutt, R. C., Jr., Shields, G. A., & Zaritsky, D. 1996, ApJ, 462, 147

Skillman, S. W., Xu, H., Hallman, E. J., et al. 2013, ApJ, 765, 21

Skrutskie, M. F., Cutri, R. M., Stiening, R., et al. 2006, AJ, 131, 1163

Smoot, G. F., Bennett, C. L., Kogut, A., et al. 1992, ApJL, 396, L1

Sobral, D., Best, P. N., Geach, J. E., et al. 2009, MNRAS, 398, 75

Sobral, D., Best, P. N., Geach, J. E., et al. 2010, MNRAS, 404, 1551

Sobral, D., Best, P. N., Smail, I., et al. 2011, MNRAS, 411, 675

Sobral, D., Best, P. N., Matsuda, Y., et al. 2012, MNRAS, 420, 1926

Sobral, D., Smail, I., Best, P. N., et al. 2013a, MNRAS, 428, 1128

Sobral D., et al., 2013b, ApJ, 779, 139

Sobral, D., Best, P. N., Smail, I., et al. 2014, MNRAS, 437, 3516

Sobral, D., Stroe, A., Dawson, W. A., et al. 2015a, MNRAS, 450, 630

Sobral, D., Matthee, J., Best, P. N., et al. 2015b, arXiv:1502.06602

Solanes, J. M., Manrique, A., García-Gómez, C., et al. 2001, ApJ, 548, 97

Stark, A. A., Knapp, G. R., Bally, J., et al. 1986, ApJ, 310, 660

Steinbring, E. 2014, arXiv:1404.7539

Steinhauser, D., Haider, M., Kapferer, W., & Schindler, S. 2012, A&A, 544, AA54

Stott, J. P., Sobral, D., Smail, I., et al. 2013a, MNRAS, 430, 1158

Stott J. P., Sobral D., Bower R., et al. 2013b, MNRAS, 436, 1130

Stroe, A., van Weeren, R. J., Intema, H. T., et al. 2013, A&A, 555, A110

Stroe, A., Sobral, D., Röttgering, H. J. A., & van Weeren, R. J. 2014a, MNRAS, 438, 1377

Stroe, A., Rumsey, C., Harwood, J. J., et al. 2014b, MNRAS, 441, L41

Stroe, A., Harwood, J. J., Hardcastle, M. J., Röttgering, H. J. A. 2014c, MNRAS, 445, 1213

Stroe A., Sobral D., Dawson W., Jee M. J., Hoekstra H., Wittman D., van Weeren R. J., Brüggen M., Röttgering H. J. A., 2015, 450, 646

Sullivan, M., Mobasher, B., Chan, B., et al. 2001, ApJ, 558, 72

Sunyaev, R. A., & Zeldovich, Y. B. 1972, Comments on Astrophysics and Space Physics, 4, 173

Tajer, M., Polletta, M., Chiappetti, L., et al. 2007, A&A, 467, 73

Tal T., Dekel A., Oesch P., et al. 2014, ApJ, 789, 164

Tanaka, M., Goto, T., Okamura, S., Shimasaku, K., & Brinkmann, J. 2004, AJ, 128, 2677

Tody, D. 1993, Astronomical Data Analysis Software and Systems II, 52, 173

Trasatti, M., Akamatsu, H., Lovisari, L., et al. 2015, A&A, 575, A45

Tribble, P. C. 1993, MNRAS, 261, 57

Umeda, K., Yagi, M., Yamada, S. F., et al. 2004, ApJ, 601, 805

Valdes, F. G. 1998, in Astronomical Society of the Pacific Conference Series, Vol. 145, 53–+

van Weeren, R. J., Röttgering, H. J. A., Bagchi, J., et al. 2009, A&A, 506, 1083

van Weeren, R. J., Röttgering, H. J. A., Brüggen, M., & Hoeft, M. 2010, Science, 330, 347

van Weeren, R. J., Hoeft, M., Röttgering, H. J. A., Brüggen, M. and Intema, H. T. and van Velzen, S. 2011a, A&A, 528, A38

van Weeren, R. J., Brüggen, M., Röttgering, H. J. A., & Hoeft, M. 2011b, MNRAS, 418, 230

van Weeren, R. J., Bonafede, A., Ebeling, H., et al. 2012a, MNRAS, 425, L36

van Weeren, R. J., Röttgering, H. J. A., Intema, H. T., et al. 2012b, A&A, 546, A124

van Weeren, R. J., Röttgering, H. J. A., Rafferty, D. A., et al. 2012c, A&A, 543, A43

Vazza, F., Brüggen, M., van Weeren, R., et al. 2012, MNRAS, 421, 1868

Vazza, F., Eckert, D., Brüggen, M., & Huber, B. 2015, arXiv:1505.02782

Venturi, T., Giacintucci, S., Brunetti, G., et al. 2007, A&A, 463, 937

Verheijen, M., van Gorkom, J. H., Szomoru, A., et al. 2007, ApJL, 668, L9

Vessey, S. J., & Green, D. A. 1998, MNRAS, 294, 607

Villar, V., Gallego, J., Pérez-González, P. G., et al. 2008, ApJ, 677, 169

Voges, W., Aschenbach, B., Boller, T., et al. 1999, A&A, 349, 389

Völk, H. J., Berezhko, E. G., & Ksenofontov, L. T. 2005, A&A, 433,229

Warren, S. J., Cross, N. J. G., Dye, S., et al. 2007, arXiv:astro-ph/0703037

Wegner G. A., Chu D. S., Hwang H. S., 2015, MNRAS, 447, 1126

Weiner B. J., Coil A. L., Prochaska J. X., et al. 2009, ApJ, 692, 187

Wentzel, D. G., & van Woerden, H. 1959, Bull. Astron. Inst. Netherlands, 14, 335

Werner, N., Simionescu, A., Million, E. T., et al. 2010, MNRAS, 407, 2063

White, S. D. M., & Rees, M. J. 1978, MNRAS, 183, 341

Wiener, J., Oh, S. P., & Guo, F. 2013, MNRAS, 434, 2209

Wright, E. L. 2006, PASP, 118, 1711

Young, J. S., & Scoville, N. Z. 1991, ARA&A, 29, 581

Zacharias, N., Finch, C. T., Girard, T. M., et al. 2013, AJ, 145, 44

AMI Consortium, Zwart, J. T. L., Barker, R. W., Biddulph, P., et al. 2008, MNRAS, 391, 1545

Zwicky, F. 1933, Helvetica Physica Acta, 6, 110

Samenvatting

Groepen sterrenstelsels, ook wel clusters genoemd, staan bovenaan de keten van structuren die zich vormen in het heelal. Deze clusters zijn de meest massieve structuren (met massa's van 10^{14-15} $M_\odot$), en bestaan uit grote aantallen sterrenstelsels in een relatief klein volume. In vergelijking met de vrij lege ruimte rondom, is een cluster vergelijkbaar met een grote stad, waar soms duizenden sterrenstelsels dicht op elkaar gepakt wonen. Echter, de meeste massa van een cluster zit tussen de sterrenstelsels, in de vorm van donkere materie, en heet gas, dat Röntgen-licht uitstraalt. Dit intra-cluster gas (*Intercluster Medium*, ICM) heeft een enorm effect op de evolutie van de sterrenstelsels in een cluster. Spiraalstelsels die veel sterren vormen, bevinden zich normaal gesproken in de dunbevolkte ruimte tussen clusters. Als een spiraalstelsel door zwaartekracht door een cluster wordt aangetrokken en erin valt, wordt het door de interactie met het ICM ontdaan van het gas dat nodig is voor het vormen van sterren. De structuur van het spiraalstelsel verandert dan drastisch, en het wordt een rood, dood, passief en elliptisch stelsel.

Grote clusters ontstaan uit het samensmelten van meerdere kleinere clusters. Bij dit proces komt enorm veel energie vrij, veel meer dan geproduceerd wordt door andere energetische processen in het heelal. Gedurende miljarden jaren nemen clusters in massa toe en vormen ze nieuwe structuren, net als steden die omliggende dorpen opslokken. Een deel van de energie die bij het samensmelten vrijkomt, veroorzaakt gigantische schokgolven die zich door het ICM voortplanten. Deze schokgolven kunnen electronen in het hete gas versnellen tot relativistische snelheden. Zo vormen clusters de grootste deeltjesversnellers in het heelal, 19 ordes van grootte groter dan de 'Large Hadron Collider'. De versnelde electronen draaien om de magnetische veldlijnen, en produceren hierdoor synchrotron-straling over enorm grote gebieden. Deze vorm van licht kan met radiotelescopen worden opgevangen. Deze gigantische, Mega-parsec grote, diffuse radiobronnen, noemen we 'radio relics'.

Schokgolven zijn van invloed op de manier waarop clusters zich vormen. Het bestuderen van clusters met diffuse radiostraling kan helpen bij het ontrafelen van de fysica van deeltjesversnelling dat plaatsvindt over grote afstanden, bij zwakke schokken, zwakke magneetvelden, en lage dichtheden. Dit zijn omstandigheden die noch in andere astronomische objecten, noch op Aarde, kunnen worden gereproduceerd. In het afgelopen decennium is er grote vooruitgang geboekt in ons begrip van samensmeltende clusters, maar door het gebrek aan geschikte radiotelescopen die 'radio relics' kunnen vinden, bouwt het onderzoek nog steeds voort op de studie van enkele, relatief nabije bronnen, en met waarnemingen op hooguit een paar frequenties. Met enkel radio en Röntgen studies van clusters, blijft het moeilijk om de eigenschappen en evolutie van sterrenstelsels die wel sterren vormen, te bestuderen. Er zijn een aantal onbeantwoorde vragen:

De oorsprong en fysische eigenschappen van diffuse radio straling in clusters: "waar komen de electronen vandaan, en hoe worden ze versneld? Hoe werkt de interactie met het magneetveld waardoor ze hun energie verliezen?"

Evolutie van sterrenstelsels in samensmeltende clusters met schokgolven: "wat is de invloed op de sterrenstelsels van het samensmelten van de clusters en de schokgolven?"

Dit proefschrift

Het onderzoek dat ik presenteer in mijn proefschrift combineert breedbandige radio waarnemingen, optische beelden, optische spectra en het modelleren van de spectrale energieverdeling. Daarmee bestudeer ik samensmeltende clusters die een radio relic huisvesten. Dit proefschrift richt zich op twee zware clusters, met als bijnamen de 'Sausage' (Worst), en 'Toothbrush' (Tandenborstel), die beide spectaculaire, dubbele relics bevatten, met een duidelijke structuur. Beide clusters lijken relatief eenvoudige geschiedenis te hebben: ze zijn het gevolg van het samensmelten van twee clusters met gelijke massa. Mijn onderzoek wil een zo compleet mogelijk beeld opbouwen van deze twee clusters, en richt zich daarbij op twee aspecten. Het eerste is de manier waarop schokgolven de electronen en het magneetveld beïnvloeden om diffuse radio straling te produceren. Het tweede aspect is hoe het samensmelten van zulke grote, massieve clusters de stervorming in de sterrenstelsels beïnvloedt. In het laatste deel van mijn proefschrift zal ik de eigenschappen van stervorming in clusters in een bredere context plaatsen, door het vergelijken van grote aantallen sterrenstelsels in zowel dicht- als dunbevolkte gebieden aan de hemel.

In **hoofdstuk 2** bespreek ik de invloed van de ontstaans-geschiedenis van clusters op de radio stelsels in het cluster, en op het versnellen van de electronen die diffuse radio straling produceren. De analyse is gebaseerd op een grote hoeveelheid radio waarnemingen van de 'Sausage' cluster, gedaan met de 'Giant Metrewave Radio Telescope' in India, en de Westerbork Synthesis Radio Telescope. Door het bestuderen van de kromming van het spectrum en de 'kleur' van de radio straling, bevestigen wij dat de twee symmetrische radio relics waarschijnlijk zijn ontstaan door symmetrische schokgolven. Dit soort schokgolven ontstaat op het moment dat de centra van de twee samensmeltende clusters elkaar passeren. De analyse geeft aan dat de electronen door de schokgolf worden versneld.

Hoofdstuk 3 vergelijkt de eigenschappen van de schokken zoals afgeleid uit radio en Röntgen waarnemingen van radio relics. We hebben voor het eerst het effect van ruimtelijke resolutie op het radiospectrum van de 'Sausage' cluster in de analyse meegenomen. . Als we dat doen, zijn de Mach-nummers afgeleid uit de radio en de Röntgen waarnemingen met elkaar in overeenstemming. Eerdere analyses vonden dat de Mach-nummers niet met elkaar in overeenstemming waren. We vinden verder een toename in de leeftijd van de radio straling vanaf de noordkant van de schok in de stroomafwaartse richting. Hieruit leiden we af dat de schokgolf in noordelijke richting beweegt, met een snelheid van ongeveer 2500 km s^{-1}. We laten zien dat er nog meer belangrijke effecten zijn (opnieuw versnellen van electronen door turbulentie en het mengen van electronen in de gezichtslijn), die tot nu toe niet zijn meegenomen in modellen voor het ontstaan van radio relics.

In **hoofdstukken 4 en 5** presenteer ik metingen van de diffuse radio straling op de hoogste frequentie ooit, namelijk 16 en 30 GHz. Deze waarnemingen zijn gedaan met de 'Arcminute Microkelvin Imager', en de 'Combined Array for Research in Millimeter-wave Astronomy'. Ze zijn essentieel om vast te stellen hoe electronen en het magnetisch veld elkaar beïnvloeden, en om onderscheid te maken tussen verschillende modellen voor de oorsprong van deze electronen. Onze waarnemingen laten zien dat het radio spectrum steiler wordt, zowel in de 'Sausage' als in de 'Toothbrush'. Dit vormt een uitdaging voor de huidige modellen voor het ontstaan van radio relics. Volgens onze analyse zijn complexere modellen nodig, waarin de electronen verantwoordelijk voor de diffuse radio straling al een keer eerder zijn versneld,

bijvoorbeeld in radio stelsels die in het verleden actief waren in het cluster.

In **hoofdstukken 6, 7, en 8** beschrijf ik waarnemingen in het zichtbaar licht, specifiek op de frequentie van de Hα lijn. Voor beide clusters is de emissie van deze lijn volledig in kaart gebracht. In de 'Sausage' cluster vinden we in de nabijheid van de relics meerdere sterrenstelsels die veel Hα uitstralen, wat aangeeft dat ze actief nieuwe sterren vormen. In de 'Toothbrush' zien we dit soort sterrenstelsels niet. We verklaren dit door de verschillende fases waarin de samensmeltende clusters zich bevinden. Simulaties laten zien dat de 'Toothbrush' al een miljard jaar ouder is dan de 'Sausage'. Mogelijk ontstaat door de schokgolf een korte, heftige fase van stervorming in de nabije sterrenstelsels, waardoor de transformatie van spiraalstelsels in elliptische stelsels wordt versneld.

Voor **hoofdstuk 9** hebben we WSRT waarnemingen gebruikt van het neutrale waterstofgas in de 'Sausage' cluster. Hiermee bestuderen we het effect dat het samensmelten en de schokgolven hebben op het koele gas dat de brandstof vormt voor stervorming in de sterrenstelsels. Eerder onderzoek liet zien dat stelsels minder koel gas bevatten naarmate ze zich dichterbij het centrum van een cluster bevinden. Wij vinden echter dat actief stervormende sterrenstelsels in de 'Sausage' cluster net zoveel koel gas bevatten als actief stervormende sterrenstelsels buiten de clusters. We vinden aanwijzingen voor radiolicht van krachtige supernova restanten, hetgeen betekent dat de stelsels al minstens 100 miljoen jaar sterren aan het vormen zijn.

In **hoofdstuk 10** voeren we een studie uit van een grote groep stervormende sterrenstelsels op een roodverschuiving van ~ 0.2. We reconstrueren hoeveel sterrenstelsels er zijn met een bepaalde lichtsterkte van de Hα lijn. We vinden zo de helderste, en meest zeldzame sterrenstelsels. Zeer lichtsterke, stervormende stelsels zijn meer gegroepeerd dan stelsels die maar mondjesmaat sterren vormen. Verder kunnen we vaststellen dat clusters met dichtheden zoals de 'Sausage' extreem zeldzaam zijn.

Rezumat

Clusterele de galaxii sunt aflate la vârful lanţului ierarhic de formare a structurilor din Univers. Clusterele sunt astfel cele mai masive structuri din Univers (cu mase de 10^{14-15} M$_\odot$) şi conţin sute de galaxii într-un mic volum cosmic. Clusterele pot fi asemănate unor metropole, unde galaxiile sunt înghesuite în comparaţie cu spaţiul pustiu din jurul lor. Marea majoritate a materiei din clustere este distribuită printre galaxii, în forma materiei întunecate si a unei plasme extrem de fierbinţi (cu temperaturi de 10^{7-8} K). Mediul din cluster are un efect profund asupra evoluţiei galaxiilor. Galaxiile spiralate, care formează în mod activ noi stele, se regăsesc de obicei în spaţiul 'viran' dintre clusterele galactice. Când o galaxie cade către miezul unui cluster, interacţiunea dintre galaxie şi mediul fierbinte inter-galactic duce la îndepărtarea gazului care alimentează formarea de noi stele. Fără acest combustibil, galaxiile suferă o transformare morfologică din galaxii spiralate in galaxii pasive, roşii şi eliptice.

Clusterele evoluează prin coliziuni cu alte clustere mai mici, acestea fiind eventimentele cele mai energetice de la 'Big Bang' încoace. De-a lungul a miliarde de ani, clusterele îşi dezvoltă structura şi masa, la fel ca oraşele în dezvoltare care înghit satele dimprejurul lor. Parte din energia eliberată în timpul coliziunilor dintre clustere este disipată în mediul dintre galaxii prin unde de şoc gigantice care traversează clusterul şi accelerează până la viteze relativistice electronii aflaţi în calea lor. Din aceast punct de vedere, şocurile din clustere sunt cele mai mari acceleratoare de particule din Univers, fiind cu 19 ordine de magnitudine mai întinse decât acceleratorul de particule al Organizaţiei Europene Pentru Cercetare Nucleară din Geneva. Electronii acceleraţi girează în jurul liniilor de câmp magnetic şi produc energie sincrotronă împrăştiată pe arii întinse. Radiaţia sincrotronă poate fi detectată cu telescoape radio. Undele de şoc din clustere duc astfel la formarea unor surse radio enorme, de ordinul megaparsecilor, cu caracter difuz, numite relicve radio.

Şocurile influenţează evoluţia clustereleor în context cosmologic. Studiul clusterelor cu emisie radio difuză poate dezvălui felul în care funcţionează procesul de accelerare a particulelor în contexte astronomice şi în condiţii ce nu pot fi reproduse pe Pământ: dimensiuni foarte mari, şocuri supersonice, câmpuri magnetice slabe şi densităţi foarte scăzute.

În ultimul deceniu s-au facut progrese semnificative în domeniul clusterelor aflate in coliziune. Totuşi din cauza lipsei intrumentelor astronomice potrivite, multe studii se bazează încă pe cercetarea relicvelor individuale, aflate în Universul local, folosing observaţii la una sau doua frecvenţe radio. În prezent, avem o imagine incompleta a clusterelor în coliziune: natura şi evoluţia galaxiilor spiralate din aceste clustere rămâne încă neexplorată. Întrebări încă fără răspuns în acest domeniu includ:

Natura şi fizica emisiei radio difuze din clustere: Cum sunt electronii acceleraţi pentru a forma relicve radio? Cum interacţionează electronii cu câmpul magnetic spre a-şi pierde energia?

Evoluţia galaxiilor din clusterele în coliziune cu unde de şoc: Influenţează coliziunea şi şocurile evoluţia galaxiilor din cluster?

Această dizertaţie

Cercetările prezentate în această teză de doctorat combină date complementare radio, optice, spectroscopie şi modelare, cu scopul de a studia coliziunea clusterelor şi relicvele radio asociate. Această teză este focalizată pe două clustere masive, fiecare dintre ele aflate în perioadă de coliziune, poreclite 'Sausage' ('cârnatul') şi 'Toothbrush' ('periuţa de dinţi'), care găzduiesc relicve duble spectaculoase, cu o morfologie deosebit de regulată. Clusterele par să aibă o istorie simplă, rezultând din coliziunea în planul cerului a două sub-clustere de aceeaşi masă. Am obţinut astfel o imagine completă a acestor două clustere. Am studiat interacţiunea dintre undele de şoc şi electronii din gazul inter-galactic pentru a produce emisie difuză radio. Deasemenea, am cercetat influenţa coliziunilor dintre clustere asupra formării de noi stele în galaxiile membre. În ultima parte a tezei, am pus proprietăţile acestor două clustere în context mai larg, comparându-le cu rezultate obţinute printr-o cartografiere a galaxiilor spiralate aflate atât în medii cosmice dense cât şi în volume goale.

Capitolul 2 discută influenţa coliziunilor asupra galaxiilor radio şi asupra accelerării de particule în contextul emisiei difuze radio. Analiza este bazată pe date radio asupra clusterului 'Sausage', obţinute cu telescoapele radio Giant Metrewave şi Westerbork la frecvenţe între $150-2300$ MHz. Prin tehnici de mapare a indexului spectral, curburii spectrale şi a graficelor de coloare-versus-culoare, confirmăm că relicvele gemene din clusterul 'Sausage' au fost cel mai probabil accelerate de şocuri simetrice, declanşate la coliziunea între două sub-clustere. Analiza noastră arată că după ce electronii sunt acceleraţi de către unda de şoc, unghiul dintre electroni şi câmpul magnetic este isotropizat în mod continuu.

Capitolul 3 adresează problema nepotrivirii dintre numerele de şoc Mach obţinute din date radio şi raze X. Am făcut prima mapare spectrală a unei relicve radio pentru a investiga efectul rezoluţiei imaginilor radio asupra măsurării numărului Mach în relicva 'Sausage'. Arătăm că datele radio confirmă rezultatele numărului Mach obţinute din date X-ray. Găsim o creştere sistematica a vârstei spectrale de la marginea de nord a relicvei 'Sausage' către zona post-şoc. Şocul se deplasează către nord cu o viteză de aproximativ 2500 km s^{-1}. Această analiză reprezintă un test direct că electronii pierd energie prin emisie sincrotronă şi împrăştieri Compton inverse. Arătăm de asemenea că efecte, precum reaccelerarea prin turbulenţă şi amestecarea emisiei în linia de vedere, trebuie luate în considerare în modelele de formare a relicvelor.

Capitolele 4 and 5 prezintă detecţiile de emisie difuză de la cele mai înalte frecvenţe de până acum, la 16 şi 30 GHz, posibile cu ajutorul telescopelor Arcminute Microkelvin Imager şi Combined Array for Research in Millimeter-wave Astronomy. Astfel de măsurători sunt cruciale pentru a cuantifica interacţiunea electronilor cu câmpul magnetic şi pentru a diferenţia între diferitele modele pentru originea electronilor sincrotron. Spectrul integrat al relicvelor 'Sausage' şi 'Toothbrush' devine mai abrupt la frecvenţe înalte, ceea ce este în tensiune cu modelul acceptat în acest moment pentru formarea relicvelor radio. Analiza noastră indică necesitatea dezvoltării unor modele mai complicate, care iau în considerare populaţii de electroni pre-acceleraţi, de exemplu de activitate nucleară din centrul galaxiilor radio.

Capitolele 6, 7 şi 8 prezintă cartografierea liniei de emisie Hα în clusterele 'Sausage' şi 'Toothbrush', aducând prima dovadă directă că şocul afectează formarea de noi stele în galaxiile din cluster. Găsim numeroase galaxii care au emisii Hα, aflate în aproprierea relicvelor

radio din clusterul 'Sausage'. Aceste galaxii sunt extrem de masive, bogate în metale şi produc stele noi. Nu găsim astfel de exemple în clusterul 'Toothbrush'. Interpretăm aceste rezultate în contextul diferitelor istorii ale celor două clustere: clusterul 'Toothbrush' s-a format cu ∼ 1 miliard de ani mai devreme decât 'Sausage'. Propunem că trecerea şocului induce formarea temporară de noi stele, accelerând evoluţia galaxiilor din spirale bogate în gaz către eliptice.

În **Capitolul 9**, folosim date obţinute cu telescopul Westerbork în clusterul 'Sausage' pentru a investiga efectul coliziunii clusterelor şi al şocurilor asupra rezervoarelor de gaz care alimentează formarea de noi stele în galaxii. În mod contradictoriu faţă de cercetari anterioare care arată că galaxiile au din ce în ce mai puţin hidrogen neutru de la marginea către centrul clusterelor, noi observăm că în clusterul 'Sausage' galaxiile spiralate au la fel de mult hidrogen neutru ca şi galaxiile asematoare aflate în spaţiul liber dintre clustere. Detectăm emisie radio viguroasă produsă de supernove, ceea ce indică că aceste galaxii formează stele de cel puţin 100 milioane de ani.

În **Capitolul 10**, facem cea mai largă cartografiere a galaxiilor care formează stele, aflate la o deplasare spre roşu de $z ∼ 0.2$. Construim funcţii de luminozitate Hα care depăşesc variaţia cosmică şi detectează cele mai luminoase şi rare galaxii. Galaxiile luminoase, care formează stele la o rată foarte ridicată sunt mai grupate decât cele care formează mai puţine stele. Deşi există multă varianţă cosmică de-a lungul mapării noastre, observăm că sunt foarte rare zonele cu densitate foarte mare de galaxii, precum cele din clusterul 'Sausage'.

287

Publications

Refereed Publications

1. **Stroe, A.** et al. The 'ultimate' cluster radio relic spectrum: observations from 150 MHz to 30 GHz. MNRAS (submitted, 2015)

2. **Stroe, A.** and Sobral, D. A large narrow band Hα survey at $z \sim 0.2$: the bright end of the luminosity function, cosmic variance and clustering across cosmic time. MNRAS (in press, 2015)

3. **Stroe, A.** et al. Neutral hydrogen gas, past and future star-formation in galaxies in and around the 'Sausage' merging galaxy cluster. MNRAS (in press, 2015)

4. **Stroe, A.** et al. The rise and fall of star-formation in $z \sim 0.2$ merging galaxy clusters. MNRAS, 450, 646 (2015)

5. **Stroe, A.**, Harwood, J. J., Hardcastle, M. J., Röttgering, H.J.A. Spectral age modelling in the 'Sausage' radio relic. MNRAS, 445, 1213 (2014)

6. **Stroe, A.**, Rumsey, C., Harwood, J. J., Röttgering, H.J.A., Saunders, R. D. E. Highest frequency detection of a radio relic: 16 GHz AMI observations of the 'Sausage' cluster. MNRAS, L59 (2014)

7. **Stroe, A.**, Sobral, D., Röttgering, H.J.A., van Weeren, R. J. The role of cluster mergers and travelling shocks in shaping the Hα luminosity function at $z \sim 0.2$: 'Sausage' and 'Toothbrush' clusters. MNRAS 438, 1377 (2014)

8. **Stroe, A.**, van Weeren, R. J., Intema, H.T., Röttgering, H.J.A., Brüggen, M. and Hoeft, M. Discovery of spectral curvature in the shock downstream region: CIZA J2242.8+5301. A&A 555, A110 (2013)

9. **Stroe, A.**, Snellen, I.A.G., Röttgering, H.J.A. A stringent upper limit to 18cm radio emission from the extrasolar planet system τ Boötis. A&A 546, A116 (2012)

10. Sobral, D., **Stroe, A.** et al. *MC^2: Boosted AGN and star-formation activity in CIZA J2242.8+5301, a massive post-merger cluster at $z = 0.19$.* MNRAS, 450, 630 (2015)

11. Jee, M. J., **Stroe, A.** et al. *MC^2: Constraining the dark matter contribution of the violent merging galaxy cluster CIZA J2242.8+5301: Piercing through the Milky Way.* ApJ, 802, 46 (2015)

12. Dawson, W., Jee, M. J., **Stroe, A.**, et al. *MC^2: Galaxy imaging and redshift analysis of the merging cluster CIZA J2242.8+5301.* ApJ, 805, 143 (2015)

13. Emonts, B., Mao, M., **Stroe, A.**, et al. *A CO-rich merger shaping a powerful and hyperluminous infrared radio galaxy at $z = 2$: the Dragonfly Galaxy.* MNRAS, 451, 5544 (2015)

14. Heald et al. (including **Stroe, A.**) *The LOFAR Multifrequency Snapshot Sky Survey (MSSS) I. Survey description and first results.* (submitted to A&A in October 2014)

15. Akamatsu et al. (including **Stroe, A.**) *Suzaku X-ray study of the double radio relic galaxy cluster.* A&A (in press, 2015)

16. van Weeren, R. J. et al. (including **Stroe, A.**) A distant radio mini-halo in the Phoenix Cluster. ApJ Letters, 786, L17 (2014)

17. van Weeren, R. J. et al. (including **Stroe, A.**) The discovery of a radio halo in PLCK G147.3–16.6 at $z = 0.65$. ApJ Letters, 781, L32 (2014)

18. Emonts, B. et al. (including **Stroe, A.**) CO(1-0) survey of high-z radio galaxies: alignment of molecular halo gas with distant radio sources. MNRAS, 438, 2898 (2014)

19. Griffin, R.F. and **Stroe, A**. Photoelectric radial velocities, Paper XX: 45 years' monitoring of the radial velocities of the Redman K stars. JOAA 33, 245 (2012)

Conference Proceedings

1. **Stroe, A.**, van Weeren, R. J., Sobral, D., Rumsey, C., Intema, H. T., Röttgering, H. J. A., Harwood, J. J.; Saunders, R., Brüggen, M., Hoeft, M. Spectral and morphological signatures of cluster merger shocks: CIZA J2242.8+5301. Proc. of 'The Metre Wavelength Sky: Celebrating 50 years of Radio Astronomy at TIFR' (2014)

2. Harwood, J. J. et al. (including **Stroe, A.**) The spectral structure and energetics of powerful radio sources Proc. of 'The Metre Wavelength Sky: Celebrating 50 years of Radio Astronomy at TIFR' (2014)

3. Röttgering, H. J. A. et al. (including **Stroe, A.**) The 'Sausage' and 'Toothbrush' clusters of galaxies and the prospects of LOFAR observations of clusters of galaxies. AN, 334, 333 (2013)

Curriculum Vitae

I was born on the 19th of November 1987, in Constanța, Romania, on the beautiful coast of the Black Sea. I was fascinated by the Cosmos ever since I was a small child and wanted to become an astronaut when I grew up.

I completed my pre-university education in 2007 as valedictorian at the 'Mircea cel Batrân' National College, with a focus on Mathematics, Computer Science, Physical and the English language and literature. Upon realising that my chances of becoming an astronaut were very slim, I decided I wanted to move people into space, so I participated in a series of space settlement design competition organised by NASA, where I designed habitable space settlements orbiting around the Earth, Mars and located on the Moon and on Mars.

My strong interest in all things space related lead me to to study Physics and Astronomy at Jacobs University in Bremen, Germany. During my undergraduate degree, I took part in a number of research internships. In the summer of 2008, I returned as a mentor for the 15th NASA International Space Settlement Design Competition. In the winter of 2009, I spent one month researching an innovative deployment mechanism for solar cells installed on spacecrafts within the OHB System satellite company in Bremen. During the first half of the 2009 summer, I analysed data from the Cluster II spacecraft to understand the physics of the neutral sheet of Earth's magnetosphere, within the Department of Space Plasma at the Max Planck Institute for Extraterrestrial Physics in Garching bei München, Germany. I spent the second half of the summer within the Optical Interferometry group at the Cavendish Laboratory, University of Cambridge, UK, where I wrote the `visim` software, an imaging simulator used for the upcoming Magdalena Ridge Observatory Interferometer. I also gained teaching experience by supervising the 1st year physics laboratory. I was also teaching assistant for the second year Analytical Mechanics course. I graduated in 2010 with honours, in the top 5% of my class, with two degrees: a Bachelor of Science in Physics and a Bachelor of Science in Earth and Space Sciences, with the focus Astrophysics. I wrote two theses on the topics the Earth's neutral sheet (*Multipoint Analysis of Local Magnetohydrostatic Equilibria in the Earth's Magnetotail using Cluster II data*, under the guidance of Prof. Dr. Joachim Vogt) and on simulated optical interferometric observations of a star with a disk (*Assessment of the Feasibility of Proposed Observations for the Magdalena Ridge Observatory Interferometer with the* `visim` *Software*, under the supervision of Prof. Dr. Marcus Brüggen).

I then moved on to University of Cambridge, where I pursued a Master of Advanced Study in Experimental and Theoretical Physics, hosted by the Cavendish Laboratory. I wrote my Master's thesis under the supervision of Dr. Manda Banerji and Prof. Dr. Richard McMahon, at the Institute of Astronomy, on the topic *Infra-red Properties of Galaxy Clusters Selected Using the Sunyaev-Zel'dovich Effect*. I graduated in 2011 with Merit.

My MSc work sparked my interest for multi-wavelength studies of galaxy clusters. As a result, I chose to do a PhD in Astronomy at Leiden Observatory, with Prof. Dr. Huub Röttgering, working on merging clusters hosting diffuse radio emission, combining radio and optical imaging and spectroscopy with modelling to study the effect of cluster merger shocks on the intra-cluster medium and the cluster galaxies. I have presented my work at national and international conferences in Nice (France), Bonn (Germany), Pune (India), Nijmegen (Nether-

lands), Dubrovnik (Croatia), Jeju (South Korea), Ringberg (Germany) and at other institutes (Hertfordshire, UC Davis, U Porto, U Lisbon, IAC Tenerife, INTA/CSIC Madrid, UCLA, UC Riverside, Stanford, Berkeley, Caltech, Harvard, ESAC Madrid, MPIA Heidelberg). I attended meetings, workshops and schools in Madrid (Spain), Bielefeld (Germany), Socorro (US), Garching (Germany), Manchester (UK) and Seattle (US).

In October 2015, I will move to Garching bei München to take up an ESO Fellow position.

Acknowledgements

I would not have made it this far without the support and help of many people.

I would first like to thank the Leiden Observatory staff, who ensured my stay here was smooth and pleasant, especially the management (Alexandra, Evelijn, Els), the computer group (Erik, Aart, David) and the secretaries (Anita, Liesbeth, Debbie).

There were many who supported me in becoming an astrophysicist: my high school physics teacher, Ion Bǎraru, my undergraduate supervisors, Joachim Vogt and Marcus Brüggen, my summer project supervisors, Roger Griffin and John Young, and my Master's project supervisor, Manda Banerji. Thanks for giving me the opportunity to do real research before starting my academic career!

At Leiden Observatory, I was fortunate to be part of a diverse and stimulating research group. I would like to thank present and past members of the 'radio astronomy' group (even though we do much more than radio) for many interesting scientific discussions: Leah and Emma (thanks for being great office mates), Wendy, Tim, Julius, George, Duy, Edwin, Gabriela, Aayush, Bas, Reinout, David R., Laura.

I am grateful for having the opportunity to work with amazing people during my PhD. David S., thanks for being a great mentor, collaborator, friend and for offering me the opportunity to do real independent research. Annalisa, you were the one who taught me how to do radio interferometry! Reinout, I learned so much from you! Jeremy, it was great to come up with our own research projects! Julius, I understand theory so much better after our discussions. Will, James and David W., thanks for the fruitful collaboration and for hosting me in Davis. Bjorn, Clare, Henk, Huib, Maja, Marcus, Martin, Matthias, Rainer, Richard, Tom O., Tom J. (what a nice referee you were!), many thanks for the support, ideas, theoretical input and data. Jorryt, Ana, Sérgio, Aayush, João: thanks for the great company during observing trips. François and Igone, thanks for organising the clusters meetings. I would like to also thank Annalisa, Jarle, Jelle, Koen, Marijn, Paul and Tom for taking the time to read my thesis and for being part of my reading/opposition committee. Credits go to Logan Apple and Tatyana Zabanova for allowing me to use their beautiful art as cover and bookmark for my thesis and to Ilse van Bemmel for translating the summary of the thesis in Dutch.

I am grateful for all the amazing friends I had while in Leiden. Thanks for the nice discussions, parties, trips and for your continued support. Alex North, Alex South, Berenice, Bernard, Caroline, David, Francisco, Heather, Irene, Marco, Matteo, Mattia, Monica, Nienke, Nicola, Tiffany, thanks for making Leiden Observatory a fun place to work. Heather, Alex South, Marco, Mattia, Monica, thanks for the amazing memories we made together. Thanks for being there and listening when I needed it. Thanks for all the advice, for always caring whether I am doing alright and for listening to all my complaining. Mattia, Matteo, Francisco, Simon, the short-lived 'Redshift district' was a nice escape from daily research. David C., thanks for being a great house mate and for always listening to me at the end of the day. Catarina, you always cared and listened, thank you!

My first friend ever, Cristina, even though we see each other so rarely these days, I always feel your support and friendship close. I am so grateful to the amazing NASA crew: Adela, Bǎbe, Daiana, George, Ioana, Lavinia, Mircea, Oana (Crina), Raluca. We've been friends

for years and it's great to see you all grow into amazing scientists, entrepreneurs, engineers and doctors (the useful kind). Friends I met during my undergrad, Maria, Sonia, Cosmina, Marja, Irina, you helped me stay sane during those stressful Jacobs years. Andreea, Dominika, Malwina, you made Cambridge a wonderful place.

My deepest gratitude goes to my parents and grandparents for their unconditional love, support and encouragement. Tata, you taught me to be critical, analytical and to push myself to reach my potential. Mamaie, tataie, you always worry about my well-being and always make sure I am happy and healthy. I am so happy that you consider me a real scientist.

Victor, I am so incredibly lucky to have you by my side. Your support, patience, care and love are invaluable. You always manage to lift me up when I am down and make me smile. You have brought balance into my life and without you, I would have not made it sane to where I am now. We have shared more than five amazing years and I am looking forward to the next hundred. I am grateful to Elena and Constantin for welcoming me in their family.

Finally, this thesis is dedicated to my mother, who has been the single most important driving force in my life and career. Mama, I miss you more every day.